Seismic character and interaction of intrabasinal mass-transport deposits in deep-water continental margins (Espírito Santo Basin, SE Brazil)

Omosanya, Kamaldeen Olakunle

Submitted in partial fulfilment of the requirements for the degree of PhD

School of Earth, Ocean, and Planetary Sciences,
Cardiff University.

December, 2014

Declaration

I hereby declare that this thesis represents my own work and is submitted in fulfilment of the requirements for the degree of Doctorate of Philosophy. This work has not been previously submitted to Cardiff University, or any other institution, for any degree, diploma or other qualification.

Author's note and status of publications

The technical Chapters of this thesis were published as research articles and conference proceedings. Chapter 4 was published in "*Marine and Petroleum Geology, February, 2013*"; Chapter 5 was published in "*Marine Geology in April, 2013*" and Chapter 6 was published in "*Tectonophysics, May, 2014*". Sections of Chapter 4 and 5 are published in "*Earthdoc*" as proceedings from the EAGE conference, 2013 in London. Detailed notes on the publications are provided at the beginning of each of the technical Chapters. It should be noted that these publications are the work of the lead author Omosanya, Kamaldeen Olakunle. The articles are jointly co-authored by the project supervisor, Dr T.M. Alves, who provided editorial comments in line with a normal PhD thesis.

Acknowledgments

To Allah be the glory and adoration for a successful completion of the thesis.

I appreciate the support and understanding of my family during the PhD period. The moral, financial, and spiritual support of my parents Alhaji and Alhadja K.A. Omosanya is greatly acknowledged. The remarkable and unquantifiable emotional, moral and financial support of my wife Hawa is appreciated. Aisha and Maryam are commendable for their patience and understanding during the PhD. I love you all. To the rest of my family (Monsur, Suraj, Abdul Kabir, Abd Hafeez, Abd Azeem) and my in-laws (Alhadji and Alhadja M.G. Saka), I am very grateful for your prayers and support. Thank you very much.

I appreciate the criticism, guidance and encouragement from my supervisor, Dr T.M. Alves. I acknowledge his swift response to the different drafts of the thesis and manuscripts.

I am grateful to TETFund and OOU, Nigeria for the research grant that led to the completion of this project. Also, I thank CGG-Veritas for the permission to publish the Chapters of this thesis, and Schlumberger for provision of Geoframe[@] and Petrel[@] for seismic interpretation. The wonderful comments and opinions of the anonymous reviewers are recognised and greatly valued. I thank the 3D Lab cohort for a wonderful co-existence and shared experience, Gwen Pettigrew, Davide Gamboa, Iqbal, Hamood, Duartes, Aldina, Qin, Usman, Oluchi, Tuvierre, Daniel, Pete, Chris K and Chris W.

Finally, I am grateful to Allah, my source of repose and comfort for the strength to carry on despite the numerous detours. Indeed, he is the sovereign ruler of the universe.

Abstract

The aim of this thesis is to assess the spatial and temporal recurrence of mass-transport deposits (MTDs) within salt withdrawal basins to unravel the complex interaction between mass-wasting processes and salt halokinesis. A high-quality 3D seismic dataset from the mid-continental slope of Espírito Santo Basin, SE Brazil, was used to assess the provenance of mass-transport deposits and their potentials as structural markers for seafloor perturbation and fault activity.

A new proposition from this work includes scale-independent classification of mass-transport deposits into homogeneous and heterogeneous types. Heterogeneous MTDs are composed of seismic facies corresponding to slides, slumps and debrites. Homogeneous MTDs comprise consolidated debrites considered in this work as comprising barriers to fluid flow. In addition, MTD composed of rafted blocks displayed a disproportionate relationship between their shape, transporting distance and degree of remobilization.

Drag zones denote sections of MTDs that are uplifted during salt diapir rise. These drag zones are extended and shortened along their long and short axis respectively. Ramps flanking salt diapirs are formed by either complete or partial erosion of paleo-seafloors and pre-existing fault scarps. In this thesis, it is shown that the risk of remobilized sediments is highest within drag zones.

The erosive nature of mass-wasting processes is justified by the decoupling history of faults eroded by MTDs. An innovative method to assess fault decoupling history on continental margin is the use of cumulative throw character. MTD-decoupled faults are

characterised by shorter propagation rate and cumulative throw and are potentially sealing compared to their non-decoupled counterparts.

The information from this study is crucial information for successful hydrocarbon exploration and risk assessment in deep-water environments. The methodologies and results from this thesis are applicable to continental margins worldwide.

Table of Contents

List of Figures

List of Tables

List of Equations

Chapter 1

Introduction and Literature Review

1. Rationale

Mass-wasting is ubiquitous on continental slopes, where the combined action of local tectonics, sediment input and gravitational instability can generate complex structures (Urgeles et al., 1997; Goldfinger et al., 2000; Mienert et al., 2003; Hunerbach and Masson, 2004; Hjelstuen et al., 2007; Tailing et al., 2007). In nature, a continental slope fails when downslope directed shear stress exceeds the shear strength of seafloor sediment (Varnes, 1978). Following seafloor failure, mass-wasting processes are triggered and involve the transport of sediments over a detachment surface called the basal shear surface. Once failure is initiated, materials continue to move downslope at different speeds and volumes over the basal shear surface, until shear strength overcomes shear stress and material inertia (Richardson et al., 2011). The sedimentary deposits generated during mass-wasting events are called mass-transport deposits (MTDs) or complexes (MTC) when they are the product of multiple failure events.

The term ‘‘mass-transport complex’’ has been used to describe all kinds of gravity-induced or downslope deposits, except for turbidites (Norem et al., 1990; Masson et al., 1997, 1998; Gee et al., 1999; Sohn, 2000; Wach et al., 2003; Martinez et al., 2005). Mass-transport complexes were firstly considered to develop during sea-level falls towards lowstand periods, when sediment transported onto the shelf edge is at its maximum and water overburden weight is being reduced over shelf regions (Masson et al., 1997; Posamentier and Kolla, 2003). Resulting MTDs usually occupy areas on the slope and on the basin floor, accumulating near the toe of slope. The volume of MTDs can thus vary enormously, ranging from a few meters in thickness and a few hundred square meters in area, to more than 200 m (660 ft.) in thickness and tens of thousands of square kilometres in area (Hampton et al., 1996; Posamentier and Martinsen, 2011). As a result of these differences in thickness and area distribution, MTDs commonly

develop initial bathymetry which later influences sedimentation in deep-water settings, in both carbonate and siliciclastic settings (Shanmugam, 2000; Marr et al., 2001; Posamentier and Kolla, 2003; Jackson and Johnson, 2009).

Mass-transport deposits are usually composed of muddy sediments, although in some cases, sands can be also present. Log responses tend to show an increase in resistivity, compressional velocity, density, and low-porosity when compared to confining strata (Weimer, 1990; Shipp et al., 2004). Geotechnical measurements indicate an increase in shear strength, particularly towards their base, with a corresponding decrease in void ratio and water content (Piper et al., 1997; Shipp et al., 2004). All these characteristics suggest that MTDs may be considerably more consolidated shortly after deposition than other deepwater deposits (Moscardelli et al., 2006).

Classifying MTDs is a difficult task due to their significant variability. A good classification scheme will provide information on the lithology of the source area and invariably, the provenance. Previous classification schemes described these deposits based on their transport mechanism, their sedimentary composition and recognizable seismic features. Well referenced classification methods include those of Dott (1963), Nardin et al., (1979) and Moscardelli and Woods (2007). These schemes classified MTDs into slides, slumps, debris flows and sometimes turbidites (See Figures 1.2 to 1.5).

Moscardelli and Woods (2007) used aspect ratios to classify MTDs as slope-attached, shelf attached and shelf-detached offshore Trinidad and Tobago. Their study highlighted the importance of source areas relative location on the continental slope as a

major classification criterion. A similar technique was adopted by Twichell et al., (2009) to classify Quaternary submarine landslides on the US Atlantic continental margin. In addition to these latter publications, the provenance of MTDs was previously determined from seismic profiles by analysing the orientation and geometry of kinematic indicators, or by correlating sub-surface data with geomorphological information from outcrop analogues (Boe et al., 2000; Bull et al., 2009; Frey Martinez et al., 2005a; Frey-Martínez et al., 2006a; Gee et al., 2005; Haflidason et al., 2004; Laberg and Vorren, 2000; Laberg et al., 2000; Lastras et al., 2006; Lucente and Pini, 2003; Schnellmann et al., 2005; Strachan, 2002a, 2002b; Wilson et al., 2004).

A practical result of published data is that there is still the need to study MTDs on seismic data and provide information on the lithologies of their source areas. Other important parameters to investigate are the sediment processes involved in mass-wasting and their relationship to the degree of homogeneity of the material being transported, and the erosion/abrasion of the transporting medium below MTDs. Seismic descriptions of MTDs include the recognition of an upper surface that is usually hummocky, rugose or ridged located above discontinuous, chaotic to moderately deformed low-high amplitude reflections (Sangree and Widmier, 1977; Posamentier and Kolla, 2003; Richardson et al., 2011). In these deposits, a basal shear surface separates chaotic and disrupted strata within MTDs from the much more continuous facies of non-MTD deposits (Hampton et al., 1996; Winker and Booth, 2000; Beauboeuf and Friedman, 2000; Armentrout, 2003; Piper and Behrens, 2003; Frey-Martínez et al., 2006; Bull et al., 2009; Frey Martinez, 2010). In essence, there are still few well documented reports on the seismic facies of MTDs using seismic attributes such as continuity, amplitude, lap geometries, and frequency of reflections.

Statistical analyses are invaluable tools for the study of submarine MTDs. For instance, Gamboa et al., (2011) used descriptive statistics to document the distribution of failed blocks along salt ridges in southeast Brazil with a view to understanding their capability as conduit for vertical fluid flow. Other work include Alves and Cartwright (2009), Alves (2010) and Gamboa et al., (2010). From these works I found that the distribution and recurrence of MTDs is often controlled by a) halokinesis and the geometry of the associated salt structures, b) major tectonic episodes that cause localised uplift, faulting and ultimately can lead to the exhumation of near-seafloor sediment. In the particular case of salt-rich continental slopes, halokinetic movements can alter slope gradient and trigger local mass-wasting events on the seafloor (e.g. Gee et al., 2006; Alves, 2010). As a consequence, mass-transport deposits are often thin at the crest of active diapirs and thicker on their flanks (Rowan et al., 1998; Tripsanas et al., 2004). Published data highlights the fact that it is imperative to recognise what products of mass-wasting in salt-rich continental margins are distinctly different from those of margins with no salt.

Mass-transport deposits found around salt diapirs are often regarded as the product of erosion of adjacent diapir crests. In addition, the gliding surfaces of the MTDs in such environments are marked by distinctive kinematic indicators. On the basal shear surfaces, ramps are found close to the diapir crest. Furthermore, rugged topographies or irregularities on these basal shear surfaces are related to faults propagating from the crest of salt diapirs (e.g. Alves et al., 2009; Davison et al., 2000; Richardson et al., 2011). These faults presumably influence failure on the glide surfaces. Fault scarps often are cannibalized, eroded and draped by younger MTDs as shown in Chapter 6 of this thesis.

In this thesis, the spatial and temporal recurrence of MTDs in salt-rich continental margins such as the Espírito Santo will be used to test the following research hypotheses (Figure 1.1).

- Mass-transport deposits are often found around salt structures. If sedimentation is totally controlled by gravity, with little influence of tectonics, it will be possible to establish the history of mass-wasting and provide information on the provenance of MTDs. If MTDs are sourced close to a salt structure, the deposits will taper away from the salt structure. If they are sourced from regions distant from salt structures, the thickness of the MTDs will increase towards the source area. Consequently, the provenance of MTDs in salt-rich continental margins can be assessed by systematically recording thickness variations. Salt-controlled basins will show distinctly different geometries in MTDs from non-salt rich basins. It is therefore possible to use specific MTDs from salt-rich continental margins to establish a new classification scheme for this type of deposits.

- Mass-transport deposits in salt-rich basins record the growth of adjacent salt structures and, subsequently, the palaeo-strain conditions near the seafloor. If MTDs are affected by the growth of salt structures they should appear deformed closest to the region of salt piercing. If not, the MTDs will not show any evidence of deformation. In the case of a clear salt-MTD relationship, palaeo-strain conditions will be measured by the dimension of 'drag zones' within the interpreted MTDs.

- The translation of MTDs over any surface is generally erosive. If MTDs are deposited after salt growth, the crestal and synclinal faults emerging from the

salt structures will have their scarps eroded and cannibalized. If not, the MTDs will be faulted during the upward propagation of the crestal faults. The interaction between MTDs, salt and faults can therefore be assessed using displacement analyses. Moreover, the deposition of the MTDs in these conditions can influence fluid flow properties of adjacent faults.

The research hypotheses, if tested, are important for the successful exploration of hydrocarbon in salt-rich deepwater continental margins, on which the vast majority of oil plays are located in areas prone to slope instability (Hjelstuen et al., 2007; Tailing et al., 2007).

1.1 Aims of the PhD

This work investigates the interaction between MTDs and tectonics on a salt-rich passive continental margin. Using a high-quality 3D seismic data from the Espírito Santo Basin, the thesis presents novel techniques useful for ongoing exploration in new frontiers on salt-rich continental margins. The aims of this work are:

1. To document spatial and temporal recurrence of MTDs on the continental slope offshore Espírito Santo Basin.
2. To propose a new method to estimate the provenance of MTDs on salt rich-continental margins using 3D seismic data. In this aim are included:

   (a) The assessment of the seismic heterogeneity of MTDs on a salt-rich continental slope;

(b) The quantification of the degree of disaggregation experienced by MTDs in relation to their transporting distances; and

(c) A more complete understanding of how interactions between MTDs and growing salt diapirs can provide information on the provenance areas of such strata.

3. To investigate how the morphology of MTDs relates to diapir growth and near-seafloor strain, presenting new data on:

a) The extent to which perturbation imposed by growing diapirs is reflected on the seafloor;

b) The analysis of whether basal ramps and flats affect the geometry of mass-transport deposits ;

c) The proposition of new methods to assess the effect of ramps and flats on the type of sediments deposited on and around growing salt diapirs.

4. To characterise the effect of mass-transport deposits on vertical fault propagation and their importance as stratigraphic markers of fault activity. Three main questions will be addressed:

a) Can mass-transport deposits impose lithological controls on the propagation of faults on continental margins?

b) Can mass-transport deposits be used as stratigraphic markers to assess fault propagation histories on structurally decoupled and non-decoupled fault families?

c) What methods can be used to distinguish different fault families in terms of their propagation histories?

In the next section, a detail background is given on the processes, types and significance of MTDs. This is followed by an organised and generalised literature review on vertical salt flow. In order to provide hints into the results Chapters, the last sections in Chapter 1 provide key data on the expected interaction between mass-wasting processes and halokinesis.

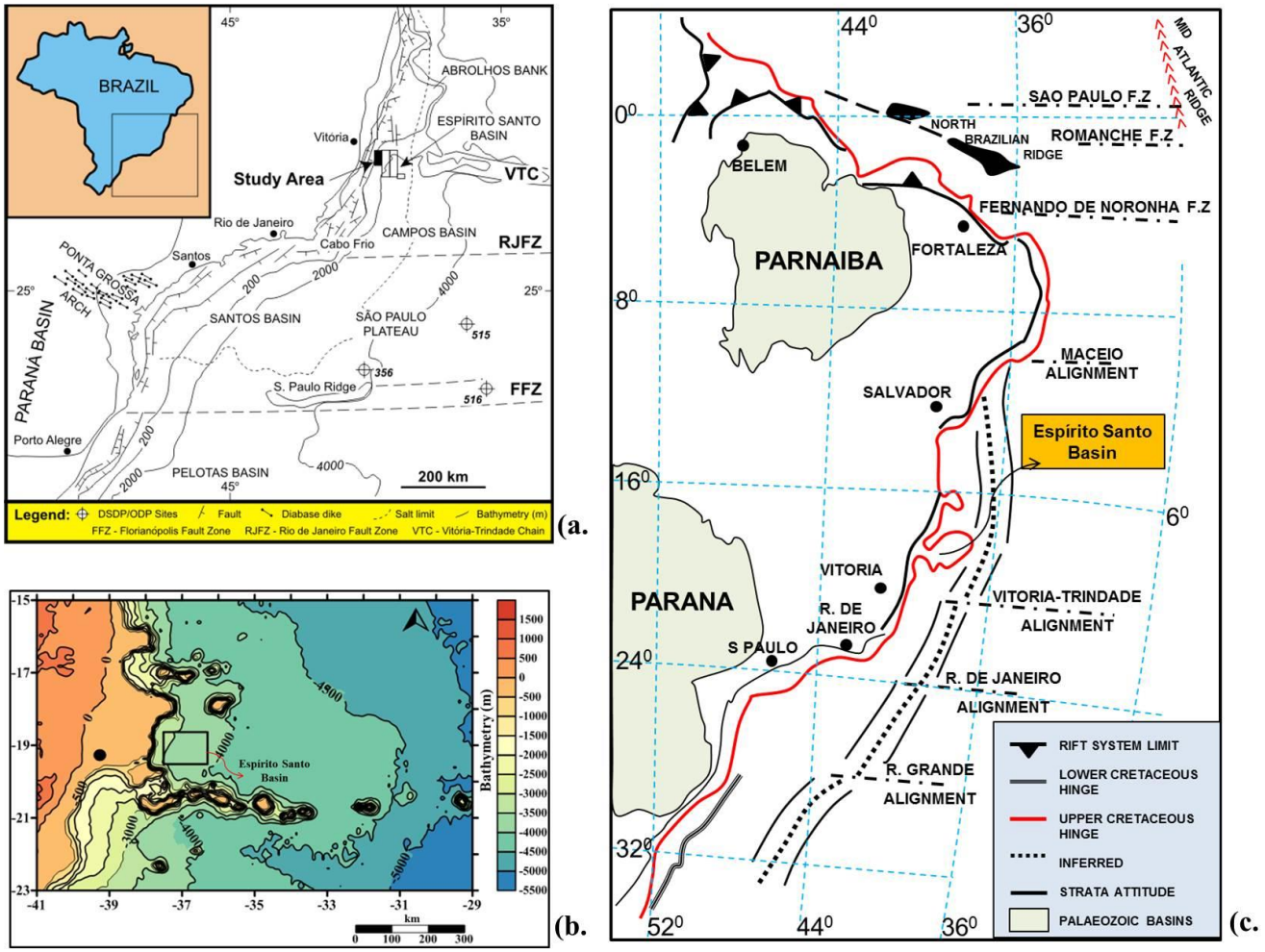

Figure 1.1: a) Map of the southeast Brazilian margin showing the location of the Santos, Campos and Espírito Santo basins in relation to main fault zones b) Bathymetry map of Espírito Santo basins and environments and c) Tectonic outline of Brasilian continental margin (Modified after Ojeda, 1982)

1.2 Mass-transport deposits

Mass-transport deposits (MTDs) comprise sediment packages emplaced during a single event of slope failure. In turn, the term mass-transport complex is used where multiple slope failures have coalesced into a larger unit or package (Gamberi et al., 2011; Hampton et al., 1996; Masson et al., 2006a; Mulder and Cochonant, 1996; Posamentier and Walker, 2006; Varnes, 1978). Mass-transport deposits are ubiquitous features on submarine slopes, and in all geological settings, including rift and transform margins, convergent and passive continental margins (Urgeles et al., 1997; Goldfinger et al., 2000; Laberg et al., 2000; McAdoo et al., 2000; Hunerbach and Masson, 2004). They occur at all water depths, especially in areas where soft sediment predominate (Morgan et al., 2009). Large MTDs usually cover tenths to hundreds of kilometres, they are formed by shelf break or mid-slope failure, in contrast to smaller scale MTDs formed by collapse of canyon walls or elevated gradients on the flanks of salt diapirs (Hampton et al., 1996; Masson et al., 2006a; Posamentier and Walker, 2006).

1.2.1 Importance of mass-wasting processes

- Mass-wasting processes are fundamental processes in shaping and infilling sedimentary basins (Frey Martinez et al., 2005a; Gee and Gawthorpe, 2006; Gee et al., 1999; Masson et al., 1998; Norem et al., 1990; Richardson et al., 2011). They transport significant amount of sediment to offshore areas, comprising 10% to 27% of continental slope strata (Hühnerbach et al., 2004; Mienert et al., 2003; Hjelstuen et al., 2007; Tailing et al., 2007). As a result, the distribution of these transported masses is crucial to hydrocarbon reservoir assessment in deep-water domains.

- Mass-wasting processes can be related to climate-change events when they are formed via gas hydrate dissociation (Richardson et al., 2007) or can be associated with eustatic events (Rothwell et al., 1998). They can also cause tsunamigenic waves as a result of disruption of the sea water column (Hampton et al., 1996; Nisbet and Piper, 1998; Locat and Lee, 2002; Maslin et al., 2004; Fryer et al., 2004). The understanding of the inter-relationship between slope failure and gas hydrate stability is crucial in the global understanding of climate change and ocean margin systems. Examples of geohazards associated with mass-wasting processes are provided below:

    - **2002-** The Stromboli Island volcanic activity and associated submarine landslide and tsunami caused harm to housing and infrastructures but with no fatalities (Tinti et al., 2005).
    - **1998-** Submarine landslide off Papua-New Guinea that caused a tsunami resulting in loss of 2200 deaths (Tappin et al., 2001).
    - **1996**- Submarine landslide in Finneidfjord, Norway caused destruction of a highway and three residential houses in which four persons were killed (Longva et al., 2003).

- The quest for hydrocarbons has recently moved into deepwater areas where MTDs occur. The triggering of small- and large-scale slope-instabilities has the potential to jeopardize installations and other anthropogenic structures on the seafloor. Furthermore, shallow MTDs are common drilling hazards due to their complex internal structure and inherent potential to contain local gas pockets (Barley, 1999; Weimer and Shipp, 2004; Butler and Turner, 2010; Mosher et al., 2010). For example:

    - The cost of damage to offshore pipelines is ~$400 million per year (Mosher et al., 2010).

- On December 26, 2006, a submarine landslide in the **Luzon Strait** caused failure of undersea cables, halting the entire internet network between Taiwan, Hong Kong, and China and affecting communications between Thailand, Malaysia, Vietnam, South Korea and Singapore for 12 hours (Hsu et al. 2009). This caused a severe economic impact on the daily GDP of Taiwan, Hong Kong and China which was approximately $7.56 billion/day *(courtesy: http://www.igcp585.org/significance visited 23/01/2014).*
- Twelve submarine transatlantic cables were broken by the 1929 Grand Bank earthquake and associated submarine landslide (Piper et al., 1999)

1.2.2 The physics of mass-wasting

Mass-wasting occurs over a basal shear surface and can result in little-deformed to intensely folded, faulted and brecciated masses that have translated downslope from the original site of deposition (Bull et al., 2009; Posamentier and Martinsen, 2011). Once initiated, the shear surface will propagate upslope from its nucleation point leading to a scoop-shaped, concave-downslope slide scar, often with an irregular outline (Martinsen, 1994).

The stability of a slope is governed by the Coulomb criterion, enhanced by external and internal forces acting on the slope for long or short term periods. The Coulomb theory states that shear stress applied to the slope must exceed the shear strength to generate failure. The shear stress, however, is dependent on the coefficient of static friction, normal stress and coefficient of cohesion (Eq. 1.1). External stimuli for slope failure are regarded as "triggering mechanisms" (Sultan et al., 2004). Long-term stability factors include the steepness of a slope and the strength/cohesion of the lithologies involved, controlled by erosion, tectonics, substrate, and anthropogenic factors (Erismann and Abele, 2001; Glade et al., 2005; Jakob and Hungr, 2005). Short-term factors include physical loading and seismic shaking.

Most submarine slopes are inherently unstable but require external, often transient effects to trigger mass-wasting. Elevated pore pressures, related to processes such as earthquake shaking or rapid sedimentation appear to be critical factors in most submarine landslides. Such pore pressures support part or all the weight of the overlying sediment, thus lowering the frictional resistance to mass-wasting (see Mohr-Coulomb Eq. 1.1). When concentrated in specific geological layers, they create weak layers, which fail in a characteristic bedding plane parallel style (Dykstra, 2006).

The factor of safety, FS, represents mathematically the equilibrium conditions between the factors favouring slope failure and those preventing it. In Figure 1.2 it is shown how external and internal factors drive slope instability while gravitational forces resist slope failure. When FS > 1 slope is thought to be stable; the slope is unstable when FS < 1, and the condition of the slope is relatively unpredictable when FS = 1. Partly contradicting the Coulomb theory, Hühnerbach et al., (2004) documented that the occurrence of submarine landslides is not greatly influenced by slope gradients, except at the shallowest gradients where relatively few landslides occur. The authors stated that the largest landslides on the continental slope occur on the lowest slopes, often as low as 1°. In addition, the greatest number of landslide headwalls occurs on the mid-slope, with a peak at 1000 to 1300m water depth, rather than at the shelf edge or on the upper slope as might be expected (Huhnerbach et al., 2004).

$$T = (\delta n - \mu) \tan \emptyset + C \quad \text{----------} \quad \text{Eq 1.1}$$

N.B: T = resistance (shear strength), δn = normal stress, μ = hydrostatic stress Ø = angle of shearing resistance or internal friction, C = cohesion of sediments intercept (Terzaghi, 1962).

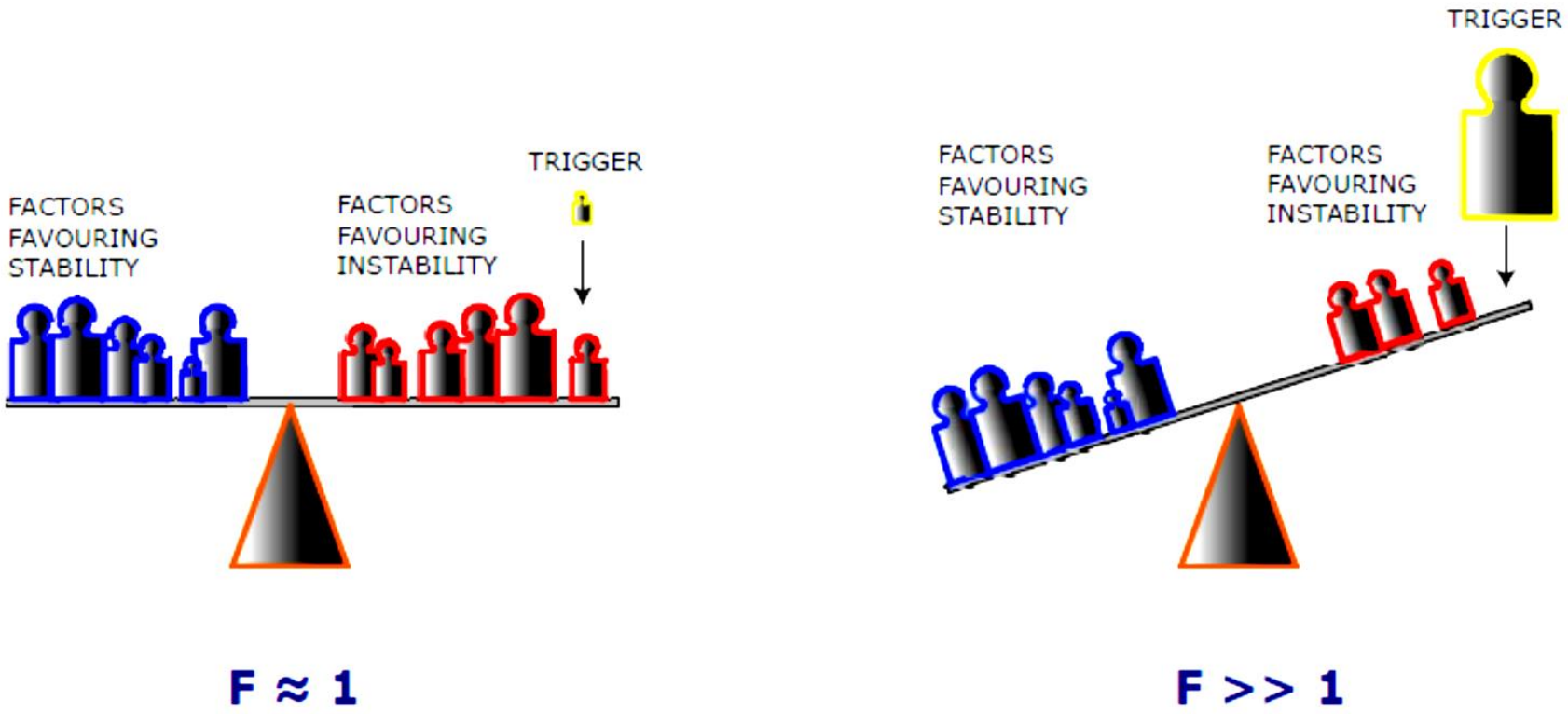

Figure 1.2: The factor of safety FS reflects the equilibrium conditions between pre-conditioning factors and triggering mechanisms. The factors favouring stability of the slope are highlighted in blue where factors triggering failure are shown in red. The slope fails when the FS is < 1 (Modified after Camerlenghi, 2013). N.B: *F in the figure refers to FS in the caption.*

1.2.3 Triggering mechanisms for mass-transport deposits

The common triggering mechanisms for mass-wasting are presented below with historic examples from the literature. In this section, landslides are used as a generic term for all kind of mass-transport deposits.

1.2.3.1 Presence of weak geological units

Evidence from sea floor technology and mapping techniques such as swath bathymetric mapping and 3D seismic data suggests weak geological units as a factor contributing to submarine mass-wasting at all scales (Bryn et al., 2005; Kvalstad et al., 2005). Weak geological layers may include degraded soft clays, loose and saturated granular silts and sands, and quick clays (Pestena et al., 2000). For example:-

- Geotechnical assessment of the Storegga slide revealed that it was triggered by a combination of one or more weak layers (contourites) deposited during interglacial periods (Locat et al 2003; Kvalstad et al., 2005; Masson et al., 2006).
- The 1979 tsunamigenic landslide along the Ligurian continental margin in the Western Mediterranean is associated with the presence of weakened clay-rich deposits (Steggmann et al., 2011).

1.2.3.2 High Sedimentation rate/ underconsolidation

Rapid deposition associated with high-sedimentation rates can result in underconsolidation of buried layers of clay-rich sediment, in which upward hydraulic gradients can reduce the internal shear strength of the sediment and lead to slope instability (Aksu and Hiscott, 1989; Prior and Coleman, 1982; Hiscott and Aksu, 1994; Laberg and Vorren, 2000). Thus, high sedimentation rates and undercompaction can often lead to overpressuring of weak geological layers such as mudstones (e.g. Kvalstad

et al., 2005). Environments where sediments are quickly deposited such as fjords, river deltas, fan systems and open continental slopes are characterised by unconsolidated sediment (Masson et al., 2006). For example:-

- The 1975 Kitimat Arm slide northwest of Douglas Channel in Canada is an example of fjords where slope failure was associated with unconsolidated sediments (Conway et al., 2012).
- Following Hurricane Camile (1969), the submarine landslide of the Mississippi Delta was found to have been triggered by overpressuring associated with high sedimentation rates (Locat and Lee, 2002).

1.2.3.3 Earthquakes

A great part of submarine landslides are triggered by earthquakes (Lewis, 1971; Dingle, 1977; Keefer, 1994; Hampton et al., 1996; Imbo et al., 2003). Earthquakes can provide significant environmental stresses and promotes elevated pore water pressures, leading to seafloor failure. Similarly, storm wave loading, hurricanes and typhoons can lead to submarine landslides in shallow regions.

- Earthquakes triggered the Grand Banks landslide of 1929, where a 20 km^3 submarine landslide was initiated after a magnitude 7.2 earthquake (Nisbet and Piper, 1998; Masson et al., 2006).
- The 1607 Bristol flooding, which was recorded on plaques in a number of churches at Kingston Seymour in Somerset and in Monmouthshire at Goldcliff, St. Brides, Redwick and Peterstone, was caused by a submarine landslide triggered by an earthquake with epicentre on the Irish coast (http://www.burnham-on-sea.com/1607-flood.shtml visited January 24, 2014)

1.2.3.4 Gas hydrates

The dissociation of gas hydrates on continental slopes due to changes in sea level or increase in bottom water temperature can produce large amounts of free gas within sediment layers (Bouriak et al., 2000; Sultan et al., 2004). This increase of free gas within the sediment column will decrease the bulk shear strength of the slope material and can potentially lead to slope failure (Mienert et al., 1998).

- Gas hydrate dissociation at water depths of 1000 to 1300 m caused slides off the east coast of the United States and the Storegga slide off the east coast of Norway (Locat and Lee, 2002; Hunerbach and Masson, 2004)

1.2.3.5 Groundwater seepage

Groundwater seepage and elevated pore water pressure can cause submarine landslides. Elevated pore water pressure causes reduced frictional resistance to sliding and can result from normal depositional processes, or can be coupled with other causes such as earthquakes, gas hydrate dissociation and glacial loading.

- Nice international airport submarine landslide of 1979 is a good example of the effect of hydrogeology on slope instability. The spatial and temporal variations in the Var aquifer was driven by precipitation and melt water fluxes hence weakening the associated clay-rich deposits (Steggmann et al., 2011)

1.2.3.6 Oversteepening

Slopes are stable as long as the angle of internal friction (ϕ) is greater than the slope angle (α) (Hampton et al., 1996). Oversteepening is caused by scouring due to oceanic currents and can result in the triggering of submarine landslides. In salt rich-continental

margins, elevated slope gradient are produced during active diapirism (e.g. Fiduk et al., 2004). Other factors that can initiate slope failure from geotechnical point of view included storm-wave loading, low tides, glacial loading and volcanic island processes (Table 1.1).

Table 1.1: Historically documented submarine landslides and their predicted triggering mechanisms (Modified after Masson et al., 2006).

Historically documented	**Examples**	**References**
Earthquakes	Grand Banks	(Fine et al., 2005)
Hurricanes or cyclic loading	Mississippi delta	(Prior and Coleman, 1982)
Loading or oversteepening of slopes	Nice, Canary islands	(Assier-Rzadkiewicz et al., 2000)
Underconsolidation (overpressure)	Mississippi delta	(Prior and Coleman, 1982)
Rainfall (where landslides have a subaerial extension)	Norway, Hawaii	(Longva et al., 2003)
Slope parallel weak layers in bedded sequences	East coast US, Storegga, west Africa	(O'Leary, 1991; Haflidason et al., 2003; Bryn et al., 2005)
Suggested (but less well documented)		
Gas hydrate dissociation	East coast US, Storegga	(Sultan et al., 2003)
Sea-level change	Madeira Abyssal Plain	(Weaver and Kuijpers, 1983)
Volcanic activity	Hawaii, Canaries	(Moore et al., 1989)
Salt diapirism	Espirito Santos, Trinidad and Tobago	Moscardelli and Woods, 2007, Gamboa et al., 2011

1.2.4 Classifying mass-transport deposits

This section appraised the published classification schemes for MTDs in order to highlight the gap in research and find a common scheme to characterise this type of deposits. A simple, scale-consistent and common classification scheme that focuses on descriptive and morphological factors is necessary for all MTDs (Posamentier and Martinsen, 2011). Previous classification schemes were based on mass-wasting processes per se, and on the deposits and rheology of the transporting medium. For example mass-wasting processes causing MTDs were defined by Masson et al., 2006b as:

- Slides, which involve movement of coherent mass of sediment bounded by distinct failure planes;
- Debris flows involve laminar, cohesive flow of clasts in a fine-grained matrix;
- Debris avalanche presents the rapid flow of cohesionless rock fragments with energy dissipation by grain contact;
- Turbidity current includes gravity flows in which sediment grains are maintained in suspension by fluid turbulence.

In the next few pages, other classification scheme including those of ISSMGE (International Society for Soil Mechanics and Geotechnical Engineering) are shown and briefly discussed in Figure 1.2 to Figure 1.8.

Mass-wasting processes form a continuum, with moderate degrees of deformation recorded initially and the last deposits reflecting high degrees of remobilization. The majority of published classification schemes are scale-dependent or only applicable to sub-aerial landslides. For example, sediment creep occurs as an extremely slow process

on the order of a few mm to cm/yr. and is essentially a sub-seismic event, i.e. below the resolution of industry seismic data (Posamentier and Martinsen, 2011). For any classification scheme to be universal, it should be applicable at all scales and depositional environments. A straightforward option is to classify MTDs using their lithological character as it is readily observable both in outcrops and seismic profiles. The processes leading to these deposits, however, can only be analysed through laboratory simulations and models. Description and geotechnical details of MTDs are, in turn, obtained from buried in situ deposits. Due to the difficulty of integrating laboratory and in situ information at distinct scales, seismic data are often used to abridge distinct datasets providing reliable information on the processes forming MTDs

1.2.5 Geomorphological classification of mass-transport deposits

Submarine landslides, slumps and debris flow can co-occur during the same slope instability event and result in characteristic seafloor morphologies (Figure 1.9). The geometry and internal deformation of MTDs is a consequence of the mechanisms of failure and the morphology of the slope over which translation occurs (Strachan, 2002; Lucente and Pini, 2003). Thus, the morphological characteristics of MTDs is commonly expressed by different geological structures or features that record information related to the type and direction of transport at the time of emplacement. These features are generally referred to as kinematic indicators; they are geological structures that can unravel the history of mass-wasting from initiation, dynamic evolution and to cessation of slope failures (Bull et al., 2009)

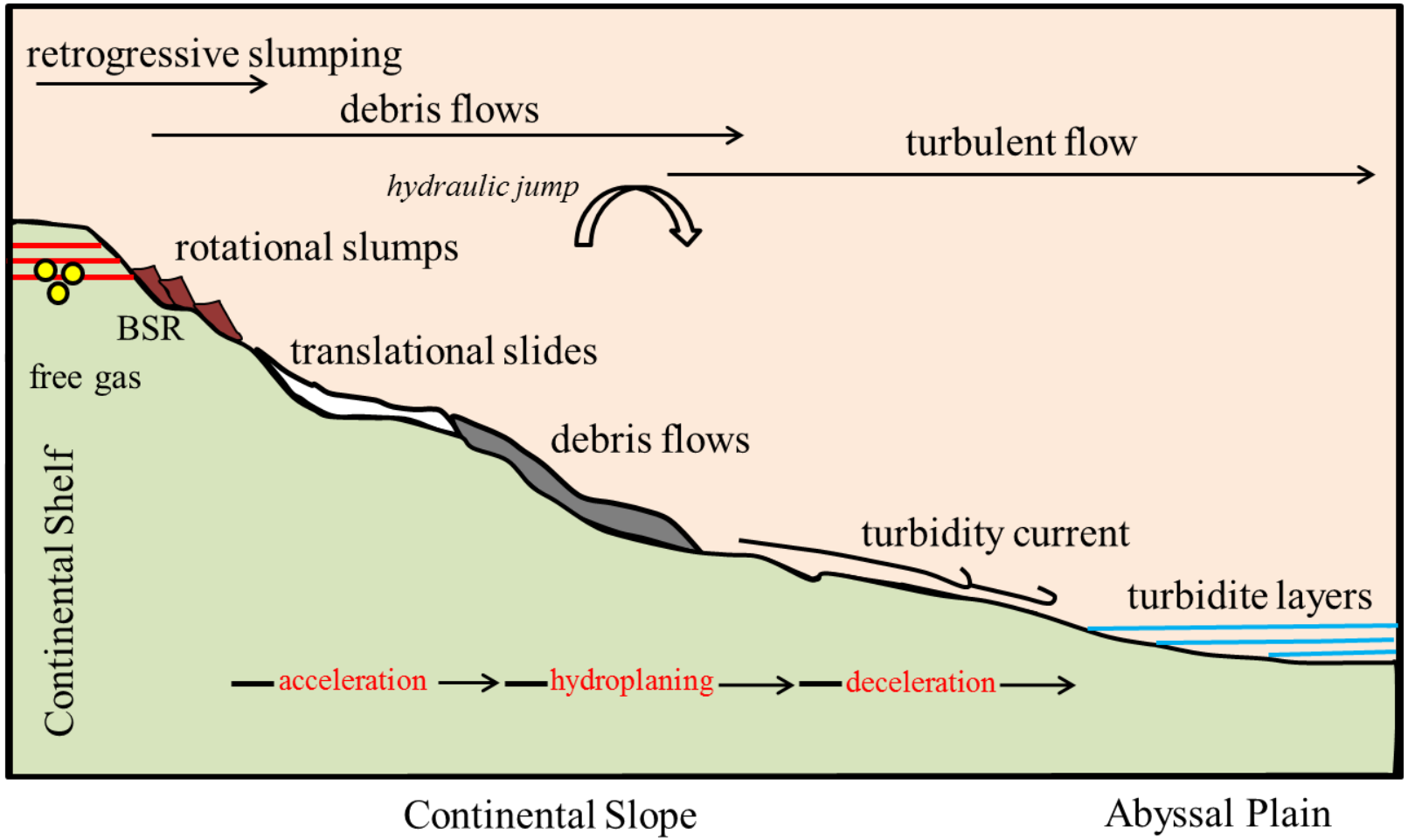

Figure 1.3: Schematic diagram for downslope mass-movements on continental margins. The classification and the type of deposits in the figure are based on the flow mechanisms and the kind of deposits produced after each failure event. The process is a continuum when materials transits from slumps near upper slope area into debris flow on the mid-continental slope - Process and deposit-based classification (Modified after Mienert et al., 1998). *N.B BSR is Bottom Simulating Reflector indicating the presence of gas hydrate on seismic section.*

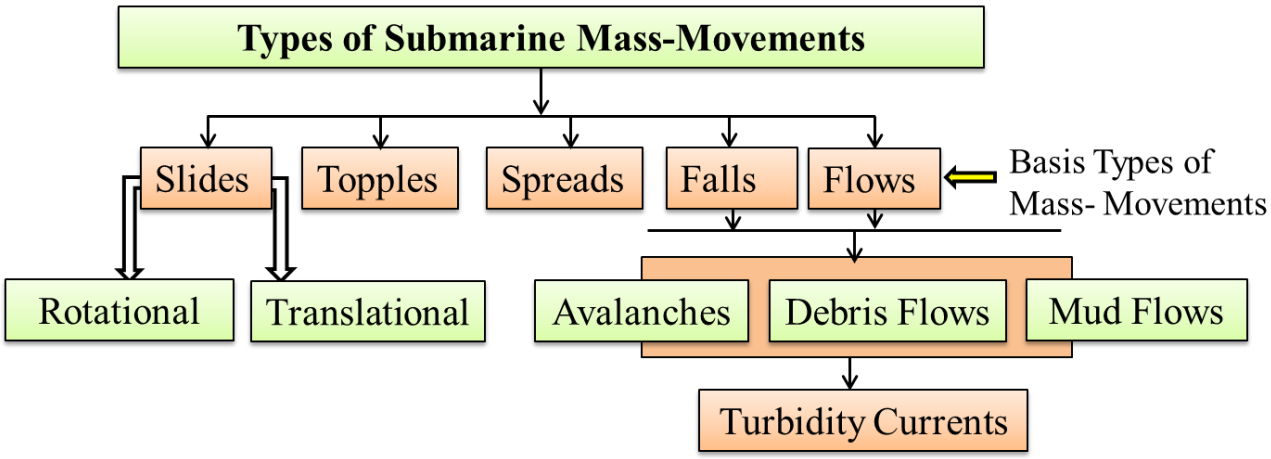

Figure 1.4: Classification of submarine mass-movements. This classification is solely based on the kinematics and the kind of mass-movements - Process-based classification (modified after ISSMGE Technical Committee on Landslides, TC-11)

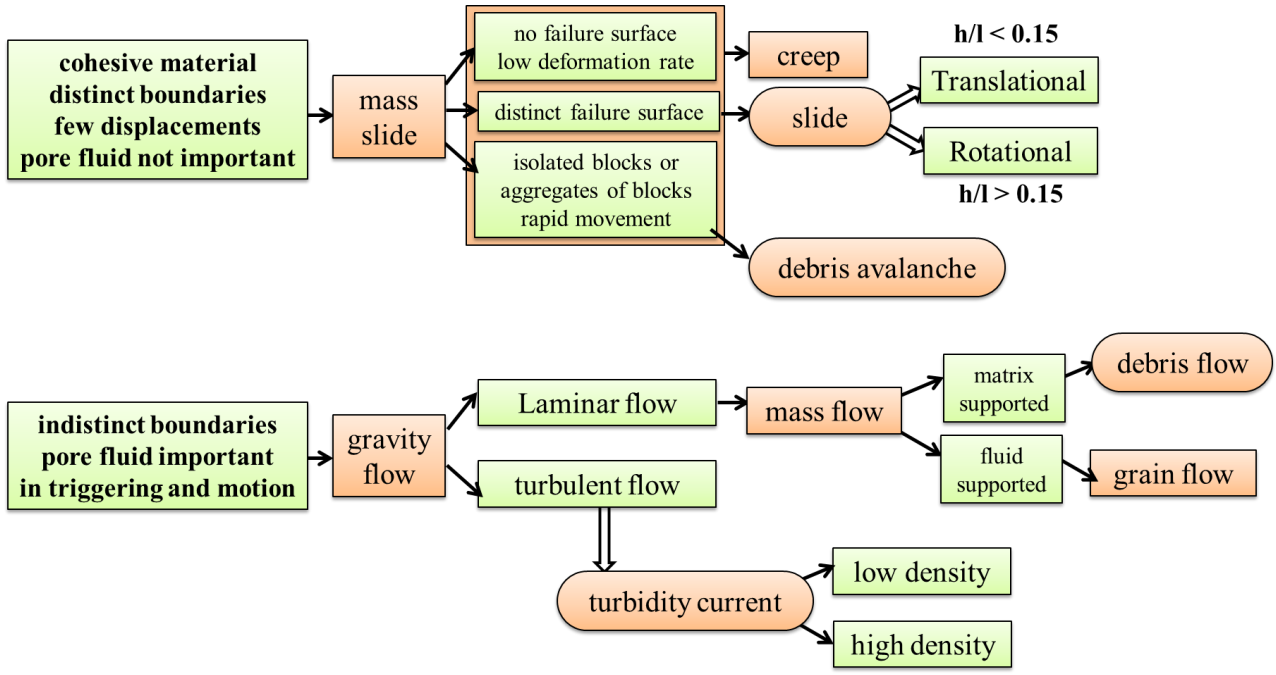

Figure 1.5: Key flow types in the classification are highlighted in the figure (Mulder and Cochonant, 1996). Slides, debris flows and turbidity currents are the main gravity-driven processes by which marine sediments are transported down slope. All have related hazards. Debris avalanches, although relatively rare in the submarine realm, are highlighted due to their specific hazard threat - Process and deposit-based classification (Masson et al., 2006c).

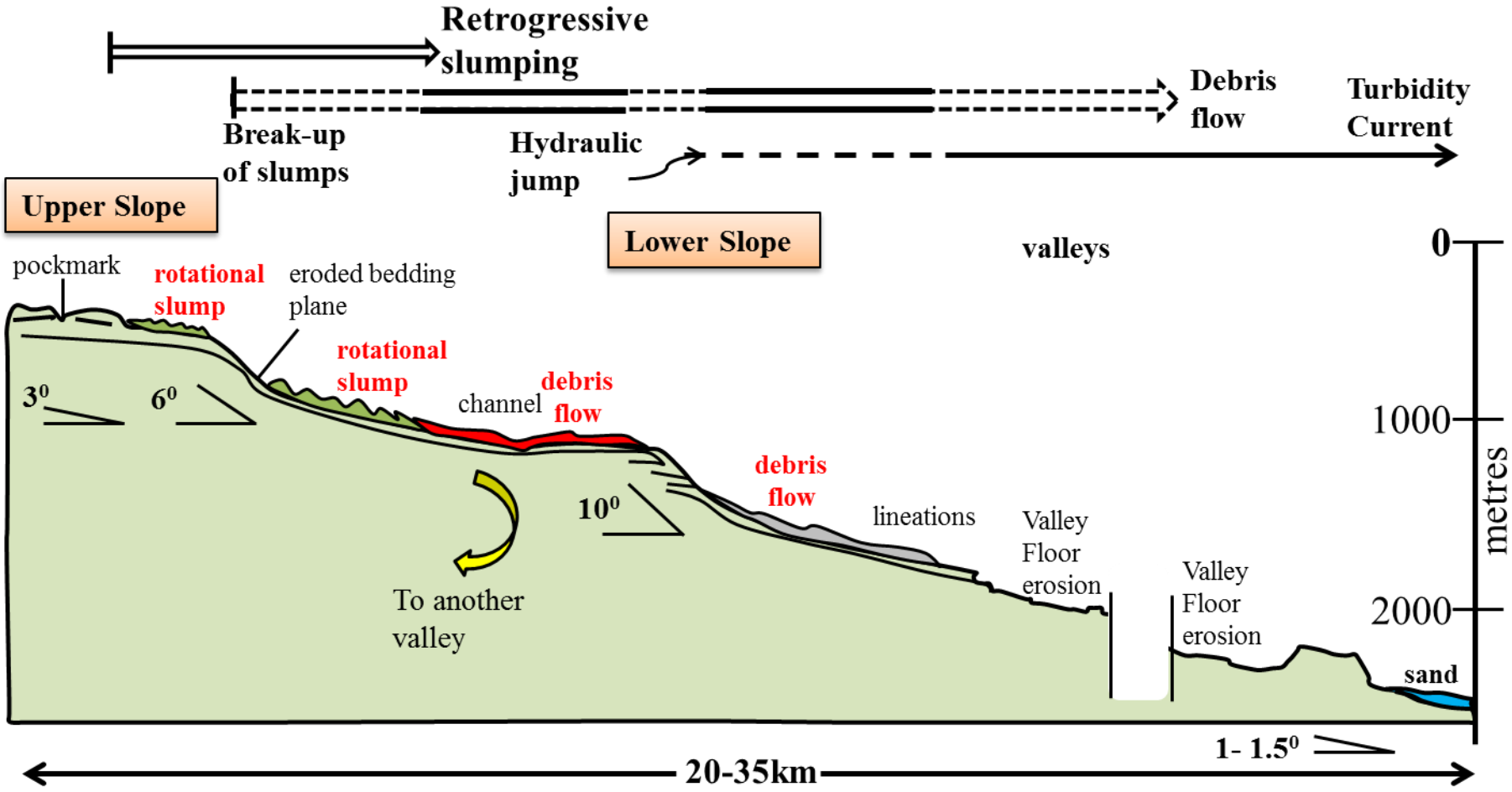

Figure 1.6: Classification of mass-transport deposits on continental margins. The classification includes the process, depth and geomorphology of the surfaces over which sliding takes place - Process and deposit-based classification (Modified after Piper et al., 1999)

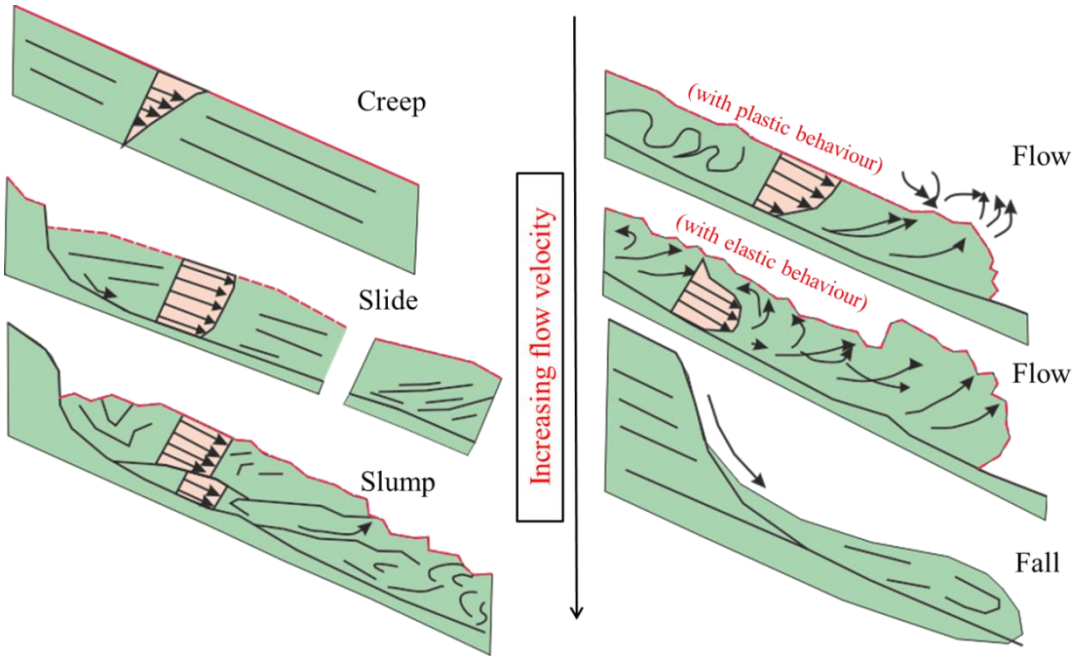

Figure 1.7: Nemec's (1991) classification of slope deformational processes and other processes. Some of these processes produce mass-transport deposits. The classification considers the rheology of the material being transported during mass-wasting - Process, deposit and rheology-based classification (Modified after Nemec (1991), Nemec and Martisen, 1994).

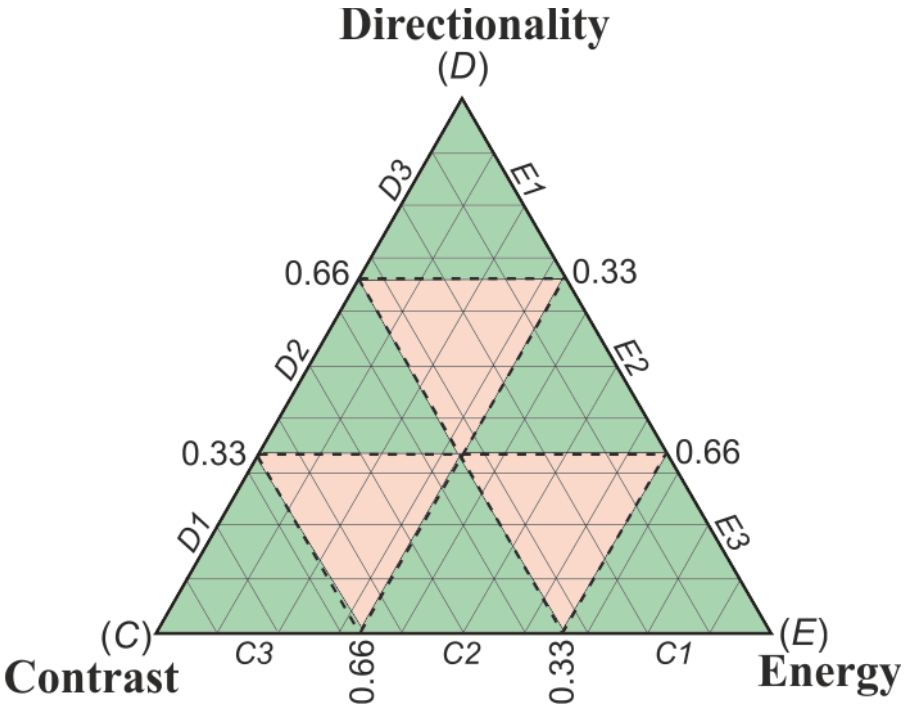

Figure 1.8: The CDE method distinguishes MTD from hemipelagites using their lithological heterogeneity and degree of disaggregation, the presence of structural fabrics such as faults, and their acoustic properties - Deposit-based classification (Adapted from Alves et al., 2014).

MTDs can be organized into structural domains reflecting characteristic kinematics and strain (Lewis, 1971; Bull et al., 2009). These structural domains include an 'extensional domain' located at the head of the failure containing predominantly extensional strain and a volume reduction relative to the stable slope, a 'translational domain' in the mid-slope containing relatively undeformed strata, and a 'compressive domain' at the toe of the failure reflecting contractional strain and a height increase with respect to the stable slope (Figure 1.9). However, this classification comprises an oversimplification of the structural division of MTDs often observed in nature. In larger complexes of coalesced deposits, the tripartite scheme is broken down into multiple domains (Martinsen, 1994; Gardner et al., 1999).

The focus of this study is not entirely on kinematic indicators. Of importance to this study are ramps and flats and the mode of frontal emplacement of MTDs. These geomorphic features are briefly discussed in the following section. A succinct description of other kinematic indicators is provided in Appendix IV.

1.2.5.1 Ramp and flats

A ramp is defined as comprising a segment of the basal shear surface that cuts discordantly across bedding, whereas the 'flat' sections are bedding-parallel segments of the basal shear surface. The ramps, therefore, connect 'flat' segments of the basal shear surface at different stratigraphic levels (Trincardi and Argnani, 1990). Lucente and Pini (2003) suggested the ramp and flat geometry to be similar to shallow level deformation in accretionary wedges, and Gawthorpe and Clemmey (1985) assigned the terms 'contractional' if the basal shear surface cuts up section and 'extensional' if it cuts down. Gawthorpe and Clemmey (1985) and Trincardi and Argnani (1990) reported that

most ramps trend perpendicular to the main flow or movement direction. In turn, slots are kinds of ramps that run parallel to the transport direction of MTDs (O'Leary, 1986; Bull et al., 2009).

1.2.5.2 Toe domain/Accumulation Zone

The toe domain represents the downslope region of the MTD, including the downslope termination point, or 'toe' of the deposit. Toe domains often have an overall convex-downslope morphology (Prior and Coleman, 1984; Frey Martinez et al., 2005), and the main kinematic indicators observed in these regions are pressure ridges and thrust-and-fold systems. Frey Martinez et al. (2006) subdivided the toe domain into those which are 'frontally confined', in which the translated mass is buttressed downslope against undisturbed strata; and 'frontally emergent' occurring when the translated mass is able to ramp up the basal shear surface and move freely across the seafloor (Figure 1.10).

Frontally-confined MTDs are characterized by developing large-scale thrust-and-fold systems (Huvenne et al., 2002; Frey-Martínez et al., 2006; Gafeira et al., 2007), while the frontally-emergent typically exhibit pressure ridges (Prior et al., 1984). There is overlap between these two extremes, with some frontally emergent MTDs developing impressive fold and thrust systems when the translating material becomes buttressed against a seafloor obstacle (Lewis, 1971; Moscardelli et al., 2006).

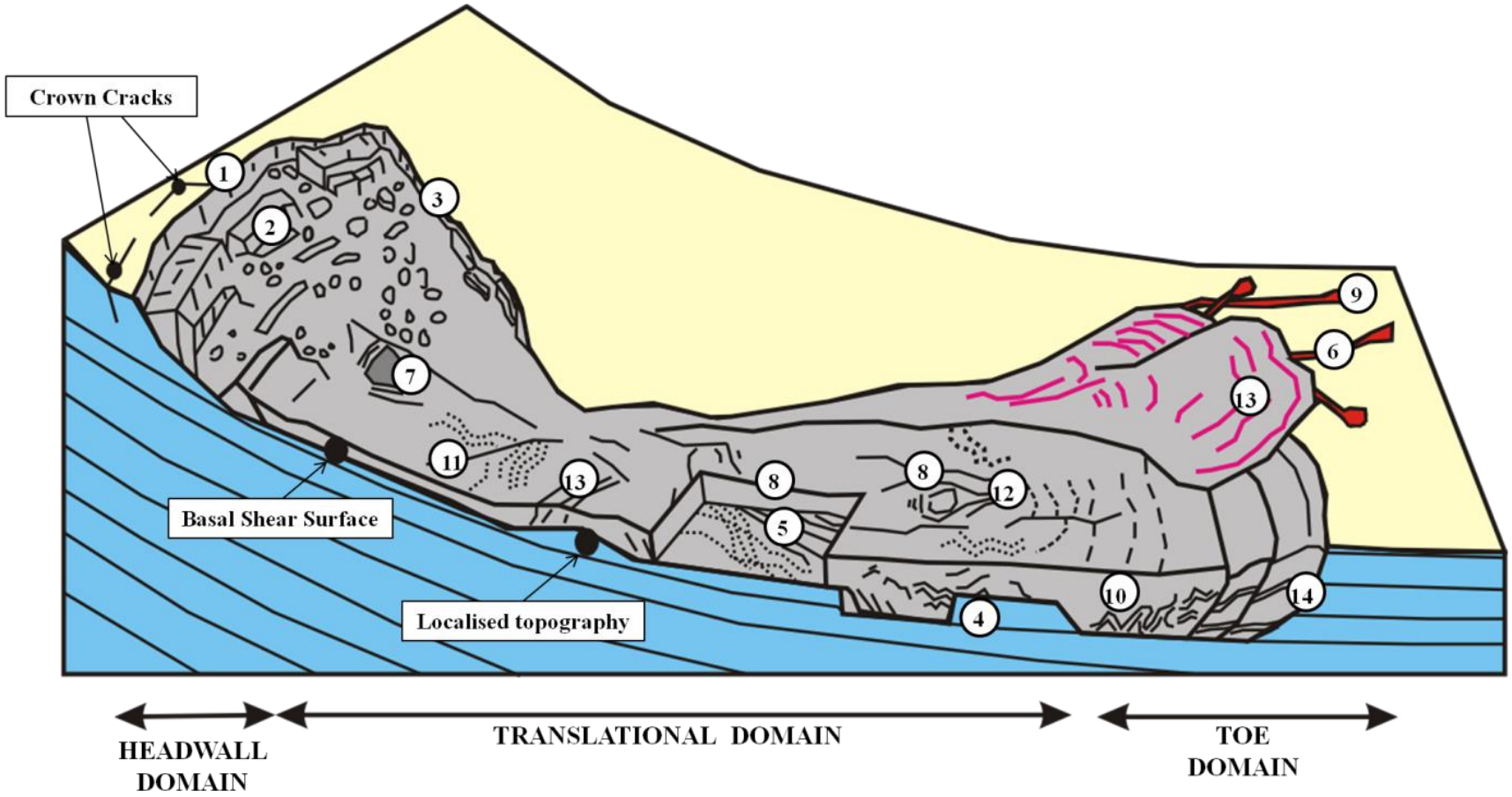

Figure 1.9: Geomorphologic division of a mass-transport deposit and the likely occurrence of kinematic indicators relative to its various domains. (1) Headwall scarp, (2) Extensional ridges and blocks, (3) Lateral margins, (4) Basal shear surface ramps and flats, (5) Basal shear surface grooves, (6) Basal shear surface striations, (7) Remnant blocks, (8) Translated blocks, (9) Outrunner blocks, (10) Folds, (11) Longitudinal shears/first order flow fabric, (12) Second order flow fabric, (13) Pressure ridges, (14) Fold and thrust systems (from Prior and Coleman, 1984).

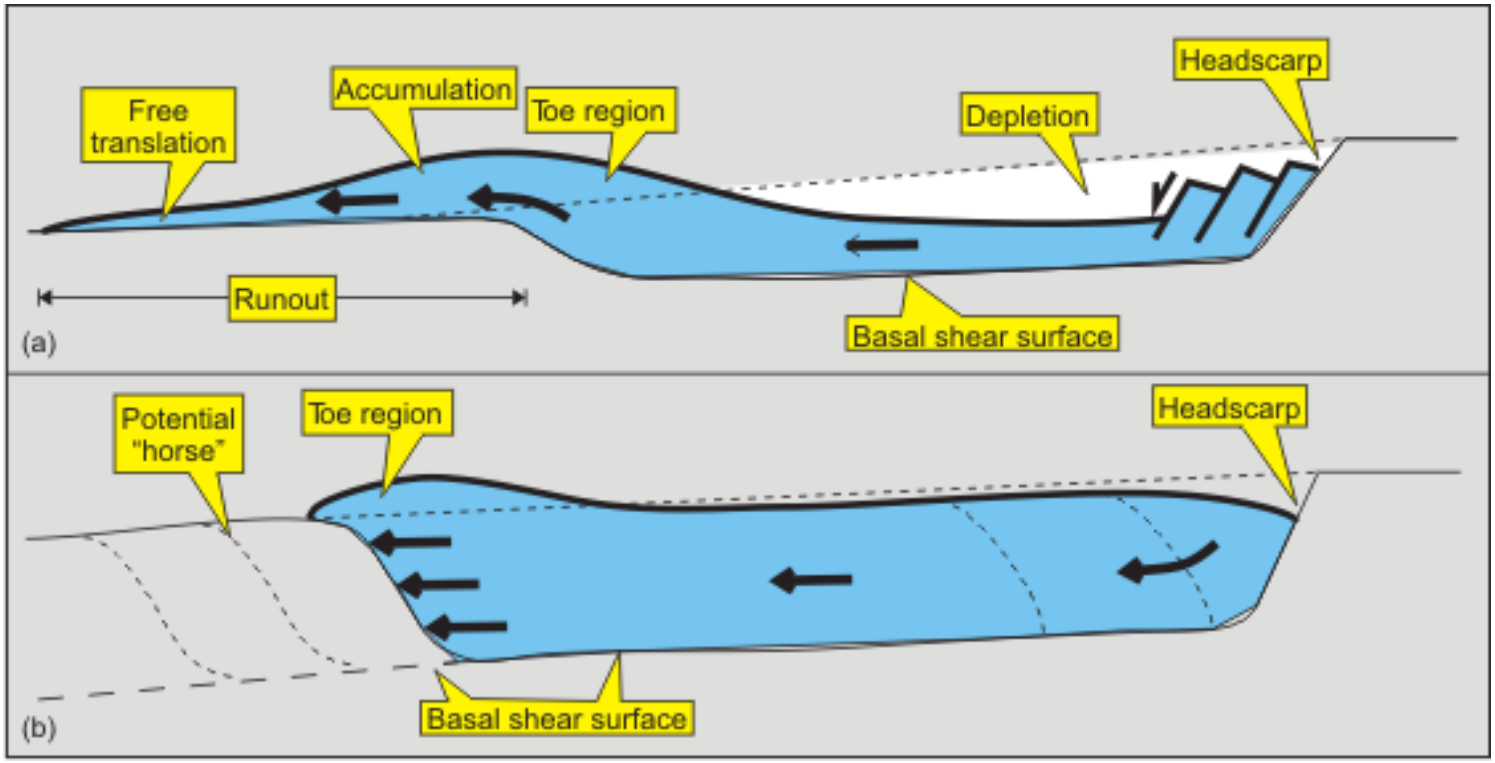

Figure 1.10: Classification of mass-transport deposits according to their frontal emplacement. (a) Frontally-emergent MTD, in which material ramps out the basal shear surface onto the seabed and is free to travel considerable distances over the undeformed slope position and, (b) Frontally-confined MTD where the leading edge of the landslide is buttressed against a frontal ramp (Modified after Frey-Martínez et al., 2006).

1.3 Mechanics of salt flow

Salt tectonics is defined as deformation involving flow of salt (Jackson and Talbot, 1991; Hudec and Jackson, 2007). Differential loading is the dominant force driving salt flow while ability of salt to flow could be impeded by both the strength of the overburden and boundary friction within the salt layer (Hudec & Jackson, 2007). In practice, salt flows when the driving forces are sufficient to overcome resisting forces. Salt can remain static in the subsurface for tens or even hundreds of millions of years if driving forces are too weak, subject only to groundwater dissolution, diagenesis, and metamorphism (Hudec & Jackson, 2007).

1.3.1 Differential loading

The depth of salt burial, geometry of the salt body, geologic setting, and thermal conditions of the salt determine whether the salt flow is driven by one of gravitational loading, displacement loading, and thermal loading (Hudec and Jackson, 2007). Gravitational loading is produced by the combined effect of the weight of rocks overlying the salt and the gravitational body forces within the salt (Figure 1.11).

Regional shortening or extension can cause the flanks of a salt body to move (Figure 1.10a). Displacement loading results from the forced displacement of one boundary of a rock body relative to another (e.g. Suppe, 1985), and it is common where basins having pre-existing salt structures are deformed because the weak salt structures typically focus regional strain. Thermal loading on the other hand can result from volume changes caused by changes in temperature. Hot salt expands and becomes buoyant, producing intra-salt convection, which is enhanced by increases in thermal gradient or decreases in thermal diffusivity and kinematic viscosity.

1.3.2. Boundary friction within the salt layer and strength of the overburden

Sedimentary rocks typically increase in both shear strength and frictional strength with depth of burial and confining pressure (Hudec and Jackson, 2007). Thick sedimentary roofs are, therefore, generally more difficult to deform than thin roofs (Figure 1.12). Roofs more than several hundred meters thick are unlikely to be deformed by salt of modest structural relief without assistance from either regional extension or shortening (Hudec and Jackson, 2007).

The viscosity of salt makes the periphery of most salt bodies to be marked by a zone of restricted flow as the salt is sheared past non flowing country rocks (Figure 1.12). This zone produces a drag along the top and bottom surfaces of the salt layer which impedes the flow of the salt within a buried layer.

1.3.3 Vertical salt flow

Vertical salt movement (Halokinesis) can take place through three (3) stages (Figure 1.13 and Figure 1.14):

(a) Reactive Stage producing salt mounds and pillows. In this setting, the development of the salt is controlled by regional thin-skinned shortening, differential loading and by residual highs located between rising salt diapirs (Vendeville and Jackson, 1992a; Vendeville and Jackson, 1992b). The overburden is extended through normal faulting (Hudec and Jackson, 2007). Normal faulting of the overburden allows the underlying salt to rise reactively even in the absence of density inversion. The grabens and their underlying reactive diapirs are raised above the regional datum while the adjacent overburden blocks subside and are flexed synformally (Vendeville and Jackson, 1992b).

(ii) The Active Stage comprises the period during which the salt flows upward and arrives at the surface or sea floor (Hudec and Jackson, 2007). This is possible because the stresses driving the subsidence of the depocenter flanks are related to gradients in the loading imposed by the overburden and to the density contrast between the salt and the overburden (Vendeville & Jackson, 1992b). Conversely, the strength of the overburden rocks is related to their dip. This implies that gentle flanks can readily subside and deform while steeper flanks are stronger and can rarely deform. Thin-skinned extension after grounding of the depocenter can cause subsidence of diapirs (Vendeville & Jackson, 1992b). Extension greatly lowers stresses within the salt body; therefore, depocenters that have inverted turtle structures to form secondary depositional sinks may have initially had gentle flanks or had been subjected to late extension (Hudec and Jackson, 2007). In extension, active diapirism is driven by buoyancy while displacement loading is the controlling factor for active diapirism in contraction.

(iii) The Passive Stage creates apparent diapirism. The salt does not deform the sediments of the overburden. Salt flows upward as sedimentation progresses on the condition that the salt dome is connected with the mother layer (Hudec and Jackson, 2007; Vendeville & Jackson, 1992a,b). However, diapirs located in tectonically quiescence areas simply stop rising after source layer depletion and remain dormant. Diapirs subject to one or more pulses of late tectonic shortening are episodically rejuvenated. Because rock salt is uncompressible and much weaker than the adjacent overburden rocks, thin-skinned shortening is accommodated by squeezing of the diapirs, which, therefore, continue to rise and deform their roofs (Vendeville and Nilsen, 1995).

1.2.4 Structural style in salt-rich passive continental margins

Deformation on passive continental margins is chiefly driven by gravity over a décollement surfaces, either evaporites or shales (Fort et al., 2004; Rowan et al., 2012). Evaporites are considered as a viscous material with very low strength. Consequently, evaporites start to deform very soon after its deposition generating symmetric detachment folds, shortened salt diapirs and inflated and thickened salt massifs and nappes (Fort et al., 2004; Rowan et al., 2012). The upper slope of salt-rich continental margins is commonly dominated by extensional processes, where salt pillows, mounds and rollers are attached to large listric faults e.g. (Gulf of Mexico, Persian Gulf, North Sea, Lower Congo Basin, Campos Basin, and Pricaspian Basin; Fort et al., 2004; Hudec and Jackson, 2007; Rowan et al., 2012). The salt structures grow into diapir and salt walls in the mid-continental slope, essentially a transition between extensional upper-slope and contractional lower-slope domains. The toe region is characterised by contractional structures. These compressive zones are dominated by salt ridges, thrusts, allochthonous salt sheets and canopies (Demercian et al., 1993; Brun and Fort, 2004;).

The relatively large accommodation space created for sediments during salt flow provides stratigraphers with high-resolution datasets to investigate the relationship between tectonism and sea-level change in controlling facies distributions (Beauboeuf and Friedman, 2000; Prather, 2000). The salt/sediment interaction has a strong impact on all four components of petroleum systems. Reservoir presence is determined by reconstructing minibasins geometry and its relationship with the surrounding salt and faults. Sediment fairways must be mapped for deepwater fans and turbidites, and areas of sediment entrapment vs. bypass must be determined (Roy and Martinsen, 2008).

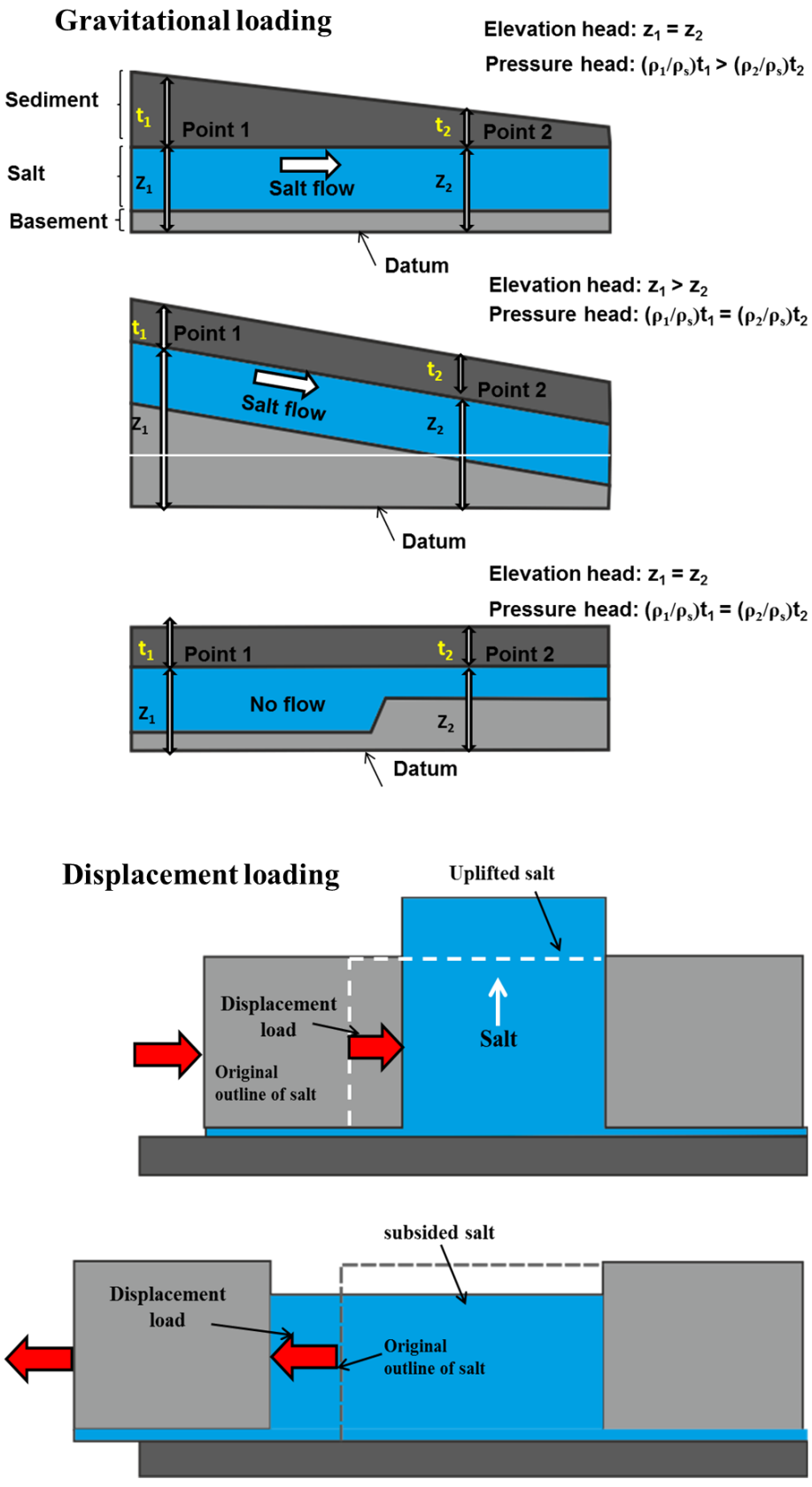

Figure 1.11: Factors promoting salt flow includes gravitational loading, displacement loading and thermal loading (Modified after Hudec & Jackson, 2007).

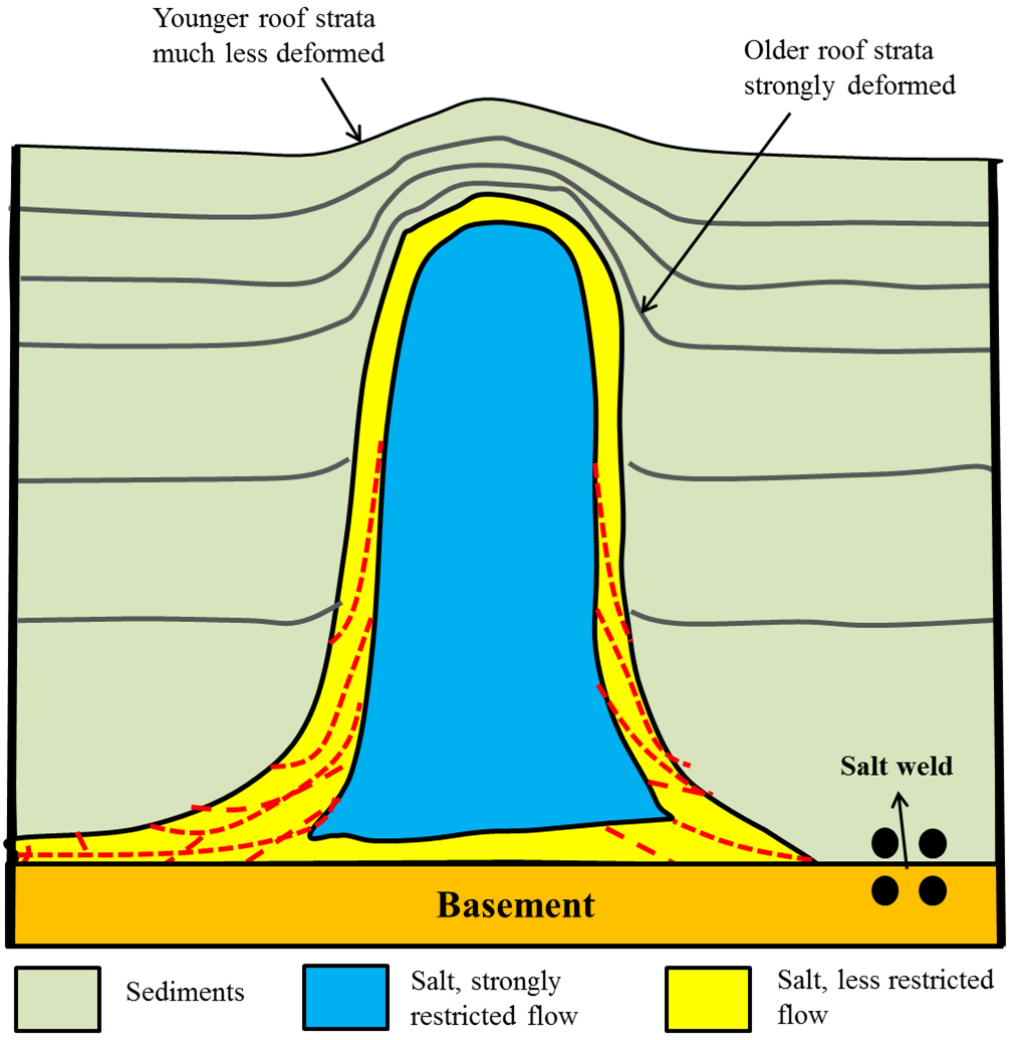

Figure 1.12: Factors resisting salt flow include the strength of the overburden and boundary friction within the salt layer. Salt deformation is accomplished if the roof is thin and weak but becomes progressively more difficult as roof thickness increases. Secondly, salt is strongly sheared near the edges of salt bodies during flow, a phenomenon causing resistance to deformation. If a salt layer becomes too thin, salt flow is restricted (Modified after Hudec & Jackson, 2007).

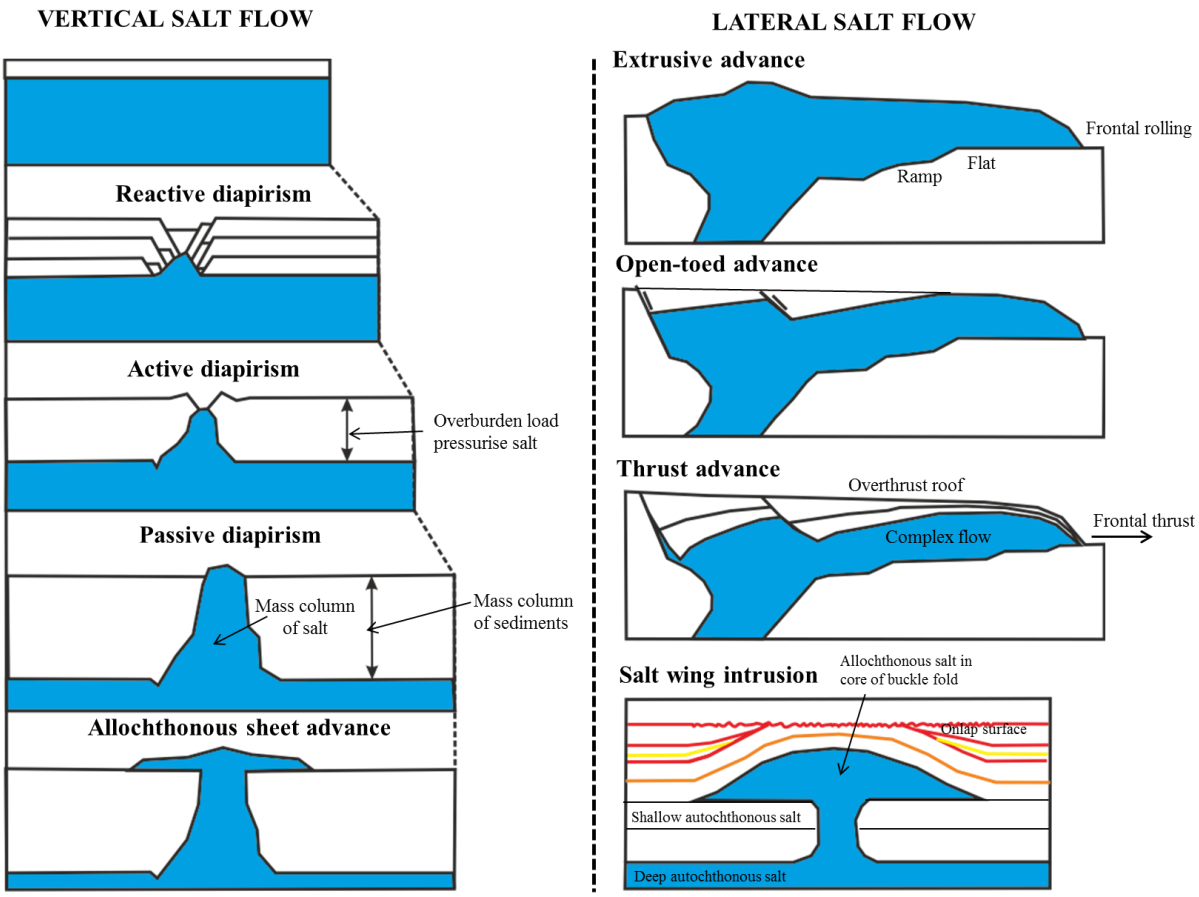

Figure 1.13: Vertical vs. lateral salt flow. Salt flows laterally because the pressure produced by the salt against the sediments is not balanced by the pressure produced by the sediments against the salt. In this case, salt has a propensity to flow upward, because the confining pressure in the sediments is always higher than the confining pressure above the salt. Vertical salt flow does not necessarily progress through all of these stages. The maturity of a given structure depends on availability of salt, total amount of extension, and relative rates of extension and sedimentation. Modified after Vendeville and Jackson (1992a) and Hudec and Jackson (2006)

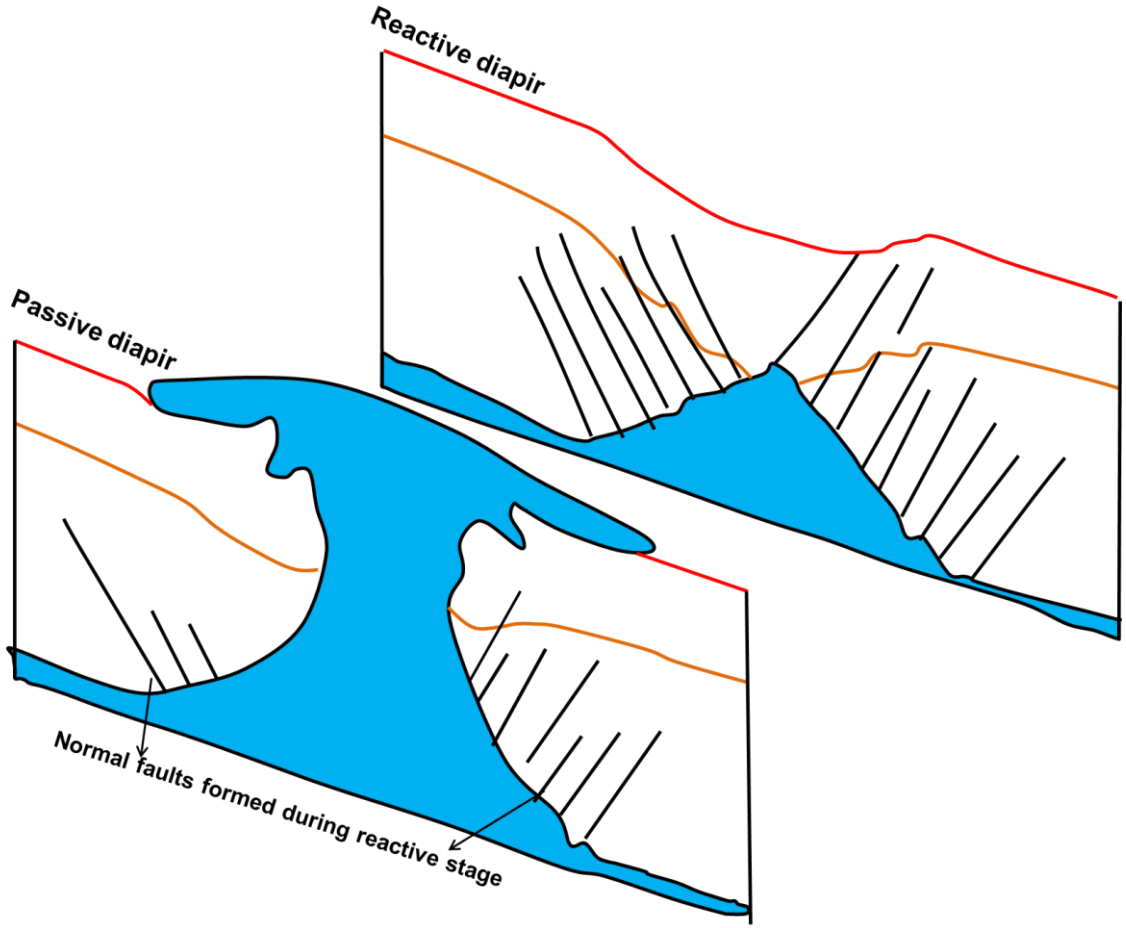

Figure 1.14: Serial sections depicting structures formed during reactive and passive stages of salt development. Modified after Vendeville and Jackson (1992a) and Hudec and Jackson (2006).

1.4 Fault geometry and techniques for displacement analyses

A fault comprises a surface or narrow zone with visible shear displacement (Fossen, 2010). In contrast to shear fracture, fault is used to describe composite structures with offsets in the order of a meter or more. Faults are categorised on the basis of the overall sense of slip, either as dip-slip or strike-slip faults (Twiss and Moore, 2007; Fossen, 2010). Dip-slip faults include normal, reverse and thrust faults while strike-slip faults are described as dextral or sinistral depending on their sense of lateral movement (Twiss and Moore, 2007). As the petroleum industry is chiefly interested in subsurface faults that could trap hydrocarbon, 3D seismic data offers the best dataset to identify and map faults in the subsurface. Discontinuous reflectors indicate fault locations, and the dip separation is estimated by correlating seismic reflectors across the faults (Badley, 1985; Brown, 2004; Schultz and Fossen, 2008). However, sub-seismic faults are often unresolved in a seismic volume. Increasingly, the industries have found alternative to model the behaviour of these from similar outcrop exposures e.g. (Jackson et al., 2006; Rotevatn and Fossen, 2011)

In order to test the third hypothesis provided in the rationale, a succinct description of displacement analyses used for characterising faults is provided in section 1.4.1. In addition, a list and definition of fault terminologies used in the thesis are provided in Appendix VIII.

1.4.1 Fault displacement profiles

Displacement distributions along normal faults usually show maximum displacements (d_{max}) at the centre of the fault plane, gradually decreasing towards the tips (Barnett et al., 1987). Displacement profiles may vary from mesa-type, cone-type to hybrid profiles

comprising both C- and M-types (Figure 1.15; after Muraoka and Kamata, 1983; Kim and Sanderson, 2005). The position of d_{max} for C-type profiles corresponds to the nucleation point where fault propagation was initiated (Mansfield and Cartwright, 1996). Importantly, variations on the M-type profiles have been attributed to resistance at the tip of the propagating fault by a mechanically competent rock (Muraoka and Kamata, 2003). Hybrid displacement and distance plots hint at fault linkage and segmentation (Baudon and Cartwright, 2008; Walsh and Watterson, 1989). Elliptical fault displacement profiles are consistent with the propagation of blind faults (Baudon and Cartwright, 2008). In addition, blind faults are characterised on seismic profile by (1) plunging upper-tip line and throw contours geometry, (2) presence of upper-tip propagation folds, and (3) absence of stratigraphic evidence for the fault intersecting a free surface, i.e. seafloor (Baudon and Cartwright, 2008).

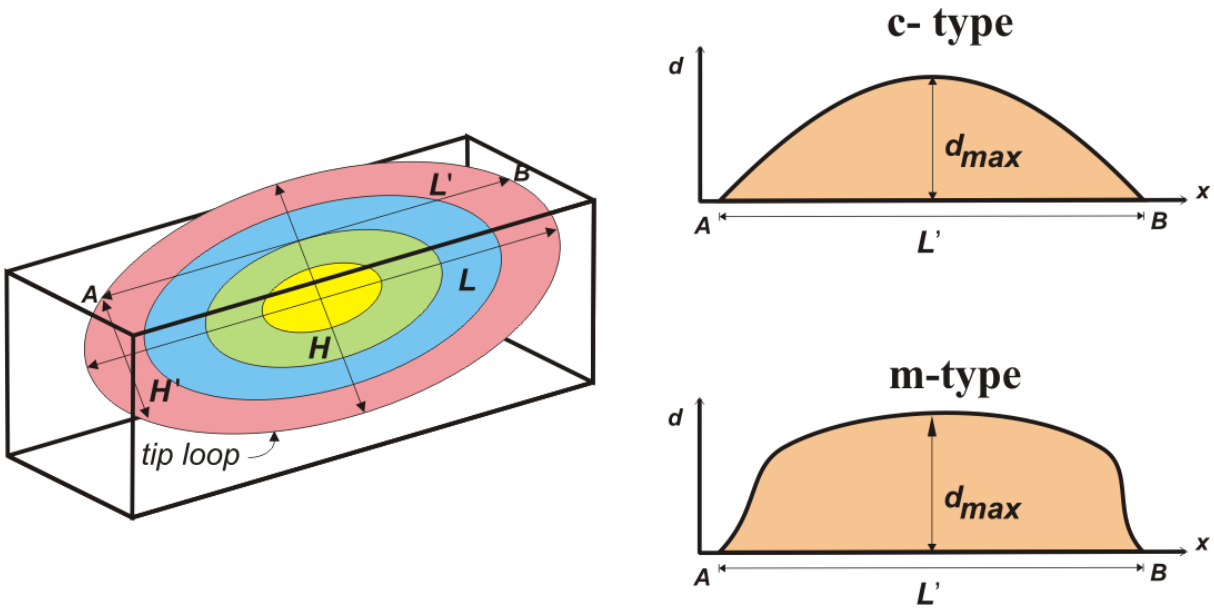

Figure 1.15: Displacement distribution on an elliptical fault surface with a length L and height H. Displacement is highest at the centre and zero at the tips. The fault intersects the upper surface of the block along line A–B. Displacement (d)–distance (x) plot for faults of the C- and M-types along line A–B. Modified after Muraoka and Kamata (1983) and Kim and Sanderson (2005)

1.5 Mass-transport deposits and salt structures: Expected geometries and impacts on MTD recurrence

Overburden strata over growing salt structures are generally thinned or completely removed by erosion, which result in the accumulation of the eroded strata in peripheral salt minibasins (Giles and Lawton, 2002). Deformation related to halokinesis is expressed not only as faulting of the overburden but also as regional folding and localized subsidence, followed by the gravitational collapse of flanking strata to salt structures (Davison et al., 2000; Tripsanas et al., 2004). The eroded strata eventually is described as MTDs and based on their internal cohesion are classified as "slides," "slumps" and "debris flows" (Nemec, 1990; Masson et al., 2006a).

Submarine slides are composed of coherent strata with minor internal deformation. The presence of slump deposits in a mass-transport deposit implies larger travel distances and internal deformation than with slides (Gamboa et al., 2011). Debris flows are characterized by presenting highly disaggregated strata and no preservation of internal strata within a cohesive matrix (Masson et al., 2006b). Large blocks of remnant or rafted strata can be ubiquitous within the debris flow deposits, either close to the MTD source areas or transported to toe regions of submarine landslides through gravitational processes such as hydroplaning (Ilstad et al., 2004; Minisini et al., 2007; Urgeles et al., 2007; Deptuck et al., 2007; Dunlap et al., 2010).

Individual blocks are named as "remnant" if left in situ, or "rafted" if substantially translated during slope failure. Remnant and rafted blocks have a wide range of sizes, from meters to hundreds of meters, but this tends to decrease with larger travel distances (Canals et al., 2004; Davison, 2004; Gee and Gawthorpe, 2006; Bull et al., 2009;).

Rafted blocks have been comprehensively identified in the vicinities of salt structures, either derived from local slope instabilities (Davison et al., 2000; Tripsanas et al., 2004) or distant (upslope) landslides (Dunlap et al., 2010). However, no data has yet been presented on the effect of salt diapirs neither on slope stability, nor on the relative distribution of remnant /rafted blocks over salt structures. Remnant blocks are considered as being *in situ* elements from the pre-failure strata that were not removed by erosion. Such blocks show vertical stratigraphic continuity with underlying non-MTD strata, with the absence of any gliding surface, similar to the features described by Moscardelli et al. (2006) and Alves (2010).

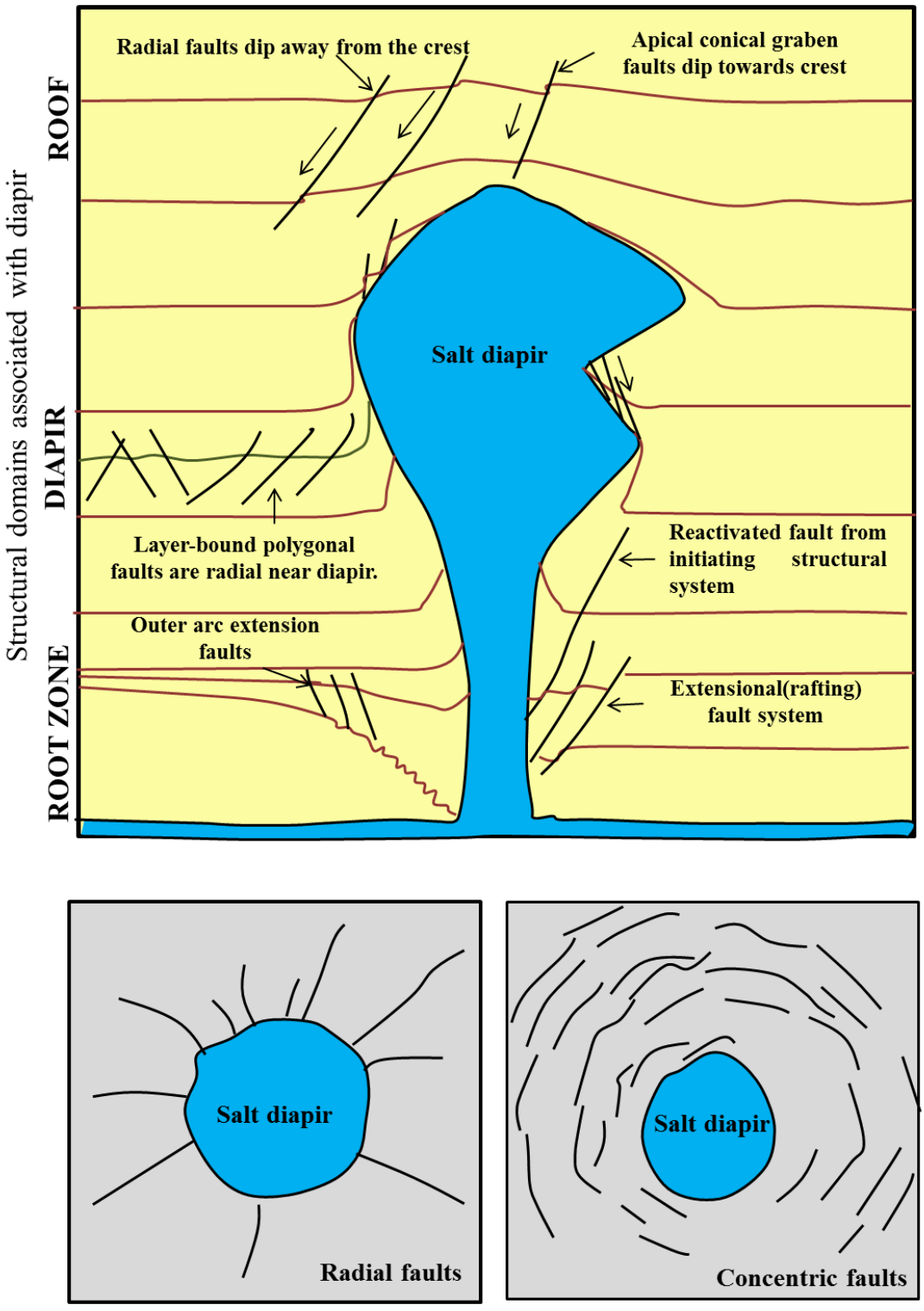

Figure 1.16: Fault geometry around a salt diapir. Radial and concentric faults are shown conspicuously in map or plan view (Modified after Stewart, 2006).

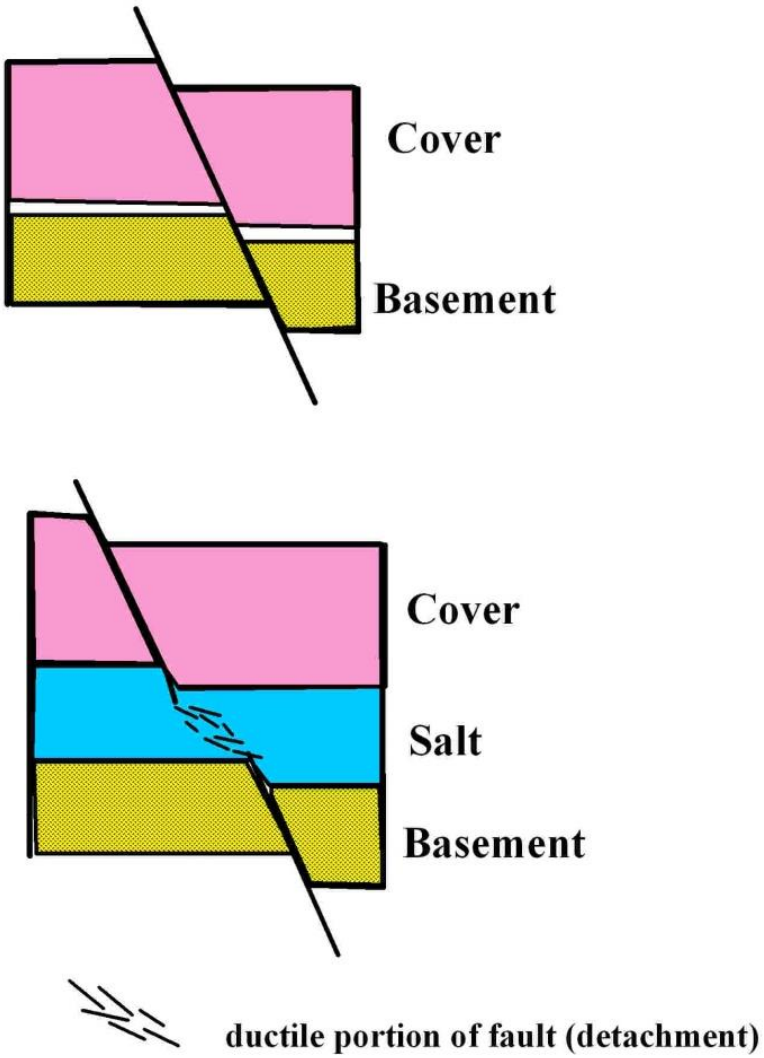

Figure 1.17: The rate of basement fault displacement is governed by the displacement ratio (Dr). D (basement fault displacement), T (viscous layer thickness), Dr = T, /D (a) Tv < D, Dr < 1. Basement fault 'hard' linked to cover in a continuous brittle strand. (b) T, > D, Dr > 1. Basement fault 'soft' linked to cover fault via ductile detachment in the salt, resulting in an extensional ramp-flat geometry (Modified after Koyi et al., 1993).

1.6. Fault systems and mass-transport deposits around active diapirs

Fault propagation close to salt diapirs can be thought of as occurring in two modes, (1) as fault propagation directly related to diapirism, whereby the influence of basement fault is neglected (Figure 1.16) and , (2) as fault propagation beneath the salt structure, which affect the salt and its overburden cover (Figure 1.17). In the first instance, overburden layers are extended and deformed during diapir growth (Davison, 2004; Stewart, 2006). Faults produced by extension of the overburden rocks include radial, crestal, collapsed crestal graben and concentric normal faults (Alsop, 1996; Rowan, 1999; Stewart, 2006). Extensional faults parallel to the salt structure are formed during reactive diapirism (Hudec and Jackson, 2007; Vendeville and Jackson, 1992b). Radial faults are formed normal to the orientation of salt diapirs (Stewart, 2006). During active diapirism, parallel faults are formed displaying concentric pattern in map view (Stewart, 2006). Generically, these faults are called crestal faults, displaying varied geometries and arrangements. The propagation of these faults is reliant on the dimension and behaviour of the salt body and is independent of the basement tectonics. In addition, synclinal faults are formed in salt withdrawal basins adjacent to salt anticlines e.g. (Alves et al., 2009).

In basement-linked fault propagation, a single fault strand does not always pass directly from the basement to cover. The cover and basement faults are kinematically linked and could be considered to represent a single fault surface, composed of brittle and ductile portions (Figure 1.17). The magnitude, direction, and rate of basement fault displacement is governed by the displacement ratio, *Dr* (Koyi et al., 1993). Dr is the ratio of the thickness of the viscous layer, Tv divided by the basement fault displacement D (Figure 1.17).

The following models are suggested to explain the possible impact of mass-wasting on geological structures formed adjacently to active salt diapirs.

1. **Erosion, cannibalisation and draping of faults scarps/scouring of palaeo channels**: The erosive nature of the basal shear surface is often expressed as erosional truncations, scours, striations, and grooves on seismic profiles and attribute maps (*cf.* Gee et al., 2005, 2006; Bull et al 2009). This implies that fault scarps present on the margin of active diapirs will be eroded by moving MTDs. The eroded materials are transported and deposited elsewhere in the basin (cannibalized) or possibly incorporated into the resulting deposits (*cf.* Alves et al, 2009, Richardson et al 2011). In a similar manner, palaeo seafloors are sometimes eroded or scoured by newer MTDs. This often results in the evacuation of the headwall region of older MTDs by younger ones. This mechanism has been used to explain some cases of MTDs lacking discernable headwall scarps (*cf.* Bull et al 2009).

2. P**referred rotation of radial and crestal faults in the direction of slumping**: It is often possible to associate the stages of slumping to development of crestal and radial faults on the tip of the growing diapirs. Continued rotation of previously formed faults closest to MTDs was recorded in Central Graben, North Sea (Davinson et al, 2000a). The location of the faults may be in the direction of the rotation of the eroding strata off the salt tip.

3. **Blanketing/decoupling of previously formed synclinal faults**: - As slumping occurs at the tip of growing salt diapirs, MTDs derived from these latter structures will be deposited closest to the flanks of the diapir or transported farther away into adjacent

withdrawal basins. The new MTDs can blanket earlier formed faults, most especially synclinal faults formed in salt withdrawal basins adjacent to growing salt structures (*cf.* Alves et al 2009).

4. **Strain absorbers**: MTDs can serve as strain absorbers, partitioning or balancing the deformation beneath and above. MTDs are sometimes faulted as a result of renewed faulting underneath them. Common fault types include normal, reverse and strike slip faults with relatively small throws (Richardson, 2011). The movement of salt of an active diapir may cause inversion of the previously formed faults in and around the MTD. MTDs crossed by these kind of faults have implications for vertical fluid flow in sedimentary basins (Gamboa et al., 2010).

5. **Strain Markers**: Mass-wasting sometimes occurs on a deformed palaeo-seafloor, with the deformation resulting from extension, compression or both. Since the mass-wasted material is translated over the palaeo-seafloor, the deformation history of this same surface can be preserved within the MTDs. This characteristic is most prominent in salt-rich continental margins where diapirs have compressed the seafloor producing elliptical structures in map view. The translated mass-transport deposit could be reflected, deflected, ponded or constricted by the pre-existing salt structure.

Post-MTD diapirism implies that the perturbation imposed by rising diapirs will be preserved in a MTD. The strata closest to the diapirs experience the highest strain relative to the rest of the MTDs. The highest strained region can be mapped with confidence using thickness map and other attributes maps.

1.7 Structure or layout of the thesis

The thesis is divided into seven Chapters and seven Appendices. The Introduction written in Chapter 1 highlights the rationale for the PhD, an extensive review of literature on MTDs, salt tectonics and a brief overview of fault behaviours on a salt rich-continental margin. In Chapter 2 is presented a general overview of the geologic setting of the Espírito Santo Basin with its known petroleum systems. Chapter 3 includes the methods used for the research, and description of seismic interpretation techniques. A concise explanation of the descriptive statistical methods and graphs used in Chapter 4 is also presented in Chapter 3. Chapters 4, 5 and 6 comprise the main results Chapters of the thesis. A new method for assessing the source areas of MTDs on salt-rich margins was introduced and investigated in Chapter 4. The importance of MTDs as strata useful to unravel palaeo-strain conditions, and the physics of material translated within the MTD is shown in Chapter 5. Chapter 6 introduced and investigated the relevance of MTDs to the structural decoupling of adjacent fault families. Conclusion and discussions of the major findings in this work are provided in Chapter 7. The appendices include a brief summary of the processing algorithm, additional seismic profiles, data analysed in Chapters 4 to 6 and atlases of MTDs and kinematic indicators for MTDs.

Important contributions to knowledge from this research are:

- The proposition of a novel method for assessing provenance of mass-transport deposit in salt-rich margins.
- The demonstration of how valid is the application of statistics to seismic interpretation.

- The assessment of MTDs importance for different stages of diapirism, and associated overburden faulting.
- An explanation of the enigma around ramps and flats bordering diapirs.
- The demonstration of the importance of MTD as indicators of fault duration and activity.

Chapter 2

Geologic Setting of the Espírito Santo Basin

2. Location of the study area

The Espírito Santo Basin is located on a passive margin that evolved during the Late Mesozoic breakup of Gondwana (Figure 1.1). The basin is located on the southeast continental margin of Brazil, and covers an area of ~18, 000 km^2 onshore and ~200, 000 km^2 on its submarine domain (Mohriak, 2003). The Espírito Santo is separated from the Mucuri and Cumuruxatiba Basins by the Abrolhos Plateau, a volcanic plateau originating in the Palaeogene (Mohriak, 2005). To the south, the basin gradually extends into the Campos Basin (Ojeda, 1982; Chang et al., 1992; Fiduk et al., 2004).

2.1. Tectonic framework and stratigraphic evolution

As most sedimentary basins in the South Atlantic, the tectonic evolution of the Espírito Santo Basin is divided into four stages, which resulted in five depositional Megasequences (Fiduk et al., 2004; Figure 2.1 and 2.3). A first pre-rift stage of Late Jurassic to Berriasian age was followed by the syn-rift stage (Berriasian to Late Aptian). The transitional stage spans the late Aptian to Early Albian, and the drift stage starting in the Early Albian up to the Holocene (Ojeda, 1982; Gibbs et al., 2003; Figure 2.2 and Figure 2.3). The stratigraphic column of the Espírito Santo basin comprises pre-rift packages deposited prior to the rift/breakup of the Western Godwana. This phase coincided with the onset of crustal uplift and development of peripheral rift basins (Ojeda, 1982; Chang et al., 1992; Mohriak, 2003).

Syn-rift tectonics is characterized by intense tectonic activity and formation of rift basins associated with the divergent movement of the South American and African plates (Franca et al., 2007). Rift-related packages are divided into Syn-rift I and II (Fiduk et al., 2004). Syn-rift sedimentation therefore is dominated by deposition of lacustrine materials in fault-controlled depressions, and carbonates over adjacent

structural highs. Syn-rift megasequences include the Cricaré and Mariricu Formation, which are composed of fluvial sandstones and syn-tectonic conglomerates intercalated with magmatic extrusives (Ojeda, 1982; Chang et al., 1992; Mohriak 2003; Fiduk et al., 2004).

Deposition during the transitional phase from syn-rift to the marine drift phase coincided with a period of tectonic quiescence and cessation of basement fault activity (Figure 2.3; Ojeda, 1982). During the transitional phase there was significant erosion of the crest of rotated rift blocks, and topographic smoothing occurred on the margin (Mohriak 2003; França et al., 2007). In parallel, the transitional phase is marked by deposition of thick sequences of anhydrite and halite resulting from extreme evaporation in an arid climate (Demercian et al., 1993; Mohriak, 2003; Franca et al., 2007). Two evaporitic cycles were recorded on the Eastern Brazilian margin during the transition from rift to drift stages; the Paripueira and Ibura evaporites (Ojeda, 1982). The early Aptian Paripueira evaporites are continuous with their West African correlatives. The late Aptian Ibura evaporites are marginal deposits restricted to the Brazilian margin (Ojeda, 1982).

Evaporites in the Espírito Santo Basin were later deformed by a combination of differential sediment loading, gravity spreading and downslope gravity gliding (Demercian et al., 1993; Fiduk et al., 2004). As a result of such a complex halokinesis, six salt fairways were developed offshore (Fiduk et al., 2004). Included in these fairways are composite structures such as salt rollers, vertical salt diapirs, allochthonous salt canopies, shallow canopies coalescing from the combination of two different tongues, deep salt canopies, and thrusted salt nappes (Fiduk et al., 2004). The area of

interest to this study lies in the region of the vertical salt diapirs (Figure 2.1). Some of these diapirs ceased their movement in Cretaceous times, while others are still growing and exposing their crests on the seafloor (Fiduk et al., 2004).

Cenozoic successions in the Espírito Santo Basin are composed of aggrading strata deposited during transgressive and highstand episodes (Mohriak et al., 1995). The lower transgressive succession, the São Mateus Formation, comprises shallow-water Albian strata intercalated with coarse sandstones. Coincidentally, the carbonate platforms of the Regência Formation were deposited in a distal slope position during the earlier transgressive episodes (Figure 2.3). Late Albian deepening of the basin resulted in the deposition of dark mudstones, turbiditic sandstones and carbonate breccias which were overlain by mudstones of the Urucutuca Formation (Fiduk et al., 2004; França et al 2007).

Prograding strata marking regressive episodes and periods of submarine canyon incision are observed in seven specific stratigraphic intervals (Fiduk et al., 2004; Moreira and Carminatti, 2004). As a result, thick carbonate and clastic sequences were accumulated on the continental shelf during the late Cenozoic, with important volumes of strata prograding to the region where the study area is located (Figure 2.1). In this same region, late marine regressive Megasequences are associated with reactivation of ancient rift structures and emplacement of Abrolhos Plateau, a volcanic high emplaced from Eocene-Oligocene times (Demercian et al., 1993; Cobbold et al., 2001; Franca et al., 2007). A resulting unit, the Abrolhos Formation (Eocene-Oligocene) resulted from the erosion of this new magmatic plateau. Neogene deposition is dominated by mudstones and turbidites of the upper Urucutuca Formation, sandstones of the Rio Doce

Formation and bioclastic calcarenites from the Caravelas Formation (França et al., 2007; Figure 2.2)

During the drift stage, there was a continued spreading of the South American and African plates with eastward tilting, increased thermal subsidence and sediment loading affecting the deeper part of the Espírito Santo Basin (Mohriak, 2003). Uplift and erosion of the Abrolhos Plateau during the late drift stage culminated in the deposition of mixed siliciclastic and volcaniclastic material by turbiditic flows along submarine channel systems, fans and mass-wasting (Bruhn and Walker, 1997; Mohriak, 2003; Franca et al., 2007; Gamboa et al., 2010). In such a setting, mass-wasting events in the interpreted seismic volume result from regional tectonic movements (Mohriak et al., 1995; Duarte and Viana, 2007), and slope instability events related to prolonged halokinesis and diapir growth (Fiduk et al., 2004).

In summary, the post-Jurassic stratigraphy of the Espírito Santo Basin can be divided into the Nativo, Barra Nova and the Espírito Santo Groups (França et al 2007; Figure 2.2). The Nativo Group sits unconformably over the Precambrian basement and is Neocomian to Cenomanian in age. The upper Mucuri Member of the Mariricu Formation is composed of alluvial, fluvial and lacustrine sandstones with interbeds of organic-rich shales (Figure 2.2). The Albian Barra Nova Group consists of sandstone deposited in fan delta systems, as well as carbonate platform sediments. The carbonates are known as the Regência Member and the sandstones are part of the São Mateus Member (Fiduk et al., 2004; França et al., 2007).

The Espírito Santo Group is diachronous and was deposited from the Upper Cretaceous to the Quaternary (Turonian to Pliocene). The group comprises three distinct lithostratigraphic members; Urucutuca, Caravelas and Rio Doce (Bruhn and walker, 1993; Fiduk et al., 2004; França et al., 2007). The Urucutuca Formation is composed of shale and calcareous shale intercalated with turbidites sands at its base. Lithologically the unit grade into sandy turbidites, marls and turbidites composed of volcaniclastic materials at its upper part. The Rio Doce Formation and Caravelas member are composed of sandstones and turbidite sands with marls respectively (Franca et al., 2007; Alves 2012).

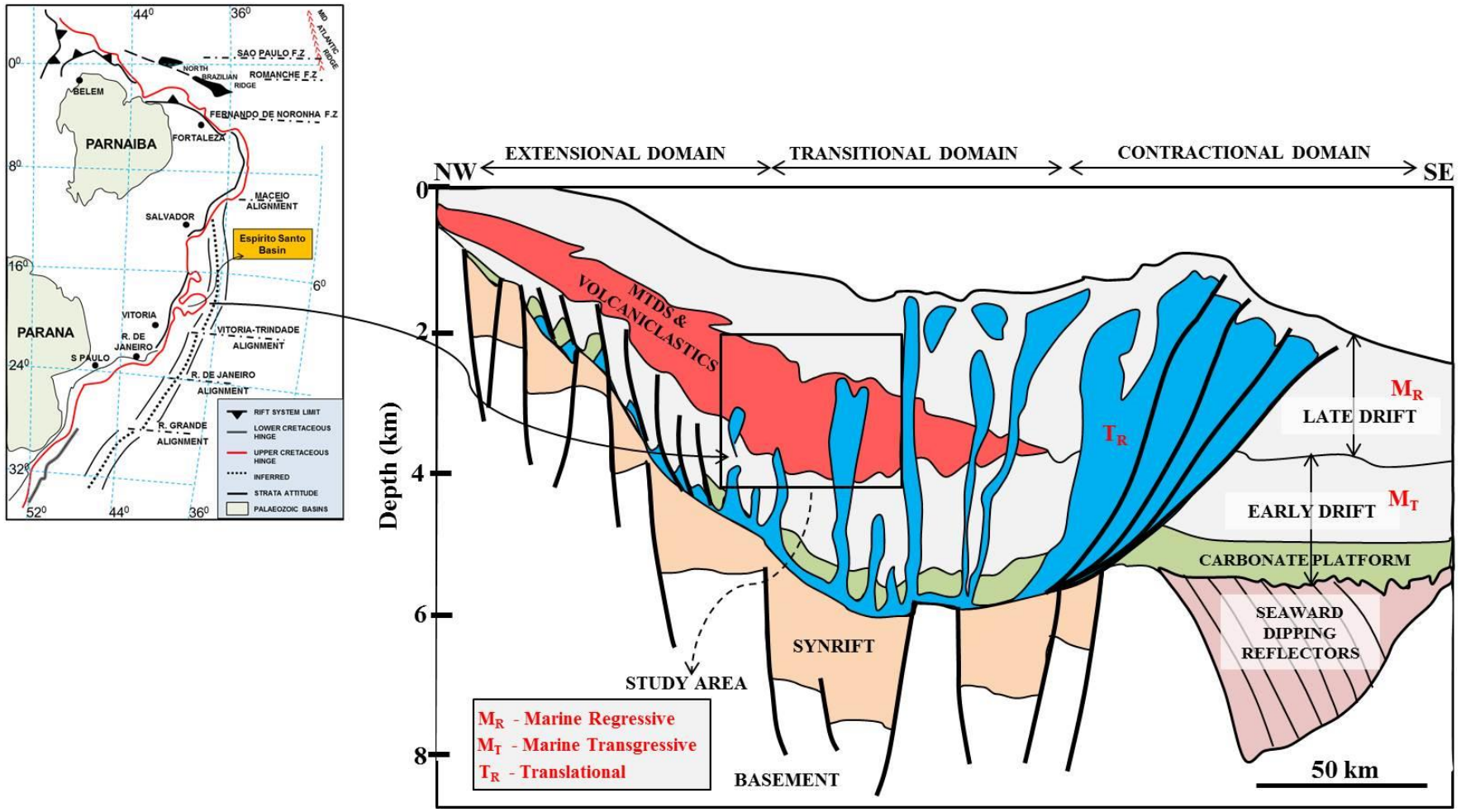

Figure 2.1: Relative location of the study area on the continental slope of Espírito Santo. Modified after Fiduk et al. (2004) and Gamboa et al. (2010, 2011). *Inset: Tectonic outline of Brazilian continental margin (Modified after Ojeda, 1983).*

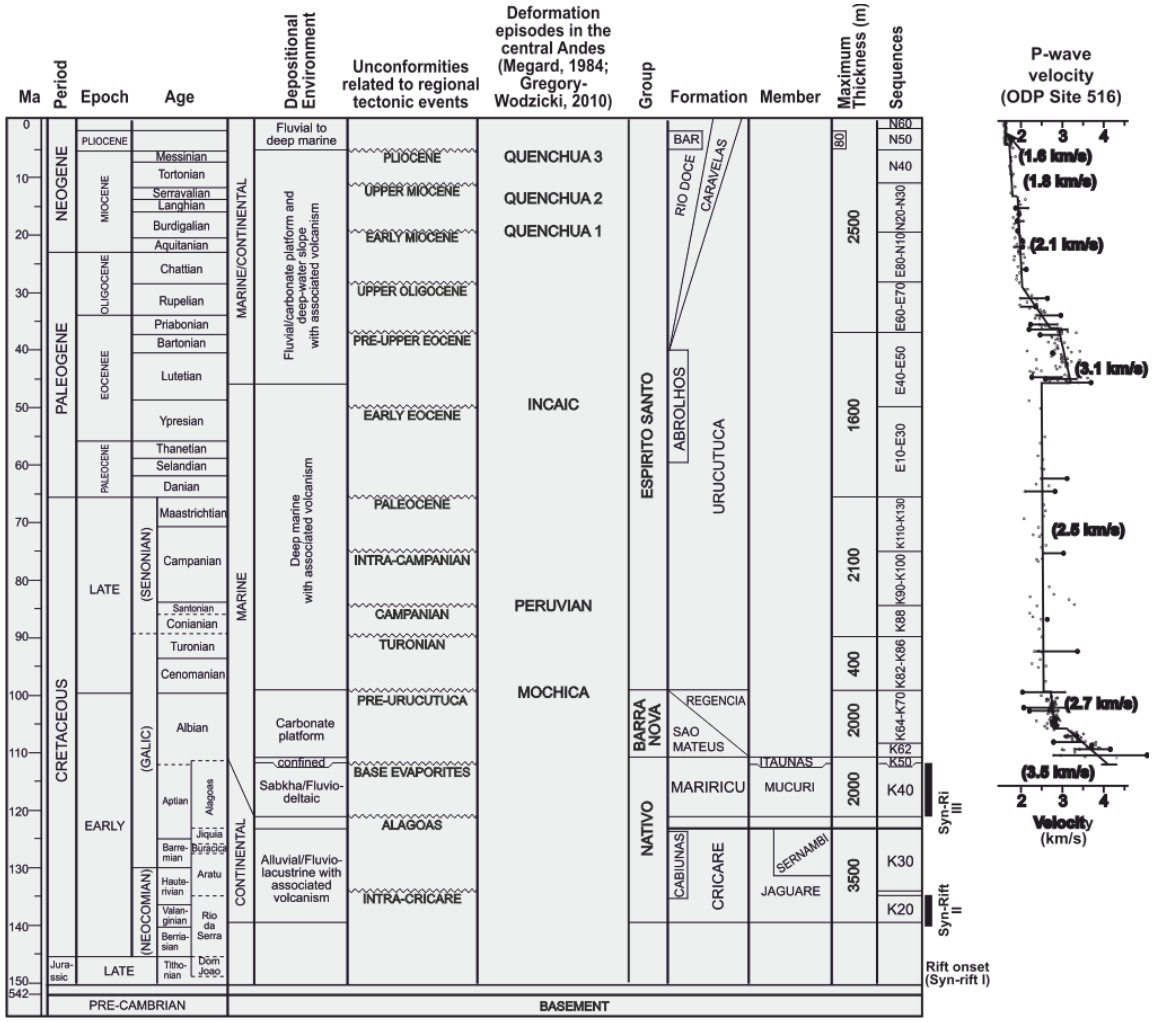

Figure 2.2: Stratigraphic column of the Espírito Santo basin, showing major megasequences and distinctive regional unconformity surfaces (Modified from Alves et al., 2009 and França et al., 2007). Also shown is the velocity information for depth conversion as obtained from DSDP Site 515 (Barker et al., 1983).

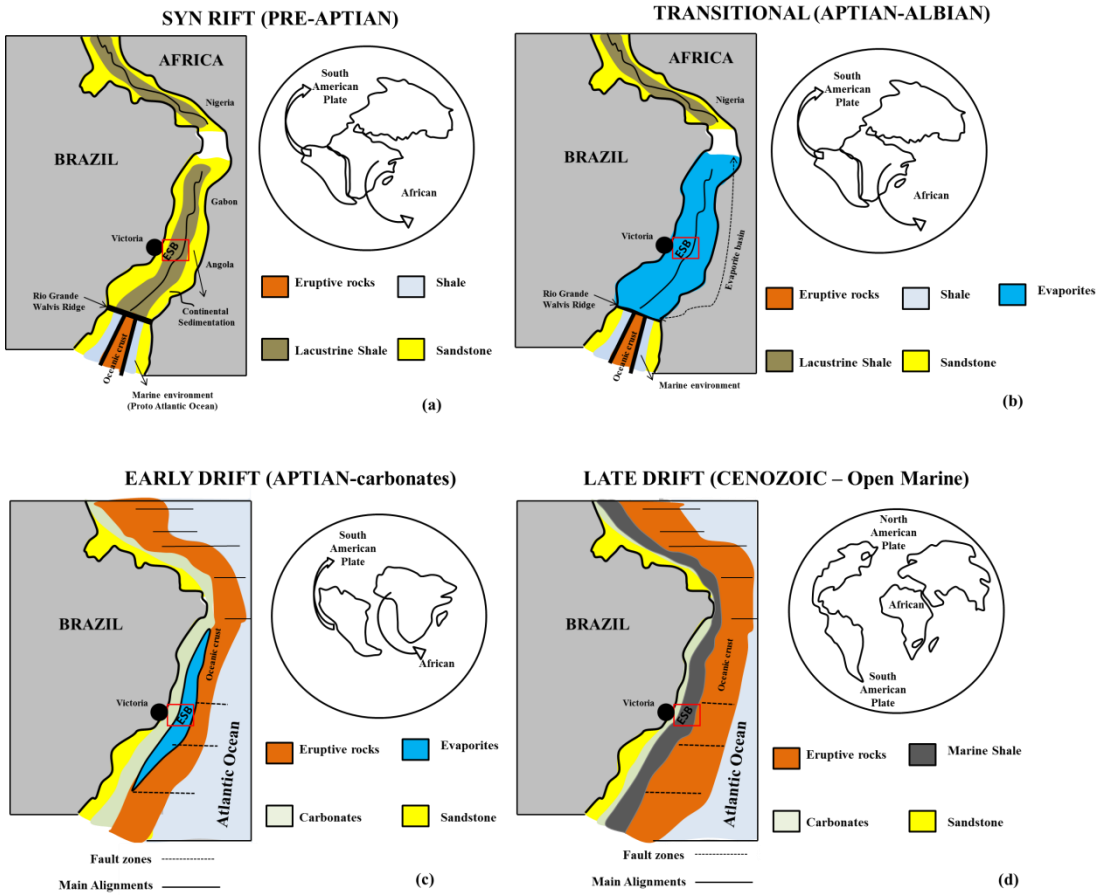

Figure 2.3: Paleogeography and plate reconstruction of the Espírito Santo Basin during the opening of the South Atlantic, from Aptian to Holocene. The syn-rift stage is dominated by continental environments, followed by the deposition of thick masses of evaporates. The drift phase is characterised by shallow--water carbonate platforms and open marine sedimentation. The relative location of the Espírito Santo Basin is highlighted by the red box (Modified from Ojeda, 1982 and Chang et al., 1992).

2.1.2 Structural setting of the Espírito Santo Basin

The structural framework of the East Brazilian Rift System (EBRIS) is reflected in the Espírito Santo Basin. This framework includes: a) antithetic tilted step-fault blocks, b) synthetic un-tilted step-fault blocks, c) structural inversion axes, d) hinges with compensated grabens, e) homoclinal structures, f) growth fault with rollovers, g) shale or salt diapirs, and h) igneous structures (Ojeda, 1982). These structures reflect continental extension and rifting associated with the opening of the Southern Atlantic Ocean (Ojeda, 1982; Chang et al., 1992; Mohriak 2003; Fiduk et al., 2004).

Specifically, the Espírito Santo Basin comprises a series of horsts, grabens, and halokinetic faults. The study area lies in the region of vertical salt diapirs on the mid-continental slope (Figure 2.1). Post-salt potential reservoir units were structural compartmentalized by halokinesis through Cenozoic times. This resulted in the development of three main phases of fault growth, which included normal and reverse faulting of overburden strata on salt crests linking adjacent diapirs (Alves, 2012; Tiago M. Alves et al., 2009; Baudon and Cartwright, 2008b).

1. In early Palaeocene to late Eocene, halokinesis triggered the growth of closely spaced sets of extensional faults on the crests of rising salt anticlines. These faults propagated through the Late Cretaceous and Eocene strata and were mostly truncated by the mid-Eocene unconformity.

2. These fault sets were eroded during the deposition of thick mass-transport complexes (MTCs) and submarine channels in late Eocene to Oligocene times during a period of tectonic quiescence.

3. Reactivation of older faults sets by vertical propagation and dip linkages in late Cenozoic was dependent on movements of Aptian rafts and cessation of tectonic tilting of the slope (Alves, 2012). Faulting of Late Eocene to Holocene strata is less expressive, reactivated faults have poor or no expression on the modern seafloor (Baudon and Cartwright, 2008; Alves et al., 2009).

Fault reactivation in the study area is therefore related to regional-scale reactivation that affected the Southeast Brazilian margin. Structural inversion on the EBRIS was influenced by plate-wide horizontal compression associated with the Andean orogeny (Cobbold et al., 2010). Early Cretaceous and older structures on the obliquely rifted margin of south eastern Brazil were reactivated during the Late Cretaceous and Cenozoic as a result of far-field stresses and hotspot activity. Reactivation occurred in right-lateral mode during three main phases (Late Cretaceous, Eocene, and Neogene), which correlate with changing conditions of convergence at the Andean margin of South America (Cobbold et al., 2001,2010).

2.2 Cenozoic breakup of Africa and Southern America and palaeogeography of the Espírito Santo Basin.

The Gondwana super-continent comprised South America, Africa, Australia and India (Figure 2.4). They were grouped around Antarctica as a central core, with a number of smaller continental fragments. By the early Cretaceous, some 130 million years ago, Gondwana had begun to break up (Chang et al., 1992). The first split divided the continent into two sections, a western half, made up of Africa and South America, and an eastern half with Antarctica, India and Australia. Later in the Cretaceous period, some 120 million years ago, the next of the fragments, India, broke away and began its northward journey through the Indian Ocean (Chang et al., 1992).

The western Gondwana breakup started in the Late Jurassic in the southern extreme of the South Atlantic (Argentina/Namibia-South Africa) and advanced towards the Eastern Brazilian/Western African continental margins by Early Cretaceous (Chang et al., 1992; Mohriak et al. 2008). Rifting started in the south, and propagated toward the north. Consequently, emerging basins on either side of the continents are characterized by similar tectono-sedimentary evolutions; for example, the magma-rich Argentina–Namibia margins, the moderately magmatic Santos-Campos-Espírito Santo-Angola margins, and the magma-poor Bahia-Sergipe-Gabon margins (Figure 2.3). However, these basins can differ from very wide rifted basins with a thick layer of Aptian salt, and to very narrow basins with no evaporite deposition (Davison, 2007).

The south Atlantic rift system created two very different margins in Brazil; the north and East Brazilian rift systems (NBRIS and EBRIS). The North Brazilian Equatorial margin evolved in response to strike-slip motion between Brazil and Africa, producing

complex shear-dominated basins. The EBRIS evolved into a passive margin, as consequence of orthogonal crustal extension (Chang et al., 1992). The EBRIS consists of rifted continental margins which include Pelotas, Santos, Campos, Espírito Santo, Mucuri, Cumuruxatiba, Jequitinhonha, Camamu/Almada, Jacuipe, Reconcavo, Tucano, Jatoba and Sergipe-Alagoas basins (Chang et al., 1992).

2.3 Deformational styles in the case study area

The study area represents a classical example of gravity-controlled passive margins. The Espírito Santo Basin consists of extensional margin near the continental shelf, with progression into a translational area between the shelf and the slope (characterised by vertical salt diapirs) and a contractional part in deepwater regions (around the lower slope). Salt (evaporites) is often considered as a viscous material having a very low strength, and formed the décollement layer for the gravity-controlled systems observed in the study area. Salt starts to deform very soon after its deposition. It leads to symmetric detachment folds, shortened salt diapirs and/or inflated and thickened salt massifs and nappes (Rowan et al., 2004; Brun and Fort, 2011).

2.4 Petroleum system of the study area

Onshore exploration in the Espírito Santo Basin was initiated during the early 1960s, while offshore operations began in 1968 (Vieira et al., 2007). Present day oil production in the Espírito Santo Basin is about 20,000 barrels per day (Vieira et al., 2007). The principal production comes from turbiditic reservoirs enclosed in thick Tertiary and Upper Cretaceous marine slope deposits, near the bottom of Cretaceous submarine canyons (França et al., 2007).

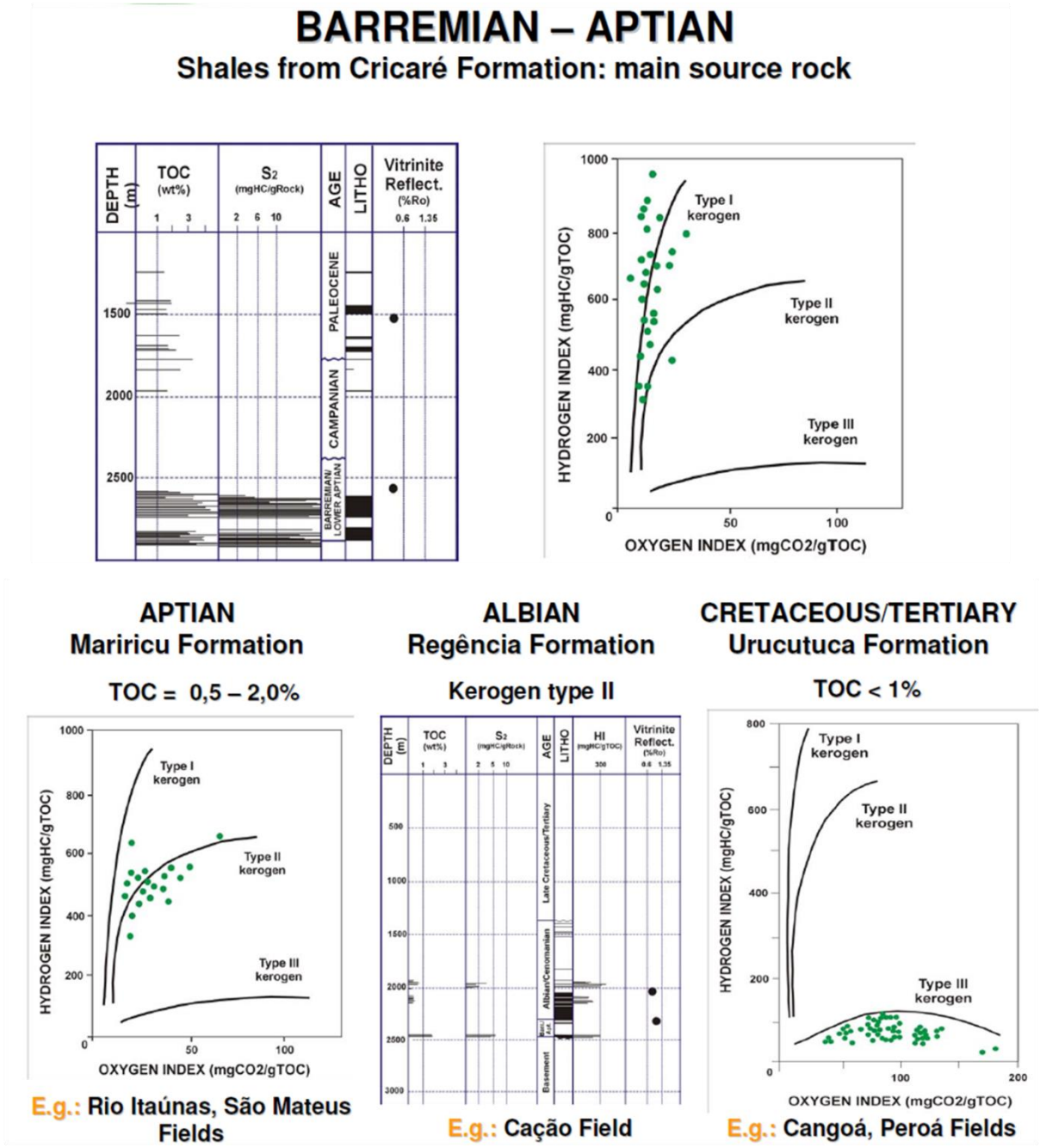

Figure 2.4: Source rock characterization for the Espírito Santo Basin (After Mello and Maxwell, 1990).

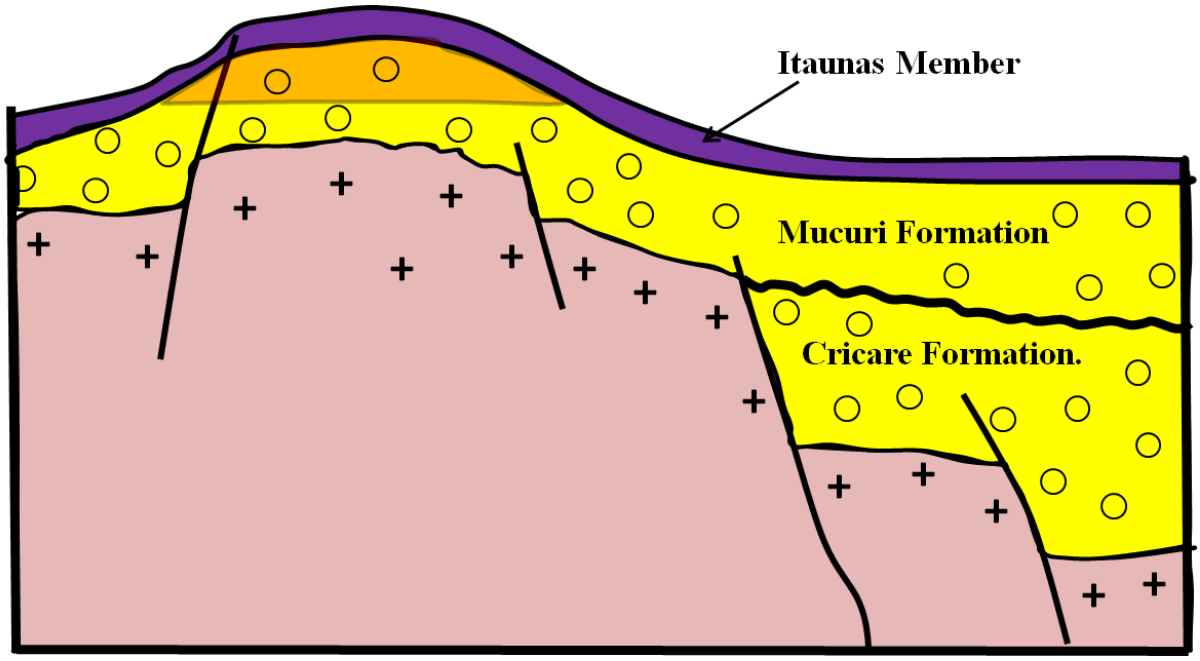

Figure 2.5: Figure highlighting the main trapping mechanisms in rift units, which are linked to the presence of horsts and grabens (Modified after ANP/COPPE, 2008).

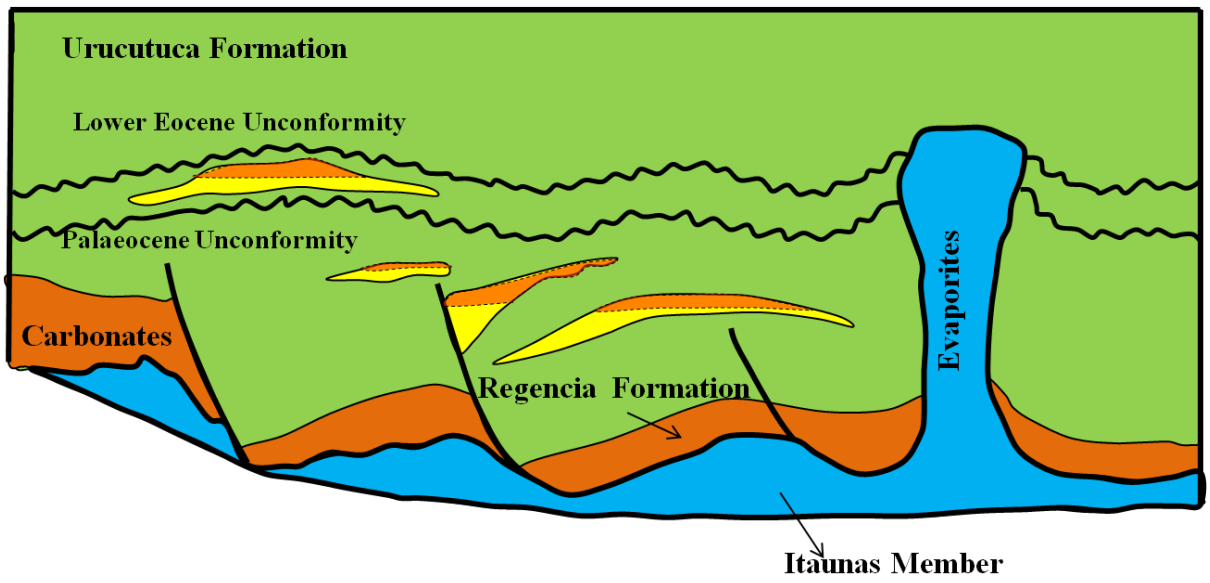

Figure 2.6: Trapping mechanisms in the Espírito Santo Basin also include four-way closures in rollover anticlines located on the flank of salt diapirs (Modified after ANP/COPPE, 2008).

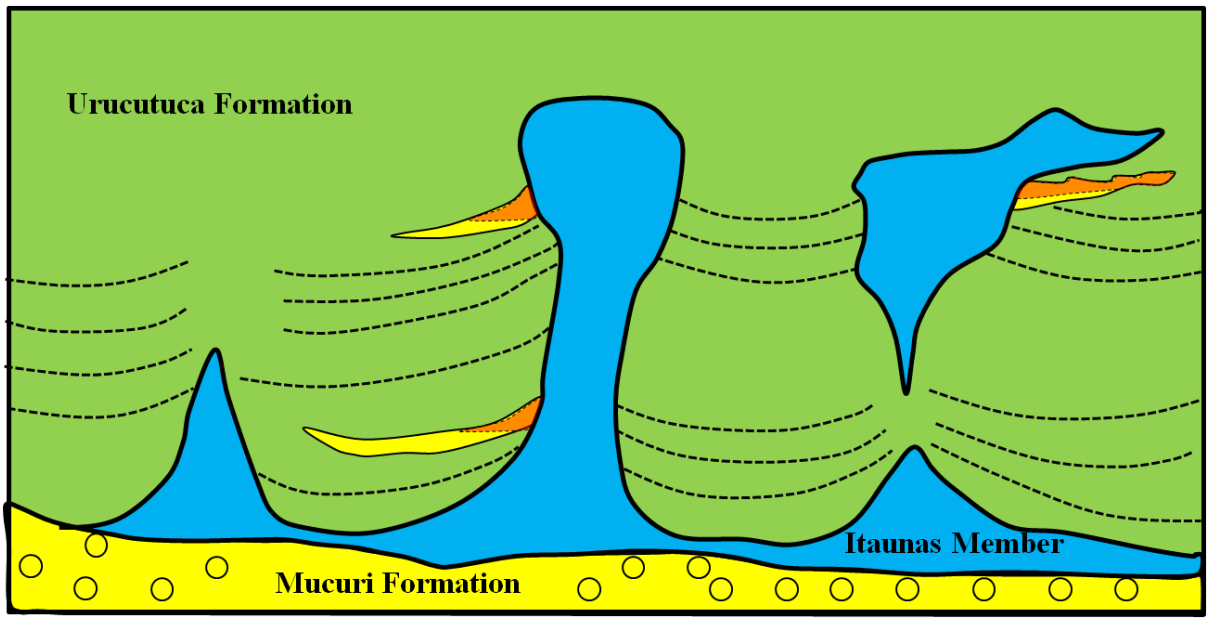

Figure 2.7: Other traps include stratigraphic pinchouts and salt canopies (Modified after ANP/COPPE, 2008).

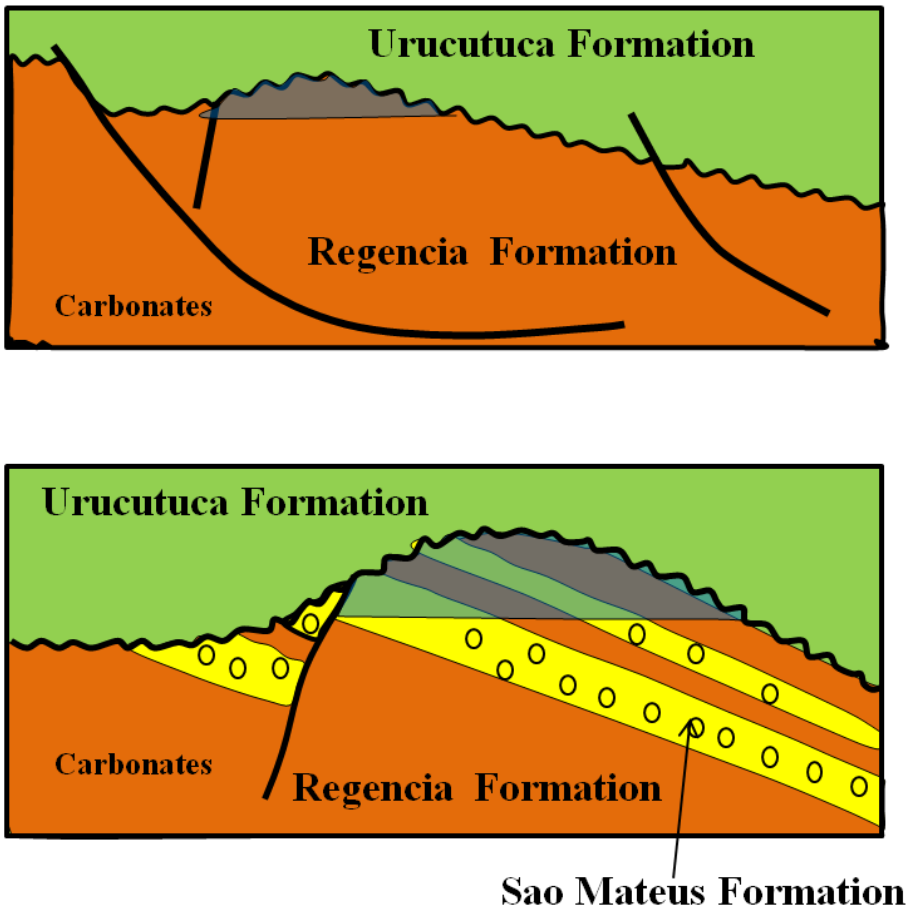

Figure 2.8: Palaeogeomorphic traps are common in drift units and are associated with the incision of submarine canyons and channels (Modified after Carvalho et al., 1989).

2.4.1 Source rocks

The main source rocks in the Espírito Santo Basin comprise the Cenomanian/Turonian deep marine shales of the Urucutuca Formation, shallow to deep marine marls of the Albian Regencia Formation (Post–rift I), Fluvio-marine shales of Aptian Mariricu Formation/Mucuri Member (Transitional), and Lacustrine shales of the Barremian/Aptian Cricaré Formation/Sernambi member (Syn-rift) (Mello and Maxwell, 1990). Fine-grained lacustrine sediments consist of fine sand, silts and dark shales in syn-rift depocentres (Ojeda 1982; Chang et al., 1992; Fiduk et al., 2004). The extreme anoxic conditions in the depocentres allowed the right quality and abundance of organic matter in extensive shale units (Mello et al., 1994; Mohriak 2004).

The Barremian/Aptian Cricaré Formation is characterized by presenting Type I kerogen with average TOC of >5% (Figure 2.4) (Ferreira et al., 2009; Schenk, 2000a). The Urucutuca Formation is dominated by Type III kerogen while the Regência and Mariricu Formations have TOC of 0.5 – 2.0%, respectively, and a predominance of Type II kerogen (Mello and Maxwell, 1990; Coward et al., 1999; Schenk 2000a).

2.4.2 Reservoir rocks

Reservoir rocks mainly comprise turbidites of the Urucutuca Formation. Hydrocarbons are associated with upper Cretaceous and tertiary turbidites sandstones of the Fazenda Cedro palaeo-canyon. The Regência Platform is located in the southern part of the basin where the main producing reservoirs are Albian sandstones and carbonates. Reservoir rocks located north of the Espírito Santo Basin are sandstones of the São Mateus platform. Potential oil bearing sediments also include Cretaceous continental deposits located in rift valleys and transitional shallow-marine

strata stratigraphically trapped below an Aptian evaporite seal. The main reservoir units in the Espírito Santo Basin can be grouped as:

- Cretaceous/Palaeogene (Turbidites-Urucutuca Formation)
- Albian (-Regencia Formation)
- Aptian (Mariricu Formation/Mucuri Member)
- Valanginian/Barremian (Cricare Formation/ Jaguare member)

2.4.3 Traps and seals

Trapping mechanisms in the Espírito Santo Basin include pre-salt horsts and graben, three-way closures (Figure 2.5), and traps related to rollovers on the flank of salt diapirs are common in drift successions (Figure 2.6). Paleogeomorphic traps are commonly associated with the erosion of drift phase sediments by channels and canyon (Figure 2.8). These kinds of traps are common in drift stage carbonate platforms. Other types of traps include stratigraphic pinchouts and complex traps created by allochthonous salt structures such canopies and tongues (Figure 2.7). Cretaceous shales of the Urutuca Formation are the major sealing units for post-salt rocks. Others include Albian calcilutites and marls of the Regência Formation, and salts and shales of the Itaúnas and Mucuri Members, respectively.

2.5 Seismic stratigraphy of the study area

In Chapters 4 and 5, nine horizons were interpreted in order to constrain the geometry of the mass-transport deposits around five salt diapirs. Similarly in Chapter 6, five megasequences and 6 horizons corresponding to the tops and bases of the three MTDs were interpreted. Velocity information for depth conversion was obtained from the

Barker et al., 1983. The correlation panel is presented in Figure 2.9 while the attributes of the horizons are briefly discussed in Tables 2.1, 2.4, section 6.2 and 6.3, respectively.

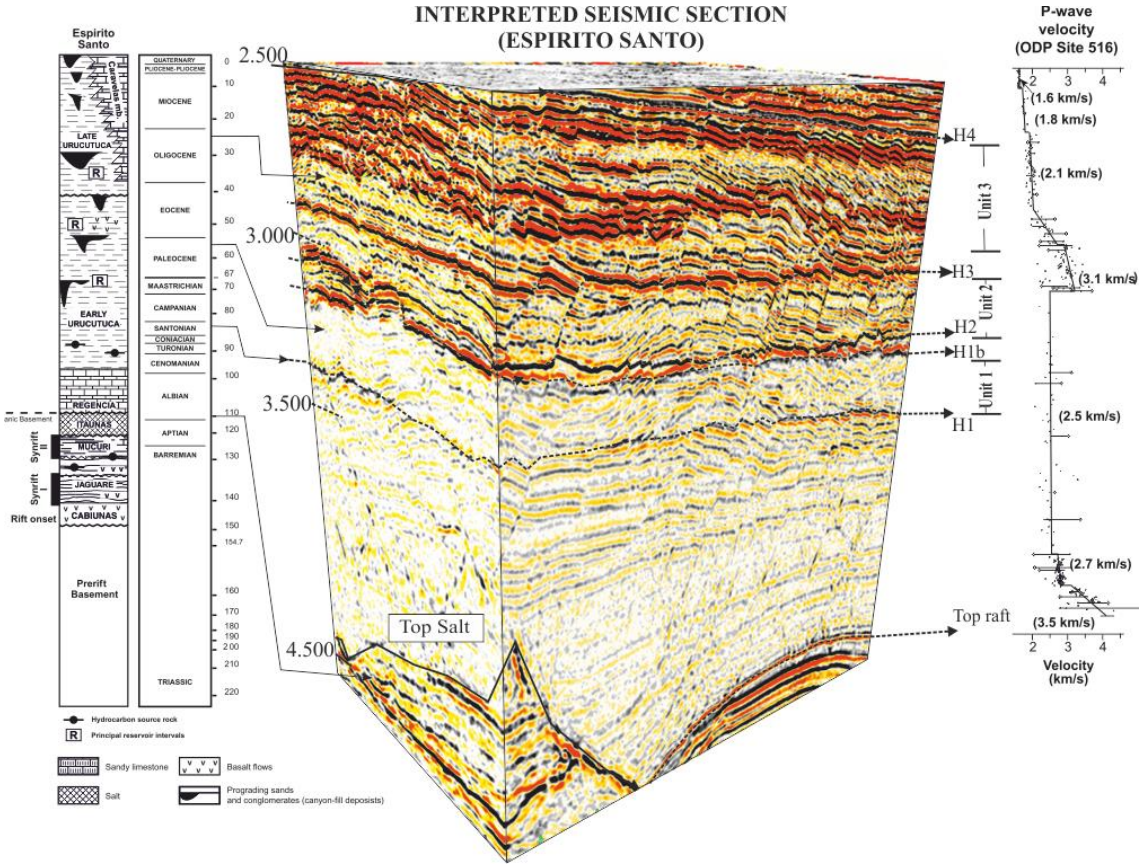

Figure 2.9: Correlation panel for the interpreted seismic horizons. Horizons 1 to 4 reflect regional unconformity surfaces identified by França et al., (2007). The stratigraphic column is modified from Alves et al., (2009) and França et al., (2007). The velocity information for depth conversion was obtained from DSDP well of Barker et al., 1983.

Table 2.1: Seismic character and features hroizons used to constrain the geometry of MTDs interpreted in Chapters 4 and 5.

Horizon	**Seismic Unit**	**Age (Fiduk et al 2004) (Mohriak 2003, 2005)**	**Seismic character**
1	H0	Eocene	Continuous, high amplitude
2	H1	Eocene	Continuous, high amplitude.
3	H2	Late Eocene	Very discontinuous, rugged, low to moderate amplitude
4	H3	Late Eocene	Very discontinuous moderate high amplitude, often stair-cased
5	H4	Oligocene	Continuous, high amplitude
6	H5	Miocene	Continuous, irregular, high amplitude
7	H6	Miocene	Continuous, high to moderate amplitude
8	H7	Miocene	Continuous, high to moderate amplitude

Table 2.2: Seismic character of hoizons interpreted in Chapters 6

Horizon	**Seismic Unit**	**Age (Fiduk et al 2004) (Mohriak 2003, 2005)**	**Seismic character**
1	H1	Late Santonian	High-amplitude, discontinuous reflection
2	H1b	Campanian to Santonian	High-amplitude, discontinuous and faulted layer beneath horizon H2
3	H2	Maastrichtian	High amplitude, discontinuous reflection and densely faulted
4	H3	Early Eocene	High amplitude, moderately faulted reflection
5	H4	Miocene	High amplitude reflection

Chapter 3

Materials and Methods

3. Basic concepts on seismic reflection method

Seismic reflection surveying has greatly improved our understanding of subsurface geology and associated hydrocarbon, mineral, and energy resources (Cartwright and Huuse, 2005). The current state of sophistication of the technique results from the huge investment from the hydrocarbon industry, coupled with the development of advanced electronics and computing technology (Kearey et al., 2002; Cartwright and Huuse, 2005). Seismic data allow geoscientists to map subsurface geological structures and stratigraphic features (Sheriff, 2002). However, the technique involves acquisition, processing and interpretation common with other geophysical methods. A review of techniques of seismic surveying is provided below and methods used in this research are outlined.

3.1 Seismic data acquisition

Seismic waves are created by a controlled source and propagate through the subsurface (Kearey et al., 2002). Some waves will return to the surface after refraction or reflection at geological boundaries at the subsurface. Instruments distributed along the surface detect the ground motion caused by these returning waves and hence measure the arrival times of the waves at different ranges from the source (Figure 3.1). Arrival times may be converted to depth values providing information on the subsurface geological interfaces (Kearey et al., 2002). Body waves generated at seismic source include compressional (P-primary wave) and shear waves (S-waves). Body waves propagate through the interval volume of an elastic solid, P-waves travel in the direction of wave travel while shear waves propagate by a pure shear strain in a direction perpendicular to the direction of wave travel (Sheriff and Geldart, 1995; Kearey et al., 2002; Bacon et al., 2007).

Seismic sources include dynamite, vibroseis, mini-sosie (or wacker), shotguns, electrical sparkers, boomers, weight drops and hammers, air guns and water guns (Figure 3.2; Kramer et al., 1968). The choice of seismic source is dependent on the environment in which the survey is done (land or offshore), the desire to obtain the sufficient energy across the broadest possible frequency, the necessity to obtain a repeatable source waveform, and environmental issues. The main goal of any survey is to reduce the noise ratio compared to the signal produced from the geological interfaces (Sheriff and Geldart, 1995; Kearey et al., 2002). In marine reflection seismic surveys the energy source is typically an array of air guns (a single gun in the case of a vertical seismic profile) with receivers in various combinations towed by a vessel at the sea surface (Figure 3.1). Marine seismic reflection surveys are mostly concerned with P-wave reflections, as fluids do not transmit S-waves (Sheriff and Geldart, 1995; Kearey et al., 2002; Bacon et al., 2007).

Fundamental to the seismic reflection method is the property of a layer termed acoustic impedance (Z), which can be defined as:

$$Z = \rho V \quad \text{---------- (Eq. 3.1)}$$

Where ρ is the density of the rock or sediment and V is the velocity of a P-wave through the rock or sediment. Contrasts in acoustic impedance determines the reflection coefficient at normal incidence (Sheriff and Geldart, 1995; Kearey et al., 2002). The velocity of a P-wave through an isotropic, homogenous solid is controlled by the elastic constants and density of the material (Sheriff and Geldart, 1995). Rocks and sediments are rarely isotropic or homogenous, and as such the velocity of wave will vary

depending on composition, porosity, and fluid content, which may all vary in the three-dimensions (Sheriff and Geldart, 1995; Kearey et al., 2002; Bacon et al., 2007).

3.1.1 3D seismic survey

Seismic surveys are achieved through the design of appropriate line geometry for source and geophone locations. The general practice is to lay out geophones and source set in a rectangular grid, called dip lines and strike lines (2D) or inlines and crosslines (3D) (Stone, 1994). A *dip line* follows (at least approximately) the line of steepest descent down the structure; it minimizes the problem of reflections originating out of the plane of section. A *strike line* follows (at least approximately) a contour line on the structure (Stone, 1994). Initial knowledge of the structure could be derived from surface geology, or regional geology, or satellite imagery, or previous geophysical surveys such as gravity and magnetics (Weimer and Davis, 1996; Vermeer, 2000). For example, if the structural trend of the prospect area trends northwest-southeast, the dip lines will be in NE-SW and while strike lines NW-SE. A simple rectangular grid will suffice for simple structures such as anticlines, faults and simple stratigraphic sequences. For complex structures such as salt dome or a patch reef, an additional number of radial lines will be required to map the flanks of the structure. Planning the survey layout may include planning for both surface and sub-surface factors potentially affecting the seismic processing algorithm, particularly structural local dips and local topography (Stone, 1994).

The layout of 3-D lines involves a greater volume of work that 2-D seismic although their principles are the same. Most surveys are planned using workstations. These allow the planner to superimpose the survey on a topographic map so that operational

problems can be integrated into the planning process. Marine streamer 3-Ds and oblong land 3-Ds have longer offsets in a defined azimuth (Weimer and Davis, 1996; Vermeer, 2000). The choice of this azimuth will depend on the structure and processing methods to be applied. If the long offsets are parallel to dip, then the NMO correction will vary according to dip, and may be difficult to achieve accurately. This problem is mitigated by the use of DMO or pre-stack depth migration. If the long offsets are parallel to strike, then there will be no variation in stacking velocity as a function of dip and the processing becomes simpler (Weimer and Davis, 1996; Vermeer, 2000). However, this method may require closer CMP spacing in the cross-line direction, which may be expensive to achieve (Vermeer, 2000). In addition, the acquisition parameters can sometimes be designed to obliterate certain kind of multiples before the data is processed. These will be discussed further in the next section.

3.1.2 Seismic Processing

The main goal of seismic processing is to obtain the most precise representation of the subsurface information inferred from the seismic. It is central to the seismic prospecting technique, hence, the reason why it is ambiguous and extremely time consuming. The goal of seismic processing is to produce higher signal-to-noise ratios (SNR) than raw seismic data. A typical processing flowchart and algorithm is provided in Figure 3.3 and Appendix I. The readers can refer to Seismic processing technique of Sheriff and Geldart (1995) and Yilmaz (2001) for further details.

3.1.3 Seismic interpretation

The main approaches to seismic interpretation include structural and stratigraphic analyses (Kearey et al., 2002; Bacon et al., 2007) (Figure 3.4 and Figure 3.5). The

former reflect studies of reflector geometry on the basis of reflection times with the sole goal of searching for structural traps containing hydrocarbons. On the contrary, stratigraphic interpretations involve the analysis of reflector sequence as the seismic expression of lithologically-distinct depositional sequences (Kearey et al., 2002; Bacon et al., 2007). In seismic stratigraphy, reflectors are considered to define chronostratigraphical units (e.g. unconformities) and genetically related sedimentary sequences composed of onlap, toplap, downlap and truncations distinguishing overlying and underlying sequences (Emery et al., 1996; Vail et al., 1977). Two dimensional (2-D) seismic data provide a cross-section beneath the Earth's surface unlike 3-D data, which images the subsurface geology as a volume in x, y, z direction. Seismic profiles are usually displayed with vertical (z) axis in two way travel time [TWTT (s/ms)] or depth (m) and horizontal (x, y) axis in metres (m) or kilometres (km). Two-way travel time (TWTT) can be converted to depth using appropriate P-wave velocities (*cf.* Brown, 2005a). A generalised interpretation workflow is shown in Figure 3.6.

3.2 Dataset utilised in this study

The data set in this research consist of a high-quality seismic volume covering ~1310 km^2 in water depths ranging from 100 m to 1800 m (Figure 3.7 and Figure 3.8). The data set was acquired using a dual air gun array and six, 5700 m long streamers. Bin spacing for this zero-phased migrated volume was 12.5 × 12.5 m at a vertical sampling rate of 2 ms. Data processing integrated resampling, spherical divergence corrections, and zero-phase conversions, which were undertaken before stacking 3-D prestack time migration using the Stolt algorithm, and one-pass 3-D migration. Further details on the processing algorithm are provided in Appendix I.

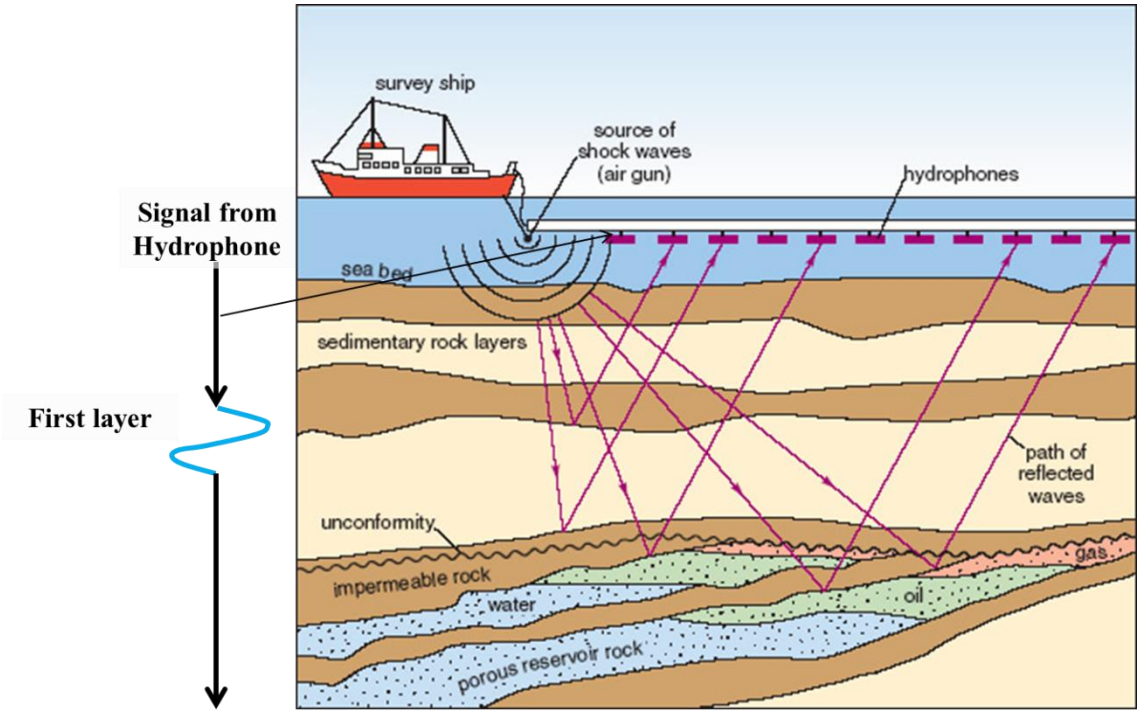

Figure 3.1: The principles and techniques of seismic reflection survey in offshore area (Modified from http://www.epa.gov/esd/cmb/GeophysicsWebsite).

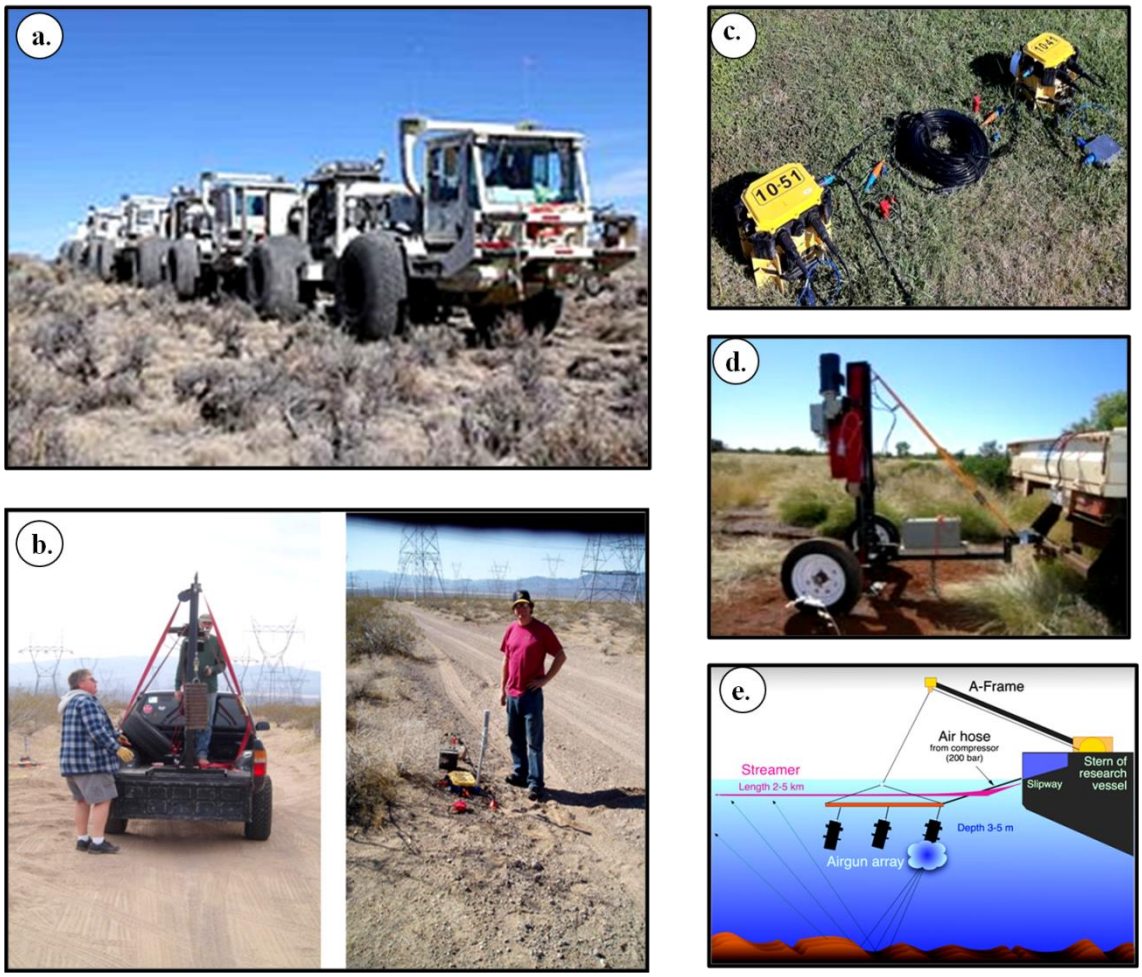

Figure 3.2: Examples of seismic acquisition sources (a.) Vibroseis in a set (http://www.cflhd.gov) (b.) Weight dropping and sledge hammer (http://mettechnology.com) (c.) geophones (http://iseis.com) (d.) weight dropping (http://geophysics.curtin.edu.au (e.) Air gun used for marine survey (http://upload.wikimedia.org/wikipedia/commons/1/1d/Airgun-array_hg.png).

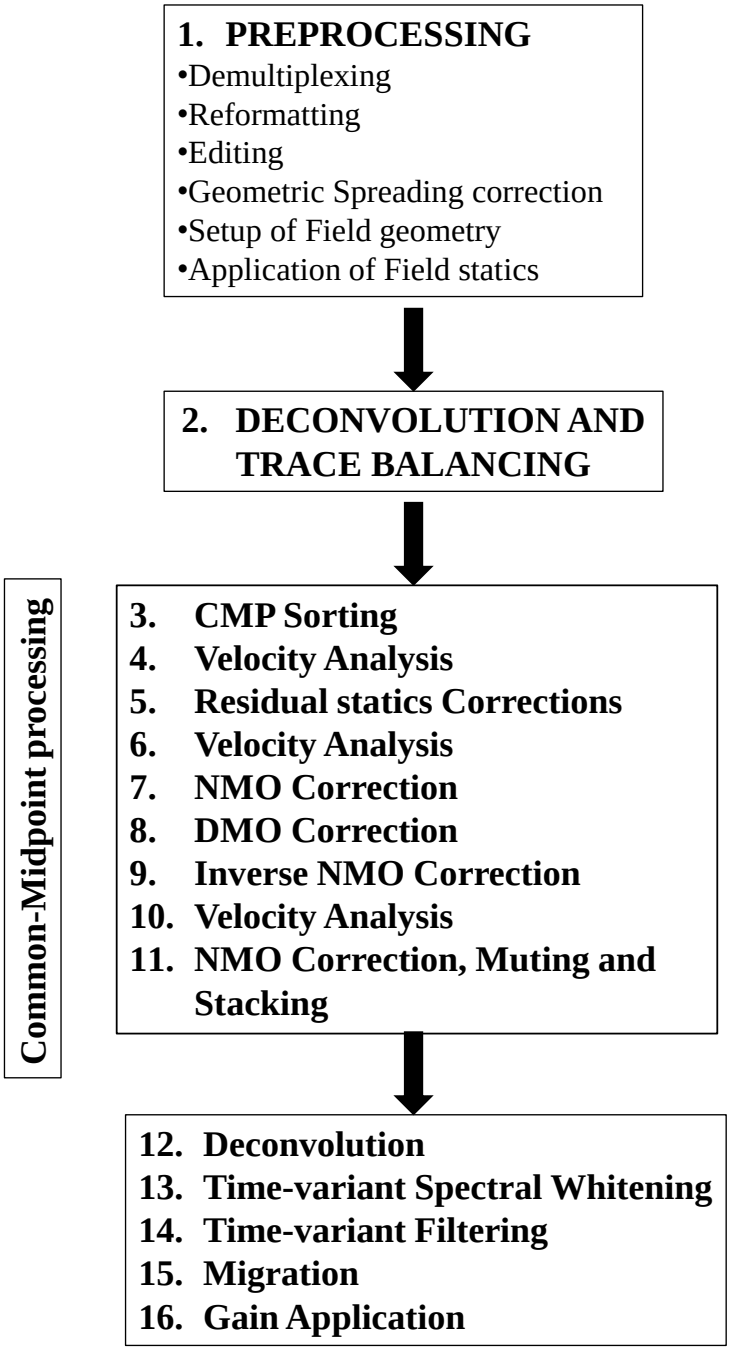

Figure 3.3: Flow chart for conventional seismic processing (Yilmaz, 2001).

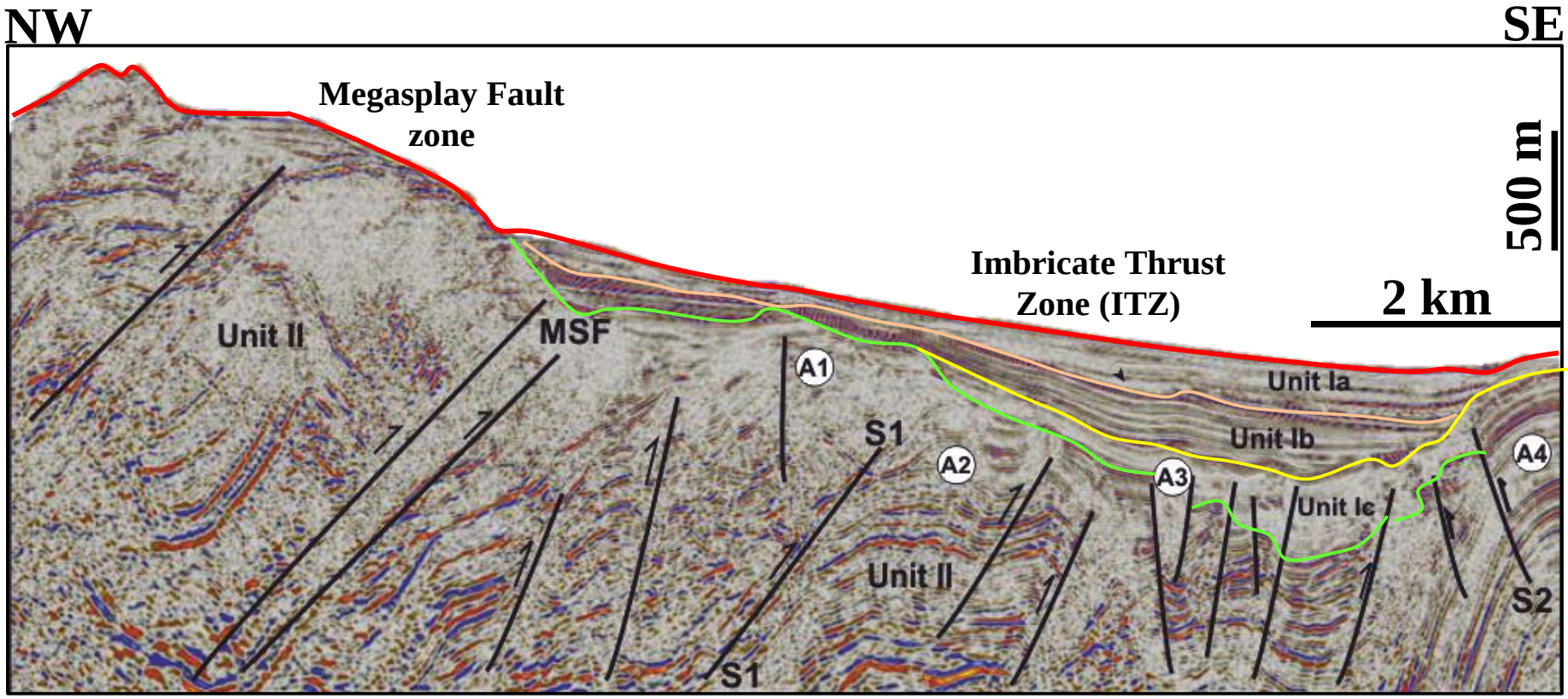

Figure 3.4: Examples of structural and stratigraphic seismic interpretation. The seismic section shows post-kinematic sediments that are deposited above a complex thrust-fold system of the Nankai trough (Modified after Alves et al., 2013).

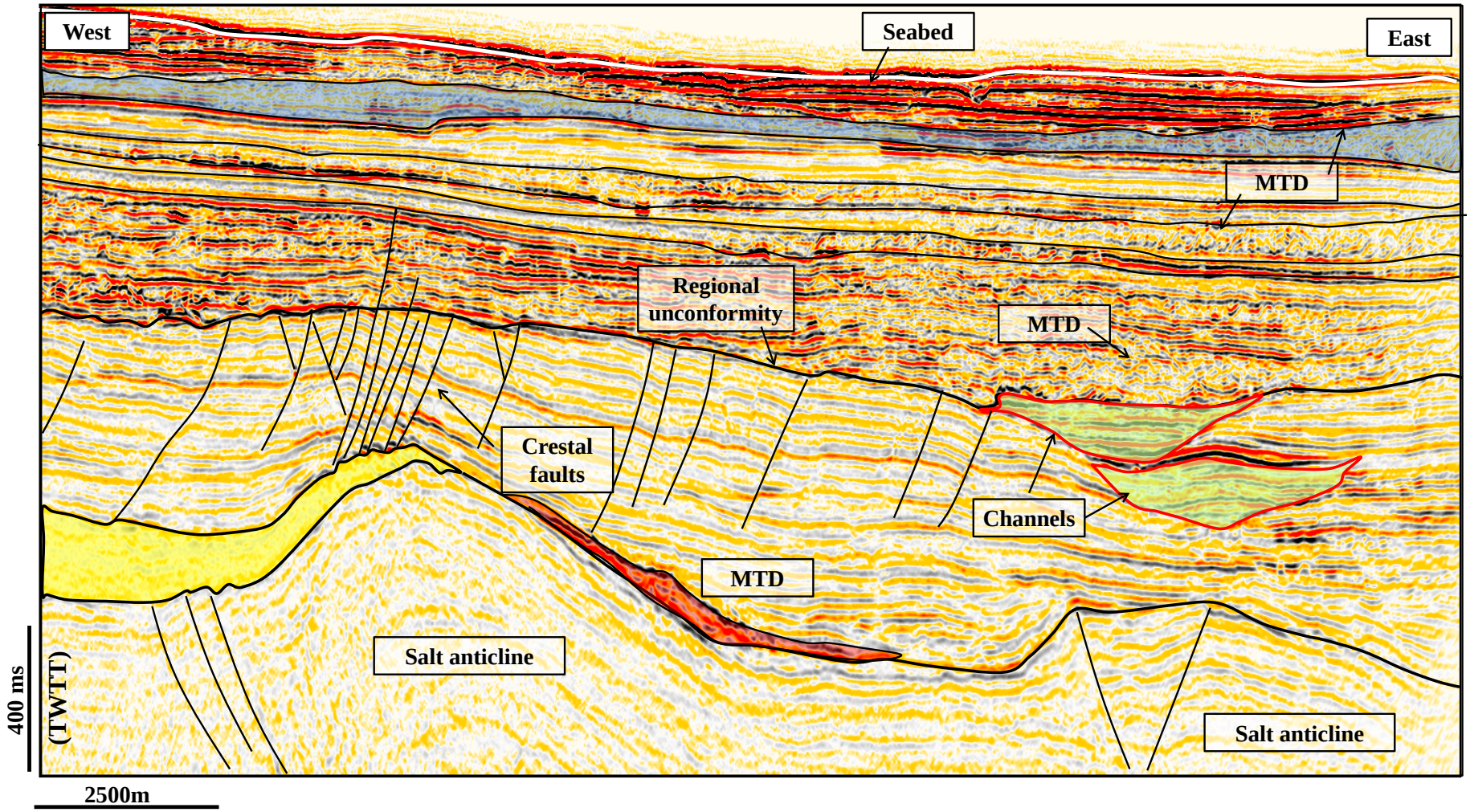

Figure 3.5: Another example of complex seismic interpretation involving both structural and stratigraphic mapping of a basin. The seismic section was interpreted from a section of the dataset used for this thesis.

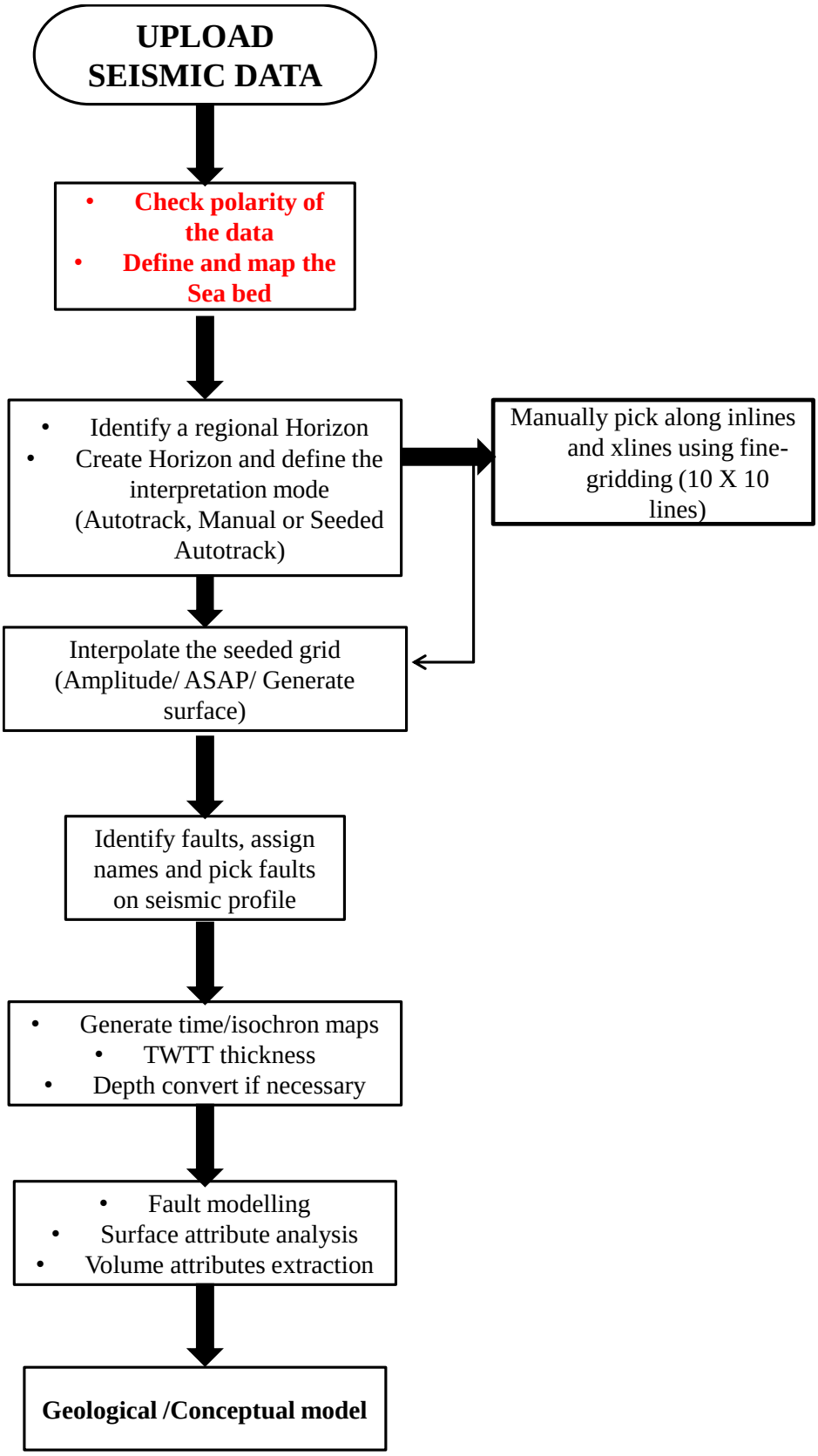

Figure 3.6: A simplified seismic interpretation workflow for Petrel and Geoframe.

3.2.1 Phase of the seismic data

A fundamental question prior to any seismic interpretation should include: What is the defined polarity of the data? Is it zero-phase or a minimum-phase wavelet? Is there a phase shift in the data, because phase often varies both laterally and vertically across a dataset? Seismic amplitude can be maximum, minimum and zero-phase (Figure 3.9), with the latter type being ubiquitous in present-day seismic interpretation practices (Brown, 2004). The zero-phase data implies that the wavelet is symmetrical and the majority of energy is coincident with its peak, which has a great advantage on seismic stratigraphic interpretations as the centre of the wavelet is coincident with the geological interface causing the reflections. Thus, an interpreter with a zero-phase data will pick the horizons or surfaces through the central part of the reflection.

3.2.2 SEG Convention/ Picking Parameters

When picking the horizons, the Society of Exploration Geophysicists (SEG) convention was adopted for a reflection that is associated with an increase in acoustic impedance. The normal SEG polarity is positive and displayed as a peak (Figure 3.10). If the signal arises from a decrease in acoustic impedance, the polarity is negative and is shown as a trough (Sheriff and Geldart, 1995; Kearey et al., 2002).

The normal SEG convention is otherwise referred to in this thesis as American convention in contrast to trough-peak polarity of the European convention. The seismic volume for this research is displayed in normal polarity with an increase in acoustic impedance with depth shown as a peak (Figure 3.9). The peaks were displayed as black while the troughs shown as red reflectors, white reflections are the zero-crossings.

The polarity of a reflected wave is dependent on the reflection coefficient (RC). Acoustic impedance is the product of velocity (V) and rock density (ρ) (Brown, 2004; Kearey et al., 2002). The reflection coefficient can be obtained from equation 3.1.

$$\text{Reflection coefficient} =$$

$$\text{Amplitude reflected}/\text{Amplitude incident} = \frac{V2\rho1 - V_1\rho1}{V_2\rho2 + V_1\rho1}$$

Where $V_1\rho_1$ is the acoustic impedance of layer 1

and $V_2\rho_2$ is the acoustic impedance of layer 2 ---------- **(Eq. 3.2)**

If the acoustic impedance of layer 2 > layer 1, the resulting reflection will be positive. A negative reflection is obtained where the acoustic impedance of layer 2 < layer 1.

3.3 Horizon Mapping

In the absence of a well data, a seismic tie could not be done and interpretation was done using traditional methods of seismic facies analysis. The facies parameters used in mapping the horizons include strong amplitude, continuity, and frequency variation (Mitchum et al., 1977). Interpreted horizons defined seismic packages by identifying zones of high/low frequencies and strong, medium or low amplitude reflection. Seismic packages can be defined as a sedimentary unit which is different from adjacent units in its seismic character. Continuity describes the lateral persistence of a reflection (Badley, 1985). It can comprise a good lithology indicator if zones of continuous and discontinuous reflections are taken as different lithological units (Figure 3.11).

An abrupt increase in seismic amplitude can indicate the presence of hydrocarbons, although such anomalies can also result from processing problems, geometric or velocity focusing or changes in lithology. Amplitude anomalies that indicate the presence of hydrocarbons can result from sudden changes in acoustic impedance, such as when gas sand underlies shale, and in that case, the term is used synonymously with hydrocarbon indicator. Where amplitudes can be differentiated, the qualifying terms of high, medium and low were used in this thesis. Most of the horizons interpreted were high amplitude reflections. Low amplitude zones are associated with fault planes and evaporites (Figure 3.12).

3.3.1 Seed gridding and mis-ties

The greatest advantage of 3-D seismic data over 2-D data is that visualization and interpretation of geologic features can be undertaken in the x, y and z directions (Kearey et al., 2002; Sheriff and Geldart, 1995). A seed grid technique was used to obtain an overview of the geometry of the reflectors. This included the picking of horizons of interest through a number of widely-spaced crosslines and inline at regular intervals. Horizon interpretations done at a 10 inlines or crosslines spacing implies a picking interval of 125m in this survey. Seed gridding is necessary to ensure that the interpretation loop is accurately tied (Figure 3.14).

Inline and cross lines not picked within the interpretation loop were amplitude interpolated or tracked using Automatic Seismic Area Picker (ASAP) prior to generating time/isochron and attribute maps. Mis-ties were corrected by re-picking along the problem area with the aid of the seed grid (e.g. Figure 3.15).

3.3.2 Seismic frequency and resolution

Frequency or spacing describes the number of reflectors per unit time (Figure 3.13). It is a good sedimentary facies discriminator. As vertical changes in reflector spacing can be used as a guide to locating boundaries between depositional sequences, restraints must be used when using this parameter as an interpretation criterion (Badley, 1985).

Interval velocity = distance or depth (m) / OWTT (s) ---------- (Eq. 3.3)

The resolution of a seismic volume can defined as the minimum separation between two features. Resolution varies both vertically and laterally, the vertical seismic resolution is defined as the minimum separation between two interfaces such that we can identify two interfaces rather than one (Sheriff and Geldart, 1995). In turn, horizontal resolution is how far two features involving a single interface must be separated to show as separate features. The best resolution can be obtained at ¼ of λ and the minimum resolution at 1/30 of λ (Sheriff and Geldart, 1995; Badley, 1985). The seismic velocity (v) is the product of frequency (f) and wavelength (λ), such that:

$v = f \times \lambda$ ---------- (Eq. 3.4)

The vertical resolution of the dataset with a dominant frequency of 40 Hz is ~15.6 m and 19.375 m assuming velocity of 3100 m/s and 2100 m/s for deeper and shallow horizons (Barker et al., 1983; Fiduk et al., 2004). The dominant frequency is the frequency of the highest amplitude which is obtained from the processing algorithm. For a migrated data, horizontal resolution is equal to the bin size and is ~12.5 m for the interpreted volume.

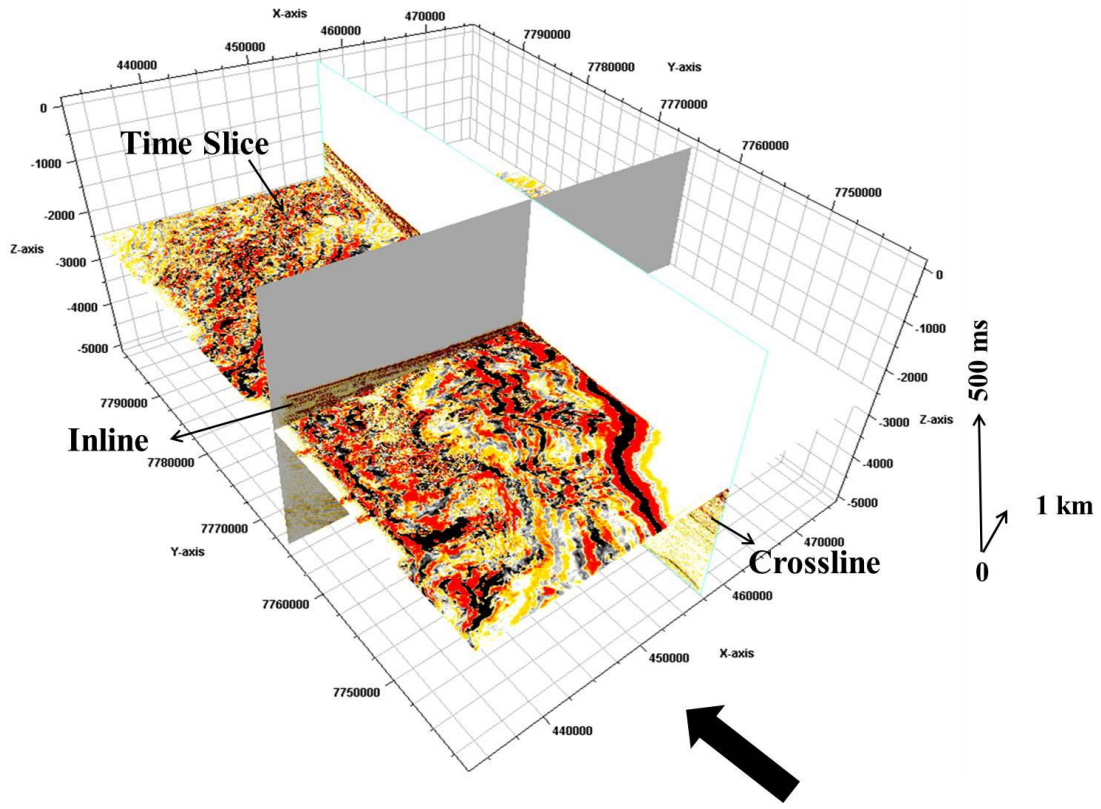

Figure 3.7: Seismic cube through the study area. Also shown in the figure are examples of an inline, crossline, and time slice. The interpreted seismic cube covers ~1310 km^2 in Espírito Santo Basin, SE Brazil.

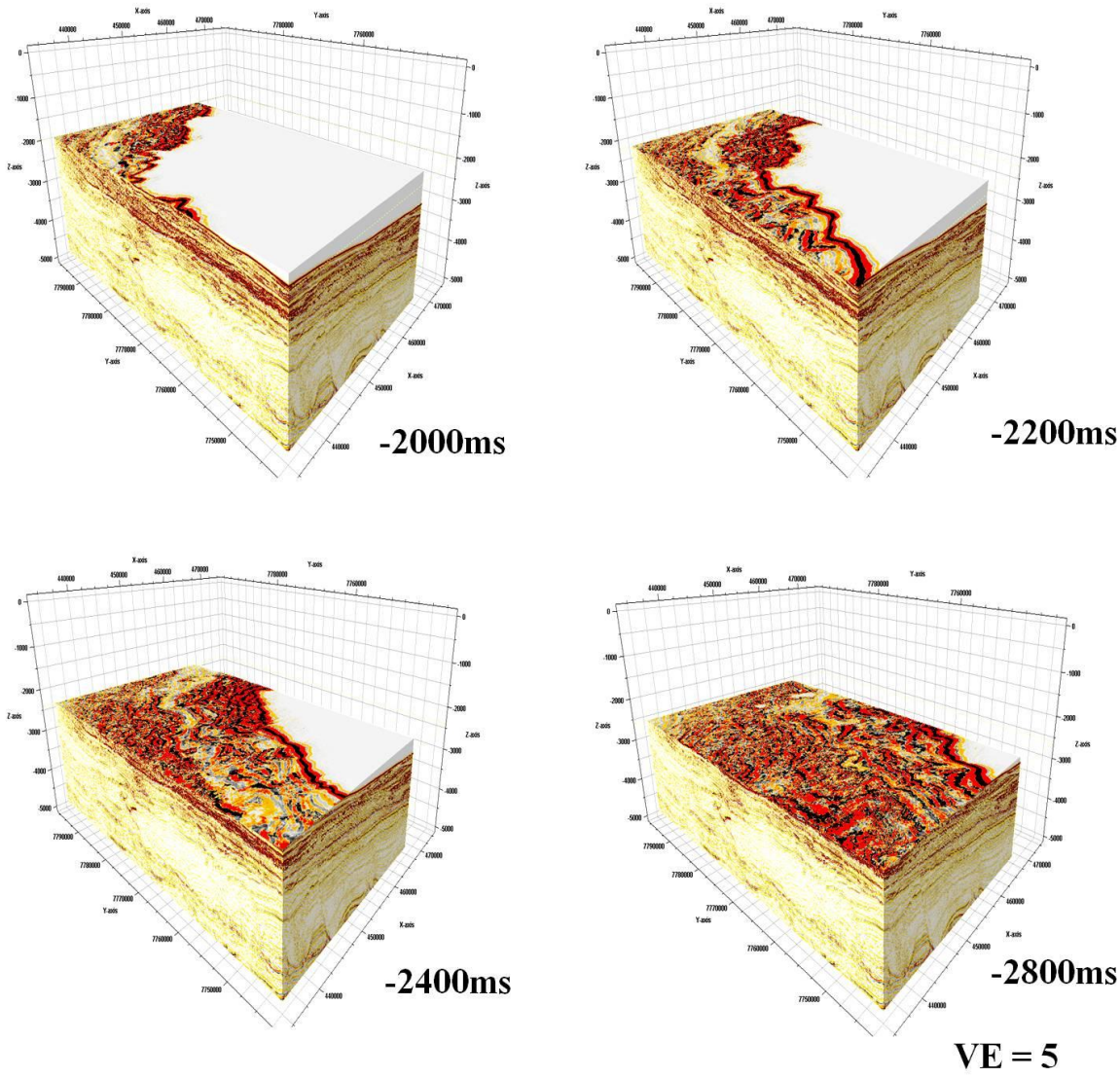

Figure 3.8: Example of 3D seismic visualisation techniques used in this work. The seismic volume interpreted in this study covers water depths of 100 to 1800m offshore the Espírito Santo Basin. The seismic cubes in the figure show how the water depth varies along slope.

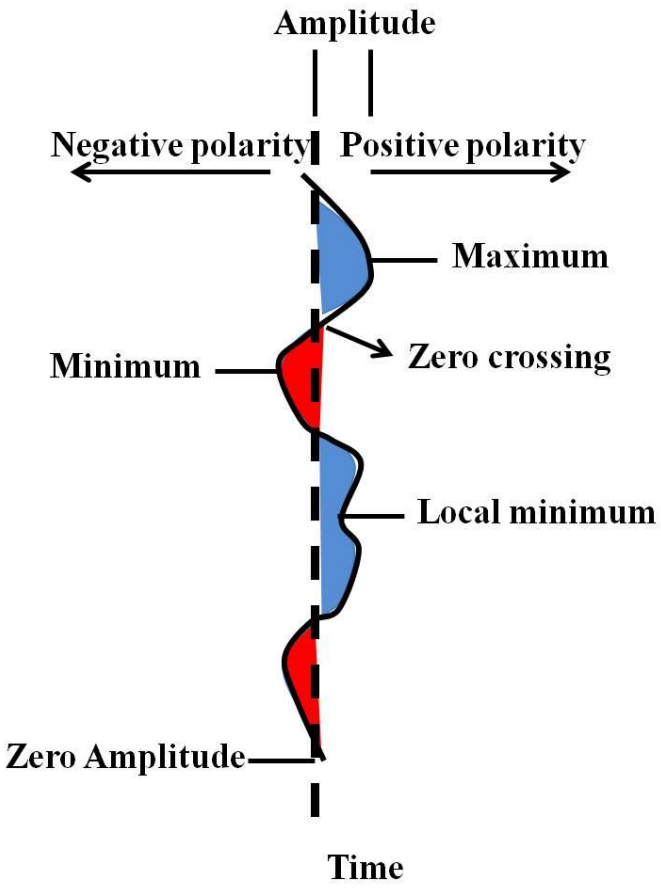

Figure 3.9: Maximum, minimum and zero-phased seismic amplitude. Polarity or phase of seismic amplitude. The American convention displays an increase in acoustic impedance with depth as a peak (Modified from Sheriff and Geldart, 1995).

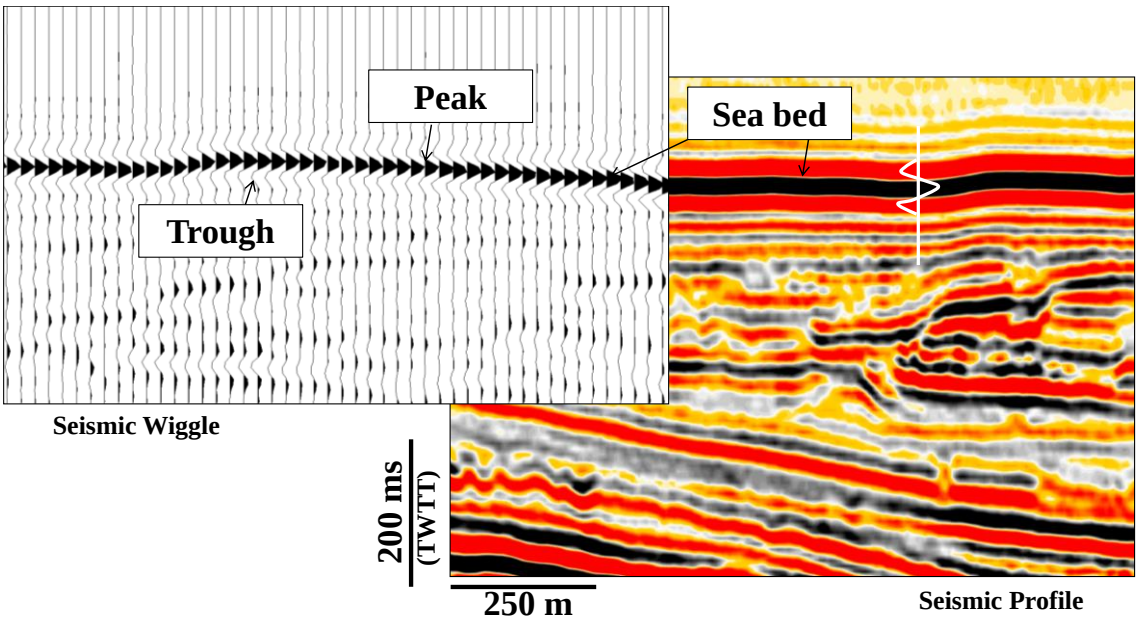

Figure 3.10: The seismic volume for the study is displayed in normal SEG convention.

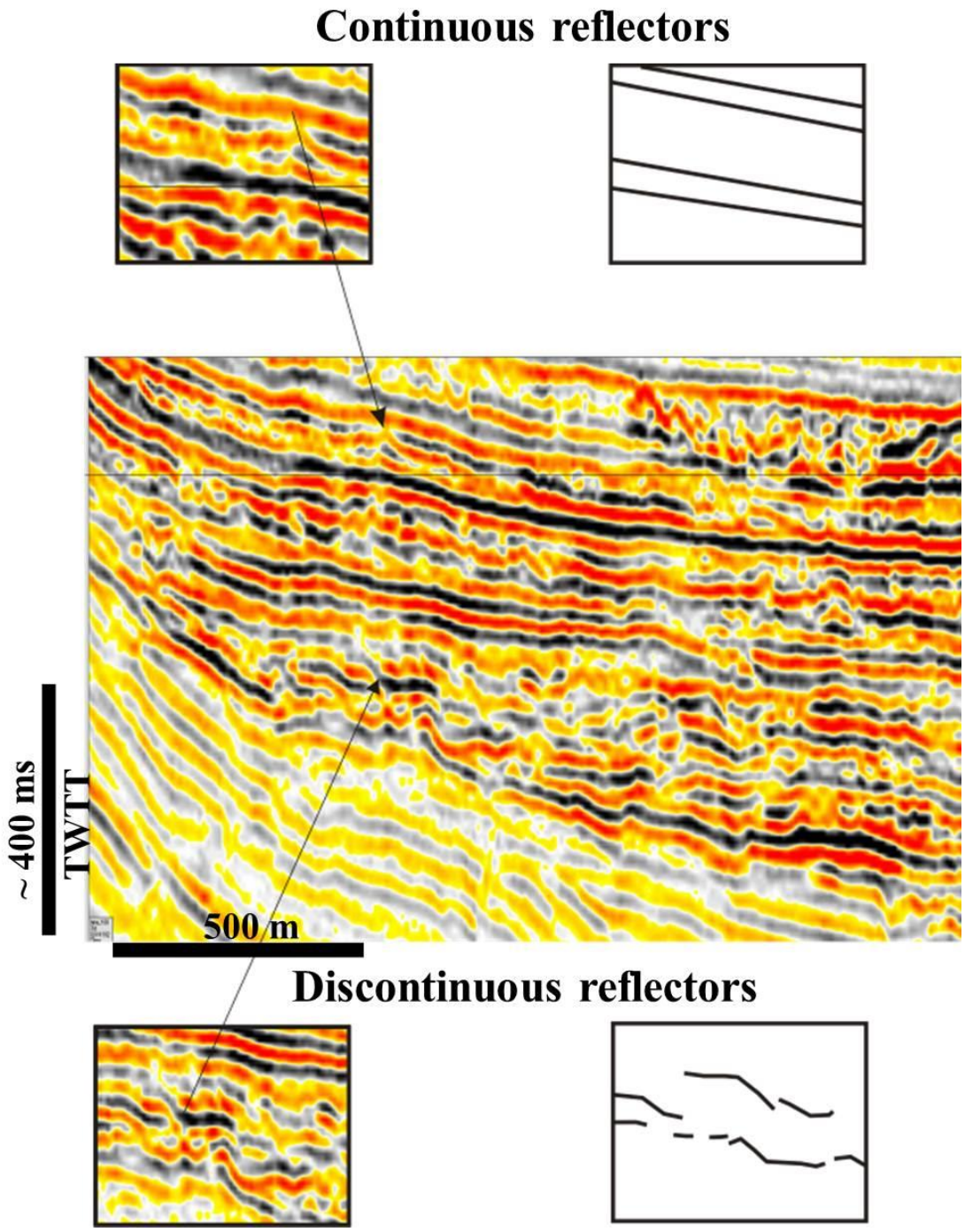

Figure 3.11: Examples of continuous and discontinuous reflectors from the seismic volume. Modified after Badley (1985).

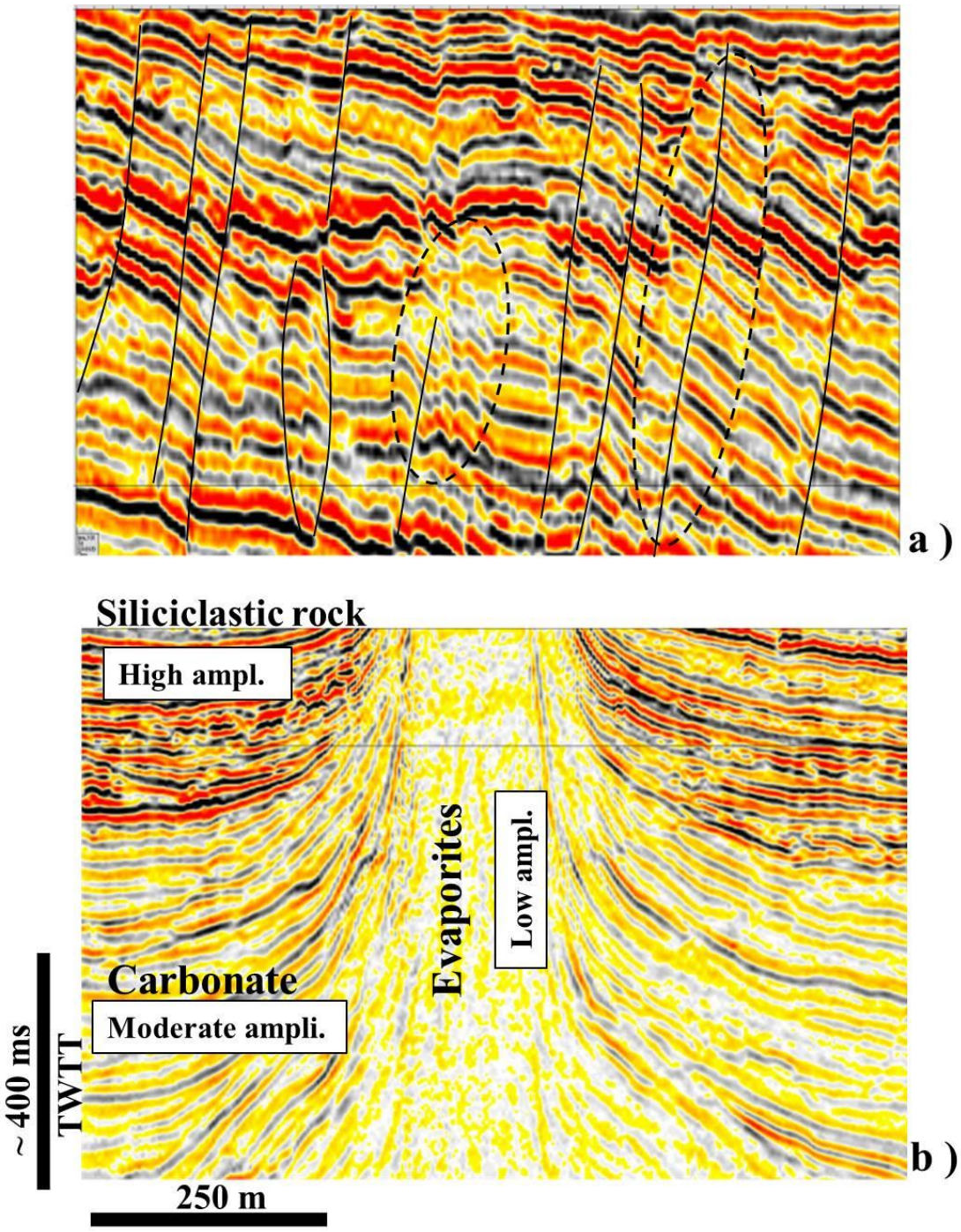

Figure 3.12: Seismic example of low amplitude associated with fault planes and evaporites. Moderate seismic amplitudes are associated with carbonate rocks. The magnitude of the amplitude is dependent on the AGC (Amplitude Gain Control) used for the interpretation.

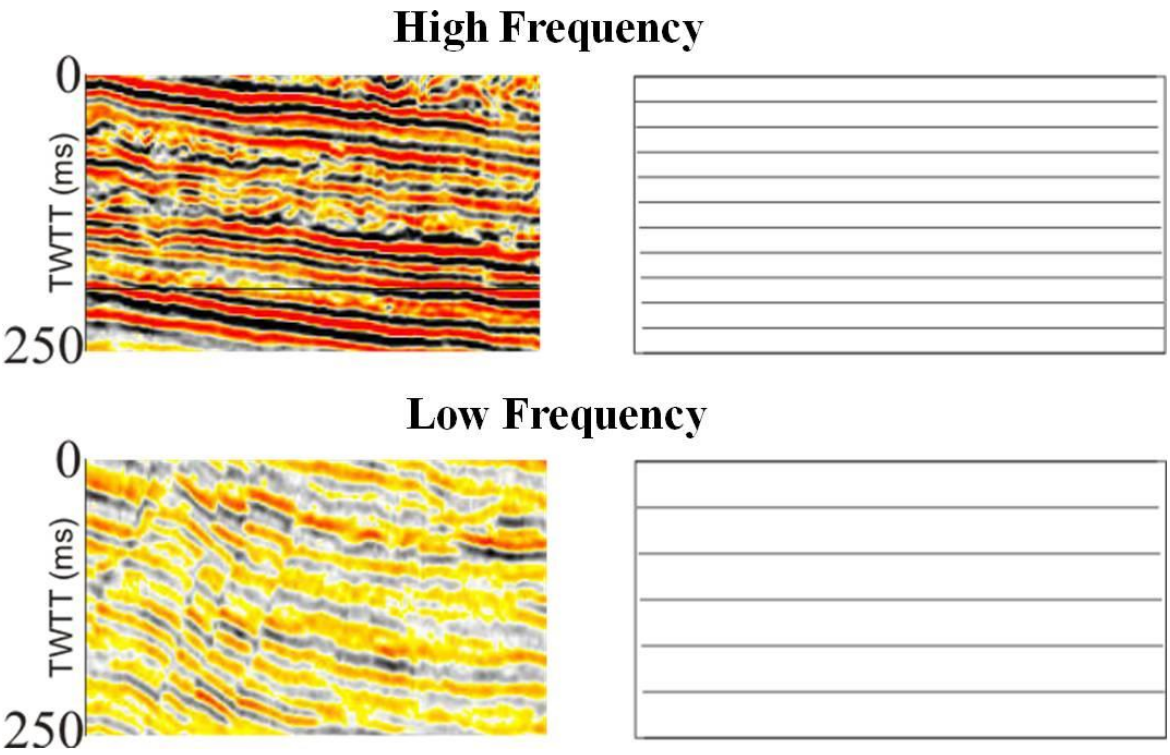

Figure 3.13: Frequency is a good lithological discriminator. In this instance very high frequency reflectors are associated with siliciclastic rock while carbonates can be defined as very low frequency packages. The frequency is defined as the number of reflectors by unit time (Modified after Badley, 1985).

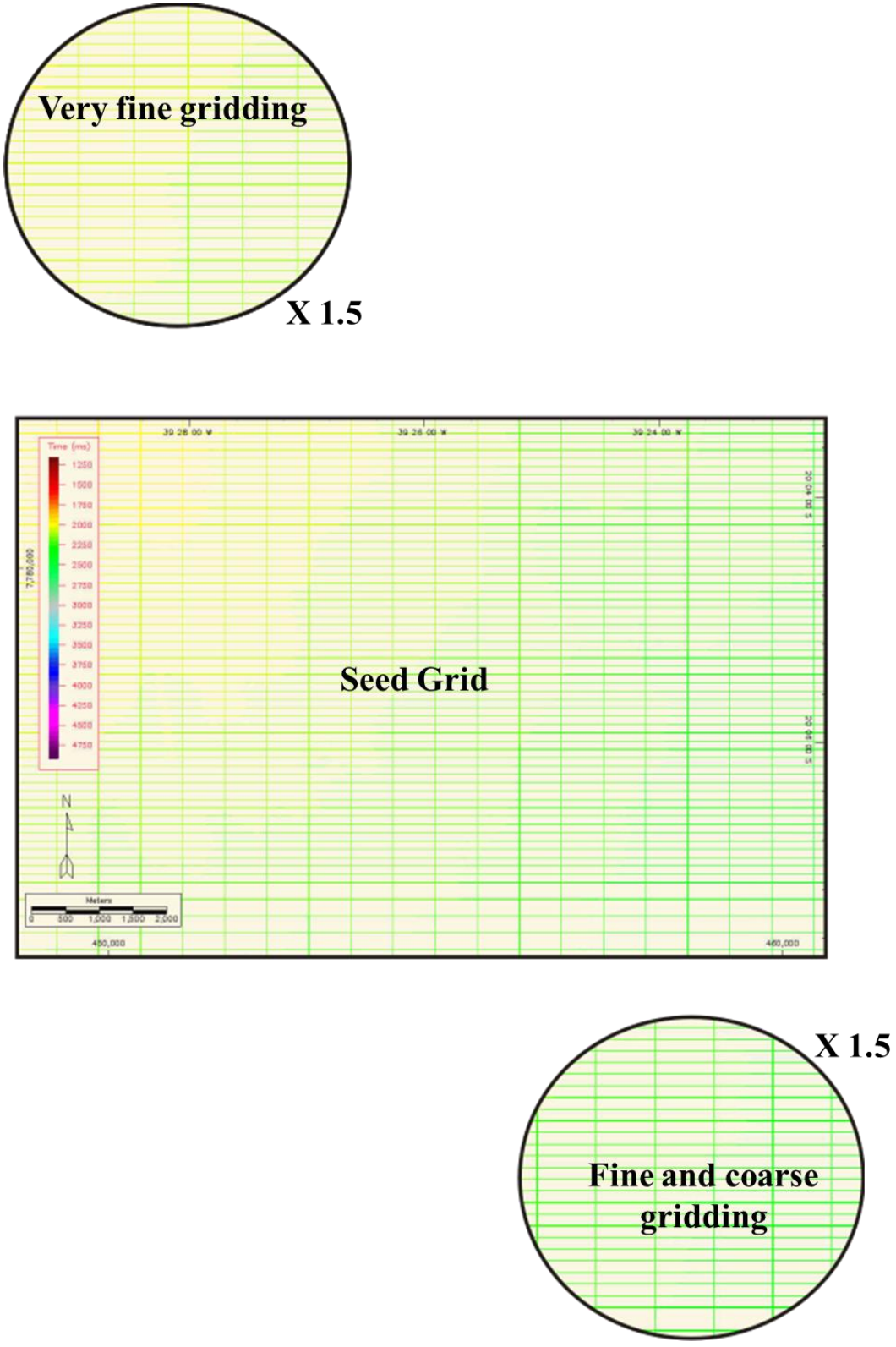

Figure 3.14: Seed gridding used for 3D seismic interpretation in the case study area. The fine gridding in this thesis included the interpretation of data at intervals of 10 inline or crosslines (i.e. done at intervals of ~125 m).

3.3.3 Mapping of mass-transport deposits

The boundaries of MTDs are imaged as distinctive tops and basal shear surfaces contrasting with the relative continuous strata above and below. The upper surface of a MTD is usually a rugged or ridged surface located above chaotic to moderately deformed reflections of variable amplitude (Richardson et al., 2011), while the basal shear surface separates disrupted strata within the MTD from the much more continuous deposits underneath (Frey Martinez et al., 2005b; Frey-Martínez et al., 2006b). Seismic expressions of the top and basal surfaces of some MTDs are shown in Figure 3.16 and Figure 3.17.

Nevertheless, the internal character of the mass-transport deposit is variable on seismic, depending on their interior architecture derived from their source materials. Based on the preservation of some or all of their original stratigraphy, mass-wasting deposits are classified as slides, slumps and debris flow deposits (Masson et al., 2006b), the latter being an entirely homogeneous, chaotic, disaggregated material with no original stratigraphy preserved (Figure 3.16).

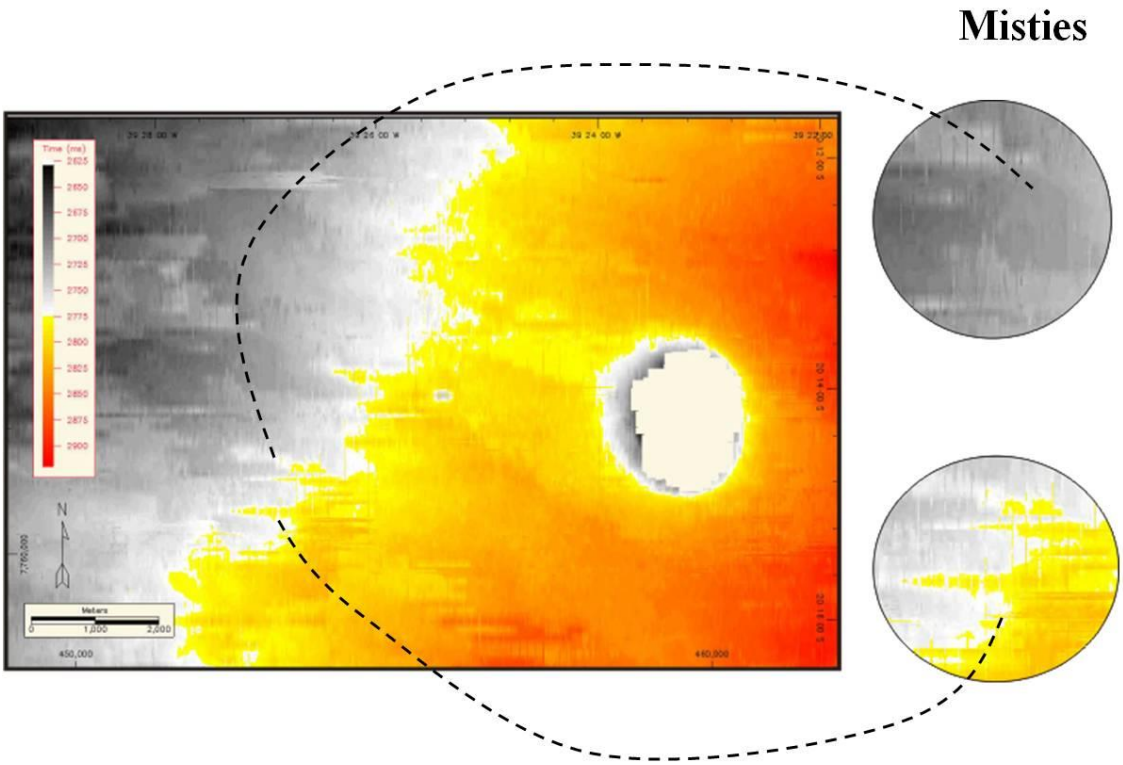

Figure 3.15: Mis-ties during seismic interpretation were identified after the seeded grid was amplitude interpolated or ASAPed.

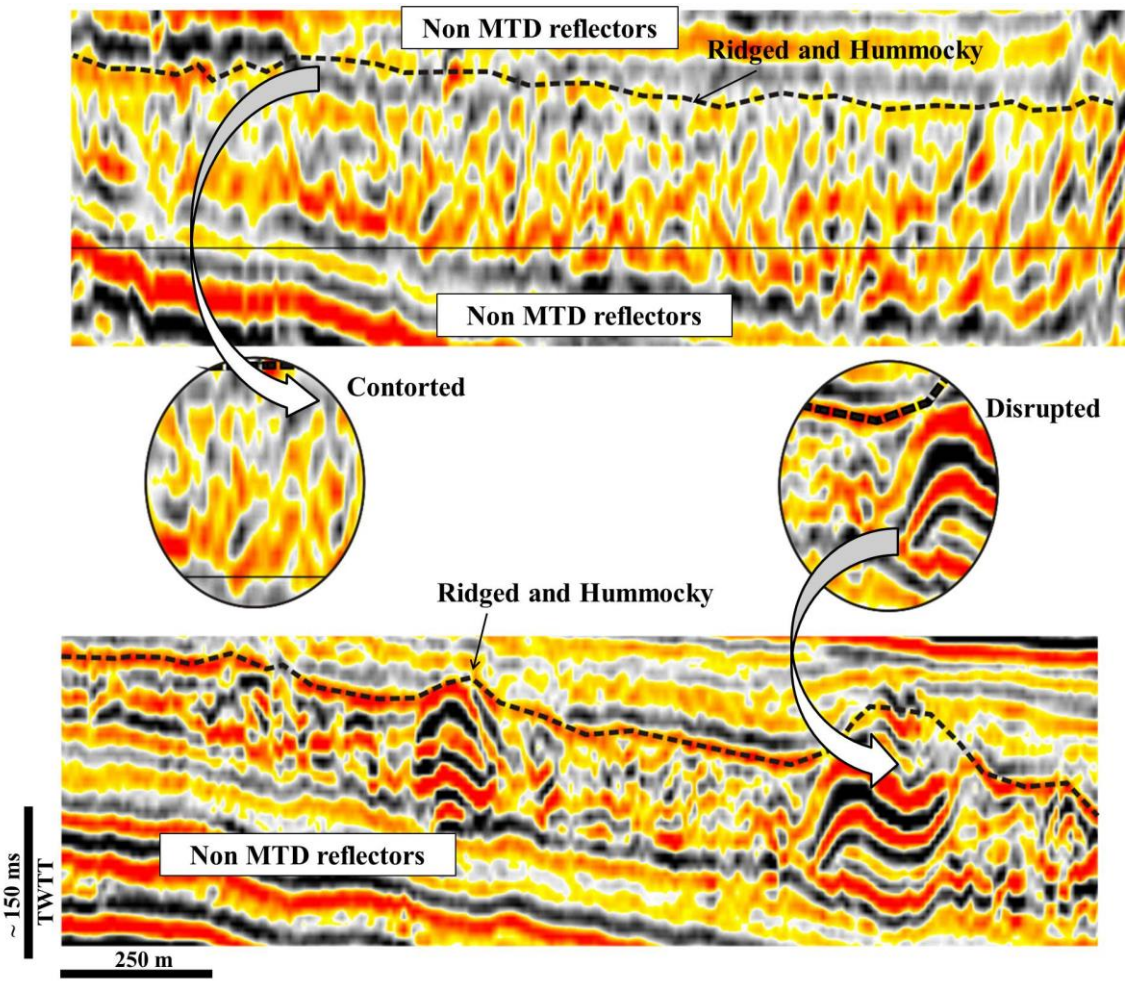

Figure 3.16: Seismic reflection of the top reflection in a MTD and corresponding internal character of this same deposit. The top of a mass-transport deposit is shown as rugged and hummocky reflection. From Richardson et al., (2011).

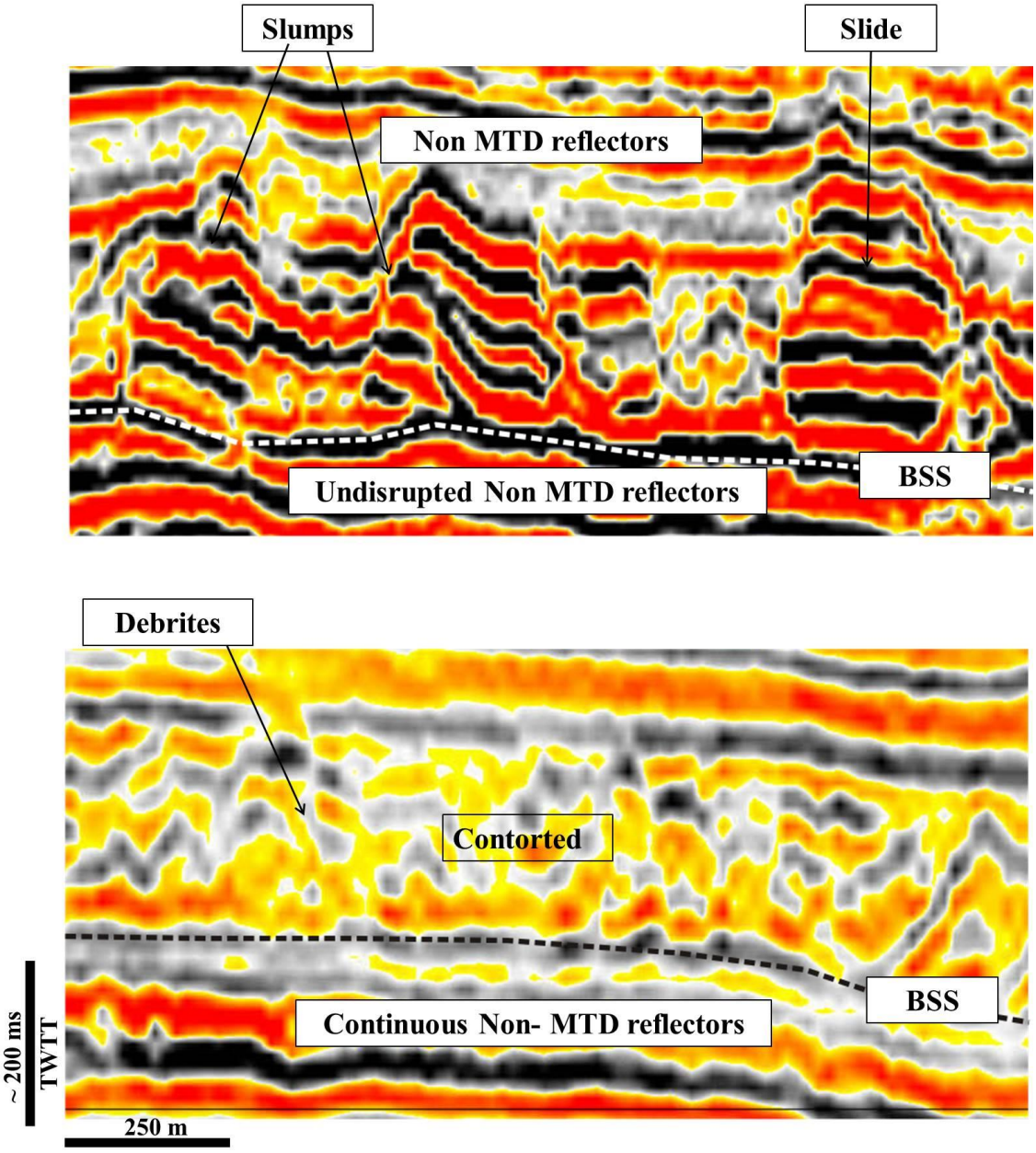

Figure 3.17: Seismic expression of the basal shear surface of a mass-transport deposit. Also shown are examples of slides, slumps and debrites. N.B: BSS is the basal shear surface along which material was translated along slope. Slope failure occurs when downslope-directed shear stress exceed the shear strength of seafloor sediment (Richardson et al., (2011) and Varnes (1978)).

3.3.4 Fault mapping and modelling

Faults were mapped at a very fine grid of 1 to 5 inline/crossline spacing equivalent to 12.5 m to 62.5 m. After picking the faults, fault models were created in petrel in which most of the faults were quality-controlled and converted into fault surfaces. The fault model was populated with horizons, zones and arbitrary sedimentary layers to observe the effect of the fault offset on horizons. The very subtle faults were picked using attribute maps, mainly dip, amplitude and coherence maps. Automatic fault extraction was used to pick the polygonal faults in the study area (Figure 3.26).

Specifically in Chapter 6, fault planes were manually mapped in Latest Cretaceous-Holocene strata showing three main MTDs (Figures 6.3b and 6.4b). In densely faulted regions, we used ant tracking algorithms to extract fault patches (Randen, 2000). Faults automatically extracted by this method were manually checked to ensure that the automatic fault picks were valid. In order to achieve an effective automatic fault extraction, the volume was divided into four zones comprising both MTD and non-MTD areas (Figure 6.1). Two thousand two-hundred and eighty-two (2282) faults were automatically extracted and analysed in this work.

Fault propagation histories were analysed using throw-depth (t-z) techniques (Walsh and Watterson, 1989; Peacock and Sanderson, 1991; Dawers and Anders, 1995; Cartwright and Mansfield, 1998; Mouslopoulou et al., 2007; Baudon and Cartwright, 2008). In detail, throw values were estimated on faults using seismic profiles orthogonal to fault strikes at the inflection points closest to the hanging wall and footwall cut-offs (Mansfield and Cartwright, 1996). Throw values were contoured for twenty four (24) representative faults to further elucidate the styles of fault growth, linkage styles and

reactivation in the study area. Errors in throw estimate were dependent on the vertical sampling rate of 2 ms. Hence, the correlation of synchronous strata across hangingwall and footwall section was completed with a high degree of confidence. The sampling interval, rather than the vertical stratigraphic resolution, determines accuracy when matching two correlative seismic reflection peaks or troughs (Baudon and Cartwright, 2008a).

Throw values were contoured for representative fault families and presented as maps to further elucidate fault growth, linkages and reactivation (e.g. Figure 3.18 and Figure 3.19). Contour values are consistently sampled as strike-projections of the fault seen from the footwall side (Figure 3.19).

Fault decoupling geometries were further analysed by estimating the propagation rate for faults and the relative age of sediments they cut through (see techniques of Childs et al, 2003 for estimating fault propagation rate). The ages of mapped horizons were estimated from well data and regional sections of Barker et al. (1983), Fiduk et al. (2004) and França et al. (2007). Half-lengths of faults were measured from the point of maximum displacement on the mapped fault trace to the fault tip-point. In parallel, the ratio of half-lengths to the time-interval between mapped horizons was also measured. Sedimentation rate is defined in this work as the mean thickness of the interval from both hangingwall and footwall section divided by the time interval between mapped horizons.

Pitfalls when calculating both rates derive from accurate estimation of tip-line locations, time interval over which propagation rates were calculated, seismic resolution and

differing seismic interval velocities. The effect of sediment compaction due to burial was not considered; the rate used is the thickness of compacted sediment per unit time. While this may lead to a substantial underestimation of the absolute rate of deposition, it may not influence the fault analysis because (a) this depends on the relative rate not the absolute rate, and (b) all the faults are buried to about the same depth, and therefore the sediments they cut have undergone approximately the same amount of compaction.

Detailed styles of fault interaction and specific fault families were interpreted using isopach maps (Figure 6.5). These maps were used to recognise variations in the geometry of the interpreted MTDs, regions affected by extension, and growth packages related to syn-sedimentary faulting. Graphical descriptions of fault families were also completed using rose diagrams in Figure 6.1.

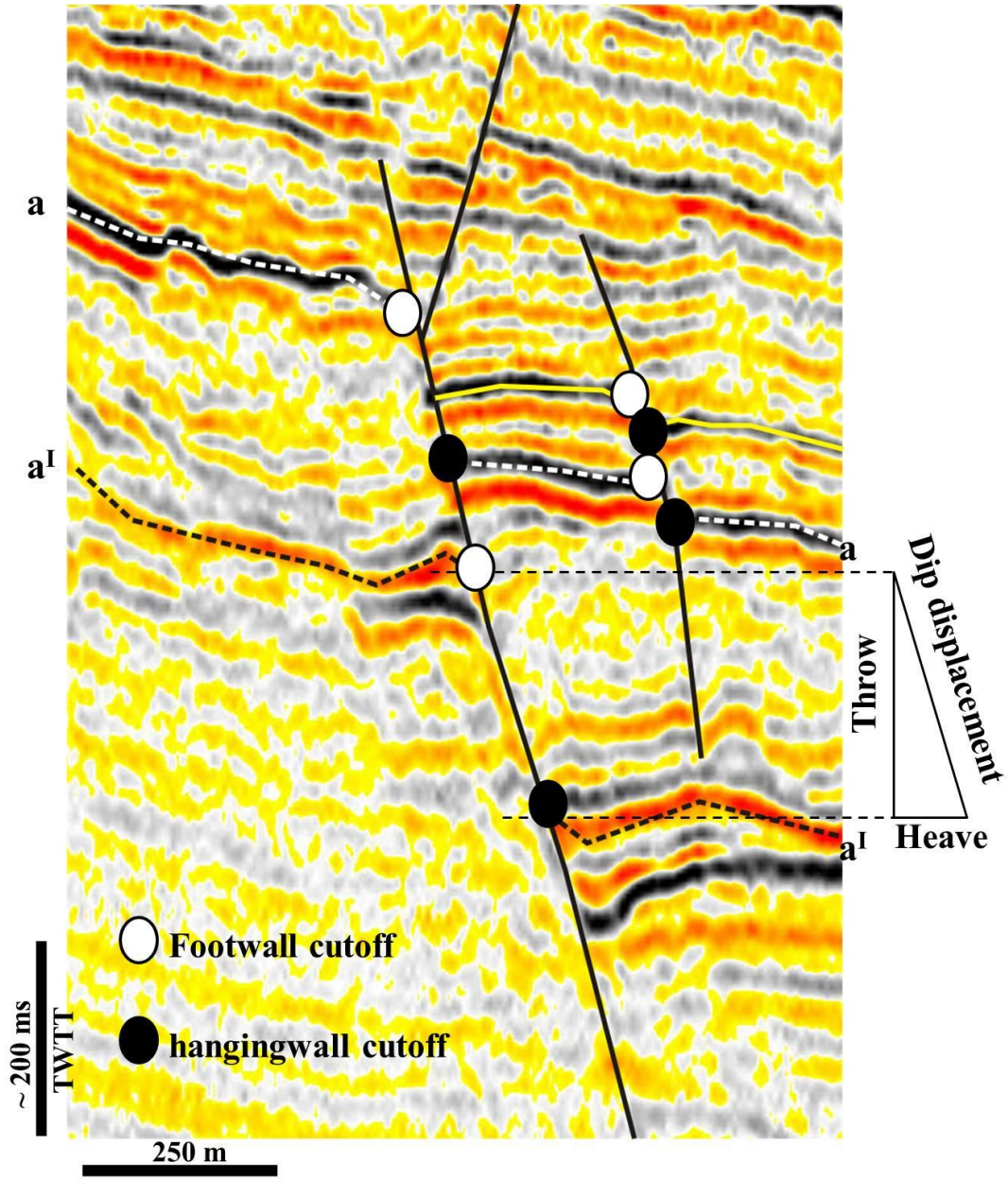

Figure 3.18: Fault planes are expressed as truncations or terminations of seismic reflections on profiles. Also shown in this figure is the technique used for estimating throw from hanging-wall and footwall cut-offs. The dip displacement is the square root of the sum of the square of the throw and heave.

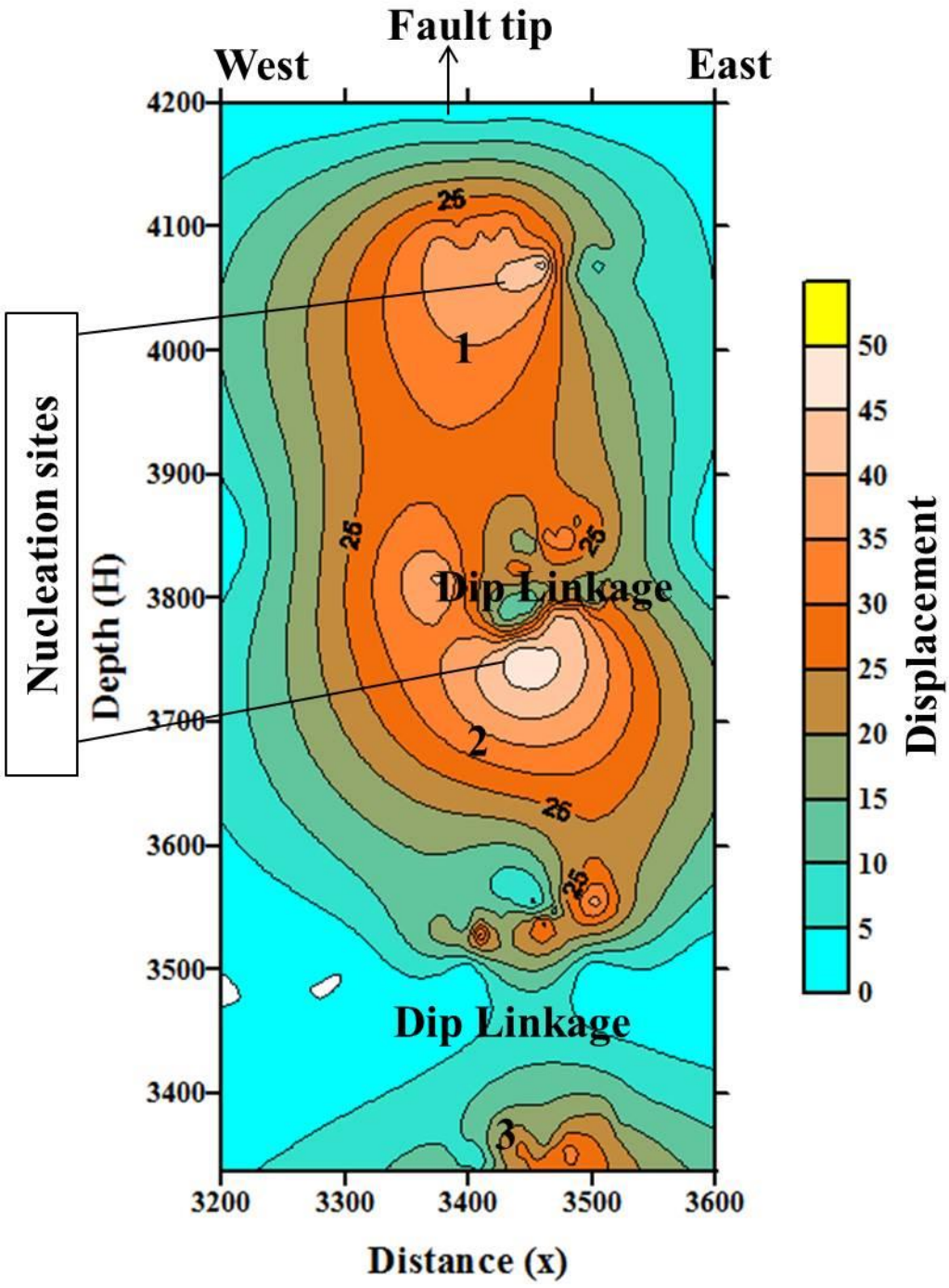

Figure 3.19: Throw contours providing hints on fault growth, linkage and reactivation. The point of nucleation for the fault is the position of maximum displacement (d_{max}), fault propagates from d_{max} with displacement reaching zero at the tips (Barnett et al., 1987; Walsh and Watterson, 1989). The figure shows the displacement profiles of three faults reactivated by dip linkage into a single fault (Baudon and Cartwright, 2008).

3.4 Seismic attribute analysis

3.4.1 Amplitude

This attribute displays the amplitude value at any point along an interpreted seismic horizon (Randen et al., 2000; Brown, 2004). The amplitude of a seismic reflection is weakened along structural lineaments such as faults. It is thus possible to map fault traces along an interpreted seismic reflection by analysing seismic amplitude data. Minor structures are difficult to identify on amplitude maps, and is therefore appropriate to always use amplitude data in conjunction with dip maps (See Figure 3.21). Amplitude data may be further computed as maximum, minimum, average amplitudes, number of zero crossing, maximum magnitude, etc.

3.4.2 RMS amplitude

Root-mean square (RMS) amplitude maps were generated in this work to highlight the presence of high-amplitude strata and associated structural fabrics. RMS amplitude maps calculate average amplitude values by squaring individual data samples over a defined time window, boosting any high amplitude in the mapped interval (Brown, 2004). RMS attribute maps can emphasise structural fabric because seismic wavelets are diminished across basal ramps/faults as a result of the destructive interference of seismic energy (Fairbairn and Ward, 1984) and the incomplete reflection of energy from the Fresnel Zones on both sides of the ramps (Townsend et al., 1998).

In this thesis, RMS amplitude maps helped the identification of heterogeneous MTDs, basal ramps and flats, as well as any drag zones around growing salt diapirs. On RMS amplitude maps, near-seafloor uplift is shown as elliptical features around the salt diapirs, marked by differences in amplitude and character from strata away from these

elliptic zones. In addition, these same regions are characterised by ramps of variable dimensions (Figure 3.20).

3.4.3 Dip Maps

Time-derived dip maps across remnant or rafted blocks show marked changes in dip when compared with disaggregated strata, provided the vertical resolution is high enough to resolve dip offsets (Yilmaz, 1987). Time-structure maps were used to describe the morphological division of individual MTDs into their headwall, translational and toe domains. Changes in dip associated with basal shear surfaces were underlined using time-dip maps (Figure 3.21). The latter maps highlight changes in dip of an interpreted seismic reflection. Since ramps offset near-seafloor strata, a continuous interpretation across the ramps will result in a change in dip of the interpreted horizon, provided the vertical resolution is high enough to resolve the offset (Yilmaz, 1987). How abrupt the change in dip across a ramp is, depends on the bin size of the seismic volume as well as its lateral resolution (Yilmaz, 1987).

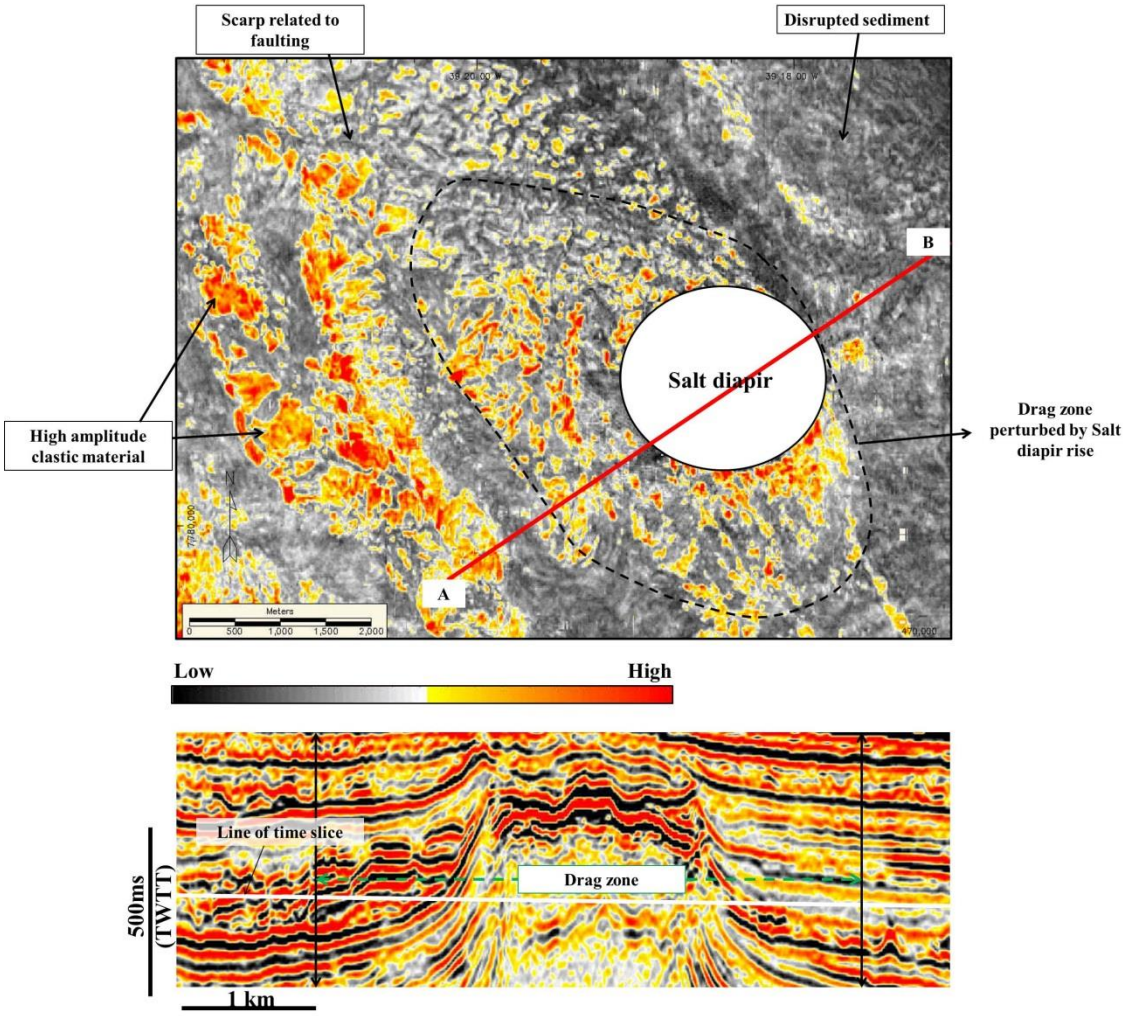

Figure 3.20: RMS amplitude maps are useful to identify structural fabrics such as ramps, faults within a pre-established depth window. It is also a good lithology discriminator especially when it is necessary to characterise heterogeneous deposits. In this work, RMS amplitude maps were used to elucidate segments of the palaeo seafloor that were pierced and uplifted during the rise of salt diapirs.

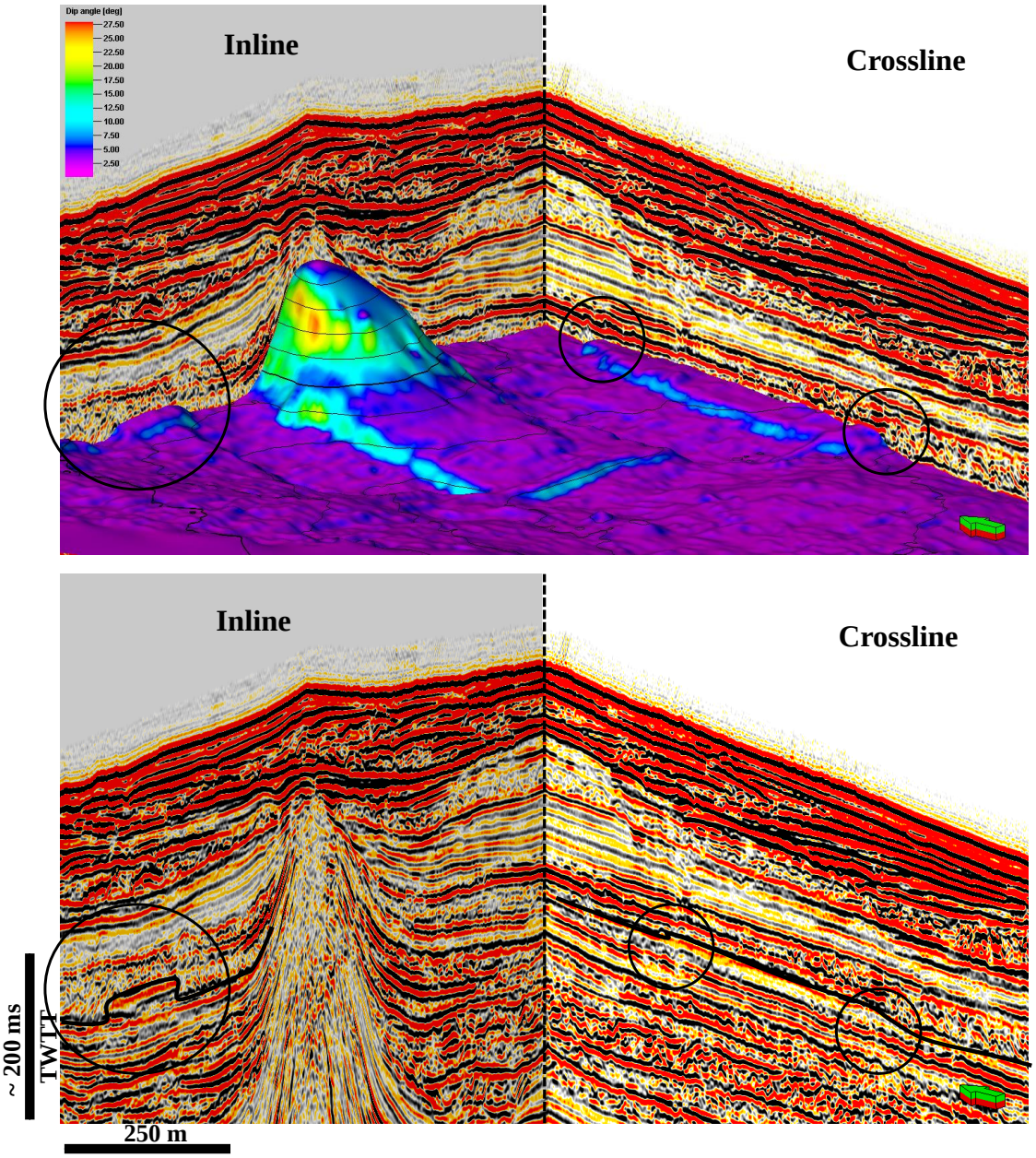

Figure 3.21: Dip maps are useful to identify changes in slope gradient. Dip maps are very sensitive to acoustic noise in the seismic volume and should be used in combination with other attributes, such as coherence and amplitude, when mapping subtle structures.

3.4.4 Coherence or variance data

This is a cube of coherence coefficients generated from the input 3D seismic data volume. It is a measure of the waveform similarity i.e. how a trace is similar to its neighbour. High coherence areas are typically shown as white to light grey and may indicate slow rates of deposition. Low or non-coherence areas are shown as dark grey or black (Figure 3.22 to Figure 3.24). Similar traces are mapped as high coherence coefficients while discontinuities have low coefficients (Bahorich and Farmer, 1995; Brown, 2003). Sharp discontinuities may result from fracturing, faulting, diagenesis, erosion, fluvial systems, or changes in the rate of deposition (Bahorich and Farmer, 1995; Brown, 2003).

Coherence provides an accurate first estimation of subtle changes in a waveform of a seismic trace over an entire cube. It is a useful reconnaissance mapping tool because it gives an unbiased view of the features in the seismic volume without any prior interpretation. In addition to faults, channels and beaches, it has been successfully utilized in the visualisation of mud volcanoes, salt intrusions, MTDs and polygonal faults (Chopra and Marfurt, 2005) (Figure 3.22 to Figure 3.24).

For this study, coherence was used to map polygonal fault systems, fractures at reservoir level and evaporites. Coherence maps at the base of MTDs were also used to validate the position of ramps observed on time-dip maps (Figures 5.5 to 5.8).

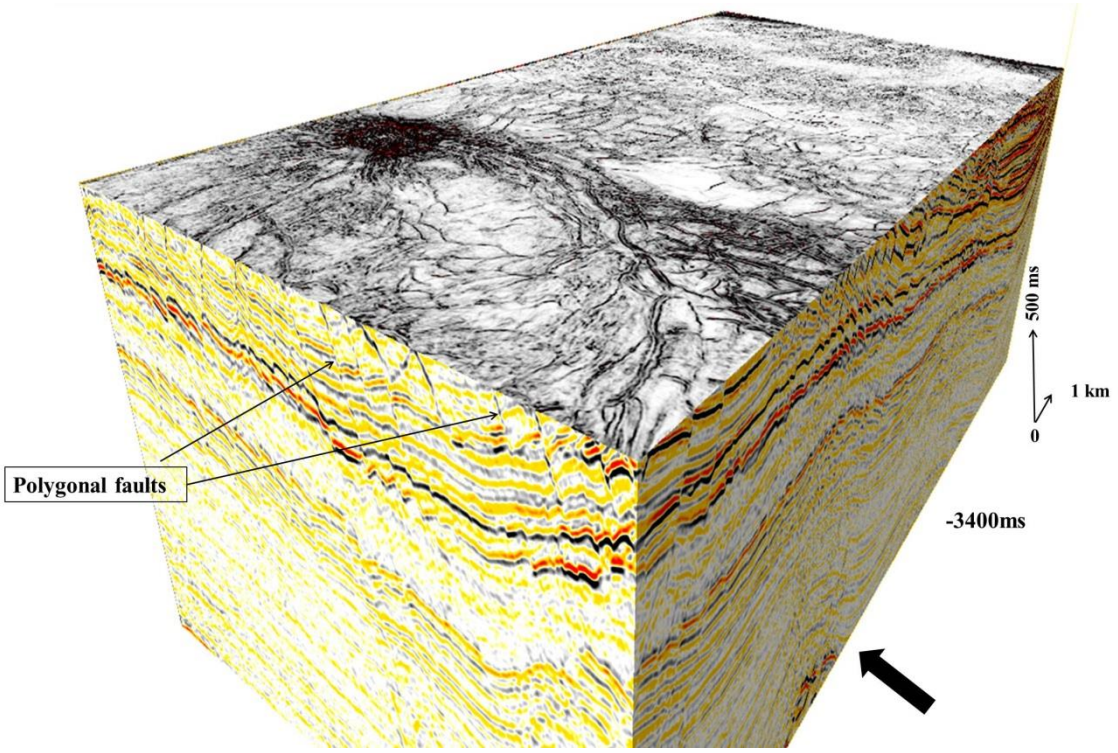

Figure 3.22: Coherence maps highlighting the presence of polygonal faults. Similar traces are mapped as high coherence coefficients, while discontinuities have low coefficients. From Brown (2003) and Bahorich and Farmer (1995).

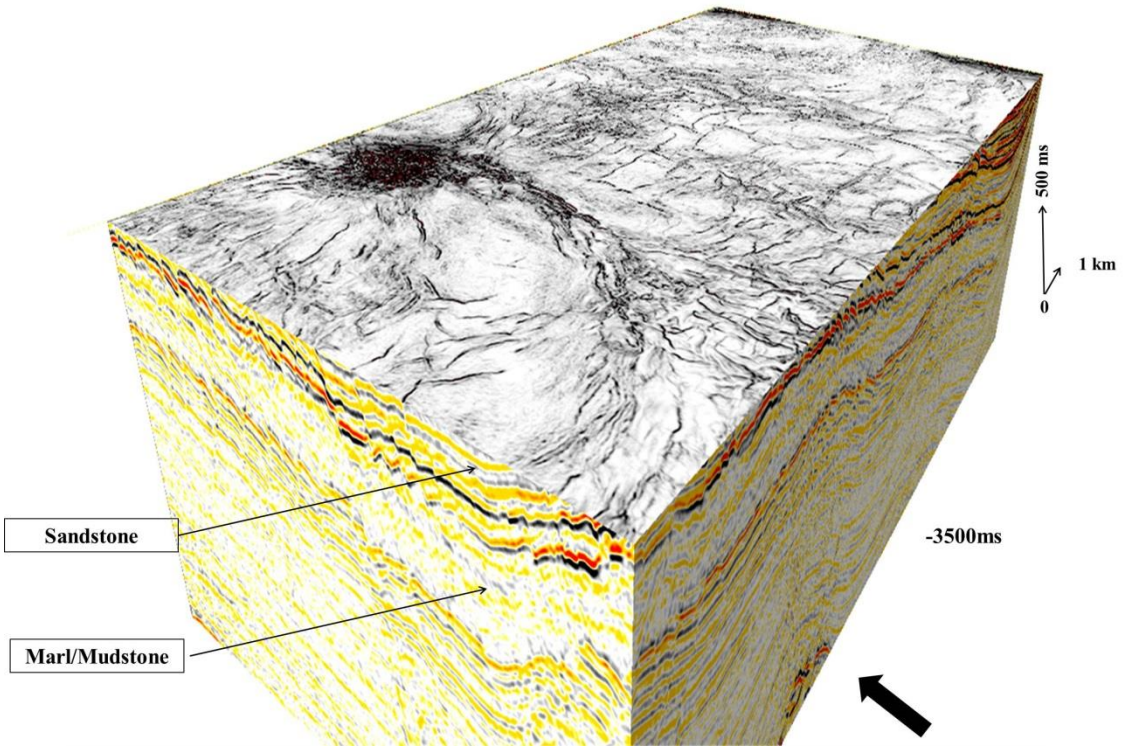

Figure 3.23: Coherence data used in lithology identification. Gray/white colour represent slow rate of deposition common in carbonates and shales.

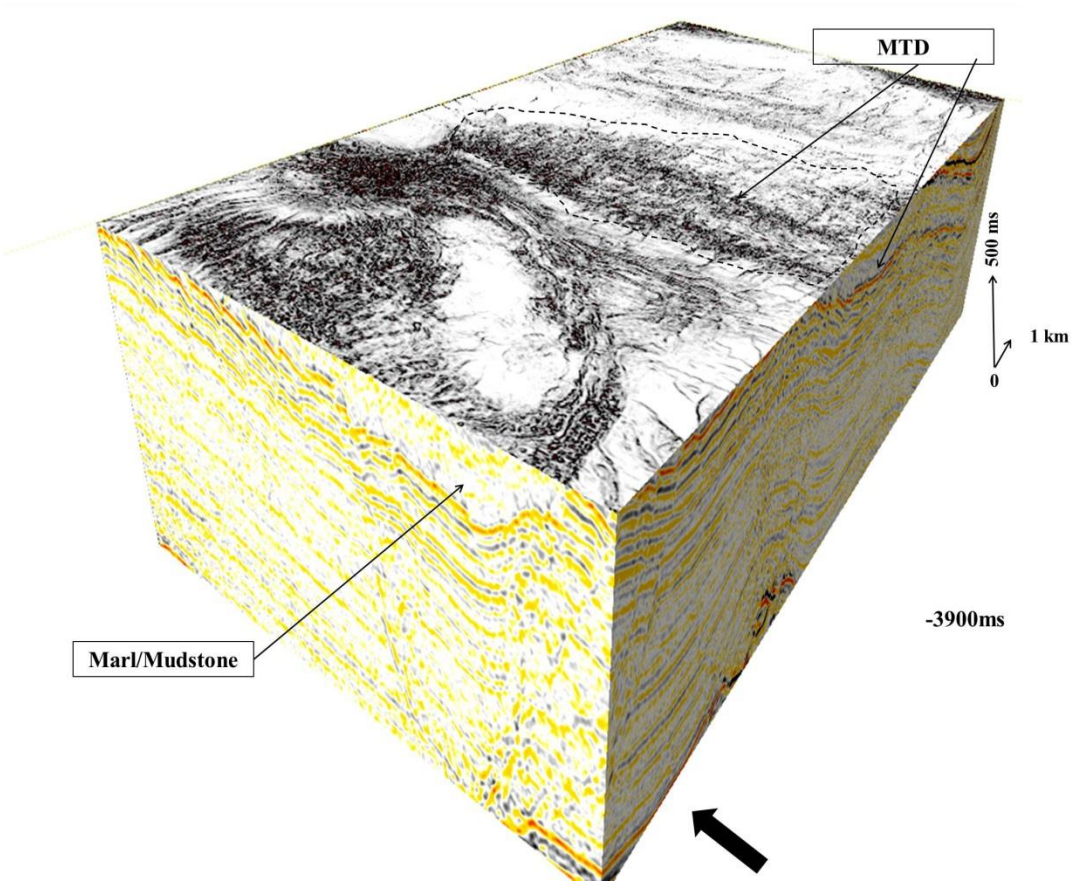

Figure 3.24: Coherence map for lithology identification. Mass-transport deposits are characterised by a relatively chaotic combination of low and high coherence coefficients..

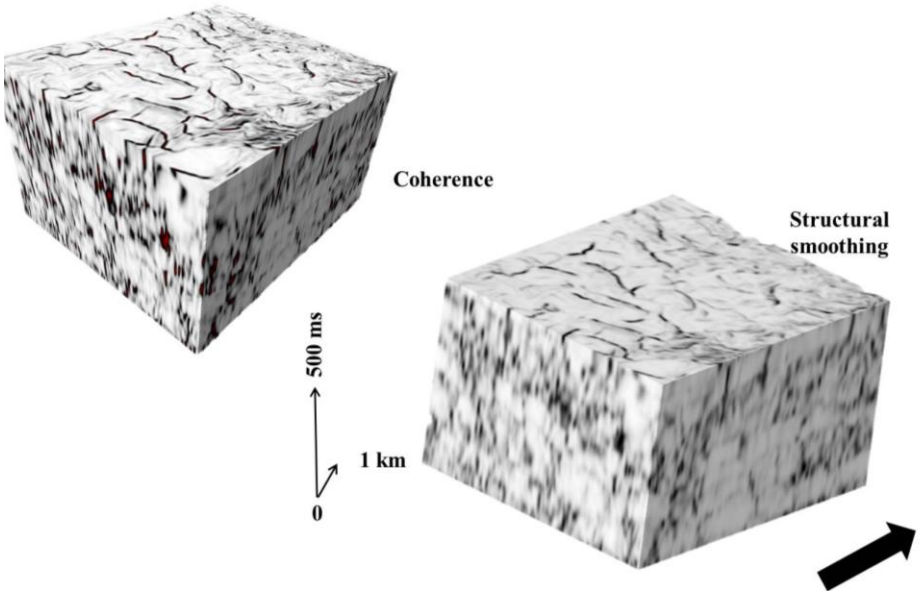

Figure 3.25: Structural smoothing as a key attribute for fault enhancement prior to automatic fault extraction.

3.4.5 Structural Smoothing

Structural smoothing algorithms calculate changes in local dip by smoothing the input signal to increase the continuity of the seismic reflector (Randen, 2000). Structural smoothing attributes are useful for pre-conditioning the seismic for automatic fault extraction (see Kadlec et al., 2010; Basir et al., 2013; Figure 3.25).

3.4.6 Ant tracking

The ant tracking attribute uses an analogy of ants' colony depending on pheromones to find the shortest path between their nest and their food source, the pheromones is a chemical substance that attracts other ants (Cox and Seitz, 2007). The shortest path will be marked with more pheromones than the longest path and so the next ant is more likely to choose the shortest route, and so on (Figure 3.26). The idea is to distribute a large number of these electronic "ants" in a seismic volume; and let each ant move along what appears to be a fault surface while emitting "pheromone." Ants deployed along a fault should be able to trace the fault surface in three dimensions before being terminated (Kadlec et al., 2010; Basir et al., 2013;). The automatic fault extraction algorithm is shown as a flowchart in Figure 3.26.

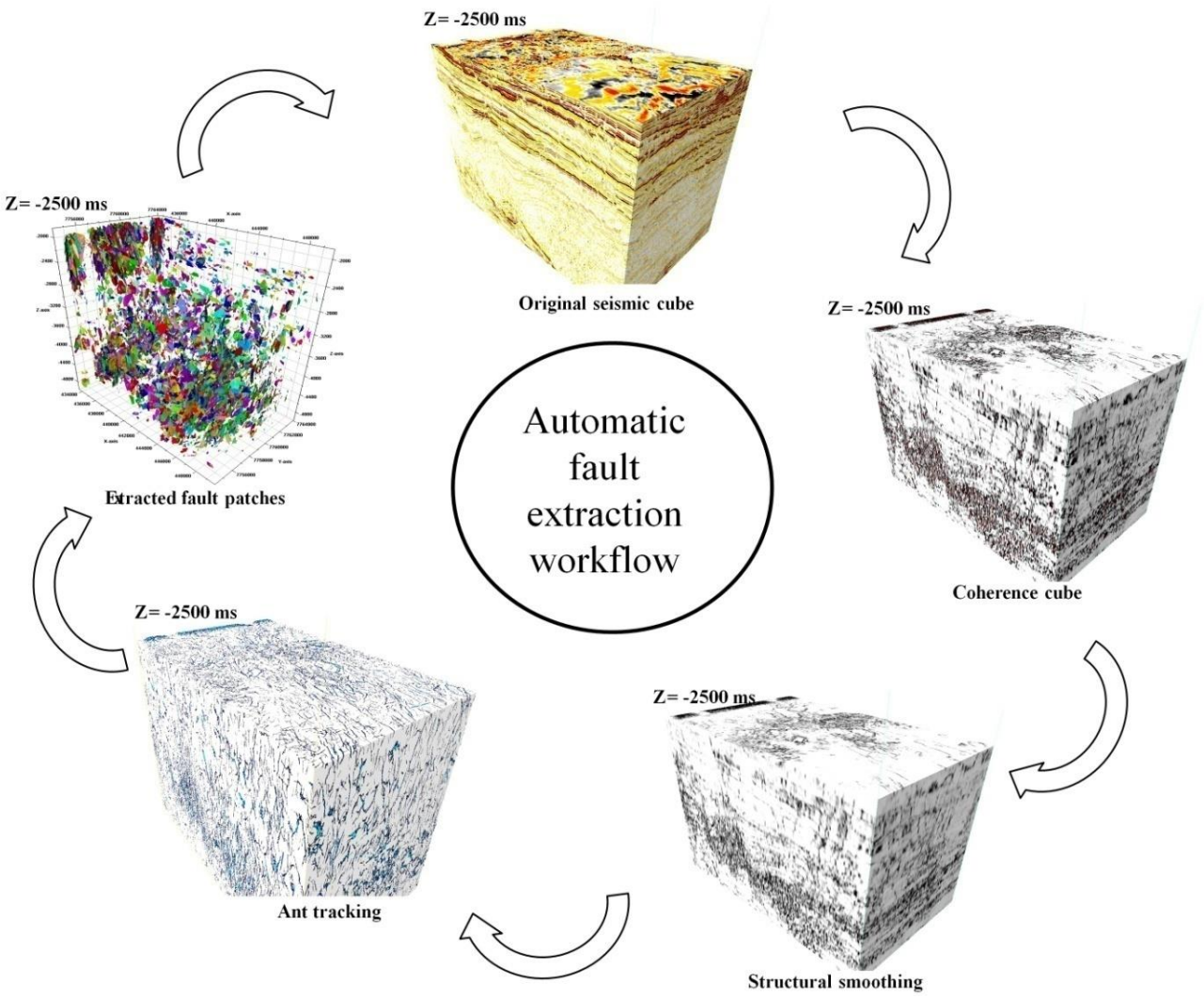

Figure 3.26: The Ant Tracking and automatic fault extraction workflow. The Ant Tracking algorithm involves the flattening of seismic volumes and data pre-conditioning for automatic fault extraction.

3.5 Erosion parameters

Grain-size analyses have wide applications in the characterization of depositional processes (Evans, 1939; Greenwood, 1978; Bryant, 1982; McLaren and Bowles, 1985) and sedimentary facies (Bigarella et al., 1969; Tucker and Wacher, 1980; Ponçano, 1986; Guedes et al., 2011). Significantly, grain-size techniques have also been used to estimate the provenance of sub-aerial landslides, particularly when of the analysis of poorly sorted debris-flow deposits with clasts reaching several 10's of metres in size, typical of landslide dams (Casagli et al., 2003; Dunning, 2006; Zhang et al., 2011). In this work, we present a variation of these techniques to investigate the provenance of MTDs as these present, in the study area, increasing degrees of disaggregation with transporting distances.

The orthogonal axes of eighty two (82) blocks were identified in computed attribute maps and measured at regular intervals (Figure 4.9). A-and b-axes were measured on individual seismic sections, time slices, isochron and attribute maps, while the height of blocks was plotted as the c-axis (Figure 3.27). Parameters tested for each block include their flatness and elongation ratios (Luttig, 1962), the Maximum Projection Sphericity index (MPSI, Sneed and Folk, (1958)), and the Oblate Prolate Index (OPI; Dobkins and Folk, 1970).

Flatness ratio is the ratio of the c-axis (thickness) to a-axis (length), while elongation ratio is the fraction of b-axis (width) to the a-axis (length) (Lin and Miller, 2005) (Figure 3.28). The MPSI is used to estimate the sphericity of a particle, a property related to its hydraulic behaviour (Dobkins and Folk, 1970). The new technique presented in this thesis relies only on the dimension of the orthogonal axes, which are

independent of each other. The need to correctly elucidate the structure of the blocks prompted the use of both the Sneed and Folk (1958) and Zingg (1934) diagrams. These ratios were plotted on Sneed and Folk (1958) triplots and Zingg (1934) charts with the aim of correlating blocks' transporting distance with their shapes.

As far as the interpreted MTDs are concerned, the Folk and Sneed tri-plot is simpler, flexible and applicable to all kind of clast analysis (Hockey, 1970) while the Zingg (1934) diagram is better suited to discriminate between certain types of sedimentary deposits (Howard, 1992).

3.6 Statistical analyses

Computed statistical parameters include the mean, standard deviation, correlation coefficients (r), and coefficient of determination (R^2) as defined in Fieller et al. (1957) and Kendall and Stuart (1973). The mean represents the average thickness of blocks. Standard deviation shows the spread of the blocks. Correlation coefficients are a measure of the linear relationship between two variables. The coefficient of determination (R^2) measures the strength of the coefficient of correlation (Fieller et al., 1957).

3.6.1 Statistical analyses in Chapter 4

In this Chapter were analysed thickness variations of MTDs accumulated around salt diapirs with a view to investigate their proximity to source areas, and infer the relationship between the timings of halokinesis and MTDs spatial distributions. Thickness data were collected every 625 m. The data obtained were used to compute

box and scatter plots of MTD thickness vs. diapir diameters and relative distances from diapir centres (Figures 4.21). Correlation coefficients are a measure of the linear relationship between blocks and salt diapir geometries. Correlation coefficients range from negative (-0.6) to positive (0.6) in the box plots computed for the study area.

In blocky MTDs, the orientations and dimensions of blocks were recorded along the flanks of interpreted diapirs. Data for individual blocks were collected in a N-S direction every 63 m. The diameters of salt diapirs were measured on time-structure maps of key horizons (*cf.* Figure 4.10 for a detailed description of the statistical parameters used in this study).

3.6.2 Statistical analyses in Chapter 5

In order to understand the mode of formation of basal ramps and how they relate to observed promontories, the thickness of interpreted MTDs was estimated within individual depressions, or coves as named in this work, created by ramps and promontories (Figures 5.15 and 5.16). In addition, the lengths of distinct ramps, the widths of coves and of adjacent promontories were measured as a way to estimate the erosion power of the investigated MTDs. Correlation coefficients between the width of coves and the maximum thickness of MTDs were calculated for the study area. The transporting distance of MTDs along slope, and the diameters of associated salt diapirs were also correlated.

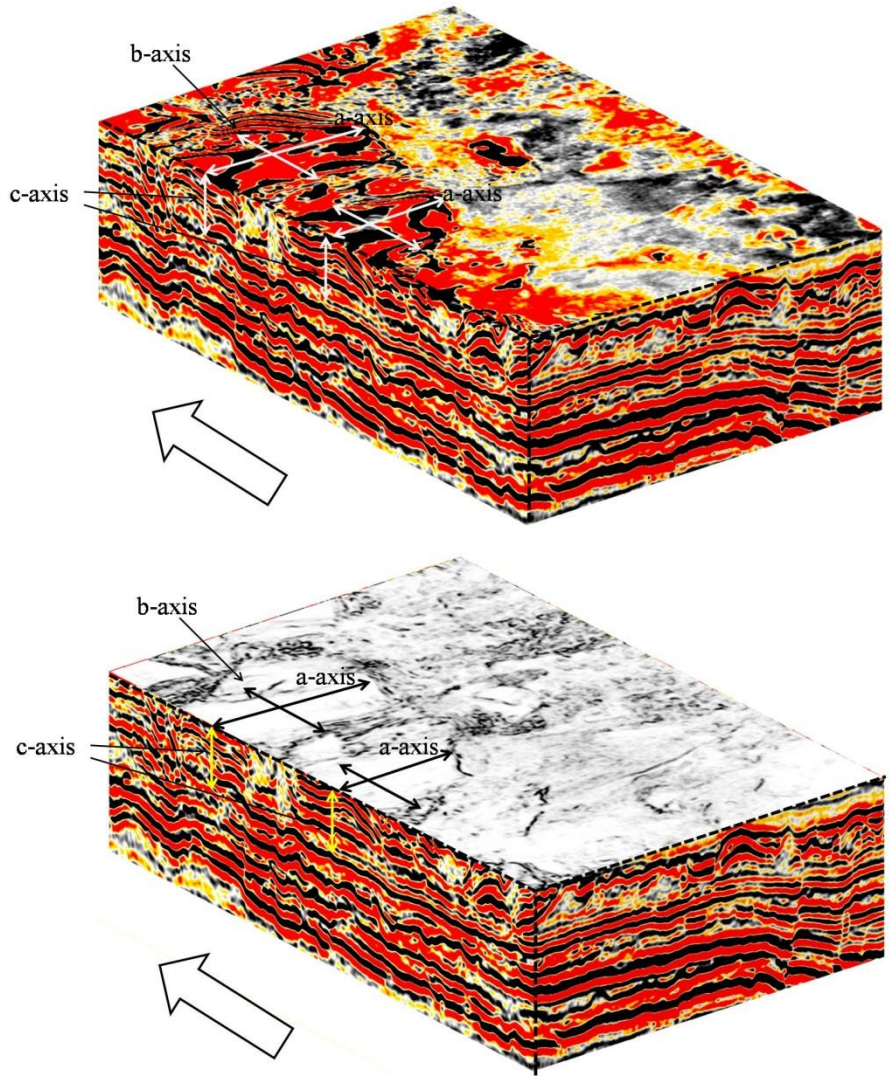

Figure 3.27: The a- and b-axis of the blocks were measured on TWTT and attribute maps while the c-axis was taken the height or thickness of the blocks.

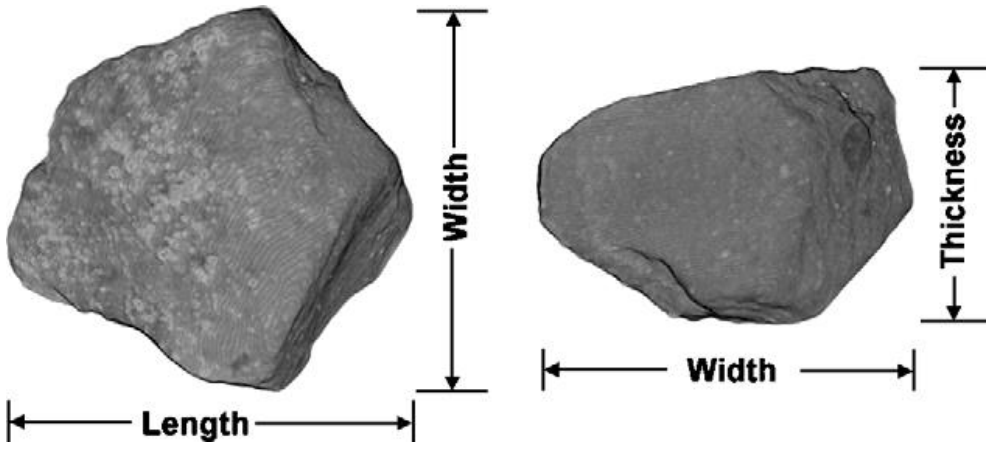

Figure 3.28: Elongation and Flatness ratios from Lin and Miller (2005).

3.7 Graphical analysis

- Histograms: A histogram is used to plot the underlying frequency distribution (shape) of a set of continuous data that has been divided into classes, called bins (Stengel et al., 2008). The histogram is a useful plot for showing the dominance of a part class interval in a set of continuous data (c*f*. Figure 3.29).

- Box plot: A box plot, otherwise known as *five-number summary*, consists of the median, the quartiles, and the smallest and greatest values in the data distribution (Lem et al., 2013). The box plot is a simple way of presenting descriptive statistics of huge volume of data (c*f*. Figure 3.30).

- Scatter plot: This is a graph for plotting bivariate data as points on a two-dimensional Cartesian plane. Scatter plots are used to analyse the association of two variables (Heo et al., 2008; Johnson and Bhattacharyya, 2010). This is a graphical inferential statistics method to test the degree of correlation between two variables as direct or inverse association (c*f*. Figure 3.31).

- Rose Diagram: Rose diagrams are circular frequency histograms that are used to plot directional (azimuthal) data e.g. strikes of beds, wind direction, or ocean current directions (Robson, 1994). In structural geology, rose diagrams are very useful for unravelling the tectonic history of deformed rocks and regions. The dominant frequency class is indicating the principal strain direction for the deformed rocks (c*f*. Figure 3.32).

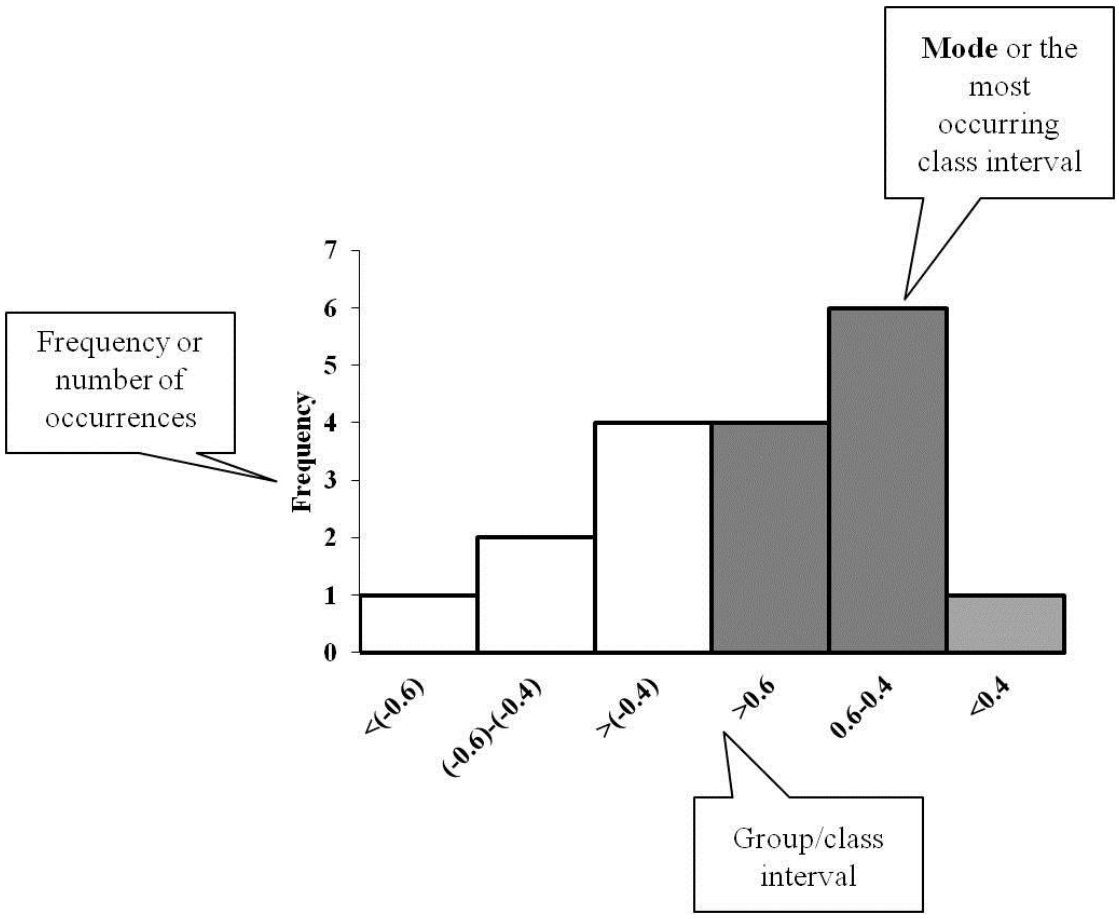

Figure 3.29: Annotated histogram highlighting the key parameters used in the statistical analyses presented in this work.

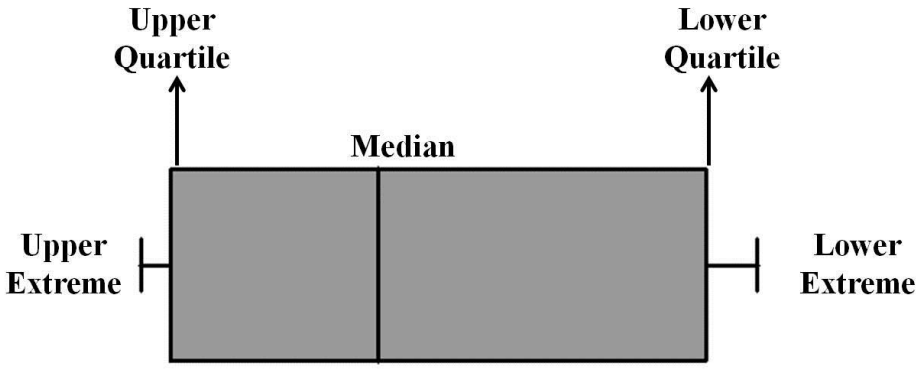

Figure 3.30: Box-Plot organised as a five-summary figure, a very powerful descriptive statistical tool used in this study.

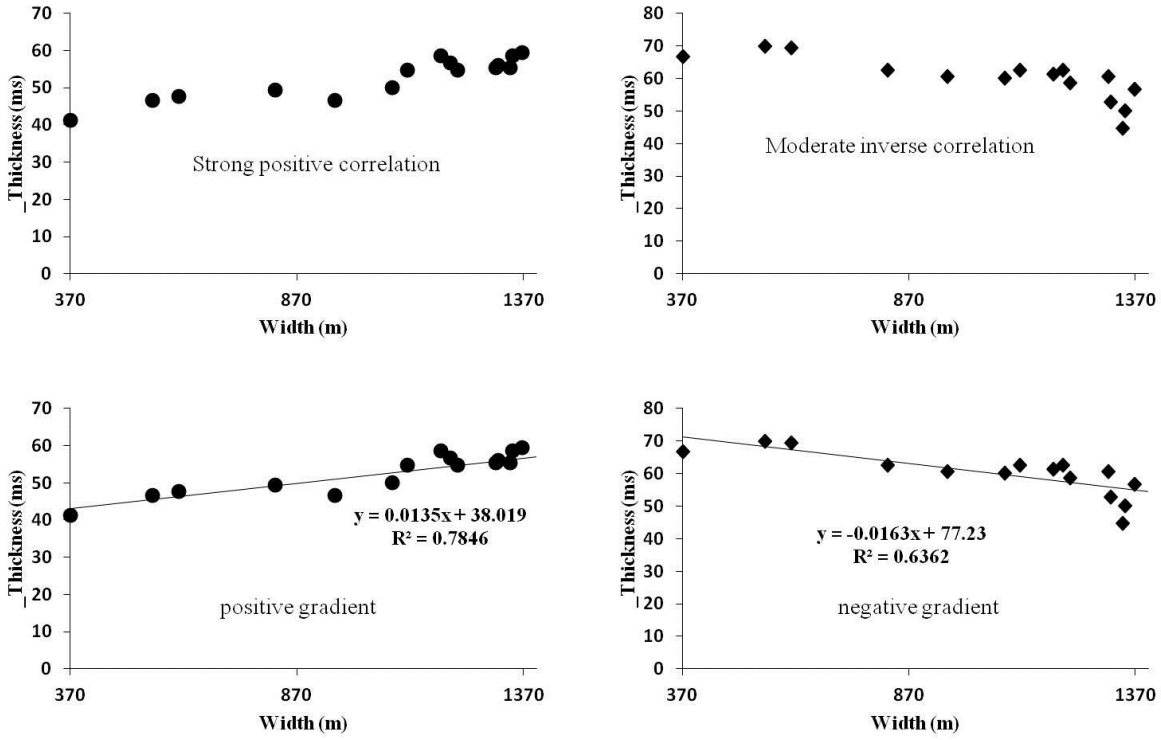

Figure 3.31: Scatter plot and its relevant for establishing association for bivariate data.

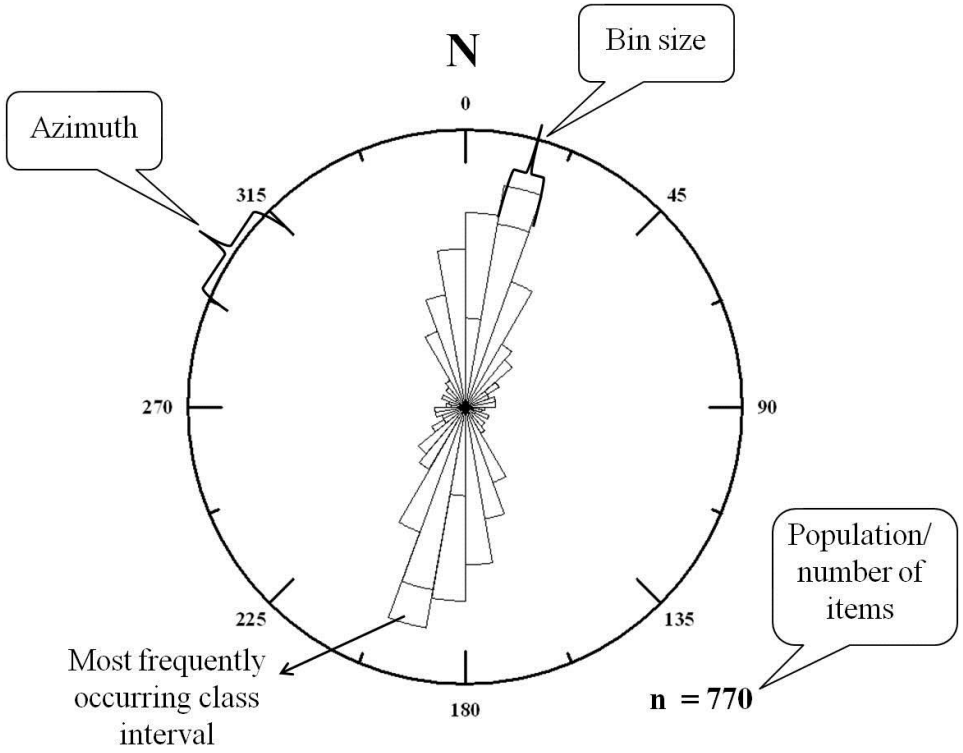

Figure 3.32: Annotated rose diagram highlighting salient parameter considered in this work.

Chapter 4

A 3-dimensional seismic method to assess the provenance of Mass-Transport Deposits (MTDs) on salt-rich continental slopes (Espírito Santo Basin, SE Brazil)

This Chapter is published as:

a) **Omosanya, K.O**., Alves, T.M. (2013), A 3-dimensional seismic method to assess the provenance of Mass-Transport Deposits (MTDs) on salt-rich continental slopes (Espírito Santo Basin, SE Brazil), Marine and Petroleum Geology 44, 223- 239 http://dx.doi.org/ 10.1016/j.marpetgeo.2013.02.006

b) KO Omosanya, TM Alves Provenance of a Blocky Debris Flow Deposit in Mid-continental Slopes (Espírito Santo Basin, SE Brazil) - 75th EAGE Conference & Exhibition incorporating SPE …, 2013

Abstract

Provenance studies of Mass-Transport Deposits (MTDs) frequently rely on the analysis of kinematic indicators. In this work, we use seismic facies analyses, measurements of preserved blocks, and correlations between MTDs thickness and salt diapir geometry to introduce a new method to estimate the provenance of MTDs on 3D seismic data. The method, applied to a high-quality 3D seismic volume from the Espírito Santo Basin (SE Brazil), provides information on the location of source areas of MTDs, their bulk composition, and their directions of transport. Whenever blocks of strata are found, their orthogonal axes are measured to estimate parameters such as Maximum Projection Sphericity Index (MPSI), Oblate Prolate Index (OPI), and ratio of short and intermediate axes (ds/di). These parameters are used to quantify the relative degrees of remobilization and transport of MTDs. Statistical data of importance include the variation of MTDs thickness with the diameter and distance from the centre of growing salt diapirs. In addition, the presence of cubic or equant blocks with $c/a > 0.4$ and $c/b > 0.65$ ratios are typical of proximal areas in MTDs, reflecting small transporting distances. Our work is important because it shows that distinct correlation coefficients exist between the thickness of MTDs and diameter of salt diapirs. Positive coefficients of correlation between diapir diameter and MTD thickness characterise active diapirism during the deposition of MTDs. This quantification allows the interpreters to distinguish MTDs sourced from local diapirs from MTDs sourced from more distal regions on the continental slope. Thus, the new method used in this research provides an alternative technique to kinematic indicators for determining the provenance of mass transport deposits on continental margins.

4.1. Introduction

Mass-wasting events are primary processes both shaping and filling sedimentary basins (Masson et al., 1998; Norem et al., 1990; Gee et al., 2005; Gee and Gawthorpe, 2006; Gee et al., 2008; Richardson et al., 2011). Mass-transport deposits (MTDs) comprise 10%-27% of continental slope strata (Hunerbach and Masson, 2004; Mienert et al., 2003; Hjelstuen et al., 2007b; Tailing et al., 2007). They occur on both passive and active margin settings (Urgeles et al., 1997; Goldfinger et al., 2000) and at all latitudes, from glacial to equatorial regions (Laberg and Vorren, 2000; Laberg et al., 2000; McAdoo et al., 2000; Alves, 2010b; Alves and Lourenço, 2010; Hunerbach and Masson, 2004). However, the provenance of MTDs can seldom be interpreted in 3D seismic volumes of limited extent, particularly if their headwall regions are not imaged e.g. (Frey Martinez et al., 2005; Moscardelli et al., 2006). In these situations, the provenance of MTDs is often inferred using kinematic indicators, or correlating sub-surface data with geomorphological information from outcrop analogues (Boe et al., 2000; Laberg and Vorren, 2000; Laberg et al., 2000; Strachan, 2002a, b; Lucente and Pini, 2003; Haflidason et al., 2004; Wilson et al., 2004; Frey Martinez et al., 2005; Gee et al., 2005; Schnellmann et al., 2005; Frey-Martínez et al., 2006; Lastras et al., 2006; Bull et al., 2009). Kinematic indicators, however, might be elusive in some MTDs or can represent local instability events, particularly in regions recording intense seafloor deformation. Outcrop analogues can be used to tackle some of these limitations but they are, in turn, of limited extent, poorly exposed or often not preserving the original MTD morphology due to subsequent surface erosion (Callot et al., 2008; Alves and Lourenço, 2010).

In the specific case of salt-rich continental margins, halokinetic movements can substantially modify slope gradient and trigger complex mass-wasting events. MTDs

are often thinner at the crest of active diapirs and thicker on their flanks (Rowan et al., 1998; Davison et al., 2000b; Tripsanas et al., 2004). In parallel, the geometry of blocks provides useful data to assess the hydrodynamic behaviour and transport directions of mass-wasting deposits sourced from active salt structures (Canals et al., 2000; Moscardelli et al., 2006; Vizcaino et al., 2006; Alves and Cartwright, 2009; Alves, 2010a; Alves, 2010b; Gamboa et al., 2010; Gamboa et al., 2011). Knowing this, the aims of this Chapter include: (a) examine the seismic heterogeneity of MTDs on a salt-rich continental slope; (b) quantify the degree and styles of disaggregation of MTDs in relation to their transporting distances; and (c) understand how interactions between blocks of strata and growing salt diapirs can provide information on the provenance of MTDs.

This Chapter starts by presenting the internal character of interpreted MTDs. It then assesses their transport history by quantifying the geometry of remnant and rafted blocks. We use basic concepts on particle size analysis e.g. (Sneed and Folk, 1958; Luttig, 1962; Dobkins and Folk, 1970) and statistical data to characterise the provenance of interpreted MTDs. In the discussion, we use the new methods in this paper to conclude on the main directions of sediment transport, the proximity of source areas of MTDs, timing of diapirism, and the styles of basal erosion and internal deformation in MTDs. Our approach grants the new methods importance and applicability, as similar blocky MTDs to those in this chapter have been found on continental margins around the world (Masson et al., 2002; Posamentier and Kolla, 2003; Lastras et al., 2005; Callot et al., 2008; Armitage et al., 2009; Armitage and Jackson, 2010).

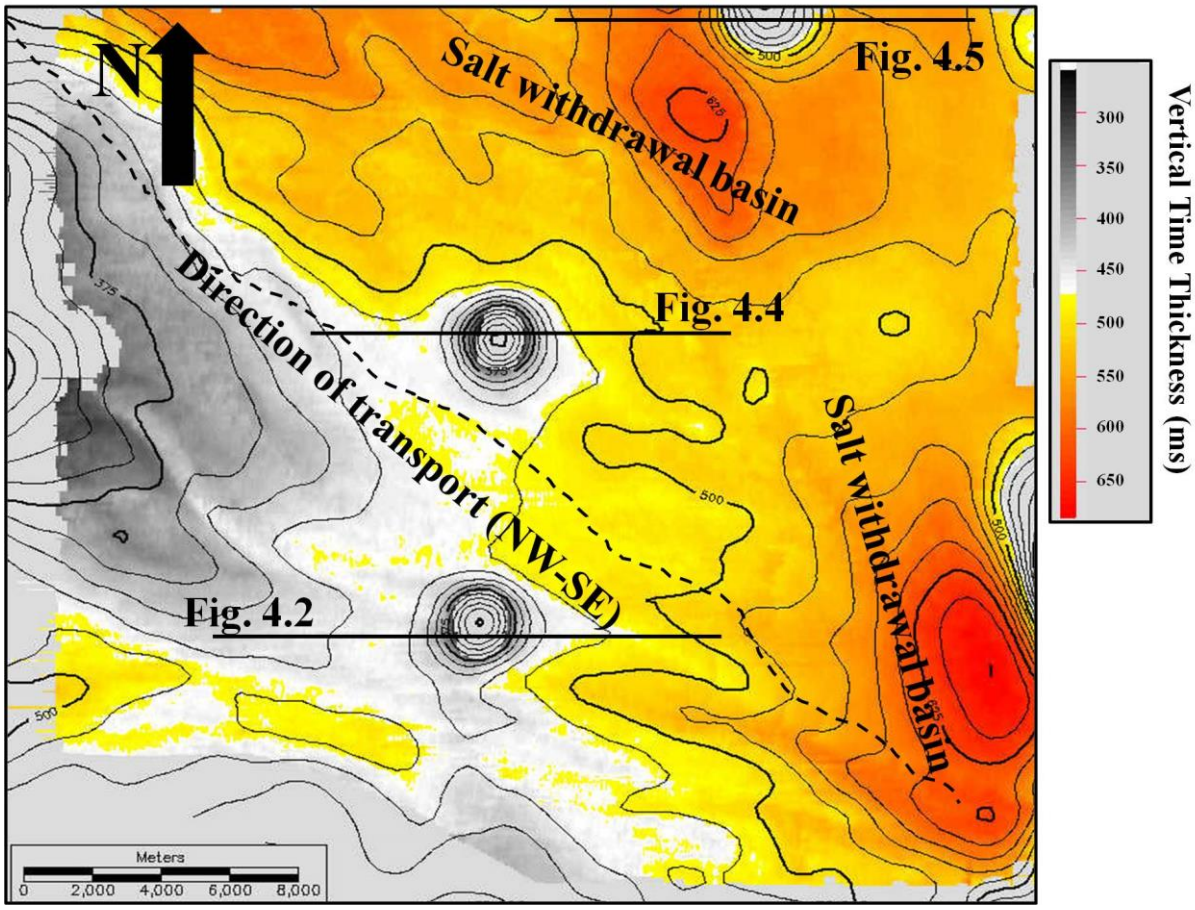

Figure 4.1: Two-way travel-time (TWTT) thickness map of Eocene (Horizon H0) to Holocene (seafloor) strata highlighting the position of three of the five salt diapirs referred to in this work. Also shown is the location of seismic lines in this chapter

4.2 Results

4.2.1 Internal character of MTDs 1-4

The top and basal surfaces of four (4) MTDs were mapped as nine (9) separate horizons, numbered H0-H8 (Figures 4.2 to 4.6). The upper surface of a MTD is usually a rugged or ridged surface located above chaotic to moderately deformed reflections of variable amplitude (Richardson et al., 2011), while the basal shear surface separates disrupted strata within the MTDs from the much more continuous deposits underneath the MTDs (Frey-Martínez et al., 2006; Frey Martinez, 2010). The main characteristics of the interpreted MTDs are summarised as follows:

4.2.1.1 MTD 1

MTD 1 is the oldest in the study area (Figures 4.2 to 4.6). It is located around diapirs D4 and D5 (Figure 4.1). Its upper and lower surfaces consist of continuous, high-amplitude reflections (H1 and H0, respectively). The headwall of MTD 1 is located northwest of diapir D5, with the MTD striking at approximately N43^{0}W. The basal surface (H0) is characterised by striations, grooves and ramps (Figure 4.8). Striations are oriented NW-SE, which is the inferred direction of transport of MTD 1 (Figure 4.8). MTD 1 is Early Palaeogene in age (Mohriak, 2003, Fiduk et al., 2004; Mohriak, 2005) and runs ~38 km downslope with a width of ~37 km over an area of ~749 km^2.

4.2.1.2. MTD 2

This MTD is of probable Eocene age (Mohriak, 2003, Fiduk et al., 2004; Mohriak, 2005), and is limited by diapirs D1, D2 and D3 (Figure 4.8). It is ~53 km in length and ~25 km in width (Figure 4.8). Its upper limit is marked by a discontinuous, ridged, low

amplitude reflection (H3) that pinches out underneath the H4 horizon towards the west. The base of MTD 2 is a low-amplitude horizon characterised by ramps and promontories on its eastern margin (Figure 4.3 and 4.4). The headwall region of MTD 2 is not preserved, likely a consequence of quick burial and erosion on a seafloor deformed by halokinetic movements.

4.2.1.3. MTD 3

The Late Eocene MTD 3 (Fiduk et al., 2004; Mohriak 2003, 2005; Alves, 2012), has a discontinuous basal surface (H4) that is highly erosive (Figure 4.8). Its upper surface is also bounded by a discontinuous reflection of moderate amplitude (H5). The basal surface shows features such as erosive scours and ramps, particularly towards the western margin of MTD 3. The MTD is ~48 km long and ~28 km wide, with a surface of area of ~851 km^2. Its headwall region is inferred to be located NW of diapir D4 (Figures 4.5 and 4.9).

4.2.1.4. MTD 4

MTD 4 is the shallowest of the MTDs in the study area (Figure 4.6). It comprises relatively continuous, high-amplitude internal reflections. MTD 4 is likely composed of Miocene marine sand (Mohriak, 2003, Fiduk et al., 2004; Mohriak, 2005) and it has area coverage of ~326 km^2. Downslope, MTD 4 is ~30 km long and ~14 km wide. Its headwall is located between diapirs D2 and D3 (Figure 4.6) and shows closely-spaced extensional faults (Figure 4.7). At its basal shear surface are observed grooves, striations, and ramps (Figure 4.8). Its headwall is characterised by moderate amplitude to transparent reflections, their amplitude increasing towards the toe region where deformation is observed in the form of small-scale thrust faults in rafted blocks (Figure 4.7). The estimated strike of MTD 4 is approximately $N47^0W$ (Figure 4.8).

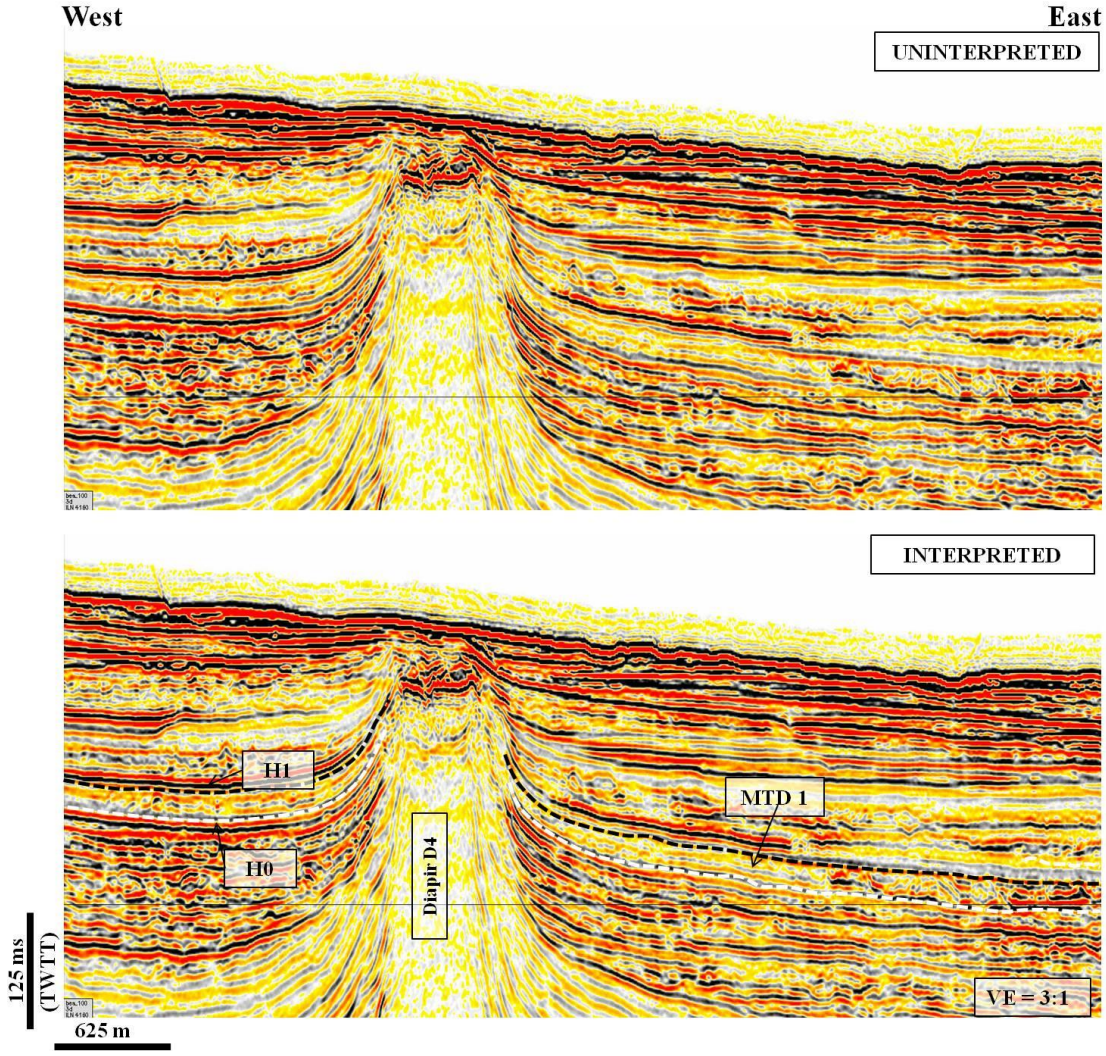

Figure 4.2: The boundaries of MTD 1 are restricted to the region around diapirs D4 and D5, and its headwall region is inferred to be NW of D5 in an area characterized by polygonal faulting..

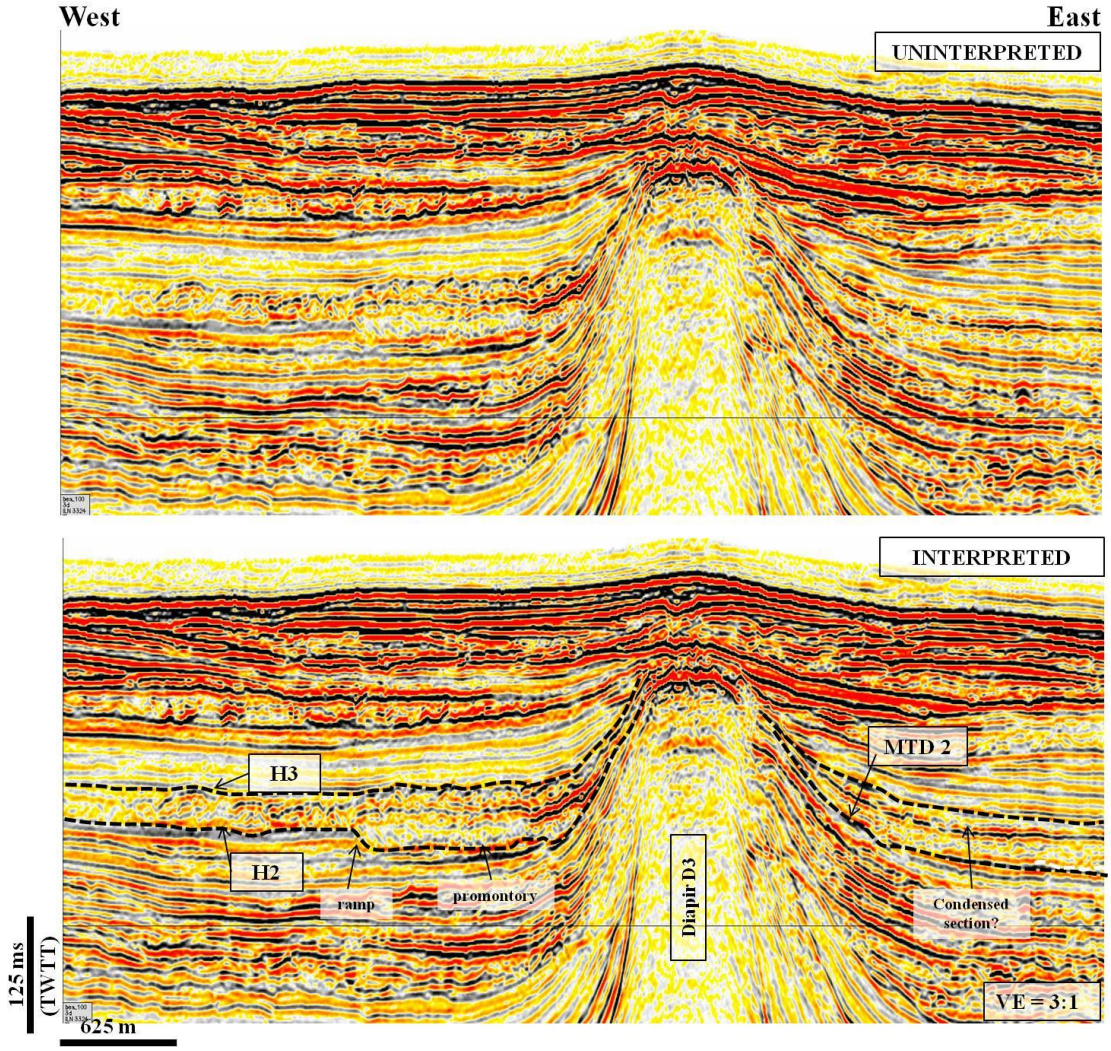

Figure 4.3: MTD 2 is Late Eocene in age. In contrast to the other MTDs in this chapter, its headwall region is not imaged in the interpreted seismic volume. *See figure 4.8 for location.*

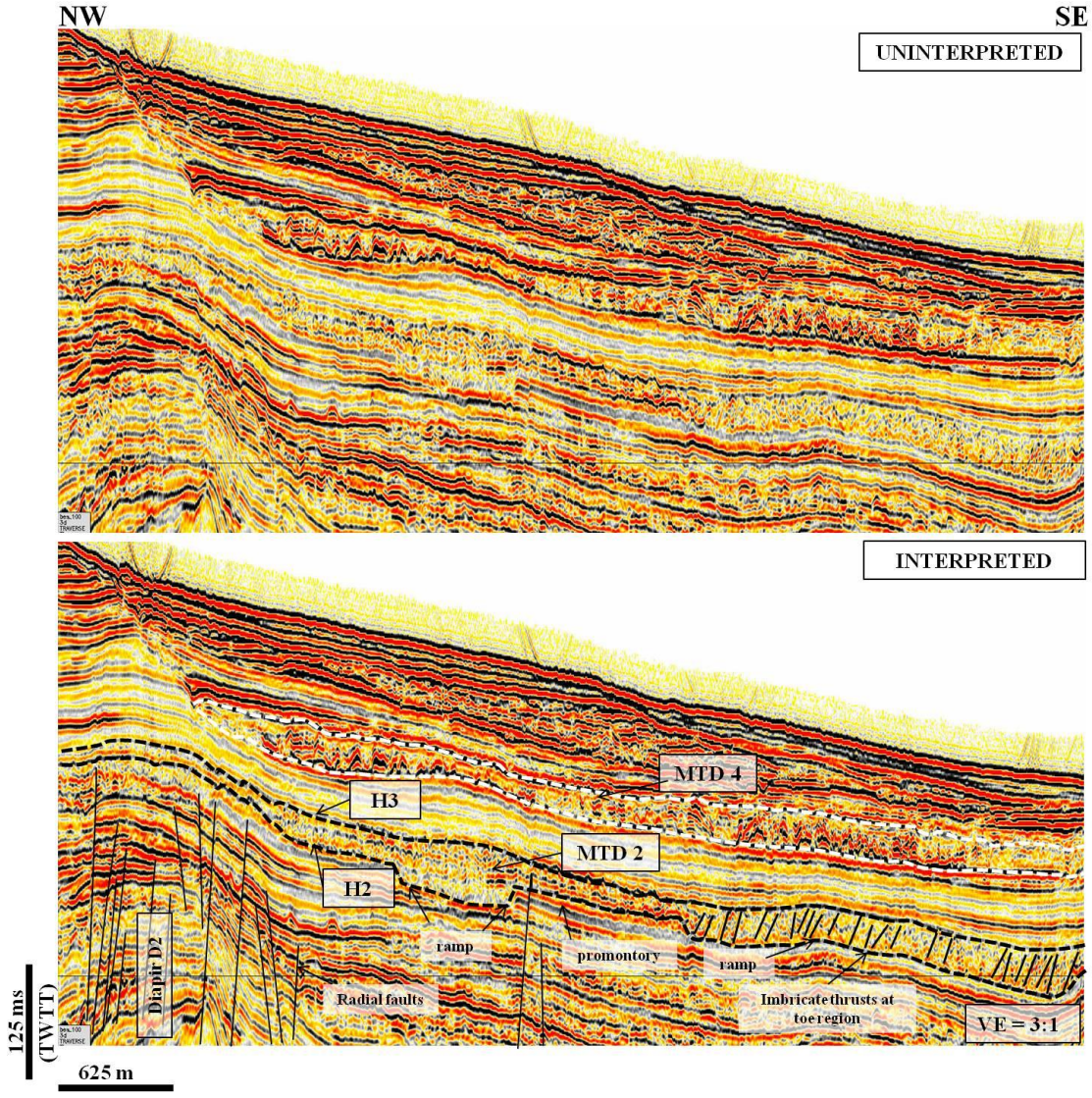

Figure 4.4: The basal shear surface of MTD 2 is characterized by ramps surrounded by protrusions, which are generically named as 'promontories' by Bull et al. (2009).

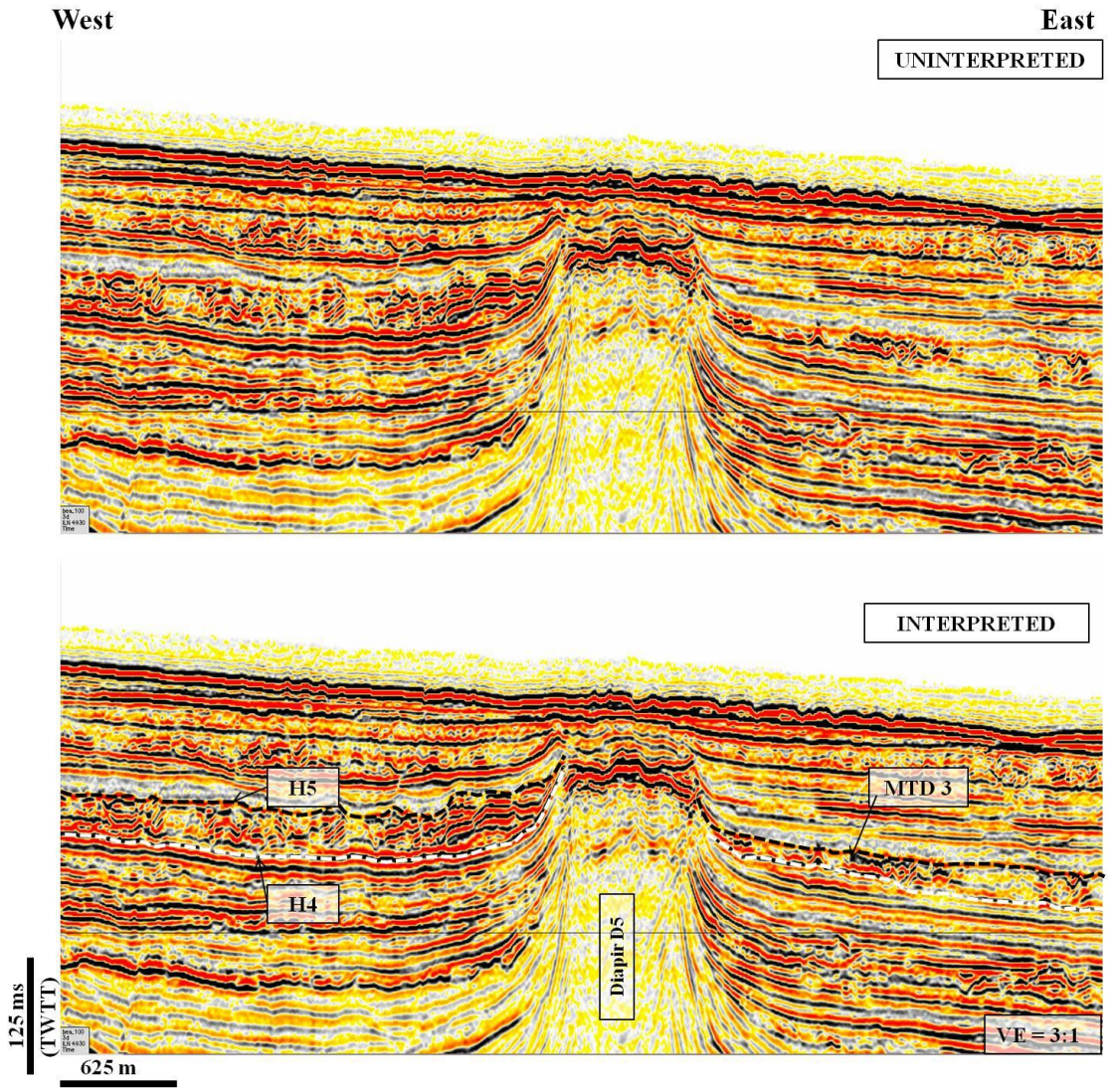

Figure 4.5: MTD 3 is located on the flanks of diapirs D4 and D5. Its headwall region is located NW of D4.

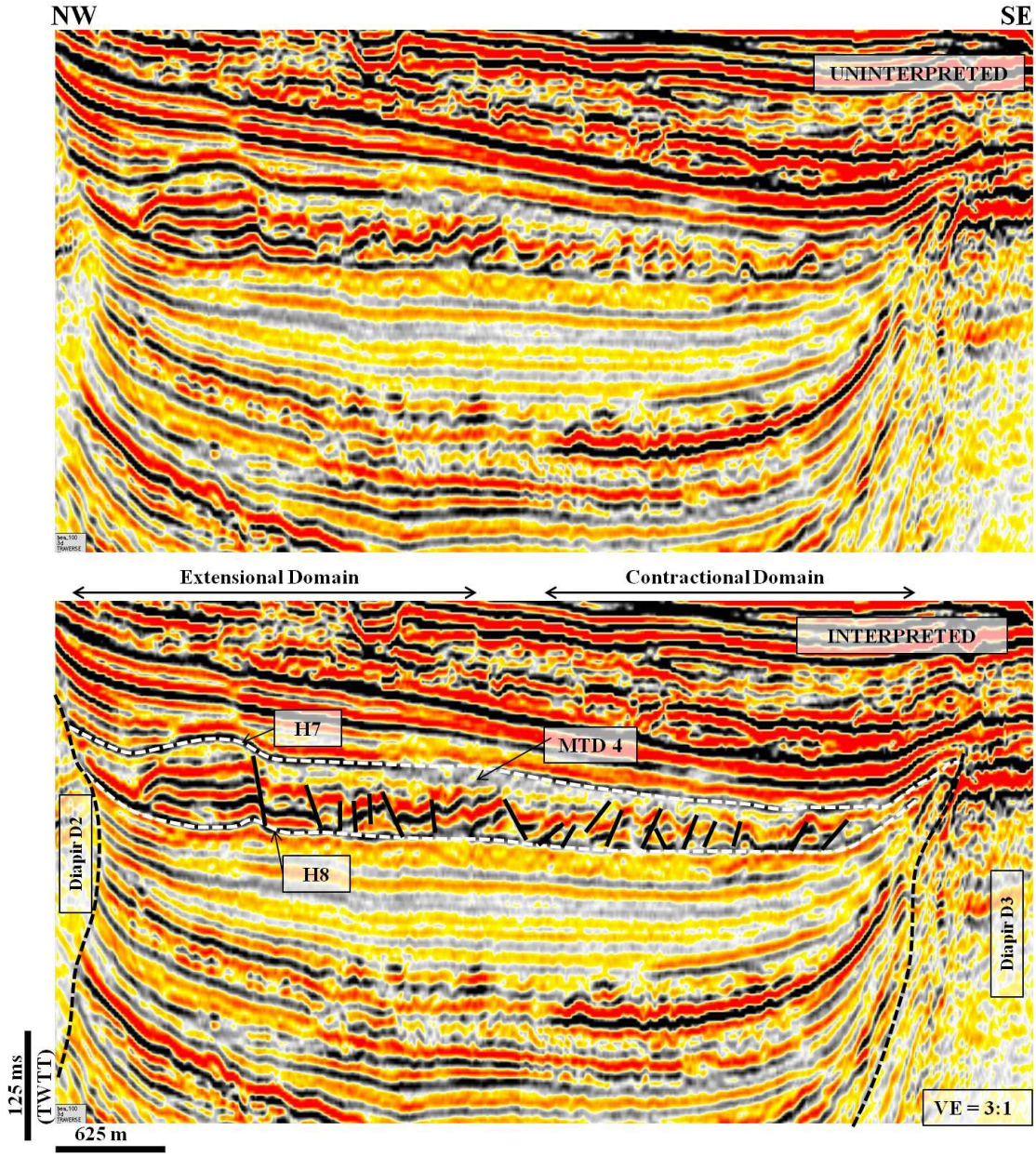

Figure 4.6: MTD 4 is Miocene in age and is the youngest mass-transport deposit mapped in the study area. *See figure 4.8 for location.*

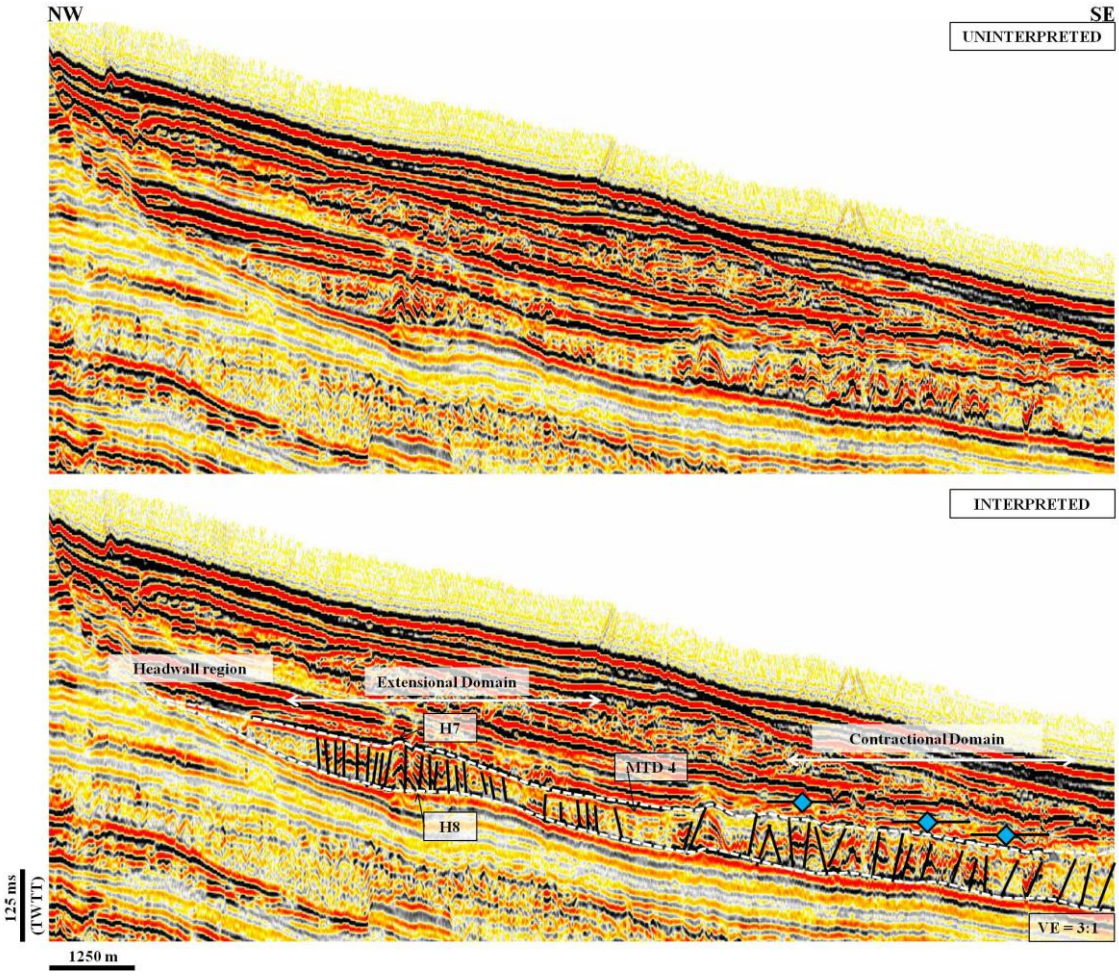

Figure 4.7: The upper region of MTD 4 is characterized by extensional structures, and its toe region is frontally emergent. *See figure 4.8 for location.*

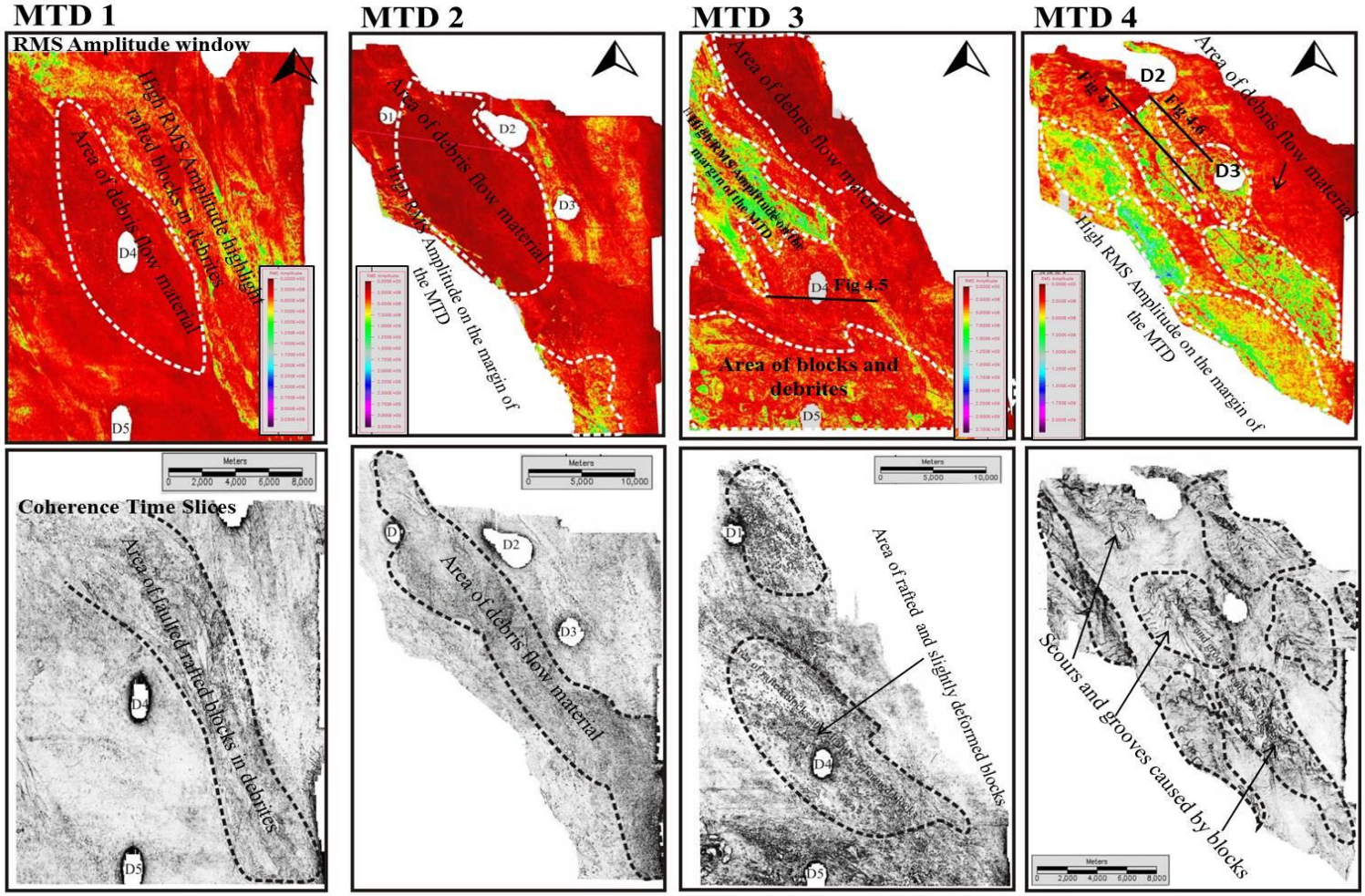

Figure 4.8: Attribute maps illustrating the internal character of MTDs 1 to 4 in the study area. RMS amplitude maps were computed for all MTD intervals. Debrites are shown with hot colours (red) while interpreted hemipelagic materials are orange-coloured, particularly in MTD 2. Green colours at the marginal areas of MTDs relate to high amplitude strata deposited as the MTD thins out. Coherence time slices were computed for the four MTDs. Grey colours represent areas of hemipelagic sediment and debrites. Rafted blocks are shown as dark patches with chaotic character, i.e. low coherence. Highlighted on the coherence maps are areas with different block geometries.

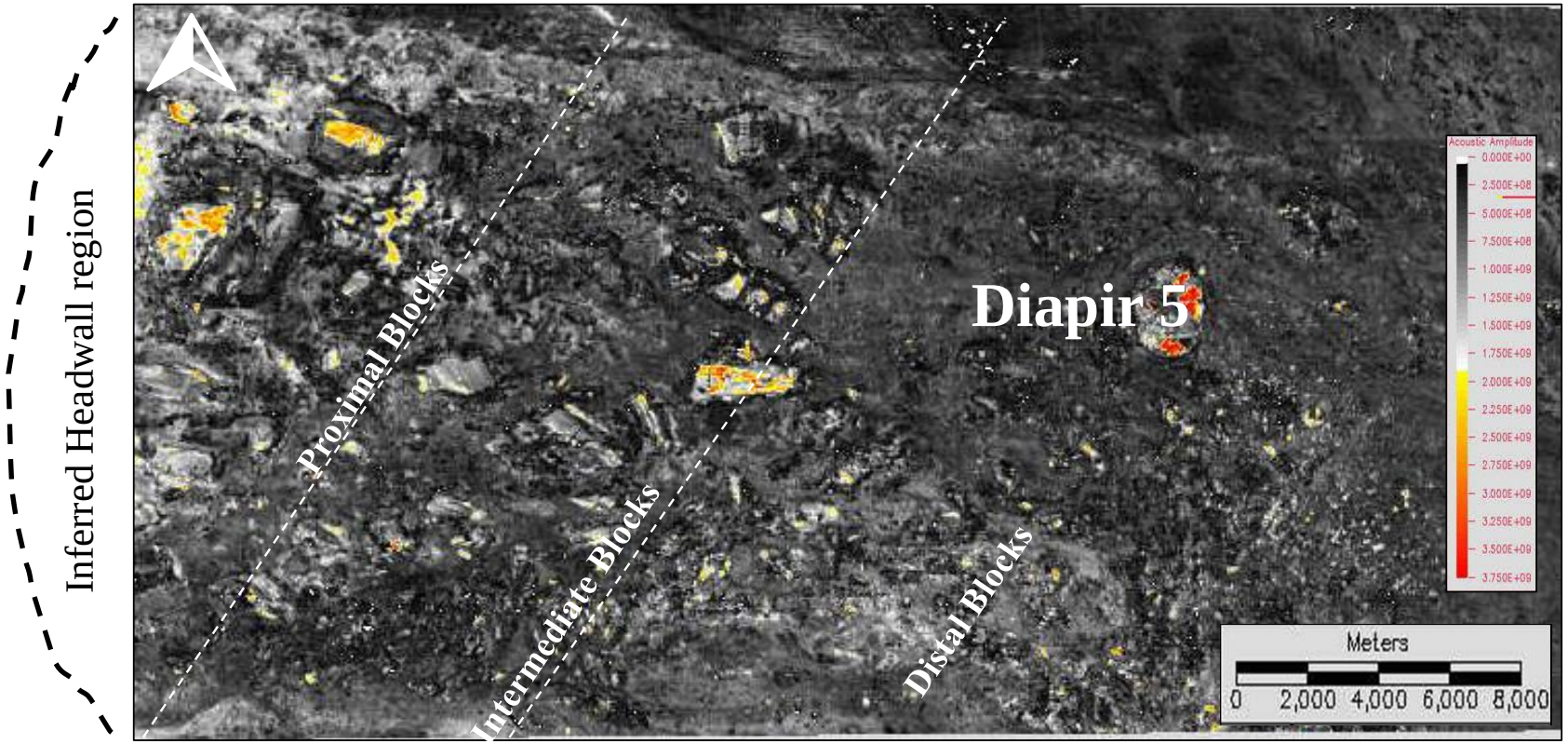

Figure 4.9a: RMS amplitude map of MTD 3 depicting the geometry of rafted blocks.

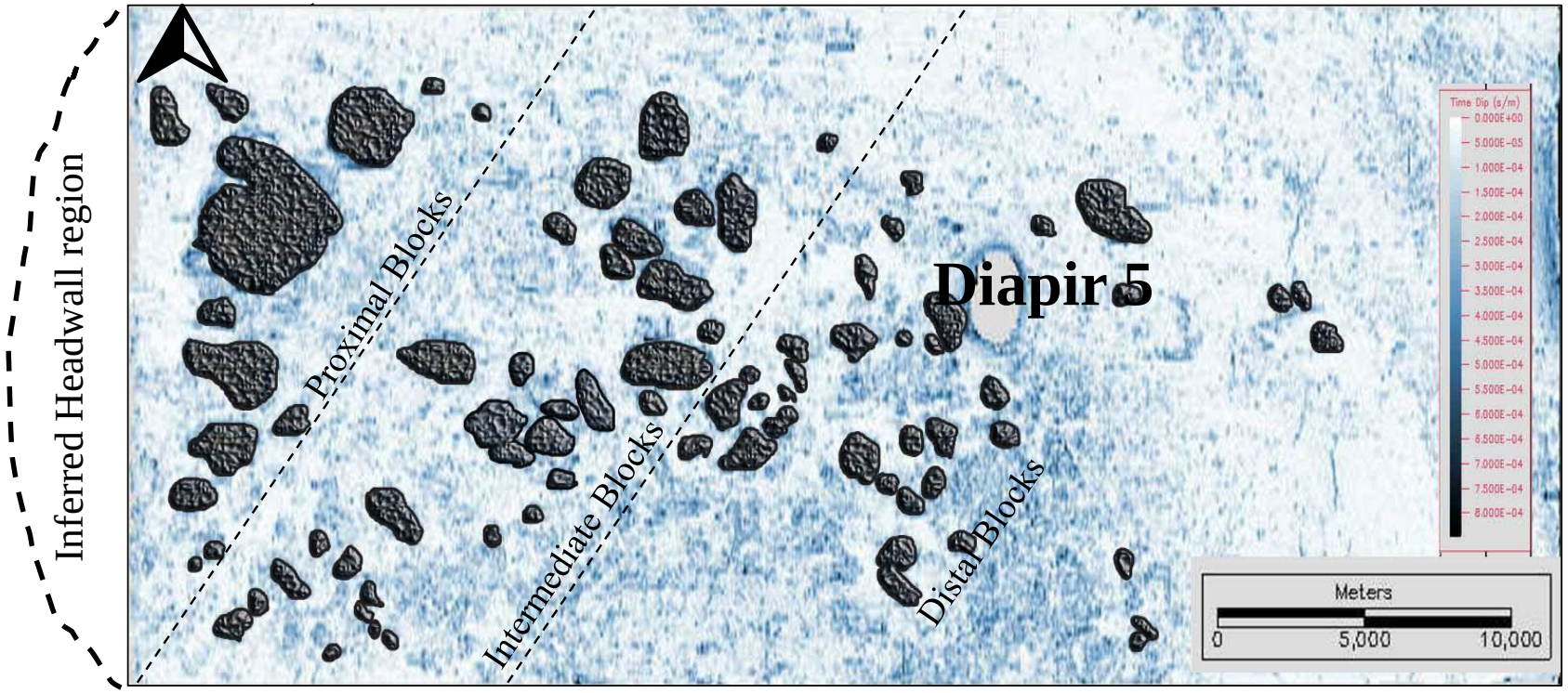

Figure 4.10b: Time dip map highlighting changes in gradient on the flanks of imaged blocks. The blocks were categorised into those at distance (distal), intermediate and proximal to the inferred headwall region

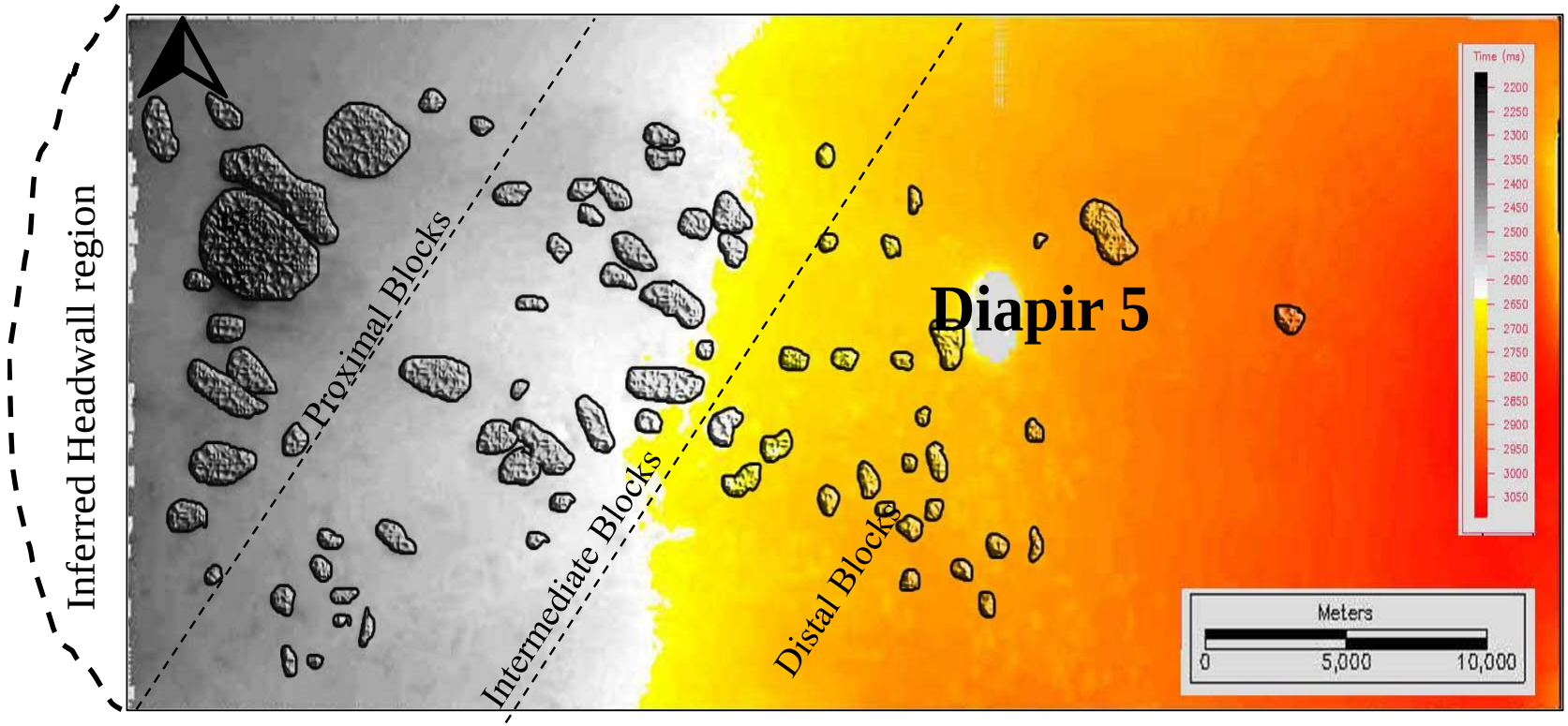

Figure 4.11c: Individual blocks stand out as topographic highs amidst the lower relief debris in which they are translated

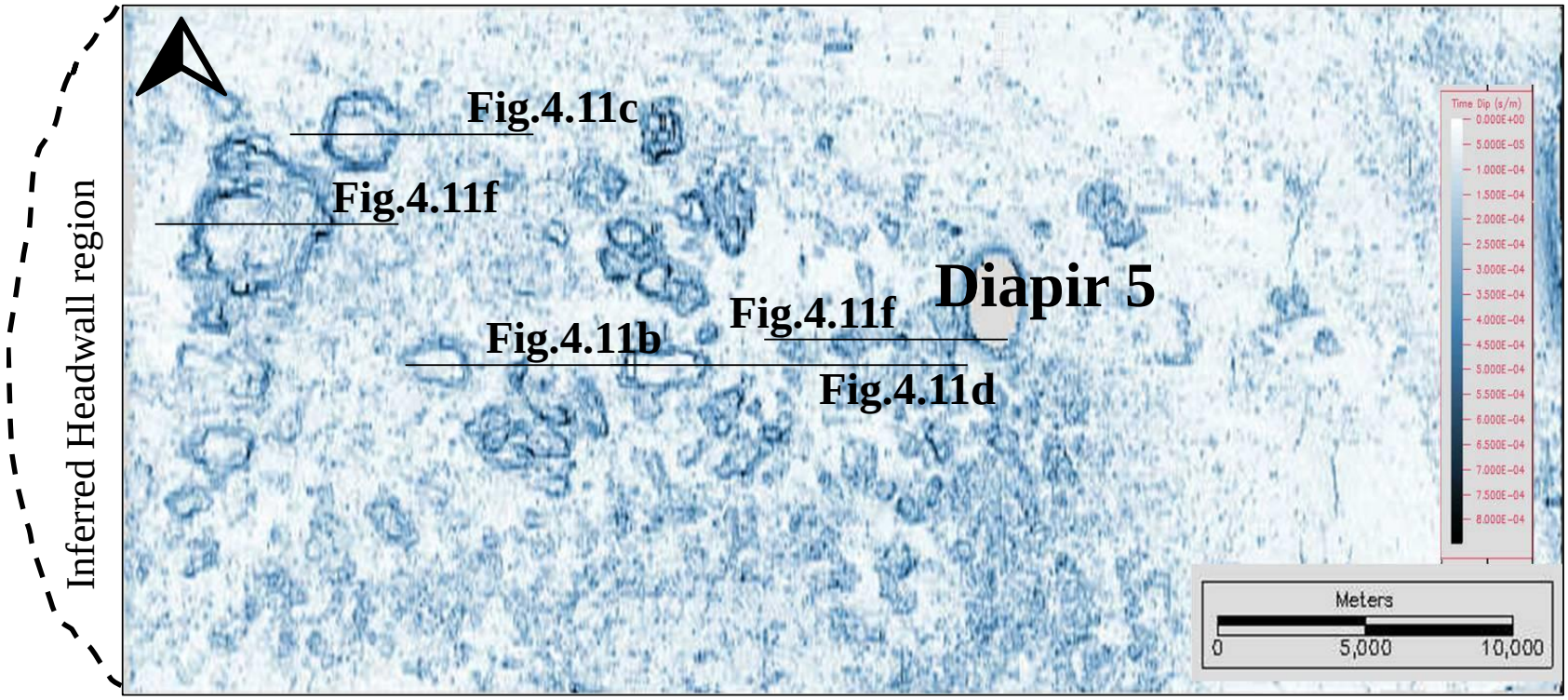

Figure 4.12d: Approximate positions of some of the blocks in Figure 4.10.

4.3 Additional statistical analyses

In the study area, we analysed thickness variations of MTDs accumulated around salt diapirs with a view to investigate their proximity to source areas, and infer the relationship between the timings of halokinesis and MTDs spatial distribution. Thickness data were collected every 625 m. The data obtained were used to compute box and scatter plots of MTD thickness vs. diapir diameters and relative distances from diapir centres (Figures 4.20 and 4.21).

4.4. Heterogeneity of strata in MTDs

In order to test the degree of heterogeneity of strata in the interpreted MTDs, their internal character was analysed on RMS amplitude, coherence maps and time-dip maps (Figure 4.8). Four seismic facies and depositional end-members were identified: coherent or unrotated blocks (CUBs), or blocks in Dott (1963) and Moscardelli et al. (2006); Deformed blocks/slides (DBS), or moderately deformed blocks in Gamboa et al. (2010, 2011); rafted blocks (RB) comprising highly deformed blocks that were transported through large distances; and debrites (DB), or debris flow deposits in Posamentier and Kolla (2003). Coherent or unrotated blocks (CUBs) are shown as high-amplitude strata within low-amplitude debrites and hemipelagites (Figure 4.8). Deformed blocks/ slides (DBS) have planar reflections in the centre and rotated edges. On coherence maps, CUBs and DBSs show high coherence values, high relief, and are embedded in low-coherency strata.

Planar, non-chaotic topography is observed in areas where the MTDs pinch-out (Figure 4.8). Rafted blocks of strata (RBs) display internal architectures resembling deposits transported and expanded. In addition, rafted blocks have rotated edges and are

characterised by high-amplitude reflections on their tops (Figure 4.11f). Strata in CUBs and DBSs are well preserved *cf*. (Glade et al., 2005), while rafted blocks still maintain some evidence of the initial stratigraphy but with some added structural complexity. Debrites (DB) are characterised by very chaotic to contorted reflections on seismic profiles (Figures 4.11b to f).

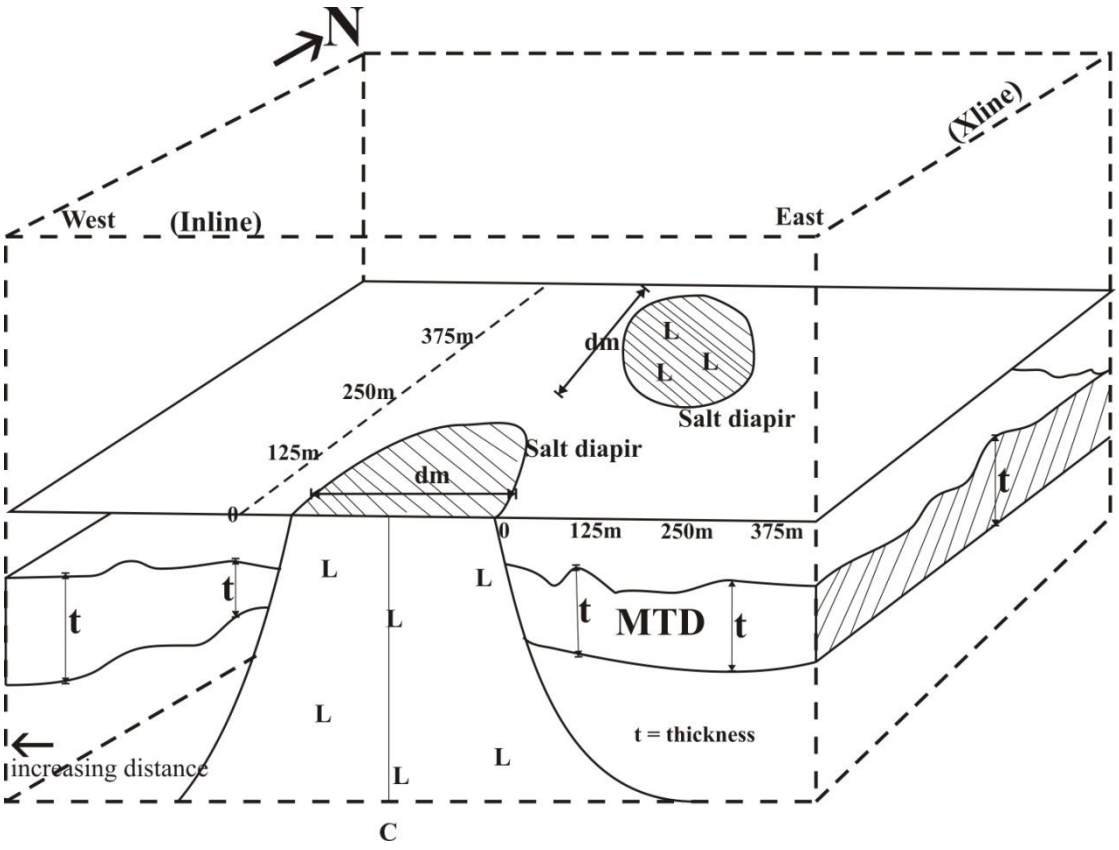

Figure 4.13: Summary of the parameters used in our statistical analysis. The thickness of the MTD comprises the difference between the lower and upper limit of the MTD shown as 't'. 'dm' is the diameter of the salt diapir; 'C' is the inferred centre of the salt diapir. Data was collected along inlines and crosslines at 625 m intervals (every 50 lines) for MTDs and at 63 m intervals (every 5 lines) for blocks.

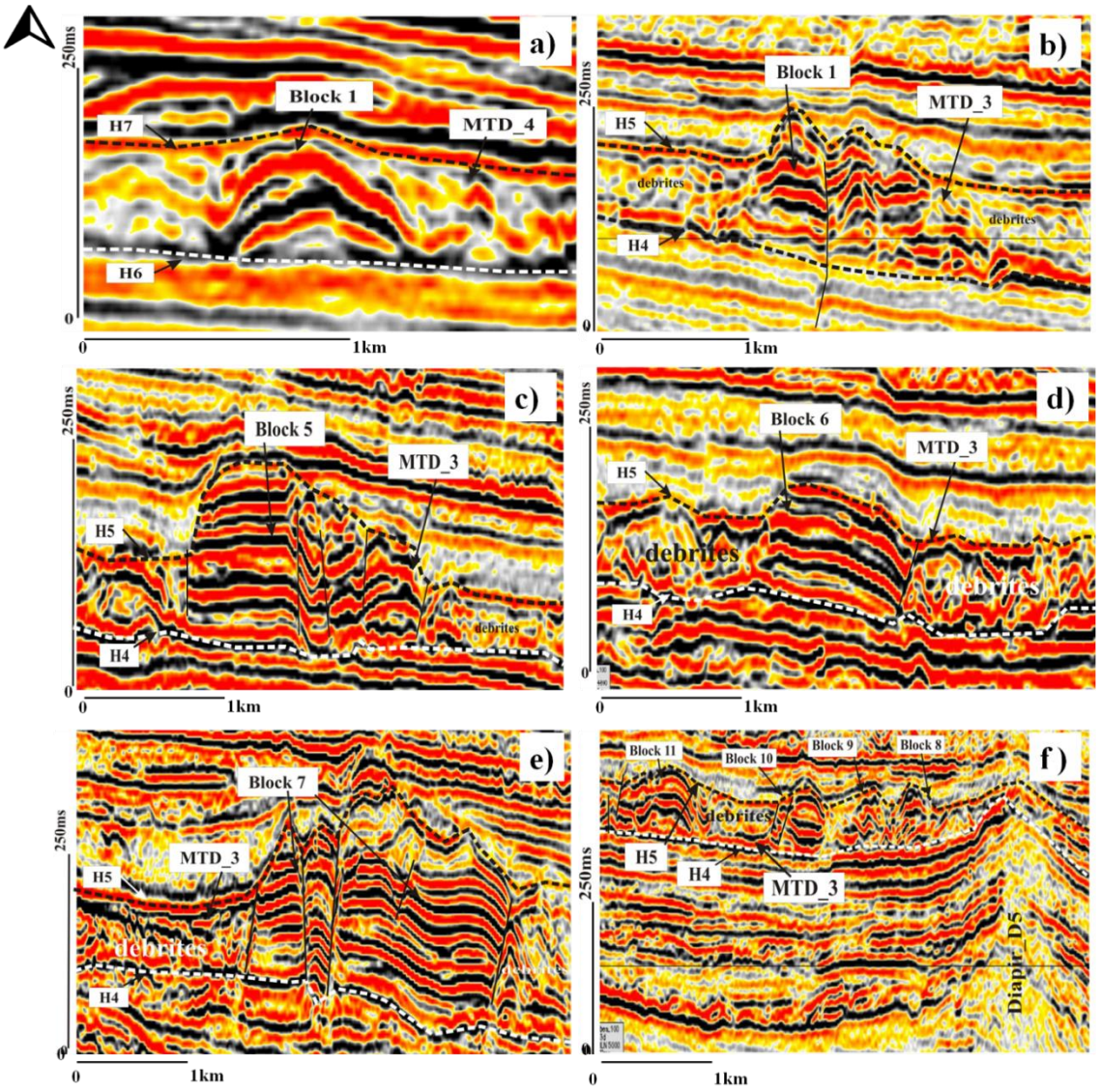

Figure 4.14: Internal geometry of rafted blocks as observed in MTD 3 and MTD 4. a) Block 1 (MTD 4) is a rafted block located on the western flank of diapir D3 (V.E = ~3). b) Highly deformed, faulted block in MTD 3. c) Coherent to internally undeformed-faulted block. d) Rotated to slightly deformed block. e) The biggest block mapped in the study, it is highly faulted (V.E = ~2). f) Rafted blocks 8 to 11. The imaged blocks are located on the western margin of diapir D5, with their size decreasing towards the diapir (V.E = ~1.5).

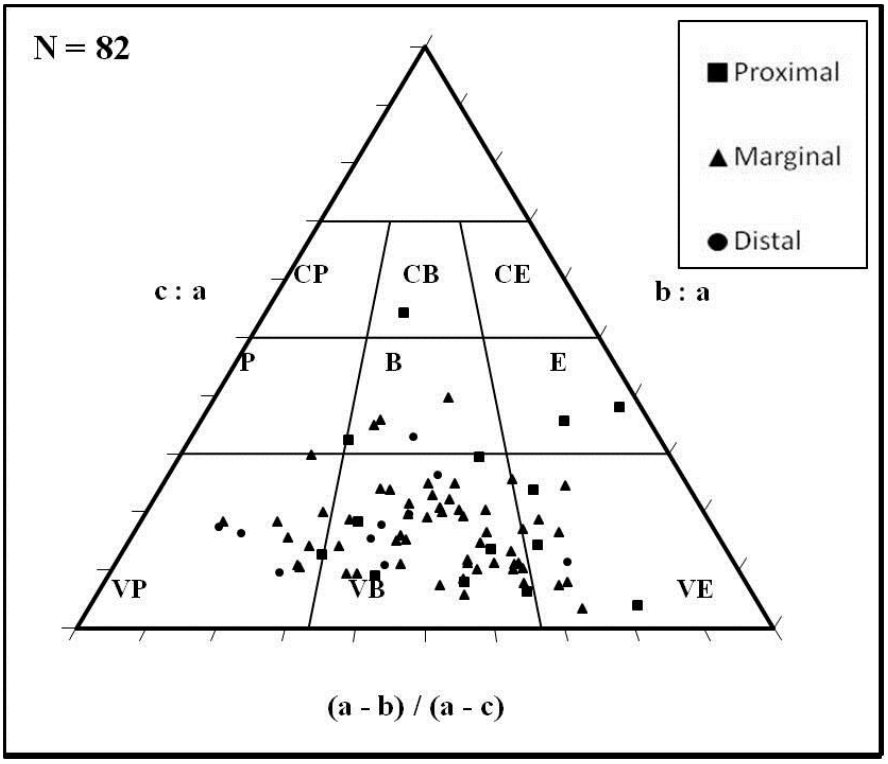

Figure 4.15: Folk and Sneed's tri-plot for eighty-two (82) blocks preserved in MTD 3. All the blocks plot outside the field of compact platy and compact elongate blocks. The Excel template used to populate the tri-plot was designed by Graham and Midgley (2000) and made available for academic use.

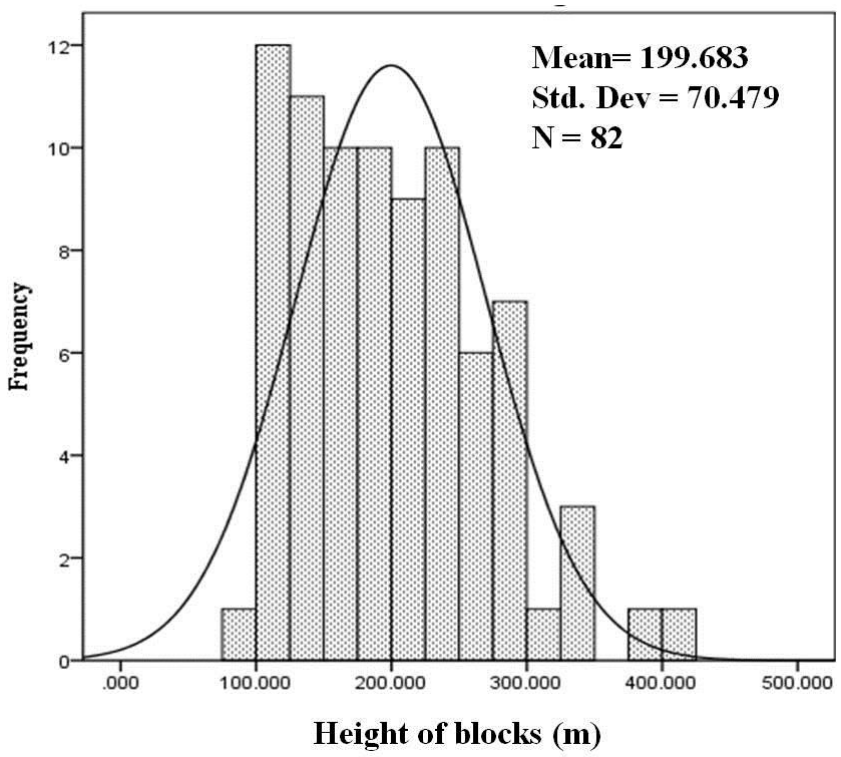

Figure 4.16: Average thickness of the blocks is ~200 m

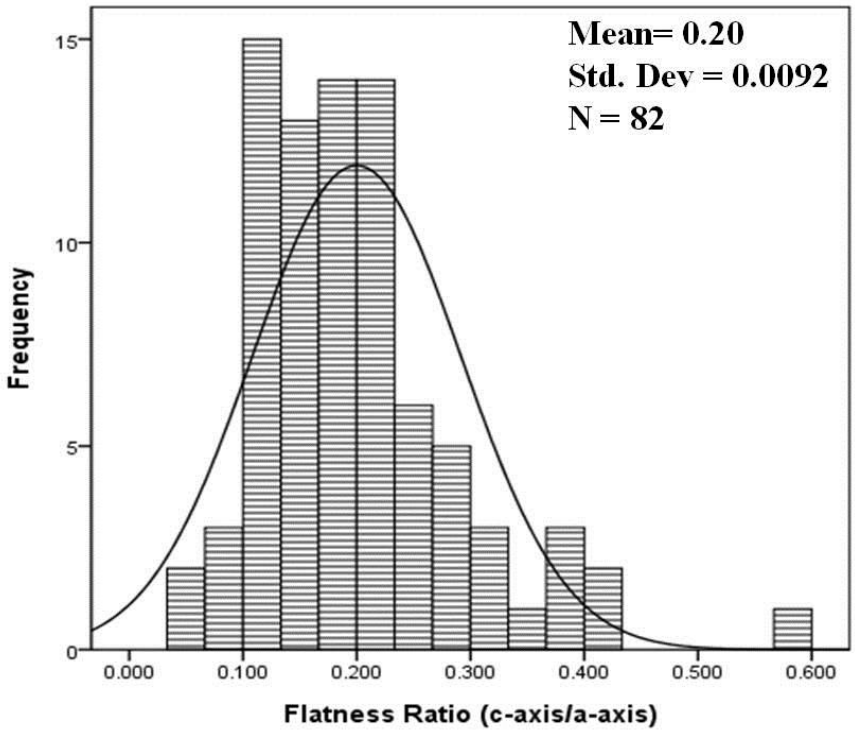

Figure 4.17: Flatness ratio is nearly normally distributed, with an average of ~0.2.

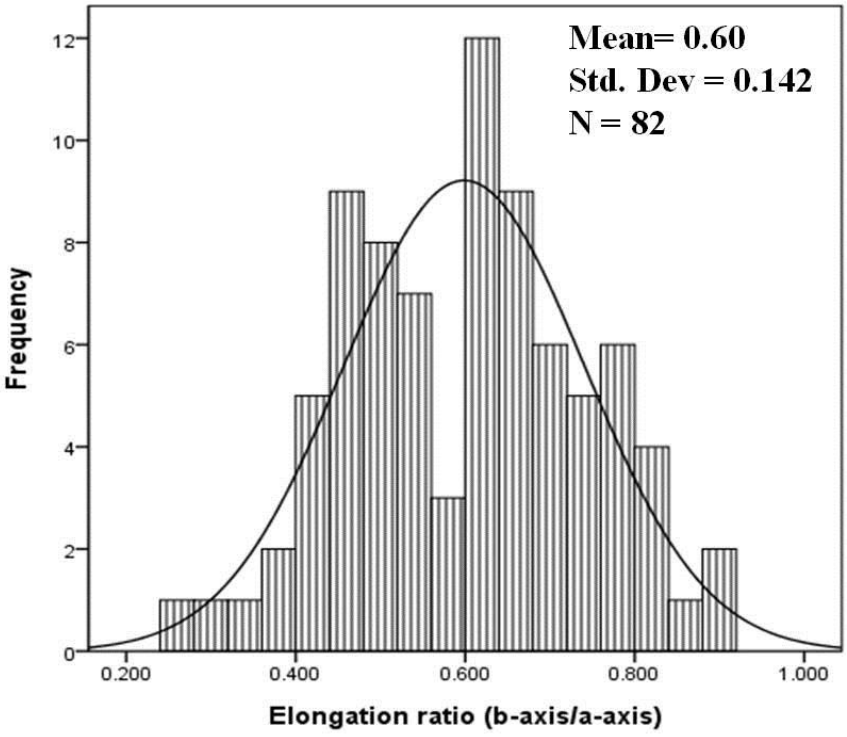

Figure 4.18: Elongation ratio is nearly normally distributed with mean of 0.6

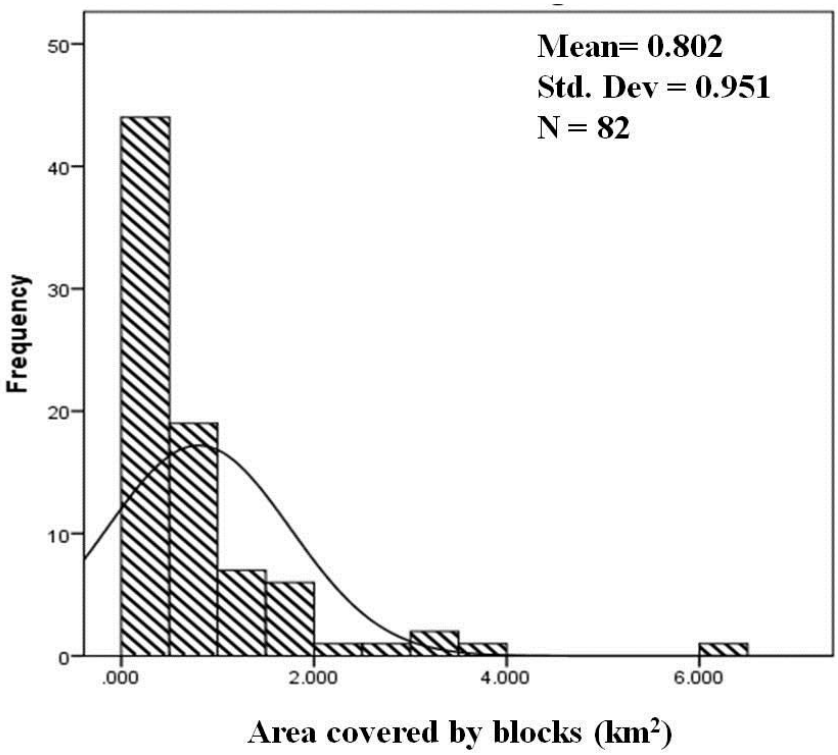

Figure 4.19: Area covered by the blocks in MTD 3. The mean coverage area of the observed blocks is ~ 0.8 km^2.

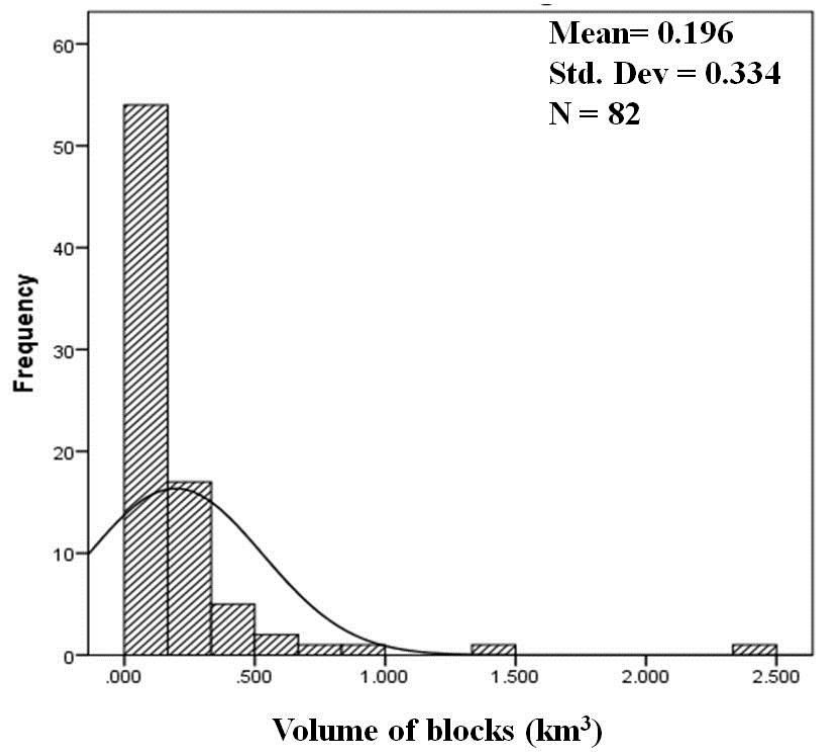

Figure 4.20: Average volume of blocks, shown in the order of ~ 0.2 km^3.

The larger blocks observed in the study area occur in MTD 3 and include rafted (Figure 4.11a), coherent (Figure 4.11c), slightly deformed (Figure 4.11d), coherent and faulted (Figure 4.11c), rafted and faulted, and highly deformed blocks (Figure 4.11b). The larger blocks comprise CUBs and DBSs but these are restricted to the NW margin of diapir D5.

Rafted blocks (RBs) are predominantly observed at the southern and eastern boundary of diapir D5. Geometrically, block height ranges from 90.94 m to 407.14 m, with an average thickness of 199.68 m (Figure 4.13). The average area and volume of the blocks are respectively 0.802 km^2 (Figure 4.14) and 0.196 km3 (Figure 4.15). Estimated block shape parameter shows that blocks in MTD 3 have an average MPSI and OPI value of 0.398 and 0.991 (Table 4.1). The elongation and flatness ratios of the blocks follow a normal distribution with means of 0.599 and 0.200 respectively. A MPSI value of up to 0.666 and an OPI greater than -1.15 shows that the blocks are poorly sorted (Dobkins and Folk, 1970; Ogala et al., 2010).

The orthogonal axes of interpreted blocks were plotted on the Sneed and Folk (1958) tri-plot shown in Figure 4.12. The majority of the blocks are very bladed (62.20%), with very platy (13.41%) and very elongate blocks (12.2%) being less frequent in the study area. Elongated blocks are distributed distally in MTD 3, close to diapir D5 (Figures 4.9 and 4.18). On the modified Zingg (1934) and Le Roux (2004) chart (Figures 4.18), 92.7% of blocks plotted in the field of bladed or triaxial shapes. Equant blocks only occur in proximal areas, while the intermediate and distal zones of MTD 3 show a cluster of bladed and bladed/triaxial blocks, some of them of small dimensions. Importantly, there is a cluster of bladed/ellipsoid blocks in intermediate and distal areas

of MTD 3, while blocks with ratios c/a > 0.4 and c/b > 0.65 only occur in proximal areas, together with smaller blocks.

Table 4.1: Descriptive statistics and geometries of blocks in MTD 3

S/N	Parameter	Mean	Minimum	Maximum	Range	Std dev	Median
1	a(long)	1178.41	377.90	3660.00	3282.10	660.63	1007.35
2	c(short)	199.68	90.94	407.14	316.20	70.48	190.12
3	b(inter)	663.04	187.60	2150.00	1962.40	331.58	587.80
4	F.R(c/a)	0.200	0.059	0.569	0.509	0.092	0.181
5	E.R(b/c)	0.599	0.242	0.908	0.666	0.142	0.609
6	c/b	0.337	0.127	0.925	0.798	0.141	0.297
7	MPSI	0.398	0.223	0.731	0.508	0.109	0.376
8	OPI	0.991	0.243	3.835	3.593	0.601	0.825
9	Coeff Flat	19.994	5.927	56.877	50.950	9.165	18.112
10	Thickness (km)	0.200	0.091	0.407	0.316	0.070	0.190
11	Area(km^2)	0.802	0.073	6.380	6.307	0.951	0.482
12	Volume(km^3)	0.196	0.009	2.492	2.483	0.334	0.091

N.B: The axes of the blocks were measured in metres

4.6. Statistical analyses of MTDs around salt diapirs

4.6.1. Diapir diameter vs. MTD thickness

4.6.1.1. MTD 1 vs. diapirs D4 and D5

Using the 50th percentile lines as reference in the multiple box plots in Figure 10, plots of MTD 1 thickness vs. the diameter of diapir D4 show that there is positive correlation ($-0.2<\rho<0.866$) between the two variables along the western and eastern flanks of D4 (Figure 4.20, Table 4.2). Here, the coefficient of determination (R^2) is as high as 79%. Predominantly negative correlations ($-0.632 < \rho < -0.119$) were recorded north and south of diapir D4, where the coefficient of determination is less than 20% (Figure 4.20). Positive correlation coefficients were recorded on the eastern and western flanks of diapir D5 for MTD 1, where $0.748 < \rho < 0.005$. The value for R^2 is here less than 50%, except on the eastern flank of the diapir where it reaches value of 56%; this value accounting for a 56% variation of the MTD thickness with the diapir width.

4.6.1.2. MTD 2 vs. diapirs D1, D2 and D3

A regression analysis for MTD 2 and diapir D1 was only made for the eastern and southern flank of the salt structure owing to the fact that the MTD thins out in the other two directions (Figures 4.20 and 4.21). A moderate to low negative correlation of $-0.564 < \rho < -0.072$ was estimated along the eastern flank of D1. The low R^2 value of <20% suggests a weak relationship between MTD thickness and diapir diameter. On the southern flank of D1 there is a tendency for a positive correlation between the two variables, but maximum and minimum values are scattered on the box plots (Figure 4.20). R^2 values for positive correlations reach as much as 79%.

The thickness of MTD 2 shows a more positive correlation with diameter on the western flank of diapir D2 than on the southern and eastern flanks (Figure 4.21). The

coefficient of correlation varies from poor to moderate with a R^2 value of <25%. Negative coefficients of correlation were recorded to the south and east of D2 (Figure 4.20). The thickness of MTD 2 varies inversely with the diameter of diapir D3, except for its southern flank (Figure 4.21). Correlation coefficients approach $-0.536 < \rho < 0.0001$ (Figure 4.20). R^2 values show that where there is a positive correlation on the southern flank of D3, but changes in its diameter influence the thickness of MTD 2 by an amount not more than 35%. In contrast, negative correlations show a robust coefficient of determination of 72%, particularly for the northern flank of D3 (Table 2).

4.6.1.3. MTD 3 vs. diapir D4 and D5

The thickness of MTD 3 varies negatively with changes in the diameter of diapir D4 (Figure 4.21). Conversely, coefficients of correlation are positive and in the order of $0.6 < \rho < 0.001$ for the eastern flank of D4. R^2 is <30% for positive correlations, and up to 62% for negative correlations, especially on the southern flank of D4 (Figures 4.20 and 4.21).

Also for MTD 3, positive values are recorded to the east, south and north of D5, with negative correlations estimated only on its western flank. Positive correlations range from 0.793 to the north to 0.001 to the south. R^2 values for the positive correlations suggest that changes in the thickness of MTD 3 can be explained by about 63% of the changes in the diameter of D5. The negative or inverse correlation has very low R^2 values approaching <25%.

Table 4.2: Frequency of coefficient of correlation between MTD thickness and increasing (1) Diapir diameter and (2) Distance from diapir centre.

S/N	Diapir	Direction	Negative						Positive					
			Strong		Moderate		Poor		Strong		Moderate		Poor	
			<(-0.6)		(-0.6)-(-0.4)		>(-0.4)		>0.6		0.6-0.4		<0.4	
		Diapir	diam	Dist	diam	Dist	diam	Dist	diam	Dist	diam	Dist	Diam	Dist
MTD 1	D4	W		12		5	1	1	5		1		1	
		E	1				1		4	13	1	3	1	2
		N	1	11	2		2				1		2	
		S			1	4	5	6			1		1	1
	D5	W		11		5	3			1	1		4	
		E		6		6	1	3	3		3		2	2
		N			1		3			8	2	5	2	
		S		11		2	3						5	
MTD 2	D3	W			1	6	4	9					3	
		E	1		3	1		2			2	6	2	6
		N	3		4		1	2		7		4		3
		S					3			16	1		4	
	D1	E		1	4	3	3	1		1		3	1	2
		S	3	4			2		3		1			
	D2	W		5		1	2	2		4	1	6	5	8
		E					5	2		17		4	3	
		S	2	1	1	2	3	4		4		6	2	1
MTD 3	D5	W					6			2		6	2	6
		E				1	2	1	1	12	2	2	3	1
		N		4		5	4	1	1				3	3
		S								3		9	8	1
	D4	W	2	1	2	6	1	10					3	1
		E		7		10	3	1			2		3	
		N		6	2	6	3				1		2	
		S	1				5			7		1	2	4
MTD 4	D3	W	2		1		4			14			1	
		E	3		1		3	2				6	1	6
		N		6	1	3	2			1		3	3	
		S			2		4			13	2	1		

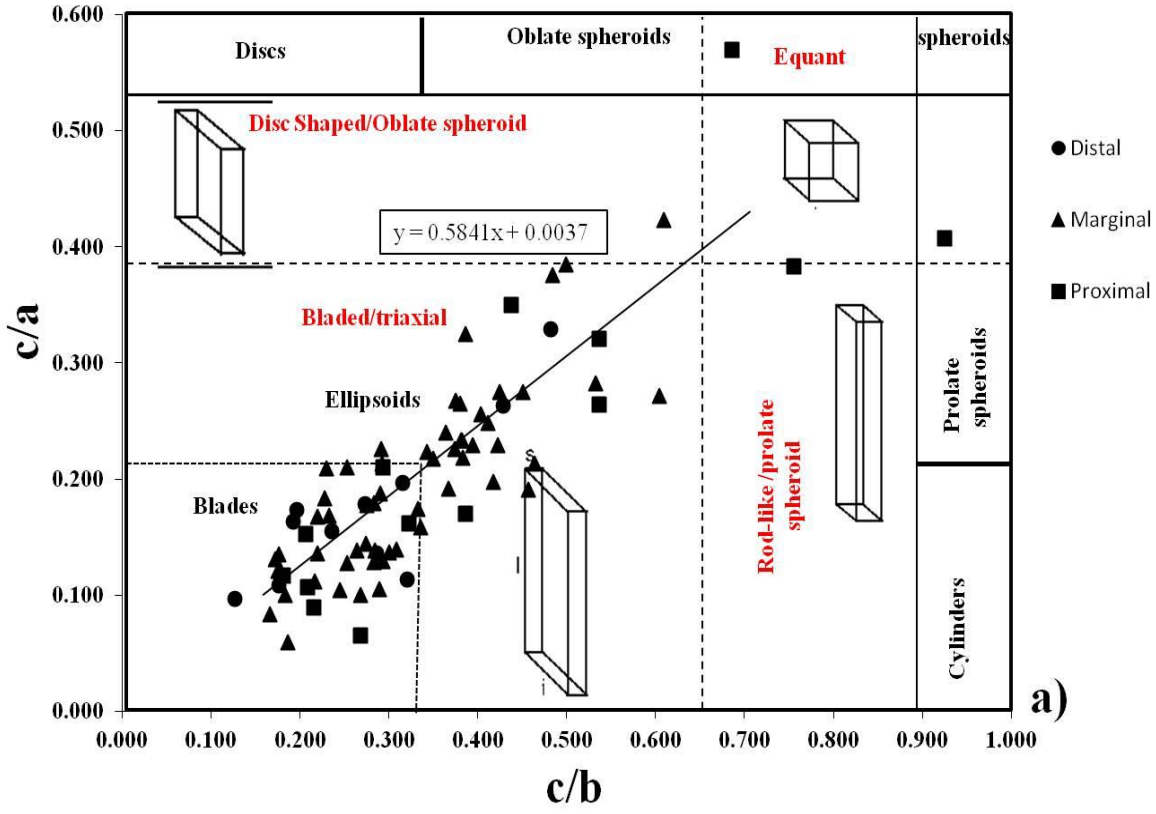

Figure 4.21: Modified Zingg's (1934) diagram for the hydrodynamic classification of particle shapes. The sections in red are the traditional Zingg's division of the chart, while the black section is modified from Le Roux (2004). The majority of the blocks are plotted in the field of Bladed/Triaxial (Zingg's) and Ellipsoids (Roux). The four main classes of grain shape are shown as block diagrams representing the ratios of the long, intermediate and short diameters of any particle (Zingg, 1934).

4.6.1.4. MTD 4 vs. diapir D3

The thickness of MTD 4 varies inversely with the diameter on diapir D3 (Figure 4.21). Coefficients of correlation approach $-0.044 < \rho < -0.790$, with R^2 between 20.5% and 62.35%.

4.7. Thickness of MTD vs. distance from diapir centre

Positive correlations are mainly observed at the northern flanks of diapirs, while the remaining flanks show a complex interplay between MTD deposition and diapir growth. The predominance of positive correlations on northern flanks relate to significant sediment transport from the upper slope region, to the northwest, with the diapirs forming effective topographic barriers. Two types of correlations should be highlighted for MTD1 and diapirs D4 and D5 and for MTD 4 and diapir 3 (Figure 4.21). The former shows a marked negative correlation between MTD thickness and distance to D4 and D5 on three of their flanks (Figure 4.21). The latter shows a predominant positive correlation (Figure 4.21).

There is a negative correlation between the thickness of MTD 1 and distance from D4 on its north, south and eastern flanks (Figure 4.21). The coefficients of correlation vary from poor to strong (0.020 to -0.877), with R^2 reaching as high as 88% closest to D4. For diapir D5, negative correlation coefficients are observed on the southern, western and eastern flanks of the structure (Figure 4.21). On its northern flank, the coefficient of correlation is positive, and ranges from 0.783 to 0.463. Also on this latter flank, the highest R^2 value (61.2%) was recorded close to the diapir centre (Figure 4.21). For MTD 4 and diapir D3, the thickness of the MTD significantly increases away from its western and southern flanks (Figure 4.21). The coefficients of correlation vary here

from 0.978 to 0.899, with a R^2 of 0.96 to 0.87. East of the diapir, the relationship is poor to moderate, with only a moderate negative correlation estimated (Figure 4.21).

4.8. Discussion

4.8.1. MTD provenance as a primary control on its internal architecture

Classifications of MTDs are usually based on the recognition of their internal architecture (Masson et al., 2006a). Slides are generally coherent, with little or no deformation. Slumps comprise essentially cohesive, but deformed, strata. Debris flow deposits exhibit the highest level of internal deformation with materials almost entirely disaggregated (Piper et al., 1999). The degree of cohesion is variable within each class, and is largely dependent on the grain-size, degree of compaction and relative amount of fluid accumulated in the sediments (Mulder and Cochonant, 1996). Thus, materials that are buried as coherent and slightly deformed MTDs reflect less deformation, and are probably closer to their source area than debris flows. This relationship between MTD architecture and transporting distances is the basis for provenance studies in MTDs deposited in the most varied tectonic settings (Gee et al., 2005; Gee and Gawthorpe, 2006; Gamberi et al., 2011).

In the study area, individual blocks of strata are recognised as high-amplitude features embedded in chaotic to contorted reflections, and reflect the presence of debris flow deposits (Lastras et al., 2005; De Blasio and Elverhøi, 2010). However, the diverse range of orientations of blocks in MTD 3 and 4 is also a characteristic of debris flow (Nichols, 2009). Diverse block orientations were described in "blocky-debris flow deposits" i.e. a deposit resulting from hyper-concentrated debris flow transporting out-

sized coherent and internally deformed blocks arranged in isolated slump folds, which possibly represent the link between slumps and debris-flow deposits (Mutti et al., 2006; Ogata et al., 2010). In such a setting, an important conclusion from this study is that the size of blocks in MTD 3 increases towards the source area, as expected, but that their shape does not change proportionally to their transporting distance. As blocks were transported downslope, they were abraded, with the larger oblong blocks disaggregating into smaller, rounder blocks, see also (Erismann and Abele, 2001). However, only equant blocks with ratios $c/a > 0.40$ and $c/b > 0.65$ correlate with smaller transporting distances, as these represent blocks kept in proximal areas with little or no disruption. MTD 3 can therefore be classified as 'blocky-debris flow deposit', an essentially heterogeneous MTD composed of a mixture of different MTD facies (slide, debrites, slump and any form beyond seismic resolution). This implies short travel distances, and moderate to no internal deformation. In contrast, homogeneous MTDs that are characterised by debrites in Figure 4.8 indicate longer travel distances, and intense deformation. Highly homogeneous MTDs comprise deposits of identical seismic and depositional facies, suggestively of uniform permeability and predictable fluid flow patterns.

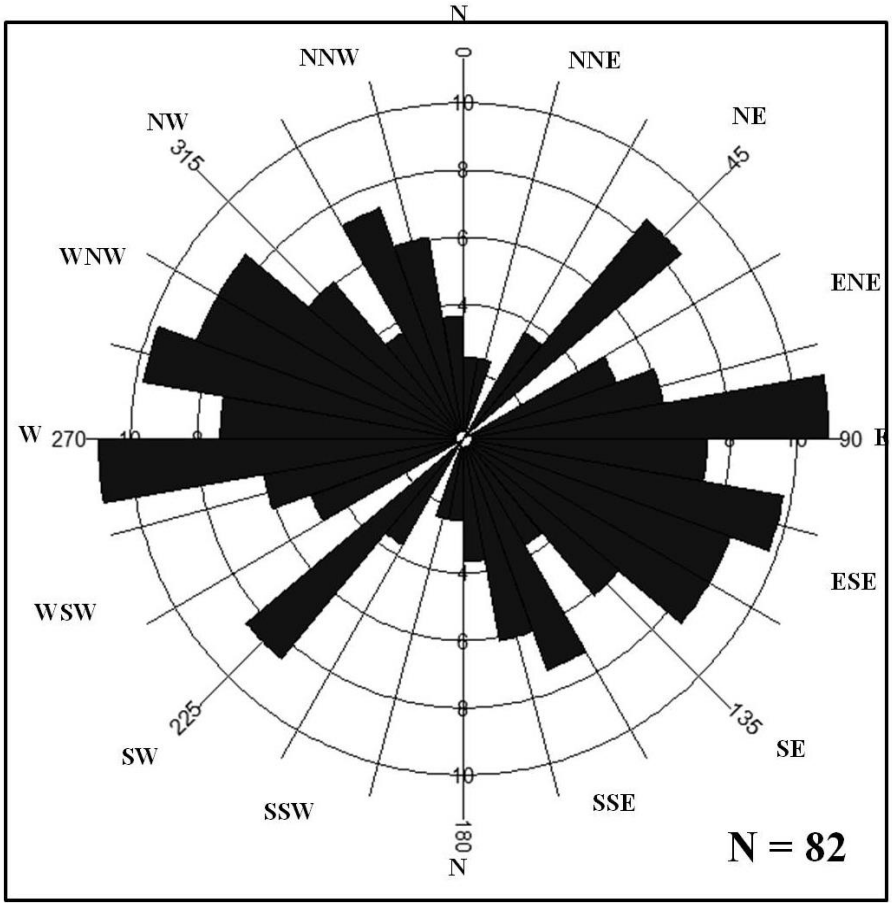

Figure 4.22: Rose diagram showing the orientation of long axes of the blocks. The elongation direction ranges from NW-SE to NE-SW with the mean aligned WNW-ENE.

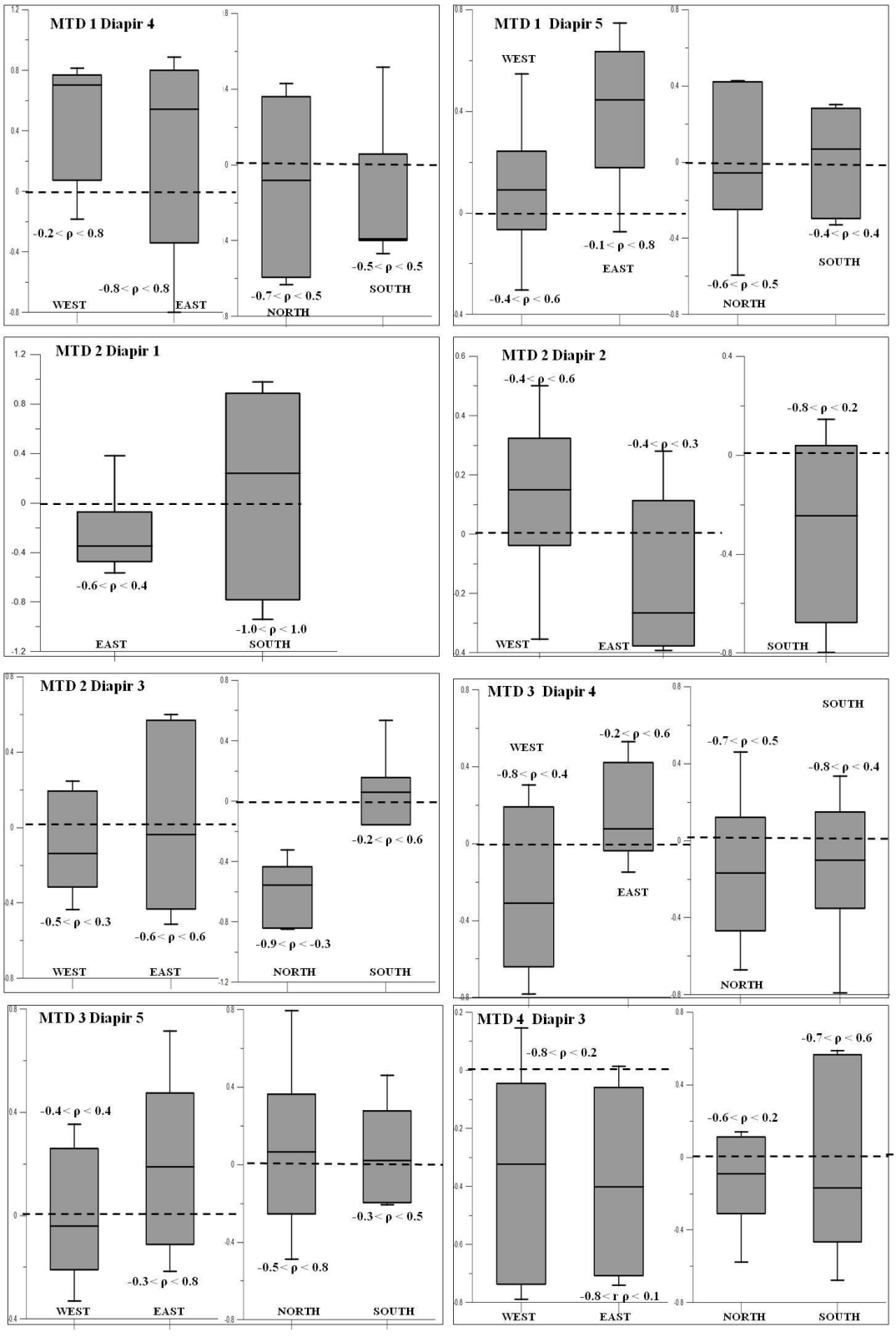

Figure 4.23: Box plot for the frequency of the correlation coefficients between diapir diameter and the thickness of MTDs. High correlations coefficients were recorded in few instances (MTD2 and diapir D3, southern flank) while inverse correlations were recorded elsewhere (e.g. MTD4 and diapir D3, east and west flanks). NB: 'ρ' is the coefficient of correlation; zero values are shown as dashed lines.

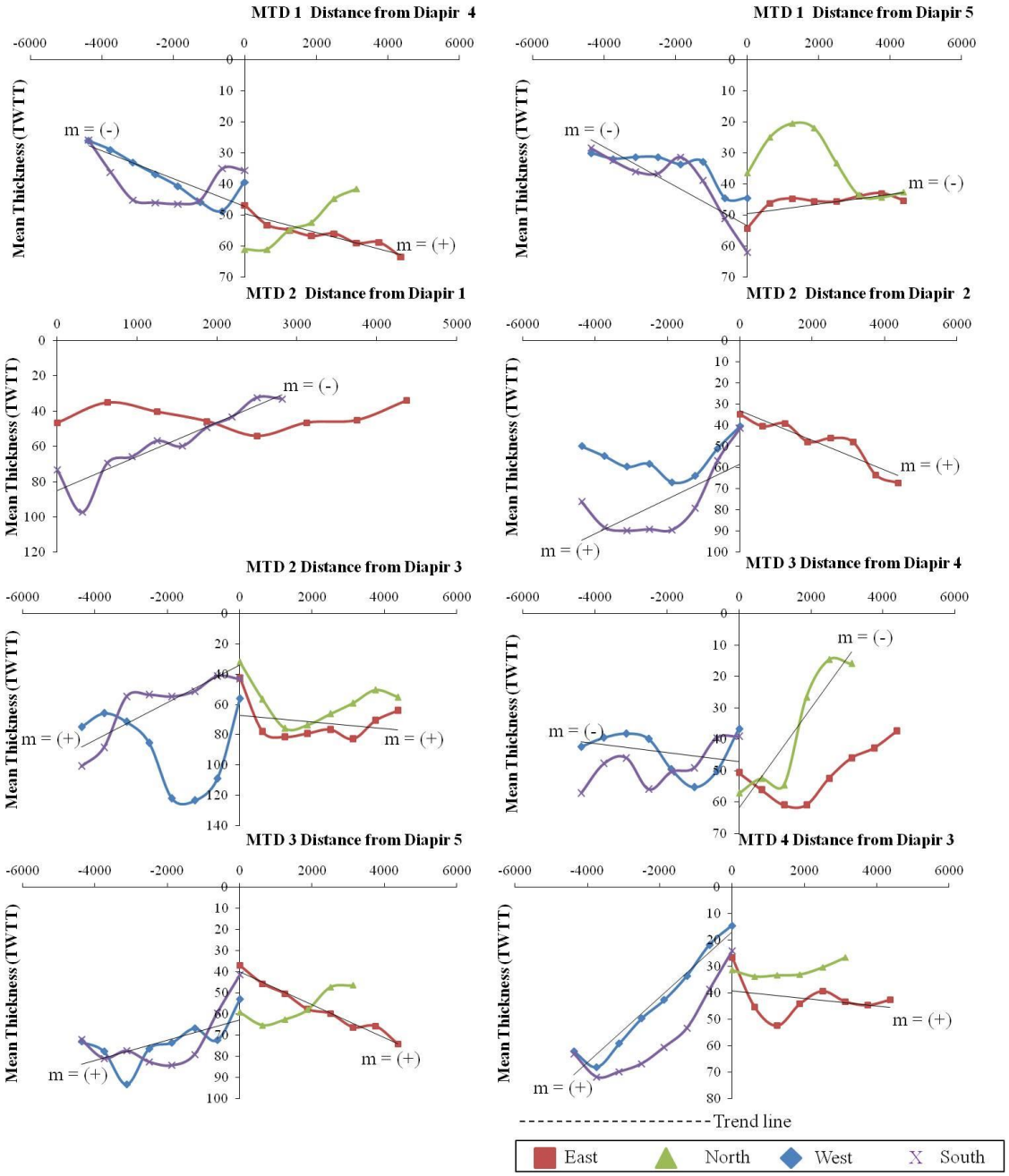

Figure 4.24: Plot of MTD thickness vs. distance from the diapir centre. Positive correlations are recorded between MTD 4 and diapir D3, and MTD 2 and diapir D3, whereas negative correlations exist between MTD1 and diapir D4 on its southern and western flank. Increasing thickness towards the diapir centres suggest small transporting distances and a relative proximity to source areas. NB: m = slope from y = mx + c.

4.8.2. Halokinesis and MTD provenance

Positive correlations between the thickness of MTDs and the diameter of diapirs indicate that salt structures controlled the deposition of MTDs. It also indicates that salt structures were actively deforming the seafloor during the transport of MTDs. Negative correlation coefficients between MTDs and the diameter of diapirs suggest that as the thickness of MTDs increased, the diameter of diapirs decreased (Figure 4.21). This implies tectonic quiescence of growing salt structures or that their growth preceded the deposition of MTDs, with no major influence of seafloor relief at the time of deposition. Places where both negative and positive correlations are recorded on different flanks indicate synchronous deposition and halokinesis.

These inferences are further supported by the geometry and nature of the studied MTDs. For MTD 1, strata above diapir D5 are thin and faulted, which is typical of overburden layers deformed by halokinesis (cf. Davison et al., 2000; Tripsanas et al., 2004). On the flanks where positive correlations are established between MTD thickness and diapir diameter, MTD 1 shows onlapping reflections onto the flank of D5, a character indicating deposition on top of a seafloor-deforming salt structure (Figure 4.2). In contrast MTD 4, showing a negative correlation between its thickness and the distance to the diapir D3, is significantly thick and relatively undeformed on the crest of this same structure (Figure 4.6). In addition, strata deposited on the crest of D3 maintain the reflection characteristics of those on the flanks of the structure (Figure 4.6).

The variation in thickness of MTDs with distance from the diapir axis can give hints on the proximity of the source area. MTD thickness tends to decrease away from the source in response to erosion and abrasion during downslope movement of material (Alves et al., 2009). The thickness is randomly distributed around diapirs when deposition pre-

dates diapirism, and thins on the diapir crests when the MTD is deposited over the diapir crest (Figure 4.2). In contrast, when MTDs are sourced from strata at the crest of diapirs, and only moderately transported, the larger thickness is recorded closer to growing salt structures, and there is a negative correlation between the thickness and distance from the diapir centre (Figure 4.21). The exception to this rule is MTD 4, with a headwall region that is located between two diapirs, D2 and D3. Strata in MTD 4 retrogressively failed in a NW-SE direction. Consequently, the thickness of MTD4 is relatively small on its headwall region due to the generation, during failure, of accommodation space on the seafloor (Kvalstad et al., 2001; Lucente and Pini, 2003; Dykstra, 2005). This process is reflected by negative correlation coefficients between diapir distance and the thickness of MTD 4 (Figure 4.21, Table 4.2), and leads to the grouping of MTDs in two main types in relation to their provenance: 1) diapir sourced, and 2) distally sourced (Figure 4.22).

The correlation coefficients used to infer the dependence of the thickness of the MTD on halokinesis do not take into account the role of other geological factors, such as faults and the position and amount of accommodation space on the slope, as major controls on MTD thickness variations. However, the absence of through-going syn-depositional faults above and below the interpreted MTDs suggests that the influence of faults is minimal in the studied stratigraphic interval. If such faults exist, they were draped and cannibalized during the mass-wasting process (Davison et al., 2000; Alves et al., 2009; Richardson et al., 2011).

4.9 Implications of provenance studies to hydrocarbon exploitation and exploration

What are the geological implications of determining the provenance of the sediment? In this paper, MTD facies types have been classified as slumps, slides and debris flows. Debris flows have very low amplitude and as such are thought to be mud-prone. They comprise relatively poor reservoir units though some have very good porosity (Jennette et al., 2000; Posamentier and Kolla, 2003). The other facies types (coherent, deformed blocks/slides and rafted blocks) have preserved the original stratigraphy to some degree and show high amplitude strata, potentially an indication of sand prone reservoir targets.

Blocks 100-400m thick have strong implications when drilling. It is important to understand how these blocks are oriented and distributed in order to plan well trajectories, especially when they are not hydrocarbon targets. The deformation suffered by the blocks may influence the sealing property of the host MTD. In situations where the blocks are highly deformed and faulted, they can act as conduits (Figure 4.11b and e) for vertical migration or seepage of hydrocarbon from lower stratigraphic units to those above. In this case, they may influence the development of gas chimneys and pockmarks on some seafloor (Gay et al., 2007; Gamboa et al., 2011).

In terms of reflection characteristics, most of the blocks are of very-high amplitude, suggesting the presence of bright spots and/or sand (Posamentier and Kolla, 2003). Thus the geometry of the blocks, especially where they are hosted in debris flow deposits, may imply the presence of hydrocarbon pockets with seal provided by the adjacent debris flows. This hydrocarbon system is quite unconventional in the real

sense, but with a maximum volume reaching 2.492 km^3, such areas hold promise for research and commercial exploration.

4.10 Conclusions

The detailed analysis in this work provided information on the position of source areas, modes of transport and spatial distribution of MTDs in relation to growing salt diapirs. The techniques used, when combined with the analysis of kinematic indicators, can provide complete and objective information on the source area of MTDs especially in salt rich continental margins. This new knowledge is vital to well planning and hydrocarbon exploration on such margins. Thus, in this study it is concluded that:

1. The geometry of MTDs, and of blocks included in them, provides data on the mode of transport, distance from source area and styles of deformation of failed strata. Homogeneous MTDs start as slide or slumps and end up as debrites or debris flow deposits due to prolonged transport and intense deformation. Heterogeneous MTD recorded less material disaggregation during transport.

2. The geometry of rafted blocks in MTDs provides estimates on the degree of transport and internal deformation experienced during failure. The shapes of the blocks hold invaluable information about their provenance. The size of the blocks decreases with increasing distance and from the source area.

Away from the source area, their shape approaches bladed and ellipsoids geometry with slight variations in the dimension of their orthogonal axes. Tall blocks with ratios $c/a > 0.40$ and $c/b > 0.65$ only occur in the proximal area of MTD 3.

3. Block geometry also provides information on the depositional processes leading to their accumulation. With MPSI and OPI of >0.666 and >-1.15, respectively, the blocks show poor degrees of sorting. This implies a lack of common preferred orientation of the blocks, which is typical of debris flow deposits.

4. Positive correlation coefficients between diapir diameter and the thickness of MTDs suggest active diapirism during their deposition. Where negative correlations exist, salt diapirs were not developed when of the deposition of the MTDs, or MTDs were not transported across the diapir crest. MTDs accumulated without any salt influence of growing diapirs have negative coefficients of correlation between their thickness and the diameter of associated diapirs;

5. The thickness of MTDs decreases away from source area. Increases in the thickness of the MTD close to the diapir axis suggest seafloor failure on their flanks, in parallel, small transporting distances.

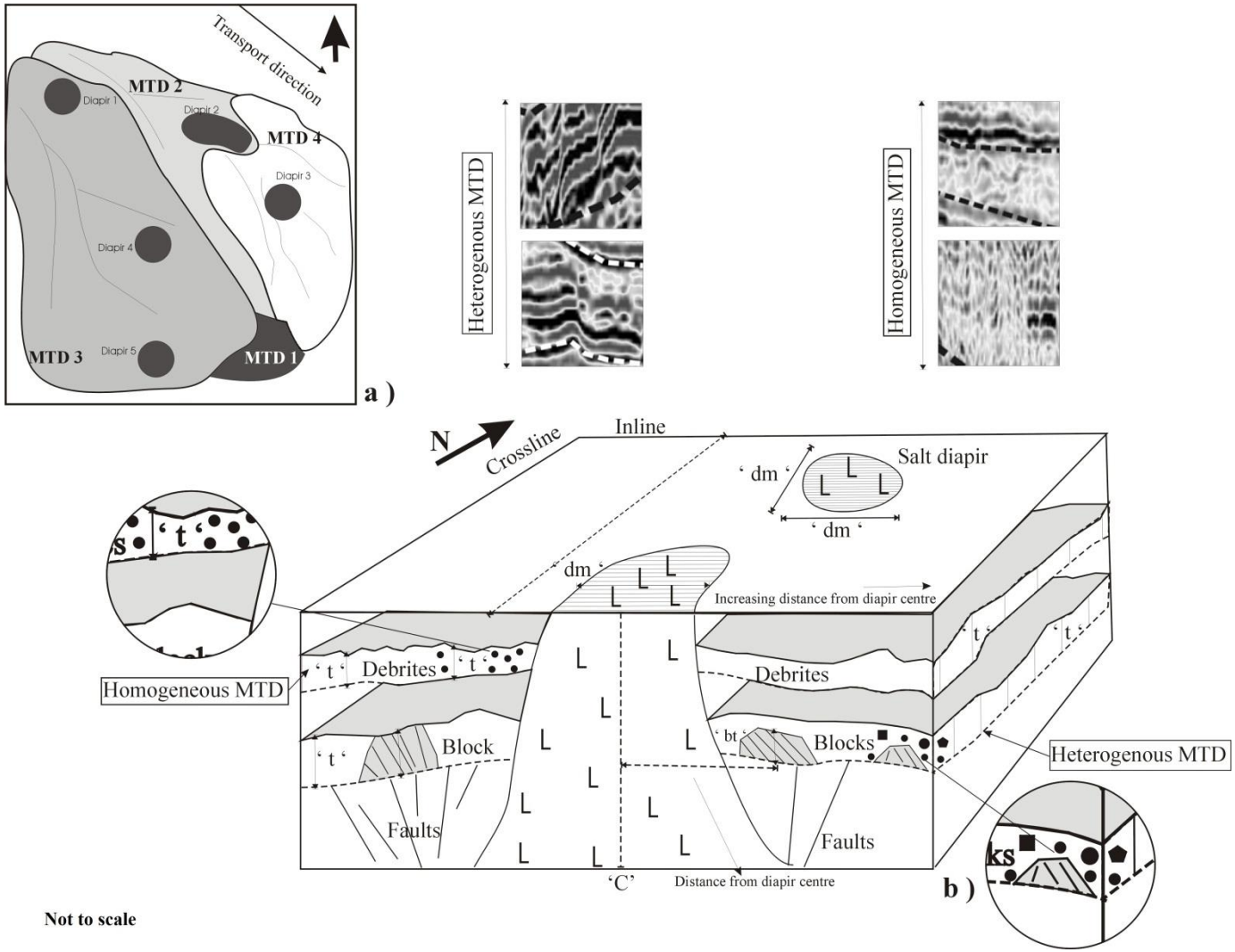

Figure 4.25: Distribution of the different MTDs adjacently to the five salt diapirs interpreted in this study. b) Summary of the main depositional controls interpreted for MTDs 1-4, highlighting the presence of blocks and debrites in their interior, and the effect of diapirs in their distribution.

Chapter 5

Ramps and flats of mass-transport deposits (MTDs) as markers of seafloor strain on the flanks of rising diapirs (Espírito Santo Basin, SE Brazil).

This Chapter is published as:

a) **Omosanya, K.O**., Alves, T.M., 2013. Ramps and flats of mass-transport deposits (MTDs) as markers of seafloor strain on the flanks of rising diapirs (Espírito Santo Basin, SE Brazil), Marine Geology http://dx.doi.org/10.1016/j.margeo.2013.04.013

b) KO Omosanya, TM Alves The Significance of Ramps and Flats of Mass Transport Deposits (MTD) as Kinematic Indicators- 75th EAGE Conference & Exhibition incorporating SPE …, 2013

Abstract

Ramps and flats reflect variations in the morphology of basal shear surfaces in mass-transport deposits (MTDs), which are often mapped without considering their potential as strain markers. In this work ramps and flats are mapped on the margins of salt diapirs, using a high-quality 3D seismic volume from SE Brazil (Espírito Santo) to investigate how the morphology of MTDs relates to diapir growth and near-seafloor strain. In parallel, aspect ratios of MTDs are used to estimate their source areas and possible causal mechanisms. Our results show diapir-related MTDs to have length/width ratios ≤3, in a region where sediment failure was triggered by faulting and seafloor tilting due to halokinesis. Sections of MTDs that were triggered and later uplifted on the flanks of growing diapirs are termed 'drag zones'. Ramps within these drag zones are shown as local changes in gradient at the basal shear surfaces, and are linked to promontories and older fault scarps. The results in this paper are important because they show that drag zones are elongated in a NW–SE direction, parallel to the dominant trend of basal ramps and promontories. Basal ramps and promontories in these drag zones constitute markers for seafloor strain around growing salt diapirs, with variations in the internal character of MTDs occurring across these same ramps and promontories. As a result, a spectrum of seismic and depositional facies can occur in specific quadrants of drag zones. In the study area are identified debrites (DBs), slightly deformed blocks (SDBs), coherent or unrotated blocks (CUBs), and rafted blocks (RBs).

5. Introduction

Mass-wasting is ubiquitous on continental slopes, where the combined action of local tectonics, sediment input and gravitational instability can generate complex structures (Norem et al., 1990; Masson et al., 1998; Goldfinger et al., 2000; Laberg and Vorren, 2000; McAdoo et al., 2000; Hunerbach and Masson, 2004; Hjelstuen et al., 2007a). Following seafloor failure, which occurs when downslope-directed shear stress exceed the shear strength of seafloor sediment (Varnes, 1978; Richardson et al., 2011), mass-wasting processes involve the transport of sediment over a basal shear surface (Lucente and Pini, 2003) or gliding plane (Gee et al., 2005). Once failure is initiated, sediment will move at different velocities and volumes over the basal shear surface until the inertia of failed material is balanced once again by glide plane shear strength (Richardson et al., 2011).

Kinematic indicators such as scours (Nissen et al., 1999; Posamentier and Kolla, 2003; Weimer and Shipp, 2004), grooves and striations (Gee et al., 2005; Gee and Gawthorpe, 2006), cat claws (Moscardelli et al., 2006), monkey fingers (Mc Gilvery and Cook, 2003), ramps and flats (Gawthorpe and Clemmey, 1985; Trincardi and Argnani, 1990; Lucente and Pini, 2003) are examples of features on basal shear surfaces that reflect the nature and physics of mass-wasted strata. Basal ramps form segments of a shear surface that are discordant with underlying bedding planes, while flats comprise the bedding-parallel portion of the surface. Ramps and flats generally run perpendicular to the flow movement direction (Trincardi and Argnani, 1990) and are seldom parallel to the flow direction (O'Leary, 1986, 2002; Bull et al., 2009). As the failed strata move across ramps, significant deformation in the sediment is observed at the shear surface (Ramsay and Huber, 1987), usually in the form of slump folds and complex compressional features (Rupke, 1967; Frey Martinez et al., 2005; Alves and Lourenço, 2010)

In addition to basal shear surface deformation, circular and elliptical features interpreted on seismic volumes provide evidence of local (palaeo) stresses associated with compression, extension, or both. They are usually associated with near-seafloor folding (Edwards et al., 2005), salt diapirs (Stewart, 2006), mud volcanoes (Medialdea et al., 2000; Milkov, 2000; Dimitrov, 2002), igneous/volcanic plumes (Garfunkel and Ben-Avraham, 1996), extension/polygonal faulting or sandstone intrusions (Shoulders et al., 2007). Salt diapirs, mud volcanoes and folds are generally associated with compressional stresses with minimum stress oriented in a vertical direction (Stewart, 2006). Such a stress distribution is recorded in the form of complex deformation around growing diapirs, which translates at the seafloor as slope instability features, or mass-transport deposits (MTDs). Significantly, some MTDs present ramps and flats in basal shear surfaces that relate to local stress fields and directions of transport during mass-wasting events (Brami et al., 2000; Lamarche et al., 2008).

This Chapter presents a quantitative analysis of ramps and flats at the base of multiple MTDs from SE Brazil (Figure 2.1). The aim of this Chapter is to relate the morphology of ramps and flats, and the relative recurrence of MTDs above them, to the growth of adjacent salt diapirs (Figure 5.1). In addition to significant seismic facies variations across basal ramps, this Chapter shows that the recurrence of MTDs varies across specific areas of elliptical 'drag zones' around growing diapirs. In addition, source areas of MTDs can also be recognised by analysing their length/width aspect ratios. In detail, this Chapter aims to:

(a) Document the extent to which stress perturbations imposed by growing diapirs are reflected on the seafloor;

(b) Analyse how basal ramps and flats affect the internal character of MTDs;

(c) Propose new methods to assess the effect of ramps and flats on the type of sediments deposited on and around growing salt diapirs.

In this Chapter attribute and isochron maps are used to define ramps and flats around the salt diapirs. In addition, we quantify thickness variations within individual ramps and flats and relate them with modes of transport of MTDs. This latter section is followed by a discussion on: a) how to recognise source areas of MTDs around growing salt structures, b) how 'drag zones' can be used to establish the relative timing of halokinesis, and c) the significance of the ramp and flats of MTDs as seafloor strain markers.

The term 'drag zone' is used to denote sections of MTDs that are uplifted during salt diapir rise (see also Stewart, 2006). Drag zones are elliptical to circular in map view and reflect the regions of the seafloor that suffered the most strain during the diapir growth (Davison et al., 2000b; Stewart, 2006). Drag zones in the study area were mapped using a combination of TWTT thickness and seismic attribute maps.

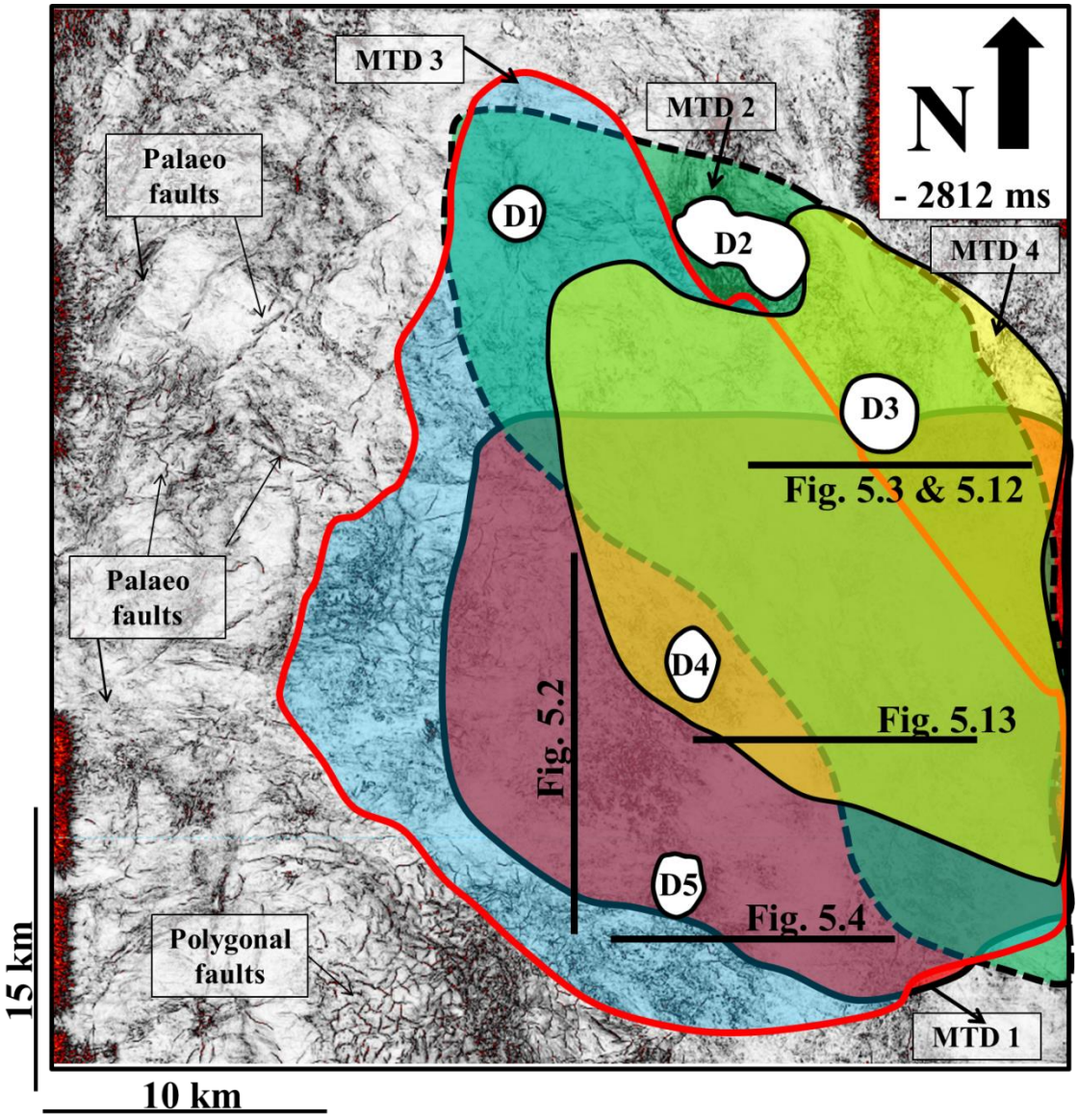

Figure 5.1: Distribution of the different MTDs adjacently to the five salt diapirs, D1 to D5, interpreted in this study.

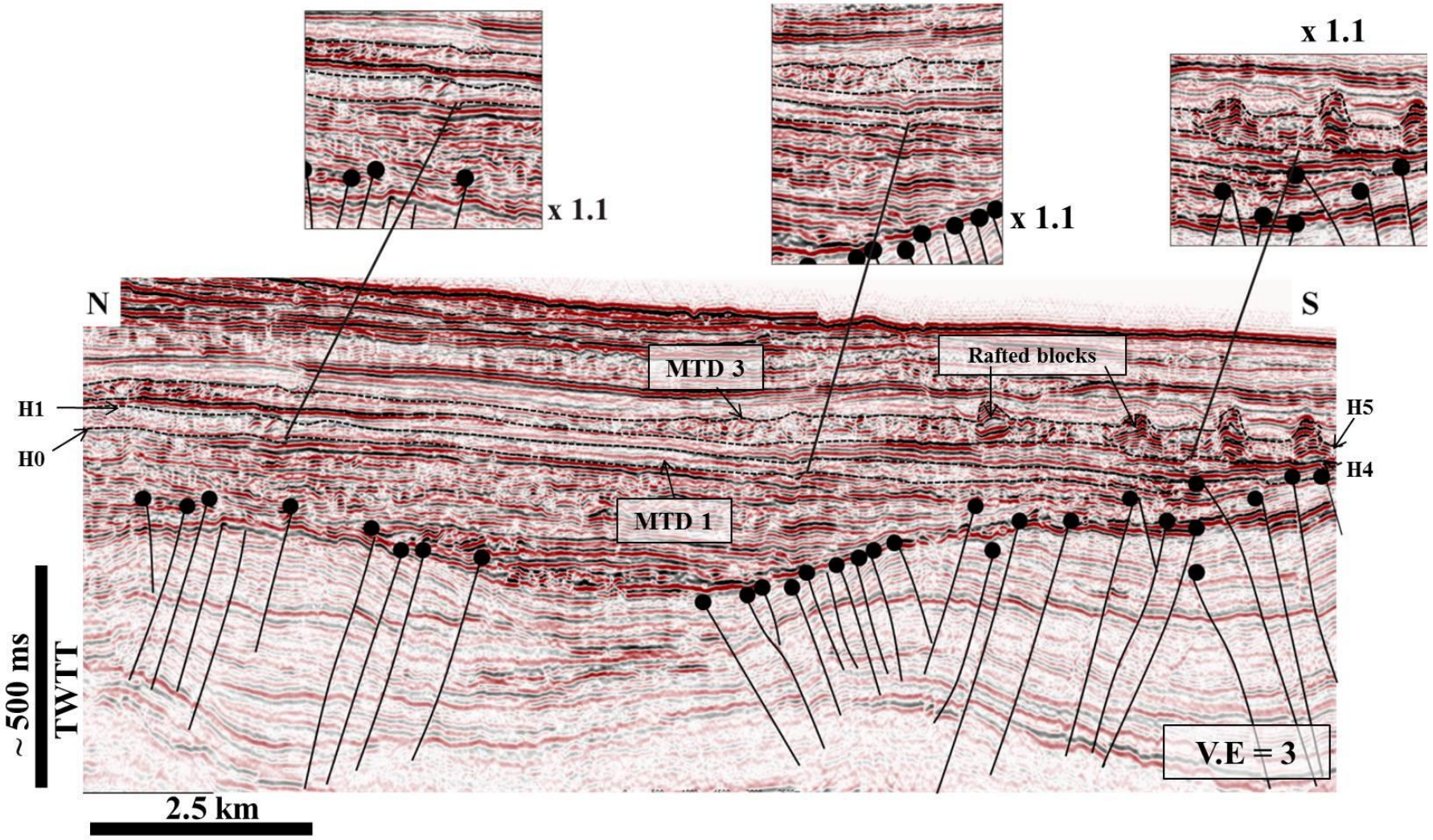

Figure 5.2: Interpreted MTDs in the study area. Ramps are highlighted in separate insets. The positions of the imaged MTDs relative to the continental slope are shown in Figure 5.1.

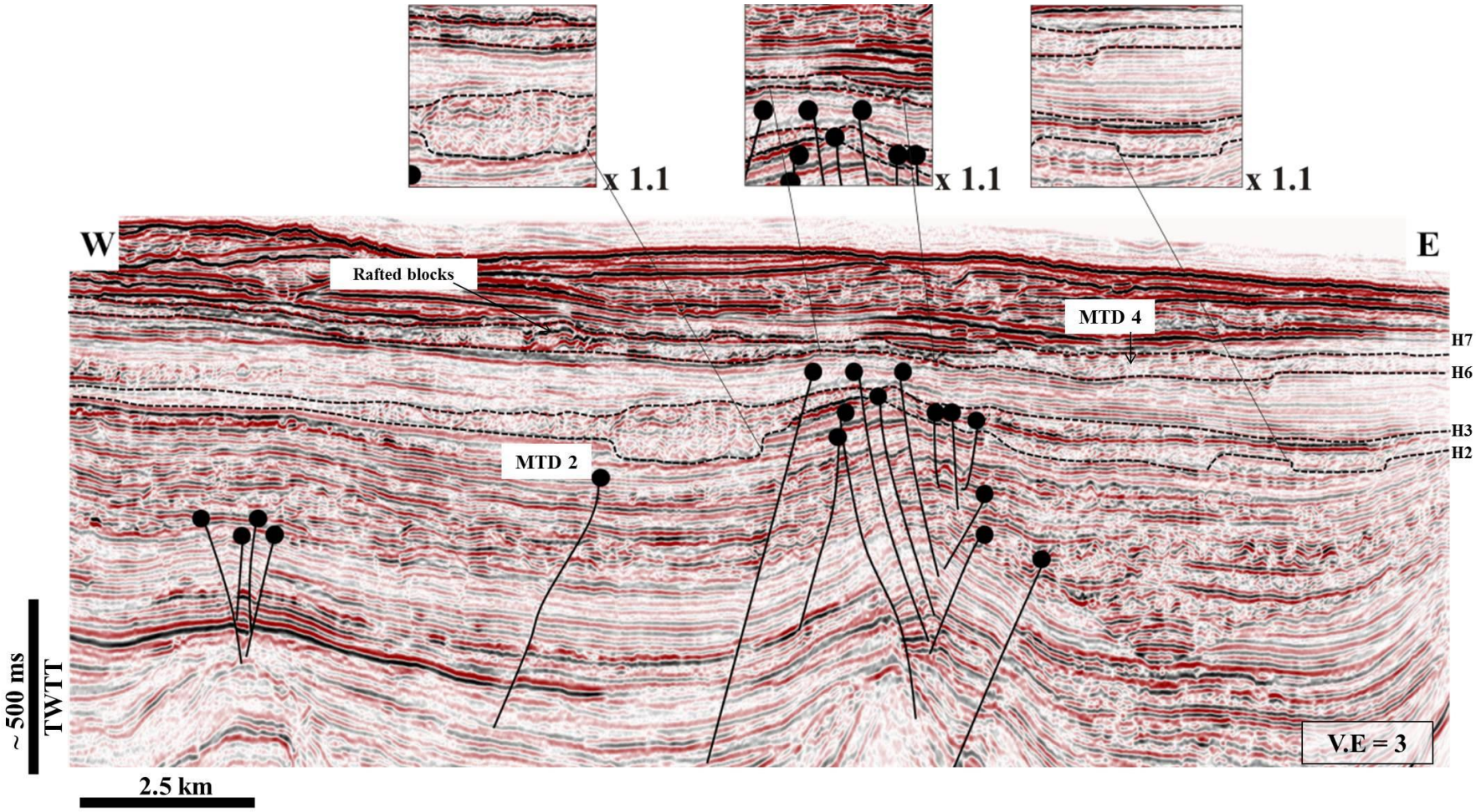

Figure 5.3: MTDs in the study area range in age from Early Eocene to Miocene and were predominantly transported in a NW–SE direction.

Table 5.2: Seismic character of the tops and bases of Mass-transport deposits interpreted in this Chapter.

MTD	Seismic Unit	Age (Fiduk et al 2004, Mohriak 2003,2005)	Associated Salt diapirs	Headwall Region	Basal Shear features
1	H0 and H1	Eocene	D4 and D5	NW of diapir D5.	Striations, grooves, ramps.
2	H2 and H3	Late Eocene	D1, D2 and D3	Headwall region not observed, interpreted as buried east of diapir D3.	Frontally confined by ramps, promontories east of the MTD. Condensed section in between promontories and basal ramps.
3	H4 and H5	Oligocene-Miocene	D1, D4 and D5	NW of diapir D5.	Ramps west of diapir D5.
4	H6 and H7	Miocene	D2 and D3	NE of diapir D2.	Minor topographic barriers, scarps, grooves and striations striking NW-SE.

5.1. Ramps and flats in interpreted MTD intervals

The top and basal surfaces of four MTDs were mapped as nine surfaces named H0 to H8 in Figures 5.2 and 5.3. The mapped surfaces range in age from Eocene to Miocene. On seismic profiles, basal shear surfaces separate chaotic and disrupted strata within MTDs from the much more continuous facies of non-MTD deposits (Hampton et al., 1996; Frey-Martínez et al., 2006; Frey Martinez, 2010; Bull et al., 2009).

The internal character and geometry of the MTDs interpreted in this study is summarised in Tables 5.1 and 5.2. The description of the trend and nature of ramps was based on time-dip, coherence and RMS amplitude maps of the basal shear surfaces shown in Figures 5.5 to 5.8 and 5.18. In this work, ramps are considered to include structures on the basal shear surface over which significant amount of sediment was transported across different stratigraphic levels (Trincardi and Argnani, 1990; Gawthorpe and Clemmey, 1985; Strachan, 2002a; Lucente and Pini, 2003; Frey Martinez et al., 2005; Bull et al., 2009). Scarps related to sub-surface faulting at the base of the MTD were categorised as fault-controlled ramps (*cf.* Richardson et al., 2011). Faults forming scarps are radial and crestal faults emerging from the salt diapirs (Figures 5.9, 5.10, 5.12 and 5.13). Other structures that contributed to changes in gradient on the basal shear surface included erosional scours, and minor topographic highs related to doming or salt diapirism (Figure 5.6).

In total, twenty-eight basal ramps were identified in the study area (Figure 5.14). Approximately, 43% of the ramps occur at the base of MTD 1, while 29%, 21% and 7% were identified on MTDs 2, 3 and 4 (Figures 5.5 to 5.8). Promontory-related ramps were confined to MTD 2 while fault-controlled ramps were characteristic of the other

MTDs. Along the slope, ramps range in length from ~3 km to ~39 km, with an average length of ~10 km.

5.1.1 MTD 1 (Early Eocene)

Ramps at the base of MTD1 have a low angle of dip (<5°) on time-dip maps. They separate areas of chaotic and fine-textured topography from undeformed, very high amplitude, continuous reflections (Figure 5.5). Ramps largely show a NW–SE orientation (N72°W to N28°W), parallel to the slope gradient. Geometrically, the length of ramps in MTD 1 ranges from ~5 km (R_7) to ~28 km (R_1). To the NW of MTD 1, two ramps formed a relay zone by the intersection of a NW-trending (N72°W) ramp, R_1 and south trending ramp, R_5 (Figure 5.5). Flat areas with no basal ramps were characterised by chaotic topography, which suggested that the basal surface was erosive at this part and that materials transported above it mainly comprise debrites (Posamentier, 2003; Posamentier and Kolla, 2003; Gee and Gawthorpe, 2006;).

5.1.2. MTD 2 (Late Eocene)

Topographic features resembling promontories *sensu.* Bull et al. (2009) are associated with depressions, or coves, created by antithetic ramps on the basal shear surface of MTD 2 (Figures 5.6, and 5.9). Promontories are peninsula-like protrusions on time-structure maps. At the base of MTD 2, they are restricted to the edges of diapir D3 and to the southern flank of D2 (Figure 5.6). These promontories comprise undeformed strata, and have an average height of ~46 ms TWTT, for an area coverage of ~24 km^2 for PR_1, ~17 km^2 for PR_2, ~13 km^2 for PR_3, and ~7 km^2 for PR_4 (Figure 5.6).

Promontories at the base of MTD 2 are characterised by chaotic and rugged topography on the time-dip and coherence maps, implying that the basal shear surface was erosive and possibly associated with the deposition of debrites above (Figure 5.6).

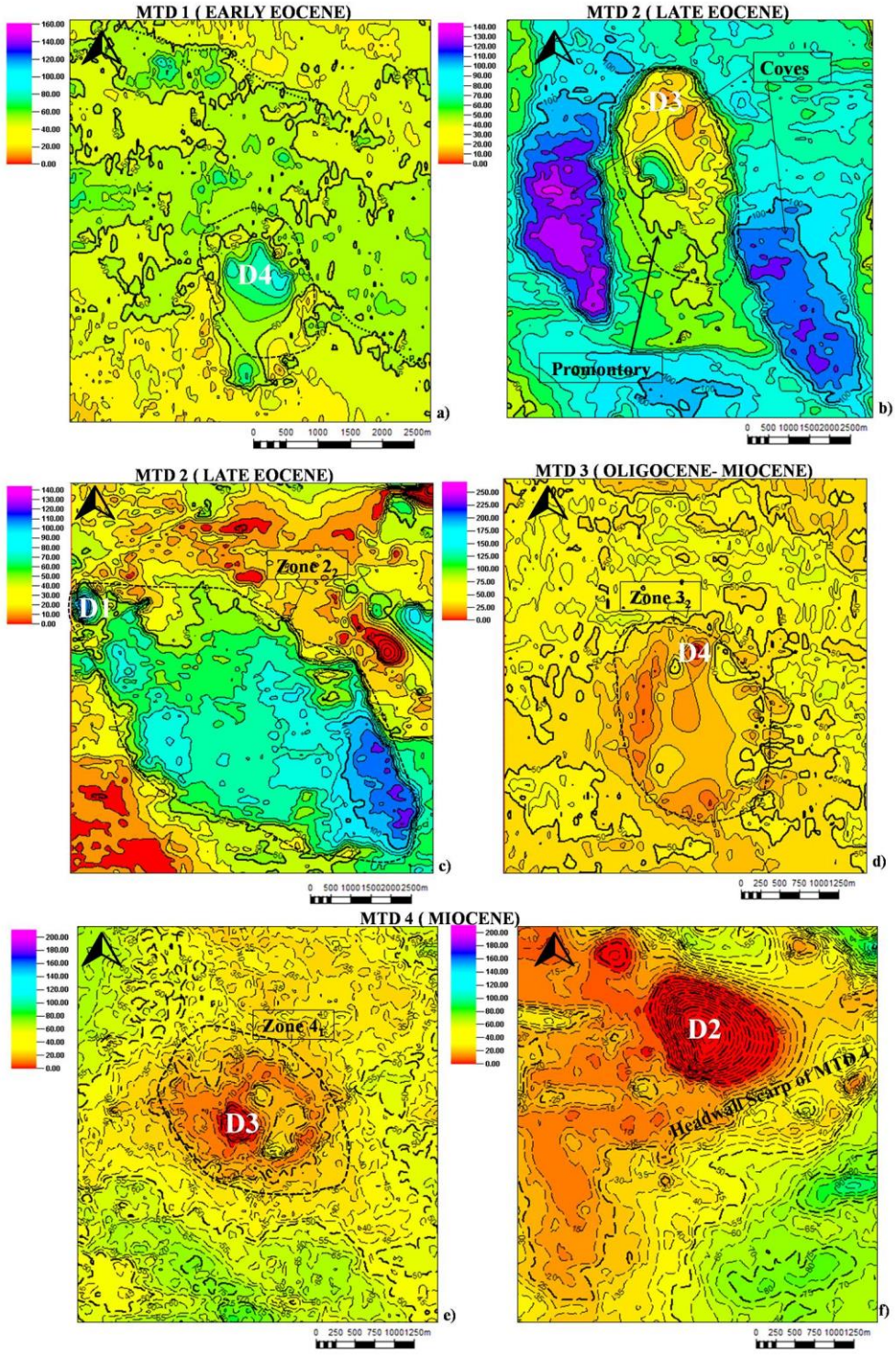

Figure 5.4: Thickness maps of MTDs and marginal strata to diapirs D1 to D4. a) MTD 1 has maximum thickness of ~200 ms TWTT. b) MTD 2 has its maximum thickness recorded in coves bounded by ramps and promontories. c) Thickness map of Zone 21 at the base of MTD 2. d) MTD 3 shows a decrease in thickness towards the North. A maximum thickness of ~200 ms is recorded SSW of MTD 3 in a region with megablocks. e) The area around D3 shows a thin MTD 4. The thickest part of MTD 4 onlaps onto the diapir. f) The headwall region of MTD 4 shows a very low thickness. N.B: Areas highlighted with dash lines are 'drag' zones inferred on the RMS amplitude maps, thickness maps are in TWTT (ms).

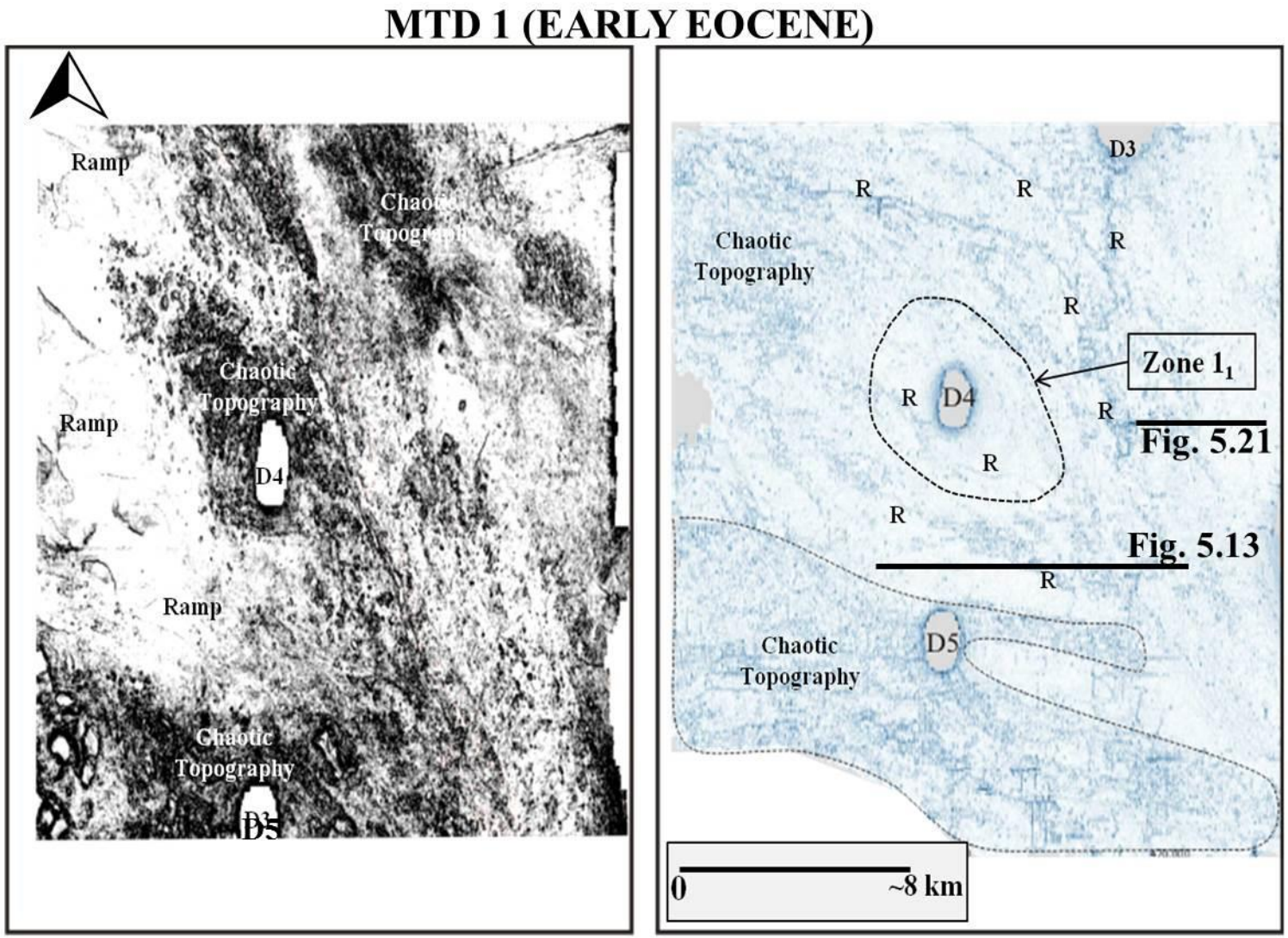

Figure 5.5: Dip and coherence maps elucidating the characteristic features of basal shear surface of the MTDs in the study area. Ramps below MTD 1 are shorter along their strike than most of the other ramps compared with Figure 5.4. N.B: *R- Ramp*

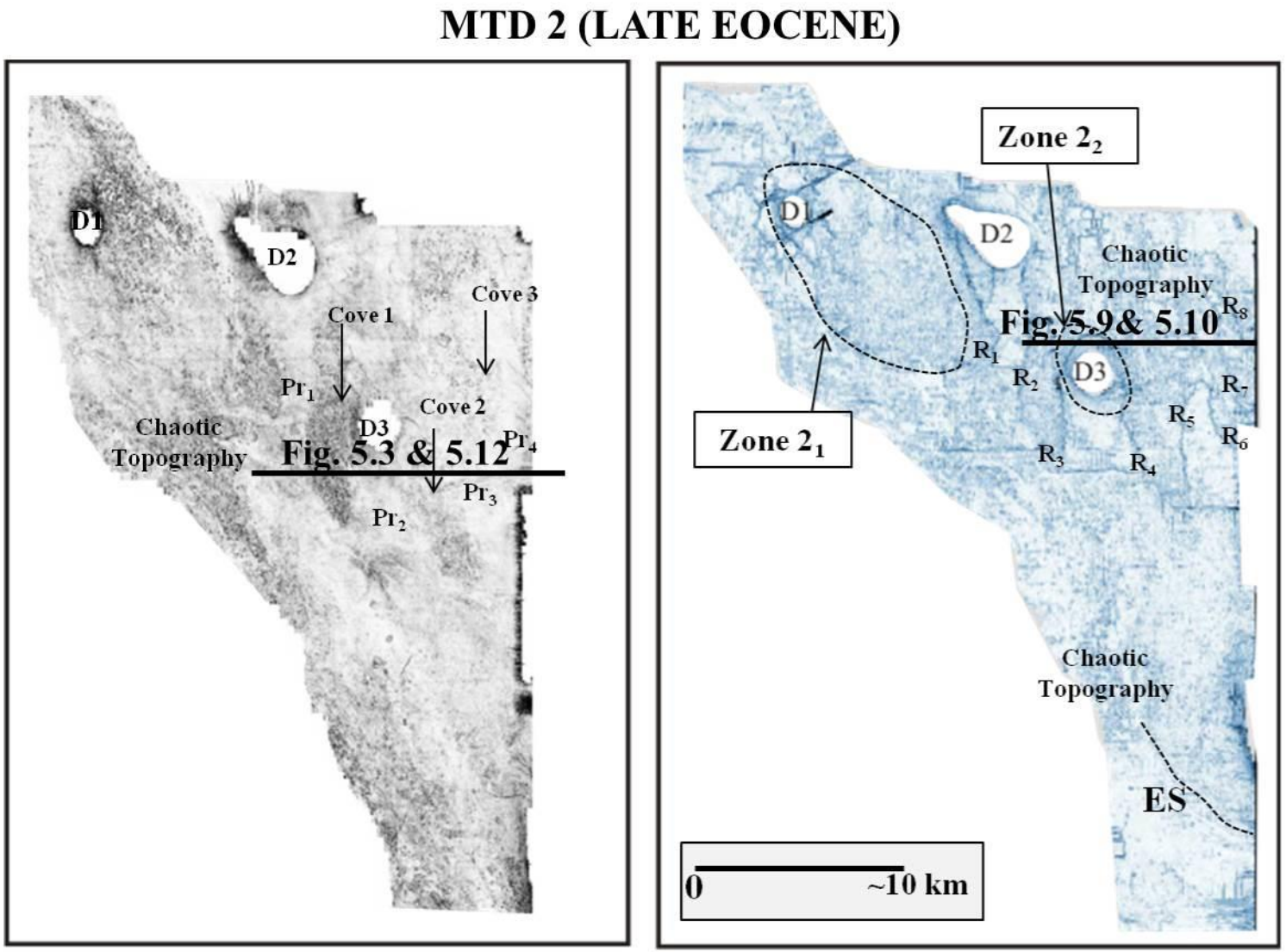

Figure 5.6: Ramps on the basal shear surface of MTD 2 present stair-case geometry where antithetic ramps created depression between promontories. N.B: *R- Ramp, ES- Erosional scour*

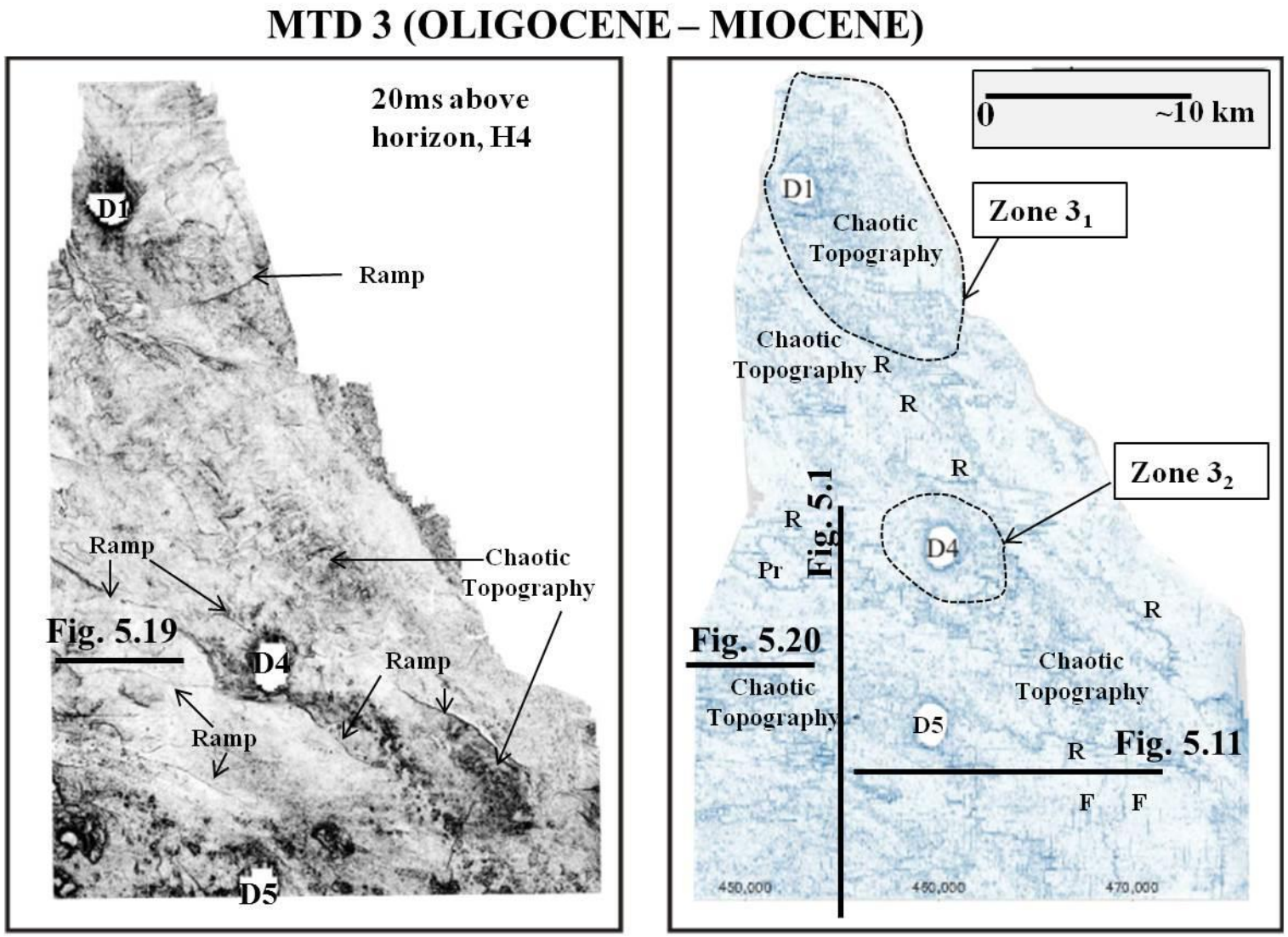

Figure 5.7: Ramps on the basal shear surface of MTD 3 are not related to the salt diapirs. They are interpreted away from the drag zones.

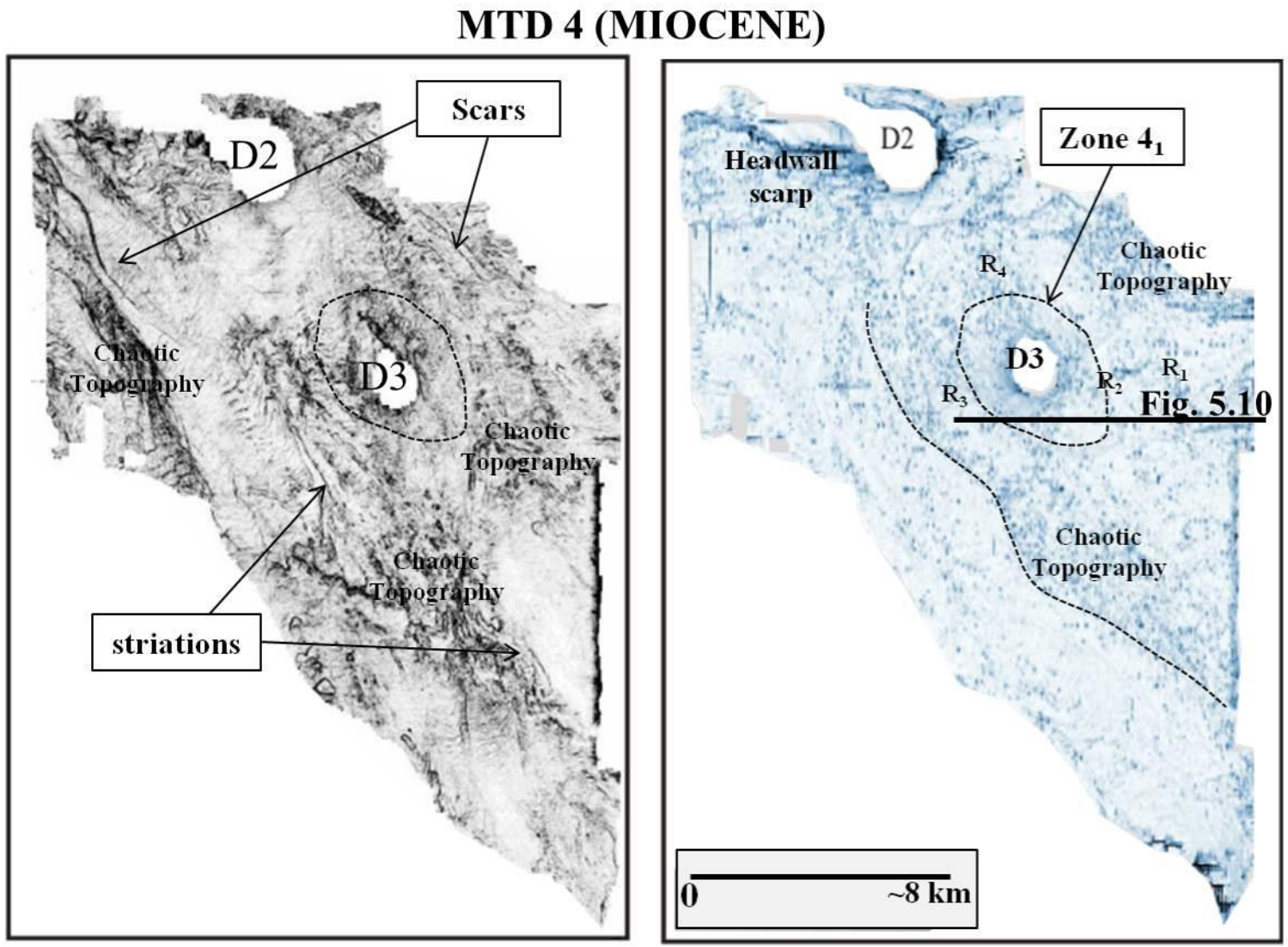

Figure 5.8: Shorter ramps on the southern margin of D3 form scarps on the palaeo seafloor. R - Ramp, Pr - Promontory, ES - Erosional scours, F-fault.

5.1.3. MTD 3 (Oligocene–Miocene)

Ramps on the basal shear surface of MTD 3 separate areas of nearly flat topography from regions with rugged basal shear surfaces (Figure 5.7). Time-derived dip and coherence maps at the base of MTD 3 show rugged topography towards the western flank of D5. This area is dominated by large rafted blocks (Figure 5.11). Most of the observed ramps are NW–SE trending (N72°W to N44°W) and anastomosed in the SE part of Figure 5.7. The point of intersection of the ramps corresponds to the position of scours into the underlying lithological unit. A striking sub-elliptical feature on the most distal margin of D4 forms a promontory flanked by a cove (Figure 5.7). Despite its shape, it differs from those described in MTD 2, as it is enclosed by debrites.

5.1.4. MTD 4 (Miocene)

Basal ramps in MTD 4 shows very low angles of dip (<5°) and are located on the NW and SE flanks of D3 (Figures 5.8 and 5.12). On the SE flank of D3, rafted blocks with heights up to 82 ms TWTT (~254.2 m) are found at the point of intersection of the basal ramps. The headwall scarp of MTD 4 is shown as subtle topographic highs on the palaeoslope (Figure 5.4f). Furthermore, striations and erosional scours on the SE part of the MTD trend NW–SE (N46°W) direction. This supports the assumption that the transport direction of MTD 4 was NW–SE (N54°W).

5.2. Drag zones around salt diapirs

For the six (6) drag zones interpreted in the study area, axial ratios of long/short axes (AR) and the orientations of the long axes (Φ) were determined from the computed time-dip and RMS amplitude maps (Figure 5.18). The aim was to map variations in the internal character of MTDs in four pre-defined quadrants in each drag zone. In the study area, seismic variations are prominent across basal ramps within the identified drag zones

(Figure 5.18). The following nomenclature was used to convey the different MTD facies located in each quadrant of the drag zones:

a) Debrites (DBs), also debris flow deposits sensu. Posamentier and Kolla (2003). Debrites are characterised by very chaotic, disrupted and contorted reflection on seismic profiles. They are shown as very low amplitude strata on RMS maps (Figure 5.19).

b) Coherent/unrotated blocks (CUBs) sensu. (Dott, 1963; Moscardelli et al., 2006). Coherent blocks usually have preserved internal geometries with parallel reflections. They are characterised by high amplitude features on RMS maps and are expressed distinctly from their surrounding low amplitude sediments (Figure 5.20).

c) Slightly deformed blocks/slides (SDBs), also moderately deformed blocks sensu. (Gamboa et al., 2010; Gamboa et al., 2011). Moderately deformed blocks have planar reflections in the centre and rotated edges. They are often faulted. They are indistinct on the RMS map except when associated with low amplitude debrites (Figure 5.19).

d) Rafted blocks (RBs) (cf. Gamboa et al., 2011). Rafted blocks comprise blocks of strata that display internal architecture resembling materials that have been transported and dilated. They have rotated edges and are characterised by high amplitude reflections at their top and base (Figure 5.21).

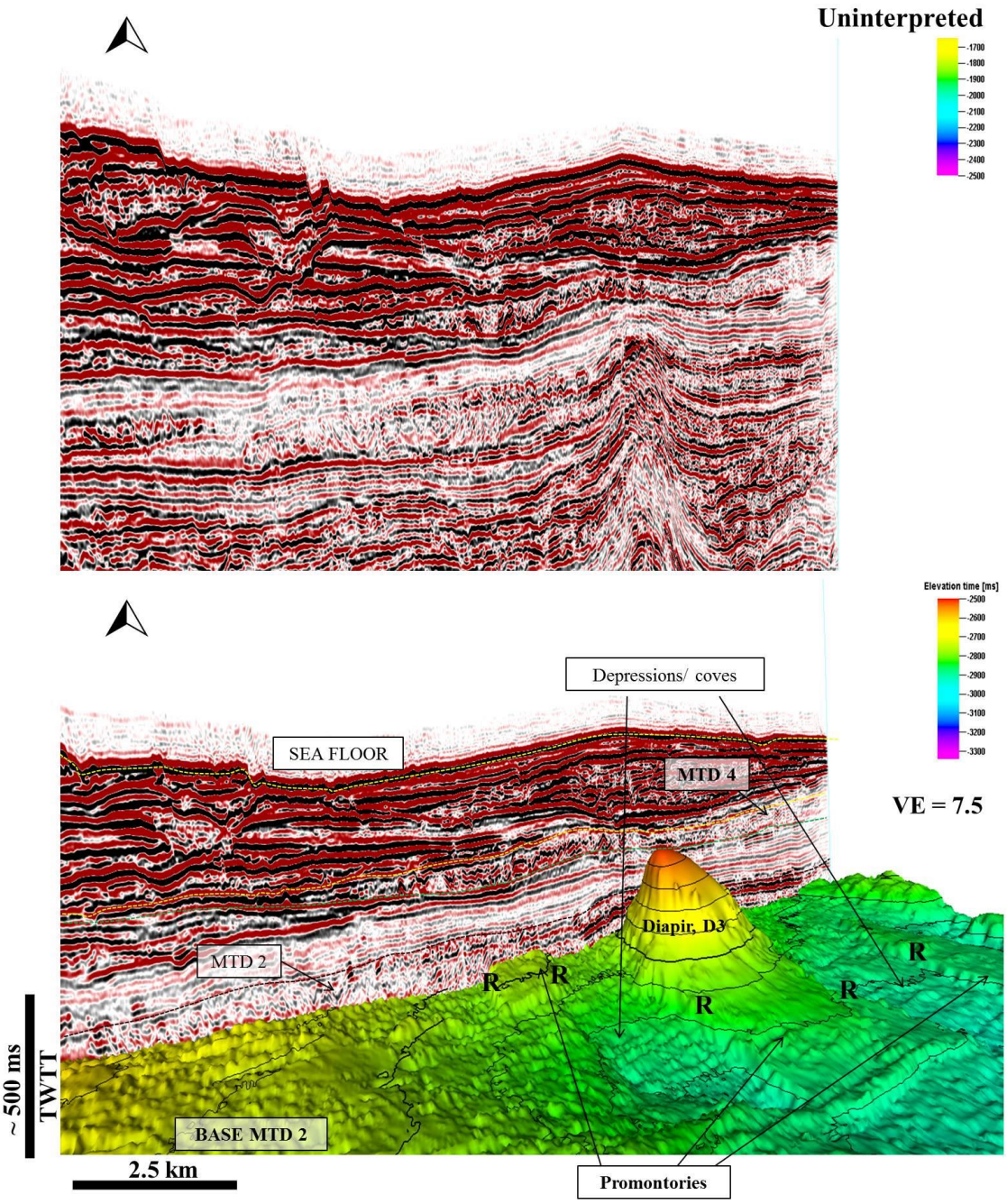

Figure 5.9: Type I ramps are flanked by promontories, and they are restricted to the base of MTD 2.

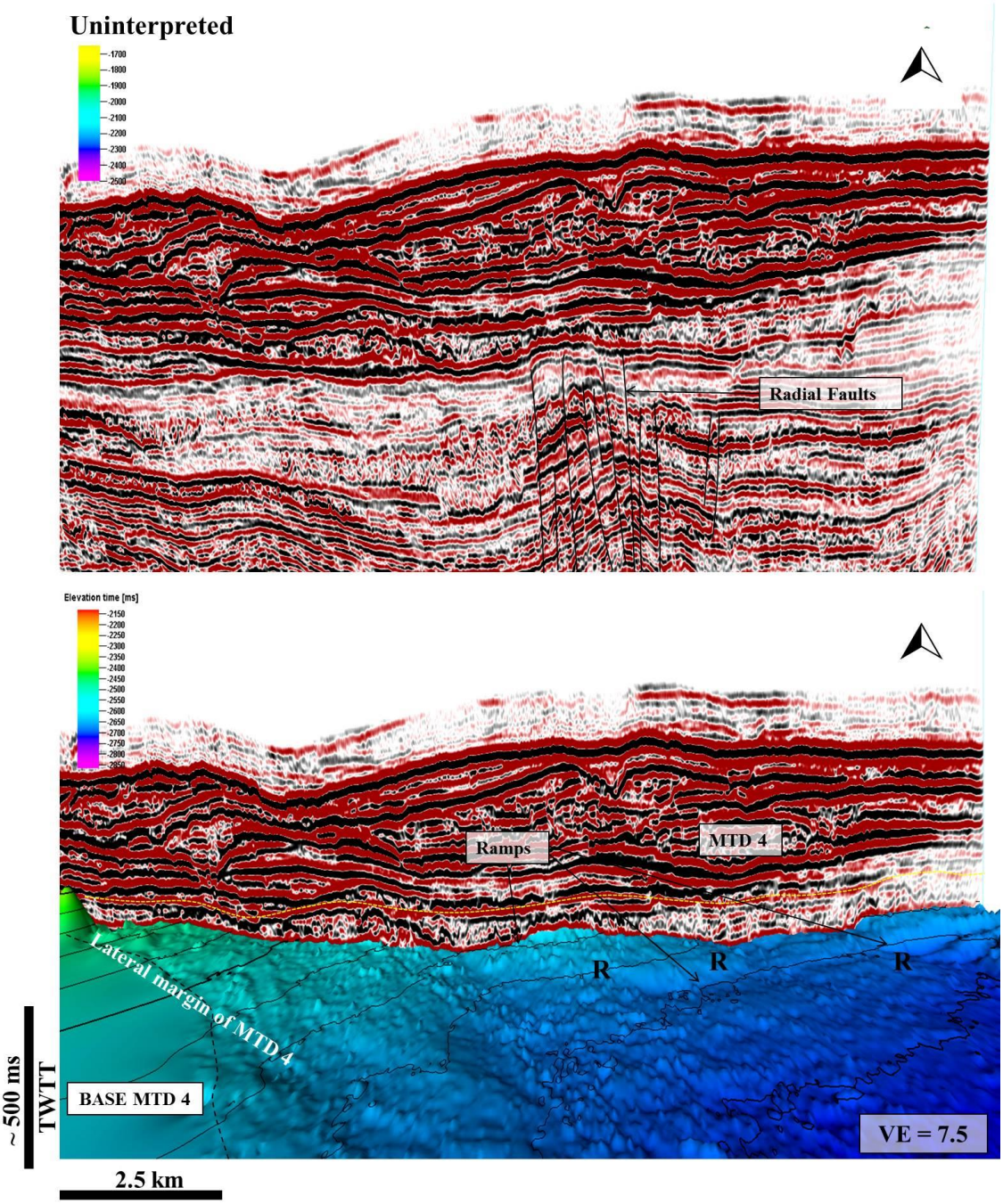

Figure 5.10: Seismic profile through Type II ramps at the base of MTD 4. R— represents the position of basal ramps.

Table 5.3: Aspect ratio and geometry of MTDs in this Chapter.

MTD	Max length	Max breadth	Aspect ratio	Max. Thickness(ms) (TWTT)	Area (sq.km)	Volume (km^3)
MTD 1	38	38	1.00	110	778.8	90.0
MTD 2	52	25	2.08	140	602.4	88.5
MTD 3	48	28	1.71	175	851.1	156.4
MTD 4	30	14	2.14	75	325.8	25.7

Table 5.4: Statistical parameters measured on inferred drag zones at the crest of the salt diapirs

S/N	Ellipse	MTD	Long(x)	Short(z)	x/z	Phi (ϕ)
1	$Z4_1$	4	8.72	5.82	1.50	54.1
2	$Z3_1$	3	12.36	7.71	1.60	57.1
3	$Z3_2$	3	7.60	4.33	1.76	51.2
4	$Z2_1$	2	12.35	6.22	1.98	46.9
5	$Z2_2$	2	7.88	6.44	1.22	54.1
6	$Z1_1$	1	11.54	5.54	2.08	26.7

5.2.1. MTD 1 — fault-controlled debrites

The drag zone mapped at the depth of MTD 1 was located around D4 (Figure 5.18a). Its boundary is marked by differences in RMS amplitude values on the northern flank of D5, and by basal ramps on the other flanks (Figure 5.5). Distinct shadow zones and scars represent changes in the composition of the MTD (Figure 5.18a). Their axial ratio was computed as ~2.08, with short and long axes of ~12 km and ~6 km respectively. This zone had the highest estimated Aspect Ratio value in the study area, with a long-axis direction of ~N27°W (Table 5.3). MTD facies in the drag zone included debrites (DBs), and coherent/unrotated blocks (CUBs) in the first quadrant, DBs in the second, and slightly deformed blocks/slides (SDBs) in the third and fourth quadrants respectively (Figure 5.18a).

5.2.2. MTD 2 — promontory-bounded debrites

The first zone on MTD 2 is mainly located around diapir D1 (Figure 5.18b). Basal ramps are ubiquitous features in the western part of zone 2_1 (Figure 5.6). The axial ratio of the zone approaches 1.98, with long and short axes of ~12 km and ~6 km. The first quadrant contains CUBs and DBs while the remaining quadrants are entirely covered by DBs. The second drag zone affecting MTD 2 is observed on the margin of diapir D3, The basal shear surface is here marked by ramps on both its western and eastern flanks (Figures 5.6 and 5.18b). A shadow zone on its western end highlights a transition from high to low amplitude strata N54°W (Figure 5.18). The estimated axial ratio of Zone 2_2 is ~1.22. DBs were deposited in the first and fourth quadrant while SDBs were found in the third and second quadrants.

5.2.3. MTD 3 — Blocky mass-transport deposit

The two drag zones identified in MTD 3 were located in areas of low to high amplitude reflections across NW–SE (N57°W and N51°W) trending ramps (Figure 5.18c). Zone 3_1 was located on the north western margin of the MTD. The estimated axial ratio of this zone was ~1.60. Its western and eastern margins are marked by very prominent ramps (Figure 5.7). To the north and south of 3_1 the ramps interconnect and are subtly revealed on the RMS amplitude window (Figures 5.7 and 5.18c). MTD facies included DBs in the second and third quadrants, CUBs and DBs in the first and moderately high-amplitude SDBs in the last quadrant (Figure 5.18c). Zone 3_2 was located south of the first zone; it had an estimated axial ratio of ~1.76, with long and short axes of ~8 km and ~4 km. Rotated/rafted blocks (RBs) were the main MTD types in the fourth quadrant while other quadrants comprise of a mixture of CUBs, SDBs and DBs (Figure 5.18c).

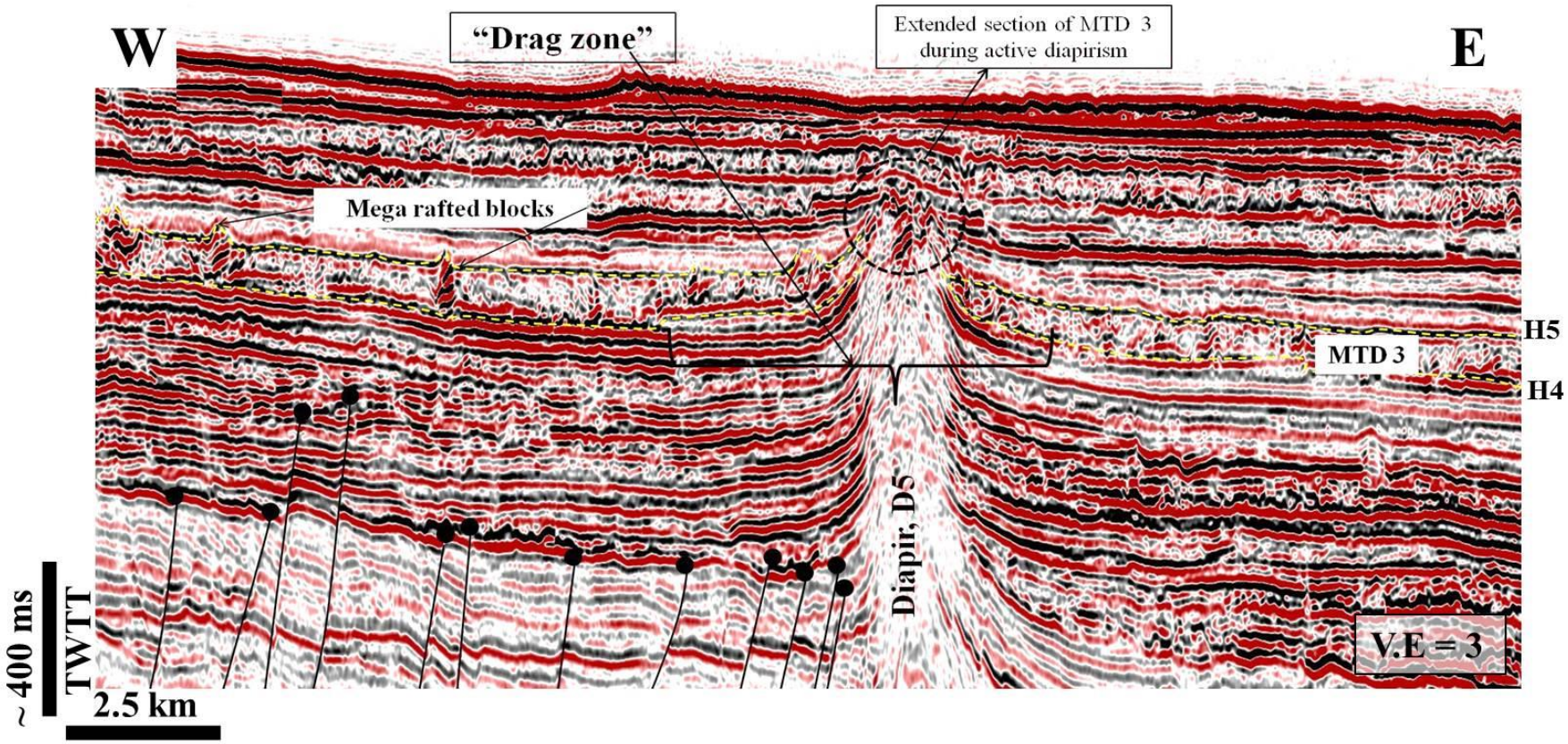

Figure 5.11: Seismic profile showing examples of 'drag zones' and rafted blocks in MTD 3. Drag zones represent the uplifted section of the MTD during diapir growth. In addition are shown faults that controlled slope gradient at the base of MTD 1.

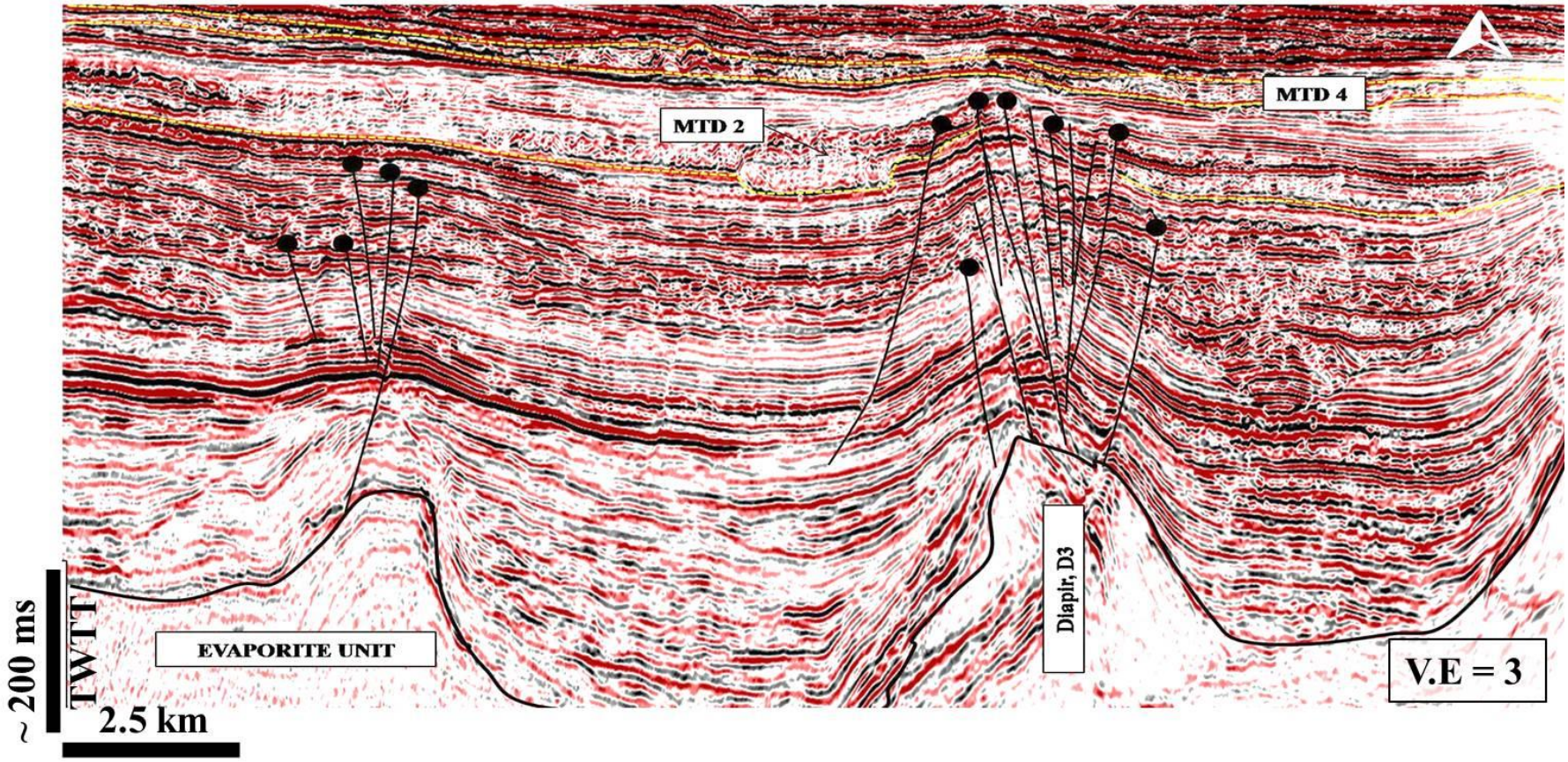

Figure 5.12: Fault controlled ramp (Type II) at the base of MTD 4. Also shown are high amplitude reflections associated promontories at the basal shear surface of MTD 2.

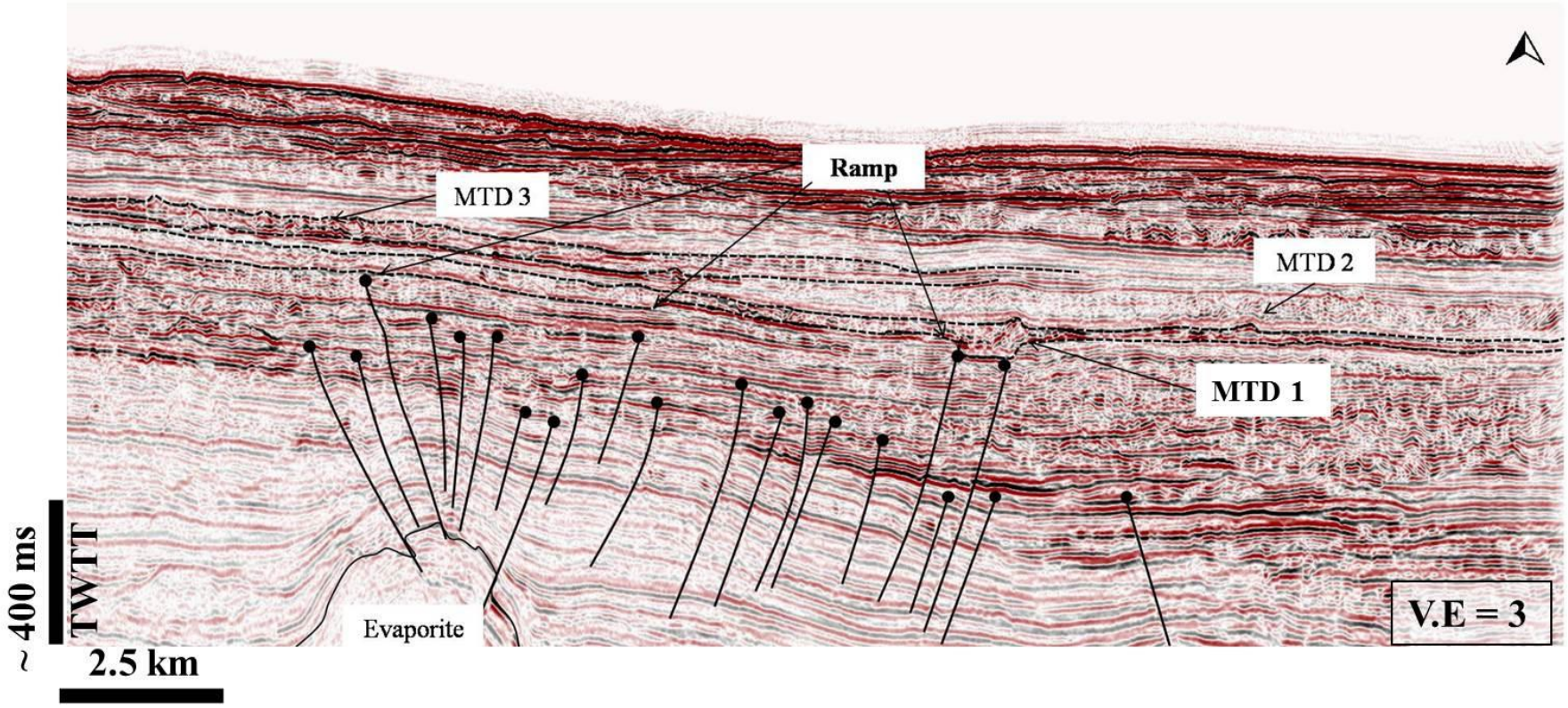

Figure 5.13: Type II ramps at the base of MTDs 1 and 3.

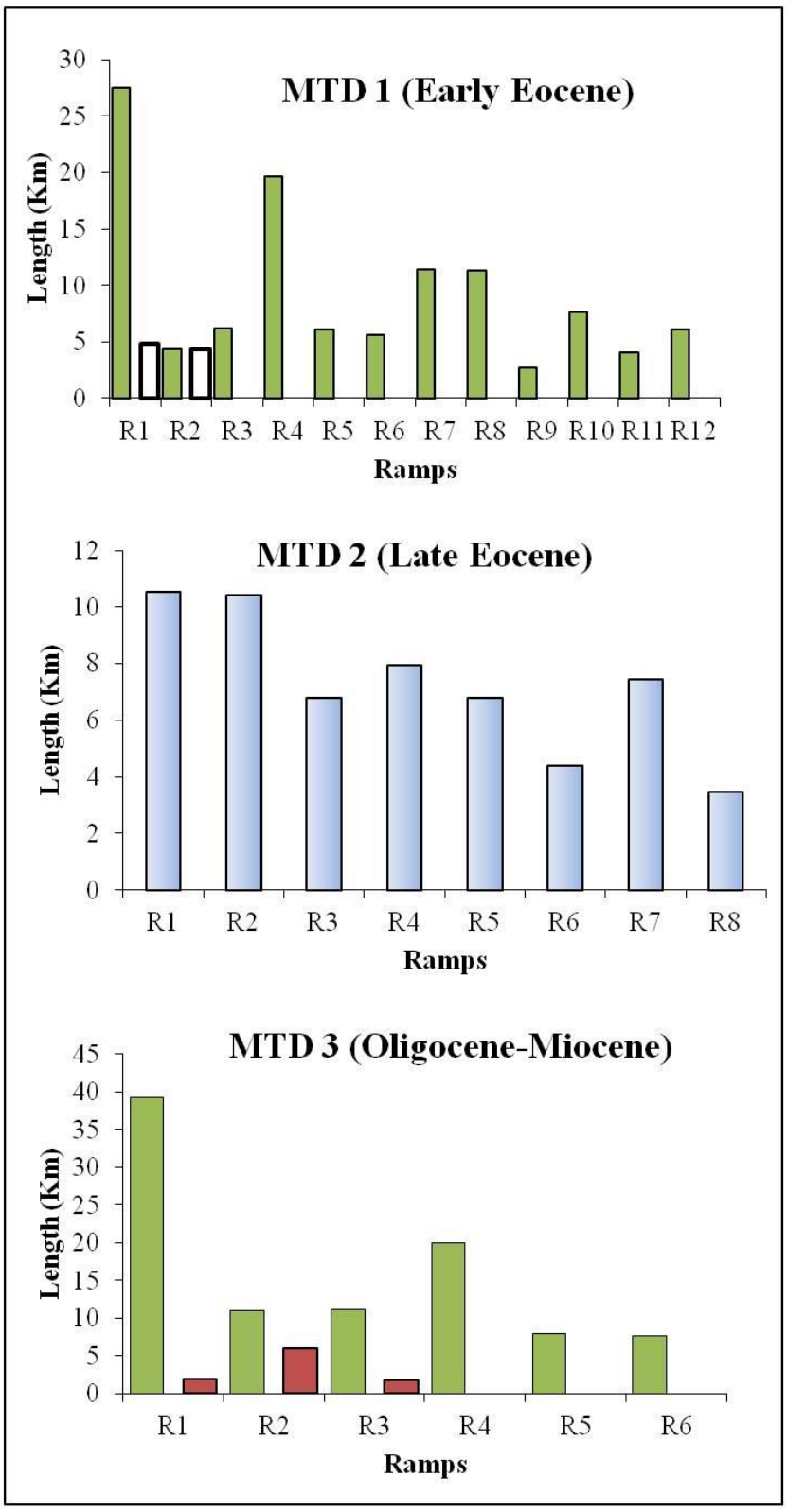

Figure 5.14: Dimensions of ramps measured on dip maps. Length of the twenty-eight ramps used in this chapter.

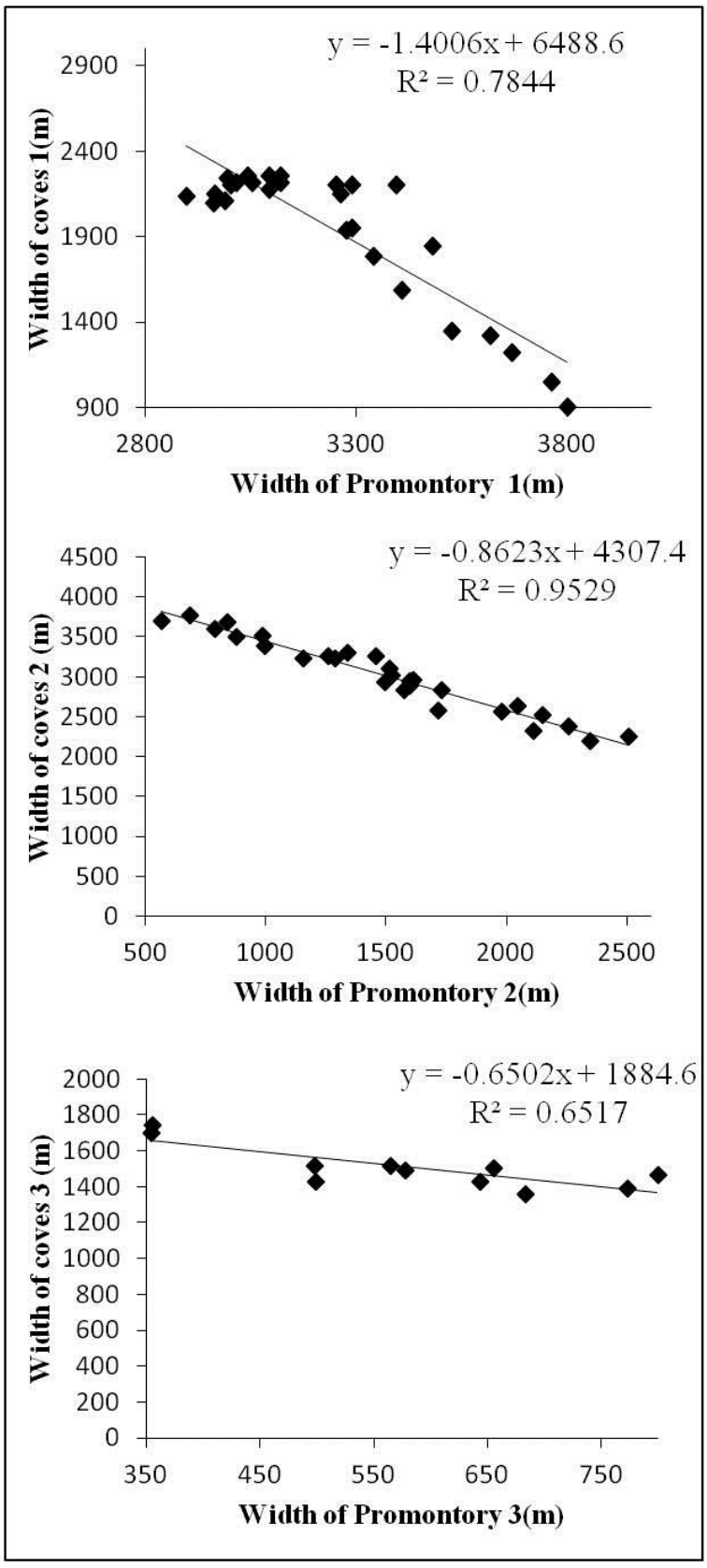

Figure 5.15: Scatter plots highlighting statistical analyses of the variations in the width of the depocenter and promontories in MTD 2.

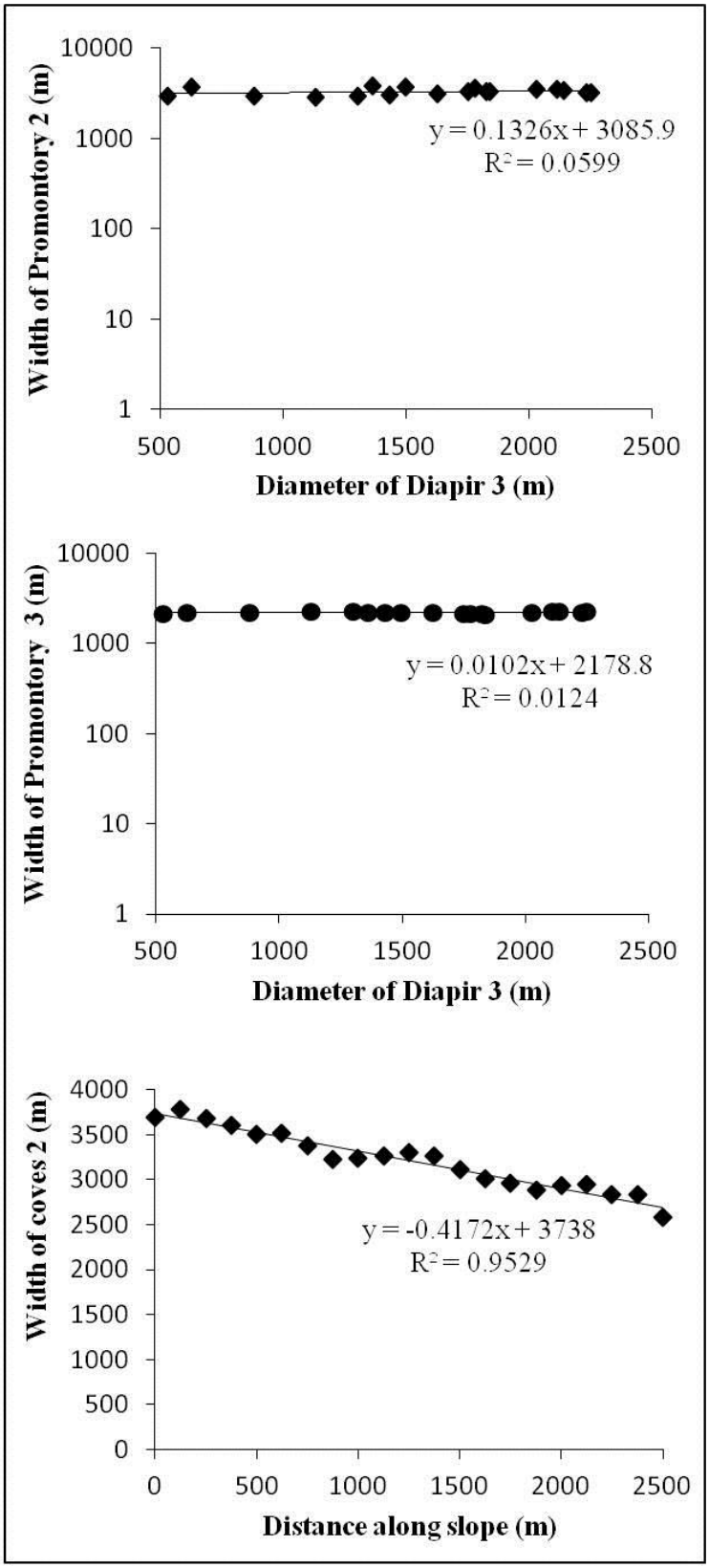

Figure 5.16: Statistical analyses of the variations in width of promontories with diameter of diapir and increasing distance towards toe regions.

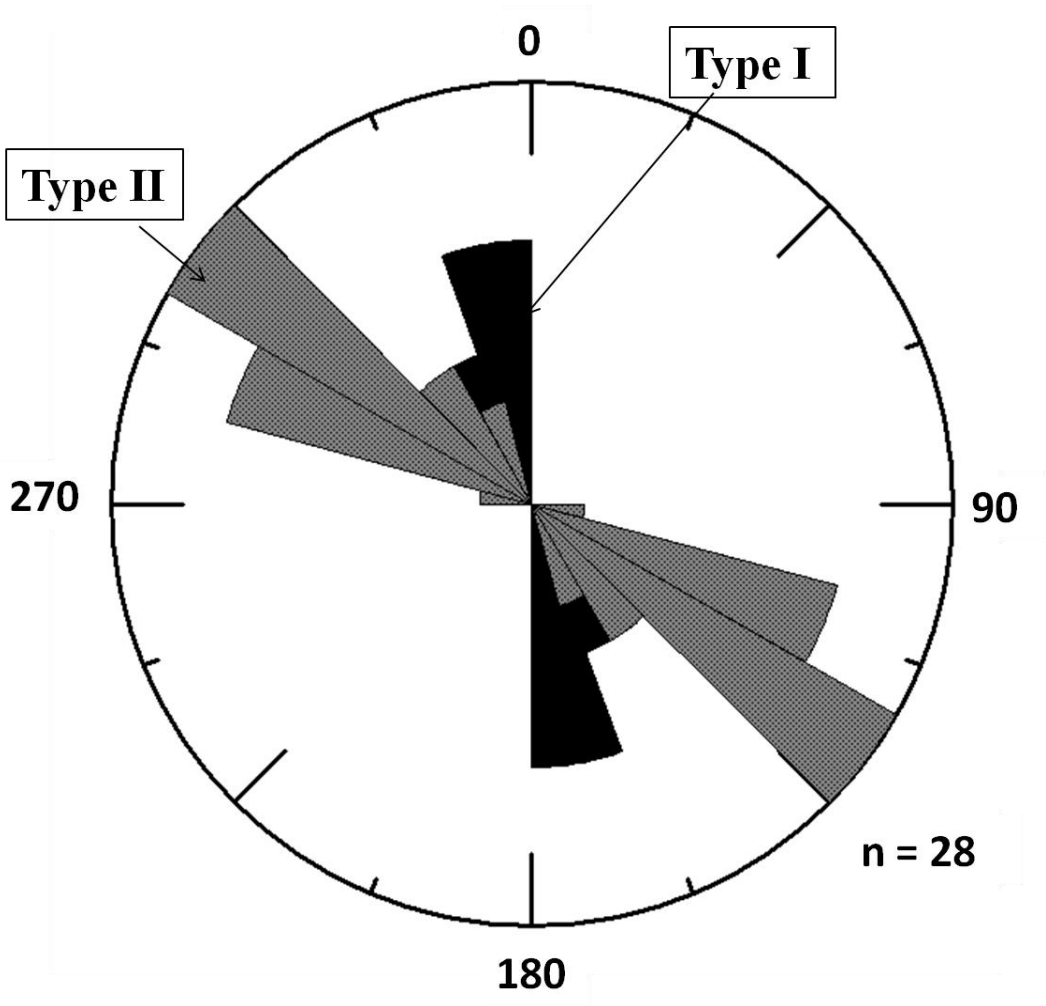

Figure 5.17: Rose diagram for the orientation of the two types of ramps discussed in the text. Type I are promontory-related ramps while Type II are fault-controlled ramps.

5.2.4. MTD 4 — Low-angle scarped MTD

Zone 4_1 is inferred around diapir D3. This diapir displayed features previously identified in older MTDs. Zone 4_1 is delimited by a ramp to the west, a shadow zone and several subtle ramps to the east. The long and short axes were ~9 km and ~6 km respectively, with an axial ratio of ~1.50. The first and fourth quadrants of the zone were dominated by CUBs and RBs while the third and second quadrants show DBs and SDBs (Figure 5.18d).

In summary, ramps within the drag zones frequently relate to the deposition of blocky MTDs, while those beyond the drag zones mostly favoured the deposition of debrites (Figure 5.23b). Geometrically, three kinds of axial ratio are common in the drag zones; these are <1.50, 1.50–2.00, and >2.00. The principal long and short axis ranges from ~12 km to ~5 km, and ~3 km to ~8 km; estimated standard deviation for these parameters are ~0.28, ~2.57, and ~1.39 respectively. The calculated harmonic and vector mean for the axial ratio and phi (ϕ) are 1.63 and ~47°. Overall, the long axes of the predicted zones are oriented in a NW–SE (~N27°W to N57°W) direction while the short axes are NE–SW-trending (~N63°E to N33°E), respectively coinciding with the direction of the maximum extension and contraction of the zones.

5.3. Reassessing diagnostic features of slope- and shelf-detached MTDs

The dimension of MTDs can be used to estimate their source area and sediment run-out distances (Hunerbach and Masson, 2004). It also provides important hints on the volume of sediment remobilised during slope instability events. Based on this assumption, aspect ratios were previously used to classify MTDs as ‘slope-detached’ and ‘attached’ offshore Trinidad and Tobago (Moscardelli and Wood, 2007), and in the

analysis of Quaternary submarine landslides on the US Atlantic margin (Twichell et al., 2009). Slope- and shelf-attached MTDs are of regional scale, covering thousands of kilometres in area and are generally sourced from extra-basinal systems such as shelf-edge deltas and upper-slope regions (Moscardelli and Wood, 2007). In contrast, detached MTDs are relatively small and confined to the margins of minibasins or bathymetric highs. Irrespective of the volume of remobilised strata, slope detached MTDs have specific aspect ratios of < 4 (Moscardelli and Wood, 2007; Twichell et al., 2009). Slope-attached MTDs usually have longer run out distances and invariably high length/ width ratios relative to those detached from the slope or shelf.

The methods in Moscardelli and Wood (2007) and Twichell et al. (2009) are valid when classifying MTDs on continental margins where the headwall scarp is imperceptible or, as in the case of the study area, salt structures are prominent and well-developed (Figures 5.4 and 5.23). However, this work highlights the existence of quadrants on the margins of rising diapirs in which the MTDs' lithology and internal characters significantly vary. In addition, these same quadrants are shown to comprise the regions on the slope recording the higher recurrence of MTDs (Figure 5.23b). This is a significant piece of new information that will be discussed in detail in the following sections.

In this study, all the MTDs have length/width ratios of <3 with the headwall scarp and toe regions prominently-imaged. The lack of headwall scarps in MTD 2 may imply quick burial, evacuation and later infilling of the headwall region by subsequent and younger MTDs, or a distal source for the failed material. This latter interpretation is favoured by the homogeneous nature of MTD 2. This MTD started out as

heterogeneous combination of different facies (slides, slumps and debris flow deposits) and, consequent to its long travel distance, ended up as homogeneous debrites (Figure 5.23).

The reactivation of previously-formed radial faults and the growth of newer faults within salt withdrawal basins triggered the deposition of MTD 3 during the Miocene–Oligocene. Rafted blocks up to 400 m in height are prominent near the inferred headwall region (Figure 5.19). Some of these blocks can be markedly faulted, with their size decreasing towards the toe region. The lack of an obviously-extended headwall region implies that materials could have failed homogeneously on the flanks of diapirs (Dykstra, 2005). In contrast, the youngest MTD 4 was formed in the Miocene by continued halokinesis and faulting. The headwall region of MTD 4 lies between D2 and D3 (Figures 5.4f and 5.8). The post Miocene reactivation of D2 led to an elevated slope gradient and the subsequent collapse of sediments on the south-eastern margin of the diapir.

The four interpreted MTDs are thus characteristic slope-detached MTDs presumably resulting from instability generated by increasing slope angles on the flanks of growing salt diapirs. Sliding on the plane of failure was promoted by near-seafloor faulting and salt diapirism. They are also found within, or restricted to, salt withdrawal basins formed on the flanks of rising diapirs. They were generated close to the present-day salt diapirs and as such can be described as locally-sourced MTDs.

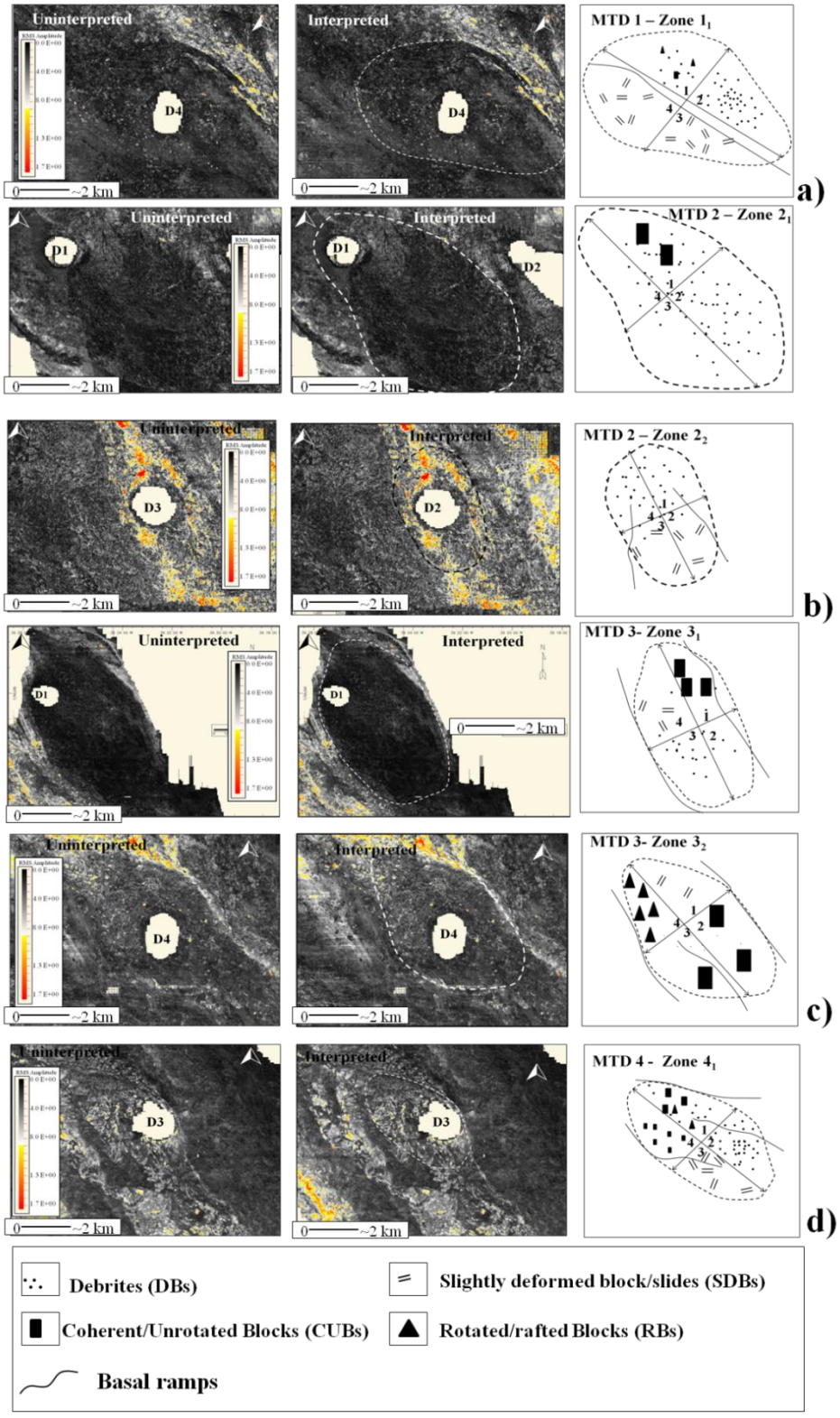

Figure 5.18: Drag zones inferred from RMS amplitude maps computed between the tops and bases of the MTDs. Areas of high amplitude separate the MTDs into bands of alternating high and low amplitude. Quadrants are labelled clockwise. Coherent unrotated blocks and debrites were recognised as near cubic and triangular features on RMS amplitude maps, while the other facies types were indistinctly separated on the maps, except in places where they were shown as low-amplitude features.

5.4. Discussion

5.4.1. Significance of basal ramps of MTDs on the flanks of rising diapirs

In the study area, basal ramps include a) low angle, <5° features around promontories (Type I) and b) fault-controlled scarps created by the reactivation of radial faults and faulting of salt withdrawal basins (Type II) (Figure 5.9). Type I ramps are only found at the basal shear surface of MTD 2 while Type II ramps predominate at the base of the other MTDs. In situations where adjacent ramps were antithetic, they formed promontories and adjacent coves were subsequently filled by debris flow deposits (Figure 5.12). Both kinds of ramps influenced the distribution of the MTDs in distinct drag zones (Figure 5.18). The origin of the two kinds of ramps described in this study can be linked to erosion of the mechanical incompetent layers at the basal shear surface (Figure 5.22b and c). Regions of enhanced erosion are marked on seismic profiles as small-scale coves flanked by undeformed promontories, which comprise the uneroded remnants and mechanical competent parts of seafloor around MTDs.

A key observation in this work is that ramps and promontories have their long axes oriented parallel to the direction of transport of the interpreted MTDs (Figures 5.5 to 5.8). Complete erosion of the palaeo-seafloor may cause the section of the ramp that is normal to the mass flow direction to be indiscernible on seismic profiles. In the study area, there is a strong inverse correlation between the widths of the promontories/flats and that of adjacent coves, with correlation coefficients ranging from 0.65 to 0.953 (Figure 5.15). These relationships suggest that erosion affected the seafloor in an uneven way and account for the evolution of the ramps and flats in the study area (Figures 5.4b and 5.6).

Thus, the promontory-related ramps in this study are not similar to extensional or compressional structures in Gawthorpe and Clemmey (1985). Instead, Type I ramps fit into the description of ramps by Trincardi and Argnani (1990); Lucente and Pini (2003); Frey-Martinez et al. (2005); and Bull et al. (2009). Seismic coherence maps show that Type I ramps are not discontinuities in the seismic volume in contrast to their Type II counterparts (Figure 5.7 and 5.8). Type I ramps are thought to be sidewalls of basal excavation areas on the basal shear surface through which sediments were transferred during the movement of MTDs. Plots of variations in the diameter of D3 versus the width of adjacent coves demonstrate that coves increase in width in the regions where the diameter of the diapir D3 is larger (Figure 5.16). In such a setting, salt diapirs preferentially grew adjacently to the observed promontories.

A possible explanation for the presence of Type II ramps is that they were created by the action of multiple beds cut by pre-existing fault scarps (Figure 5.22c). Type II ramps are, however, preferentially oriented in the direction of transport of the interpreted MTDs. Consequently, we interpret these ramps to pre-date or occur synchronously with the deposition of MTDs 1 to 4 (Figure 5.22a). In addition, the orientation of the fault controlled ramps was directly controlled by halokinesis. Salt mounds, diapirs and associated crestal and radial faults propagated to the south east in areas of lower head gradient *cf.* (Hudec and Jackson, 2007), thus the predominance of Type II ramps striking NW–SE (~N40°W) beneath MTDs 1, 3 and 4 (Figure 5.17).

5.4.2. Drag zones as indicators of seafloor strain

The seafloor and adjacent stratigraphic units draping growing salt diapirs are usually compressed or extended during diapir rise (Vendeville and Jackson, 1992a; Vendeville

and Jackson, 1992b; Davison et al., 2000a; Davison, 2004). The sub-circular shape of most diapirs indicates that the highest strain is located in their central, dome-shaped crest, and progressively distributed along the adjacent flanks of growing salt structures (Bouhallier et al., 1995).

This Chapter shows that halokinesis and diapir growth created drag zones around the studied diapirs. These zones are elliptical on thickness maps and RMS amplitude windows. On the TWTT thickness maps, they were often shown as areas of significant thickness variations when compared to their surroundings (Figure 5.4). Drag zones are therefore considered to mark the area of maximum strain endured by the palaeo-seafloor during the diapir growth. On the RMS amplitude map, they are materialised as coherently distributed zones of uplift/drag characterised by changes amplitude (Figure 5.18). In addition, subtle low amplitude linear features, or scars, observed around some of the diapirs on RMS amplitude maps correspond to the position of basal ramps (Figure 5.18).

Quantifying these drag zones provided insight into the distribution of strain within the MTD during halokinesis. Where present, ramps also influenced the geometry and type of the final drag zone. In this paper is shown a spectrum of MTD facies in drag zones with developed ramps. As drag zones represent the maximum strained section of MTD deposited during salt diapir rise, their analysis can be used to understand if MTDs were deposited before or during salt diapir movement.

The relative lack of flow structures such as deflected, reflected or imbricated MTD layers around the diapirs suggest mass flows that are not buttressed against a structural

or topographic barrier (see Figure 5.22a). In addition, the diapirs are found in the translational domain of MTDs which may indicate no significant alteration of the stress regime during the diapir growth. Also, piercement of the MTD connotes deformation of the overburden, especially during the active stage of diapirism. In contrast to the latter settings, basal ramps sub-parallel to drag zones' long axes indicates the accommodation of local strain on the flanks of diapirs when of the deposition of MTDs. This is an important finding, as it shows that this type of ramps and promontories can be used as a proxy to understand the timing of salt diapirism, and the amounts of strain experienced in the drag zones at the time of seafloor failure.

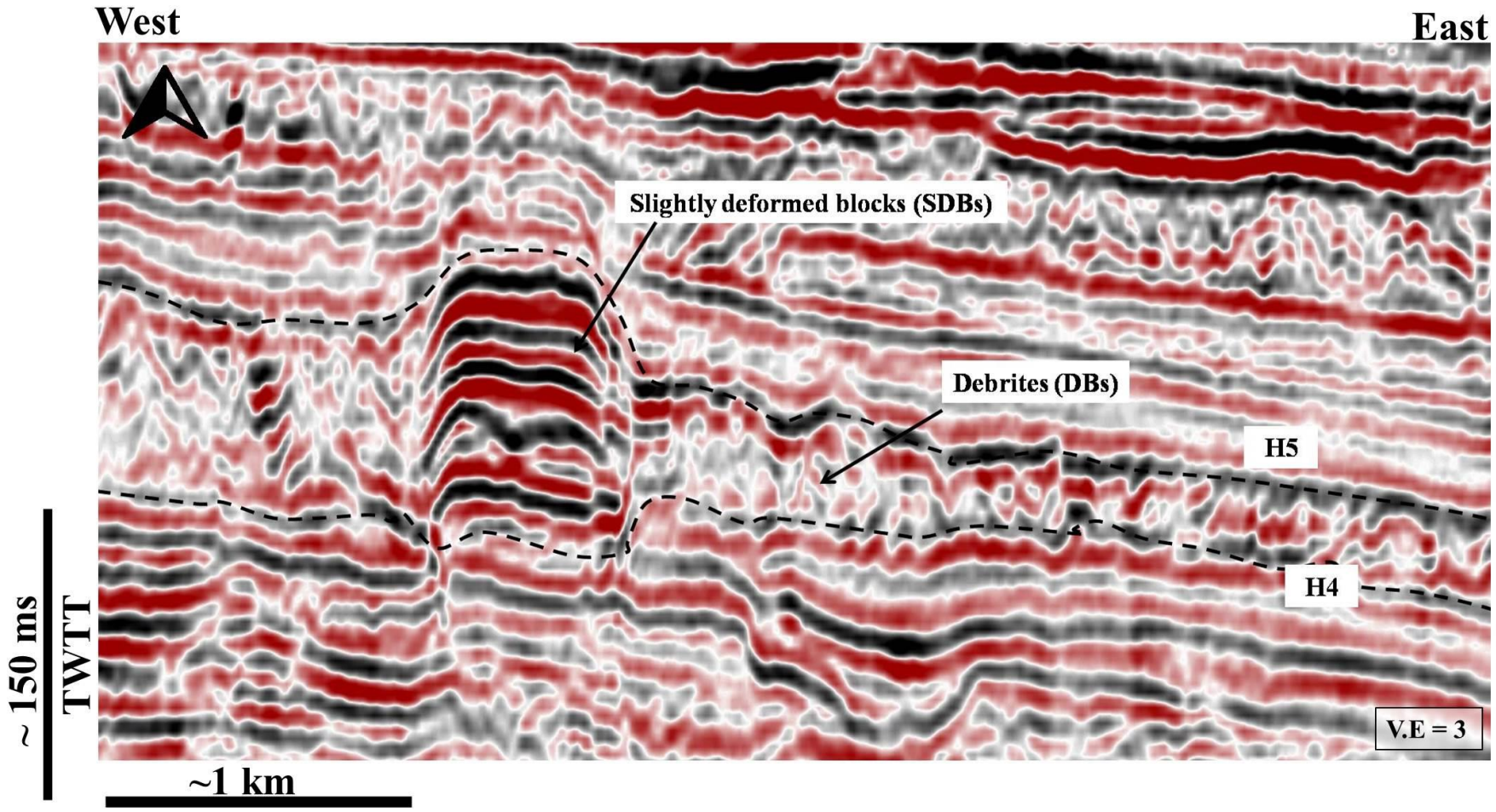

Figure 5.19: Slightly deformed blocks (SDBs) comprise moderately deformed blocks with planar reflections in the centre and rotated edges.

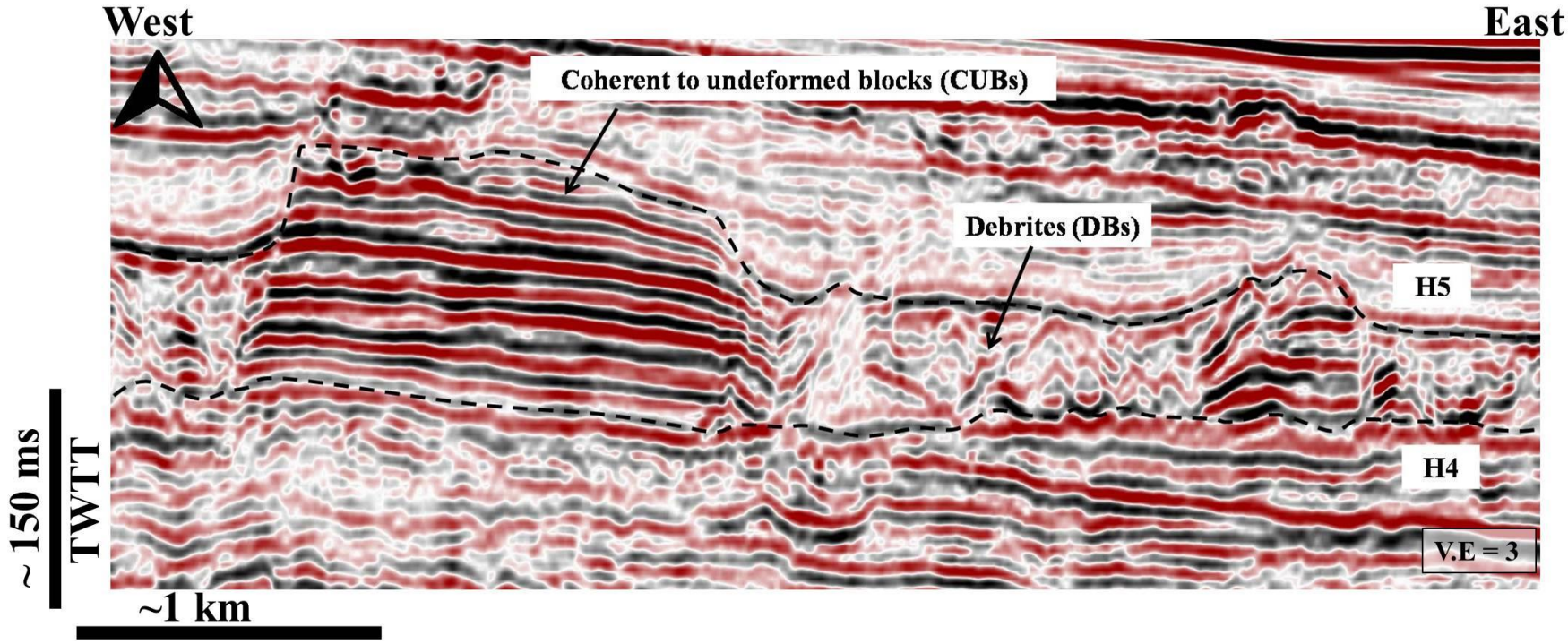

Figure 5.20: Coherent to undeformed blocks (CUBs) have preserved internal geometries with parallel reflections.

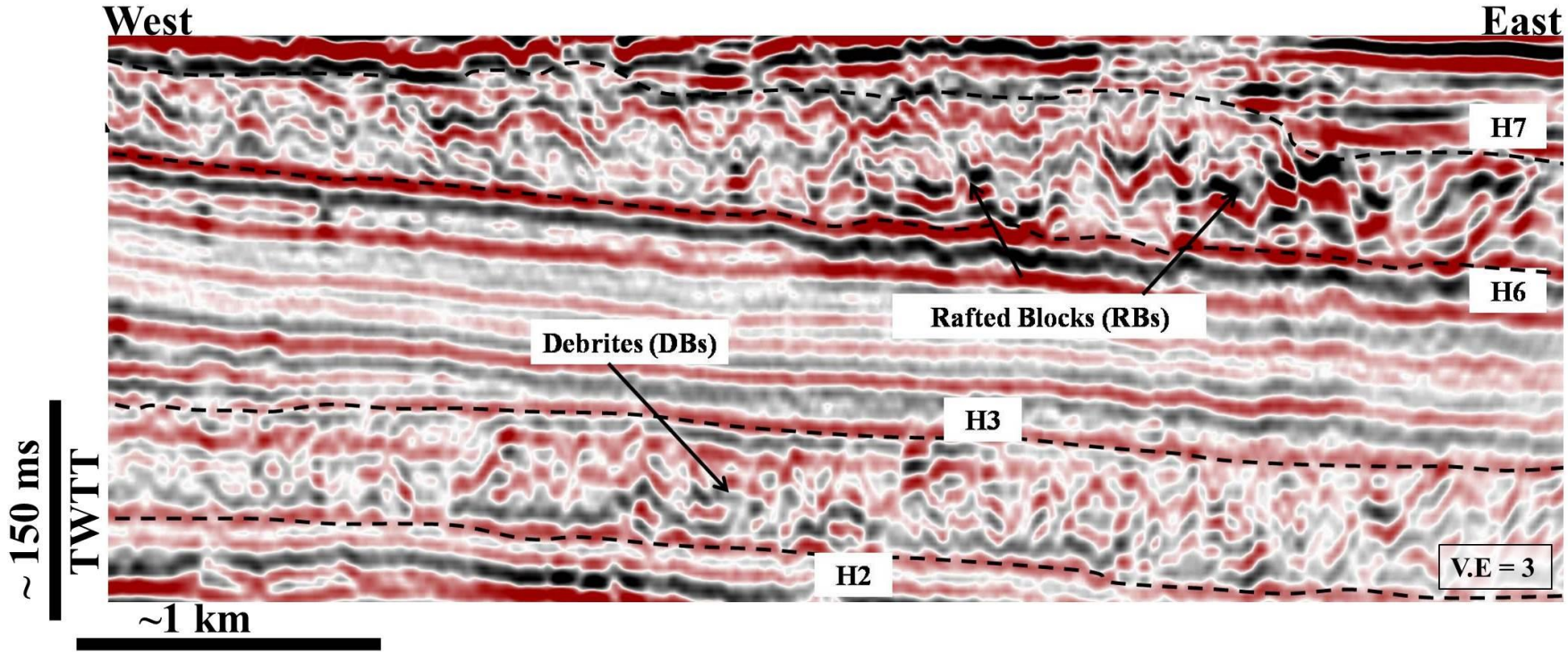

Figure 5.21: Rafted blocks (RBs) comprise blocks of strata that display internal architecture resembling materials that have been transported and dilated, while debrites (DBs) are characterised by very chaotic, disrupted and contorted reflections on seismic data.

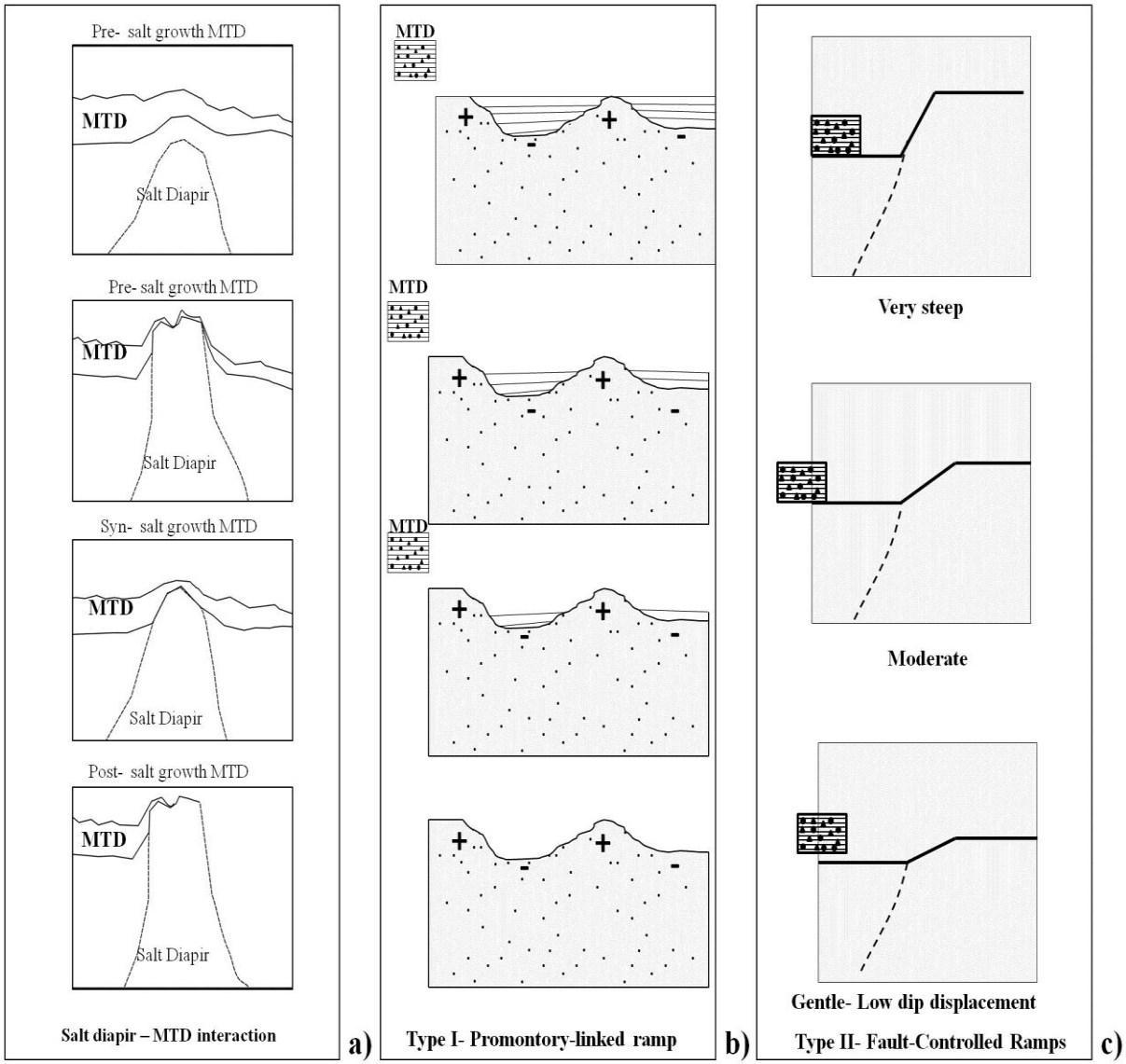

Figure 5.22: Diagram depicting: a) the possible interplay of MTDs with growing salt diapirs and their modes of formation of b) Type I ramps, c) Type II ramps. N.B: *(+) represent the mechanical competent section of the palaeo seafloor while (−) denote the less competent part.*

5.5. Conclusions

This Chapter shows that ramps at the base of MTDs could be oriented parallel to the flow direction. These ramps include those attached to promontories, and fault-controlled ramps that either predated or occurred synchronously with the deposition of MTDs. Ramps with promontories formed by the erosion of the least competent part of the basal shear surface. When there is complete erosion of the incompetent layer, they are manifested as structures normal to the direction of mass flow and parallel during partial erosion. Furthermore, the action of multiple beds and incomplete erosion of underlying fault scarps was linked with the formation of fault-controlled ramps.

The salt diapir rise and subsequent strain histories of the mass transport deposits are preserved in drag zones within the MTD on the crest of the diapirs. Distinct MTD facies were preferentially deposited in different quadrants of drag zones. The estimated axial ratios of drag zones were estimated to be b1.5, 1.5–2.0, and 2.00; with the long axes mainly oriented in NW–SE direction. Additionally, the location of drag zones and MTD facies was influenced by the position of basal ramps. The orientation (ϕ) of the long axes and axial ratios of the drag zone were important parameters for investigating the strain history of the palaeo seafloor and the MTDs.

These zones are strain markers, which could only be analysed by estimation of their aspect ratios. Drag zones, though elliptical in map view, cannot be considered as strain ellipses, as the pre-requisite for hypothetical representation of the zone as initially circular objects cannot be adequately justified from seismic. If it were possible to identify the elliptical drag zone in attribute data from near-horizontal section through the seismic volume, there would be no way to characterise the intermediate axis sufficiently to carry out a strain analysis.

In this Chapter we identified three statistical parameters (angle of dip, length along strike, orientation) defining the geometry of basal ramps, and two types of ramps. Type I is promontory-related and Type II is fault-controlled. Promontories are linked with very high-amplitude reflections, characteristic of bright spots. This implies that promontories in MTD 1 and MTD 2 can comprise potential exploration targets, similar to features described as 'Erosional Shadow Remnants' by Moscardelli et al. (2006). In addition, the drag zones mapped in this work are sites of recurring mass wasting events, and such areas should be avoided when planning well trajectories, especially when these zones are in front of salt diapirs. If located on the proximal part of the diapirs, they can act as a structural barrier to remobilised MTDs.

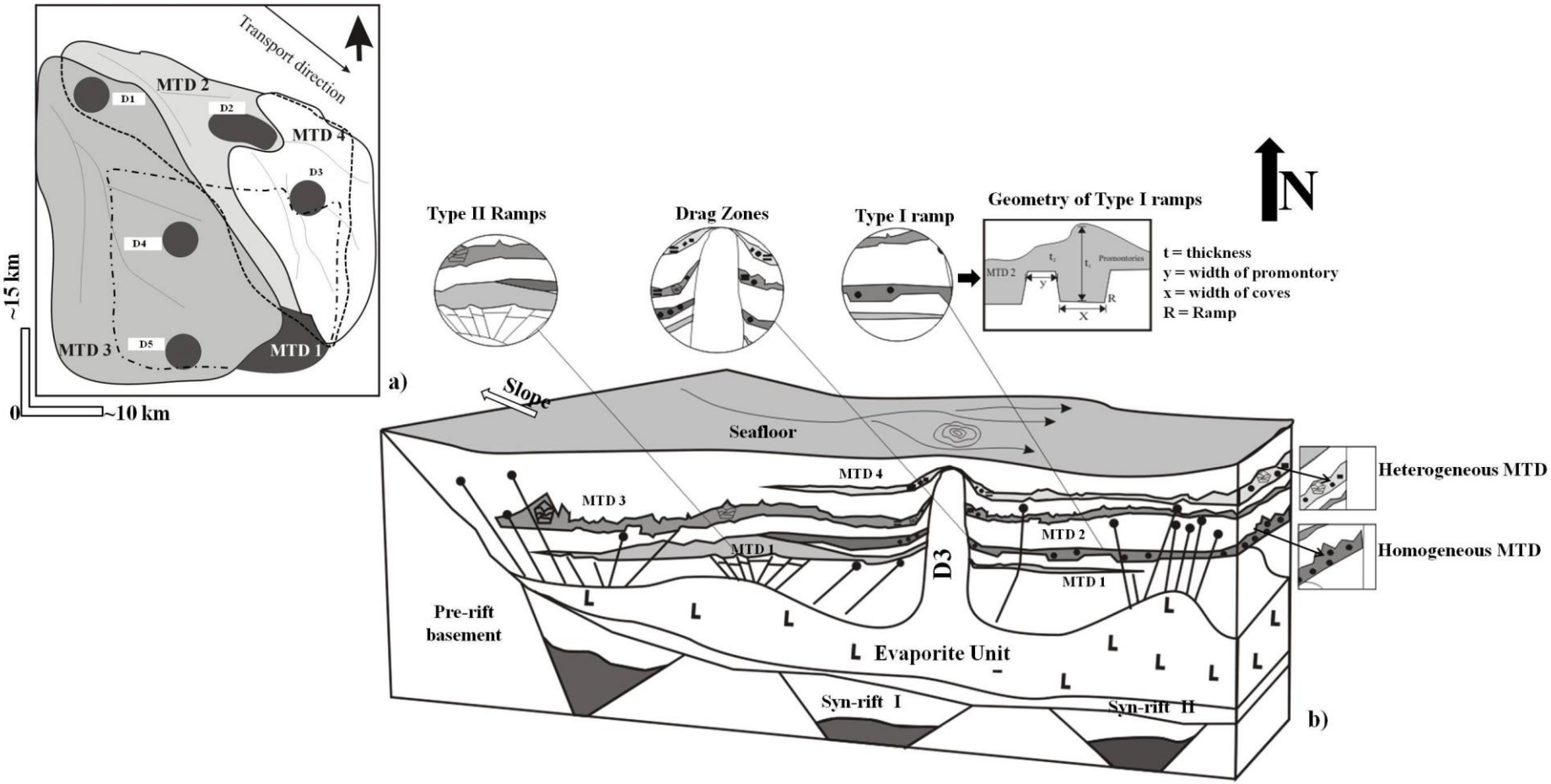

Figure 5.23: a) Relationship and geometry of MTDs on the Espírito Santo continental slope. b) Block diagram showing some of the terminologies and concepts described in the text. Shown in the figure are examples of Type I and Type II ramps, Heterogeneous and Homogeneous MTDs, and drag zones (not to scale). *N.B:The arrow point in the direction of the upper slope*

Chapter 6

Mass-transport deposits controlling fault propagation, reactivation and structural decoupling on continental margins (Espírito Santo Basin, SE Brazil)

This Chapter is published as:

Omosanya, K.O., Alves, T.M., 2013. Mass-transport deposits controlling fault propagation, reactivation and structural decoupling on continental margins (Espírito Santo Basin, SE Brazil), Tectonophysics, **10.1016/j.tecto.2014.04.045**

Abstract

This work uses high-quality 3D seismic data to assess the importance of mass-transport deposits (MTDs) as markers of fault propagation. We mapped three distinct MTDs and several fault families on the continental slope of the Espírito Santo Basin, SE Brazil. Fault mapping was based on seismic attributes such as seismic coherence and structural smoothing, and was further completed using ant tracking algorithms. Genetically related fault families were analysed in terms of their throw-depth (t-z) and throw-distance (t-x) gradient curves. A key result in this paper is that vertical fault propagation can be hindered by MTDs, as demonstrated for Eocene to Early Miocene faults in parts of the study area. Throw-depth variations in faults affected by MTDs are associated with: a) lithologic controls resulting from the presence of MTDs, b) local fault segmentation and c) reactivation by dip linkage. Based on their orientation and degree of interaction with MTDs, interpreted faults can be classified as decoupled and non-decoupled. Importantly, faults decoupled by MTDs have quasi-elliptical t-x profiles and show smaller cumulative throw values and fault propagation rates when compared to their non-decoupled counterparts. Recurrent MTDs can therefore be used as markers to estimate structural decoupling between distinct fault families.

6.1 Introduction

The contribution of mass-wasting processes to the geometry and architecture of sedimentary basins has been widely discussed in the literature (e.g. Hunerbach et al., 2004; Hjelstuen et al., 2007; Tailing et al., 2007). In particular, mass-transport deposits (MTDs) are important components of petroleum systems on continental margins (Gamboa et al., 2011; Ogiesoba and Hammes, 2012). They may comprise mud prone successions, homogeneous debris flows with good seal properties, or reservoir intervals composed of siliciclastic or volcaniclastic strata (Jennette et al., 2000; Haughton et al., 2003; Posamentier and Kolla, 2003; Welbon et al., 2007; Dykstra et al., 2011; Meckel et al., 2011; Ogiesoba and Hammes, 2012). As shown in this work, MTDs can also be used as structural markers. In fact, erosional truncation of pre-existing fault scarps during mass-wasting events can help in constraining the timing of fault growth and movement in sedimentary basins (see also Alves et al., 2009; Gamboa et al., 2010; Omosanya and Alves 2014).

The history of fault growth is commonly assessed through the collection of fault displacement data (Peacock and Sanderson, 1991; Cartwright and Mansfield, 1998; Mansfield and Cartwright, 2001; Stewart, 2001; Morley, 2002; Peacock, 2002; Baudon and Cartwright, 2008a, b; Zhang et al., 2011; Tvedt al., 2004). Throw-depth (t-z) and throw-distance (t-x) plots offer information on the nucleation, propagation, segmentation and linkage of individual faults, providing at the same time important data for fault seal prediction (Stewart, 2001; Koledoye et al., 2003; Faulkner et al., 2010). In addition, throw and displacement gradient plots have systematically been used to assess the role of lithology and tectonic reactivation on the growth of faults (Cartwright et al., 1998; Baudon and Cartwright, 2008a), as discrepancies on throw/displacement

gradients commonly result from mechanical heterogeneities, fault linkage or fault segmentation (Baudon and Cartwright, 2008b).

This Chapter aims to characterise the effect of MTDs on vertical fault propagation by providing a detailed history of fault families on the mid-continental slope of the Espírito Santo Basin, SE Brazil (Figure 6.2). We apply throw-depth (t-z) plots in an area of recurrent MTDs to investigate the history of fault growth. Cumulative throw plots are introduced to distinguish fault families and assess their propagation history. Faults identified in the study area include those found in regions where the MTDs are mapped and faults where no MTDs are observed. In essence, this paper aims to address the following questions:

a) Can MTDs impose lithological controls on the propagation of faults on continental margins?
b) Can MTDs be used as stratigraphic markers to assess fault propagation histories on structurally decoupled and non-decoupled fault families?
c) What methods can be used to distinguish different fault families in terms of their propagation histories?

To simplify the analysis in this Chapter, interpreted faults have been classified into Types A to D (see Figure 6.1 for further information). Faults types A and B are located in non-MTD regions, while Types C and D comprise faults mapped within the MTD interval. In addition, we defined decoupled faults as those faults whose tips are confined to the basal shear surfaces of the interpreted MTDs (Type D). Non-decoupled faults include Type A, B and C faults (Figure 6.2).

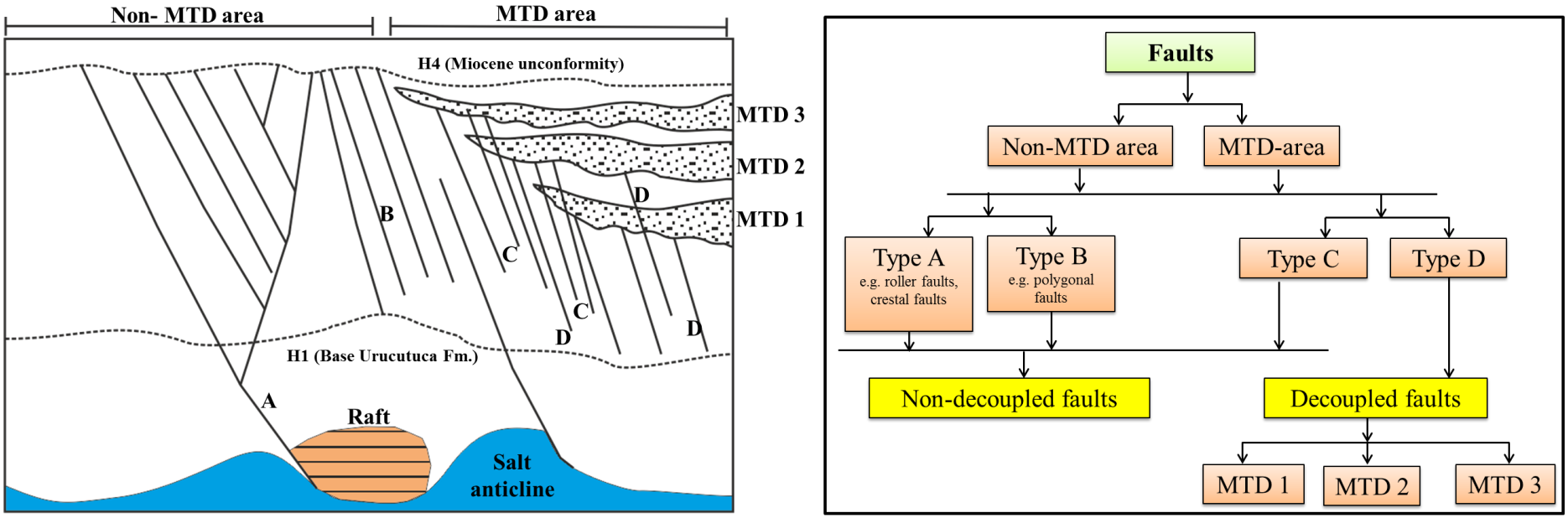

Figure 6.1: Classification of faults discussed in the text. Decoupled faults include those faults decoupled by MTD 1 to 3 while types A to C are non-decoupled faults

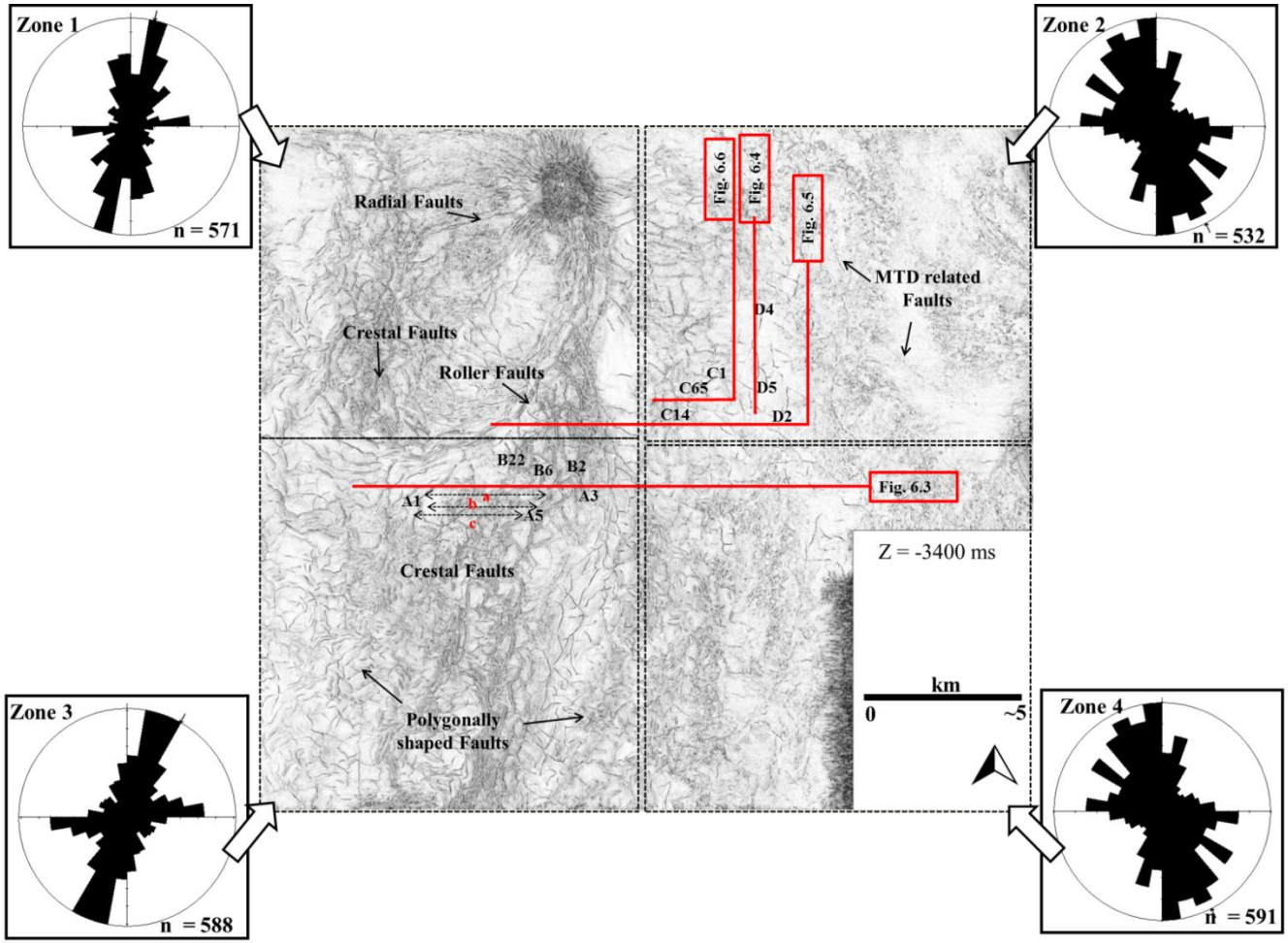

Figure 6.2: Coherence map at -3400 ms showing the major fault families described in this chapter. Zones 2 and 4 in the figure correspond to the approximate position of the MTDs. Dominant orientation of faults in non-MTD areas is NE-SW, a direction contrasting with the predominant NNW-SSE strike for faults in MTD areas. N.B: *The average perpendicular distance between fault is the mean of a, b and c. Fault length was measured along strike for 24 faults.*

6.2 3D Seismic Interpretation

Five megasequences bounded by regional unconformities (França et al., 2007) were interpreted in the study area (Figure 2.9; 6.3 to 6.6). In addition, six horizons corresponding to the top and bases of the MTDs were also interpreted (Figure 2.9; 6.3 to 6.6). The stratigraphic description of the different units and MTDs is provided in the following section.

6.2.1 Stratigraphic units

6.2.1.1 Unit 1 (Late Santonian to Campanian)

Unit 1 comprises a mixture of sandy turbidites and shales, changing into marls towards the distal part of the continental slope (França et al., 2007). The base of Unit 1 is marked by horizon H1, which correlates with a late Santonian unconformity (Table 2.2, Figure 2.9; 6.3 to 6.6). Horizon H1 separates low amplitude units capping Albian rafts and younger salt structures from high amplitude strata above (Table 2.2, Figure 2.9; 6.3 to 6.6).. Horizon H1 represents the base of the Urucutuca Formation, and shows evidence for the different phases of faulting identified in this work (Table 2.2, Figure 2.9; 6.3 to 6.6). On a regional scale, H1 is associated with the incision of a late Santonian to Maastrichtian channel system (Golfinho Field; Vieira et al., 2007). Additionally, a secondary horizon H1b was interpreted beneath horizon H2. Horizon H2 corresponds to a late Maastrichtian regional unconformity capping the low amplitude Unit 1 (Table 2.2, Figure 2.9; 6.3 to 6.6).

6.2.1.2 Unit 2 (Palaeocene to Early Eocene)

The lower boundary of Unit 2 is marked by an unconformity of Maastrichtian age, horizon H2 (Table 2.2, Figure 2.9; 6.3 to 6.6). The top of Unit 2 is horizon H3, which comprises an early Eocene regional unconformity (Table 2.2, Figure 2.9; 6.3 to 6.6). Unit 2 is composed of prograding sandstones and shales, which are ubiquitous on the SE Brazilian margin (França et al., 2007; Fiduk et al., 2004).

6.2.1.3 Unit 3 (Eocene to Early Miocene)

The lower and upper boundaries of Unit 3 comprise unconformities of early Eocene and Miocene age, respectively (Table 2.2, Figure 2.9; 6.3 to 6.6). The uppermost horizon (H4) truncates almost all of the closely spaced faults mapped in Units 1, 2 and 3. The H4 horizon represents the upper part of the Urucutuca Formation (França et al., 2007). Unit 3 comprises sandstones (Rio Doce Formation), Calcarenites (Caravelas member), turbidite channel/levee deposits and marls of the Urucutuca Formation (França et al., 2007; Alves et al., 2009). Unit 3 comprises alternating regressive and transgressive strata (Moreira and Carminatti, 2004). At the distal part of the study area, the unit presents a succession of MTDs and incising channel deposits (Table 2.2, Figure 2.9; 6.3 to 6.6).

6.3 MTDs in this chapter

The three MTDs interpreted in this chapter are found in Unit 3 (Early Eocene to Late Eocene; (Table 6.1, Figure 6.3 to 6.6). The base of MTD 1 is a discontinuous, moderate amplitude reflection presenting fault-controlled ramps and erosional scours (Figure 6.3 to 6.6). The upper and lower boundaries of MTD 2 coincide with high amplitude reflections. Its top, in particular, is rugged and hummocky displaying characteristic features of a MTD (*cf*. Posamentier and Kolla, 2003; Richardson et al 2007). MTD 3 is

a heterogeneous deposit rich in megablocks (Figure 6.3 to 6.6). The highest block in the study area is ~72 m tall, but blocks up to ~ 400 m in height occur to the NW (Omosanya and Alves, 2013). The upper boundary of MTD 3 is ridged, and of moderate amplitude reflection Figure 6.3 to 6.6). The seismic-stratigraphic and geometric characters of the three MTD are highlighted in Table 6.1.

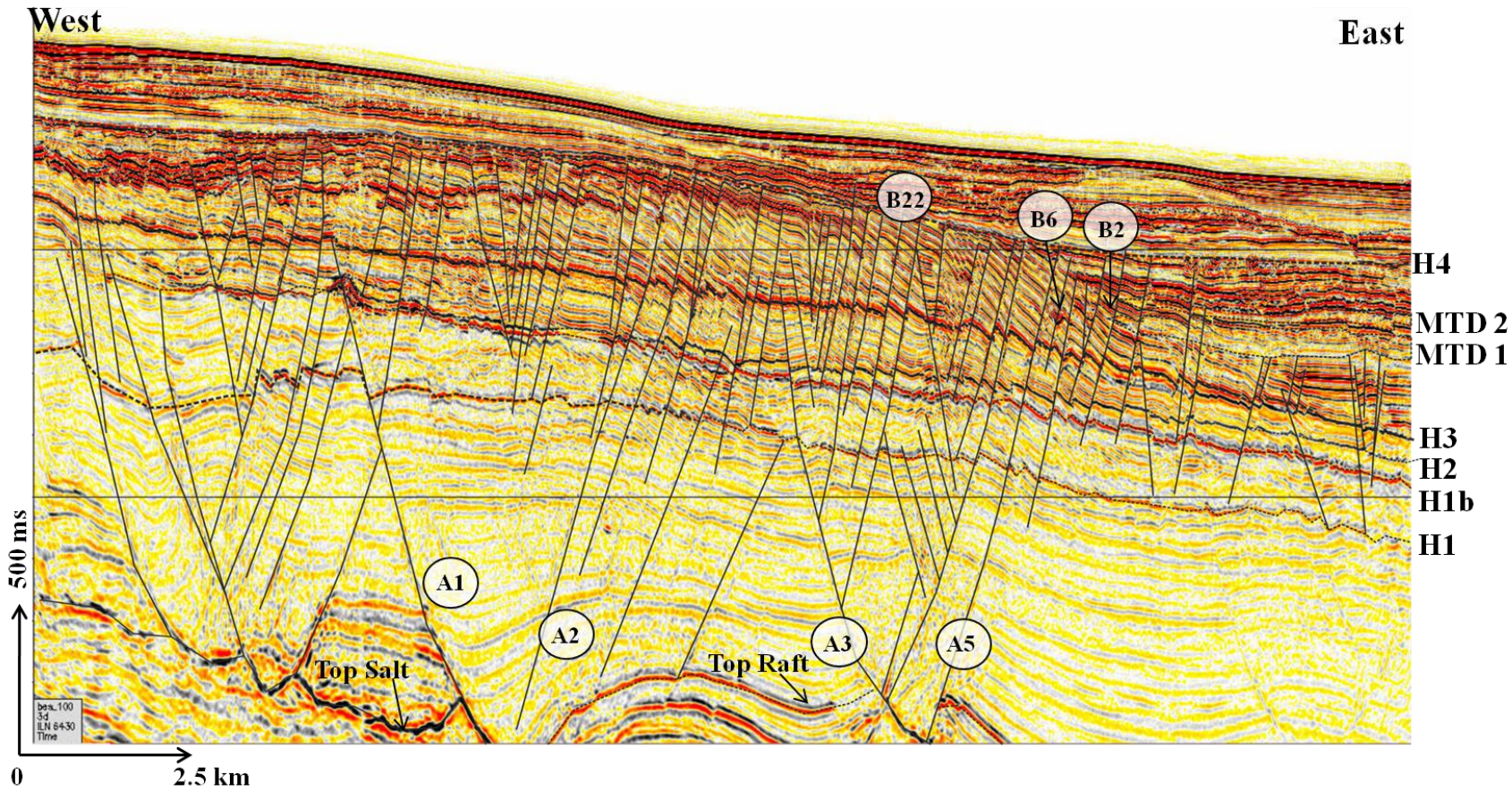

Figure 6.3: Seismic profile showing Type A and Type B faults, these faults are located in the non-MTD area. Roller faults are examples of Type A which detach onto top salt and raft horizons. Types A and B faults are restricted to the western section of the seismic volume in area without MTDs. **V.E = 3**

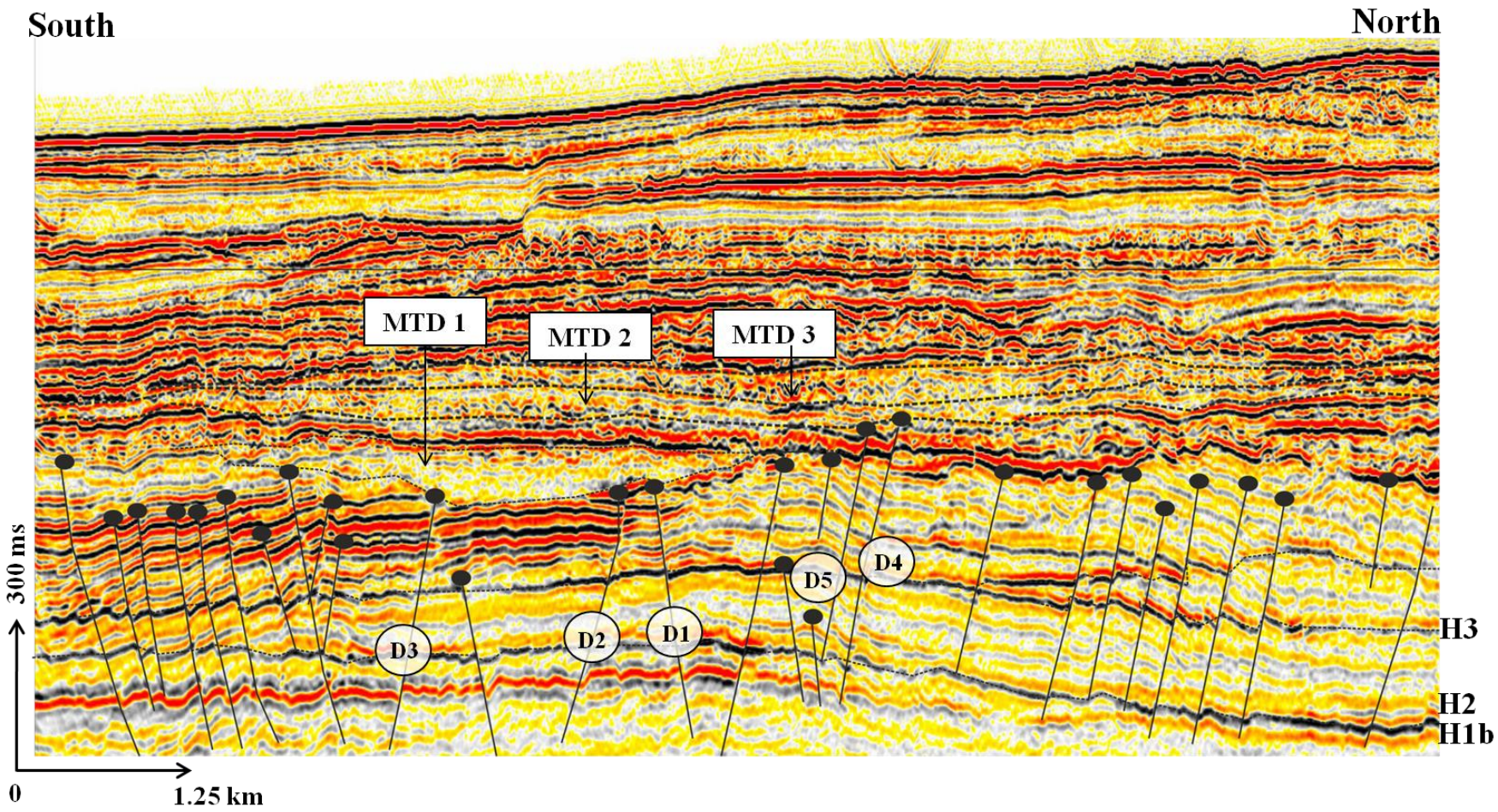

Figure 6.4: Seismic profile showing Type D faults include MTD 1, 2, and 3 decoupled faults. The highest number of faults is decoupled by MTD 2. Type C faults include those faults vertically propagating into the MTDs. **V.E = 3.**

6.4 Interpreted fault families

In this Chapter, decoupling refers to the classical definition of lateral and vertical deformation partitioning, e.g. Grocott et al., 2004. We mean that a body of sediments (in this case a MTD) absorbs and prevents the upward propagation of a fault. As far as the fault propagation is concerned, the sediments above the MTD are decoupled from the sediments below. The characteristic of both decoupled and non-decoupled faults are discussed as follows.

6.4.1 Non-decoupled faults (Types A, B and C)

In the study area, Type A faults comprise listric faults detached onto salt anticlines and rafts. Examples of Type A include roller and crestal faults (Figure 6.2 and 6.6). Along strike, the faults have average length of ~5 km (Figure 6.2). Type A faults are truncated by the Early Miocene unconformity, horizon H4 (Figure 6.4). Type B faults are polygonally shaped in map view and referred here as polygonal faults. The tips of Type B faults are eroded by the H4 horizon in most places (Figure 6.3 to 6.6). On seismic data, Type B faults have an average length and spacing of ~4 km and ~2 km respectively

Polygonal faults are laterally extensive arrays of extensional faults formed in fine-grained sediments with small throw and lateral extension. They show close spacing, high fault density, and variable strikes within polygonal planform geometry (Sun et al., 2010; Cartwright, 2011; Ding et al., 2013) (Figures 6.1, 6.3a and 6.4a). On the isopach maps, the effect of Type B faults is apparently restricted to Miocene strata away from the region of the interpreted MTDs (Figure 6.16 and 6.17). Nonetheless, Type B faults are the most segmented, dominant and linked fault systems in the interpreted seismic

volume (Figure 6.2). The principal orientation among Type B faults is NNW-SSE and NE-SW, contrasting with NNW-SSE of Type A faults (Figure 6.2).

Type C faults offset the base of MTDs 1 and 2 but do not propagate beyond the youngest MTD 3. These Late Eocene faults are accompanied by thickness variations in the Eocene, after which thin sediments were deposited across uplifted footwall blocks or eroded away. Type C faults have an average length of ~2 km and a maximum perpendicular spacing of ~1 km. The dominant orientations of these faults are NW-SE and NE-SW (Figure 6.2).

6.4.2 Decoupled faults (Type D)

Type D faults are MTD-decoupled faults found at the base MTD 1 and 2 (Figures 6.3b and 6.4b). The Type D faults offset the deeper horizons H1 to H3 and do not intersect or extend up to the early Miocene unconformity (horizon H4). These faults have average length of ~1 km and are the shortest fault types in the study area. Associated fault geometries include small-scale graben and horst structures limited to the base of MTD 1 (Figures 6.3b and 6.4b). The majority of the faults show evidence for partial reactivation, evidenced by multiple stratigraphic levels with reverse drag on hanging-wall and footwall sections (Figure 6.4 and 6.5). The dominant orientation of the MTD-decoupled faults is E-W in contrast to NNE-SSW, NW-SE and NE-SW recorded in other faults types (Figure 6.1). In addition, Type D faults are relatively unlinked and have their lower tips detached onto the H1 horizon (Figures 6.4b and 6.7d).

In the next section, we employ the analysis of throw gradient (t-z) and contoured throw (t-x) maps (*cf.* Mansfield and Cartwright, 1991; Baudon and Cartwright, 2008a, b) to

ascertain the growth history of the interpreted fault families. Based on their orientation (Figure 6.1), representative faults were chosen for each of the categories described in sections 6.4.1 and 6.4.2.

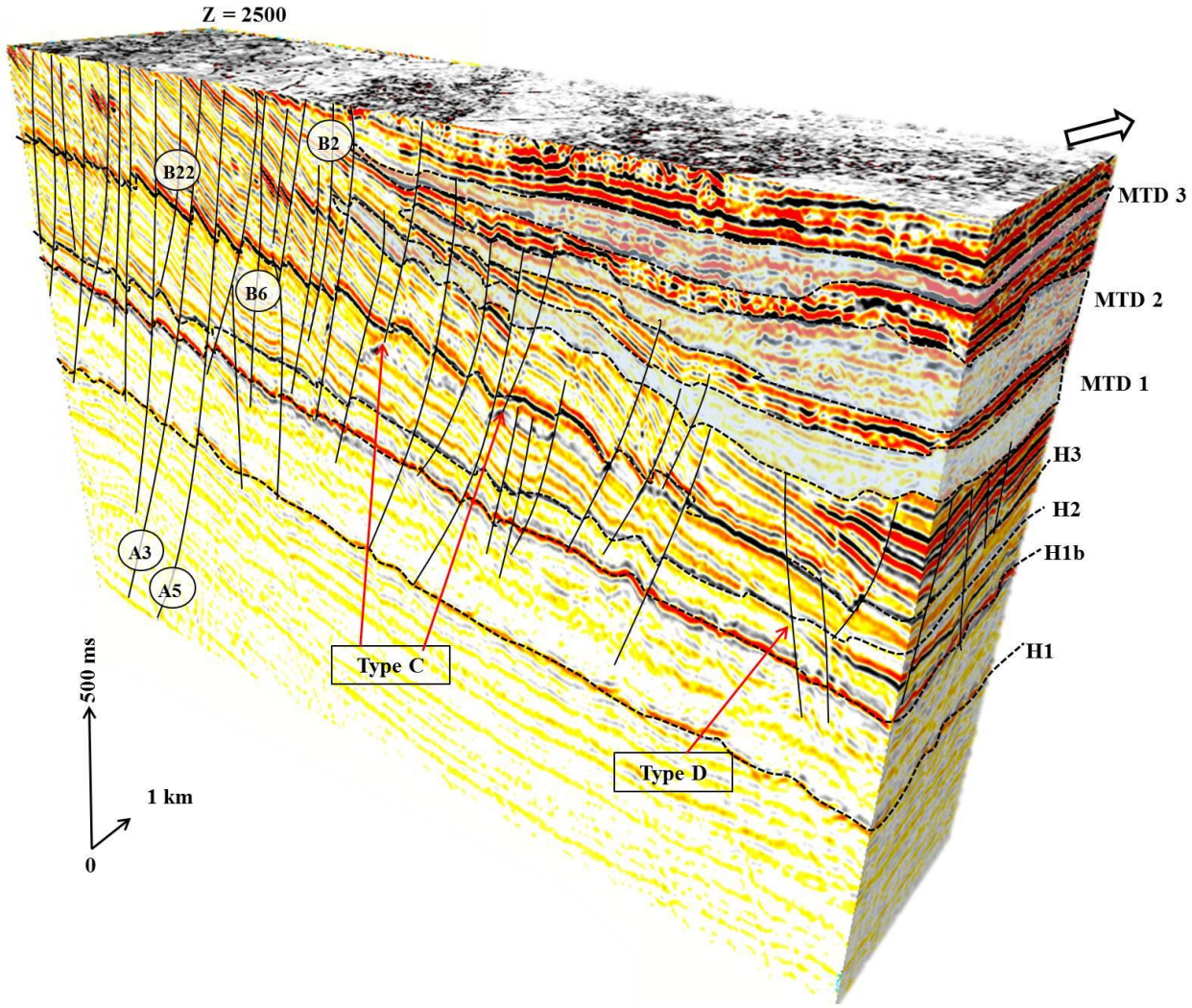

Figure 6.5: Seismic volume highlighting major fault types in the study area such as Types A to D faults. Type A faults are the only fault types extending below the Late Santonian unconformity. **V.E = 3**

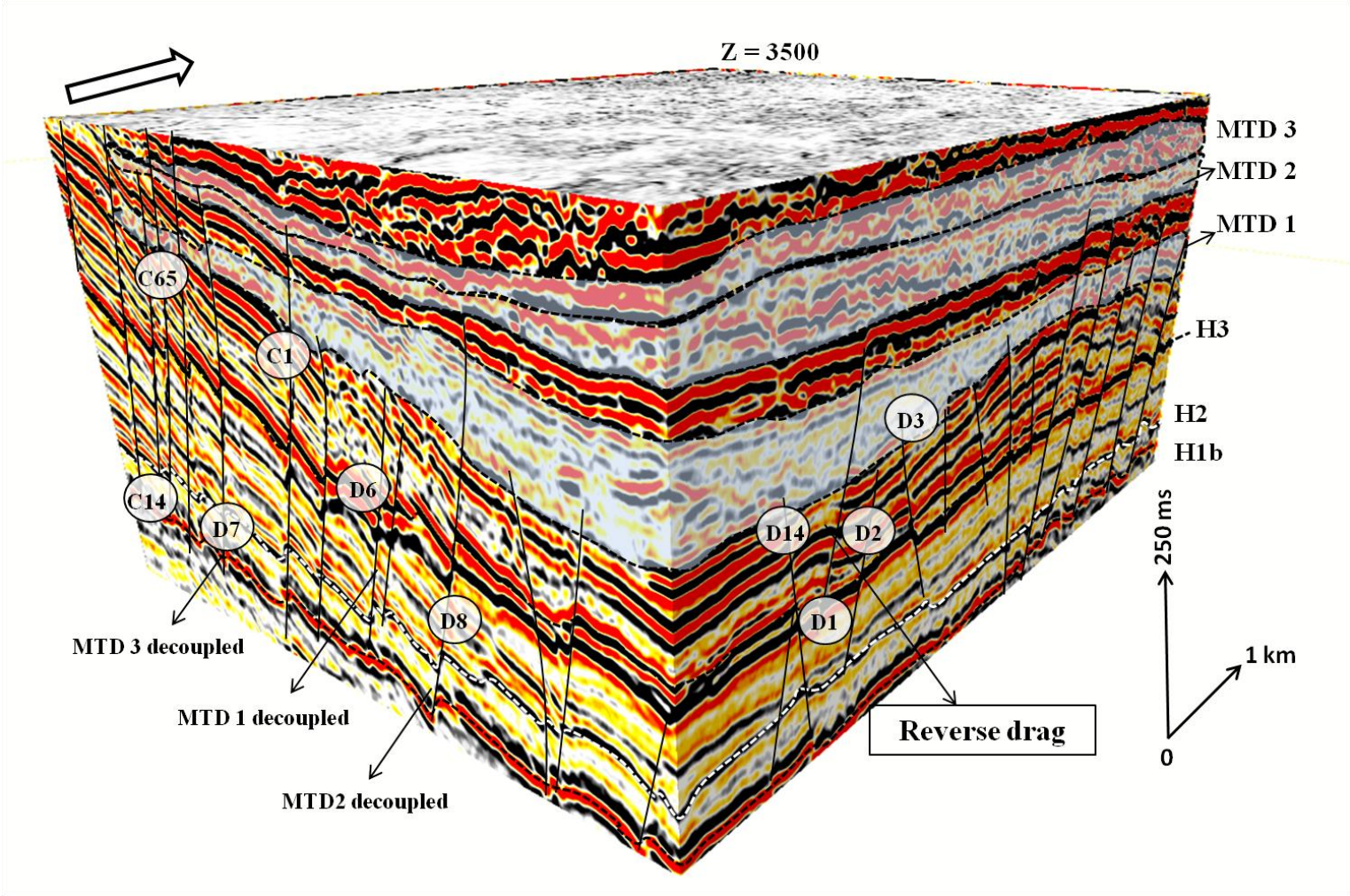

Figure 6.6: Seismic volume highlighting examples of MTD decoupled faults and their associated geometry. Reverse drag recorded in some of the faults beneath MTD 1 suggests that fault reactivation is not limited to non-MTDs areas. **V.E = 3**

6.5 Character of decoupled and non-decoupled faults

6.5.1 Throw-depth (t-z) and throw-distance (t-x) plots

Type A faults have steep t-z gradient with a maximum throw of ~90 m (e.g. fault A1), but a consistent negative gradient was recorded on the H2 horizon for all Type A faults (Figure 6.7). This gradient change is attributed to lithological changes rather than fault segmentation. Gradient plots for Type A faults show hybrid C-type and quasi-elliptical profiles of Muraoka and Kamata (1983), Barnett et al. (1987) and Walsh and Watterson (1989) (Figure 6.7 to Figure 6.9). Towards the surface, throw values decrease towards zero at the tip point, with a minimum of ~5 m where the tip of Type A faults was eroded by the H4 unconformity (Figure 6.10). Deeper in the succession, throw maxima are recorded close to nucleation sites with no shift in the position of maximum displacement (d_{max}).

The displacement gradient for Type B faults includes C-types and hybrid C-types (Figure 6.7). Negative gradients were recorded in horizon H2 for B2 and B6, and in horizon H1b for B22 (Figure 6.7). Such an inconsistency in gradient across different stratigraphic levels is attributed to fault segmentation and dip linkages (Walsh and Watterson, 1989; Baudon and Cartwright, 2008). In fact, some of the Type B faults show evidence for reactivation and interaction with other faults. Observed negative deflections of the t-z gradient in some of the Type B faults are related to reverse drag at horizon H1 (Figure 6.1).

The lack of near-zero throw values towards the surface confirms erosion of the fault tips by H4 (Figure 6.7 and Figure 6.8). In addition, the position of d_{max} for Type B faults is located at intermediate stratigraphic levels (Figure 6.8 and Figure 6.9). Along strike, the d_{max} anomaly is sub-horizontal and apparently associated to dip linkage. Observed

anomalies in d_{max} values represent local decreases in throw confined to discrete parts of the fault planes, a character implying that the linking faults are highly elliptical (*cf.* Cartwright and Mansfield, 1996).

Type C faults are characterised by negative gradients at H1b and H1, which are apparently related to lithology changes (Figure 6.8 and Figure 6.9). In addition, the relative shift in position of d_{max} suggests upward propagation of Type C faults rather than blind propagation. The positioning of d_{max} at the H3 horizon implies nucleation of the fault at shallow depths and possible reactivation by dip linkage (Figure 6.8 and Figure 6.9). This character is similar to that observed for Type B faults.

Throw gradients for Type D faults include C- and M-types (Muraoka and Kamata, 1983). Strikingly, abrupt changes in throw on the flanks of the M-type profiles are recorded at the base of MTD 2 and in horizon H3 (Figure 6.7). This character is consistent with the prediction of a brittle barrier for the flanks of the M-type gradients (Muraoka and Kamata, 1983). When anomalies in throw gradients are conflicting over different horizons, there is a hint for fault reactivation rather than lithological controls for Type D faults (Baudon and Cartwright, 2008a, 2008b). Nevertheless, throw plots for Type D faults are fairly diagnostic; throw contours are elliptical and quasi elliptical in planform view with no apparent shift in the position of d_{max} with depth (Figure 6.7). Maximum throw values include ~37 m and ~45 m for D2, D4, and D5 respectively (Figure 6.7). In particular, gradient and throw contours of the D4 signify reactivation by dip linkage and restriction of upward fault propagation by MTD 2.

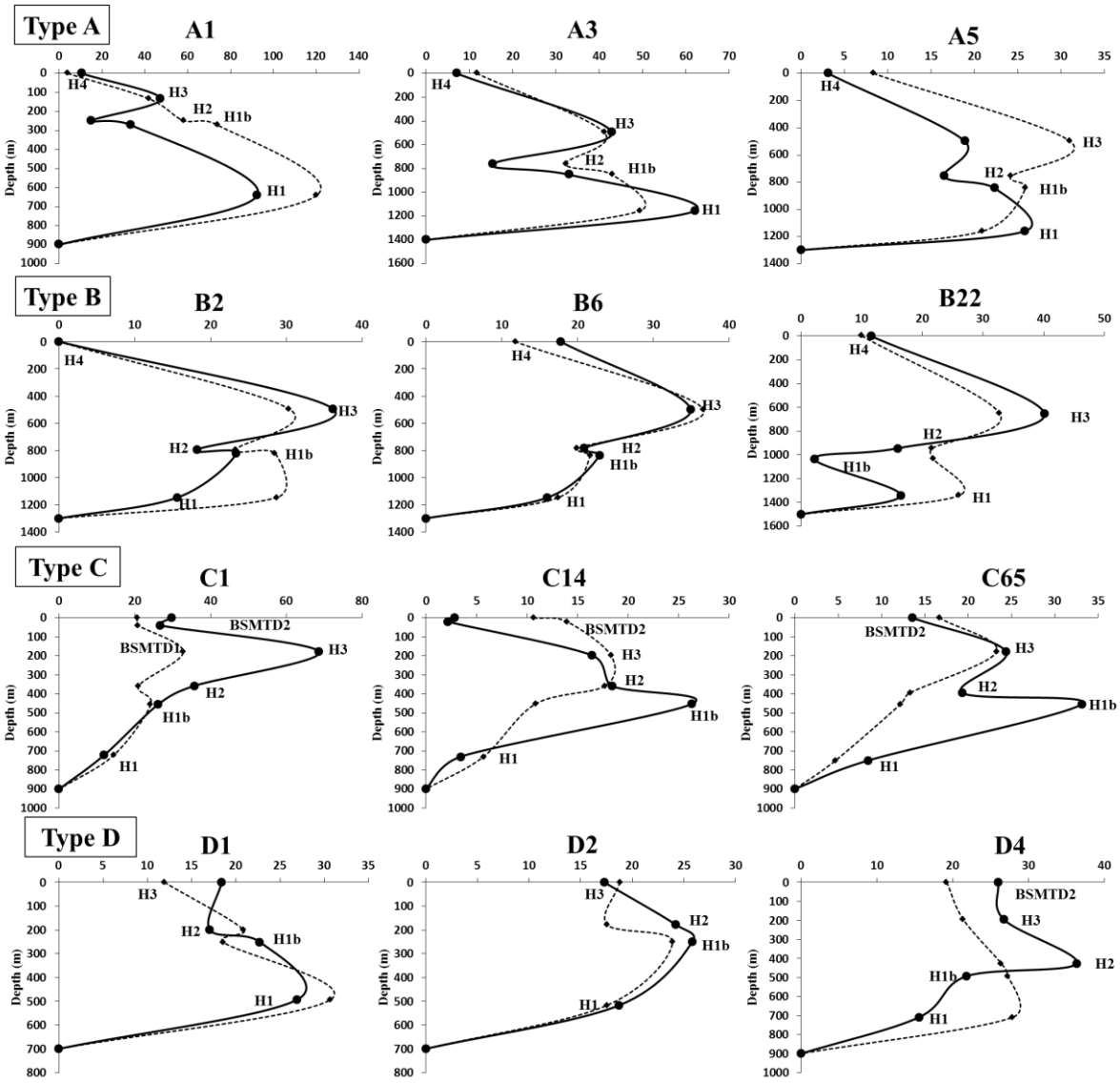

Figure 6.7: Throw gradient for representative faults in the study area. The profiles include C-types, Hybrid C-types and M-types of Muraoka and Kamata (1983). Negative gradient at the H2 and H1b horizons are attributed to lithological control and reactivation by dip linkage. The position of dmax varies depending on the fault family. N.B: Average throws are plotted as broken lines.

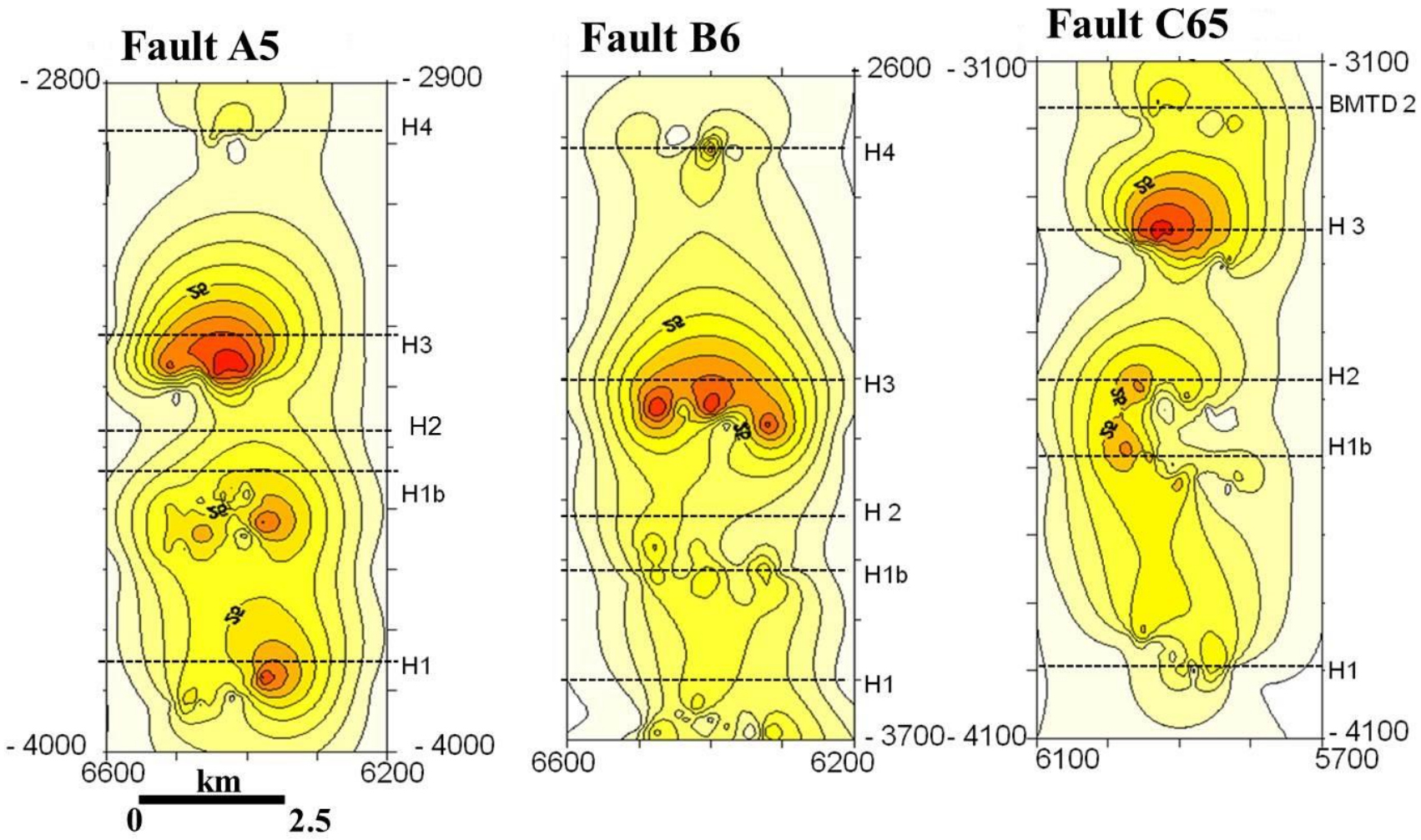

Figure 6.8: Throw contour maps for non-decoupled A5, B6 and C65. The throw contours for these faults are non-elliptical and characterised by multiple patches of d_{max}. The lack of zero throw near the surface provides further evidence for the erosional truncation of the upper tips of faults by the H4 unconformity.

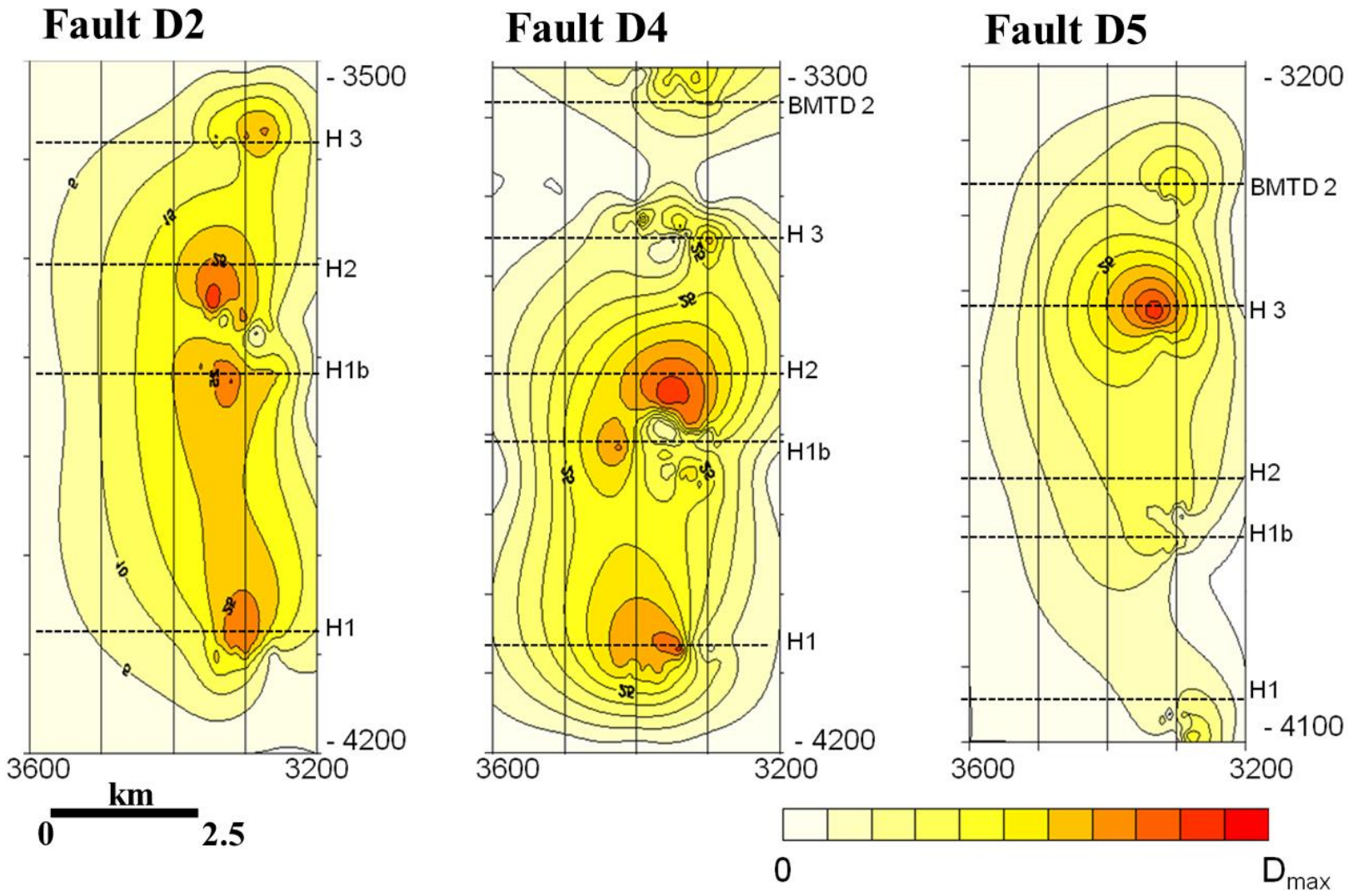

Figure 6.9: Decoupled faults D2, D4 and D5 are characterised by upper tip decrease in throw and elliptical to quasi-elliptical displacement profiles. The decoupled faults have their upper tip truncated by the mass-transport deposits.

6.5.2 Cumulative throw plots

The results so far show that Type C faults are included in the non-decoupled faults while Type D faults are decoupled by MTDs. In this work, decoupled faults are classified further into three types, i.e. faults decoupled by MTD 1, 2 and 3, respectively (Figure 6.1) An important result of our analysis is that plots of cumulative throw (m) with age (Ma) show non-decoupled faults to have higher cumulative throws than decoupled faults (Figure 6.14). These faults offset older (Urucutuca Fm.) and younger sequences (Rio Doce Fm.). The gradient of the decoupled faults is stepped and bridged contrasting with the smooth gradients of non-decoupled faults (Figure 6.14)

6.5.3 Fault propagation rate vs. sedimentation rate

We applied propagation and sedimentation rate to further examine the history of the studied fault types (Figure 6.15 and Table 6.2). Both decoupled and non-decoupled faults show decreasing propagation rate with elapsed time (Figure 6.15 and Table 6.2). Most faults in the study area show highest propagation rate during their early growth stage (Figure 6.15 and Table 6.2). A reverse trend to this latter suggests that the faults were derived at depth and subsequently reactivated (*cf*. Childs et al., 2003). Average fault propagation rate is 184 m/Ma, 120 m/Ma, 141m/Ma and 32 m/Ma for Types A to D, respectively (Table 6.2). Hence, decoupled faults have shorter propagation rate than non-decoupled faults. For example, D2 and D5 are decoupled at the base of MTD 2. These faults have propagation rates of 47 m/Ma and 12 m/Ma, contrasting with the value of 38 m/Ma for D4 which is decoupled by MTD 1 (Figure 6.15 and Table 6.2).

The half-lengths of decoupled faults correlate positively with elapsed time. In addition, decoupled faults have smaller half-lengths relative to their non-decoupled counterparts

(Figure 6.15 and Table 6.2). Highest lengths for the decoupled faults were recorded during their late growth stage. In contrast, non-decoupled faults display low correlation between their half lengths and elapsed time (Figure 6.15 and Table 6.2).

Finally, there is no correlation between fault propagation rates and sedimentation rates, as some of the faults with high vertical propagation rates occur within intervals of low sedimentation (Table 6.2). For example, C65 has the highest propagation rate in the study area yet occurs in the interval with the lowest sedimentation rate (~ 9 m/Ma; Figure 6.15). The only exceptions are the larger Type A (listric) faults, which are characterised by high propagation rates within intervals reflecting relatively high sedimentation rates (Table 6.2).

6.6. Discussion

6.6.1 Reconstructing the history of faulting in the Espírito Santo Basin

A reconstructed history for faulting in the study area is shown in (Figure 6.21). Based on the T/Z plots in (Figure 6.7 to 6.9), we favour the first of episode of faulting to have occurred in Palaeocene to Early Eocene times, during which Types A, B, and D faults were generated (Stages 1 to 2 in Figure 6.21). Type B faults initially formed isolated fault segments. MTDs in the study area were triggered after a period of tectonic quiescence in Oligocene times (Stages 3 and 4 in Figure 6.21). If seafloor failure occurred after the initial phases of faulting, original fault scarps were eroded and cannibalized during the mass-wasting events. An alternative interpretation is that MTDs were translated prior to any faulting within the basin. However, the population of faults within the interpreted MTDs contradicts an idea of post-faulting deposition. Instead,

larger numbers of faults are buried beneath MTD 1 and 2 (Figure 6.3 to 6.6). This latter interpretation is further corroborated by the isopach data in (Figure 6.16 and 6.17), which reveal significant variations in sediment thickness from Late Santonian to Miocene in non-MTD regions. The observed thickness variations prove that post-Eocene faulting was not significantly active in the region where MTDs were deposited (Figure 6.16). In addition, the presence of erosional scours at the basal shear surfaces of MTDs shows that they were erosive and truncated of some of the imaged fault scarps (Figure 6.10 to 6.13). The amount and location of sediments cannibalized from the fault scarps, however, cannot be adequately quantified on the interpreted seismic volume.

Post-MTD deposition marked the commencement of tectonic tilting of the slope (Stage 5 in Figure 6.21). The second phase of faulting occurred in the late Oligocene during which additional sets of Type B faults were formed in association with overburden compression due to raft remobilization at depth (Alves, 2012). The Oligocene also coincided with the formation of Type C faults at the tips and distal sections of the MTDs. Type C faults were formed during late-stage extension and reactivation of salt withdrawal basins. These faults are limited to distal part of the MTDs, where they are relatively thin and possibly comprising hemipelagic material (Figure 6.21)). Continued tilting of the slope and movement of rafts at depth resulted in accumulation of displacement on Type B faults which were subsequently reactivated along dip. This process ceased in late Oligocene to Early Miocene times (Stages 9 to 11 in Figure 6.21).

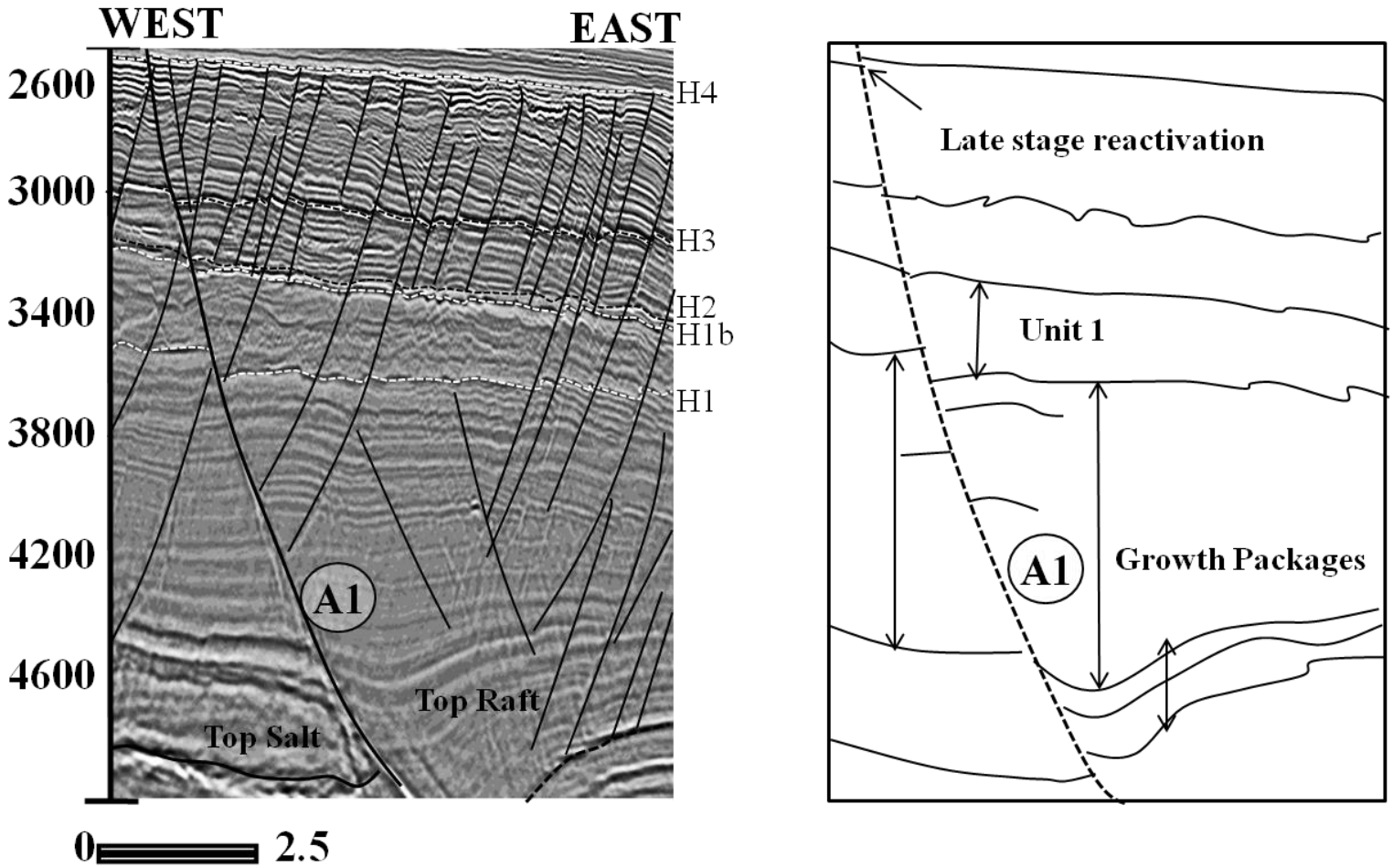

Figure 6.10: Seismic profiles showing growth packages associated with Type A faults. The growth strata are restricted to the base of the late Santonian unconformity. These packages generally show fanning geometries by thickening into fault A1. **V.E = 3**

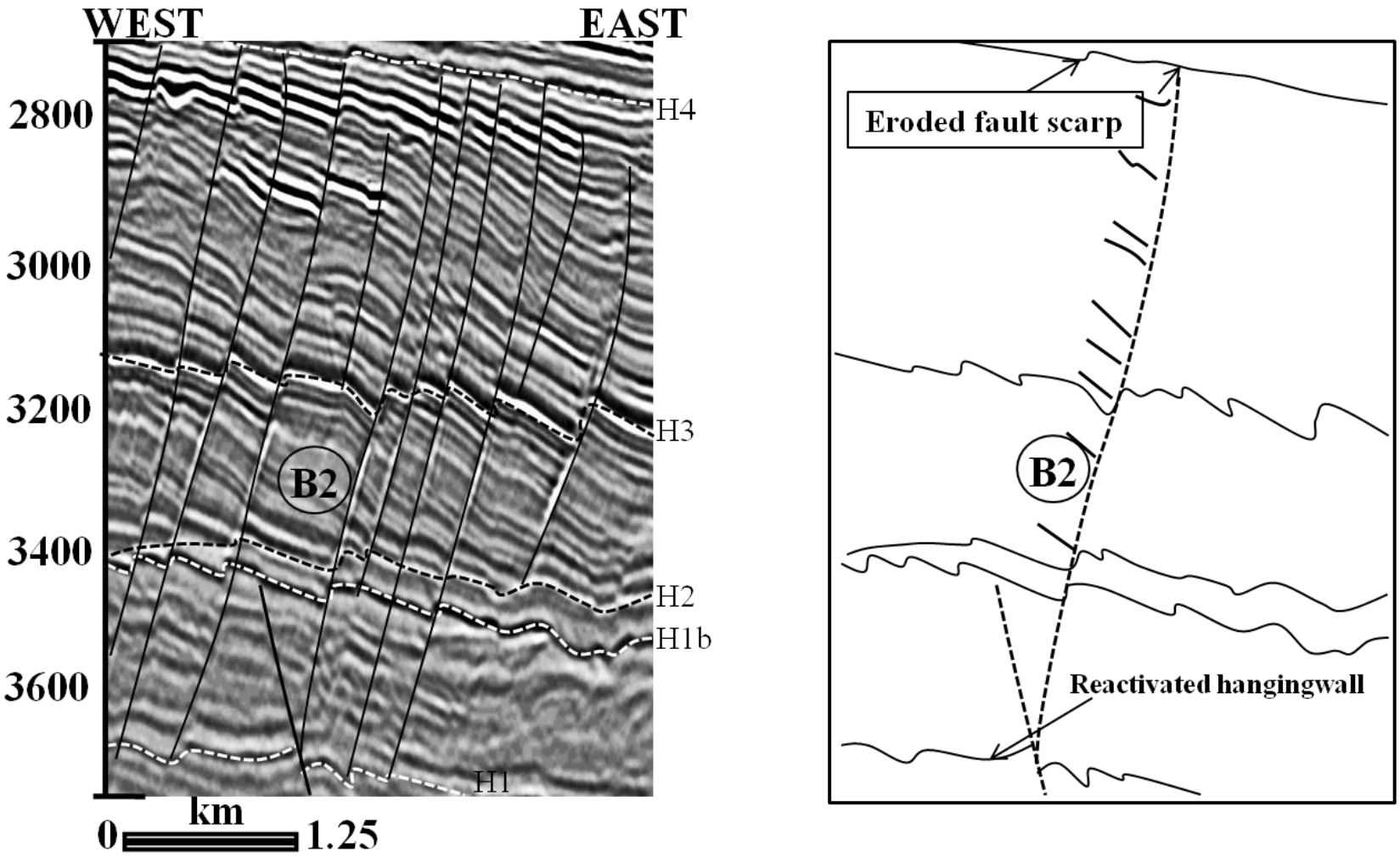

Figure 6.11: Seismic profiles showing reactivation at the base of B2 and associated propagation fold on its upper tip. Some of the hangingwall sections of the H1 horizon are uplifted relative to the strata immediately above. **V.E = 3**

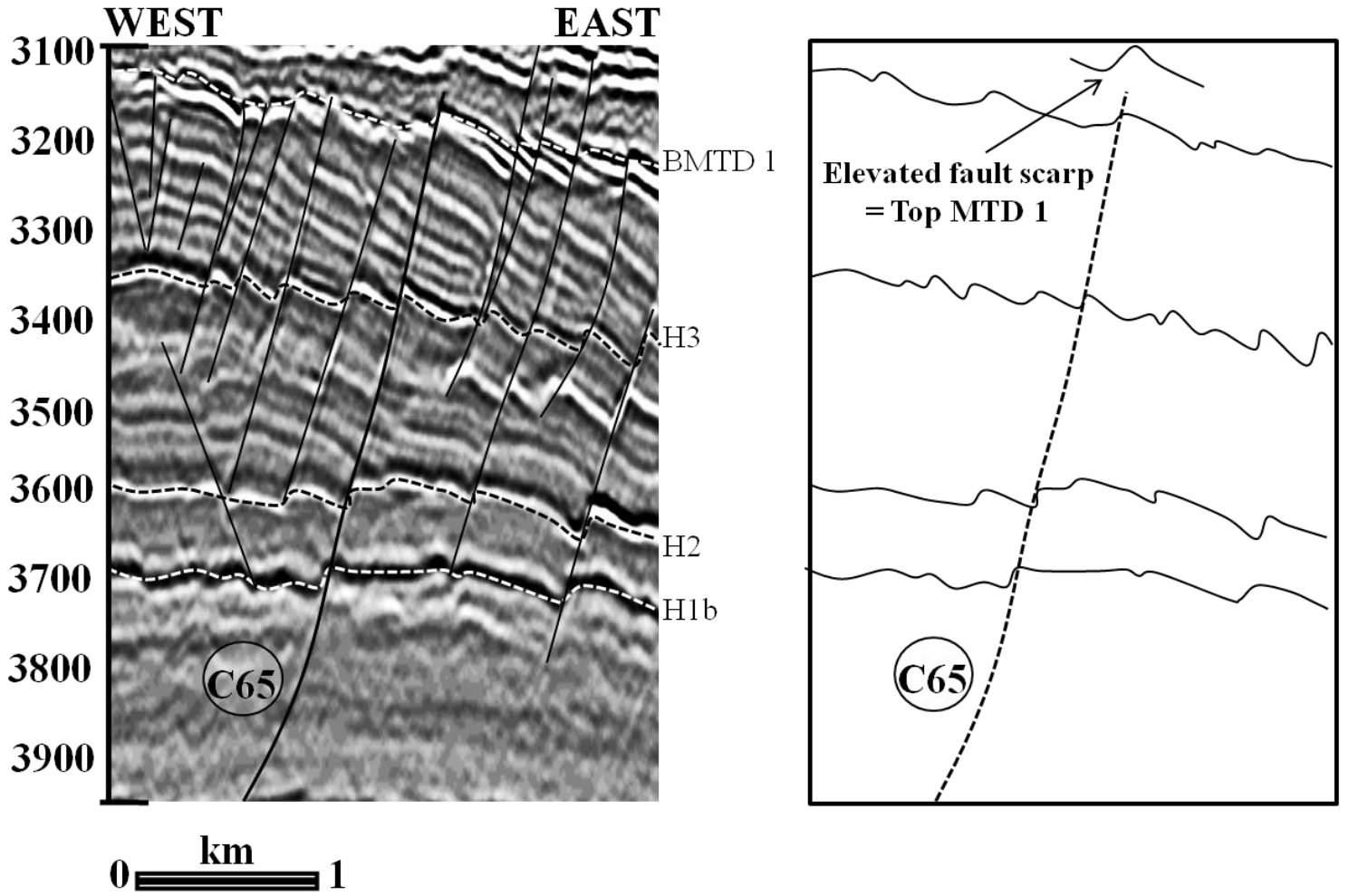

Figure 6.12: Seismic profiles showing faulting at the base MTD 1 by C65, also shown is a fault scarp created at the top of the MTD. Propagation folding at the upper tip of faults is a valid criterion to distinguish faults characterised by syn-sedimentary activity from faults showing blind propagation of the tips. **V.E = 3**

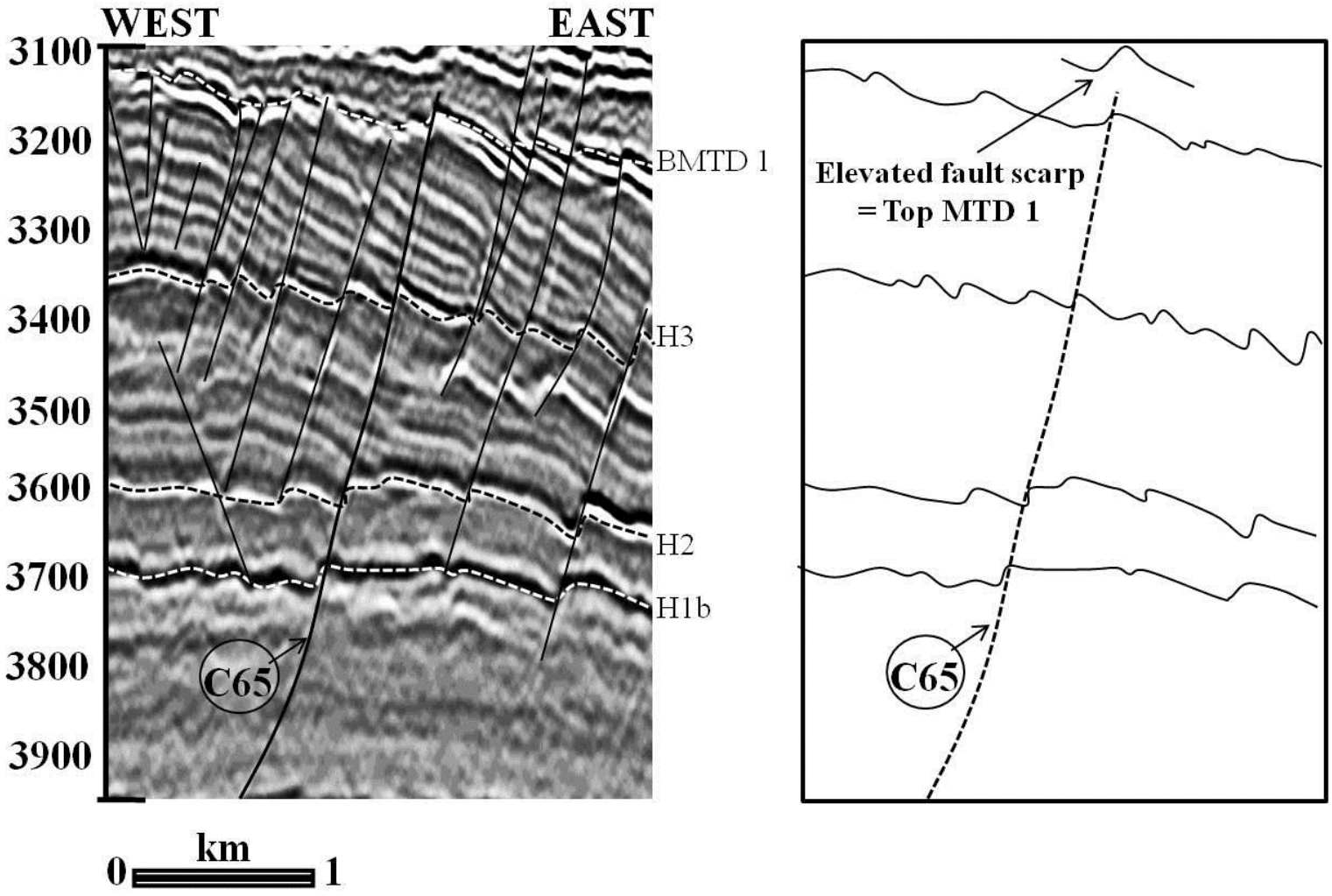

Figure 6.13: Seismic profiles showing evidence for post-MTD reactivation. The uplifted section of MTD 2 beneath the C65 fault is attributed to reactivation of D1 and D2 rather than fault propagation folding. **V.E = 3.**

Table 6.1: Geometry of the interpreted MTDs in this Chapter

MTD	**MTD 1**	**MTD 2**	**MTD 3**
Mean Length (km)	12	17	12
Mean width (km)	7	14	14
Thickness (m)	184	263	95
Volume of remobilized sediments (km^3)	15	61	15
MTD Facies	Homogeneous	Heterogeneous	Heterogeneous

Table 6.2: Fault propagation and sedimentation rate for faults and the intervals they intersected.

S/N	**Fault**	**Half Length (m)**	**Time Elapse (Ma)**	**Thickness (m)**	**Propagation rate (m/Ma)**	**Sedimentation rate (m/Ma)**
1	A1	4028	46	589	126	23
2	A3	3293	33	327	178	21
3	A5	4380	33	329	237	21
4	B2	2722	39	411	83	12
5	B22	2126	22	304	201	14
6	B6	2183	37	411	76	12
7	C1	576	33	187	21	8
8	C14	1240	30	229	47	9
9	C65	9967	30	237	386	9
10	D2	1518	34	296	47	10
11	D4	435	16	156	38	12
12	D5	369	34	289	12	10

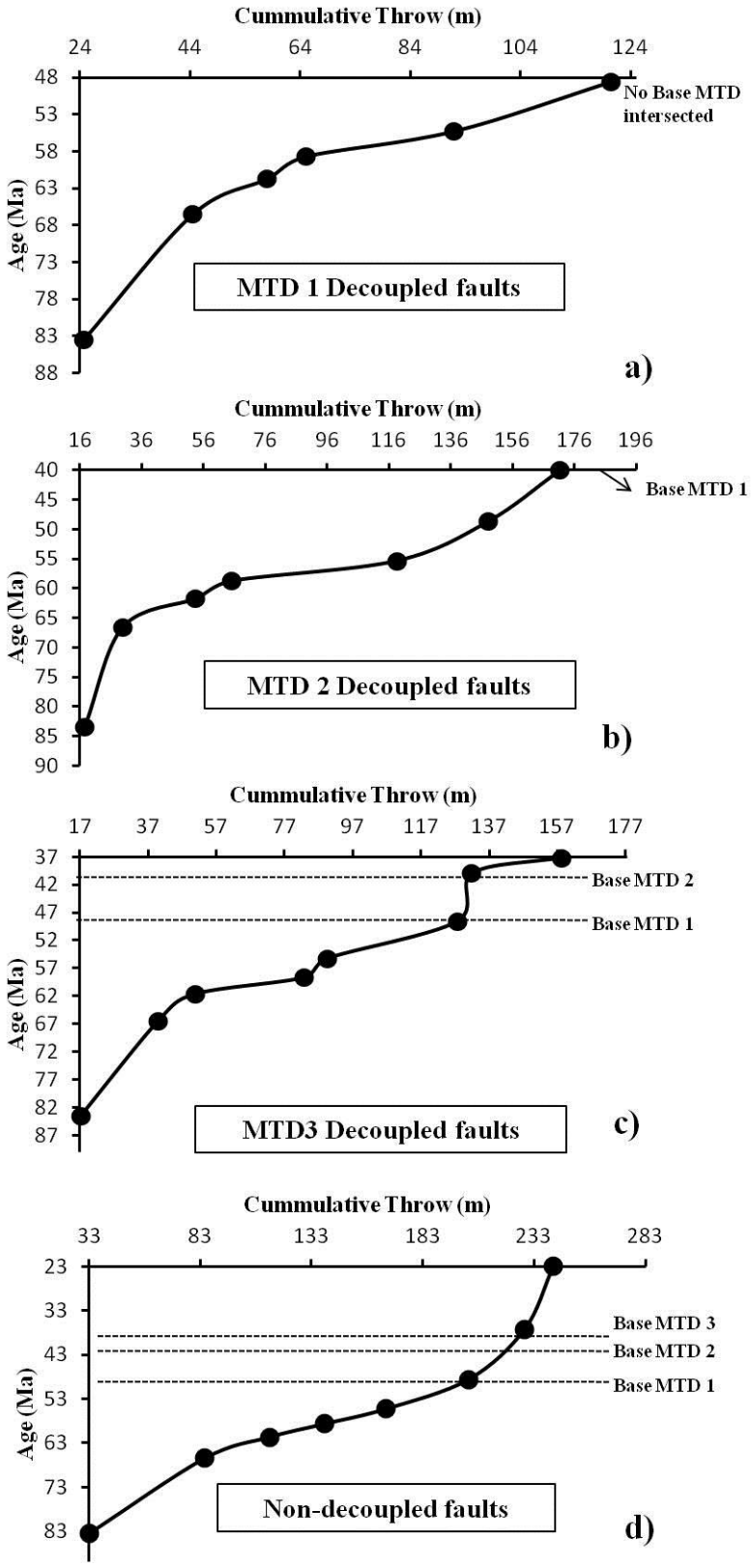

Figure 6.14: Cumulative throw vs. age for decoupled and non-decoupled faults. Type C faults vertically propagated through the MTDs. Steps on the plot for decoupled faults can be correlated with three episodes of reactivation.

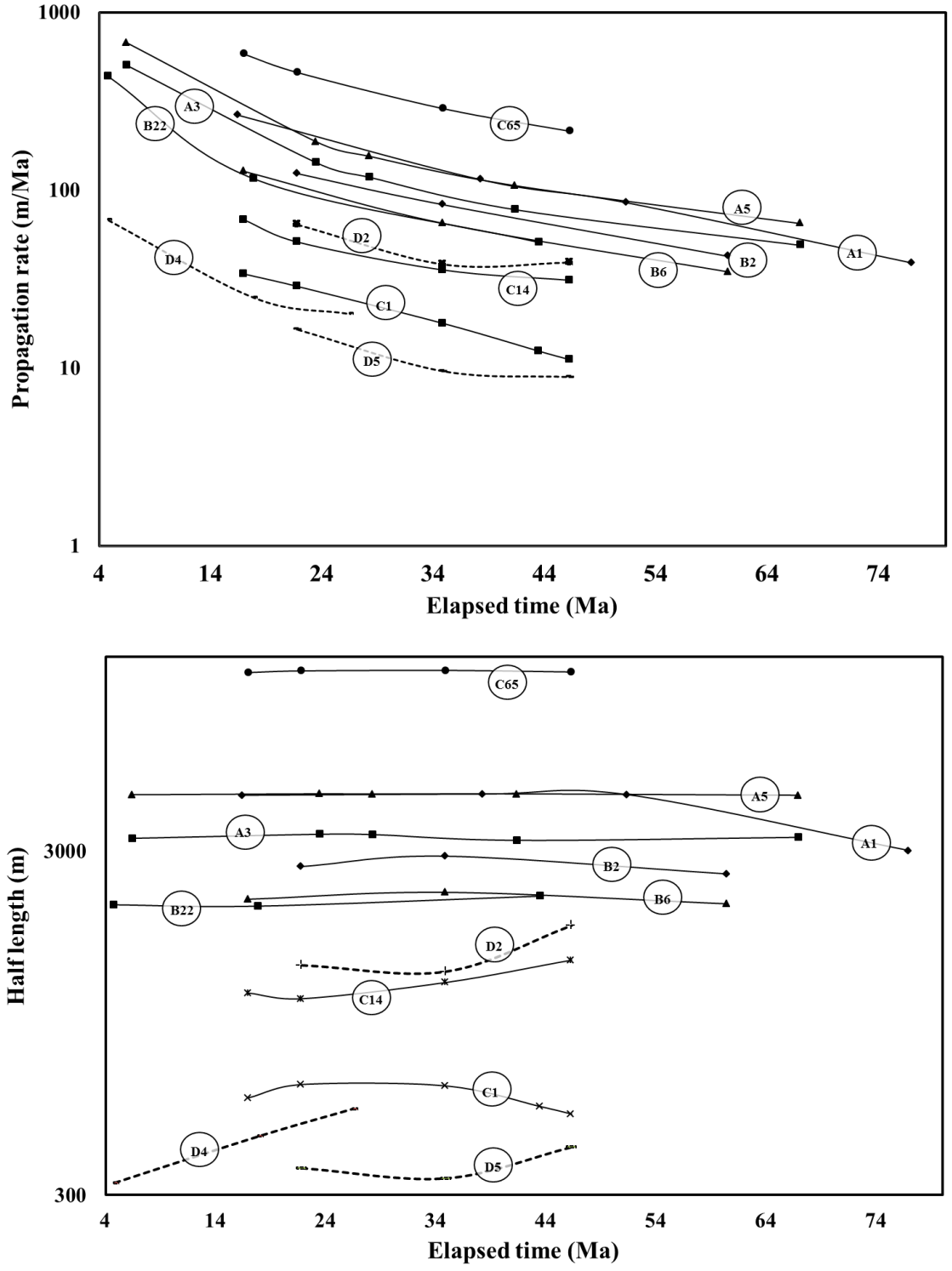

Figure 6.15: a) Plot of fault propagation rate and elapsed time. Most of the faults shows highest propagation rates during their early growth stage b) the decoupled faults are shown in dashed lines. These faults show a positive correlation between their half lengths and elapsed time. The average thickness was estimated from isopach maps, whereas the ages of the different horizons was constrained based on stratigraphic data in Alves et al. (2009) and França et al. (2007).

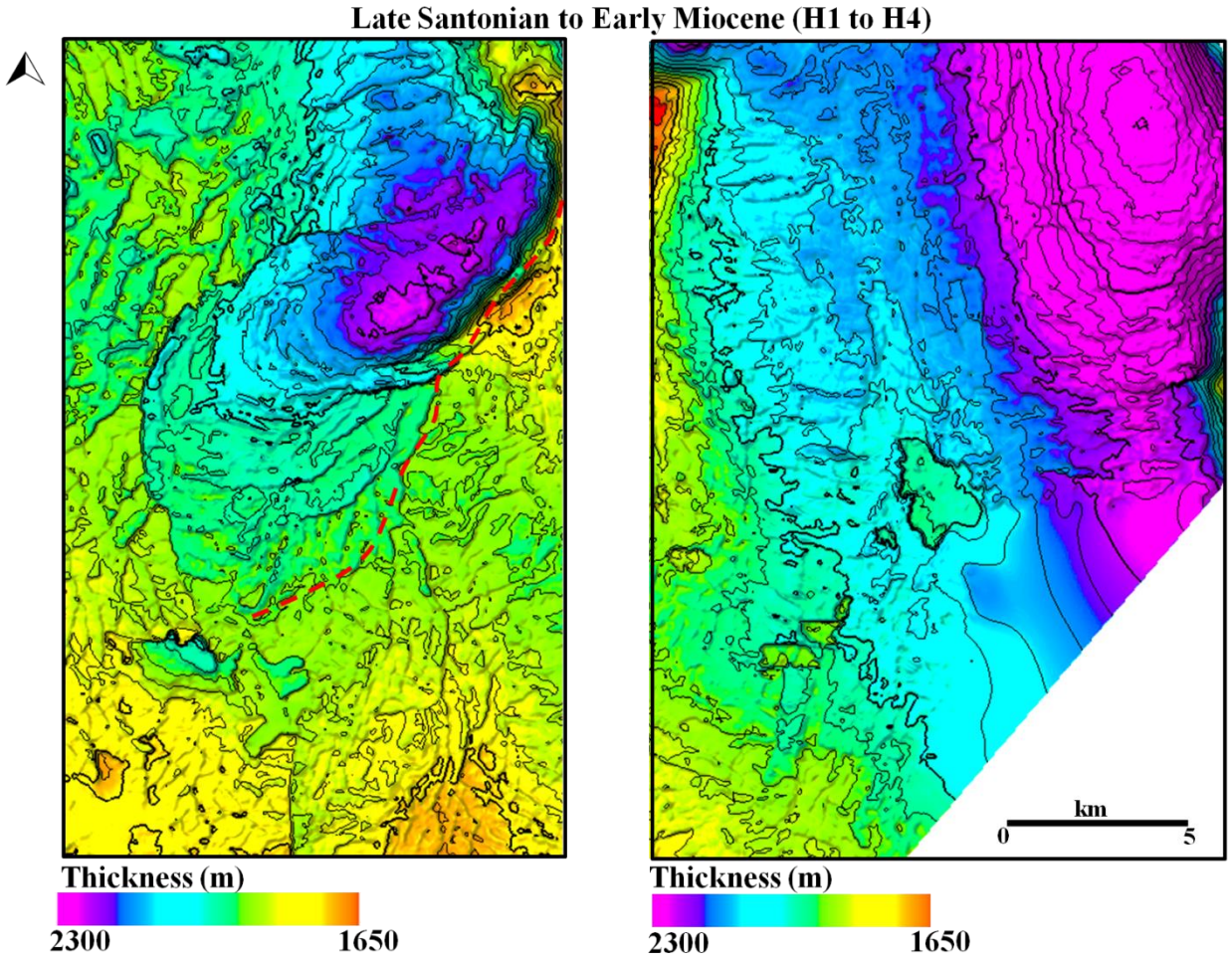

Figure 6.16: Isopach maps for the principal units interpreted in this work a) Non-MTD region where the effect of post-Eocene faulting is shown as uplifted and subsided blocks on the sides of fault scarps. The NE-SW trending fault scarps marked as dotted line correspond to the limit of the basal raft b) The MTD region is not affected by post-Eocene faulting.

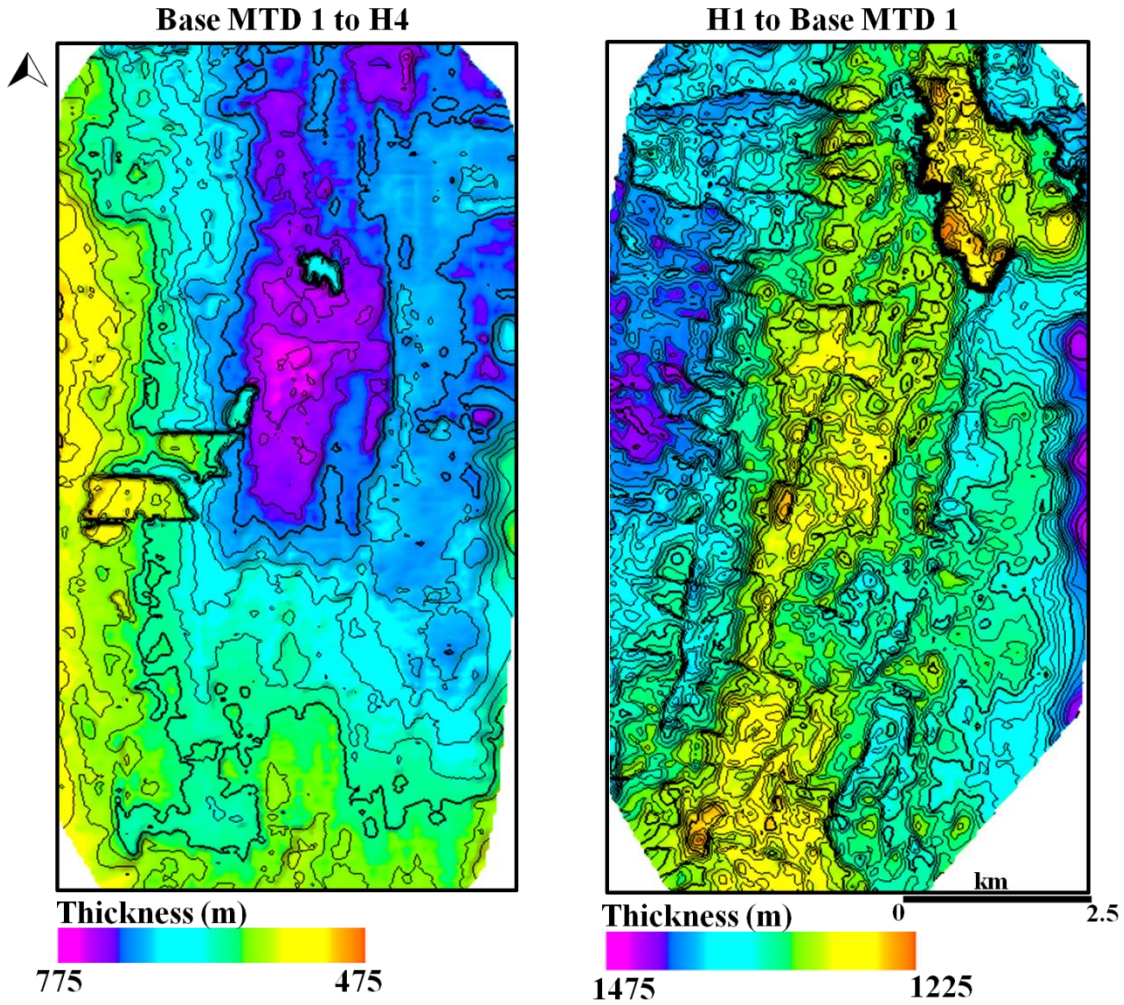

Figure 6.17: The isopach maps provide further evidence for decoupled faults at the base of the MTDs. Dominant faults in MTD regions are N-S, E-W and NNW-SSE oriented. In the MTD region, structural compartments are formed by the intersection of NNW-SSE and E-W faults at the base of MTD 1

The similar orientations of faults observed away from MTD areas imply that Types A, B and C faults are genetically different from faults observed in MTD areas (Type D; Figure 6.2). Furthermore, the discrepancies noted on throw gradients, and the fault-drag geometries of hanging-wall reflections, indicate an Early Miocene reactivation episode for Type A and B faults (Figure 6.8 and Figure 6.9). Based on these interpretations, we propose two episodes of fault reactivation for the study area, Eocene and early Miocene (See also Baudon and Cartwright, 2008 and Alves 2012 for reactivation of faults in other parts of the Espírito Santo Basin). Most of the interpreted faults were reactivated through dip linkage as noted in Figure 6.7 to Figure 6.9. Faults reactivated through dip linkage are initially isolated fault sets that coalesced into a single coherent structure by accumulating displacement over time (*cf*. Mansfield and Cartwright, 1996). The inverse relationships between the propagation rate, elapsed time and half lengths for some of these faults also show that they inherit their length at depth from pre-existing faults (*cf*. Childs et al., 2003). This condition specifically favours the propagation of Type B faults.

6.6.2 MTDs as lithological barriers to fault propagation

Decoupled faults in the study area have diagnostic cumulative throw character that can be distinguished from their non-decoupled counterparts using contour of displacements/throws. For decoupled faults with C-type profiles, if the locus of nucleation coincides with the region of maximum displacement, then the faults are classic examples of faults with radial propagation of their tips (*cf*. Walsh and Watterson, 1987; Barnett et al., 1987; Walsh and Watterson, 1987; Nicol et al., 1996). Faults formed through radial propagation have displacement contours characterised by plunging upper-tip region, propagation folds at their upper-tip and absence of syn-

kinematic strata (Watterson, 1986; Baudon and Cartwright, 2008a). Decoupled faults in the study area displayed all these criteria, while non-decoupled faults record both blind and syn-sedimentary fault activity (Figure 6.7 to Figure 6.8). Only Type A faults show evidence for syn-sedimentary faulting in the Late Cretaceous-Early Cenozoic time period (Figure 6.10). However, younger stratigraphic units display polycyclic fault activity (e.g. Cartwright et al., 1998), which include the reactivation and segmentation of individual fault strands as implied by the hybrid nature of their gradient profiles (Figure 6.7).

Based on the interpreted data, MTDs in the study area are considered as strong lithological barriers to the growth of Type D faults. The evidence in this paper suggests that Type D faults were decoupled in the Palaeocene and reactivated during the Eocene and Miocene. Significantly, steps on the plots of cumulative throw vs. age can be correlated with the two main episodes of reactivation interpreted in this work (Figure 6.14). This signifies that decoupled faults with M-type gradients illustrate the presence of lithological barriers at their upper regions (Muraoka and Kamata, 1983). MTDs acted as strain absorber inhibiting the upward propagation of Type D faults during the Eocene tectonic phases. The subsequent reactivation of the decoupled faults is implied by the presence of monoclines at top MTD units (Figure 6. and Figure 6.; *cf*. Tvedt et al., 2013 for characteristics of decoupling)

The use of throw profiles to characterise fault propagation history requires significant assumptions to be made as faults can transit between blind and syn-sedimentary activity (Childs et al., 1993; Nicol et al., 1996; Meyer et al., 2002). The point of maximum displacement can also migrate away from nucleation site of the fault due to interaction

with other faults or presence of mechanical barriers (e.g. Peacock, 1991; Cowie, 1998; Schultz, 2000). Neglecting these pitfalls, fault length and propagation rates are presented here as diagnostic data to recognise decoupled faults. In the study area, Type D faults have shorter propagation rate and half length character compared to their non-decoupled counterparts. Hence, the rate at which faults propagate in the study area is proportionate with their decoupling history. For all the faults, fault propagation and sedimentation rate are pointers to the history of fault growth and the origin of the fault lengths (Childs et al., 2009).

If post-Eocene faulting was not significantly active in regions of MTDs, was it due entirely to the presence of MTDs or other factors? We have shown that the upward propagation of Type D faults was inhibited by the presence of MTDs. This is not a coincidence as the highest percentage of faults was decoupled by MTD 2 (Figure 6.118 to Figure 6.2 and Table 6.1). In addition, ~35% of the faults within the basin were decoupled by the MTDs (Figure 6.18 to Figure 6.20). Therefore, there is a positive correlation between the size of the MTDs (i.e. amount of sediment mobilized) and the number of faults decoupled. We suggest, however, that the population and distribution of faults in the study area are also favoured by the boundary and stress conditions in MTD and non-MTD regions. Regions with MTDs have a lower surface slope compared to the updip section of non-MTD regions. Relative high slope gradients on the margins of salt withdrawal basins likely enhanced the capability of the MTD tips as strain absorbers and invariably, the population of fault families. Thus, a significant amount of faults are recorded in updip non-MTD regions likely as a consequence of the stress field being different from the downdip MTD domain.

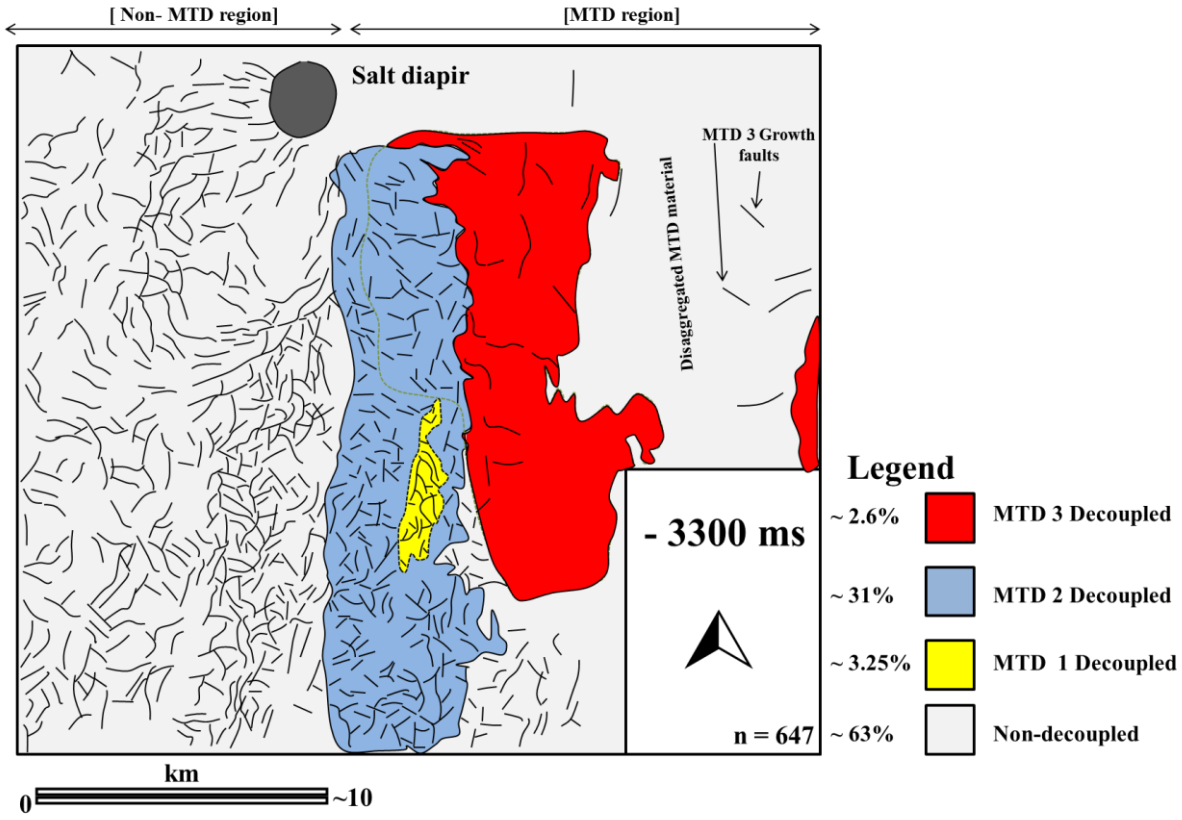

Figure 6.18: Schematic map showing the position of decoupled versus non-decoupled faults at depth of -3300 ms. At this depth, the highest numbers of fault were decoupled by MTD 2. N.B: Fault patches were extracted and interpreted from coherence slices using the ant tracking algorithm.

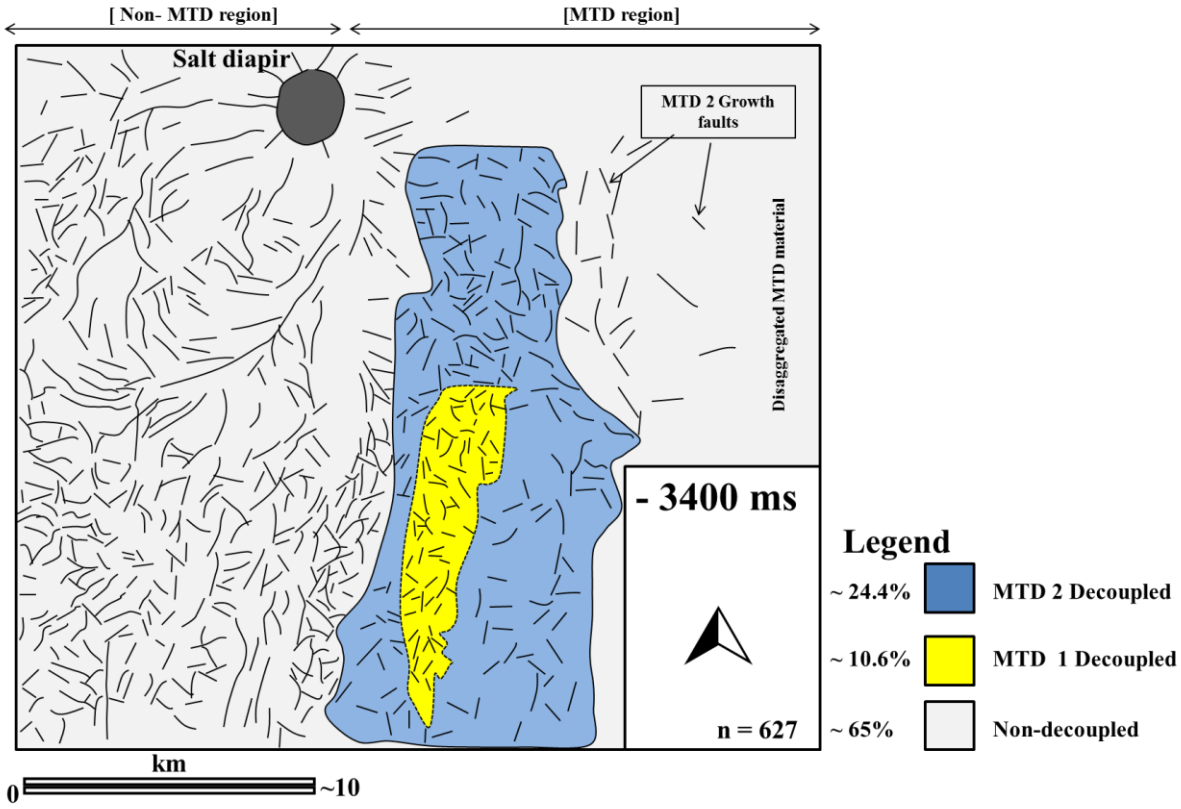

Figure 6.19: Schematic map showing the position of decoupled versus non-decoupled faults at depth of -3400 ms. N.B: Fault patches were extracted and interpreted from coherence slices using the ant tracking algorithm.

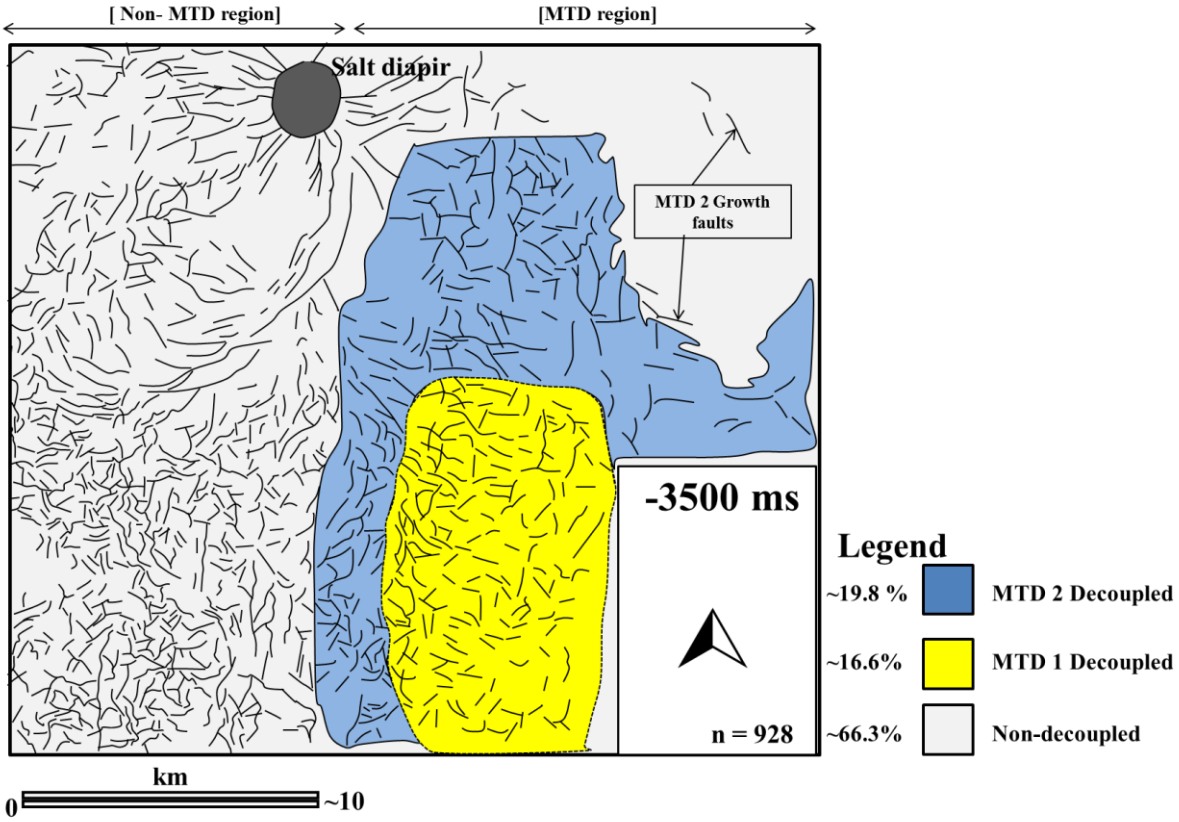

Figure 6.20: Schematic map showing the position of decoupled versus non-decoupled faults at depth of -3500 ms. The number of non-decoupled faults extracted was higher than their decoupled counterparts. N.B: Fault patches were extracted and interpreted from coherence slices using the ant tracking algorithm.

6.7 Conclusions

The importance of MTDs at modifying the infill and structural setting of a salt withdrawal basin has been proved in this study. MTDs are potential seal rocks that are often compartmentalised by faults. The major conclusions from this study include:

1. The first episode of faulting in the salt withdrawal basin is related to deformation of overburden strata by rising salt anticlines.
2. This latter event resulted in the development of synclinal faults. For the deepest part of the withdrawal basins, the scarps of first generation faults were eroded and cannibalised by two major mass-wasting events.
3. MTDs acted as lithological barriers to the growth of Type D faults, restricting their vertical propagation during early Eocene and Miocene tectonic reactivation. Discrepancies on throw-depth and throw-distance gradients, and the elliptical to quasi-elliptical nature of throw contours, indicate an important lithological control on the vertical propagation of Type D faults.
4. For Type A and B faults, reactivation is dominated by dip linkage. Early syn-sedimentary/growth packages for Type A faults are narrowed to the Palaeogene and Late Cretaceous.
5. Type D faults are decoupled by MTD 1, 2 and 3. MTD decoupled faults evolved through radial propagation of their tips and are marked by lower cumulative throw compared to non-decoupled faults.
6. Faults decoupled by MTDs are characterised by presenting concentric tip-zones, low wavelength upper-tip propagation folds, and by an absence of growth strata. In contrast, growth strata are common with Type A faults. Other non-decoupled faults are characterised by sub-vertical throw contour patterns and higher wavelengths folds at their upper-tip.

7. There is a positive correlation between the size of MTDs, the number of faults decoupled, and the decoupling history of these same faults.

In summary, discrepancies on throw-depth gradient and shapes of throw contours clearly hint at important effects of tectonic reactivation and lithological changes on the growth of faults in the study area. Dip linkage and upward propagation of faults into post-Oligocene deposits followed fault reactivation, and are potentially factors compromising MTD seal competence, both in the study area and on many other continental margins where multi-phased faulting is recorded. Importantly, this work shows that cumulative throw plots can be used to characterise decoupled from non-decoupled faults, and MTDs can be used as structural markers for blind fault propagation.

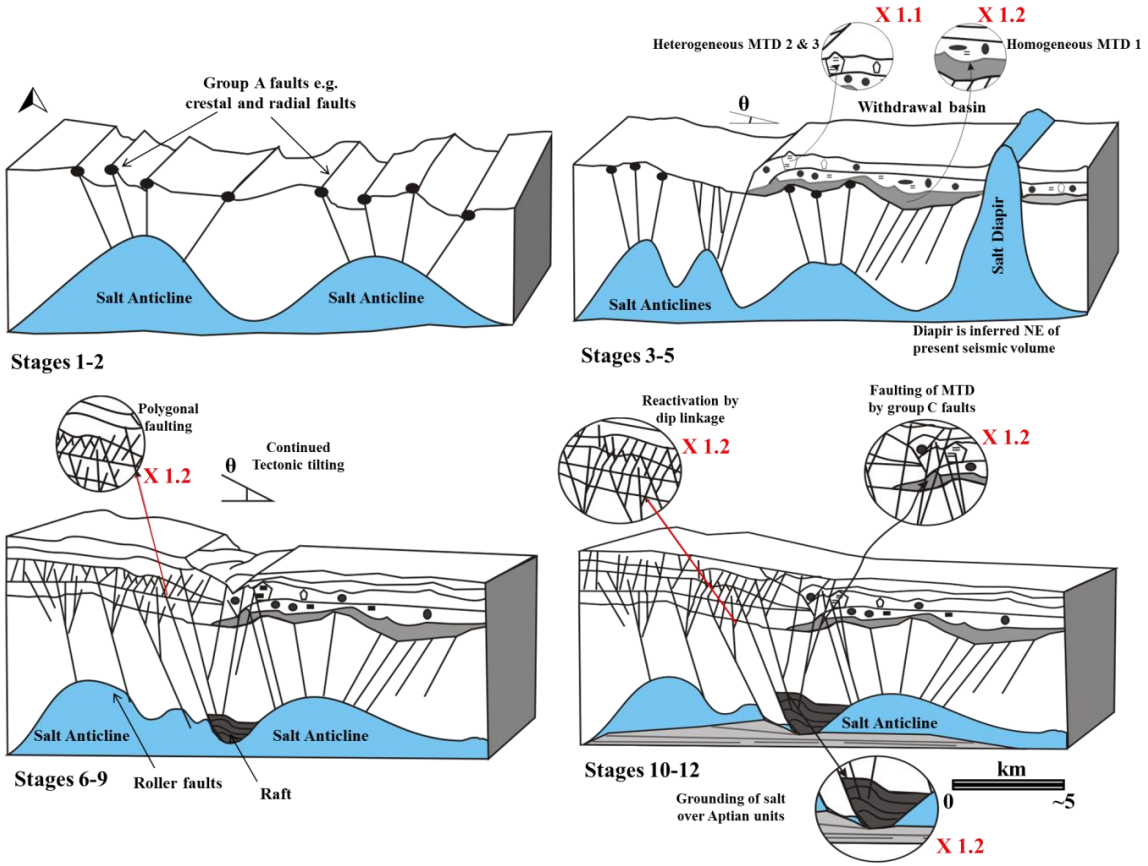

Figure 6.31: Schematic diagram summarising fault propagation and depositional histories of MTDs in the study area. 1) First episode of faulting (Palaeocene to Early Eocene), 2) Erosion of fault scarps (Early to Late Eocene), 3) Period of tectonic quiescence (Late Eocene to Oligocene), 4) Synchronous deposition of MTDs, 5) Possible commencement of tectonic tilting, 6) Second phase of faulting (Late Oligocene), 7) Growth of raft in response to depleting salt structures, 8) Development of Type B faults, 9) Continued slope tilting, 10) Reactivation of Type A and B faults through dip linkage (Late Oligocene- Early Miocene), 11) Cessation of tectonic tilting and raft tectonics at depth, and 12) Erosion of fault scarps by the Mid Miocene unconformity. N.B: X = Exaggeration.

Chapter 7

Discussion and Conclusions

7.1 Discussion

7.1.1: Relationship between MTD internal character and source area

i.) MTD geometry as pointers to transporting distance and source area

The source areas of the MTDs used in the thesis were further reassessed using their morphometric parameters in compliance with the schemes of Moscardelli and Wood (2007) and Twitchell et al. (2009). All the seven (7) MTDs interpreted in Chapters 4 to 6 have length/width ratio of <3, indicating they are shelf- and slope- detached MTDs. Triggering mechanisms for slope-detached MTDs are linked to elevated slope gradients or instability associated with palaeobathymetric highs on the seafloor e.g. the flanks of salt structures, mud-volcano ridges, and in submarine channel margins (Moscardelli and Woods, 2007). Hence, slope-detached MTDs are usually intrabasinal, topographically constrained and generally smaller than their slope-attached counterparts (Figure 7.2 and Figure 7.3, Moscardelli and Woods, 2007).

Geometrically, slope-detached MTDs have short length/width ratios (L/W) and run-out distances from their source areas (Figure 7.3). The morphometric character of the Storegga landslides and several other landslides from the US continental margins are presented in Figure 7.1. Parameters of subaerial, submarine landslides and other mass-wasted deposits can provide information on the source area and the general characteristics of the failure event. The relationship between these parameters is not a simple linear rule. For example, run-out distances have both vertical and horizontal components, the horizontal run-out distance is governed by volume (v), height (h), ground acceleration and the slope angle (Φ) (Changwei et al., 2013). There is an exponential relationship between the run-out distance and log of v, h and acceleration, and a negative exponential relationship between L and tan Φ. In parallel, there is

positive correlation between the volume of sediments remobilised and the run-out distance (Budetta and De Riso, 2004). As a result, the dimension of slope-detached MTDs can provide useful hints on the amount of sediment remobilized and run-out distances expected.

ii.) Are statistical and thickness data adequate to assess the stages of diapirism?

In Chapter 4, descriptive statistics were used to establish the timing of diapirism by comparing the thickness of MTDs with the diameter of associated diapirs. However, a major concern in the Chapter was whether statistical data are adequate to provide this piece of information. Salt flow is enhanced by differential loading which comes from gravity, displacement and thermal controls. The case study area presents an exceptional margin where gravity controls entirely the dynamics of sediments (Demercian et al., 1993; Mohriak et al., 1995; Fiduk et al., 2004). In addition, the shapes of the salt diapirs in the area provide further insights to the role of tectonics and sedimentation in their formation. The diapirs are either columnar or upward narrowing in cross section.

Columnar diapirs form when the rate of salt supply is equal to the rate of sediment accumulation and extension while upward-narrowing diapirs are formed when the rate of salt supply is less than the rate of sedimentation and extension (Koyi, 1998; Hudec and Jackson, 2007). Extension connotes piercing of the overburden layer by the upward rising diapirs, which is necessary to mechanically weaken the roof, thin the roof, create differential loading and space for diapirs to fill in (Vendeville and Jackson, 1992b; Hudec and Jackson, 2007;). Hence, the diapir shape provided additional clue into the high sedimentation rate driven by gravity in the study area.

Neglecting displacement and thermal loading the diapirs in the study area are solely gravity-driven, responding essentially to high sedimentation rate and increasing slope subsidence (tectonically and thermally driven). Thickness variations of sediments prior, during or after diapirism can effectively be tied to gravity loading. To elucidate the relationship between the effects [sedimentation (mass-transport deposits)] and causes [diapirism (gravity-driven)] a regression analysis was developed. Where inverse relationship were established the sediments displayed characteristic overburden pierced by salt (Davison et al., 2000a; Stewart, 2006). Positive correlations are noted where some MTDs show onlapping reflections onto the flank of D5, a character indicating deposition on top of a seafloor-deforming structure.

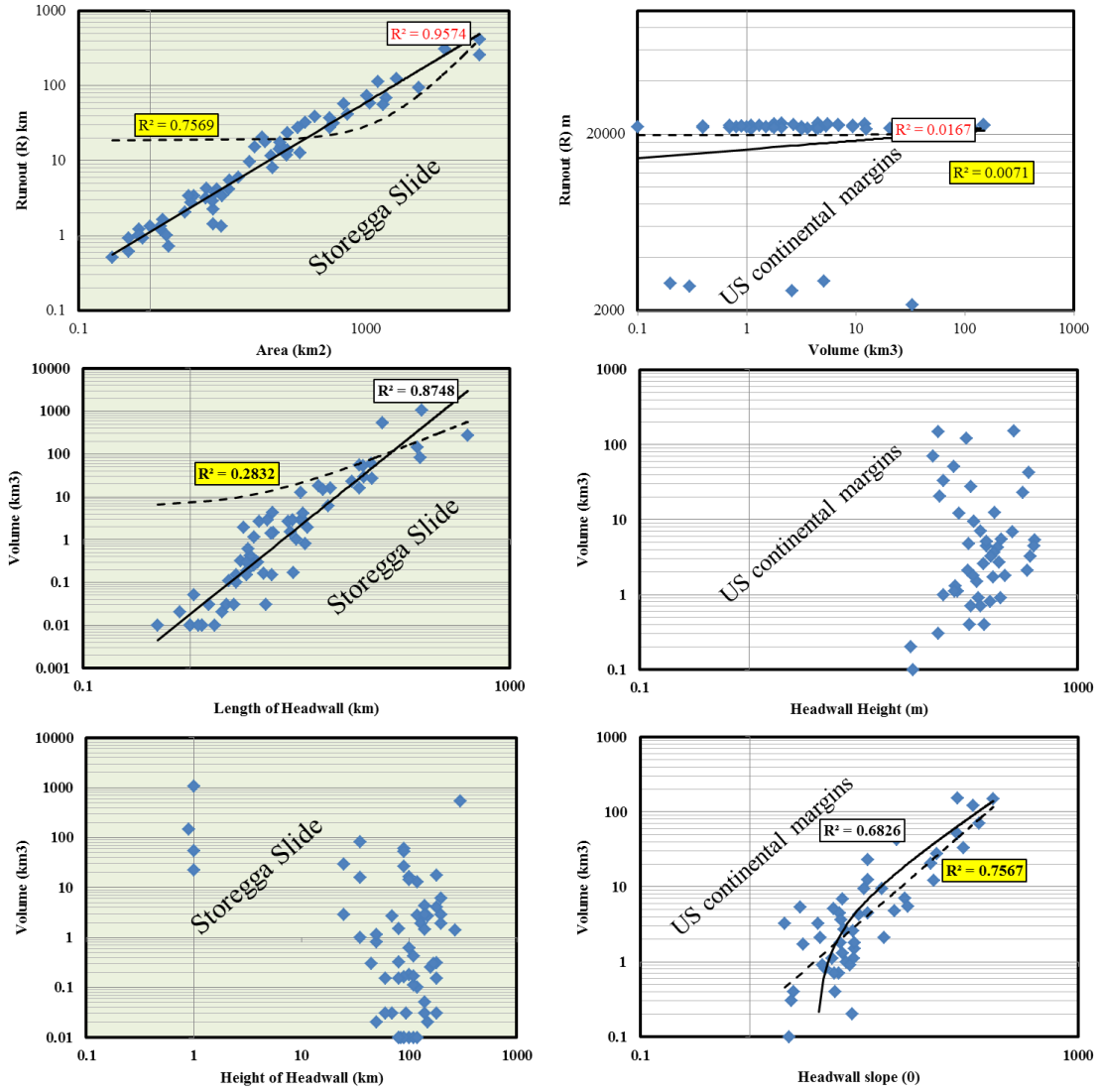

Figure 7.1: Morphometric character of the Storegga landslides and several lobes and landslides from the US continental margin (data derived from Haflidason et al., 2005 and Mc Adoo et al., 2000).

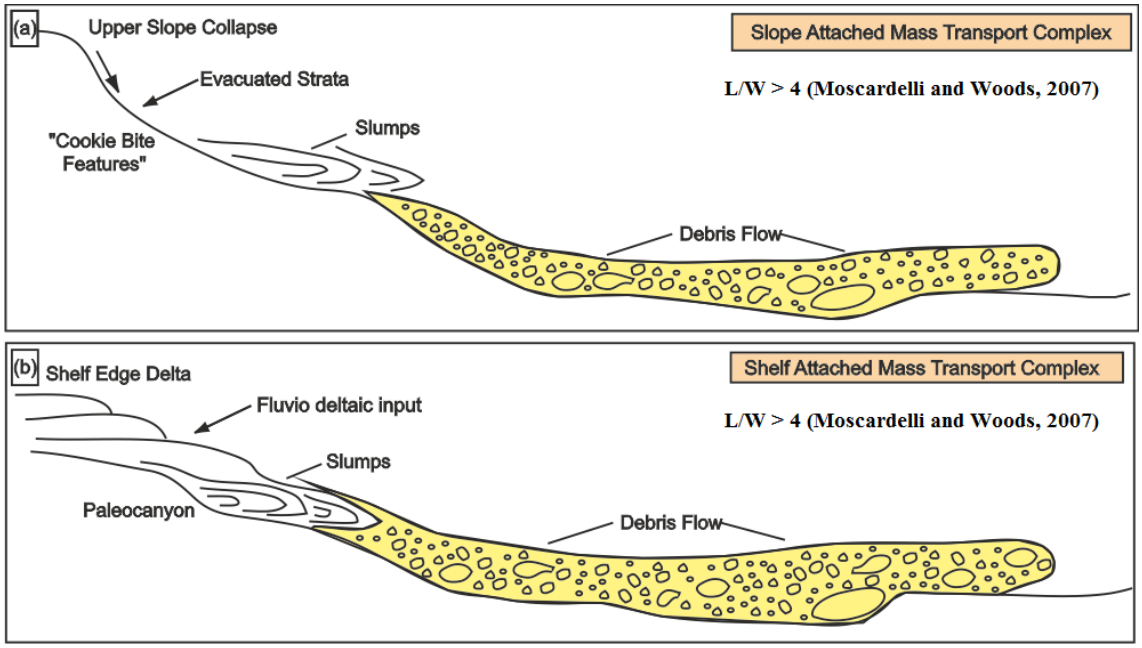

Figure 7.2: Triggering mechanisms (a) and processes (b) associated with the development of mass-transport complexes as defined by Moscardelli and Wood, 2007. Slope- and shelf-attached mass-transport complexes are produced by catastrophic collapse of the upper slope area and dumping of sediments by shelf-edge deltas into the deep marine basin. Slope- and shelf- attached mass-transport complexes have aspect ratio of >4 (Adapted from Moscardelli and Wood, 2007).

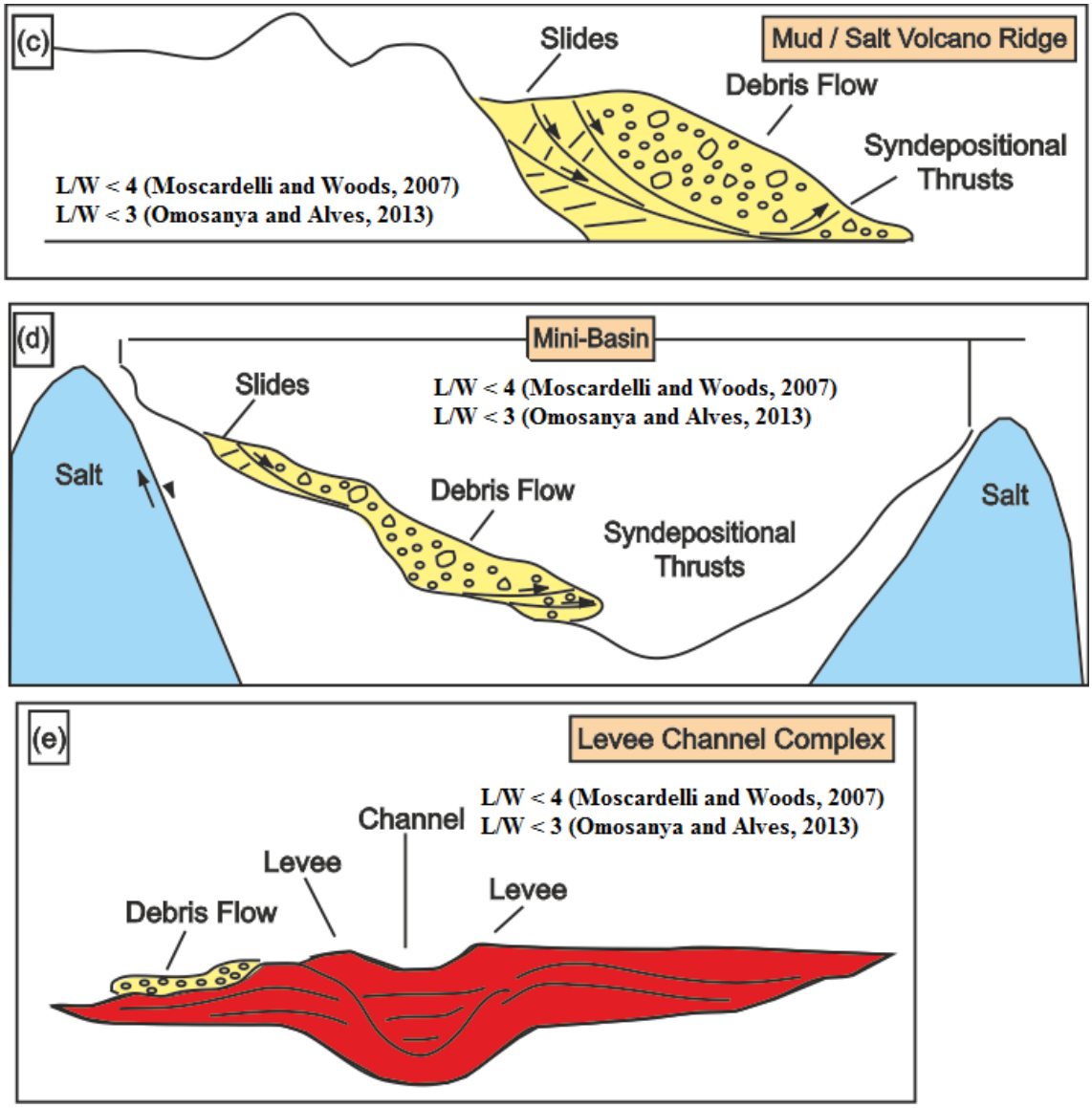

Figure 7.3: Slope- and shelf-detached mass-transport complexes are triggered by c) gravity instability and collapse of the flank of a mud volcano ridge, (d) oversteepening of one of the margins of a deep-water withdrawal basin, and (e) collapse on the margins of levee channel complex. Slope- and shelf-detached mass-transport complexes are characterised by L/W ratio < 4 (Adapted from Moscardelli and Wood, 2007).

ii) Frontal versus lateral ramps as kinematic indicators

The terms ‘frontal’ and ‘lateral’ ramps have been used to describe the geometry of hanging-wall strata of thrust-related folds (Pohn and Coleman Jr, 1991; Scott Wilkerson et al., 2002; Aridhi et al., 2011). In structural geology, a frontal ramp is oriented normal to the direction of transport of the faulted sequence (Figure 7.4). In contrast, lateral and oblique ramps are oriented parallel and obliquely to the direction of transport of the hanging wall section of the thrust fault (Scott Wilkerson et al., 1991; Scott Wilkerson et al., 2002). These structures are produced in compressional domains where rocks are contracted (Figure 7.4, Scott Wilkerson et al., 2002; Scott Wilkerson et al., 1991). The use of ramp and flats is not limited to thrust faults, but reactivated normal faults with ramps and flats are poorly documented (e.g. Axen, 1993; Hayman and Kidd, 2002).

Ramps are used to describe the mode of frontal emplacement of MTDs (Frey-Martínez et al., 2006). Frontally-confined MTDs undergo a restricted downslope translation and do not overrun the undeformed downslope strata (Figure 1.10 and Figure 7.5). The compressional toe regions of frontally confined MTDs are usually buttressed by ramps separating their fill from the foreland (Frey-Martínez et al., 2006). There is no bathymetric expression compared to their total thickening and relative modest downslope transfer of sediment. Consequently, ramps of frontally-confined MTD are linked to contractional and extensional structures characteristic of shallow deformation in accretionary wedges (Lucente and Pini, 2003). Current theories show that ramp explicitly described structures formed through different mechanisms e.g. erosion for MTD and compressional tectonics for faults (Scott Wilkerson et al., 2002; Lucente and Pini, 2003; Bull et al., 2009; Aridhi et al., 2011). Furthermore, the role of lithological control at forming ramps at the basal shear surface of MTDs was emphasized using both

seismic interpretation and statistics techniques (Bull et al., 2009; Omosanya and Alves, 2013).

This thesis shows that ramps can form at the base of MTDs, not only in frontal regions of confinement. Erosion is the dominant controlling factor on the formation of ramps at the base of MTDs. The erosional pattern observed depends on the direction of mass flow, flow regime, mechanical strength of the substrate, and the erosive power of the transporting medium (Omosanya and Alves, 2013). For example, the ramps discussed in Chapter 5 are essentially oriented in the NW-SE direction coincident with the direction of mass flow observed in the study area of the Espírito Santo Basin (Omosanya and Alves, 2013). The ramps were created as sections of the palaeo-seafloor were eroded.

Ramps associated with MTDs previously described as structure perpendicular to the mass flow direction could have been misinterpreted or are simply frontal ramps (Figure 7.6). For example, the general practise in seismic interpretation is to interpret seismic profiles along inlines and crosslines which most often are not the strike orientation of the structures. Any dip interpreted along such line would be apparent. Thus, to adequately understand the orientation of the ramp relative to the direction of mass flow entails a broad understanding of the direction of mass flow. From this work, it is apparent that ramps and flats are unreliable kinematic indicators and can be oriented differently to the direction of mass flow/transport (See Figure 7.6 for details).

iii) Coves as sediment repositories and record of cannibalised sediments

In Chapter 6, basal ramps are flanked by coves formed during the translation of the MTDs (Figure 5.9). As the ramps are thought of as the sidewalls of excavation zones,

they could provide hints on the amount of sediments cannibalised during mass-wasting events. The volume of cannibalised sediments can be estimated from $\mathbf{A.t^I}$ while the overall sediment budget is **A.t**, with **A** being total area of the coves. The parameter $\mathbf{t^I}$ is the difference of the base of the coves to the original datum for basal shear surface and t is total thickness of the MTD (See Figure 7.7 for further details). This formula is crucial for estimating sediment budgets i.e. those reworked or incorporated into the mass-wasting process. Mass-transport deposits with coves are cannibalised and homogeneous on seismic profiles. The sediments retained in the coves enhance the stiffness of the overburden unit, salt diapirs pierced through the adjacent promontories which are less stiff providing further example of overburden layer resisting salt growth (See Figure 7.7 and Figure 1.12).

7.1.2: Drag zones as strain markers around salt diapirs

In Chapter 5, MTDs were shown to form reliable strain markers, i.e. providing a record of palaeo-seafloor perturbation during salt diapirism (Omosanya and Alves, 2013). Compression and extension of the seafloor during salt diapirism were previously documented (Vendeville and Jackson, 1992a,b; Davison et al., 2000a; Davison et al., 2000b; Davison, 2004; Stewart, 2006). However, the results from this study give important hints about the amount of extension and contraction of the section of the seafloor pierced by the through-going diapirs and invariably on the strain ratio, R_s. The big scientific question in Chapter 5 is if the elliptical drag zones can be analysed using common strain analysis techniques.

Strain analysis focuses on the characterization of the change in shape of geological markers (Ramsay and Huber, 1987). Strain markers used in structural analysis include

fossils of trilobites, ammonites, belemnite, sea urchin, fishes, ooids, spherulite, pebbles of conglomerates, brecciated masses found in sedimentary rocks, and deformed crystals of garnet and quartz found in metamorphic rocks (Beach, 1979; Lisle, 1979; Hildebrand-Mittlefehldt and Oertel, 1980; Borradaile, 1984; De Paor, 1986; ; Wu and Groshong Jr, 1991; Sullivan and Beane, 2010). A starting assumption in strain analyses is that the strained objects were initially circular and record no change in area upon deformation (Wellman, 1962; Ramsay and Huber, 1987). For homogeneous strain, the deformed body is characterised by no strain gradient and is uniformly strained. In contrast, heterogeneous strain involves variations in shape and intensity of deformation from one location to another and hence, involve significant strain gradients (Ramsay and Huber, 1987). As strain involves, only changes in shape, volume, position and shape of a body in response to applied stress are accounted as deformation. In this context, the strain history of a body can be analysed using variety of techniques such as Breddin's, Centre-to-Centre, Fry's, Rf/Φ, Wellman's, Flinn's (Flinn, 1956; Wellman, 1962; Dunnet, 1969; Ramsay and Huber, 1987). These techniques work with the starting assumption that homogeneous strain transforms an imaginary sphere into an ellipsoid with three orthogonal x-, y-, and z- axes (Ramsay and Huber, 1987).

The caveat for using the drag zones in this study as strain markers relate to limited information on: a) initial the geometry of the seafloor i.e. if the initial seafloor was circular or planar around the salt diapirs prior to halokinesis; b) incorrect estimates of the third dimension of the elliptical drag zones, c) causative factors or mechanisms for deforming the seafloor i.e. is deformation brittle, ductile or viscous? d) the time-length and styles of deformation i.e. if the deformation is continuous, homogeneous or heterogeneous? This thesis defends that seafloor morphology is constantly modified by

external forces such erosion and tectonism, and thus a uniformly flat and planar seafloor is non-realistic (Ren et al., 1996; Beaman and Harris, 2003; Cattaneo et al., 2004; Dupré et al., 2007; Savini et al., 2009; Dandapath et al., 2012; Watt et al., 2012).

Posing this, the section of the seafloor studied in Chapter 5, and perturbed during diapir growth, could never have been circular or planar. From figure 5.11, the thickness of the drag zone is not constant especially on the flank of the diapir where thickness is highest relative to the crest. In addition, some of the sediments eroded at the diapir crest were slumped on the flanks of the diapir (See Figures 1.15, 5.9 and Figure 7.8). Therefore, the thickness/third dimension of the drag zone cannot be adequately accounted for. The velocity used for depth conversion can also greatly influence the true thickness of the zone, as inconsistency in depth conversion can arise from different factors (Japsen, 1994; Li and Richwalski, 1996; Rimando and Manuel, 1997; Goncharov and Nelson, 2012;). This renders any estimate of the third dimension of the drag zone as speculative and indefinite.

Salt rheology is viscous and non-Newtonian and depending on the mechanism driving the salt flow, a plethora of structures can result (Vendeville and Jackson, 1992a, b; Hudec and Jackson, 2007). Although strain produced by the salt flow is mostly continuous, it may involve discontinuous strain when crestal fractures and faults at the diapir crest deform the seafloor (Bishop, 1996; Davison et al., 2000b; Hudec and Jackson, 2009). Neglecting the possibility of the latter, the MTDs in Chapter 5 record continuous strain which is heterogeneous in nature.

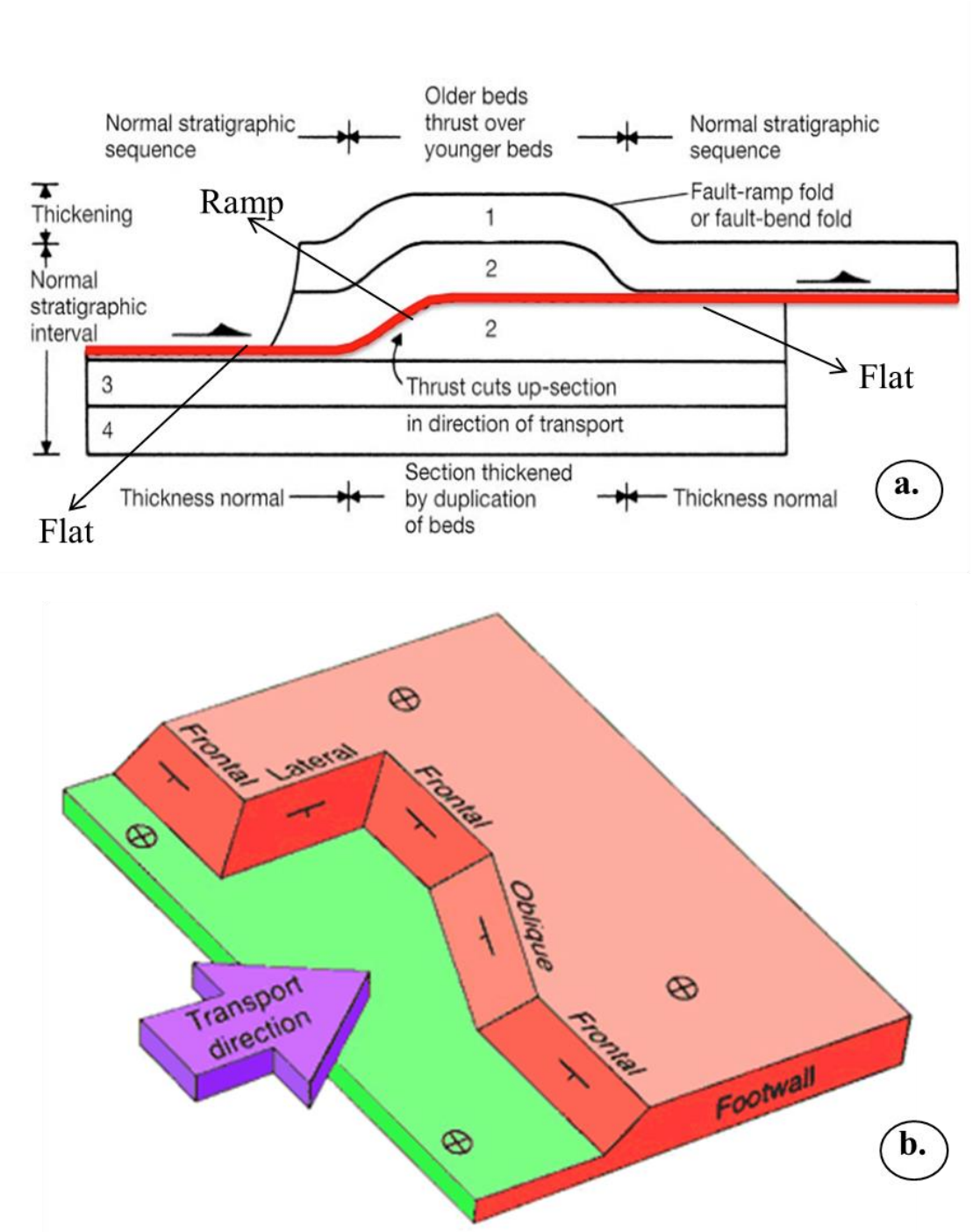

Figure 7.4: (a) In thrust tectonics, ramp and flats are formed by contraction of the hanging wall section of fault. The bedding parallel section of the thrust fault is called a "flat" while "ramps" are discordant to bedding (b) Frontal ramps are oriented normal to the direction of transport, lateral ramps are parallel while oblique ramps are oblique to the overall transport direction. Modified after Twiss Moore (1992) and McClay (1992).

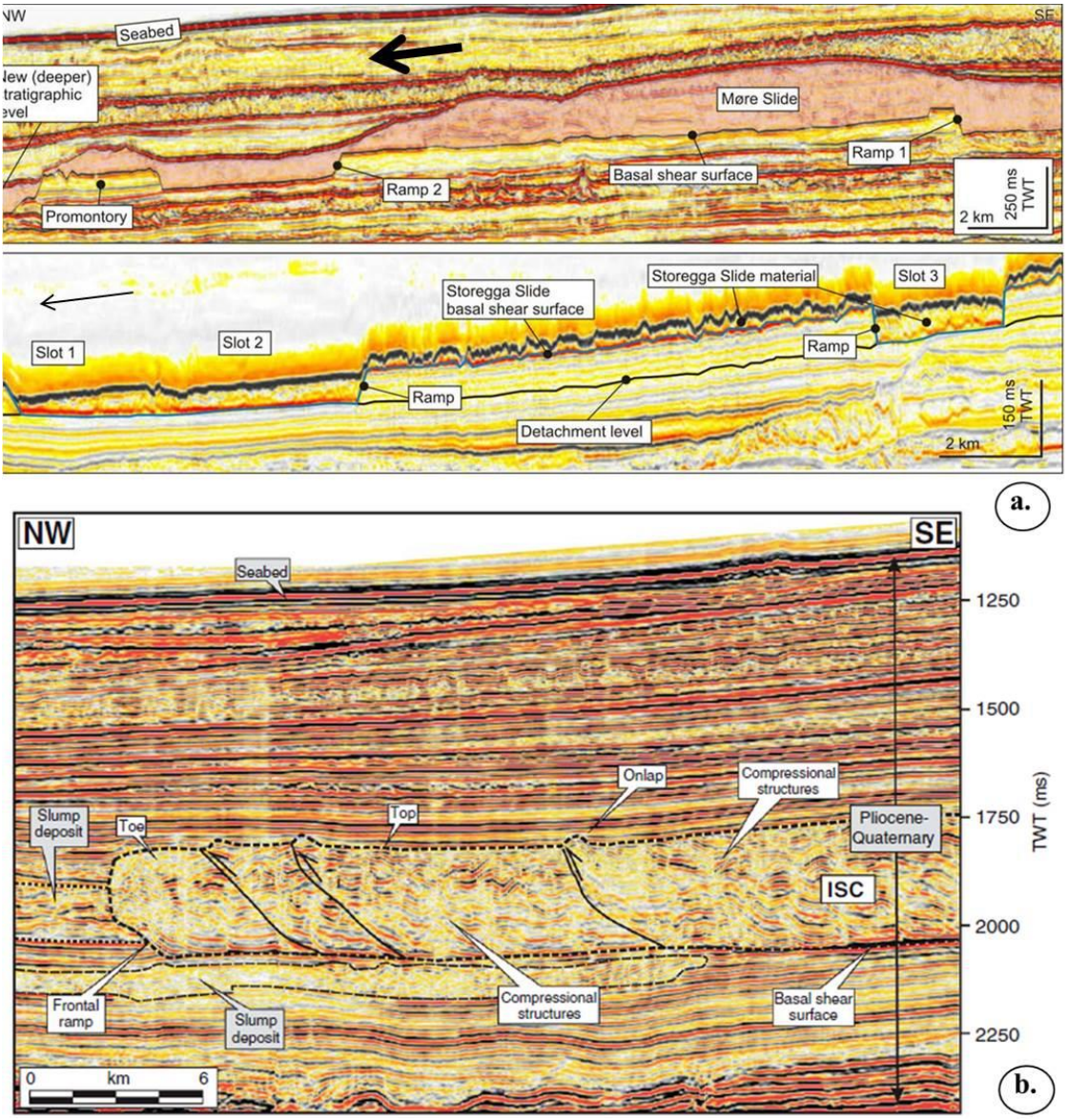

Figure 7.5: (a) Seismic section showing examples of basal ramps from the Møre slide and inlets from the Storegga slide. The ramps are steep and discordant to bedding. Arrow indicates translation direction (Bull et al., 2009) (b) Mode of frontal emplacement of MTD. Frontally confined MTC are buttressed again a frontal ramp contrasting frontally-emergent MTC that are characterised by free translation at their leading edge (Frey-Martinez, et al. 2006).

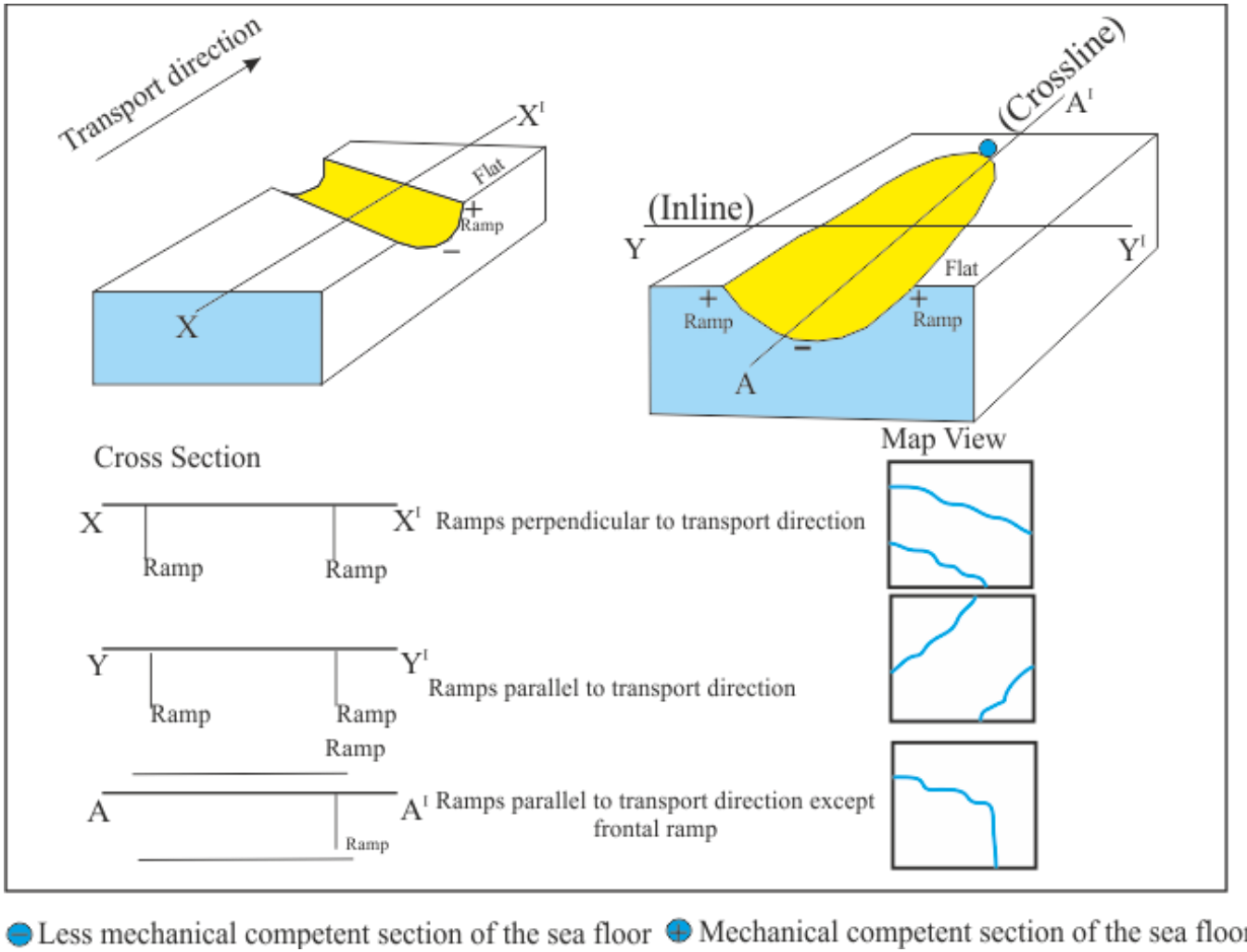

Figure 7.6: Model for explaining the unreliability of ramps and flats as kinematic indicators. The relationship between the direction of mass flow and orientation of ramps is dependent on a) the seismic mapping technique, b) the mode of erosion of the palaeo seafloor, and c) the perception and skills of the seismic interpreter.

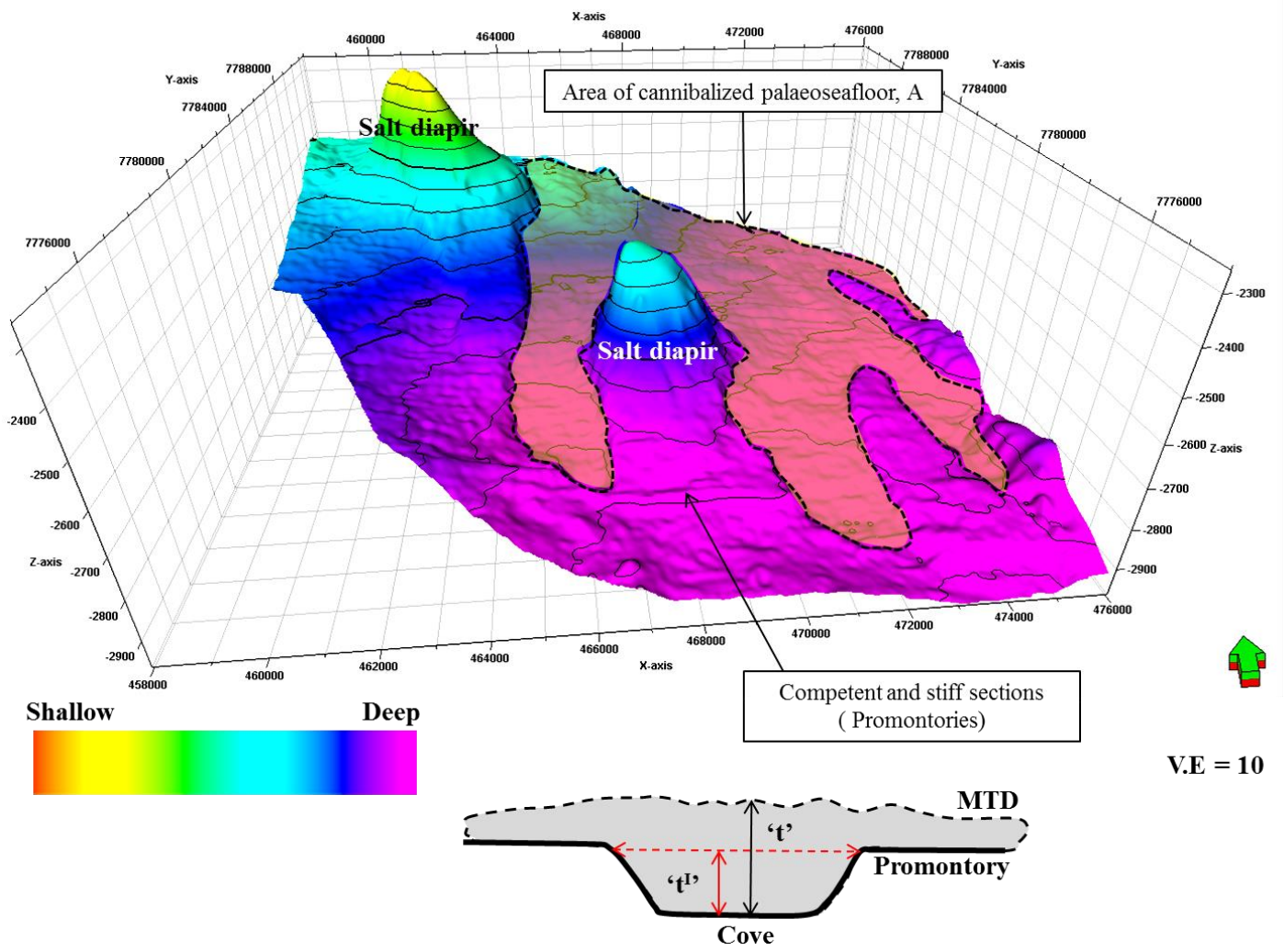

Figure 7.7: Coves provide hints on the amount of sediment cannibalised during the mass-wasting event. The ramps are thought of as walls of excavation zones during sediment transport. The amount of cannibalised sediment is $A.t^{I}$ while A.t is overall the sediment budget.

The centre-to-centre, Fry's, Breddin's and Wellman's method of strain analysis require a quite large assemblage of strain markers to be measured in a body before strain analysis can be done. However, the number of drag zones or markers in this study is less than ten (10), coupled with their disparate occurrence at different stratigraphic levels (Figure 7.8). The Rf/Φ and Flinn technique can find sparse and cautious use for the drag zones especially when using data from their short –axes. Undoubtedly, the drag zones in the study provided information on the final strain condition, $R_{s.}$ and evidence for the magnitude and degree of extension and contraction endured by the seafloor during diapir growth, but there are no means to quantify the original condition of the seafloor prior to diapirism. Nevertheless, the information provided by this strain marker is crucial to MTD recurrence studies and drilling design in offshore areas. The drag zones are marker of the maximum strain endured by the palaeo seafloor during active diapirism. Readers are referred to Appendix III for further note on the Rf/Φ technique of strain analysis

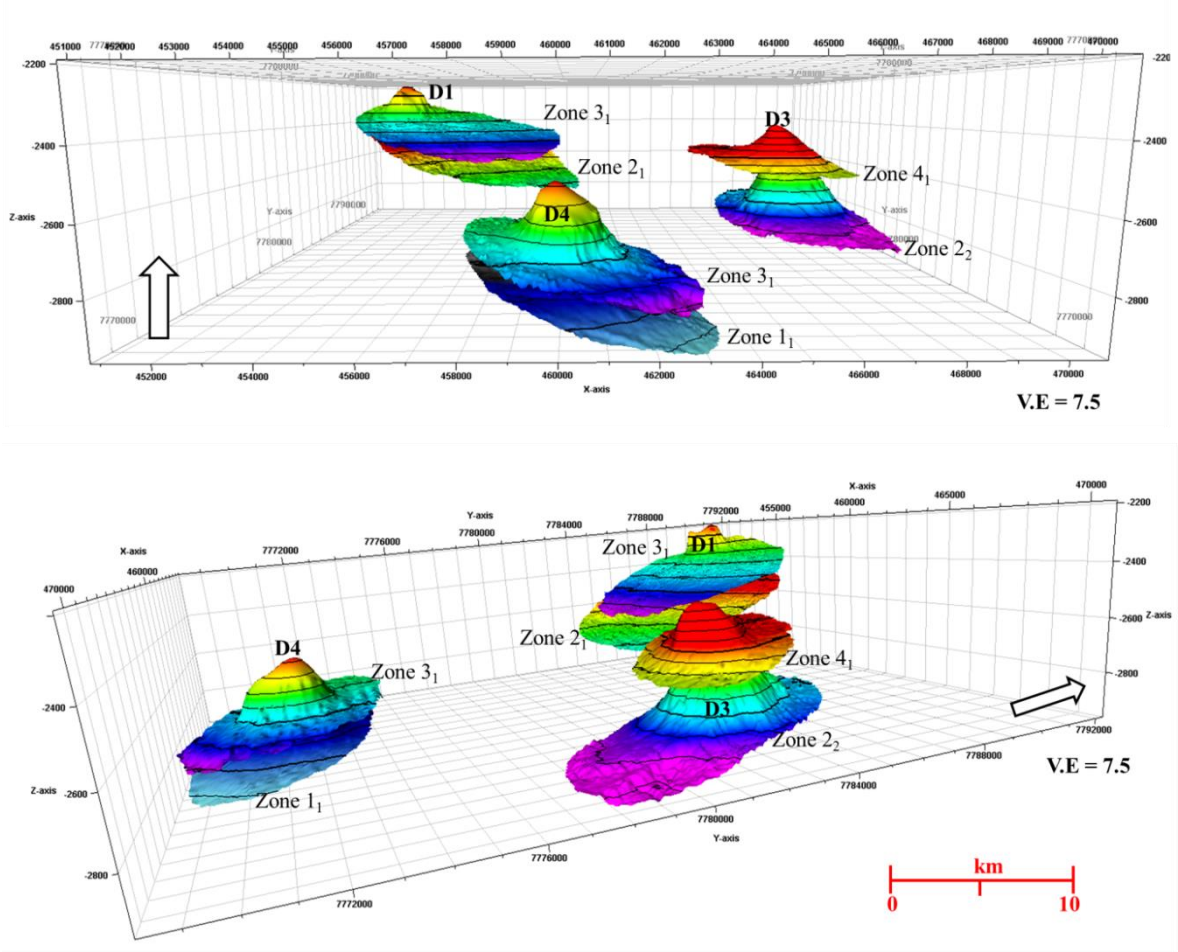

Figure 7.8: The drag zones estimated in Chapter 5 are located at different stratigraphic levels and may not meet the pre-required sample size for strain analysis. Most strain analysis techniques are applied to markers on two dimensional surfaces.

7.1.3 Mass-transport deposits as lithological barriers to fault propagation

Faults decoupled by the MTDs analysed in Chapter 6 are a classical illustration of blind faults fulfilling the criteria of structures characterised by radial propagation as suggested by Baudon and Cartwright (2008b). Furthermore, their displacement-depth characters are in accord with typical Barnett plots. The data in this thesis, however, shows that t-z plots from both restricted and unrestricted faults can have M-type profiles (Figure 6.6). This contrasts the hypothesis of Muraoka and Kamata (1983) where only restricted faults are characterised by mesa profiles. Interestingly, these observations concur with the work of Baudon and Cartwright (2008b) in the Levant Basin where unrestricted faults have mesa-profiles. Since C-type faults are connected to homogeneous incompetent materials and M-types to very rigid/competent units making their flanking section to have very steep slopes, the strata at the tip of M-type faults are considered as a strain absorber (Muraoka and Kamata, 1983). An important question is whether the MTDs are genuine barriers to the fault propagation or if external controls such as slope tilting highlighted earlier are impeding the propagation of the faults. The t-z plots for the decoupled faults in Chapter 6 are C-types and hybrid C types (Figure 6.6). Based on the observation of Muraoka and Kamata (1983), the interpreted MTDs are presumably incompetent/non rigid rock, contrasting with the interpretation of homogeneous MTDs suggested in Chapter 5. If indeed MTDs are consolidated after deposition, then the t-z plots for the Type D faults should typically be M-type profiles (Piper et al., 1997; Shipp et al., 2004; Moscardelli et al., 2006). Instead M-type profiles are found within Type A non-decoupled faults (Figure 6.8). Again, this scenario addresses the importance of MTDs to understand the evolutionary history of faults. In the absence of well and core data rendering impossible to analyse the mechanical properties, log response and geotechnical behaviours of slope strata, MTDs can give important hints about the rheological conditions (and timings) of faulting on sedimentary basins.

7.1.4: Hydrocarbon implications of MTDs vs. salt structures interactions

Mass-transport deposits are characterised by compositional and structural heterogeneity which may compromise their capability as hydrocarbon reservoirs (e.g. Weimer and Shipp, 2004; Dykstra et al., 2011). In Chapter 4, it is shown that MTDs can be classified further as homogeneous and heterogeneous, potentially an indication of the amount of clastic materials acquired during the mass-wasting process. MTDs containing hydrocarbons would require adequate porosity and permeability to conduct fluid which could be derived from their structural and lithological heterogeneity. Blocky MTDs and other clastic-rich MTDs were described by Haughton et al. (2003), Taylor et al. (2003), Welbon et al. (2007).

Lithological variability in MTDs is dependent on the provenance or staging area especially the protolith from which the MTDs were derived. Outer shelf and upper slope-derived MTDs in tectonic unstable margin are particularly prone to clastic material in their upper slope section while mid-slope-derived MTDs are generally mud-prone (Haughton et al., 2003; Posamentier and Martinsen, 2011). In addition, collapse and erosion of channel-levee complexes can provide significant amount of sand in MTDs. Structural compartmentalization of MTDs can come from architecture and complex interaction of faults and fractures. Hence, rather than the cliché of low poroperm mud-dominated sealing units (Weimer, 1990; Posamentier, 2004), the potential of MTDs as hydrocarbon reservoir has been further established in the past decade (Clayton et al., 1998; Bruso, et al., 2004 Ogiesoba and Hammes, 2012, etc.)

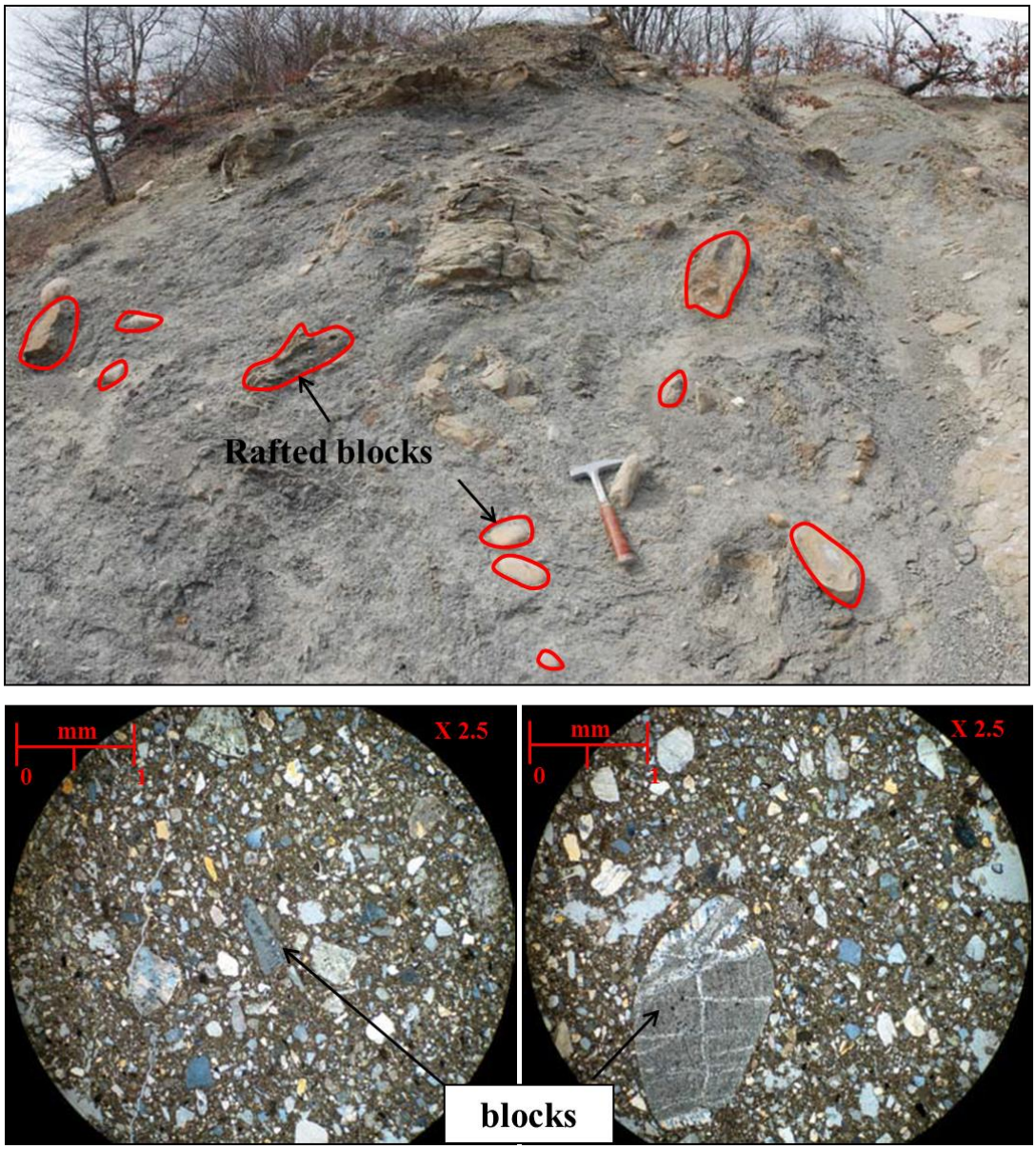

Figure 7.9: Example of a blocky debris flow deposit from the Specchio Unit in Northern Apennines. Blocks ranges in size from few meters to mm in optical sections. This is an example of heterogeneous mass-transport deposit in outcrop and thin section. At a seismic scale, this deposit would appear homogeneous as the blocks and their associated matrix would be sub-seismic (Adapted from Ogata, 2010).

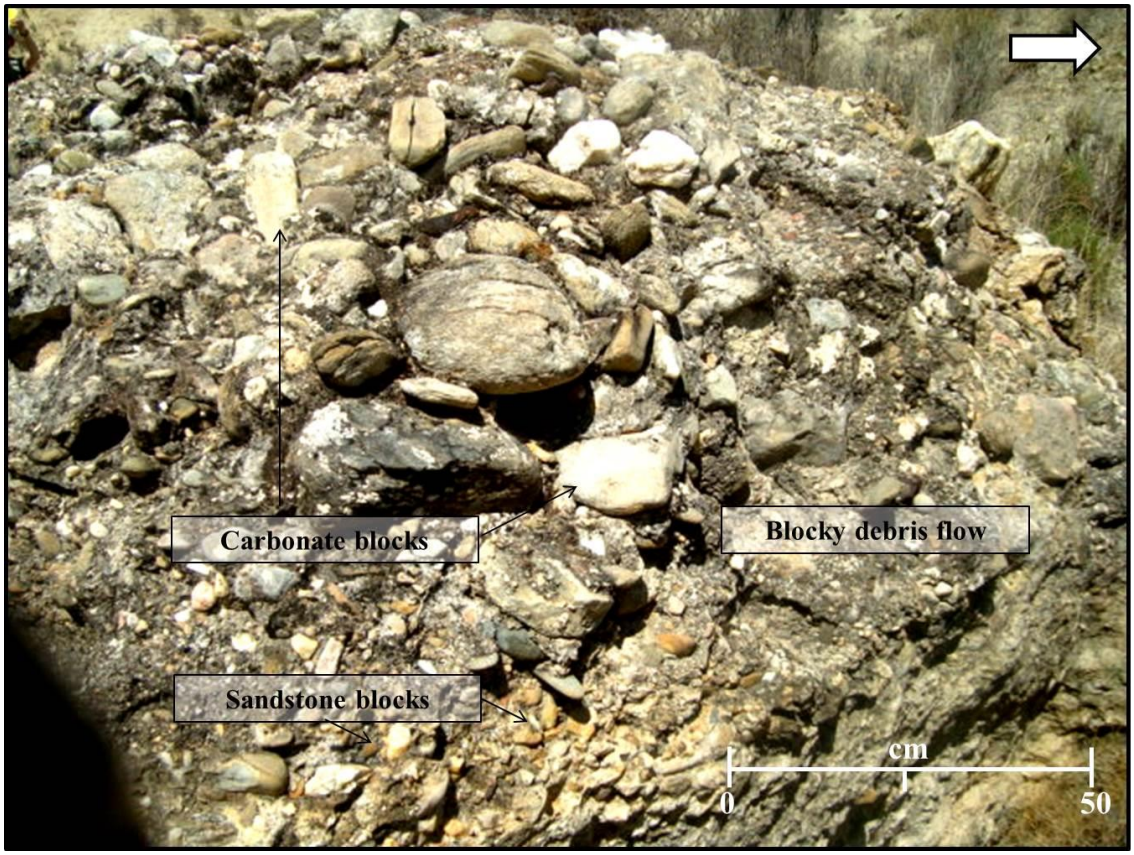

Figure 7.10: Example of a blocky debris flow deposit from the Tabernas Basin, Spain. The composition of rafted blocks varies from ferruginised sandstone to carbonate. The size and shape of the blocks do not reveal diagnostic pattern with increasing distance from source area which was inferred west of the study area. This is an outcrop example of a heterogeneous MTD. N.B: *Picture was taken during the IAS summer School in Almeria, 2012*

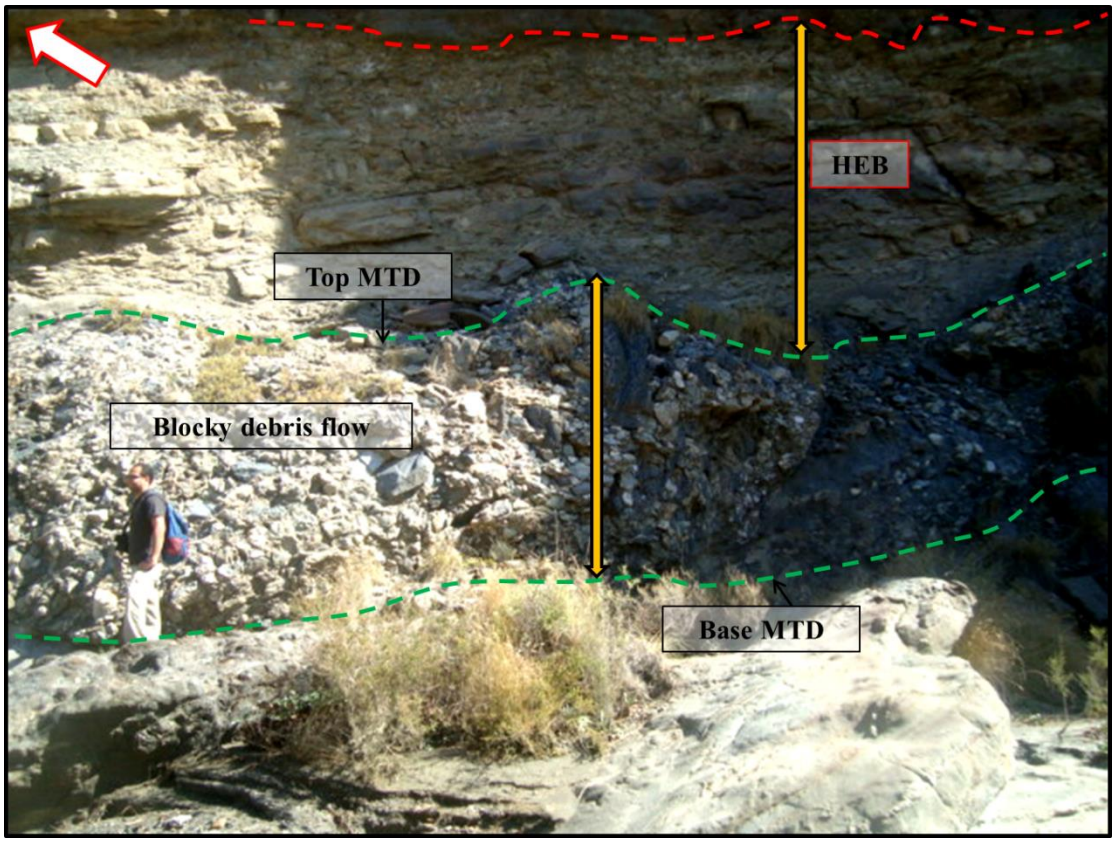

Figure 7.11: Another example of a blocky debris flow deposit from the Tabernas basin, Spain. The matrix is composed of smaller blocks and sandy debrites. This is an outcrop example of heterogeneous mass-transport deposit. N.B Picture was taken during the IAS summer School in Almeria, 2012. N.B: *HEB – Hybrid Event Bed*

The blocky debris flow deposits described in Chapter 4 are deposits that benefited from huge input of volcaniclastic and siliciclastic sediments during the uplift and erosion of the SE Brazil margin (Fiduk et al., 2004; França et al., 2007). Evidence from seismic profiles implies that the mud-prone matrix can provide a seal to the less disaggregated blocks. However, recent development of mud/shale dominated oil fields show that the matrix itself can provide unconventional means of hydrocarbon e.g. (Mohaghegh, 2013). The problem with mud-dominated reservoirs is connected to low porosity and permeability. For example, shale can possess high porosities but lack vertical permeability. The phyllosilicate structure of the dominant shale minerals means the crystals are stacked vertically and could only connect pores through horizontal pathways. To improve horizontal connectivity of pores, shale reservoirs are hydraulically fractured using a technique called 'fracking' (Mohaghegh, 2013), hence making unconventional and low poroperm reservoirs future exploration targets (Kinnaman, 2011). In this context, MTDs with porosity above certain threshold can contain important hydrocarbon reservoirs e.g. Ubit, Asabo, and Enang fields from offshore Nigeria (Clayton et al., 1998; Bruso et al., 2004) and Oligocene Frio Formation of South Texas (Ogiesoba and Hammes, 2012). In these localities, large-scale blocks or coarse-grained material were slumped, translated, and eroded on continental slopes and later covered by deep-water shales (Moscardelli and Wood, 2007).

Evidence from dip maps and some attributes in Chapter 4 shows that the degree of coarseness of the dip map topographies is derived from mixture of different materials. At vertical and horizontal resolutions of >10m, the debris flow deposits may bear clastic materials which are not seismically resolvable. Homogeneous debris flow deposits in outcrop can be heterogeneous at micro-scale. Blocks of strata controlling the

heterogeneity of the MTDs can vary in size from hundreds of meters to mm in size (Figure 7.9 to Figure 7.12). To further understand the lithological homogeneity of the debrites will involve multidisciplinary studies incorporating both core and formation evaluation.

In terms of fluid flow property of the blocks in this study, the debrites represents cohesive materials that are impermeable with the highest potential to retard fluid flow. CUB and DBS are heterogeneous and more permeable units likely composed of volcaniclastic and siliciclastic materials, hence are conduits for fluid flow especially when they are faulted. Rafted blocks on the other hand can acts as leaky reservoirs prompting the seepage of fluid from higher stratigraphic levels into younger sediments and the sea floor. The rafted blocks can display fascinating internal structures or lithological connectivity (Figure 7.13). In this context, MTDs can acts as barriers or baffles, and conduits for fluid flow in the subsurface (Readers are referred to Appendix V for the Atlas of MTD reservoir and outcrops).

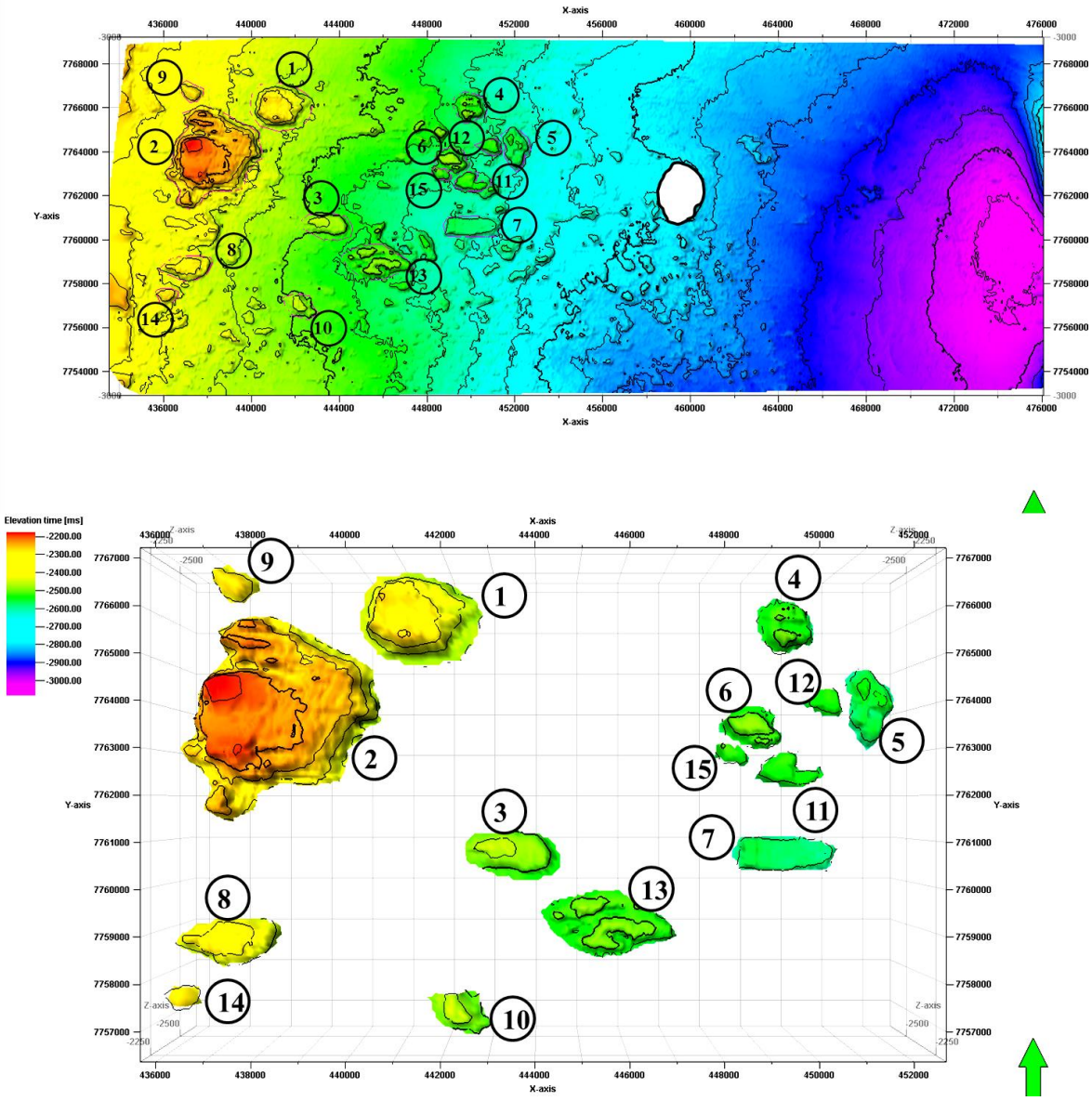

Figure 7.12: Some of the blocks discussed in Chapter 4. The size of blocks is proportionate with distance along slope in contrast to their shape.

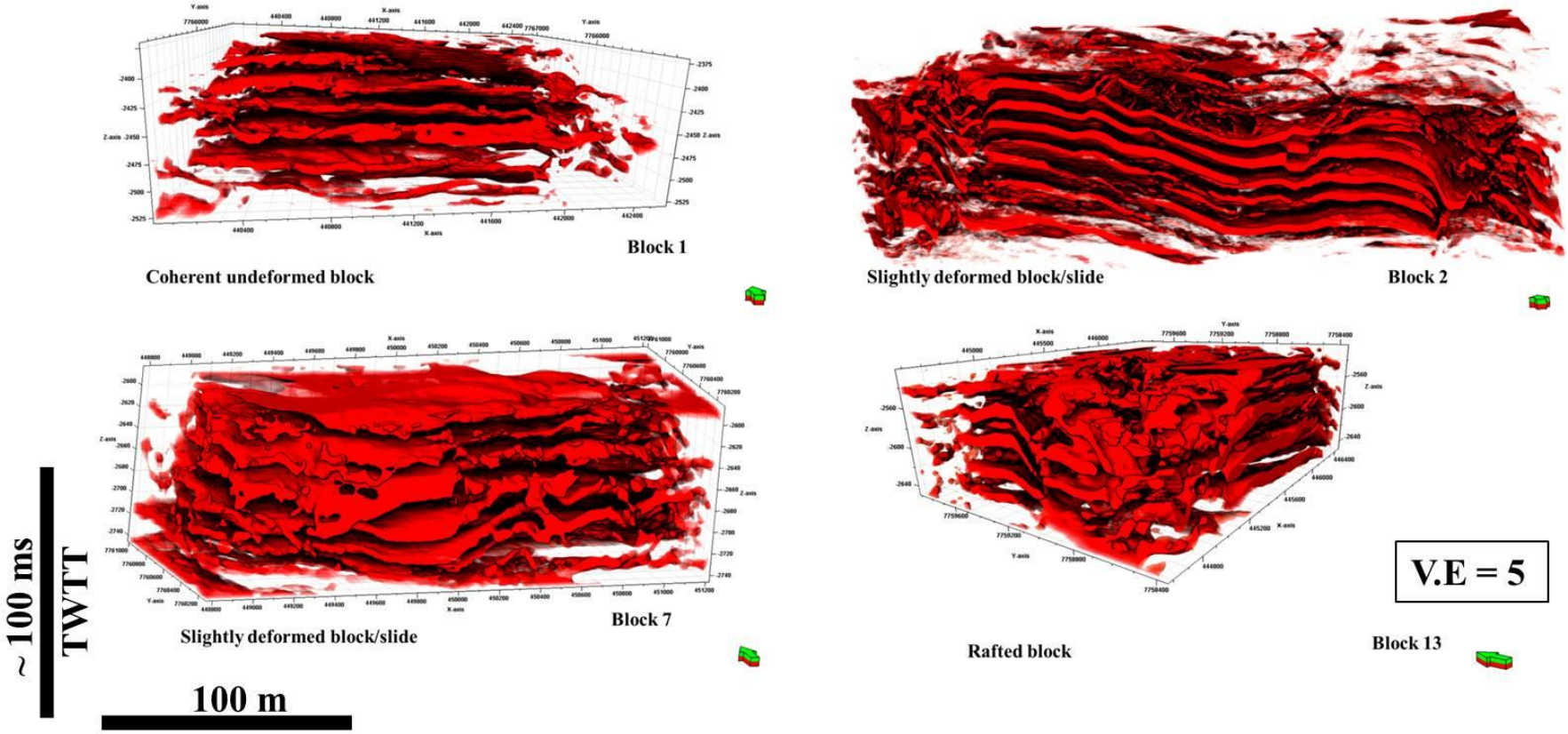

Figure 7.13: Except for debrites, the other kinds of block have a preferred sense of their initial stratigraphy. Structural heterogeneity increases from coherent undeformed block, slightly deformed blocks/slides to rafted blocks. CUB and DBS are likely conduits for fluid flow especially when they are faulted. Rafted blocks can act as leaky reservoirs.

i) Sealing potential of faults decoupled by MTDs

The ability of MTDs to serve as seal rocks has been highlighted in varied research work (e.g. Weimer, 1990; Posamentier, 2004). In addition, the importance of structural compartmentalisation in MTDs to their seal potential was discussed in Chapter 6. There are three principal components to fault seal behaviour: a) lithological juxtaposition across a fault, b) deformation product within and adjacent to the fault, and c) stress state on discontinuities within the fault zone (Smith 1980; Yielding et al, 2010). Fault seal prediction starts with a knowledge of juxtaposition character of rock on either side of a fault. Juxtaposition of permeable (e.g. sandstone) against non-permeable rocks (shale) is most likely to seal a fault than combination of rock types with similar permeability and porosity character (Morris et al, 2012).

Since juxtaposition is the *prima facie* of fault seal analysis, a thorough understanding of the fault rock sequence starts with adequate mapping of throw separation across any faults of interest. Allan juxtaposition diagrams comprise a two-dimensional graphical technique for assessing the sealing potential of juxtaposed sequences across a fault (Allan, 1989). Throw values of > 20m are usually postulated as an empirical threshold between sealing and non-sealing faults (Beach et al., 1997). This however is limited to juxtaposed sequence of permeable and non-permeable rocks (Allan, 1989;Yielding et al., 1997; Freeman et al., 1998). Allan diagrams are subsequently populated with fluid-flow characteristics of the fault at every point on its surface (Morris et al., 2012). The geometry of fault damage zones, relative amounts of clay smear, the composition of the juxtaposed sequence and the slip tendency control the overall potential of sealing faults (Yielding et al., 1997; Freeman et al., 1998). Shale gouge ratio (SGR) is commonly used to assess the clay or shale content of the fault zone. Thus, it is not necessary for

both juxtaposition and deformation process seals to be developed in order for a fault to be sealing (Jones and Hillis, 2003). In addition, fault and fractures with high slip tendencies (ratio of resolved sheared to normal stress on a surface) are more likely to be transmissive than those with low slip tendency (Fox and Bowman, 2010; Morris et al., 2012).

MTD 1 in Chapter 6 comprises essentially homogeneous, low-amplitude strata on seismic profiles, a character implying that the MTD 1 is composed of mud-rich sediment, potentially a good seal interval. Prospective reservoir rocks beneath the MTDs are presumably shielded by 17 km long, 14 km wide and ~ 90 km^3 of MTD materials. For the studied Type C faults, throw maxima for faults offsetting the Base MTD 1 are > 30m, which exceeds the threshold for fault sealing by juxtaposition of lithology (Beach et al., 1997). In addition, MTD 1 occurs at a relatively shallow depth, where faults are generally sealing in comparison to deeply buried faults (e.g. Beach et al., 1997; Knipe, 1997; Knipe et al., 1998). In places where minimum throws were recorded for MTD 1 Type C faults, similar trends were noted for MTD 2. However, the tips of these faults were terminated into MTD 2. Areas characterised by reverse drag and throw < 10m are potential seal bypass for upward migration of hydrocarbon (*cf.* Cartwright et al., 2007).

The majority of the faults in this study showed evidence for partial reactivation, evidenced by multiple stratigraphic levels with reverse drag on hanging-wall and footwall sections (Figure 6.7b). Throw at these points are relatively smaller compared to sections with normal fault drags, where maximum throw were recorded. Reactivated faults are typical baffles to hydrocarbon entrapment (Wiprut and Zoback, 2000). Hence,

the MTDs with reactivated decoupled faults are most likely leaky barriers to fluid flow. Of importance is the timing of hydrocarbon charge into the potential reservoirs. Was it prior deposition of MTDs, sealing of faults by MTDs or after reactivation of the faults beneath the MTDs?

Are MTDs therefore able to provide barriers to the upward migration of the fluid from the reservoirs? Can the MTDs reliably and consistently prevent lateral and downward migration of fluid? The dimension of the MTDs in the study area implies the sideward extent of the seal cover to be adequate. However, leakage of fluid can be connected to non-sealing faults in proximal areas of the MTDs. Type D faults are essentially E-W trending faults intersecting with NW-SE faults (Figure 6.18). This implies three-dimensional (3D) closure of faults at greater levels and apparent retardation of fluid from the reservoir beneath the MTDs. For these reasons, we postulate the MTDs to provide an adequate seal for deeper reservoirs on all fronts. In contrast, lateral migration of fluid is independent of juxtaposed sequences across a fault.

In summary, the seal competence of the MTDs is presumably derived from their geometry and interconnection of decoupled E-W and NW-SE faults. Thus fault-bounded compartments with throw of >30m are potential barriers to vertical fluid flow. The fluid retardation across the fault is also dependent on the shale gouge ratio, amount of clay smear and the overall character of the damage zones.

Spatial and temporal recurrence of MTDs in the study area

Chapters 4 & 5

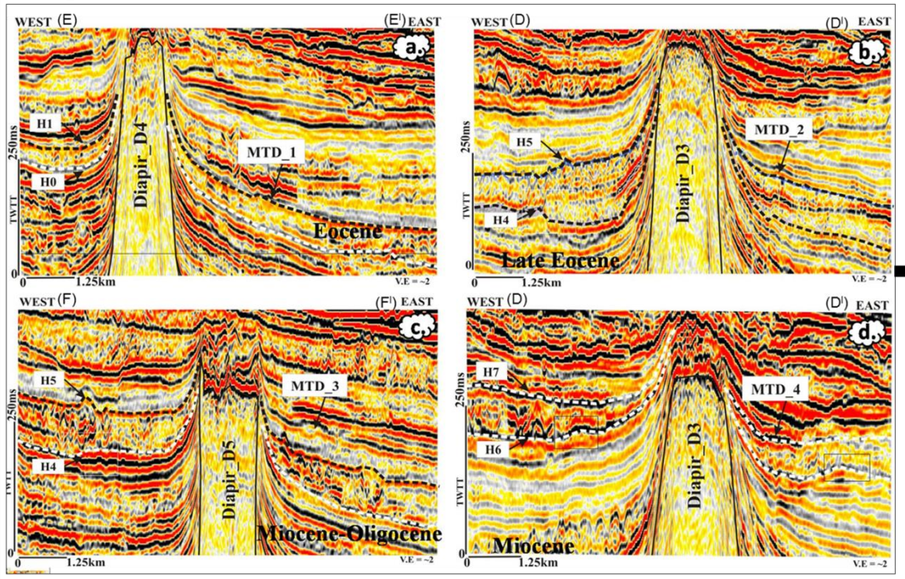

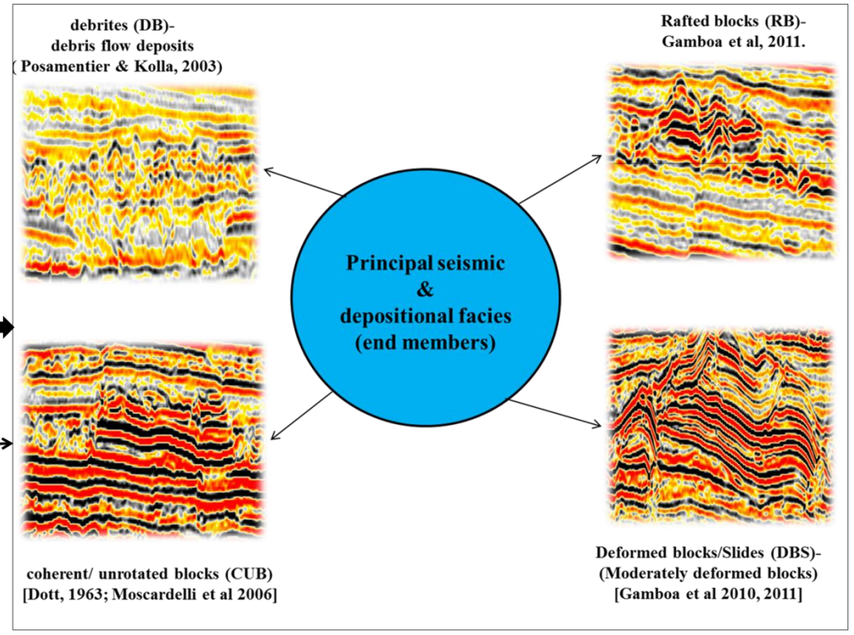

Chapters 5

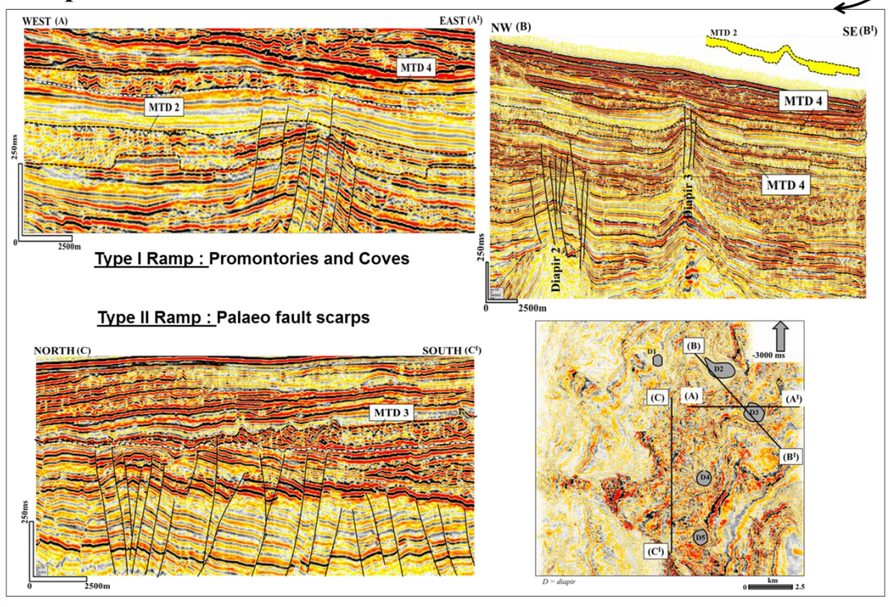

Chapters 4 & 5 — Chapter 6

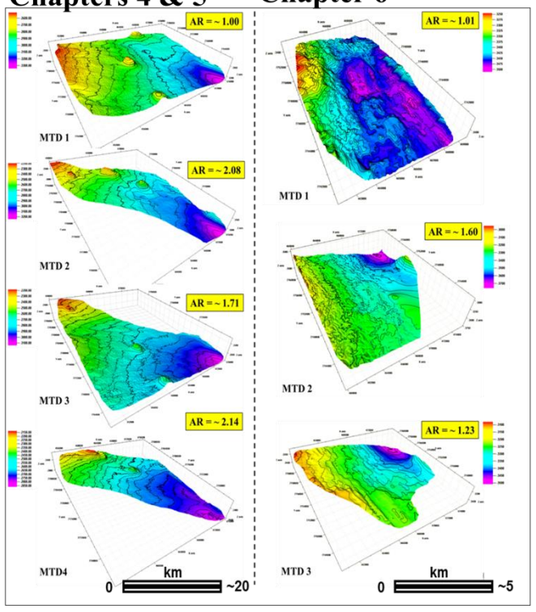

- Interpreted MTDs are distributed around five salt diapirs
- The MTDs are slope-detached MTDs with aspect ratio of <3
- The MTDs range in age from Early Eocene to Miocene
- Four depositional and seismic facies end members are defined [DB , RB, CUB and DBS]
- Causal mechanism (local instabilities on the flank of salt diapirs)
- Source area (mid-continental slope)
- Volume (MTD 1 = 90 km^3; MTD 2 = 89 km^3; MTD 3 = 156 km^3, MTD 4 = 26 km^3; Chapters 4 and 5)
- Volume (MTD 1 = 15 km^3; MTD 2 = 61 km^3; MTD 3 = 15 km^3; Chapter 6)
- Storegga (2400-3500 km^3); Andoya slides (485 km^3); Angola slides (20 km^3); Canary debris flow (400 km^3); Traenadjupet Slide (900 km^3)

CHAPTER 4

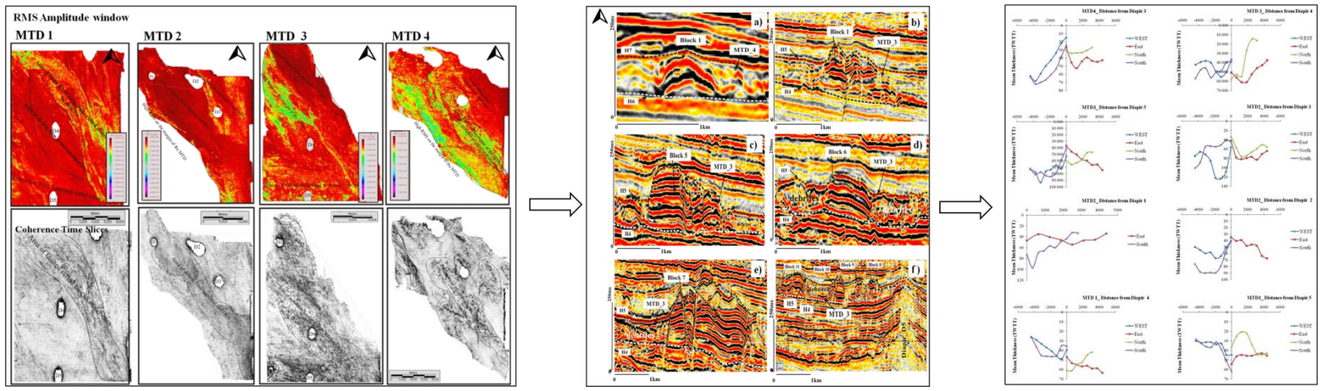

- MTDs can be divided into heterogeneous and homogeneous deposits.
- The size of blocks in blocky debris flows is proportionate with the degree of mass disaggregation and transporting distance in contrast to their shape.
- The shape of the blocks is not a reliable provenance tool
- Correlation between MTD thickness and distance from diapir axis can provide information on the nearness of the source area and seafloor failure on salt diapir flanks.

CHAPTER 5

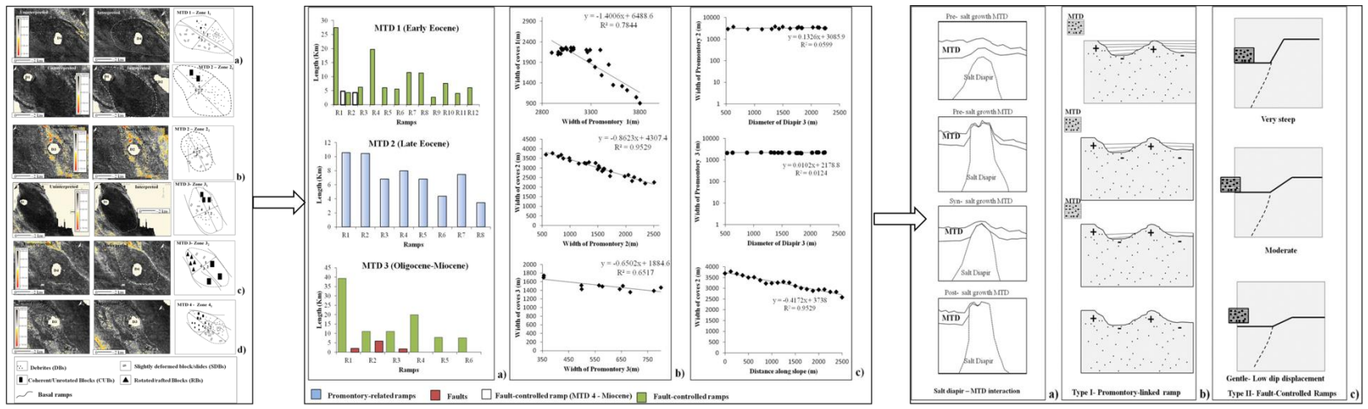

- MTDs deposited on the axis of salt diapirs can act as strain markers.
- The origin of ramps is linked to erosion at the basal shear surface
- Type I ramps are promontory-related, their long axes can be oriented normal, parallel or obliquely to the direction of mass flow.
- Types II are fault-controlled ramp created by the action of multiple beds on pre-existing fault scarps.
- Hence, this work shows that ramps are unreliable kinematic indicators.

CHAPTER 6

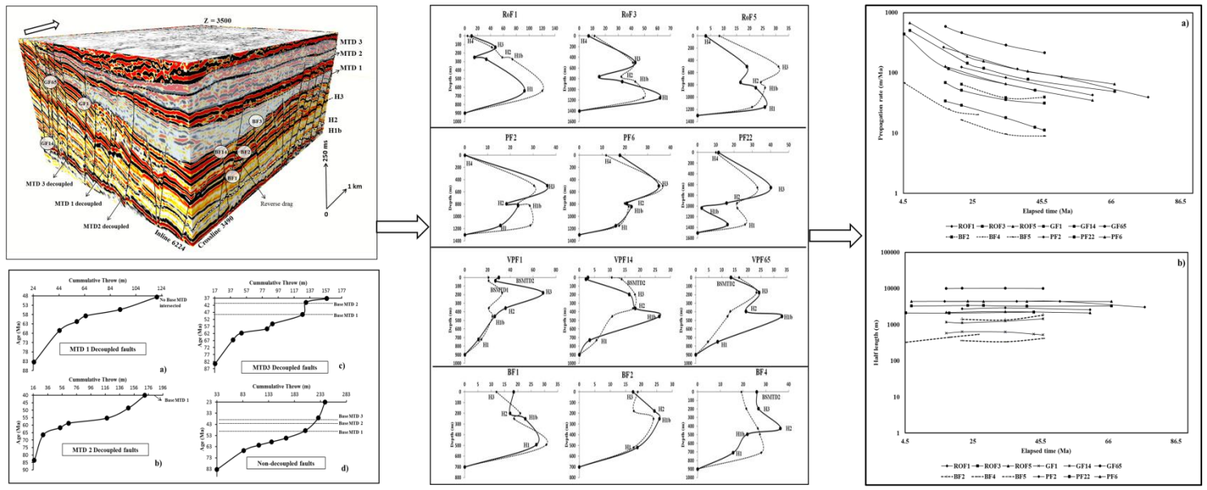

- MTDs can act as lithological barriers to the growth of faults, restricting their upward propagation especially during tectonic reactivation.
- MTD decoupled fault should have lower cumulative throw relative to non-decoupled faults.
- MTDs can introduce both stratigraphic and structural compartmentalisation into any petroleum system.

Petroleum system

- Homogeneous MTDs are highly mud-prone bodies and represent complete barrier to fluid flow. Heterogeneous MTDs are bodies with sufficient interconnected sand e.g. slumped levees and channel bodies – permeable and porous (reservoir rocks). Rafted blocks are highly deformed and faulted- Conduit for fluid flow, partial or leaky barrier to fluid
- Decoupled faults are presumably more sealing than their non-decoupled counterparts

Figure 7.14: Summary of the main findings and results from the technical chapters of the thesis.

7.2 Summary of technical Chapters

A schematic summary of the Chapters is given in

Figure 7.14. The conclusions from the technical Chapters are presented below. As a summary, Chapter 4 is concerned with the complex interaction of salt tectonics and sedimentation, and how the interaction can reveal information about the provenance or staging area of mass-transport deposits. The interrelationship of mass-transport deposits and salt diapirs can result in a plethora of seismic and depositional facies. A new seismic facies characterisation scheme was proposed for individual MTDs investigated in this thesis. These pieces of information provided additional kinematic information to understand the mode of translation of MTDs.

Furthermore, as a follow up to Chapter 4 where a new provenance technique for MTDs was introduced, an attempt was made to pinpoint the distinct character of some of the kinematic indicators found within the MTDs in Chapter 5, especially ramps and promontories. For the first time, the dimension of basal ramps of MTDs was quantified. In addition, the deformation history of seafloor perturbed by salt growth was examined. It was established that MTDs can serve as strain markers.

Since Chapters 4 and 5 focused on the effect of salt diapirs on MTDs, it was pertinent to examine how the deposition of the MTDs affected the salt and especially structures associated with the rise of salt diapirs. In other words, Chapter 6 investigated the capacity of MTD deposited within withdrawal basins to serve as barrier to the propagation of faults. This is necessary for successful appraisal of any petroleum system within these same withdrawal basins.

7.3 Conclusions

The main conclusions from the thesis are provided below:-

Chapter 4

- MTDs can display varied seismic facies and character. Hence, MTD can be divided into heterogeneous and homogenous types.

- Coherent undeformed blocks, rafted blocks, slightly deformed blocks and debrites are correlated to submarine slides, slumps and debris flow deposits at seismic scales.

- Debris flow deposits containing out-sided coherent or highly rafted blocks are further described as blocky-debris flow deposits in agreement with previous work. These deposits can be correlated to fossil Oligocene-Miocene deposits and olistostromes found in outcrops around the world.

- The degree of disaggregation during mass-wasting may increase with transporting distance. The size of blocks mapped within blocky debris flow deposits decreases with transporting and distance along slope. Their shapes are disproportionate with distance therefore the shape of blocks is a limited tool to assess the provenance of MTDs.

- On margins controlled by gravity gliding and spreading, correlations between the thickness of MTDs and the diameter and distance to salt axis can be used as provenance tool.
- The thickness of MTDs can exhibit three possible correlations with salt diapir diameter: a) a positive correlation for MTDs affected by salt movement, b) a

negative correlation for MTDs not associated with the growth of salt diapirs, and c) both negative and positive correlation for MTD deposited synchronously with salt diapir rise.

- The thickness of MTD increases towards the staging area and away from salt diapir where they were not sourced. Strong positive correlation between thickness of MTD and distance along any axis of the salt diapir indicates area of high sediment input during salt rise.

Chapter 5

- Ramps are structures formed at the basal shear surface of MTDs through erosion of a) the incompetent section of palaeo seafloor and b) pre-existing fault scarps.

- Ramps and flats are unreliable kinematic indicators. In this work, the ramps and flats are product of differential erosion and are essentially oriented parallel to the translation direction of the MTDs. Ramps can be oriented normal, parallel or obliquely to the direction of transport of a mass-transport deposit. This idea contradicts existing global opinion that ramps are oriented normal to transporting direction.

- Mass-transport deposits associated with elevated gradient and slope collapse on the flank of salt diapirs have aspect ratio of < 3. They are typical shelf- and slope-detached deposits.

- In addition, such MTDs can provide information on the degree of perturbation induced on palaeo-seafloor during diapir rise.

- The sections of the sea floor perturbed and dragged during the diapir rise are regarded as 'drag zones'.

- Drag zones within MTDs are distinct strain markers. The amount of extension and contraction in the drag zones is revealed by their aspect ratio.

- This piece of information is important consideration during drilling activities especially in margins prone to recurrent mass-wasting and continuous gravity deformation like the Espírito Santo Basin.

Chapter 6

- Mass-transport deposits found within withdrawal basin can act as structural marker for fault propagation and reactivation.

- Homogeneous MTDs are presumably stiffer than their heterogeneous counterparts and have higher tendency to restrict fault growth.

- Faults whose upward propagation is restricted by MTDs are regarded as decoupled faults.

- Cumulative throw is a criterion for recognising decoupled faults as these generally present lower cumulative throw values compared to their unrestricted/non- decoupled equivalents.

- Faults decoupled by MTDs do not have distinct propagation rate from their non-decoupled counterparts.

- In the study area, sedimentation rate had no observable effect on the propagation rate of both decoupled and non-decoupled faults.

- Seal competence in salt withdrawal basin in this study area increases with structural compartments and in zones where MTDs are found.

- In addition, we show that throw plots are insufficient to characterise evolution history of faults.

7.4 Data Limitations

Three dimensional (3D) seismic interpretations can provide information on paleogeographic setting, stratigraphic and system context, architecture and morphological expression of MTDs (Posamentier and Martinsen, 2011). This study has benefitted from a high resolution seismic dataset with a Nyquist Frequency of 250 Hz. The studied MTDs and structures are buried at shallow depths of < 3500m and have high integrity of their original depositional structures preserved. This contrasts to older MTDs that have lost sense of their diagnostic features to increasing compaction, hence, comparable to confining bedded strata (*cf.* Ogiesoba and Hammes, 2012). The MTDs and structures in this study are resolved at vertical and horizontal scales of < 20m.

Notwithstanding the powerful attributes and visualisation techniques used in the study, the uncertainties in this work are associated with the caveat of seismic processing and interpretation. The main limitation of this work is the absence of well data to tie seismic and constrain the geology. As it is often the case, the wells are often extrapolated over distances from the seismic. Well ties and correlation are useful ground-truthing exercises. However, not all beasts are equal. In the absence of the well, the seismic was

correlated to regional stratigraphic columns and DSDP well. This was done with a high level of confidence especially in Chapter 6, where the age of the different horizons was constrained using regional unconformities.

The observations made in this work are limited to the available datasets and a section of the Espírito Santo basin. Additional datasets from the basin and others elsewhere, would enable a reasonable comparative study to be done. High resolution outcrop can offer additional piece of information at macro scales. To understand the processes and products associated with mass-wasting requires an integration of both outcrop-scale and seismic-scale observations. Nonetheless, this work has given a solid argument for further investigations in other sedimentary basins around the world.

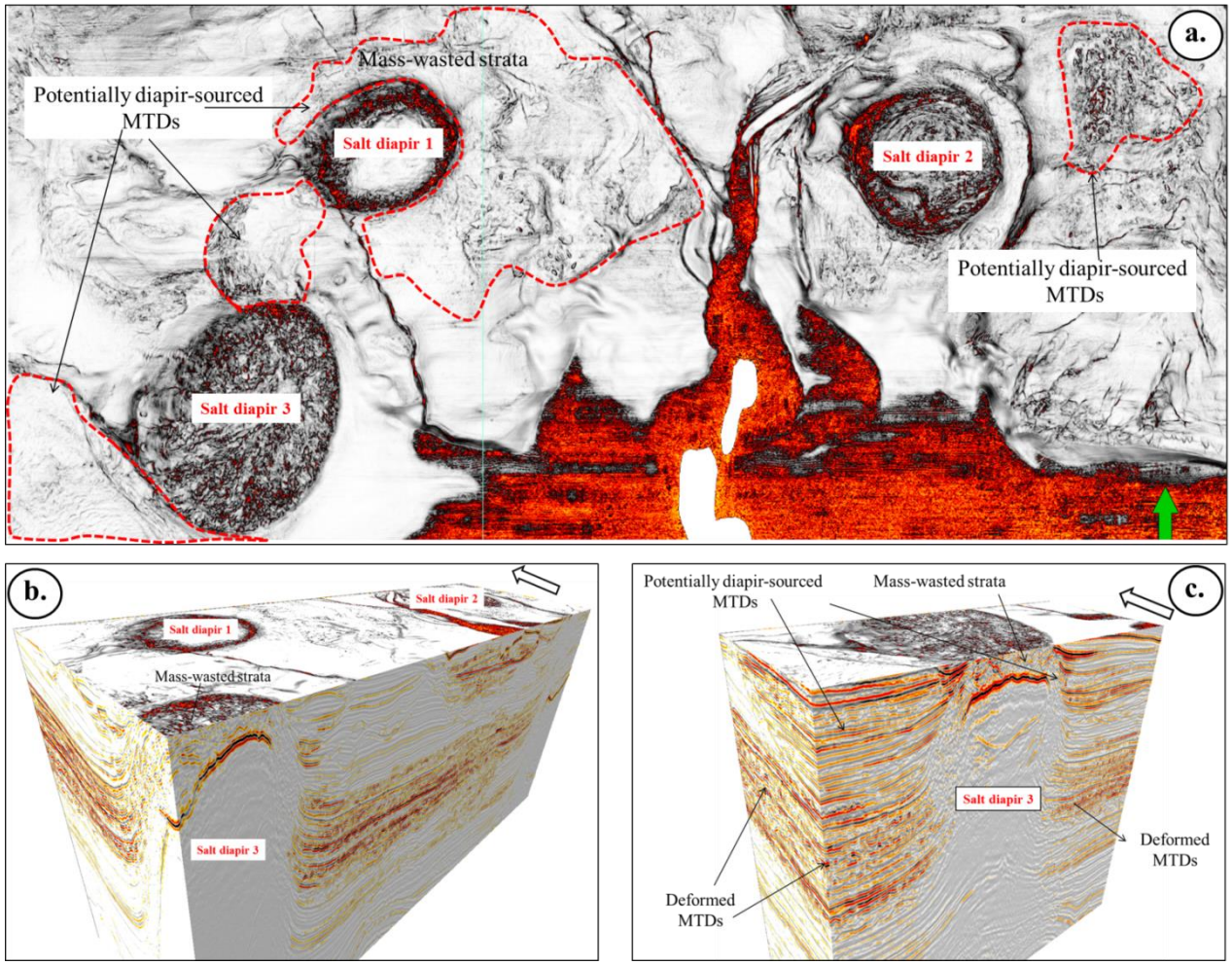

Figure 7.15: Example of potentially diapir-sourced mass-transport deposits from the lower slope of the Espírito Santo basin. Some of the salt diapirs are actively deforming the seafloor. The seismic characters of the MTDs are similar to those of the salt structures. From Chapter 4, the thickness of the mass-transport deposits should correlate positively with diameter of the salt diapir.

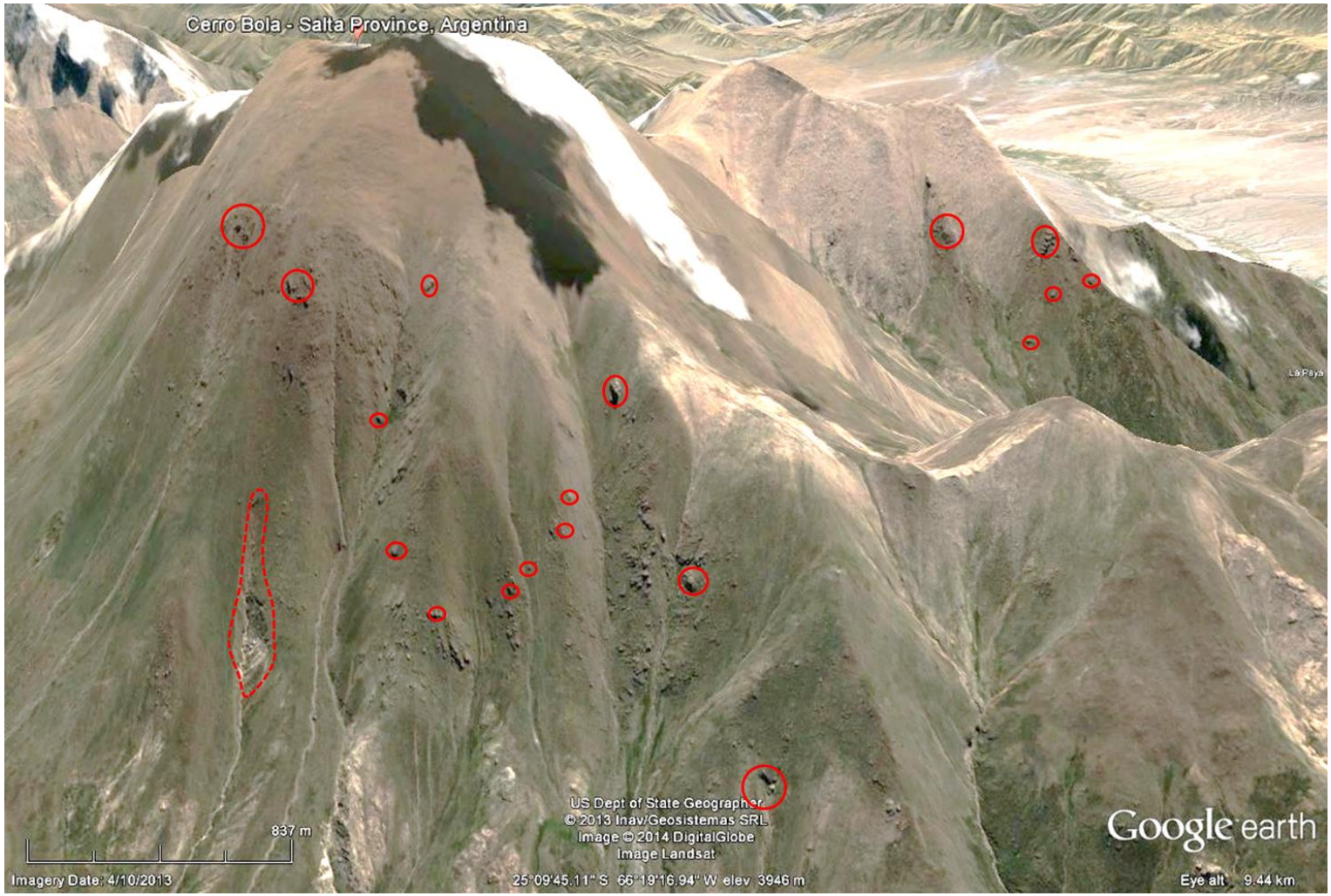

Figure 7.16: Examples of rafted blocks from the Cerro Bola province in Argentina. The red circles represent the relative size of the blocks. These blocks do not show a recognisable pattern with increasing distance along slope. Also shown in the dashed polygon is a recent subaerial landslide (Courtesy google earth, downloaded February, 10, 2014)

Figure 7.17: Examples of rafted blocks from the Tres Paso Formation in Sierra Contreras. The MTDs are composed of sandstone clast several 10s of meters in diameter buried within poorly-sorted, contorted silty shale beds (Adapted from Armitage et al., 2009 and Fildanietal, 2009).

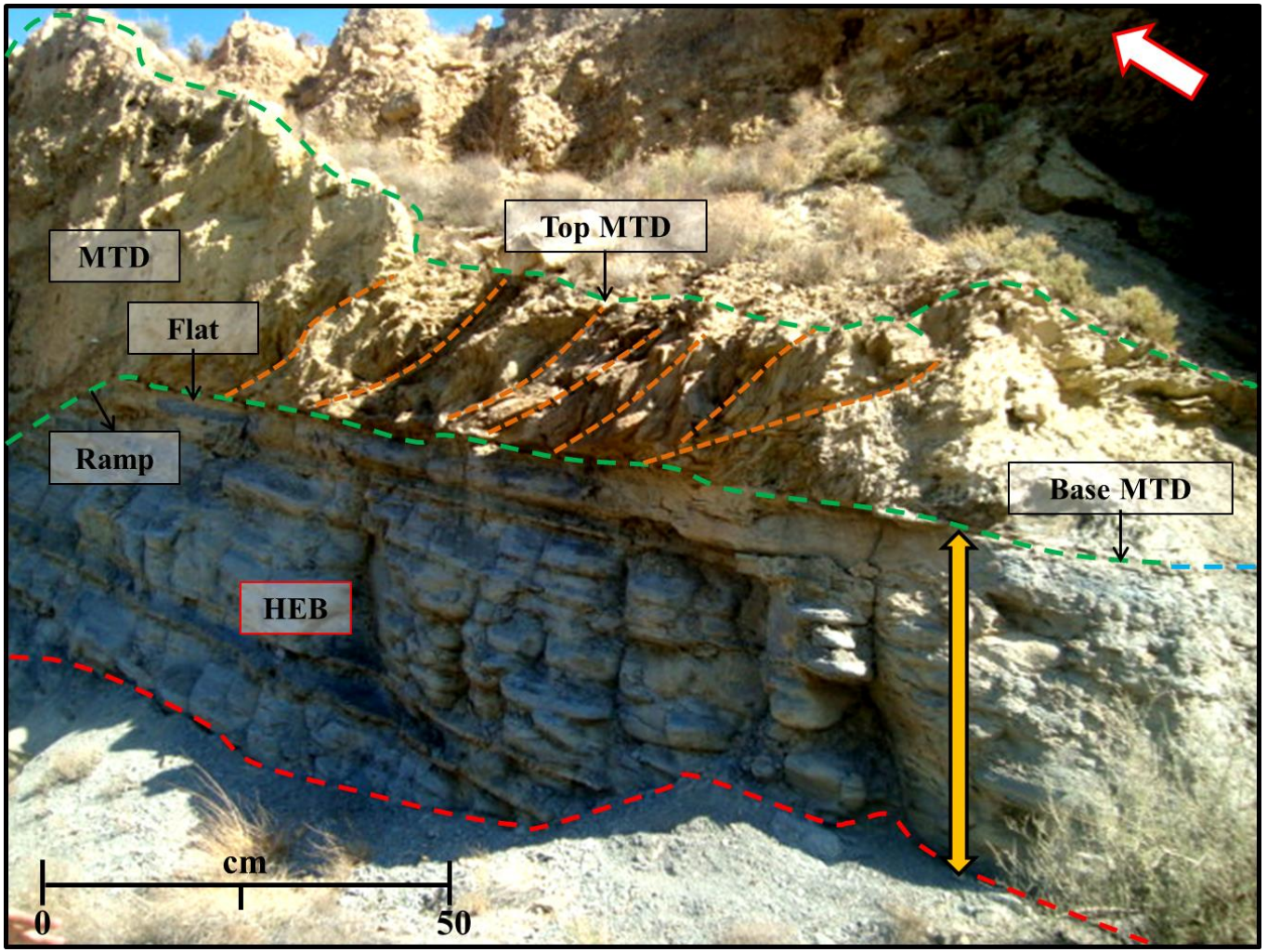

Figure 7.18: Example of a basal ramp of a mass-transport deposit from the Tabernas basin, Spain. The ramp is discordant to bedding and is thought to evolve through erosion of the top HEB unit. Based on the orientation of the thrust faults at the toe region of the MTD, the direction of transport was inferred south of the study area. N.B Picture was taken during the IAS summer School in Almeria, 2012.

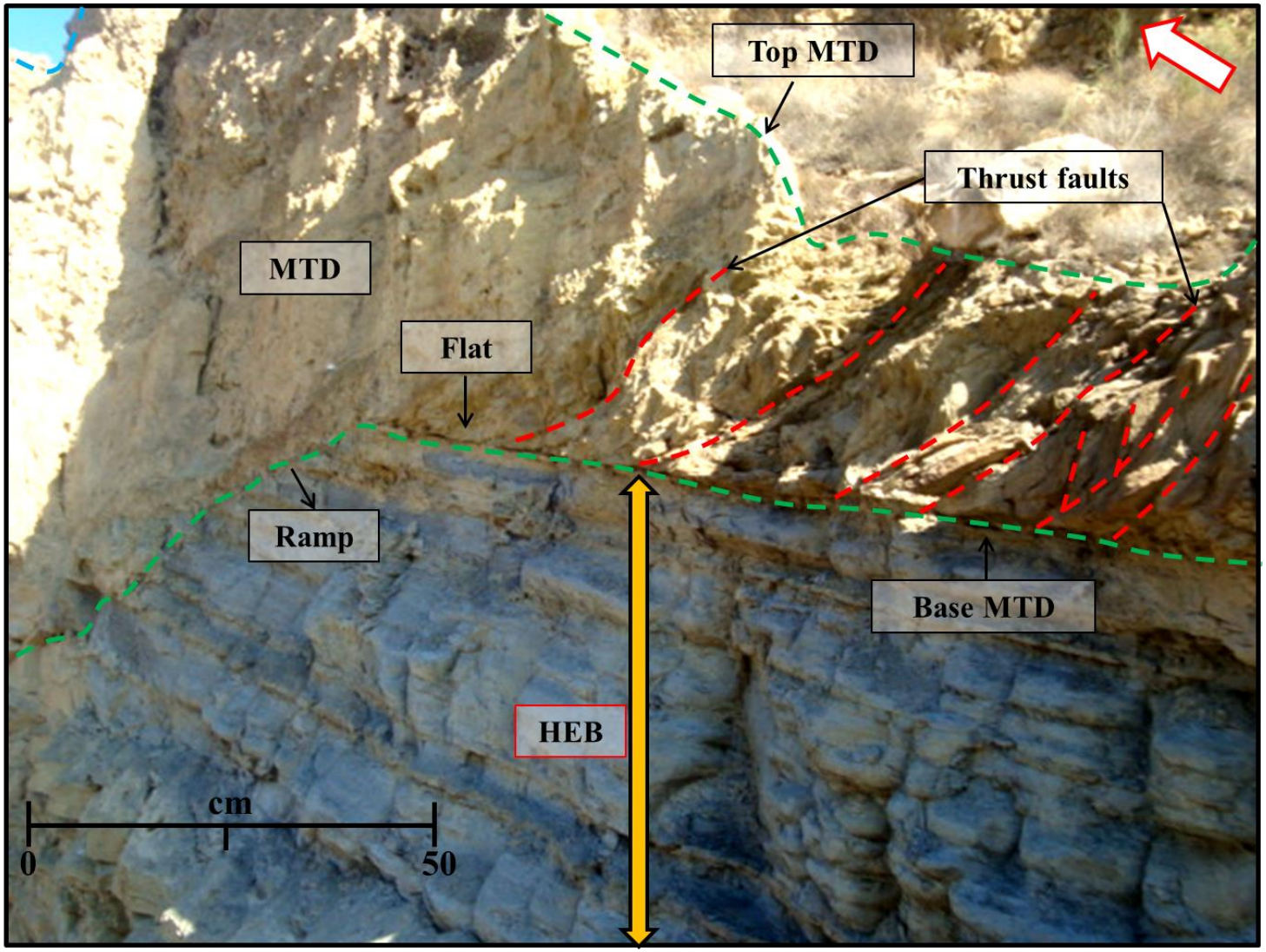

Figure 7.19: Another view to the ramp shown in Figure 7.14a. N.B: *Picture was taken during the IAS summer School in Almeria, 2012.*

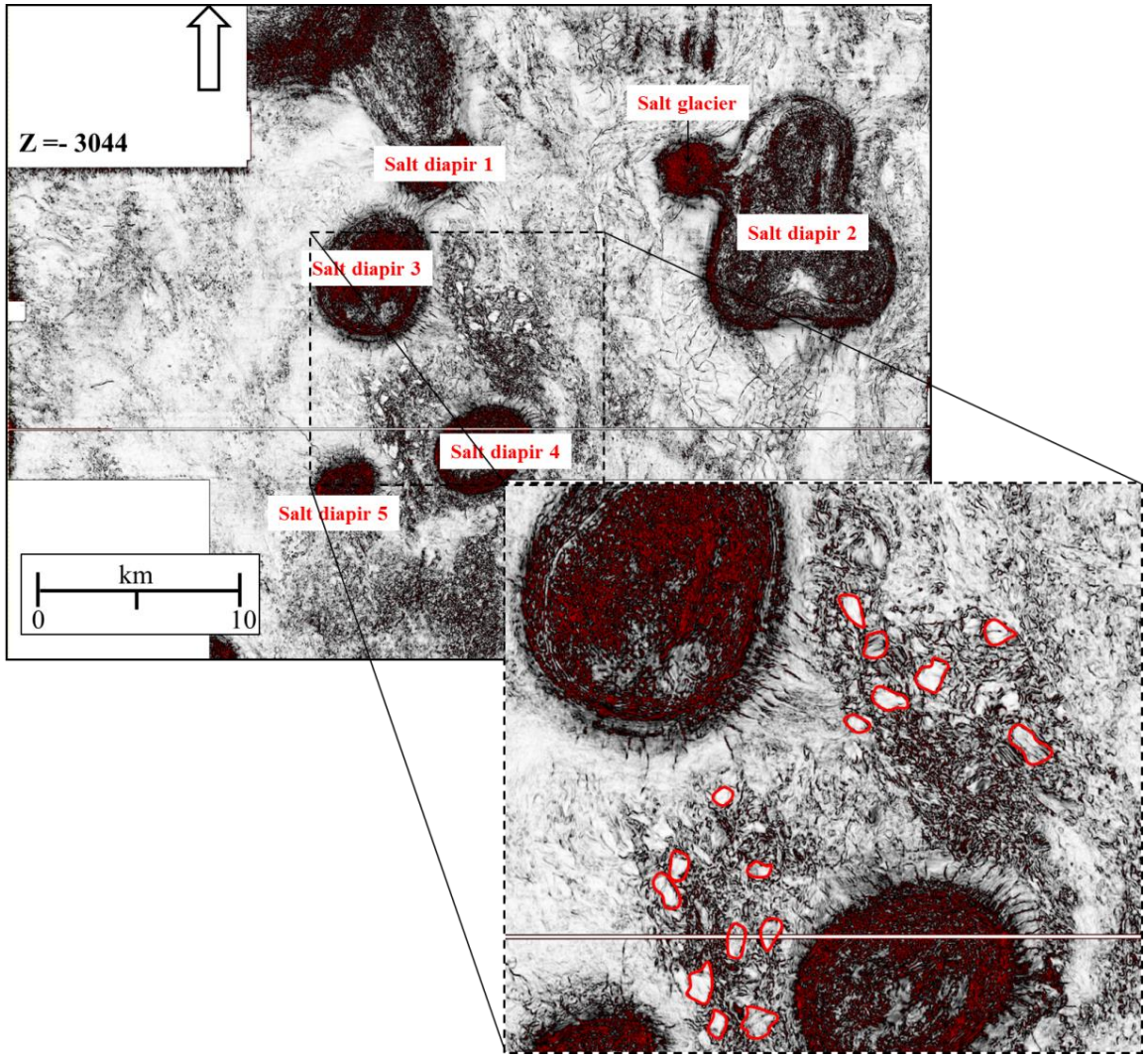

Figure 7.20: Example of rafted blocks displaying irregular size and shape with increasing distance from salt diapir in upper-mid continental slope of Espírito Santos basin.

7.5. Suggestion for future studies

Quite a number of assertions have been made in this thesis on the provenance, nature and interaction of MTDs with salt structures on the mid-slope of the Espírito Santo Basin. Nevertheless, there are still some open questions. Areas for future work that will provide extra understanding on some of the models and assertions from this work are described below:

a) Classification of locally- and distally-sourced MTDs - An integrated study of MTDs sourced directly from salt diapir crests is imminent from this work. In Chapter 4, three conditions of correlation coefficient were proposed to assess the timing of salt growth and sedimentation. The BES-200 data shows diapirs with their crest exposed at the sea floor (Figure 7.15). Some of the associated MTDs have similar seismic facies character relative to the salt and at first glance are imagined to be sourced from the diapir crest (Figure 7.15). This scenario presents an opportunity to further investigate the reliability of the regression analysis at providing information and links between active/passive diapirism and sedimentation. The physics of MTDs directly sourced from diapir crest is still sparsely investigated.

b) Statistical reassessments of the degree of remobilisation and internal reconfiguration of rafted blocks - The rafted blocks interpreted in Chapter 4 displayed increasing size with distance and transport along slope. However, this work asserted that the shape of the blocks is not commensurate with transport distance. Hence, the shape of rafted blocks is a non-diagnostic provenance tool. However, the blocks shown in Figure 7.20 which are from a section of the

Espírito Santo Basin do not show any definite pattern with transporting distance providing some impetus to investigate the suitability of size as a criterion to assess the stages of evolution of MTDs. In order to unravel this enigma, additional statistical analyses would be required. For example, correlating the morphometry of the blocks with distance and increasing diameter of salt structures. Future work should also incorporate observations at both seismic and outcrop scale. Quite a number of outcrops exist in Chile, Argentina, Crete, Norway, Italy and Spain (See Figure 7.16 and Figure 7.17). The overall objective is to establish a model where block size and shape decreases with remobilization. In addition, a seismic study to evaluate, isolate and automatically quantify the volume of the rafted blocks can be developed. This workflow may include some volume rendering and RGB blending techniques. The economic aspect of the study will include an evaluation of the fluid-flow properties of faulted blocks as either conduit or baffles to hydrocarbon.

c) Strain analysis of ramps and flat at outcrop scales – The mode of formation suggested for the ramps in this study requires additional observation from complementary seismic and outcrop data. Example of high resolution outcrop data includes ramps preserved at the base of some MTDs in the Tabernas Basin, Spain (Figure 7.18 and Figure 7.19). Mapping outcrop exposures will provide an opportunity to understand the behaviour of ramps at outcrop scales, differentiating them from tectonic ramps, and also to elucidate their character as strain markers. The findings from the study can be integrated and upscale into our model for ramps and flats.

d) Character of restricted and non-restricted faults: This work shows that there are conflicting opinions on the throw and displacement character of restricted and M-type faults. Though it is difficult to observe the true dimensionality of faults at outcrop, the potential of MTDs as barrier to fault propagation can be numerically modelled or stimulated in the laboratory. To achieve this, new research will require abundant datasets that should include well, seismic, geotechnical, outcrop and high resolution petrophysical data.

e) Reservoir potential of blocky debris flow deposits - Blocky-debris flow deposits result from hyper-concentrated debris flow conveying out-sized blocks, possibly representing the link between slumps and debris-flow deposits (Mutti et al., 2006). The aim of this future research theme is to study exposed blocky debris flows in the Northern Apennines and Tabernas Basin, understanding the lithological and structural variability within individual blocks, their spatial recurrence, and facies types. In turn, use the outcrop model to examine seismic-facies end members interpreted in blocky debris flow deposits in the Espírito Santo Basin, SE Brazil.

The outcrops in the Northern Apennine (Specchio Unit) and Tabernas Basin are classic examples of Oligocene-Miocene blocky debris flow deposits and offer unique exposures to understand the textural and structural complexities of these deposits and others elsewhere in the world. In order to achieve the set objectives, a geological mapping of lithofacies and faults in individual blocks should be undertaken. Lithological descriptions include records of the degree of sorting and matrix heterogeneity. In addition, thin sections of selected lithofacies must be attained to understand the micro-scale textural architecture. Structural

characterization of the faults will include throw pattern and displacement profiles with a view to understand their sealing capacity. This study is important to characterise blocky debris flow deposits as hydrocarbon reservoirs. On seismic profiles, debris flows have very low amplitude and such are thought to be mud-prone. In contrast, some of the blocks have preserved the original stratigraphy in some degree and show high-amplitude strata, potentially an indication of sand-prone reservoir targets sourced from siliciclastic material.

f) Characterising enigmatic high-amplitude anomalies in the Espírito Santo Basin - In the study area, high-amplitude anomalies are sandwiched within graben structures beneath the three MTDs in Chapter 6. These anomalies may imply the presence of a complete trapping and sealing system for hydrocarbons if they are DHI's. The anomalies are flat and discordant with structural reflectors and therefore imagined as flat spots. The caveat is that anomalies seen as flat spots can arise from other sources such as Opal-A to Opal-CT diagenetic boundaries, volcanic sills, or ocean bottom multiples. A detailed analysis of the high-amplitude anomalies discovered in the study area is given in a manuscript submitted to "SEG/AAPG Interpretation" journal. Further work is intended to be done on this subject. The aim of this work will include characterising several high-amplitude anomalies found within the datasets and proposing a workflow for visualising and extracting them. The main justification for relating the DHIs in this work to hydrocarbon contacts is their apparent restraint by faults forming the graben structures, their random distribution at differing stratigraphic levels and brightness which is suggestive of increasing amplitude with offset. *N.B: Submitted manuscript to "Interpretation" an AAPG and SEG journal*

References

Aksu, A., Hiscott, R.., 1989. Slides and debris flows on the high-latitude continental slopes of Baffin Bay. Geology 17, 885–888.

Allan, U.S., 1989. Model for hydrocarbon migration and entrapment within faulted structures. AAPG Bulletin 73, 803-811.

Alsop, G.I., 1996. Physical modelling of fold and fracture geometries associated with salt diapirism, G.I. Alsop, D. Blundell and I. Davison (Eds.), Salt Tectonics. Geological Society, London, Special Publications, pp. 227--241.

Alves, T. M., K. Kurtev, G. F. Moore, M Strasser, 2004. Assessing the internal character, reservoir potential, and seal competence of mass-transport deposits using seismic texture: A geophysical and petrophysical approach. AAPG Bulletin, DOI:10.1306/09121313117.

Alves, T.M., 2010. 3D Seismic examples of differential compaction in mass-transport deposits and their effect on post-failure strata. Mar. Geol. 271, 212–224.

Alves, T.M., 2012. Scale-relationships and geometry of normal faults reactivated during gravitational gliding of Albian rafts (Espírito Santo Basin, SE Brazil). Earth Planet. Sci. Lett. 331-332, 80–96.

Alves, T.M., Cartwright, J., Davies, R.J., 2009. Faulting of salt-withdrawal basins during early halokinesis: Effects on the Paleogene Rio Doce Canyon system (Espírito Santo Basin, Brazil). AAPG Bull. 93, 617–652.

Alves, T.M., Cartwright, J.A., 2009. Volume balance of a submarine landslide in the Espírito Santo Basin, offshore Brazil: Quantifying seafloor erosion, sediment accumulation and depletion. Earth Planet. Sci. Lett. 288, 572–580.

Alves, T.M., Strasser, M., G.F Moore, 2014. Erosional features as indicators of thrust fault activity (Nankai Trough, Japan): Marine Geology, doi:10.1016/j.margeo.2013.07.011.

Anderson, E.M., 1936. The dynamics of the formation of cone-sheets, ring-dykes, caldron-substances. Proceeding of the Royal Society of Edinburgh, pp. 128-157.

Apotria, T., R. Lindholm, W. Metner, M. Eze1, D. Gunn, J. Geslin, P. Rumelhart, F. Goulding, and S. Mitchell, 2004, Volume interpretation of shelf collapse processes and Biafra "disturbed" reservoirs, eastern Niger Delta joint venture: AAPG International Conference,

Apotria, T., R. Lindholm, W. Metner, M. Eze1, D. Gunn, J. Geslin, P. Rumelhart, F. Goulding, and S. Mitchell, 2004, Volume interpretation of shelf collapse

processes and Biafra “disturbed” reservoirs, eastern Niger Delta joint venture: AAPG International Conference,

Aridhi, K., Bagga, M.A.O., Abdeljaouad, S., Zargouni, F., Mercier, E., 2011. Lateral ramp-related folding evidences in the Tellian domain of Tunisia: Tectonic implications. Comptes Rendus Geoscience 343, 360-369.

Armentrout, J., 2003. Timing of late Pleistocene shelf-margin deltaic depositional and mass-transport events, East Breaks 160–161 shelf-edge minibasin, Gulf of Mexico,, in: H. H. Roberts, N. C. Rosen, R. H. Fillon, and J. B. Anderson, Eds., Shelf Margin Deltas and Linked down Slope Petroleum Systems: Global Significance and Future Exploration Potential: Gulf Coast Section. Presented at the SEPM 23rd Annual Research Conference, SEPM, pp. 91–114.

Armitage, D.A, B.W Romans, J.A Covault. S.A Graham, 2009. The influence of Mass-Transport deposit surface topography on the evolution of Turbidite Architecture: The Sierra Contreras, Tres Paso Formation (cretaceous), southern Chile. Journal of Sedimentary Research, V.79: 287-301.

Assier-Rzadkiewicz, S., Heinrich, P., Sabatier, P.C., Savoye, B., Bourillet, J.F., 2000. Numerical modelling of a landslide-generated tsunami: the 1979 Nice event. Pure and Applied Geophysics 157, 1717-1727.

Axen, G.J., 1993. Ramp-flat detachment faulting and low-angle normal reactivation of the Tule Springs thrust, southern Nevada. Geological Society of America Bulletin 105, 1076-1090.

Bacon, M., Simm, R., Redshaw, T., 2007. 3-D Seismic Interpretation. Cambridge University Press.

Badley, M.E., 1985. Practical Seismic Interpretation. International Human Resource Development, Boston MA.

Bahorich, M., Farmer, S., 1995. 3-D seismic discontinuity for faults and stratigraphic features: The coherence cube. Lead. Edge 14, 1053–1058.

Baldschuhn, R., Best, G., Kockel, F., 1991. Inversion tectonics in the north-west German basin, Spencer, A.M. (Ed.), Generation, Accumulation, and Production of Europe's Hydrocarbons. European Association of Petroleum Geoscientists, Special Publication, pp. 149-159.

Barker, P.., Buffler, R.., Gamboa, L.., 1983. A Seismic Reflection Study of the Rio Grande Rise,. in Barker, P. F., Carlson, R. L. and Hohnson, D. A. (eds) Initial

reports of the Deep Sea Drilling Program: Washington, D.C., Government Printing Office 499–517.

Barley, B., 1999. Deepwater problems around the world. Lead. Edge 18, 488–494.

Barnett, J.A., Mortimer, J., Rippon, J.H., Walsh, J.J., Watterson, J., 1987. Displacement geometry in the volume containing a single normal fault. AAPG Bull. 71, 925–937.

Basir, H.M., Javaherian, A., Yaraki, M.T., 2013. Multi-attribute ant-tracking and neural network for fault detection: a case study of an Iranian oilfield. J. Geophys. Eng. 10, 015009.

Baudon, C., Cartwright, J., 2008a. The kinematics of reactivation of normal faults using high resolution throw mapping. J. Struct. Geol. 30, 1072–1084.

Baudon, C., Cartwright, J.A., 2008b. 3D seismic characterisation of an array of blind normal faults in the Levant Basin, Eastern Mediterranean. J. Struct. Geol. 30, 746–760.

Beach, A., 1979. The analysis of deformed belemnites. Journal of Structural Geology 1, 127-135.

Beach, A., Lawson Brown, J., Brockbank, P.J., Knott, S.D., McCallum, J.E., Welbon, A.I., 1997. Fault seal analysis of SE Asian basins with examples from West Java. Geol. Soc. Lond. Spec. Publ. 126, 185–194.

Beaman, R.J., Harris, P.T., 2003. Seafloor morphology and acoustic facies of the George V Land shelf. Deep Sea Research Part II: Topical Studies in Oceanography 50, 1343-1355.

Beauboeuf, R.., Friedman, J.., 2000. High resolution seismic/sequence stratigraphic framework for the evolution of Pleistocene intra slope basins, western Gulf of Mexico: depositional models and reservoir analogs. Gulf Coast Section,, in: Deep-Water Reservoirs of the World. Presented at the SEPM, 20th Annual Research Conference, SEPM, pp. 40–60.

Biddle, K.., Christie-Blick, N., 1985. Glossary-strike-slip deformation, basin formation, and sedimentation., in: Biddle, K.T., Christie-Blick, N. (Eds.), Strike-Slip Deformation, Basin Formation, and Sedimentation. Special Publication Society of Economic Mineralogists, pp. 375–386.

Bigarella, J.., Alessi, A.., Becker, R.., Duarte, J.., 1969. Textural characteristics of the coastal dune, sand ridge, and beach sediments. Bol. Parana. Geociências 15–80.

Bishop, D.J., 1996. Regional distribution and geometry of salt diapirs and supra-Zechstein Group faults in the western and central North Sea. Marine and Petroleum Geology 13, 355-364.

Boe, R., Hovland, M., Instanes, A., Rise, L., Vassus, S., 2000. Submarine slide scars and mass movements in Karmsundet and Skudenesfjorden, southwestern Norway: morphology and evolution. Marine Geology 167, 147-165.

Borradaile, G.J., 1984. Tectonic strain of a deformed conglomerate determined from a single pebble. Tectonophysics 104, 183-186.

Bouriak, S., Vanneste, M., Saoutkine, A., 2000. Inferred gas hydrates and clay diapirs near the Storegga Slide on the southern edge of the Voring Plateau, offshore Norway. Mar. Geol. 163, 165.

Brown, A., 2004. Interpretation of Three-Dimensional Seismic Data, Sixth. ed. American Association of Petroleum Geologists (AAPG), Tulsa.

Bruhn, C.H.., Walker, R.., 1997. Internal architecture and sedimentary evolution of coarse-grained, turbidite channel-levee complexes, early Eocene Regência Canyon, Espírito Santo Basin, Brazil. Sedimentology 44, 14–46.

Brun, J.-P., Fort, X., 2004. Compressional salt tectonics (Angolan margin). Tectonophysics 382, 129-150.

Brun, J.-P., Fort, X., 2011. Salt tectonics at passive margins: Geology versus models. Mar. Pet. Geol. 28, 1123–1145.

Bruso, J. M. Jr., S. I. Getz, and R. L. Wallace, 2004, Geology will support further discoveries in Gulf of Guinea's Golden Rectangle: Oil & Gas Journal

Bryant, E., 1982. Behaviour of grain size characteristics on reflective and dissipative foreshores, Broken Bay, Australia. J. Sediment. Pet. 52, 431– 450.

Bryn, P., Berg, K., Forsberg, C.., Solheim, A., Kvalstad, T.., 2005. Explaining the Storegga Slide. Mar. Pet. Geol. 22, 11–19.

Buchanan, J.., Buchanan, P.., 1995. Basin Inversion, in: Geological Society, London, Special Publications. p. 596.

Budetta, P., De Riso, R., 2004. The mobility of some debris flows in pyroclastic deposits of the northwestern Campanian region (southern Italy). Bull Eng Geol Env. 63, 293–302.

Bull, S., Cartwright, J., Huuse, M., 2009. A review of kinematic indicators from mass-transport complexes using 3D seismic data. Mar. Pet. Geol. 26, 1132–1151.

Butler, R.W.., Turner, J.., 2010. Gravitational Collapse at Continental Margins: Products and Processes; an Introduction. J. Geol. Soc. Lond. 167, 569–570.

Camenlerghi, A. 2013. Submarine Geohazards, EGU General Assembly, Vienna.

Canals, M., Lastras, G., Urgeles, R., Casamor, J., Mienert, J., Cattaneo, A., De Batist, M., Haflidason, H., Imbo, Y., Laberg, J.S., Locat, J., Long, D., Longva, O., Masson, D.G., Sultan, N., Trincardi, F., Bryn, P., 2004. The slope failure dynamics and impacts from seafloor and shallow sub-seafloor geophysical data: case studies from the COSTA project. Marine Geology 213, 9-72.

Canérot, J., Hudec, M.R., Rockenbauch, K., 2005. Mesozoic diapirism in the Pyrenean orogen: salt tectonics on a transform plate boundary. AAPG Bulletin 89, 211-229.

Cartwright, J., Huuse, M., Aplin, A., 2007. Seal bypass systems. AAPG Bull. 91, 1141–1166.

Cartwright, J.A., Mansfield, C.S., 1998. Lateral displacement variation and lateral tip geometry of normal faults in the Canyonlands National Park, Utah. J. Struct. Geol. 20, 3–19.

Cartwright, J.A., Trudgill, B.D., Mansfield, C.S., 1995. Fault growth by segment linkage: an explanation for scatter in maximum displacement and trace length data from the Canyonlands Grabens of SE Utah. J. Struct. Geol. 17, 1319–1326.

Casagli, N., Ermini, L., Rosati, G., 2003. Determining grain size distribution of the material composing landslide dams in the Northern Apennines: sampling and processing methods. Eng. Geol. 69, 83–97.

Cattaneo, A., Correggiari, A., Marsset, T., Thomas, Y., Marsset, B., Trincardi, F., 2004. Seafloor undulation pattern on the Adriatic shelf and comparison to deep-water sediment waves. Marine Geology 213, 121-148.

Chang, H.K., Kowsmann, R.O., Figueiredo, A.M.F., Bender, A., 1992. Tectonics and stratigraphy of the East Brazil Rift system: an overview. Tectonophysics 213, 97–138.

Changwei, Y., Jianjing, Z., Zing, Z., 2013. A prediction model for horizontal run-out distance of landslides triggered by Wenchuan earthquake. Earthq Eng Eng Vib 12, 201–208.

Childs, C., Sylta, ø., Moriya, S., Morewood, N., Manzocchi, T., Walsh, J.J., Hermanssen, D., 2009. Calibrating fault seal using a hydrocarbon migration model of the Oseberg Syd area, Viking Graben. Mar. Pet. Geol. 26, 764–774.

Chopra, S., Marfurt, K.J., 2005. Seismic attributes — A historical perspective. Geophysics 70, 3SO.

Clarke, S.M., Burley, S.D., Williams, G.D., 2005. A three-dimensional approach to fault seal analysis: fault-block juxtaposition & argillaceous smear modelling. Basin Res. 17, 269–288.

Clayton, C. A., M. F. Cohen, M. Anis, T. W. Cooley, M. M. Honarpour, J. P. Wallace, and M. R. Chambers, 1998, Ubit field rejuvenation: A case history of reservoir management of a giant oil field, offshore Nigeria: Society of Petroleum Engineers Annual Technical Conference and Exhibition, doi:10.2118/49165-MS.

Cobbold, P.R., Chiossi, D., Green, P.F., Japsen, P., Bonow, J., 2010. Compressional Reactivation, Atlantic Margin of Brazil: Structural Styles and Consequences for Hydrocarbon Exploration. Search Discov. 30114.

Cobbold, P.R., Meisling, K.E., Mount, V.S., 2001. Segmentation of an obliquely rifted margin, Campos and Santos basins, southeastern Brazil. AAPG Bull. 85, 1903–1924.

Colletini, C., Niemeijer, A., Viti, C., Marone, C., 2009. Fault zone fabric and fault weakness: Nature. Nature 462, 907–910.

Conway, K.W., Barrie, J.V., and Thomson, R.E., 2012. Submarine slope failures and tsunami hazard in coastal British Columbia: Douglas Channel and Kitimat Arm; Geological Survey of Canada, Current Research 2012-10, 13 p. doi: 10.4095/29173

Cowie, P., 1998. Normal fault growth in three-dimensions in continental and oceanic crust, in Faulting and Magmatism at Mid-Ocean Ridges: Geophys. Monogr., American Geophysical Union 106, 325–348.

Cox, T. and Seitz, K., 2007, Ant Tracking Seismic Volumes for Automated Fault Interpretation in Petrel, CSEG Expanded abstract, 670-671

Dandapath, S., Chakraborty, B., Maslov, N., Karisiddaiah, S.M., Ghosh, D., Fernandes, W., Menezes, A., 2012. Characterization of seafloor pockmark seepage of hydrocarbons employing fractal: A case study from the western continental margin of India. Marine and Petroleum Geology 29, 115-128.

Davison, I., 2004. Bathymetric controls on Paleocene gravity flows around salt domes in the Central Graben, North Sea, 24th Annual Meeting, Bob Perkins Research Conference, pp. 1031-1044.

Davison, I., 2007. Geology and tectonics of the South Atlantic Brazilian salt basins., in: A.C. Ries, R.W.H. Butler and R.H. Graham (Eds.), Deformation of the Continental Crust: The Legacy of Mike Coward. Geological Society, London, Special Publications, pp. 345–359.

Davison, I., Alsop, G.I., Evans, N.G., Safaricz, M., 2000a. Overburden deformation patterns and mechanisms of salt diapir penetration in the Central Graben, North Sea. Marine and Petroleum Geology 17, 601-618.

Davison, I., Alsop, I., Birch, P., Elders, C., Evans, N., Nicholson, H., Rorison, P., Wade, D., Woodward, J., Young, M., 2000b. Geometry and late-stage structural evolution of Central Graben salt diapirs, North Sea. Mar. Pet. Geol. 17, 499–522.

Dawers, N.H., Anders, M.H., 1995. Displacement-length scaling and fault linkage. J. Struct. Geol. 17, 607–614.

De Paor, D.G., 1986. Orthographic analysis of geological structures—II. Practical applications. Journal of Structural Geology 8, 87-100.

Demercian, S., Szatmari, P., Cobbold, P.R., 1993. Style and pattern of salt diapirs due to thin-skinned gravitational gliding, Campos and Santos basins, offshore Brazil. Tectonophysics 228, 393-433.

Deptuck, M.E., Sylvester, Z., Pirmez, C., O'Bryne, C., 2007. Migration aggradation history and 3-D seismic geomorphology of submarine channels in the Pleistocene Benin-major Canyon, western Niger Delta slope. Marine Geology 24, 406-433.

Dikau, R., Cavallin, A., Jäger, S., 1996. Data bases and GIS for landslide research in Europe. Geomorphology 15, 227-239.

Dingle, R.., 1977. The anatomy of a large submarine slump on a sheared continental margin (SE Africa). J. Geol. Soc. Lond. 134, 293–310.

Dobkins, J.., Folk, R.., 1970. Shape development on Tahiti-Nui. J. Sediment. Pet. 40, 1167–1203.

Docherty, C., Sugrue, M., Willacy, C., Strong, A., 1999. Sub-salt imagery and structure recognition using Pre-SDM. World Oil 220, 80-83.

Dott, R.., 1963. Dynamics of subaqueous gravity depositional processes. AAPG Bull. 47, 104–128.

Duarte, C.., Viana, A., 2007. Santos drift system: stratigraphic organization and implications for late Cenozoic palaeocirculation in the Santos Basin, SWAtlantic

Ocean. In: Viana, A., Rebesco, M. (Eds.), Economic and Palaeoceanographic Significance of Contourite Deposits. Geol Soc Lond. Spec Pub 276, 171–198.

Dunlap, D.B., Wood, L.J., Weisenberger, H., Jabour, H., 2010. Seismic geomorphology of offshore Morocco's east margin, Safi Haute Mer area. AAPG Bulletin 94, 615-642.

Dunnet, D., 1969. A technique of finite strain analysis using elliptical particles. . Tectonophysics 7, 117–136.

Dunning, S.., 2006. The Grain size distribution of Rock-Avalanche deposits in valley-confined settings. Ital. J. Eng. Geol. Environ. 117–121.

Dupré, S., Woodside, J., Foucher, J.-P., de Lange, G., Mascle, J., Boetius, A., Mastalerz, V., Stadnitskaia, A., Ondréas, H., Huguen, C., Harmégnies, F., Gontharet, S., Loncke, L., Deville, E., Niemann, H., Omoregie, E., Olu-Le Roy, K., Fiala-Medioni, A., Dählmann, A., Caprais, J.-C., Prinzhofer, A., Sibuet, M., Pierre, C., Damsté, J.S., 2007. Seafloor geological studies above active gas chimneys off Egypt (Central Nile Deep Sea Fan). Deep Sea Research Part I: Oceanographic Research Papers 54, 1146-1172.

Dykstra, M. et al., 2011. Mass-transport deposits: combining outcrop studies and seismic forward modeling to understand lithofacies distributions, deformation, and their seismic stratigraphic expression. In: C. Shipp, P. Weimer and H. Posamentier (Eds.), Mass-transport deposits in deepwater settings. SEPM Special Publication 96, pp. 293-310.

Dykstra, M., 2005. Dynamics of Sediment Mass-Transport from the Shelf to the Deep Sea. University of California, Santa Barbara, p. 152.

Dykstra, M., 2006. Review of Submarine Slope Systems: Processes and Products, in: D.M. Hodgson and S.S. Flint. Journal of Sedimentary Research, p. 232.

Erismann, T.H., Abele, G., 2001. Dynamics of Rockslides and Rockfalls. Springere Verlag, New York.

Evans, O.., 1939. Sorting and transportation of material in swash and backwash. J. Sediment. Pet. 9, 28–31.

Evans, O.., 1939. Sorting and transportation of material in swash and backwash. J. Sediment. Pet. 9, 28–31.

Fairbairn, C.., Ward, W.., 1984. The Use of High-pass Filtering to Aid Detection of Small Reflector Discontinuities. Presented at the 46th Meeting of European Association of Exploration Geophysicists, London.

Faulkner, D.R., Jackson, C.A.L., Lunn, R.J., Schlische, R.W., Shipton, Z.K., Wibberley, C.A.J., Withjack, M.O., 2010. A review of recent developments concerning the structure, mechanics and fluid flow properties of fault zones. J. Struct. Geol. 32, 1557–1575.

Fiduk, J.C., Brush, E.R, Anderson, L.E, Gibbs, P.B, Rowan, M.G.,, 2004. Salt deformation, magmatism, and hydrocarbon prospectivity in the Espírito Santo Basin, offshore Brazil, in: In Post, P. J. (eds) Salt-Sediment Interactions and Hydrocarbon Prospectivity: Concepts, Applications, and Case Studies for the 21st Century, Gulf Coast Sect., Soc. of Sediment. Geol., Houston, Tex. pp. 370 – 392.

Fieller, E.., Hartley, H.., Pearson, E.., 1957. Tests for rank correlation coefficients. Biometrika 44, 470–481.

Fine, I.V., Rabinovich, A.B., Bornhold, B.D., Thomson, R.E., Kulikov, E.A., 2005. The Grand Banks landslide-generated tsunami of November 18, 1929: preliminary analysis and numerical modelling. Marine Geology 215, 45-57.

Fisher, Q.J., Harris, S.D., McAllister, E., Knipe, R.J., Bolton, A.J., 2001. Hydrocarbon flow across faults by capillary leakage revisited. Mar. Pet. Geol. 18, 251–257.

Flinn, D., 1956. On the deformation of the Funzie Conglomerate, Fetlar, Shetland. Journal of Geology 64, 480–505.

Fort, X., Brun, J.P., Chauvel, F., 2004. Contraction induced by block rotation above salt (Angolan margin). Marine and Petroleum Geology 21, 1281-1294.

Fossen, H., 2010. Structural Geology. Cambridge University Press.

Fossen, H., Bale, A., 2007. Deformation bands and their influence on fluid flow. AAPG Bull. 91, 1685–1700.

Franca, R.., Del Rey, A.., Tagliari, C.., Brandao, J.., Fontanelli, P.., 2007. Bacia de Espírito Santo. Boletim de Geociencias da Petrobras, 15, 501-509.

Freeman, B., Yielding, G., Needham, D.T., Badley, M.E., 1998. Fault seal prediction: the gouge ratio method. Geol. Soc. Lond. Spec. Publ. 127, 19–25.

Frey Martinez, J., 2010. 3D seismic interpretation of mass transport deposits: implications for basin analysis and geohazard evaluation., in: Submarine Mass Movements and Their consequences.Advances in Natural and Technological Hazards Research. pp. 553–568.

Frey Martinez, J., Cartwright, J., Hall, B., 2005. 3D seismic interpretation of slump complexes: examples from the continental margin of Israel. Basin Research 17, 83-108.

Frey-Martínez, J., Cartwright, J., James, D., 2006. Frontally confined versus frontally emergent submarine landslides: A 3D seismic characterisation. Marine and Petroleum Geology 23, 585-604.

Fryer, G.., Watts, P., Pratson, L.F., 2004. Source of the great tsunami of 1 April 1946; a landslide in the upper Aleutian forearc. Mar. Geol. 203, 201–218.

Gafeira, J., Bulat, J., Evan, D., 2007. The southern flank of the Storegga Slide: imaging and geomorphological analyses using 3D seismic. Springer, pp. 57-66.

Gamberi, F., Rovere, M., Marani, M., 2011. Mass-transport complex evolution in a tectonically active margin (Gioia Basin, Southeastern Tyrrhenian Sea). Mar. Geol. 279, 98–110.

Gamboa, D., Alves, T., Cartwright, J., 2011. Distribution and characterization of failed (mega)blocks along salt ridges, southeast Brazil: Implications for vertical fluid flow on continental margins. J. Geophys. Res. 116.

Gamboa, D., Alves, T., Cartwright, J., Terrinha, P., 2010. MTD distribution on a 'passive' continental margin: The Espírito Santo Basin (SE Brazil) during the Palaeogene. Marine and Petroleum Geology 27, 1311-1324.

Gardner, J., Prior, D., Field, M., 1999. Humboldt slide – a large shear-dominated retrogressive slope failure. Marine Geology 154, 323-338.

Gawthorpe, R.L., Clemmey, H., 1985. Geometry of submarine slides in the Bowland Basin (Dinantian) and their relation to debris flows. Journal of Geological Society of London 142, 555-565.

Gee, M.J.R., Gawthorpe, R.L., 2006a. Submarine channels controlled by salt tectonics: Examples from 3D seismic data offshore Angola. Mar. Pet. Geol. 23, 443–458.

Gee, M.J.R., Gawthorpe, R.L., Friedman, J.., 2006b. Triggering and evolution of a giant submarine landslide, offshore Angola, revealed by 3D seismic stratigraphy and geomorphology. J. Sediment. Res. 76, 9–19.

Gee, M.J.R., Gawthorpe, R.L., Friedmann, J.S., 2005. Giant striations at the base of a submarine landslide. Mar. Geol. 214, 287–294.

Gee, M.J.R., Masson, D.., Watts, A.., Allen, P.., 1999. The Saharan Debris Flow: An Insight into the Mechanics of Long Runout Submarine Debris Flows. Sedimentology 46, 317–335.

Gibbs, P.., Brush, E.., Fiduk, 2003. The evolution of the syn rift and transition phase of the central/southern Brazilian and W. African conjugate margins: the implications for source rock distribution in time and space, and their recognition on seismic data: Presented at the Eighth International Congress of the Brazillian Geophysical Society,, Rio de Janeiro, pp. 1–7.

Giles, K.A., Lawton, T.F., 2002. Halokinetic sequence stratigraphy adjacent to the El Papalote diapir, northeastern Mexico. AAPG Bulletin 86, 823-840.

Glade, T., Anderson, M., Crozier, M.., 2005. Landslide Hazard and Risk. John Wiley & Sons, Ltd., Chichester, UK.

Goldfinger, C., Kulm, L.., McNeill, L.., Watts, P., 2000. Super-scale failure of the southern Oregon Cascadia Margin. Pure Appl. Geophys. 157, 1189–1226.

Goncharov, A., Nelson, G., 2012. From two way time to depth and pressure for interpretation of seismic velocities offshore: Methodology and examples from the Wallaby Plateau on the West Australian margin. Tectonophysics 572–573, 26-37.

Greenwood, B., 1978. Spatial variability of texture over a beach dune complex, North Devon, England. Sediment. Pet. 21, 27–44.

Grocott, J., McCaffrey, K. J. W., Taylor, G. K., Tikoff, B.2004.Vertical coupling and decoupling in the lithosphere. Geological Society, London, Special Publications, 227, 4, 1-7. http://dx.doi.org/10.1144/gsl.sp.2004.227.01.01.

Groshong, R.H., 2006. 3-D structural geology: a practical guide to quantitative surface and subsurface map interpretation; with 453 fig. and a CD-ROM. Springer, Berlin; Heidelberg [u.a.].

Guedes, C.C.., Giannini, P.C.., Nascimento Jr., D.., Sawakuchi, A.., Tanaka, A.P.., Rossi, M.., 2011. Controls of heavy minerals and grain size in a Holocene regressive barrier (Ilha Comprida, southeastern Brazil). J. South Am. Earth Sci. 31, 110–123.

Haflidason, H., Sejrup, H.P., Berstad, I.M., Nygard, A., Richter, T., Lien, R., Berg, K., 2003. A weak layer feature on the northern Storegga slide escarpment, In European margin sediment dynamics Mienert J, Weaver P.P.E. Springer, Berlin, Germany, pp. 55-62.

Haflidason, H., Sejrup, H.P., Nygård, A., Mienert, J., Bryn, P., Lien, R., Forsberg, C.F., Berg, K., Masson, D., 2004. The Storegga Slide: architecture, geometry and slide development. Mar. Geol. 213, 201–234.

Hampton, M.., Lee, H.., Locat, J., 1996. Submarine landslides. Rev. Geophys. 34, 33–59.

Haughton, P.D.W., Barker, S.P. and McCaffrey, W.D., 2003. 'Linked' debrites in sand-rich turbidite systems - origin and significance. Sedimentology, 50(3): 459-482.

Hayman, N.W., Kidd, W.S.F., 2002. Reactivation of prethrusting, synconvergence normal faults as ramps within the Ordovician Champlain-Taconic thrust system. Geological Society of America Bulletin 114, 476-489.

Heo, J.-H., Kho, Y.W., Shin, H., Kim, S., Kim, T., 2008. Regression equations of probability plot correlation coefficient test statistics from several probability distributions. J. Hydrol. 355, 1–15.

Hildebrand-Mittlefehldt, N., Oertel, G., 1980. Strain determination from the measurement of pebble shapes: the special case of a bent foliation. Tectonophysics 67, T1-T7.

Hiscott, R.., Aksu, A.., 1994. Submarine debris flows and continental slope evolution in front of Quaternary ice sheets, Baffin Bay, Canadian Arctic. AAPG Bull. 78, 445–460.

Hjelstuen, B.., Eldholm, O., Faleide, J.., 2007. Recurrent Pleistocene megafailures on the SW Barents Sea margin. Earth Planet. Sci. Lett. 258, 605–618.

Hockey, B., 1970. An improved coordinate system for particle shape representation. J. Sediment. Pet. 40, 1054–1056.

Howard, J.L., 1992. An evaluation of shape indices as palaeoenvironmental indicators using quartzite and metavolcanic clasts in Upper Cretaceous to Palaeogene beach, river and submarine fan conglomerates. Sedimentology 39, 471–486.

Hudec, M.R., Jackson, M.P.A., 2006. Growth of allochthonous salt sheets in passive margins and orogens. AAPG Bulletin 90, 1535-1564.

Hudec, M.R., Jackson, M.P.A., 2007. Terra infirma: Understanding salt tectonics. Earth-Science Reviews 82, 1-28.

Hudec, M.R., Jackson, M.P.A., 2009. Interaction between spreading salt canopies and their peripheral thrust systems. Journal of Structural Geology 31, 1114-1129.

Hühnerbach, V., Masson, D.G., Partners, C.., 2004. Landslides in the North Atlantic and its adjacent seas: an analysis of their morphology, setting and behaviour. Mar. Geol. 213, 343–362.

Hunerbach, V., Masson, D.., 2004. Landslides in the North Atlantic 646 and its adjacent seas: an analysis of their morphology, setting and behaviour. Mar. Geol. 213, 343–362.

Huvenne, V.A.I., Croker-Peter, F., Henriet, J.P., 2002. A refreshing 3D view of an ancient sediment collapse and slope failure. Terra Nova 14, 33-40.

Ilstad, T., De Blasio, F.V., Elverhøi, A., Harbitz, C.B., Engvik, L.E., Longva, O., Marr, J.G., 2004. On the frontal dynamics and morphology of submarine debris flows. Marine Geology 213, 481-497.

Imbo, Y., De Batist, M., Canals, M., Prieto, M.., Baraza, J., 2003. The Gebra Slide: a submarine slide on the Trinity Peninsula Margin, Antarctica: Mar. Geol. 193, 235–252.

Iverson, R.M., Reid, M.E., Iverson, N.R., LaHusen, R.G., Logan, M., Mann, J.E., Brien, D.L., 2000. Acute Sensitivity of Landslide Rates to Initial Soil Porosity. Science 290, 513-516.

Iverson, R.M., Reid, M.E., LaHusen, R.G., 1997. Debris-Flow Mobilization from Landslides. Annual Review of Earth and Planetary Sciences 25, 85-138.

Jackson, C.A.L. and Johnson, H.D., 2009. Sustained turbidity currents and their interaction

Jackson, C.A.L., Gawthorpe, R.L., Sharp, I.R., 2006. Style and sequence of deformation during extensional fault-propagation folding: examples from the Hamman Faraun and ElQaa fault blocks, Suez Rift, Egypt. J. Struct. Geol. 28, 519–535.

Jackson, M.P.A., Talbot, C.J., 1991. A glossary of salt tectonics. Geological Circular. The University of Texas at Austin, Bureau of Economic Geology.

Jakob, M., Hungr, O., 2005. Debris-flow Hazards and Related Phenomena. Springer-Praxis, Berlin; Heidelberg.

Japsen, P., 1994. Retarded compaction due to overpressure deduced from a seismic velocity/depth conversion study in the Danish Central Trough, North Sea. Marine and Petroleum Geology 11, 715-733.

Jennette, D.., Garfield, T.., Mohrig, D.., Cayley, G.., 2000. The interaction of shelf accommodation, sediment supply and sealevel in controlling the facies, architecture and sequence stacking patterns of the Tay and Forties/Sele basin-floor fans, Central North Sea, in: Deep-Water Reservoirs of the World: Gulf Coast Society of the Society of Economic Paleontologists and Mineralogists Foundation. Presented at the 20th Annual Research Conference, Weimer, P.,

Slatt, R.M., Coleman, J., Rosen, N.C., Nelson, H., Bouma, A.H., Styzen, M.J., and Lawrence, D.T.,, pp. 402–421.

Johnson, R.A., Bhattacharyya, G.K., 2010. Statistics: principles and methods. John Wiley & Sons, Hoboken, NJ.

Jones, R.M., Hillis, R.R., 2003. An integrated, quantitative approach to assessing fault-seal risk. AAPG Bull. 87, 507–524.

Kearey, P., Brooks, M., Hill, I., 2002. An introduction to geophysical exploration. Wiley- Blackwell.

Keefer, D.., 1994. The importance of earthquake-induced landslides to long-term slope erosion and slope-failure hazards in seismically active regions. Geomorphology 10, 265–284.

Kehle, R.O., 1988. The origin of salt structures, Schreiber, B.C. (Ed.), Evaporites and Hydrocarbons. Columbia University Press, New York, pp. 345-404.

Kendall, M.., Stuart, A., 1973. The Advanced Theory of Statistics. In: Inference and Relationship. Griffin, ISBN 0-85264-215-6 (Sections 31.19, 31.21).

Kim, Y.-S., Sanderson, D.J., 2005. The relationship between displacement and length of faults: a review. Earth-Science Reviews 68, 317-334.

Kinnaman, T.C., 2011. The economic impact of shale gas extraction: A review of existing studies. Ecological Economics 70, 1243-1249.

Knipe, R.J., 1997. Juxtaposition and seal diagrams to help analyze fault seals in hydrocarbon reservoirs. AAPG Bull. 81, 187–195.

Knipe, R.J., Jones, G., Fisher, Q.J., 1998. Faulting, fault sealing and fluid flow in hydrocarbon reservoirs: an introduction. Geol. Soc. Lond. Spec. Publ. 147, vii–xxi.

Kockel, F., 1990. Morphology and genesis of northwest-German salt structures. Tehran University Governery of Hormozgan, pp. 225-248.

Kockel, F., 1998. Salt problems in Northwest Germany and the German North Sea sector, Kockel, F., Marschall, R. (Eds.), Geology and Geophysics of Salt Structures. Journal of Seismic Exploration, pp. 219-235.

Koledoye, B.A., Aydin, A., May, E., 2003. A new process-based methodology for analysis of shale smear along normal faults in the Niger Delta. AAPG Bull. 87, 445–463.

Koyi, H., 1998. The Shaping of salt diapirs. Journal of Structural Geology 20, 321-338.

Koyi, H., Jenyon, M.K., Petersen, K., 1993. The effect of basement faulting on diapirism. Journal of Petroleum Geology 16, 285-312.

Kramer, F.., Peterson, R.., Walton, W.., 1968. Seismic Energy Sources Handbook,. United Geophysical Company.

Kvalstad, T.., Andresen, L., Forsberg, C.., Berg, K., Bryn, P., Wangen, M., 2005. The Storegga slide: evaluation of triggering sources and slide mechanics. Mar. Pet. Geol. 22, 245–256.

Laberg, J.., Vorren, T.O., 2000. The Trænadjupet Slide, offshore Norway - morphology, evacuation and triggering mechanisms. Mar. Geol. 171, 95–114.

Laberg, J.S., Vorren, T.O., Dowdeswell, J.A., Kenyon, N.H., Taylor, J., 2000. The Andøya Slide and the Andøya Canyon, north-eastern Norwegian–Greenland Sea. Mar. Geol. 162, 259–275.

Lastras, G., Canals, M., Amblas, D., Ivanov, M., Dennielou, B., Droz, L., Akhmetzhanov, A., 2006. TTR-14 Leg 3 Shipboard Scientific Party, 2006. Eivissa slides, western Mediterranean Sea: morphology and process. Geo-Mar. Lett. 26, 225–233.

Lastras, G., Canals, M., Urgeles, R., De Batist, M., Calafat, A.M., Casamor, J., 2004. Characterisation of the recent BIG'95 debris flow on the Ebro margin, Western Mediterraenean Sea, after a variety of seismic reflection data. Marine Geology 213, 235-255.

Lem, S., Onghena, P., Verschaffel, L., Van Dooren, W., 2013. The heuristic interpretation of box plots. Learn. Instr. 26, 22–35.

Lewis, K., 1971. Slumping on a continental slope inclined at 10- 40. Sedimentology 16, 97-110.

Li, X.-P., Richwalski, S., 1996. Seismic attenuation and velocities of P- and S-waves in the German KTB area. Journal of Applied Geophysics 36, 67-76.

Lin, C.L., Miller, J.D., 2005. 3D characterization and analysis of particle shape using X-ray microtomography (XMT). Powder Technol. 154, 61–69.

Lisle, R.J., 1979. Strain analysis using deformed pebbles: The influence of initial pebble shape. Tectonophysics 60, 263-277.

Locat J, Mienert J, Longva O, Janbu N, Blikra L.H, Boe R, 2003. The Finneidfjord slide: seafloor failure and slide dynamics. In: Submarine mass movements and their consequences Locat J, Mienert J pp. 531–538. Eds. Dordrecht, Netherlands: Kluwer Academic Publishers

Locat, J., Lee, H., 2002. Submarine landslides: advances and challenges. Can. Geotech. J., 39, 193-212.

Longva, O., Janbu, N., Blikra, L.H., Boe, R., 2003. The Finneidfjord slide: seafloor failure and slide dynamics. Kluwer Academic Publishers., pp. 531-538.

Lucente, C.., Pini, G.., 2003. Anatomy and emplacement mechanism of a large submarine slide within a Miocene foredeep in the northern Apennines, Italy: a field perspective. Am. J. Sci. 303, 565–602.

Lucente, C.C., Pini, G.A., 2003. Anatomy and emplacement mechanism of a large submarine slide within a Miocene foredeep in the northern Apennines, Italy: a field perspective. American Journal of Science 303, 565-602.

Luttig, G., 1962. The Shape of Pebbles in the Continental, Fluvial and Marine Facies. Int Assoc Sci. Hydrol. Pub 59, 235–258.

Mansfield, C., Cartwright, J., 2001. Fault growth by linkage: observations and implications from analogue models. J. Struct. Geol. 23, 745–763.

Mansfield, C.S., Cartwright, J.A., 1996. High resolution fault displacement mapping from three-dimensional seismic data: evidence for dip linkage during fault growth. J. Struct. Geol. 18, 249–263.

Marr, J.., Harff, P.., Shanmugam, G., Parker, G., 2001. Experiments on subaqueous sandy gravity flows: The role of clay and water content in flow dynamics and depositional structures. Geol. Soc. Am. Bull. 113, 1377–1386.

Martinez, J.., Cartwright, J., Hall, B., 2005. 3D seismic interpretation of slump complexes: examples from the continental margin of Israel. Basin Res. 17, 83–108.

Martinsen, O.., 1994. Mass movements, in: Maltman, A. (Ed.), The Geological Deformation of Sediments. Chapman and Hall, pp. 127–165.

Martinsen, O.J., Bakken, B., 1990. Extensional and compressional zones in slumps and slides in the Namurian of County Clare, Ireland. Journal of Geological Society of London 147, 153-164.

Maslin, M., Owen, M., Day, S., Long, D., 2004. Linking continental- slope failures and climate change: testing the clathrate gun hypothesis. Geology 32, 53–56.

Masson, D., Canals, M., Urgeles, R., Alonso, B., Huhnerbach, V., 1998. The Canary debris flow: source area morphology and failure mechanisms. Sedimentology 45, 411–432.

Masson, D., Harbitz, C.., Wynn, R.., Pedersen, G., Løvholt, F., 2006. Submarine landslides: Processes, triggers and hazard prediction. Philos. Trans. R. Soc. Lond. 364, 2009–2039.

Masson, D., Van Niel, B., Weaver, P., 1997. Flow processes and sediment deformation in the Canary debris flow on the NW African continental rise. Sediment. Geol. 110, 163–179.

Masson, D.., Canals, M., Urgeles, R., Alonso, B., Huhnerbach, V., 1998. The Canary debris flow: source area morphology and failure mechanisms. Sedimentology 45, 411–432.

Masson, D.., Harbitz, C.., Wynn, R.., Pedersen, G., Løvholt, F., 2006a. Submarine landslides: Processes, triggers and hazard prediction. Philos. Trans. R. Soc. Lond. 364, 2009–2039.

Masson, D.G., Hugget, Q.J., Brunsden, D., 1993. The surface texture of the Saharan debris flow deposit and some speculation on submarine debris flow processes. Sedimentology 40, 583-598.

McAdoo, B.G., Pratson, L.F., Orange, D.L., 2000. Submarine landslide geomorphology, US continental slope. Mar. Geol. 169, 103–136.

McClay, K. R., 1992 (Ed.) Thrust tectonics. Chapman and Hall London. 447

McLaren, P., Bowles, D., 1985. The effects of sediment transport on grain size distributions. J. Sediment. Pet. 55, 457–470.

Mello, M.., Maxwell, J.., 1990. Organic, geochemical, and biological marker characterization of source rocks and oils derived from Lacustrine environments in the Brazillian continental margin, in: Katz Ed. Lacustrine Basin Exploration-Case Studies and Modern Analogs. AAPG Memoir, pp. 77–98.

Mienert, J., Berndt, C., Laberg, J.., Vorren, T.O., 2003. Slope instability of continental margins., in: In: Wefer, G., Billett, D., Hebbeln, D., Jørgensen, B., Schlüter, M., van Weering, T. (Eds.), Ocean Margin Systems. Springer Verlag, New York, p. 495.

Mienert, J., Posewang, J., Baumann, M., 1998. Gas hydrates along the northeastern Atlantic margin: possible hydrate-bound margin instabilities and possible release of methane, in: Gas Hydrates: Relevance to World Margin Stability and Climate Change, Edited by J.-P. Henriet, and J. Mienert,. Special Publication of Geological Society of London, pp. 275–291.

Minisini, D., Trincardi, F., Asioli, A., Canu, M., Foglini, F., 2007. Morphologic variability of exposed mass transport deposits on the eastern slope of Gela Basin (Sicily channel). Basin Research 19, 217-240.

Mitchum, R.., Vail, P.., Sangree, J.., 1977. Seismic stratigraphy and global changes of sea level, part 6: Stratigraphic interpretation of seismic reflection patterns in depositional sequences., in: In: C.E. Payton (Ed.), Seismic Stratigraphy - Applications to Hydrocarbon Exploration. AAPG Memoir 26, Tulsa, Ok. pp. 117–133.

Mohaghegh, S.D., 2013. Reservoir modeling of shale formations. Journal of Natural Gas Science and Engineering 12, 22-33.

Mohriak, W.U., 2003. Bacias Sedimentares da Margem Continental Brasileira, in: In: Bizzi, L.A. (Ed.), Geologia, Tectônica e Recursos Minerais Do Brasil. Presented at the CPRM,, Brasília, pp. 87–165.

Mohriak, W.U., 2005. Interpreta\ccão geológica e geofísica da Bacia do Espírito Santo e da região de Abrolhos: petrografia, data\ccões radiométricas e visualiza\ccão sísmica das rochas vulcânicas. Bol Geoc Petrobrás 14, 133–142.

Mohriak, W.U., Lira Rabelo, J., De Matos, R.D., De Barros, M.C., 1995. Deep seismic reflection profiling of sedimentary basins offshore Brazil: Geological objectives and preliminary results in the Sergipe Basin. J. Geodyn. 20, 515–539.

Mohriak, W.U., Macedo, J.M., Castelani, R.T., Rangel, H.D., Barros, A.Z.N., Latge, M.A.L., Ricci, J.A., Mizusaki, A.M.P., Szatmari, P., Demercian, L.S., Rizzo, J.G., Ayres, J.R., 1995. Salt tectonics and structural styles in the deep-water province of the Cabo Frio Region, Rio de Janeiro, Brazil, Jackson, M.P.A., Roberts, D.G., Snelson, S. (Eds.), Salt Tectonics. : A Global Perspective. AAPG Memoir, pp. 273-304.

Moore, J.G., Clague, D.A., Holcomp, R.T., Lipman, P.W., Normark, W.R., Torresan, M.E., 1989. Prodigious submarine landslides on the Hawaiian Ridge. Journal of Geophysical Research 94, 17465-17484.

Moreira, J.L.P., Carminatti, M., 2004a. Sistemas deposicionais de talude e de bacia no Eoceno da Bacia de Santos. Bol. Geociências Petrobrás 12, 73–87.

Moreira, J.L.P., Carminatti, M., 2004b. Sistemas deposicionais de talude e de bacia no Eoceno da Bacia de Santos. Bol. Geociências Petrobrás 12, 73–87.

Morgan, J., Camerlenghi, A., Silver, E., Dugan, B., Kirby, S., Shipp, C., Suyehiro, K., 2009. Addressing geologic Hazrds through Ocean drilling. Sci. Drill. 7, 15–30.

Morley, C.K., 2002. Evolution of large normal faults: Evidence from seismic reflection data. AAPG Bull. 86, 961–978.

Moscardelli, L., Wood, L., 2007. New classification system for mass transport complexes in offshore Trinidad. Basin Res. 20, 73–98. doi:10.1111/j.1365-2117.2007.00340.x

Moscardelli, L., Wood, L., Mann, P., 2006. Mass-transport complexes and associated processes in the offshore area of Trinidad and Venezuela. AAPG Bull. 90, 1059–1088.

Mosher, D.., Moscardelli, L., Baxter, C.D.., Urgeles, R., Shipp, C., Chaytor, J.D., Lee, H., 2010. Introduction to submarine mass movements and their consequences., in: Submarine Mass Movements and Their Consequences (Ed. By D.C. Mosher, L. Moscardelli, C.D.P. Baxter, R. Urgeles, R.C. Shipp, J.D. Chaytor &H.J. Lee,. Presented at the Advance in Nat.Tech.Hazards, Springer, pp. 1–8.

Mouslopoulou, V., Nicol, A., Little, T.A., Walsh, J.J., 2007. Displacement transfer between intersecting regional strike-slip and extensional fault systems. J. Struct. Geol. 29, 100–116.

Mulder, T., Cochonant, H.., 1996. Classification of offshore mass movements. J. Sediment. Res. 66, 43–57.

Muraoka, H., Kamata, H., 1983. Displacement distribution along minor fault traces. J. Struct. Geol. 5, 483–495.

Muraoka, H., Kamata, H., 1983. Displacement distribution along minor fault traces. Journal of Structural Geology 5, 483-495.

Mutti, E., Carminatti, M., Moreira, J.L.P., Grassi, A.A.. 2006. Chaotic Deposits: examples from the Brazilian offshore and from outcrop studies in the Spanish Pyrenees and Northern Apennines, Italy. - A.A.P.G. Annual Meeting, April 9-12, Houston, Texas

Nardin, T.., Hein, F.., Gorsline, D.., Edwards, B.., 1979. A review of mass movement processes, sediment, and acoustic characteristics and contrasts in slope and base-of slope systems versus canyon-fan-basin floor systems. Spec Publ Soc Econ. Paleontol. Miner. 27, 61–73.

Needham, D.T., 1989. Reactivation not inversion., in: Cooper, M.A., Williams, G.D. (Eds.), Inversion Tectonics,. Special Publication of Geological Society of London, p. 341.

Needham, T., Yielding, G., Fox, R., 1996. Fault population description and prediction using examples from the offshore UK. J. Struct. Geol. 18, 155–167.

Nemec, W., 1990. Aspects of sediment movement on steep delta slopes, Coarse-Grained Deltas. John Wiley & Sons, Hoboken, NJ, pp. 29-73.

Nemec, W., 1991, Aspects of sediment movement on steep delta slopes, *in* Colella, A., and Prior, D.B., eds., Coarse-Grained Deltas: International Association of Sedimentologists, Special Publication 10, p. 29–73.

Nilsen, K.T., Vendeville, B.C., Johansen, J.T., 1995. Influence of regional tectonics on halokinesis in the Nordkapp Basin, Barents Sea, Jackson, M.P.A., Roberts, D.G., Snelson, S. (Eds.), Salt Tectonics: A Global Perspective. AAPG Memoir, pp. 413-436.

Nisbet, E., Piper, D.J.., 1998. Giant submarine landslides. Nature (London). Nature 392, 329–330.

Norem, H., Locat, J., Schieldrop, B., 1990. An approach to the physics and the modelling of submarine flowslides. Mar. Geotechnol. 9, 93–111.

Ogata, K., 2010. Mass Transport Complexes in structurally Controlled basins: The Epiligurian Specchio unit (Northern Apennines, Italy). Ph.D. Thesis. University of Parma: Italy.

Ogiesoba, O., and U. Hammes, 2012. Seismic interpretation of mass-transport deposits within the upper Oligocene Frio Formation, south Texas Gulf Coast: AAPG Bulletin, v. 96, p. 845–868.

Ojeda, H.A.O., 1982. Structural framework, stratigraphy, and evolution of Brazilian marginal basins, AAPG Bull. 66, 732–749.

O'Leary, D.W., 1986. The Munson–Nygren slide: a major lower-slope slide off the Georges Bank. Marine Geology 72, 101-114.

O'Leary, D.W., 1991. Structure and morphology of submarine slab slides: clues to origin and behaviour. Marine Geotechnology 10, 53-69.

Omosanya, K.O., Alves, T.M., 2013. Ramps and flats of mass-transport deposits (MTDs) as markers of seafloor strain on the flanks of rising diapirs (Espírito Santo Basin, SE Brazil). Marine Geology 340, 82-97.

Peacock, D.C.P., 2002. Propagation, interaction and linkage in normal fault systems. Earth-Sci. Rev. 58, 121–142.

Peacock, D.C.P., Knipe, R.J., Sanderson, D.J., 2000. Glossary of normal faults. J. Struct. Geol. 22, 291–305.

Peacock, D.C.P., Sanderson, D.J., 1991. Displacements, segment linkage and relay ramps in normal fault zones. J. Struct. Geol. 13, 721–733.

Piper, D.J.., Pirmez, C., Manley, P.., Long, D., Flood, R.., Normark, W.., Showers, W., 1997. Mass-transport deposits of the Amazon Fan, in: R. D. Flood, D. J. W. Piper, A. Klaus, and L. C. Pederson, Eds., Leg 155 Amazon Fan Sites 930– 946. Presented at the Ocean Drilling Program, Scientific Results, IODP, pp. 109–146.

Piper, D.J.W., Cochonat, P., Morrison, M.L., 1999. The sequence of events around the epicenter of the 1929 Grand Banks earthquake: initiation of debris flows and turbidity current inferred from sidescan sonar. Sedimentology 46, 79-97.

Piper, J.., Behrens, E.., 2003. Downslope sediment transport processes and sediment distributions at the East Breaks, northwest Gulf of Mexico, in: H. H. Roberts, N. C. Rosen, R. H. Fillon, and J. B. Anderson, Eds., Shelf Margin Deltas and Linked down Slope Petroleum Systems: Global Significance and Future Exploration Potential. Presented at the Gulf Coast Section SEPM 23rd Annual Research Conference, SEPM, pp. 359–385.

Pohn, H.A., Coleman Jr, J.L., 1991. Fold patterns, lateral ramps and seismicity in central Pennsylvania. Tectonophysics 186, 133-149.

Pollard, D.D., Aydin, A., 1984. Propagation and linkage of oceanic ridge segments. J. Geophys. Res. 89, 10017–10028.

Ponçano,, W.., 1986. Sobre a interpretação ambiental de parâmetros estatísticos granulométricos: exemplos de sedimentos quaternários da costa brasileira. Rev. Bras. Geociênicas 16, 157–170.

Posamentier, H. and Martinsen, O.J., 2011. The character and genesis of submarine mass-transport deposits: insights from outcrop and 3D seismic data. In: C. Shipp, P. Weimer and H. Posamentier (Eds.), Mass-transport deposits in deepwater settings. SEPM Special Publication 96, pp. 7-38.

Posamentier, H., 2004. Stratigraphy and geomorphology of deep-water mass transport complexes based on 3D seismic data, Offshore Technology Conference, Houston, TX.

Posamentier, H.W., Kolla, 2003. Seismic geomorphology and stratigraphy of depositional elements in deep-water settings. J. Sediment. Res. 73, 367–388.

Posamentier, H.W., Walker, R.., 2006. Deep-water turbidites and submarine fans., in: In: Posamentier, H.W., Walker, R.G. (Eds.), Facies Models Revisited: Society for Sedimentary Geology, Tulsa, Oklahoma, pp. 399–520.

Prather, B.E., 2000. Calibration and visualization of depositional process models for above-grade slopes: a case study from the Gulf of Mexico. Marine and Petroleum Geology 17, 619-638.

Prior, D.., Coleman, J.., 1982. Active slides and flows in underconsolidated marine sediments on the slopes of the Mississippi Delta., in: Workshop on Marine Slides and Other Mass Movements. (Ed. by S. Saxov & J.Nieuwenhuis). Presented at the NATO Conference Series IV, Plenum Press, New York, pp. 225–234.

Prior, D.B., Bornhold, B.D., Johns, M.W., 1984. Depositional characteristics of a submarine debris flow. Journal of Geology 92, 707-727.

Prior, D.B., Coleman, J.M., 1984. Submarine slope instability, Slope Instability (Ed. by D. Brundsen & D.B. Prior). Wiley- Blackwell, Chichester, New York, pp. 419-455.

Ragan, D.M., 2009. Structural geology an introduction to geometrical techniques. Cambridge University Press, Cambridge; New York.

Ramsay, J.G., Huber, M.I., 1987. The Techniques of Modern Structural Geology. Academic Press Inc, London.

Randen, T., Monsen, E., Signer, C., Abrahamsen, A., Hansen, J., Saeter, T., Schlaf, J., 2000. Three-dimensional texture attributes for seismic data analysis. Presented at the 70th SEG Annual Meeting, Society of Exploration Geophysicists., pp. 668–671.

Ren, P., Bornhold, B.D., Prior, D.B., 1996. Seafloor morphology and sedimentary processes, Knight Inlet, British Columbia. Sedimentary Geology 103, 201-228.

Richard, P., Krantz, R.W., 1991. Experiments on fault reactivation in strike-slip mode. Tectonophysics 188, 117-131.

Richardson, S.E.., Richard, J.., Mark, B.., Grant, F.S., 2011. Structure and evolution of mass transport deposits in the South Caspian Basin, Azerbaijan. Basin Res. 23, 702–719.

Rimando, P.M., Manuel, G.A., 1997. Depth conversion in geologically complex structures: Case study in offshore southwest Palawan. Journal of Asian Earth Sciences 15, 241-250.

Robson, R.M., 1994. A multi-Component rose diagram. J. Struct. Geol. 16, 1039–1040.

Rotevatn, A., Fossen, H., 2011. Simulating the effect of subseismic fault tails and process zones in a siliciclastic reservoir analogue: Implications for aquifer

support and trap definition. Mar. Pet. Geol. 28, 1648–1662. doi:10.1016/j.marpetgeo.2011.07.005

Rothwell, R.., Thompson, J., Kahler, G., 1998. Low-sea-level emplacement of a very large late Pleistocene “megaturbidite” in the western Meditteranean Sea. Nature 392, 377–380.

Rowan, M.G., Hart, B.S., Nelson, S., Flemings, P.B., Trudgill, B.D., 1998. Three-dimensional geometry and evolution of a salt-related growth-fault array: Eugene Island 330 field, offshore Louisiana, Gulf of Mexico. Mar. Pet. Geol. 15, 309–328.

Rowan, M.G., Jackson, M.P.A., Trudgill, B.D. , 1999. Salt-related fault families and fault welds in the northern Gulf of Mexico AAPG Bulletin 83, 1454-1484.

Rowan, M.G., Peel, F.., Vendeville, B.C., 2004. Gravity-driven foldbelts on passive margins, in: K.R. McClay, Ed., Thrust Tectonics and Hydrocarbon Systems: AAPG Memoir, pp. 157–182.

Rowan, M.G., Peel, F.J., Vendeville, B.C., Gaullier, V., 2012. Salt tectonics at passive margins: Geology versus models – Discussion. Marine and Petroleum Geology 37, 184-194.

Roy, G.H., Martinsen, O., 2008. Salt: Deformation, Trapping, Recent Advances in Geosciences. GeoExpro, 56-78.

Sangree, J., Widmier, J., 1977. Seismic stratigraphy and global changes of sea level, part 9: seismic interpretation of clastic depositional facies In: Payton, C.E. (Ed.), Seismic Stratigraphy e Applications to Hydrocarbon Exploration. AAPG Memoir, pp. 165–184.

Savini, A., Malinverno, E., Etiope, G., Tessarolo, C., Corselli, C., 2009. Shallow seep-related seafloor features along the Malta plateau (Sicily channel – Mediterranean Sea): Morphologies and geo-environmental control of their distribution. Marine and Petroleum Geology 26, 1831-1848.

Scheidegger,, A., 1982. On the tectonic setting of submarine landslides, in: Marine Slides and Other Mass Movements, Edited by S. Saxov. Plenum Press, New York, pp. 11–20.

Schenk, P., Jackson, M.P.A., 1993. Diapirism on Triton: a record of crustal layering and instability. Geology 21, 299-302.

Schmatz, J., Vrolijk, P.J., Urai, J.L., 2010. Clay smear in normal fault zones – The effect of multilayers and clay cementation in water-saturated model experiments. J. Struct. Geol. 32, 1834–1849.

Schnellmann, M., Anselmetti, F.., Giardini, D., McKenzie, J.., 2005. Mass movement-induced fold-and-thrust belt structures in unconsolidated sediments in Lake Lucerne (Switzerland). Sedimentology 52, 271–289.

Schultz, R.A., Fossen, H., 2008. Terminology for structural discontinuities. AAPG Bull. 92, 853–867.

Scott Wilkerson, M., Apotria, T., Farid, T., 2002. Interpreting the geologic map expression of contractional fault-related fold terminations: lateral/oblique ramps versus displacement gradients. Journal of Structural Geology 24, 593-607.

Scott Wilkerson, M., Medwedeff, D.A., Marshak, S., 1991. Geometrical modeling of fault-related folds: a pseudo-three-dimensional approach. Journal of Structural Geology 13, 801-812.

Sedimentary Geology, 219(1-4): 77-96.

Shanmugam, G., 2000. 50 years of the turbidite paradigm (1950s– 1990s): Deep-water processes and facies models— A critical perspective. Mar. Pet. Geol. 17, 285–342.

Sharp, I.R., Gawthorpe, R.L., Underhill, J.., Gupta, S., 2000. Fault-propagation folding in extensional settings: Examples of structural style and synrift response from the Suez rift, Sinai, Egypt: GSA Bull. 112, 1877–1899.

Sheriff, R.., Geldart, L.., 1995. Exploration Seismology., Second Edition. ed. Cambridge University Press.

Shipp, R.., Nott, J.., Newlin, J.., 2004. Physical characteristics and impact of mass transport complexes on deepwater jetted conductors and suction anchor piles: Presented at the Annual Offshore Technology Conference, OTC, Houston Texas, p. 11.

Sibson, R.H., 1985. A note on fault reactivation. Journal of Structural Geology 7, 751-754.

Sneed, E.., Folk, R.., 1958. Pebbles in the lower Colorado Rivers. A study in particle morphogenesis., in: In: Lewis, Douglas, W., McConchie, David (Eds.),Practical Sedimentology. Chapman and Hall, 1993, p. 123.

Snyder, F.C., Nugent, J.A., 1996. Teak; complex subsalt trap geometry, south Timbalier Block 260, northern Gulf of Mexico (abs.), AAPG Annual Convention Official Program.

Sohn, Y.., 2000. Depositional processes of submarine debris flows in the Miocene fan deltas, Pohang basin, SE Korea with special reference to flow transformation. J. Sediment. Res. 70, 491–503.

Solheim, A., Berg, K., Forsberg, C.F., Bryn, P., 2005. The Storegga Slide complex: repetitive large scale sliding with similar cause and development. Marine and Petroleum Geology 22, 97-107.

Stengel, D., Calori, G.M., Giannoudis, P.V., 2008. Graphical data presentation. Injury 39, 659–665.

Stewart, S.A., 2001. Displacement distributions on extensional faults: Implications for fault stretch, linkage, and seal. AAPG Bull. 85, 587–600.

Stewart, S.A., 2006. Implications of passive salt diapir kinematics for reservoir segmentation by radial and concentric faults. Marine and Petroleum Geology 23, 843-853.

Stone, D., 1994. Designing Seismic Surveys in Two and Three Dimensions,, in: SEG, 244. (* Edited by Charles A. Meeder). Society of Exploration Geophysicists., Tulsa, Oklahoma.

Strachan, L., 2002a. From Geometry to Genesis: a Comparative Field Study of Slump Deposits and their Modes of Formation. University of Cardiff.

Strachan, L., 2002b. Slump-initiated and controlled syndepositional sandstone remobilisation: an example from the Namurian of County Clare, Ireland. Sedimentology 49, 25–41.

Sullivan, W.A., Beane, R.J., 2010. Asymmetrical quartz crystallographic fabrics formed during constrictional deformation. Journal of Structural Geology 32, 1430-1443.

Sultan, N., Cochonat, P., Canals, M., Cattaneo, A., Dennielou, B., Haflidason, H., Laberg, J.S., Long, D., Mienert, J., Trincardi, F., Urgeles, R., Vorren, T.O., Wilson, C., 2004. Triggering mechanisms of slope instability processes and sediment failures on continental margins: a geotechnical approach. Mar. Geol. 213, 291–321.

Sultan, N., Cochonat, P., Foucher, J.P., Mienert, J., Haflidason, H., Sejrup, H.P., 2003. Effect of gas hydrates dissociation on seafloor slope stability. Kluwer Academic Publishers., pp. 103-111.

Tailing, P., Wynn, R., Masson, D., Frenz, M., Cronin, B., Schiebel, R., Akhmetzhanov, A., Dallmeier-Tiessen, S., Benetti, S., Weaver, P., 2007. Onset of submarine debris flow deposition far from original giant landslide. Nature 450, 541–544.

Talbot, C.J., 1998. Extrusions of Hormuz salt in Iran, Blundell, D.J., Scott, A.C. (Eds.), Lyell, the Past is the Key to the Present. Geological Society, London, Special Publications, pp. 315-334.

Talbot, C.J., Jarvis, R.J., 1984. Age, budget and dynamics of an active salt extrusion in Iran. Journal of Structural Geology 6, 521-533.

Tappin, D. R., Watts, P., McMurty, G. M., Lafoy, Y. & Matsumoto, T. 2001 The Sissano, Papua New Guinea tsunami of July, 1998—offshore evidence on the source mechanism. Mar. Geol. 175, 1–24. (doi:10.1016/S0025-3227(01)00131-1)

Taylor, S.R., Almond, J., Arnott, S., Kemshell, D. and Taylor, D., 2003. The Brent Field, Block 211/29, UK North Sea. Geological Society, London, Memoirs, 20(1): 233-250.

Terzaghi, K., 1962, Stability of steep slopes on hard unweathered rock: Geotechnique, v. 12, p. 251–270.

Tinti, S., A, Manucci, G., Pagnoni, A., Artigliato, F. Zaniboni, 2005. The 30 December 2002 landslide-induced tsunami in Stromboli: sequence of events reconstructed from the eyewitness accounts, Natural Hazards Earth Science, 5, 763-775.

Tinti, S., A, Manucci, G., Pagnoni, A., Artigliato, F. Zaniboni, 2005. The 30 December 2002 landslide-induced tsunami in Stromboli: sequence of events reconstructed from the eyewitness accounts, Natural Hazards Earth Science, 5, 763-775.

Townsend, C., Firth, I.., Westerman, R., 1998. Small seismic-scale fault identification and mapping. In: Jones, G., Fisher, Q.J., Knipe, R.J. (Eds.), Faulting, Fault Sealing and Fluid Flow in Hydrocarbon Reservoirs. Geol. Soc. Lond. Spec. Publ. 147, 1–25.

Townsend, C., Firth, I.., Westerman, R., 1998. Small seismic-scale fault identification and mapping. In: Jones, G., Fisher, Q.J., Knipe, R.J. (Eds.), Faulting, Fault Sealing and Fluid Flow in Hydrocarbon Reservoirs. Geol. Soc. Lond. Spec. Publ. 147, 1–25.

Trincardi, F., Argnani, A., 1990. Gela submarine slide: a major basin wide event in the Plio–Quaternary foredeep of Sicily. Geo-Marine Letters 10, 13-21.

Tripsanas, E.., Bryant, W.., Phaneuf, B.., 2004. Slope instability processes caused by salt movements in a complex deep water environment, Bryant Canyon area, northwest Gulf of Mexico. Aapg Bull. 88, 801–823.

Tvedt B.M.T, A. Rotevatn, C.A.L. Jackson, H. Fossen, R.L. Gawthorpe, 2013. Growth of normal faults in multilayer sequences: A 3D seismic case study from the Egersund Basin, Norwegian North Sea, Journal of Structural Geology, Volume 55, 1-20 http://dx.doi.org/10.1016/j.jsg.2013.08.002.

Tucker, R., Wacher, H., 1980. Effectiveness of discriminating beach dune and river sands by moments and the cumulative weight percentages. J. Sediment. Pet. 50, 165–173.

Tueckmantel, C., Fisher, Q.J., Knipe, R.J., Lickorish, H., Khalil, S.M., 2010. Fault seal prediction of seismic-scale normal faults in porous sandstone: A case study from the eastern Gulf of Suez rift, Egypt. Mar. Pet. Geol. 27, 334–350.

Twichell, D.C., Chaytor, J.D., ten Brink, U.S., Buczkowski, B., 2009. Morphology of late Quaternary submarine landslides along the U.S. Atlantic continental margin. Mar. Geol. 264, 4–15.

Twiss, R. J., and Moores, E. M., 1992: Structural geology W.H. Freeman & Company, New York, 532.

Twiss, R. J., and Moores, E. M., 1992: Structural geology W.H. Freeman & Company, New York, 532.

Twiss, R.., Moore, E.., 2007. Structural Geology, 2nd Edition. ed. Freeman and Company, New York.

Urgeles, R., Canals, M., Baraza, J., Alonso, B., Masson, D., 1997. The most recent mega landslides of the Canary Islands: El Golfo debris avalanche and Canary debris flow, west El Hierro Island. J. Geophys. Res. 109, 20305– 20323.

Urgeles, R., Locat, J., Dugan, B., 2007. Recursive failure of the Gulf of Mexico continental slope: Timing and causes. Springer, pp. 209-219.

Vanneste, M., Mienert, J., Bu¨ nz, S., 2006. The Hinlopen Slide: A giant, submarine slope failure on the northern Svalbard margin, Arctic Ocean. Earth and Planetary Science Letters 245, 373-388.

Varnes, D.J., 1978. Slope movement types and processes, Schuster, R.L., Kruse, R.J. (Eds.), Landslides, Analysis and Control. : Special Report, 176. National Academy of Sciences, Washington, pp. 11-33.

Vendeville, B.C., Jackson, M.P.A., 1992a. The fall of diapirs during thin-skinned extension. Marine and Petroleum Geology 9, 354-371.

Vendeville, B.C., Jackson, M.P.A., 1992b. The rise of diapirs during thin-skinned extension. Marine and Petroleum Geology 9, 331-354.

Vendeville, B.C., Nilsen, K.T., 1995. Episodic growth of salt diapirs driven by horizontal shortening, 16th Annual Research Conference. Society of Exploration Palaeontologists and Mineralogists Foundation, pp. 285-295.

Vendeville, B.C., Rowan, M.G., 2002. 3-D kinematics of minibasin and salt ridges remobilised by late contraction: physical models and seismic examples (southeast Mississippi canyon, Gulf of Mexico) (abs). AAPG Annual Meeting Official Program 11.

Vermeer, G.J.., 2000. 3-D Seismic Survey Design. Society of Exploration Geophysicists., Tulsa, Oklahoma.

Wach, G.., Bouma, A.., Lukas, T., Wickens, H.., Goldhammer, R.., 2003. Transition from shelf margin delta to slope fan— Outcrop examples from the Tanqua Karoo, South Africa, in: H. H. Roberts, N. C. Rosen, R. H. Fillon, and J. B. Anderson, Eds., Shelf Margin Deltas and Linked down Slope Petroleum Systems: Global Significance and Future Exploration Potential: Gulf Coast Section. Presented at the SEPM 23rd Annual Research Conference, SEPM, pp. 849–861.

Walker, R.J., Holdsworth, R.E., Imber, J., Faulkner, D.R., Armitage, P.J., 2013. Fault zone architecture and fluid flow in interlayered basaltic volcaniclastic-crystalline sequences. J. Struct. Geol. 51, 92–104.

Walsh, J.J., Watterson, J., 1989. Displacement gradients on fault surfaces. J. Struct. Geol. 11, 307–316.

Warren, J., 1999. Evaporites: Their Evolution and Economics. Blackwell Science, Oxford.

Watt, S.F.L., Talling, P.J., Vardy, M.E., Masson, D.G., Henstock, T.J., Hühnerbach, V., Minshull, T.A., Urlaub, M., Lebas, E., Le Friant, A., Berndt, C., Crutchley, G.J., Karstens, J., 2012. Widespread and progressive seafloor-sediment failure

following volcanic debris avalanche emplacement: Landslide dynamics and timing offshore Montserrat, Lesser Antilles. Marine Geology 323–325, 69-94.

Weaver, P.P.E., Kuijpers, A., 1983. Climatic control of turbidites deposition on the Madeira Abyssal plain. Nature 306, 360-363.

Weimer, P., 1990, Sequence stratigraphy, facies geometries, and depositional history of the Mississippi Fan, Gulf of Mexico: American Association of Petroleum Geologists, Bulletin, v. 74, p. 425–453.

Weimer, P., Davis, T., 1996. Applications of 3-D Seismic Data to Exploration and Production, SEG, 270. Society of Exploration Geophysicists., Tulsa, Oklahoma.

Weimer, P., Shipp, C., 2004. Mass transport complex: musing on past uses and suggestions for future directions. Presented at the Offshore Technology Conference, Houston Texas.

Welbon, A.I.F., Brockbank, P.J., Brunsden, D. and Olsen, T.S., 2007. Characterizing and producing from reservoirs in landslides: challenges and opportunities. In: S.J. Jolley, D. Barr, J.J. Walsh and R.J. Knipe (Eds.), Structurally Complex Reservoirs. Geological Society London, Special Publications 292, pp. 49-74.

Wellman, H.G., 1962. A graphical method for analysing fossil distortion caused by tectonic deformation. Geological Magazine 99, 348–335.

White, S.H., Bretan, P.G., Rutter, E.H., 1986. Fault-zone reactivation: kinematics and mechanisms. Philosophical Transactions of the Royal Society of London. A317, 81-97.

Wilson, C.., Long, D., Bulat, J., 2004. The morphology, setting and process of the Afen Slide. Mar. Geol. 213, 149–167.

Winkelmann, D., Geissler, W., Schneider, J., Stein, R., 2008. Dynamics and timing of the Hinlopen/Yermak Megaslide north of Spitsbergen, Arctic Ocean. Marine Geology 250, 34-50.

Winker, C., Booth, J., 2000. Sedimentary dynamics of the salt-dominated continental slope, Gulf of Mexico: Integration of observations from the seafloor, near-surface, and deep subsurface., in: P. Weimer, R. M. Slatt, J. Coleman, N. C. Rosen, H. Nelson, A. H. Bouma, M. J. Styzen, and D. T. Lawrence, Eds., Deep-water Reservoirs of the World: Gulf Coast Section. Presented at the SEPM 20th Annual Research Conference, SEPM, pp. 1059–1086.

Wiprut, D., Zoback, M.D., 2000. Fault reactivation and fluid flow along a previously dormant normal fault in the northern North Sea. Geology 28, 595.

Wu, S., Groshong Jr, R.H., 1991. Strain analysis using quartz deformation bands. Tectonophysics 190, 269-282.

Yielding, G., Freeman, B., Needham, D.T., 1997. Quantitative fault seal prediction. AAPG Bull. 81, 897–917.

Yilmaz, Ö., 1987. Seismic data processing., 2. Society of Exploration Geophysicists.

Zhang, L., Xu, Y., Huang, R.., Chang, D.., 2011. Particle flow and segregation in a giant landslide event triggered by the 2008 Wenchuan earthquake, Sichuan, China. Nat. Hazards Earth Syst. Sci. 11, 1153–1162.

Zhang, Likuan, Luo, X., Vasseur, G., Yu, C., Yang, W., Lei, Y., Song, C., Yu, L., Yan, J., 2011. Evaluation of geological factors in characterizing fault connectivity during hydrocarbon migration: Application to the Bohai Bay Basin. Mar. Pet. Geol. 28, 1634–1647.

Zingg, T., 1934. Beitrag zur Schotteranalyse. Schweiz. Miner. Petrogr. Mitteilungen 15, 39–140.

Websites

- http://mettechnology.com/storage/Passive%20Seismic%20Sensors_4.jpg?__SQUARESPACE_CACHEVERSION=1286822981911
- www.ngdc.noaa.gov/mgg/gdas/gd-designagrid.utml visited 13/04/2014
- http://iseis.com/images/sigma2.jpg
- http://www.cflhd.gov/resources/agm/images/fig148.jpg
- http://geophysics.curtin.edu.au/local/images/current_students/facilities/fieldequipment/accelweightdrop.jpg
- http://upload.wikimedia.org/wikipedia/commons/1/1d/Airgun-array_hg.png
- www.see.leeds.ac.uk
- http://www.igcp585.org/significance visited 23/01/2014
- http://www.cflhd.gov/resources/agm/engApplications/SubsurfaceChartacter/611DeterminDepthStructureFractureBedrock.cfm visited 25.04.2014
- http://crystal.isgs.uiuc.edu/sections/geophys/seisref.shtml visited 25.04.2014
- http://www.epa.gov/esd/cmb/GeophysicsWebsite/pages/reference/methods/Marine_Geophysical_Methods/Marine_Seismic_Methods.htm visited 25.04.2014
- www.earth.google.co.uk visited 06.12.2013

Appendices

Appendix I: Chapter 3

Seismic acquisition and processing parameters of BES-100 survey

Acquisition parameters

Vessel: CGG Harmattan

Source: Airgun Dual

Shotpoint Interval: 25 m flip-flop

CMP xline: 25 metres

Group spacing: 12.5 m

Streamers: 6 x 5700 m

Record length: 8.0 sec

Sample interval: 2ms

Nominal fold: 56

Processing Sequence

Reformat from SEGD

Navigation/seismic merge

Resample from 2 ms to 4 ms with anti-alias filter

Spherical divergence correction

"SPARN" – signal preserving attenuation of random noise and swell noise

Zero phase conversion using modelled far field signature

Q phase only compensation (referenced to water bottom)

FX shotpoint interpolation and radon multiple attenuation

3D Kirchhoff Bin centring DMO

3D V(c) pre-stack time migration using Stolt algorithm

0.5 Km grid Final velocity analysis

Full offset stack

Post stack demigration

Crossline FX trace interpolation

Zhimming Li steep dip one pass 3D time migration

#Final Product

Raw stack in SEGY format

Raw migration in SEGY format

Final stacking velocities in VelTape format

Final migration velocities in VelTape format

Migrated bin centre positions in UKOOA P1/90 format

Final report

Appendix II: Chapters 4 to 6

Additional seismic lines and figures

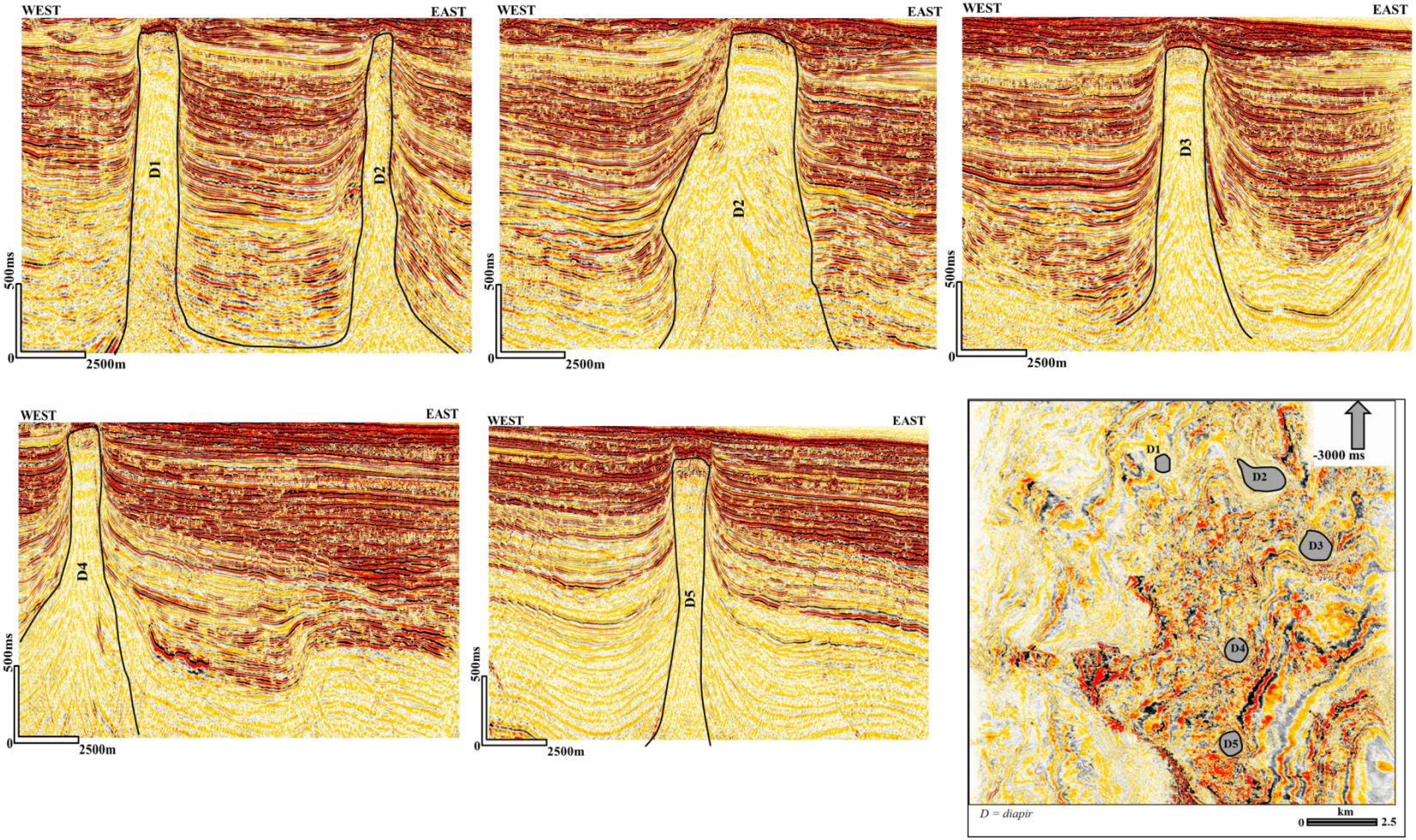

AII. 1: The salt diapirs used for this study are columnar and upward narrowing in cross section. Columnar salt diapirs are formed when the rate of salt supply is equal to the rate of sedimentation while upward narrowing develops when sedimentation rate is greater than the rate of salt supply (Koyi, 1993).

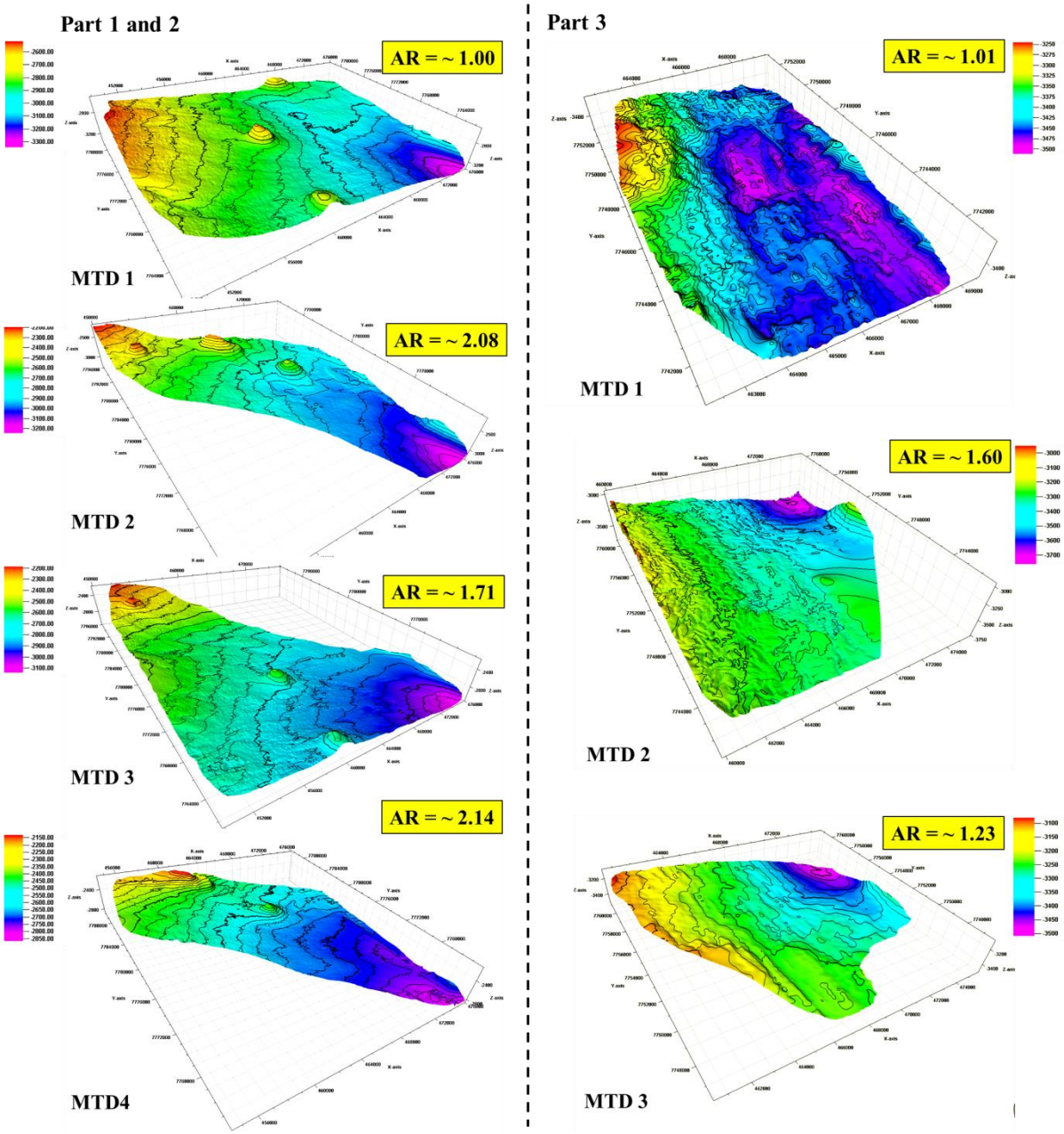

AII.2: The mass-transport deposits in this study have aspect ratio of less than 3. They are characteristic shelf- and slope-detached MTDs and are formed as a result of elevated slope gradients on the flanks of the salt diapirs. N.B: *Color bar shows the depth of occurrence of each of the MTDs.*

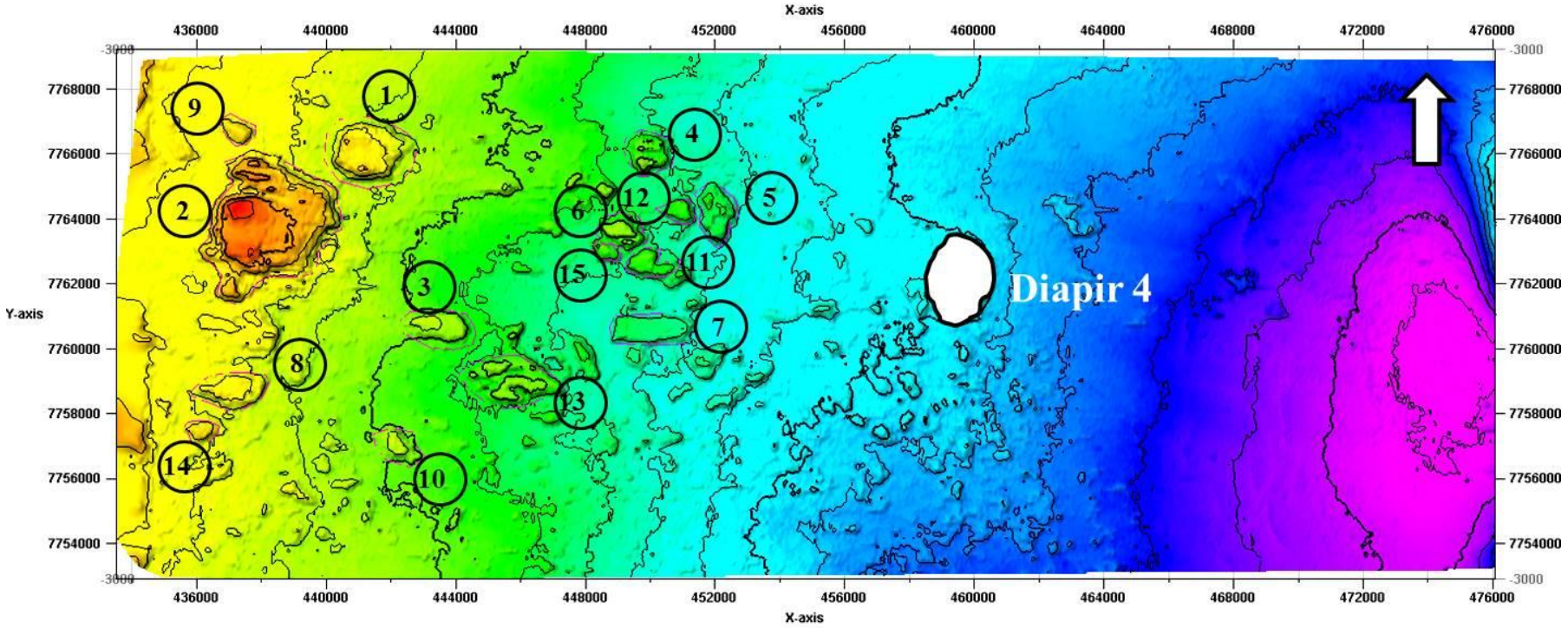

AII.3: Some of the rafted blocks analysed in Chapter 4. The isochron map is the top of MTD 3 interpreted in Chapters 4 and 5.

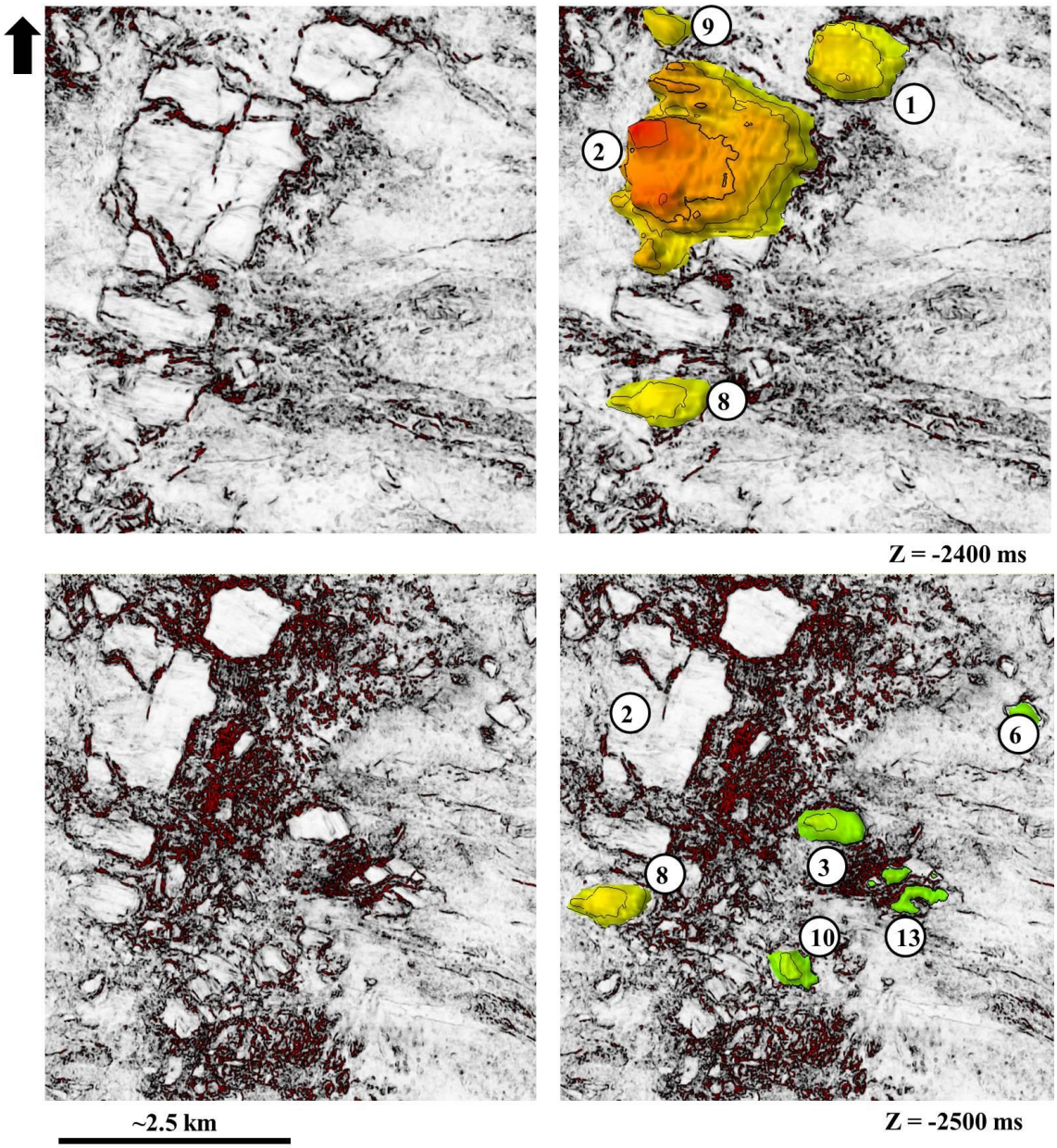

AII. 4: Coherence slices through some of the blocks shown in Figure AIII-3. The edges of the rafted blocks are marked by high coherence coefficient that is discordant with the expression of the background MTD body.

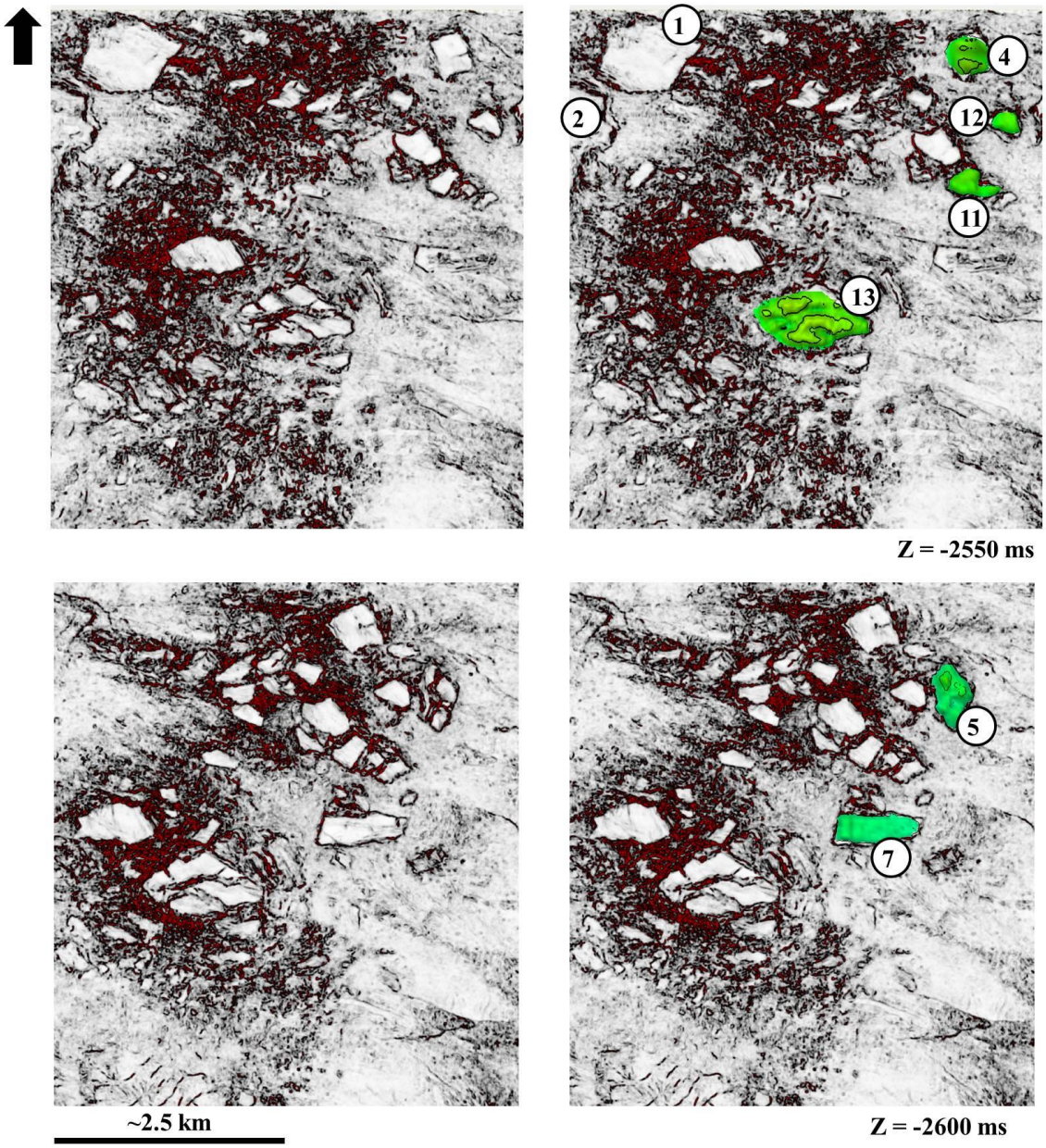

AII. 5: Coherence slices through some of the blocks shown in Figure AIII-3

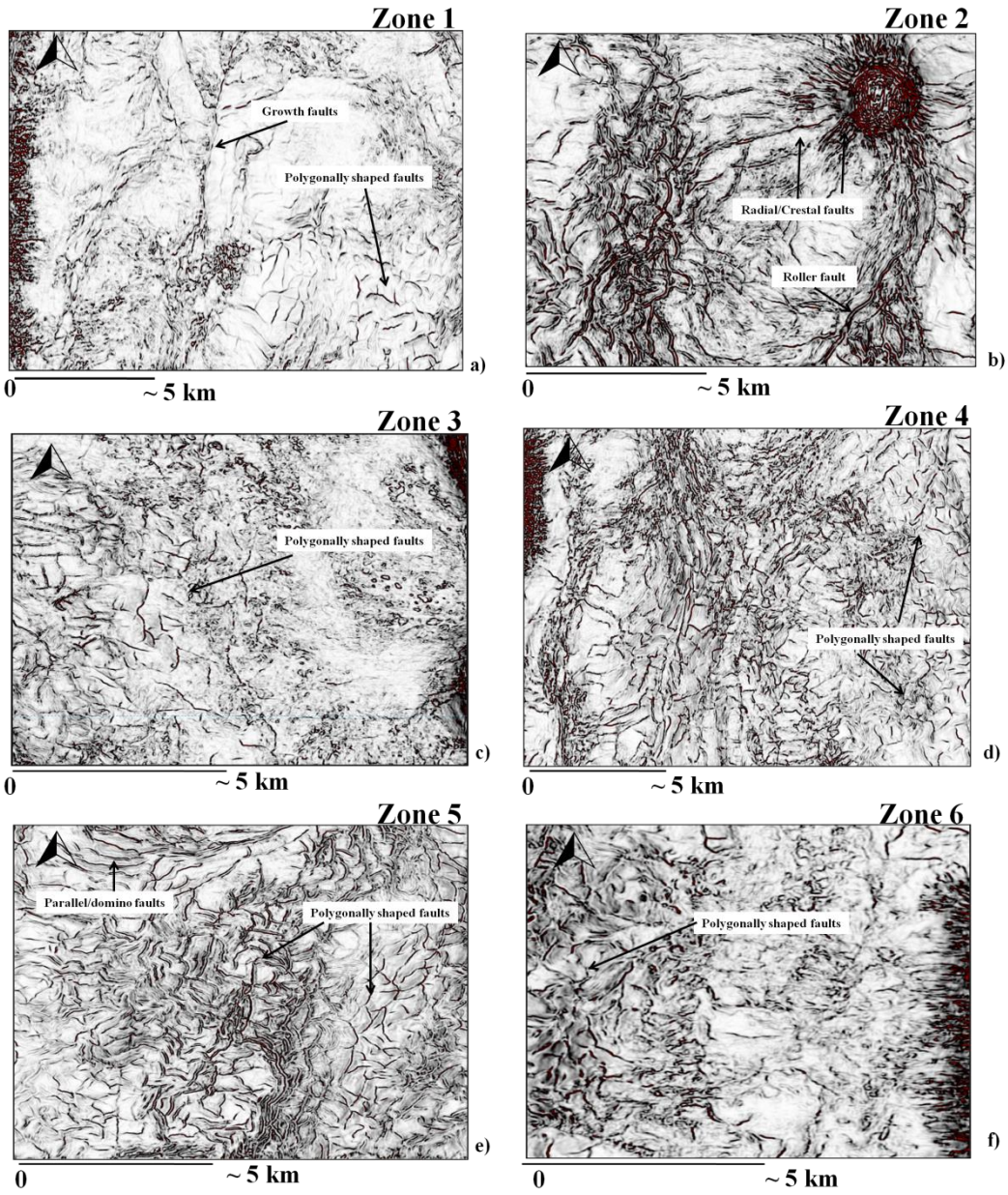

AII. 6: Expression of some of the fault shown in figure 6.2. Radial faults are limited to the crest of the salt diapirs. In map view, polygonally-shaped faults linked up to form geometrical pattern. The areas where the MTDs of Chapter 6 are located is characterized by a complex mixture of low and high coherence coefficients.

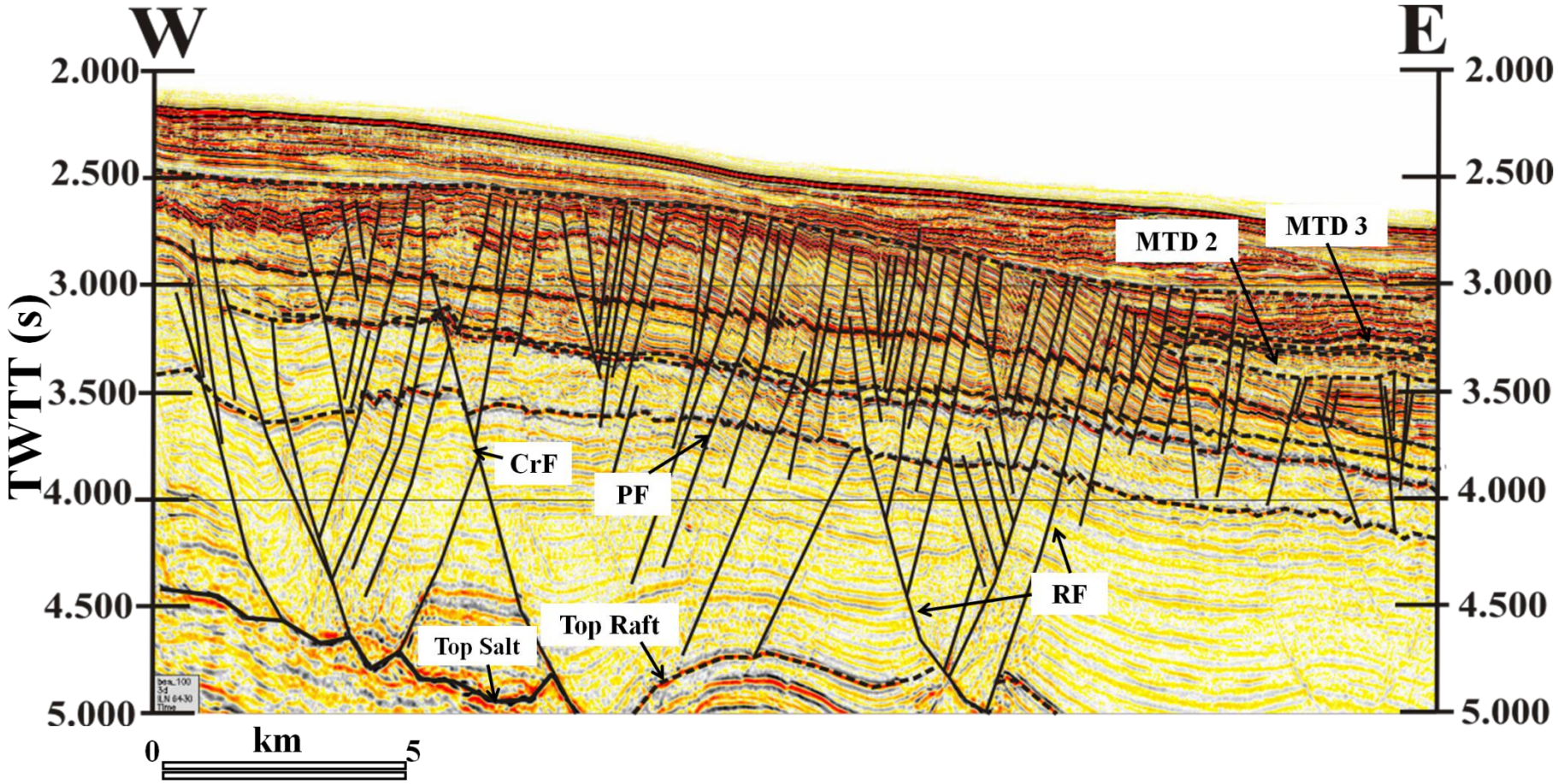

AII. 7: Seismic profile highlighting major fault families in Chapter 6. Shown in the figure are roller faults soling out at top salt level. Also observed are polygonal faults formed by buckling of overburden layers during salt diapir growth. The remaining fault families are associated with MTDs. *N.B: MTD- Mass-transport deposits, PF- Polygonal fault, RF- Roller Fault and CrF- Counter regional fault*

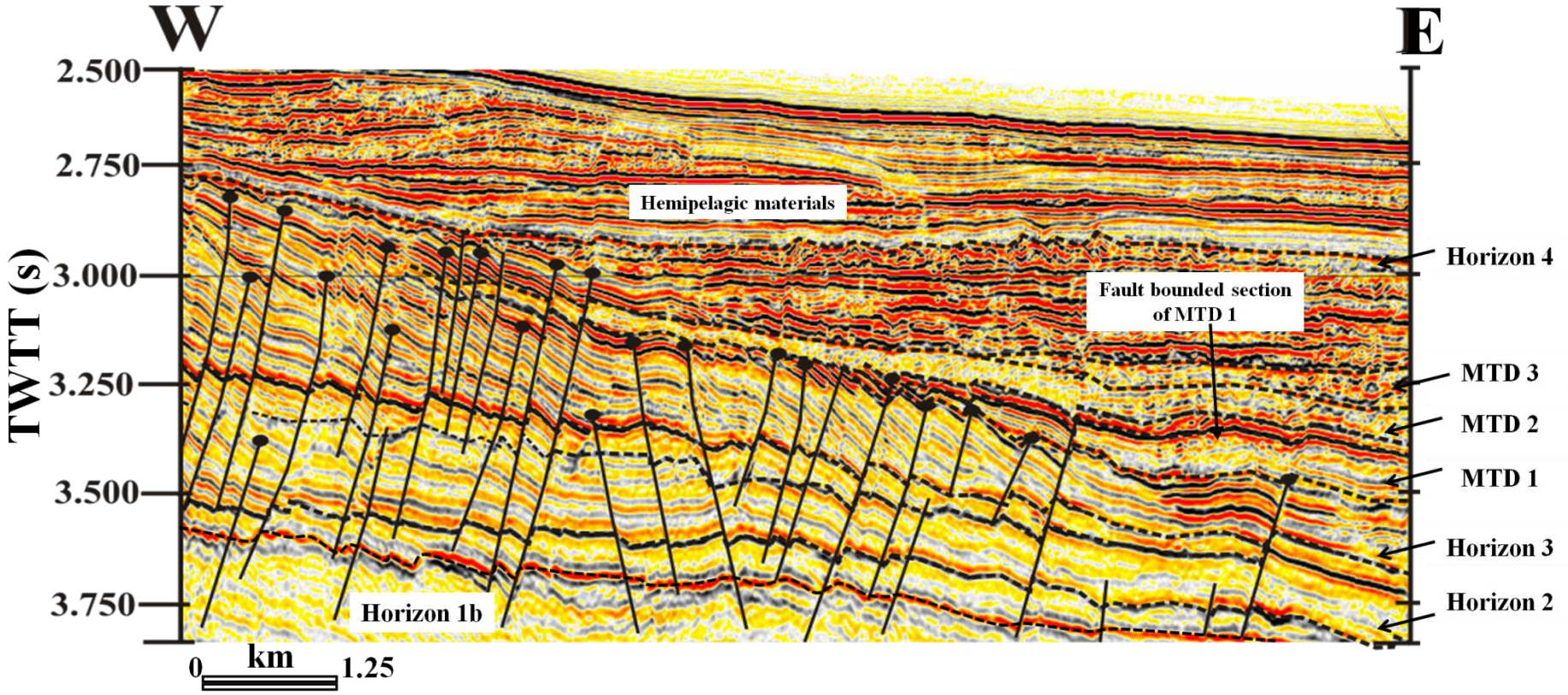

AII. 8: Detail of MTD 1 of Chapter 6 in which evidence for erosion and cannibalisation of pre-existing fault scarps is observed. Erosional scours are relatively large and clearly truncate the tips of faults buried under the MTD.

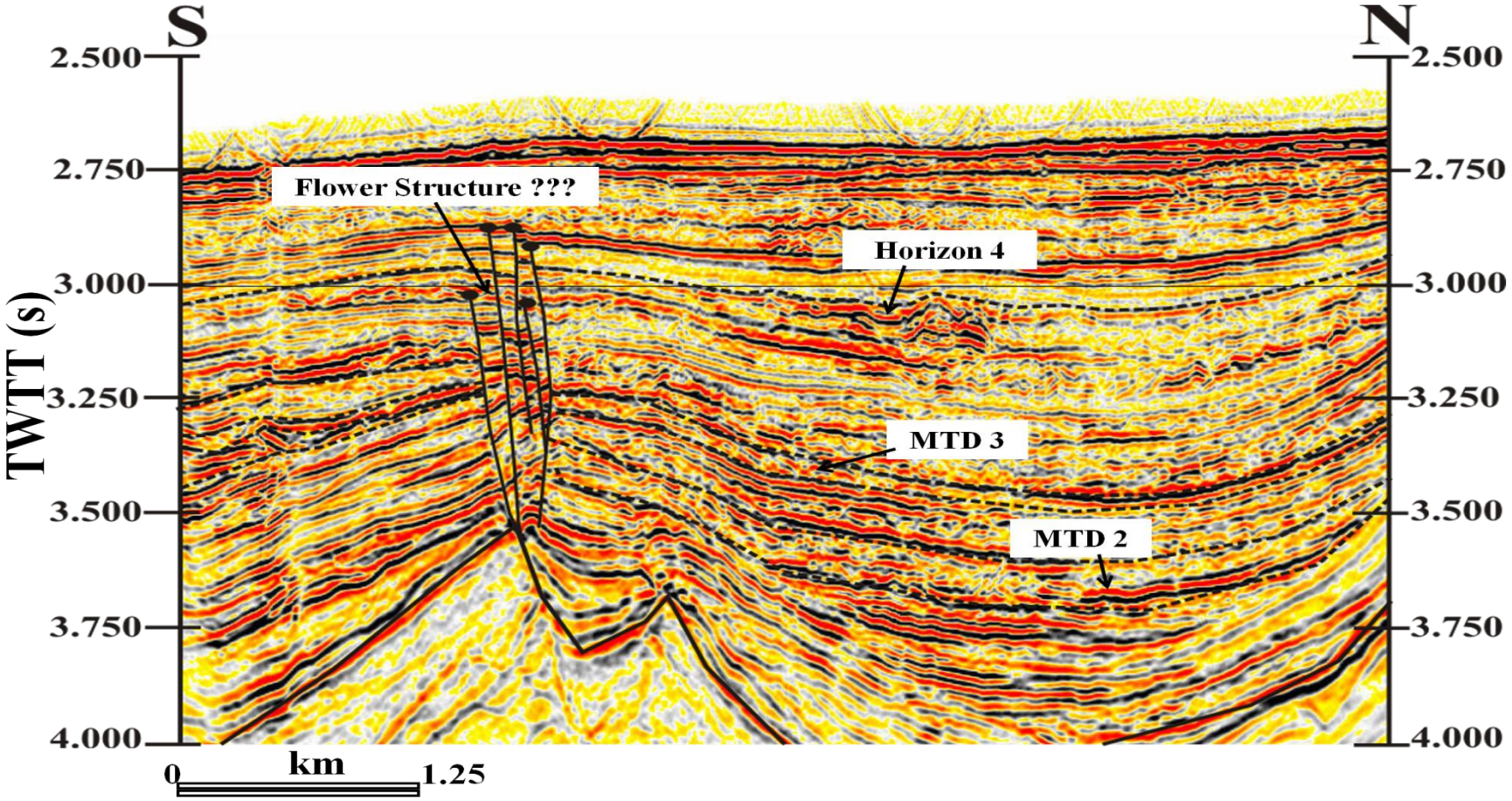

AII. 9: Seismic section showing crestal and radial faults to growing salt diapirs. These faults deviate from normal disposition and include some steeply dipping faults which are interpreted as strike-slipe faults.

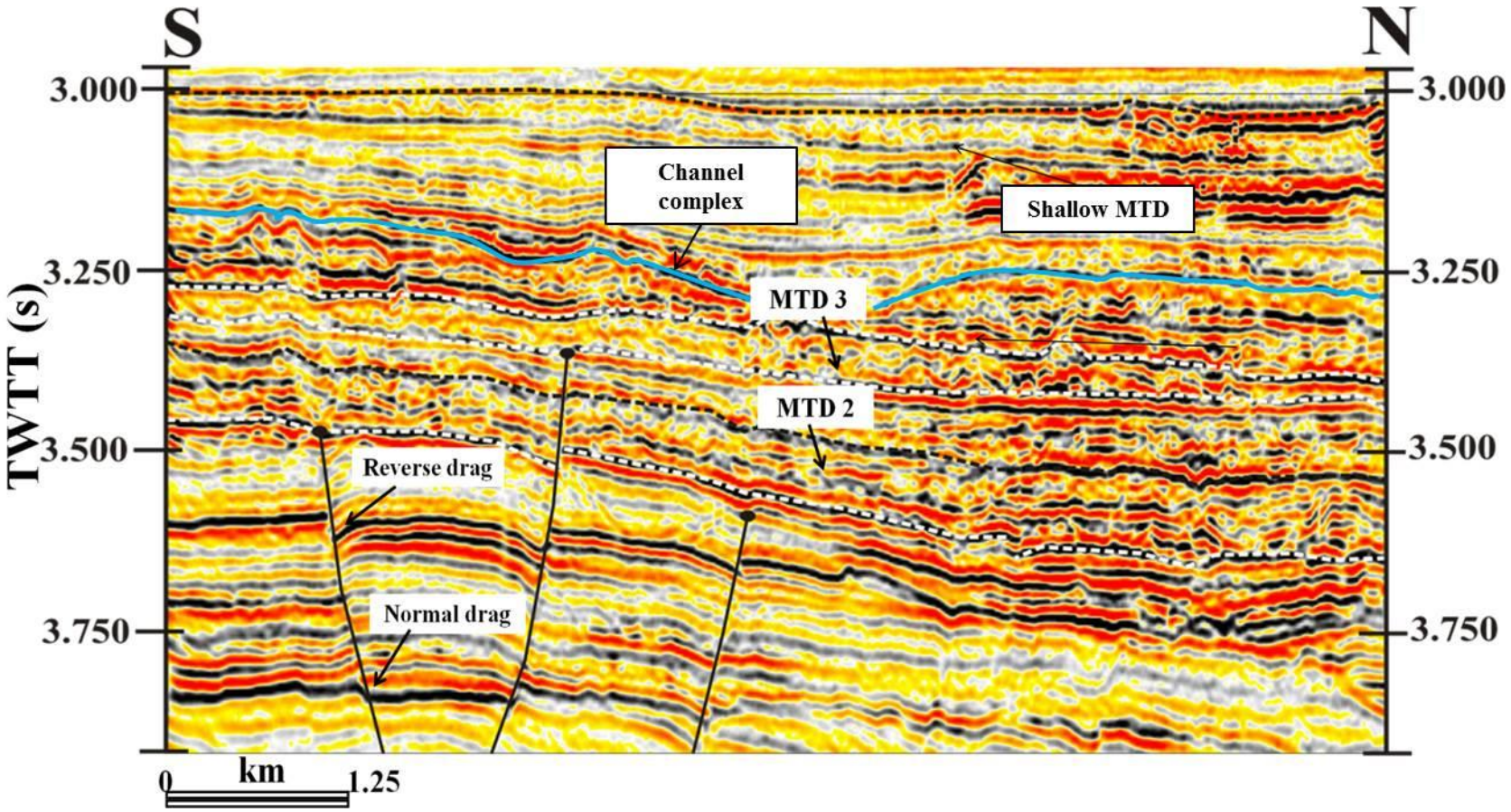

AII. 10: Reverse drag recorded in some of the faults beneath MTD 2 of Chapter 6 suggests that fault reactivation is not limited to non-MTDs areas.

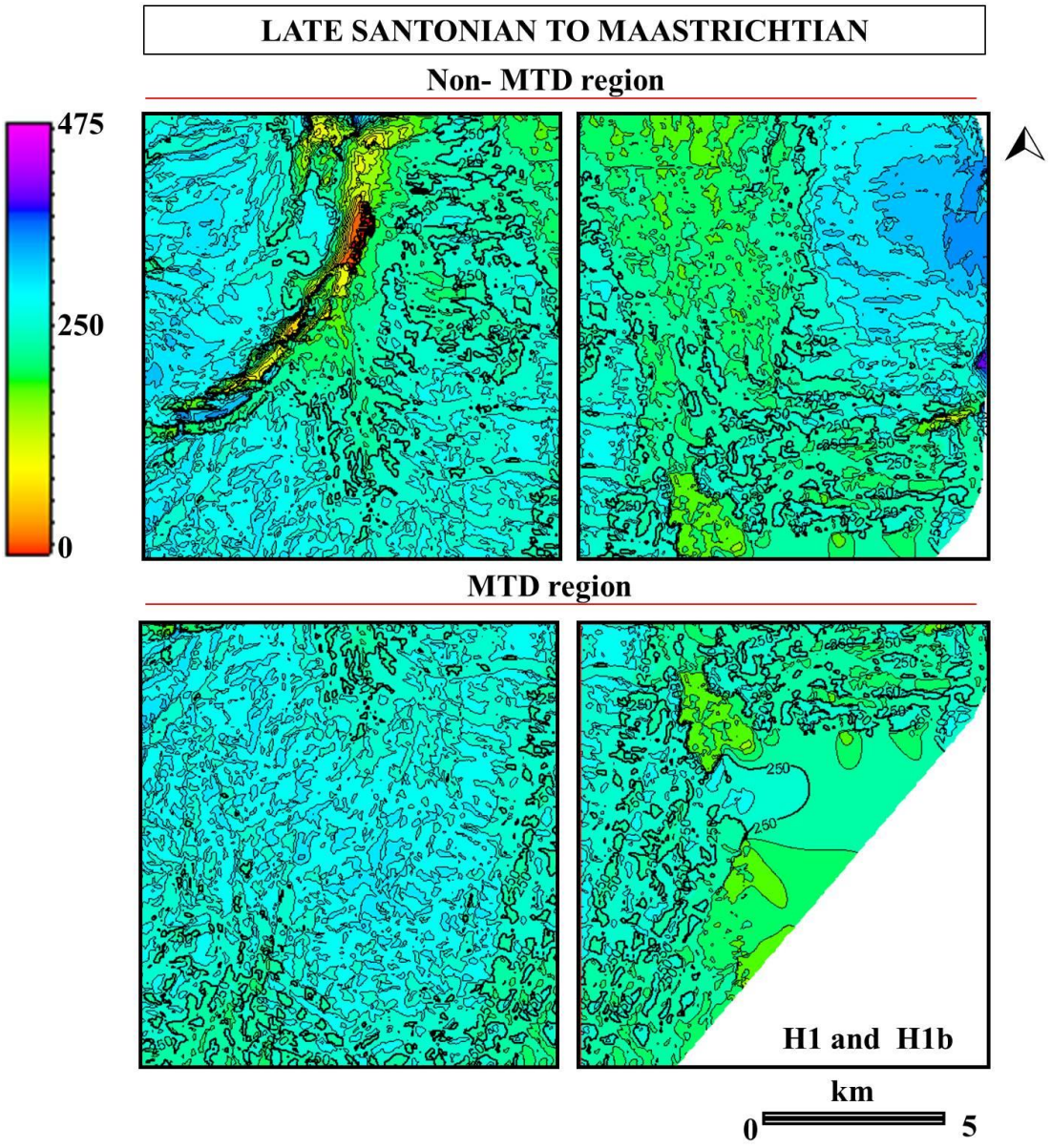
LATE SANTONIAN TO MAASTRICHTIAN
Non- MTD region
475
250
0
MTD region
H1 and H1b
km
0
5

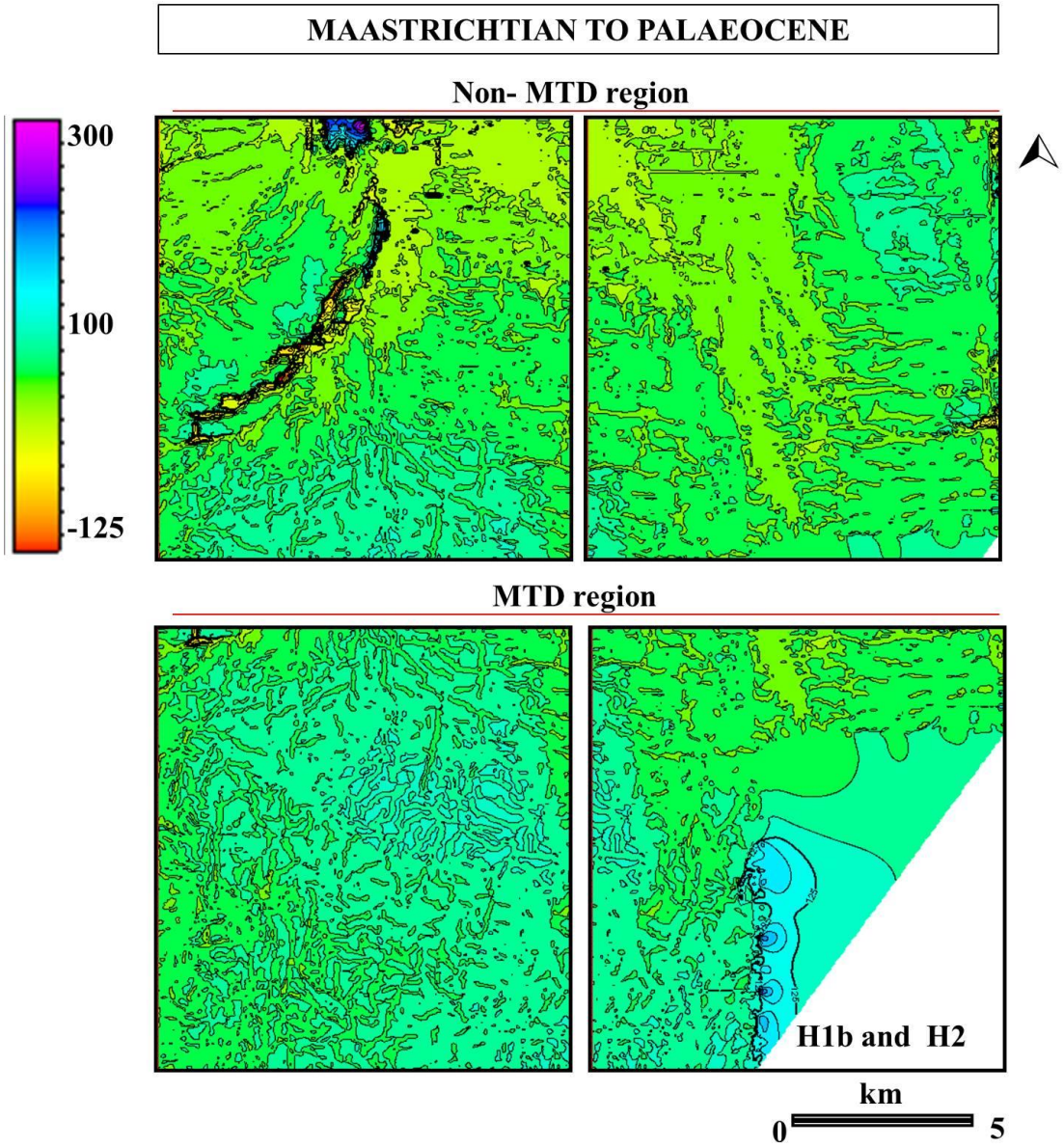
MAASTRICHTIAN TO PALAEOCENE
Non- MTD region
300
100
-125
MTD region
H1b and H2
km
0
5

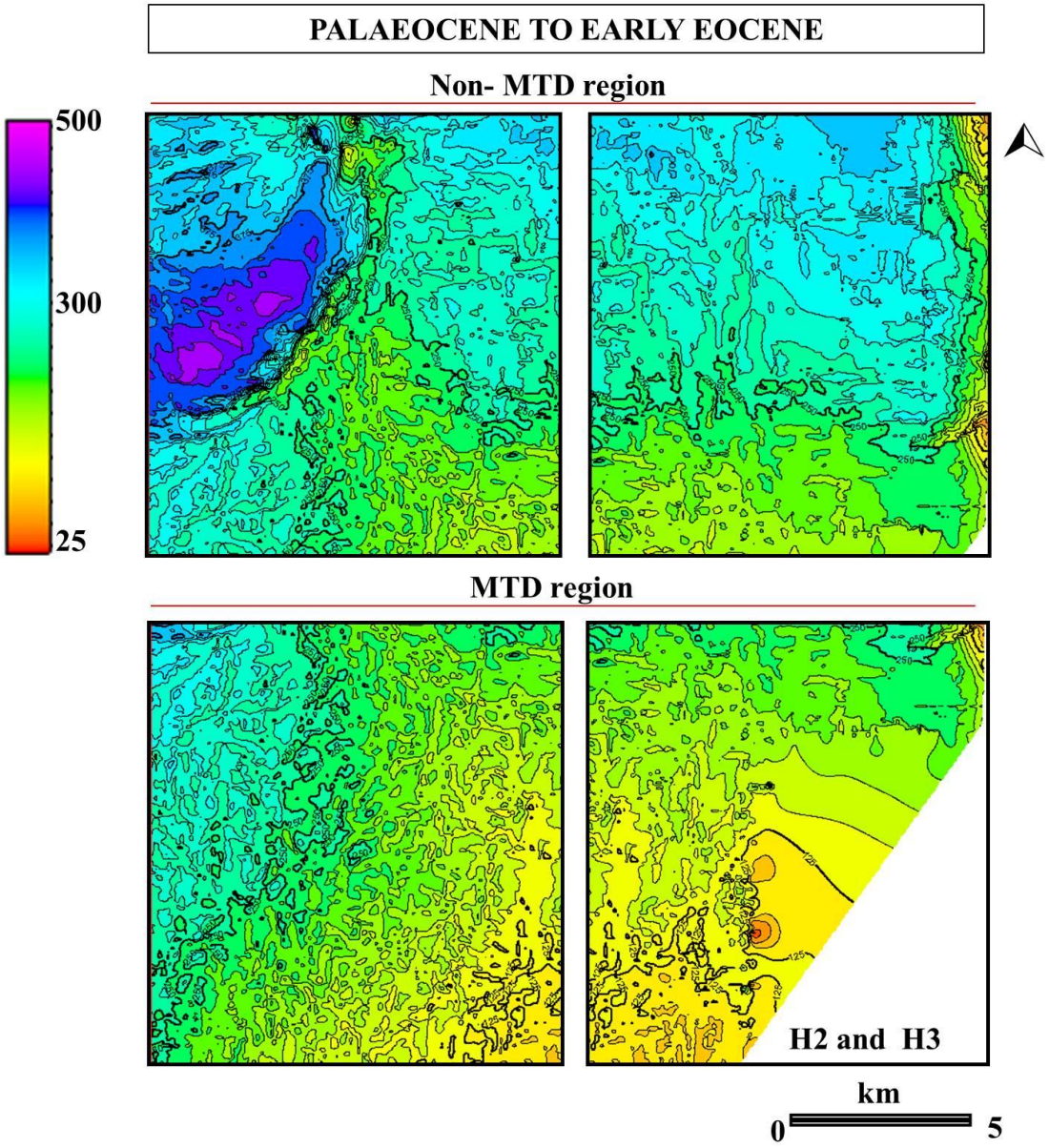
PALAEOCENE TO EARLY EOCENE
Non- MTD region
500
300
25
MTD region
H2 and H3
km
0
5

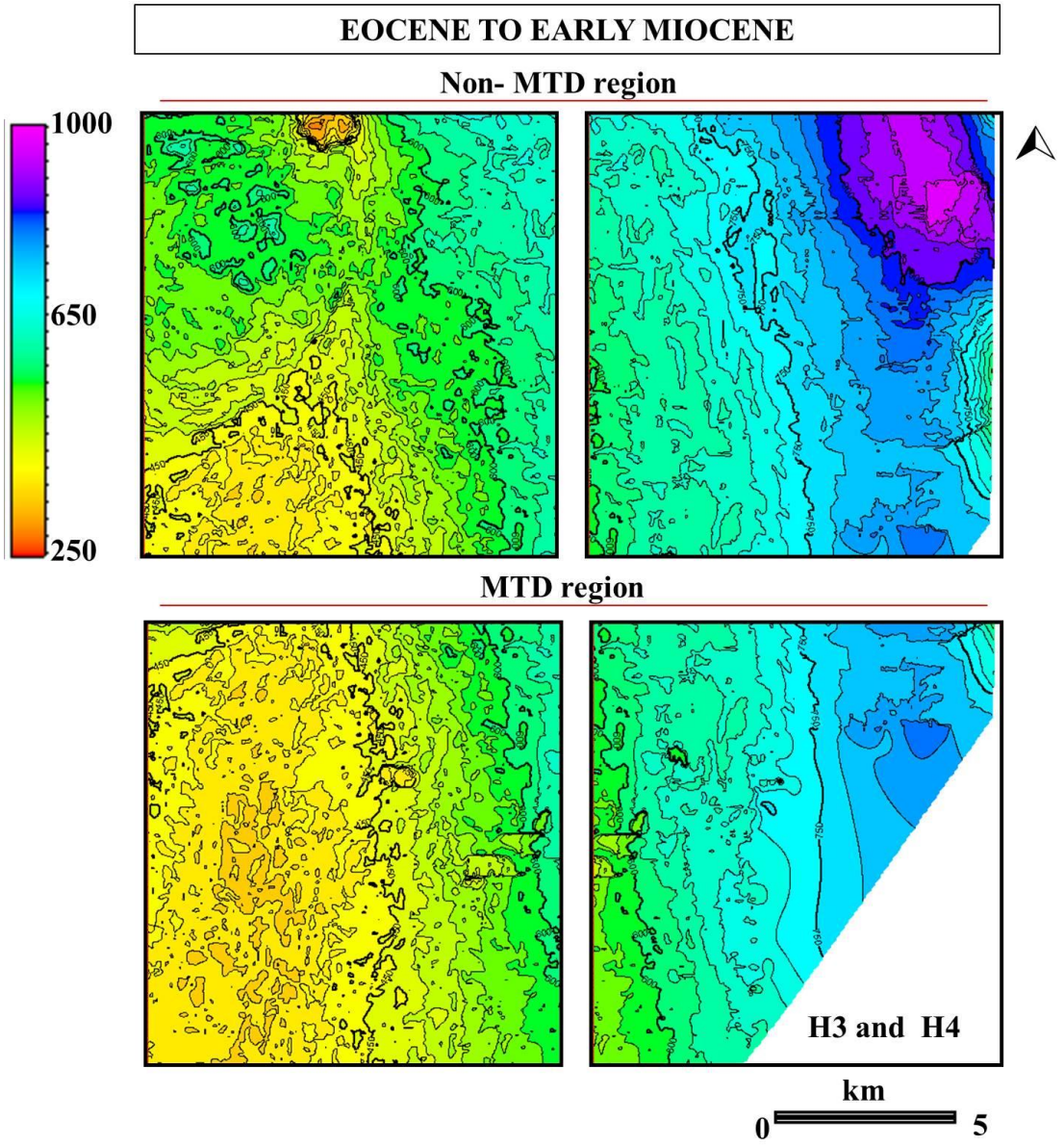

AII. 11: TWTT thickness maps for the principal units interpreted in Chapter 6. Evidence for post-Eocene faulting is manifested as thickness variations recorded in non-MTD areas. The NE-SW trending fault scarps south of the salt diapir correspond to the limit of the basal raft shown in Figure 6.18. *N.B: Zones 1 and 2 are non-MTD areas.*

Appendix III: Chapter 5

Ramps and flats as marker of strain on the flanks of rising diapirs (an attempt to do strain analysis from seismic)

1.1 The Rf- Phi Method

Strain analysis in geology is carried out using any of the following technique; Breddins, Fry's, center to center, and R_f- Φ Technique. Strain markers deform by being transformed from initially circular materials to elliptical features that can be mapped in outcrops. Assumptions during strain analysis include (a) that deformation is homogeneous as it is often very difficult to analyse heterogeneous deformation, and (b) that area is conserved during deformation.

The R_f- Φ technique of strain analysis reconstructs the strain history of initially elliptical objects by finding the strain ellipse that produced the final ellipticity in the strain marker. When an initial ellipse with ellipticity R_i is homogeneously deformed, the resultant form is also elliptical with a final ellipticity of R_f. The R_f is a product of the R_i (initial ellipticity) and R_s (a strain ellipse). The shape of the final ellipse R_f is a function of four factors; the initial shape (form and orientation of the ellipse) and the form and orientation of the strain ellipse.

For a surface containing a number of constantly shaped initial ellipse with R_i of 2.0 (Fig 1a), oriented at different angle phi to an initial marker direction x ($\Phi = 90^0, 75^0, 60^0, 45^0, 30^0, 15^0, 0^0$). The graph shows a plot of constant R_i against Φ for a range of values of Φ. When a homogeneous strain with strain ellipse ratio $R_s = 1.5$ is imposed on the ellipses, their form and orientation changes (fig 1b). The shapes of the initially constant ellipses are changed depending on their orientations with respect to those of the axes of the strain ellipse, and the orientations of the axes of the new ellipses (Φ^1) also change (except with those with initial orientations $\Phi=90^0, 0^0$), the long axes of the combined ellipses come to lie closer to the direction of the long axis of the strain ellipse. The

initial ellipse which had its long axis parallel to the maximum elongation of the strain ellipse ($\Phi=0^0$) takes on a new form which is more elliptical than that of the strain ellipse, whereas the ellipse which had its long axis parallel to the minimum elongation of the strain ($\Phi=90^0$) becomes less elliptical than the strain ellipse. The ellipticities of the other ellipse lies within this range but most of them have ellipticities higher than that of the strain ellipse. The arithmetic mean value of the ellipticities will be greater than the true ellipticity of the strain ellipse.

Imposing a homogeneous strain of twice the R_s value in Fig 1b on the same ellipses in Fig.1a will result in a strain ellipse shape greater than the ellipticity of the initial elliptical form. The range of the orientation of the particle ellipse long axes is much more restricted. The fluctuation, F is the range of orientation of the long axes. At the initial stage, the F is 180^0 which is also the same value when the tectonic strain ellipse had a lower ellipticity than the original elliptical object. As deformation becomes stronger than the initial elliptical form of the objects, the fluctuation decreases to less than 90^0 and the R_f/ Φ^I become closed.

1.1.1 The Rf- Φ Algorithm.

- The long, short and intermediate axes of the ellipses were designated as X, Z and Y respectively. Here, the Z axis was measured 45^0 from the X axis intersecting both the X and Z axes at the origin.
- The strain ellipses were inferred from the location of the basal ramps on the dip maps
- The ellipses obtained in step 2 were overlain on those inferred from the RMS amplitude map in order to pick the final ellipses

- The axes of the inferred ellipses were measured
- The R_f was estimated from the ratio of XZ, XY, and YZ.
- The I_{SYM} was performed to assure that the data is consistent with the original assumption than no previous fabric was present on the sea floor.
- The harmonic and vector mean of the R_f and Φ value were determined and were plotted as lines on the R_f Vs Φ.
- When graphed as lines, the two means produce four quadrants with the plot.
- The I_{SYM} was calculated from $I_{SYM} = 1-(|n_A-n_B| + |n_C-n_D|)/N$
- n_A denotes the number of strain markers in quadrant A etc and N = the number of markers
- I_{SYM} value of 0.5, 0.5 and 0.75 were estimated for XZ, XY and YZ respectively.
- High I_{SYM} suggest the data are symmetrical, while low values suggest that the data are markedly asymmetric and hence the assumption of no preferred initial orientation of the strain markers is incorrect (Lisle, 1985, Chew 2003). If a previous fabric were present, the final Rs value would be a measure of the strain on that fabric, and not of the original sea floor.
- The samples fit the original assumption, so the plots were overlain with Rs value plots as provided by Lisle (1985).
- The appropriate Rs value was selected from the overlay that shows the best fit.
- From this plot the strain ellipse ratio R_s, original axis ratios (R_i), and orientations (θ) for the ellipses was determined.
- The average R_s value is shown for the all the ellipses

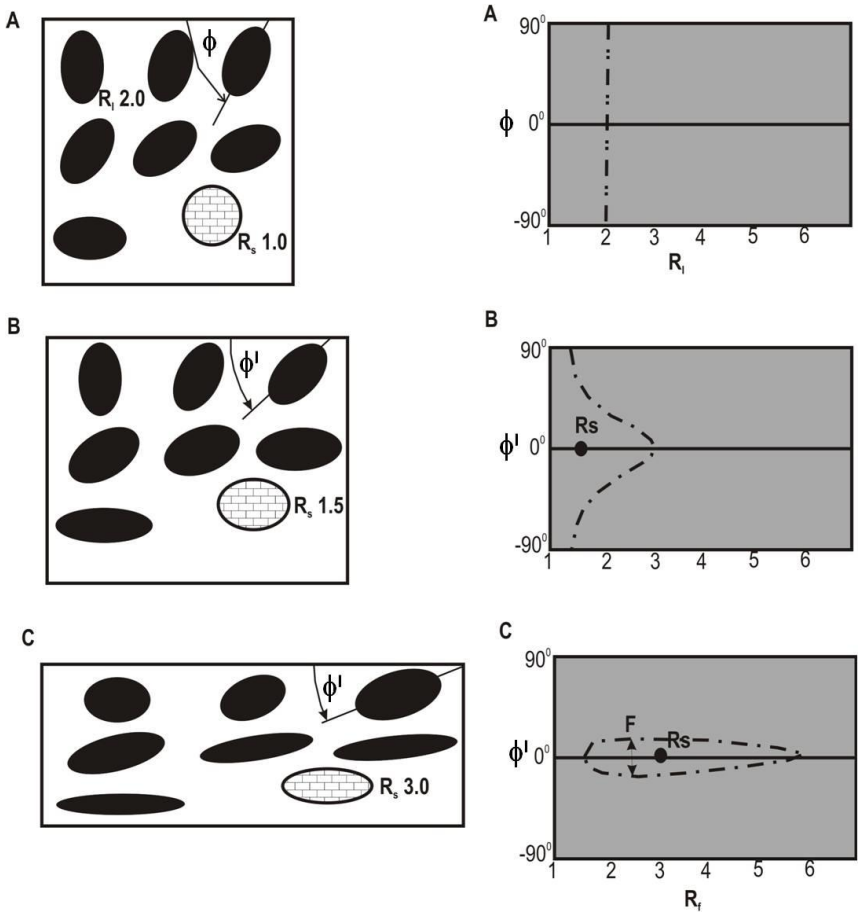

AIII. 1: The Rf/ ϕ technique of strain analysis. The effect of deformation on a series of elliptical objects with initial orientation of ϕ and ellipticity R_i. After deformation (ellipticity R_s of strain ellipse) the original marker ellipses change shape (ellipticity, R_f) and orientation (ϕ^I). F is the fluctuation which is the range of orientation of the long axes (Modified after Ramsay & Huber, 1983)

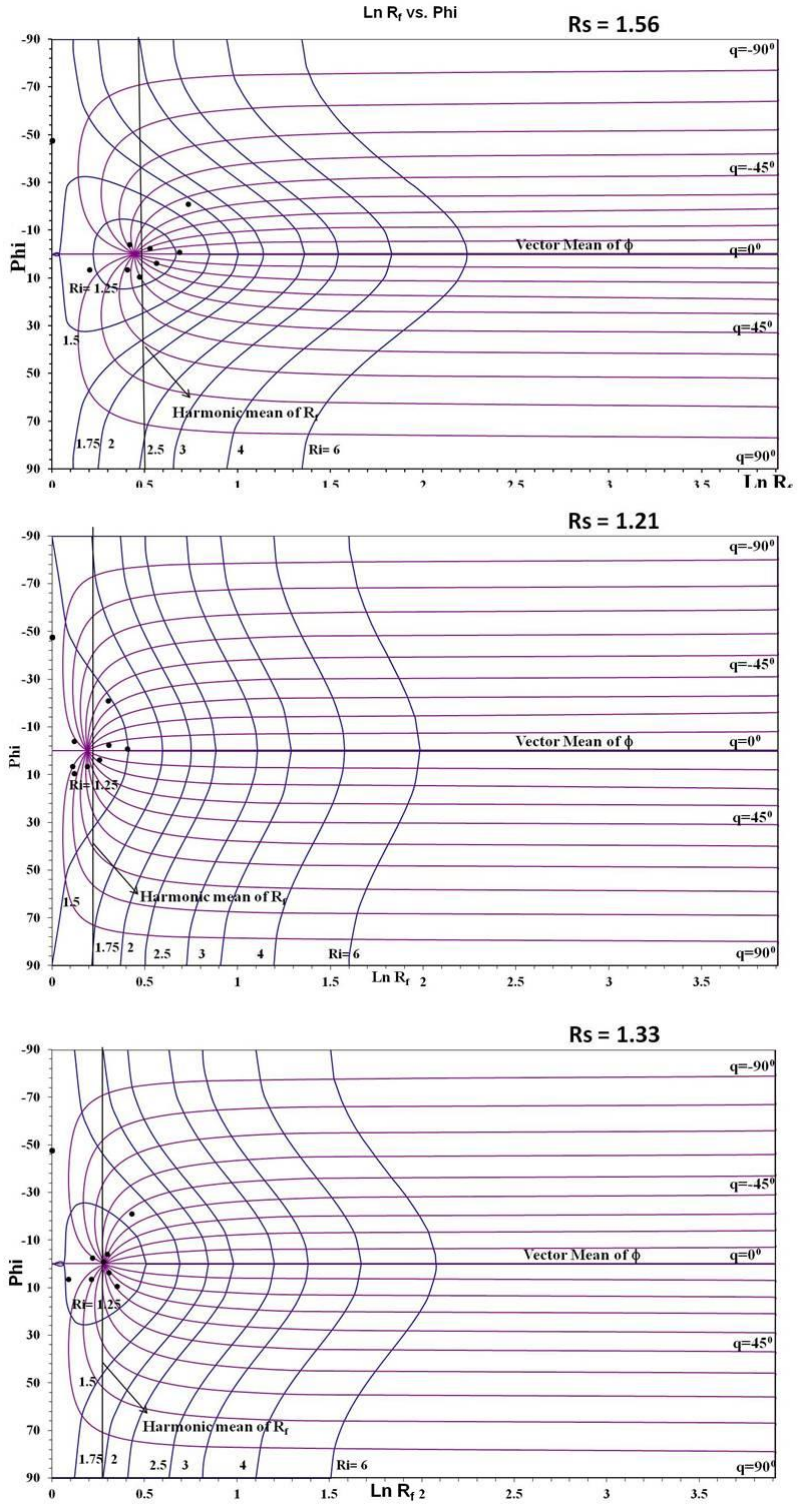

XZ (long/Short)
Rs = 1.56

XY(long/Intermediate)
Rs = 1.21

YZ(Intermediate/short)
Rs = 1.33

AIII. 2: "ln Rf Vs ϕ" chart for the ellipses in the study area. The elliptical drag zone have Rs value of 1.56 and when view in 3D dimension on seismic, the ellipsoid have Rs of 1.21 and 1.33 for the XY and YZ axes, respectively.

1.1 Coherence map at the base of the MTDs

The coherence seismic attribute is a measure of the waveform similarity i.e. how a trace is similar to its neighbour. Similar traces were mapped with high coherence coefficients while discontinuities have low coefficients and when combined with dip maps, the two attribute provided an unbiased interpretation of the basal shear features.

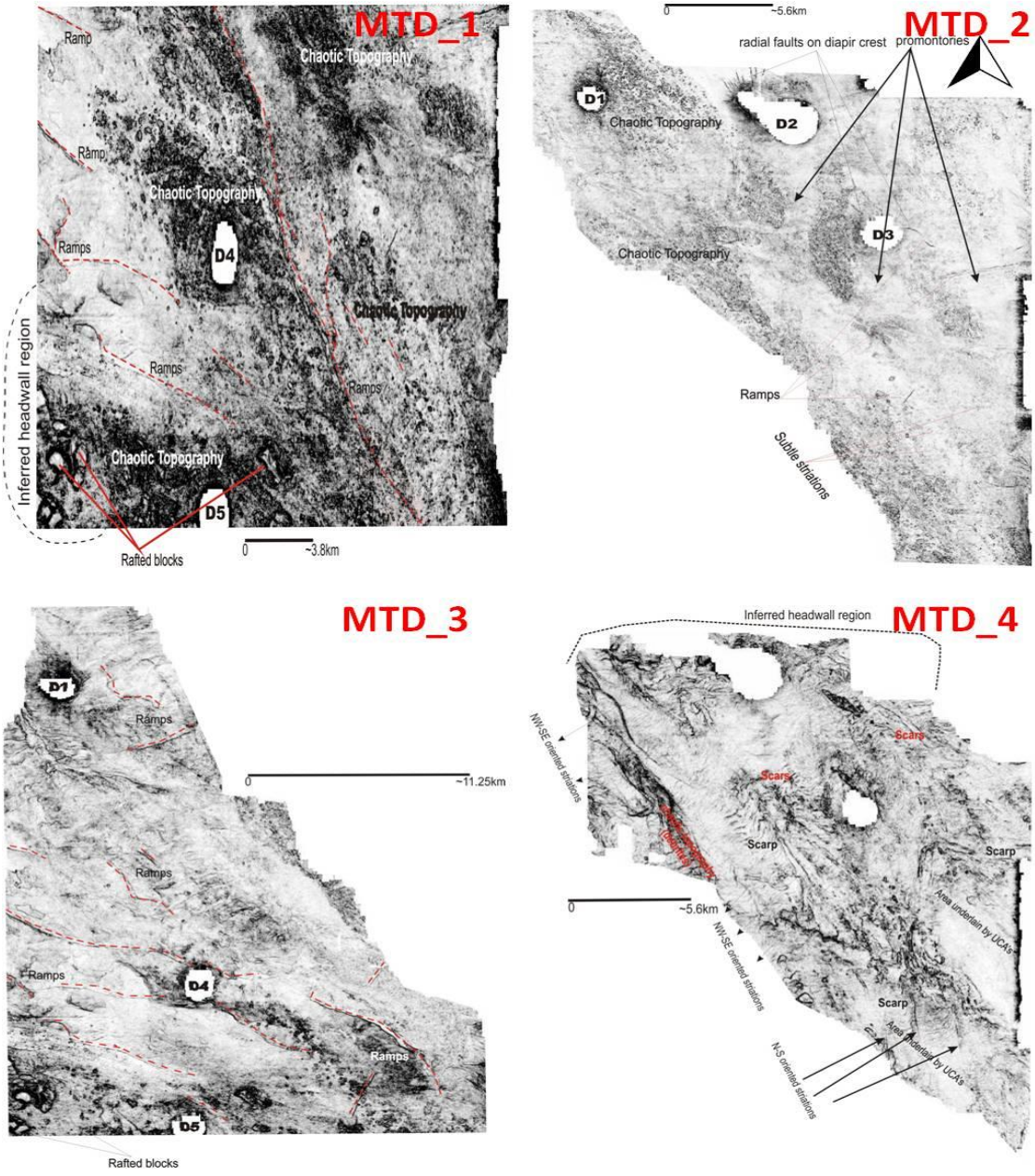

AIII. 3: Coherence map highlighting the characteristic features of the basal shear surface of MTDs in Chapters 4 and 5. (a) Ramps on MTD 1 are shorter along strike than most of the other ramps (b) The ramps at the base of MTD 2 are characterised by stair case geometry produced when antithetic ramps created coves between promontories. (c)

The larger ramps on the basal shear surface of MTD 3 are unrelated to the salt diapirs (d) Shorter ramps on the southern margin of diapir, D3 are form scarps in the palaeo sea floor. To the west of the D3, the ramps form a relay zone.

1.2 RMS Map and distribution of the MTD facies within the drag zones

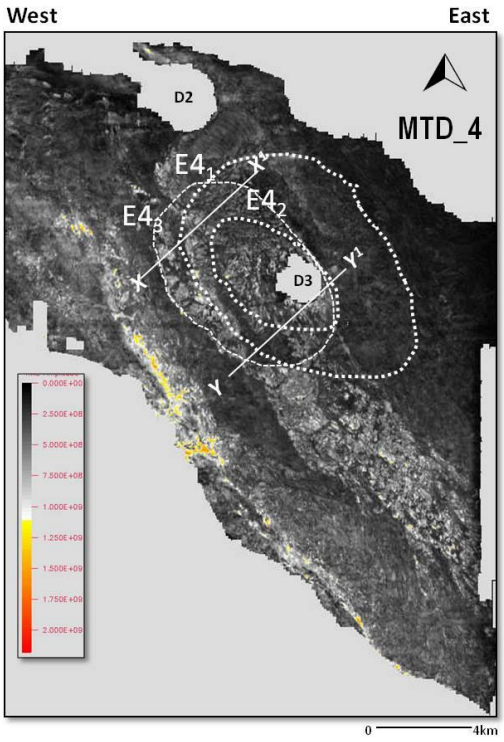

RMS Amplitude between H7&H6 (**MTD_4**)

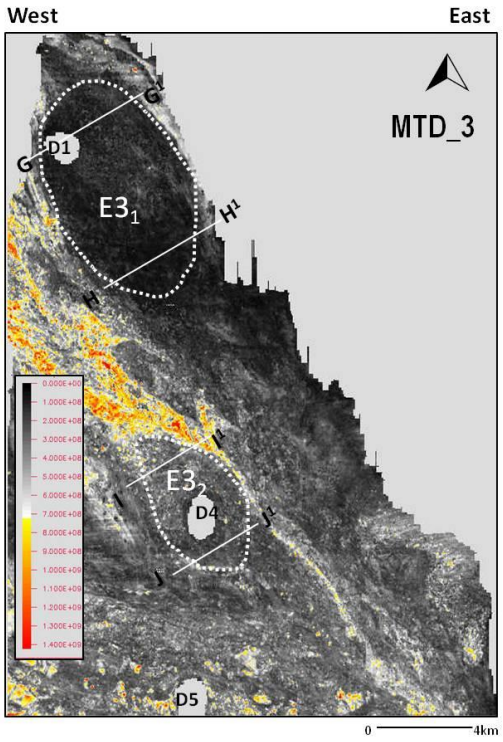

RMS Amplitude between H5&H4 (**MTD_3**)

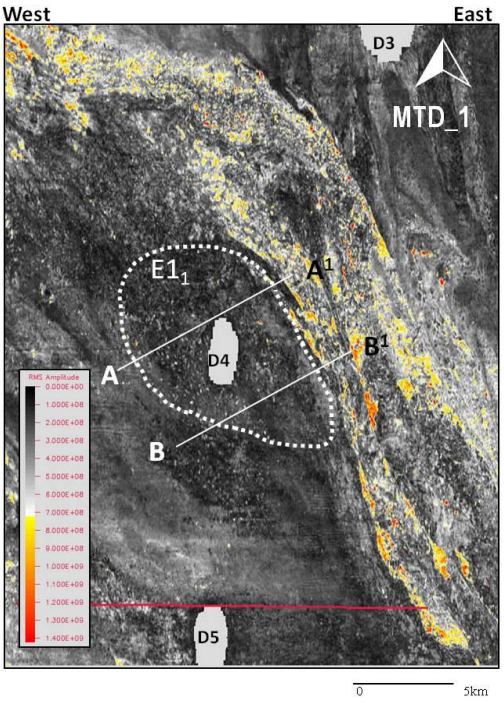

RMS Amplitude between H1&H0 (**MTD_1**)

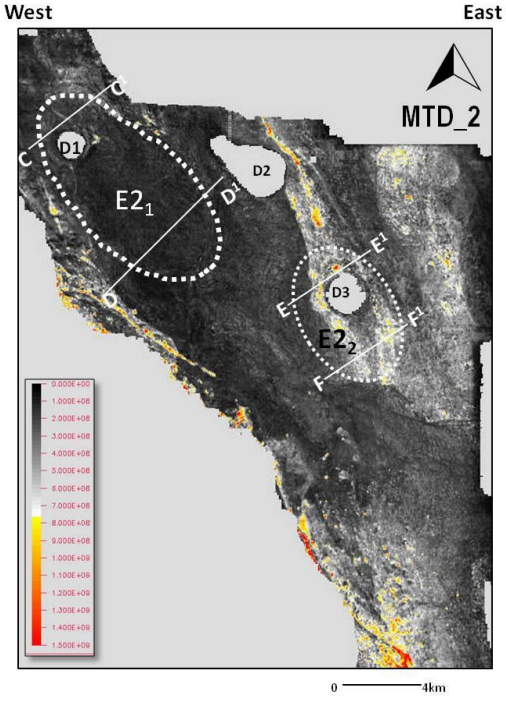

RMS Amplitude between H3&H2 (**MTD_2**)

AIII. 4: Strain ellipses inferred from the RMS Amplitude maps between the tops and bases of the MTDs (a) Ramps dissected the MTD into zones of high and low amplitude reflection, a NW-SE ramp produced this distinct boundary especially at the centre of the

map. Scarps observed on the map are related to ramps on the basal shear surface. Moderately high amplitude up north of diapir, D5 reflects the presence of undeformed blocks in the MTD (b) Low amplitudes are recorded to the west of D2 and D3 in a NW-SE trend. The areas of high amplitude separated the MTD into bands of alternating highs and lows especially on the eastern part of the unit. High amplitude in the vicinity of D3 coincided with zones of promontories identified on the dip map, ramps truncates this reflections. (c) MTD 3 shows is charcaterised by very low amplitude from north to south on the RMS amplitude map. This zone is separated by a NW-SE ramp (d) MTD 4 is characterised by very high amplitude from NW to SE, and low amplitude on the WSW margin. Blocks are prominent features on the SE margin of D2. The density and size of the blocks decrease toward the NW margin of D3.

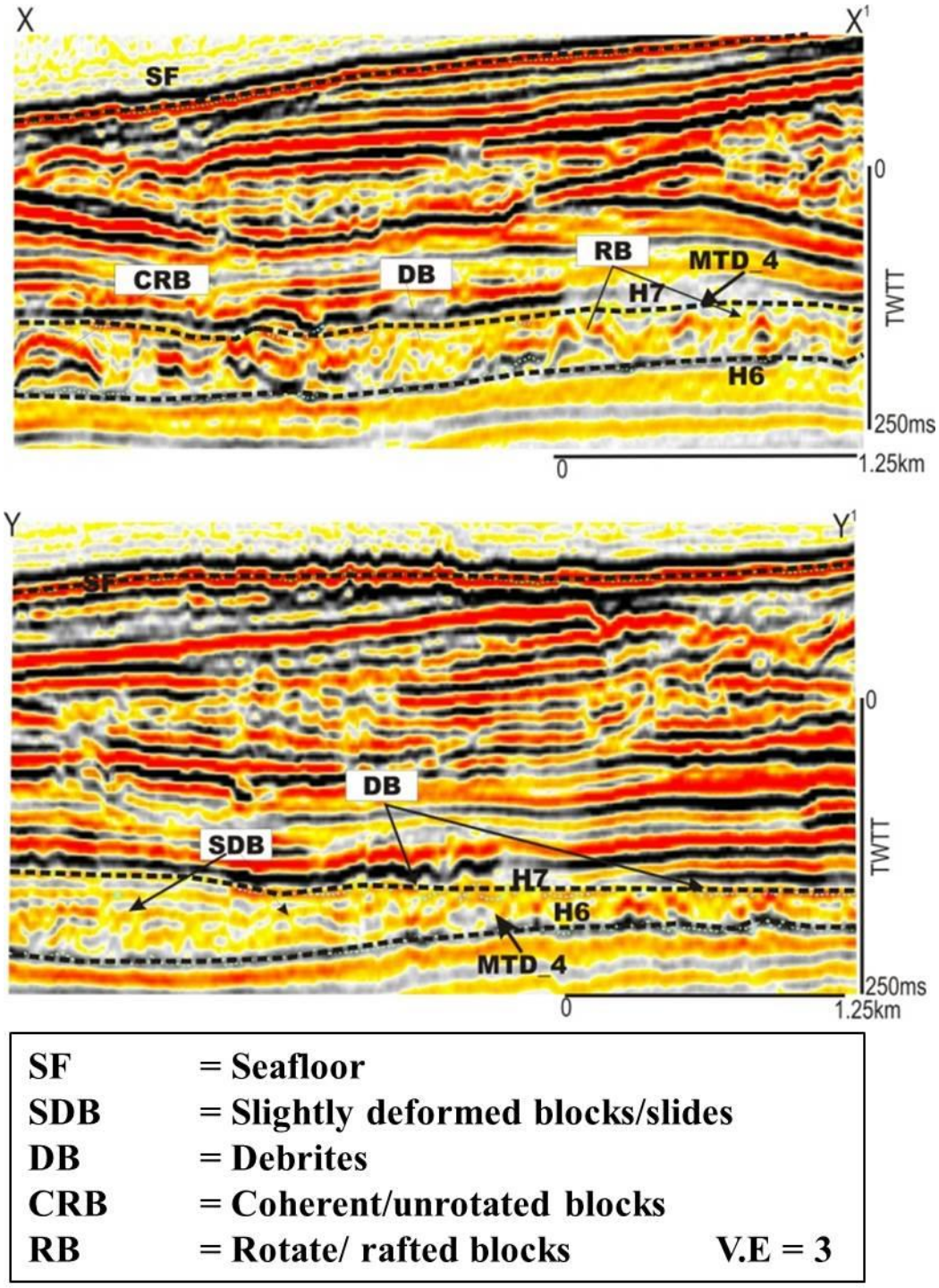

AIII. 5: MTD facies interpreted within drag zone 4_1.

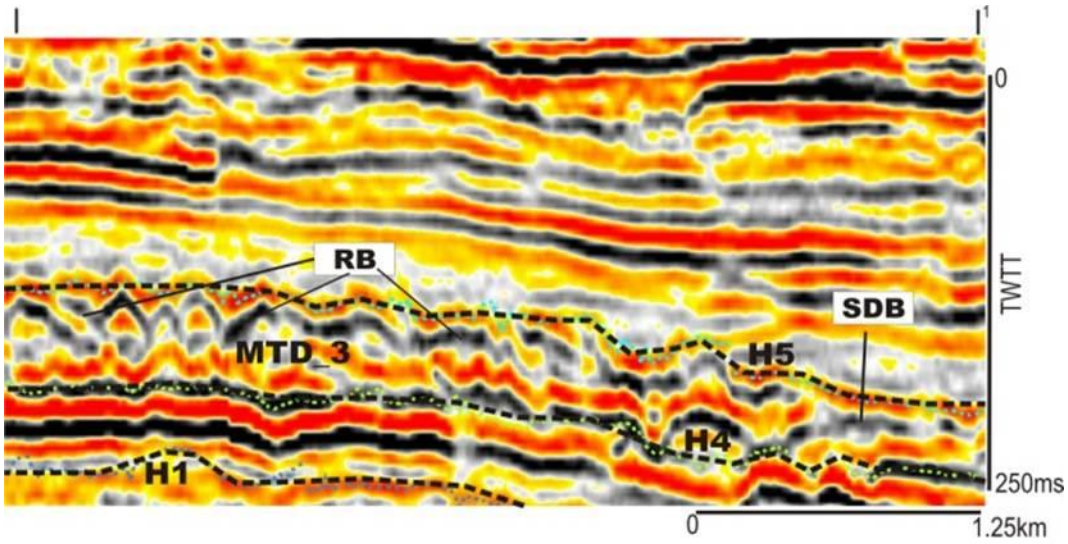

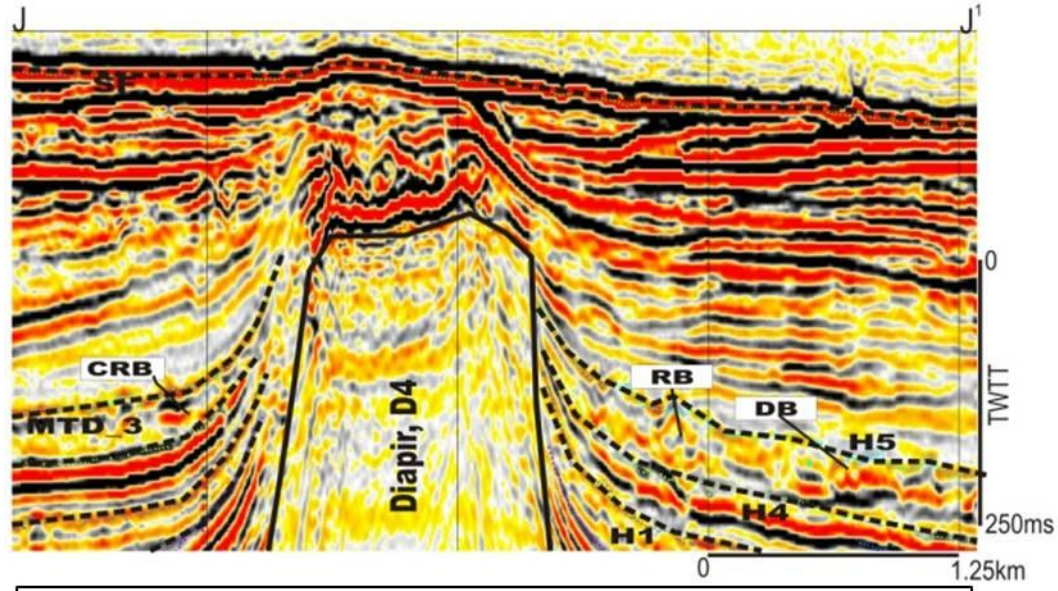

SF	**= Seafloor**	
SDB	**= Slightly deformed blocks/slides**	
DB	**= Debrites**	
CRB	**= Coherent/unrotated blocks**	
RB	**= Rotate/ rafted blocks**	**V.E = 3**

AIII. 6: MTD facies interpreted within drag zone 3_2.

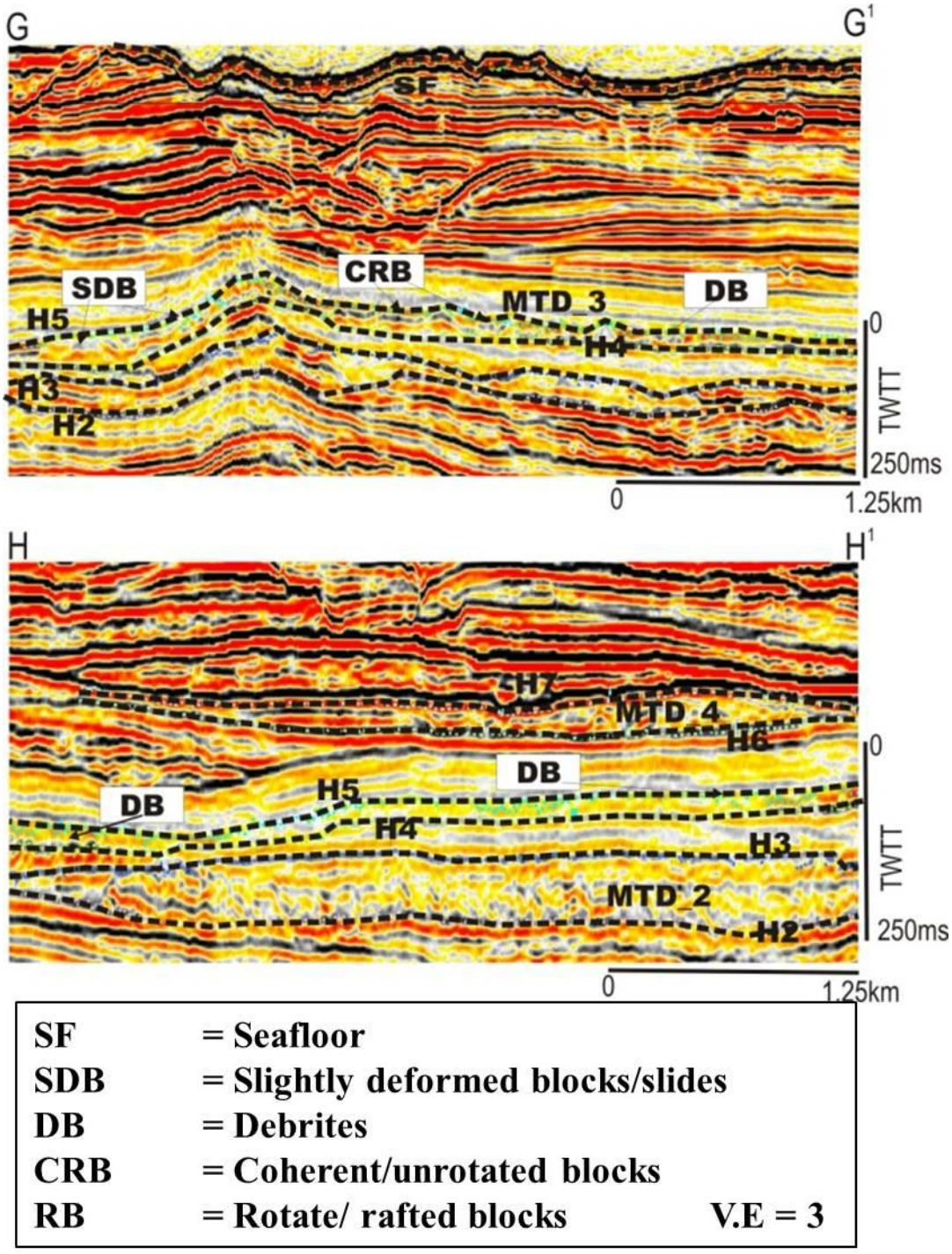

AIII. 7: MTD facies interpreted within drag zone 3_1.

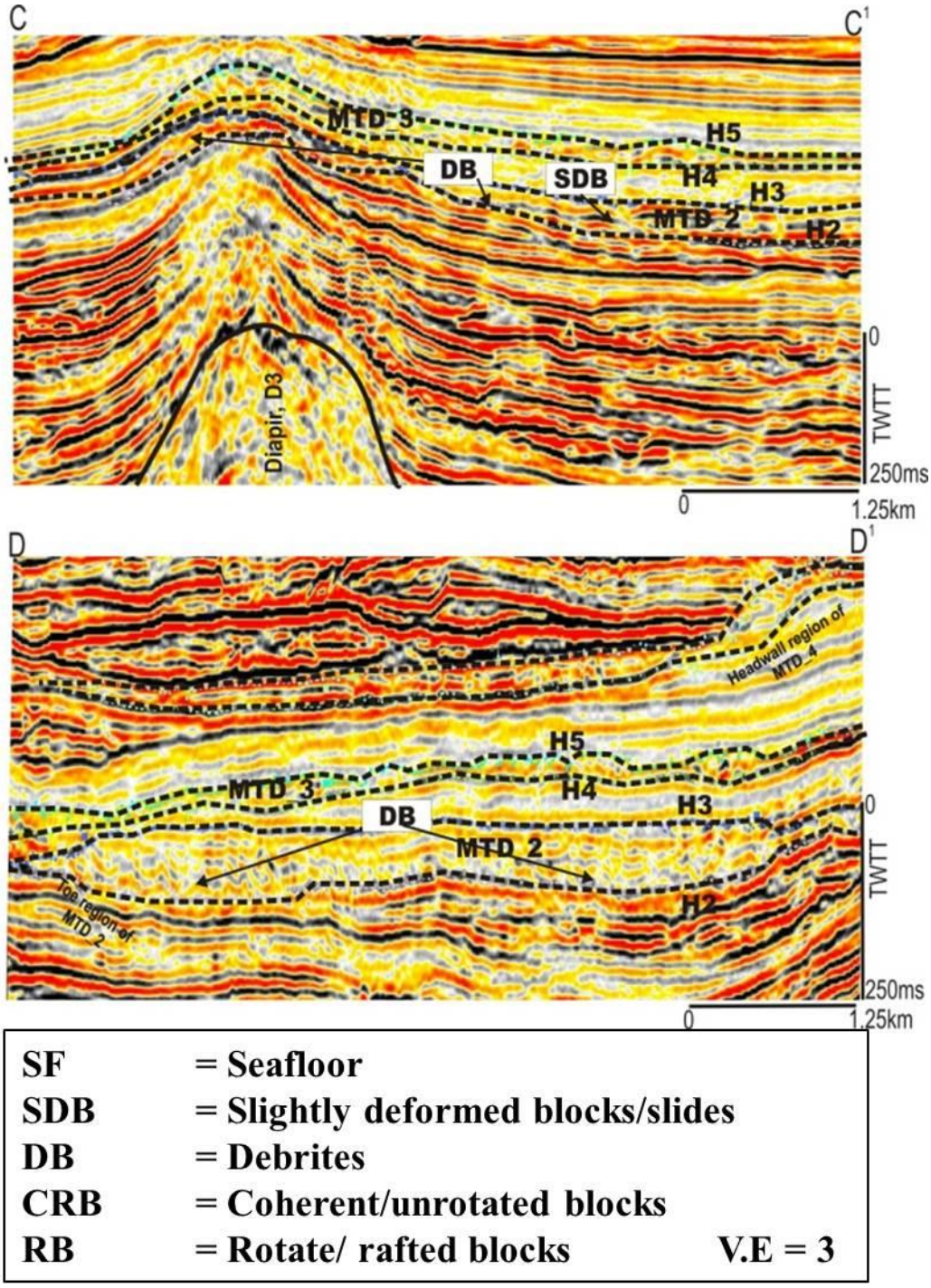

AIII. 8: MTD facies interpreted within drag zone 2_1.

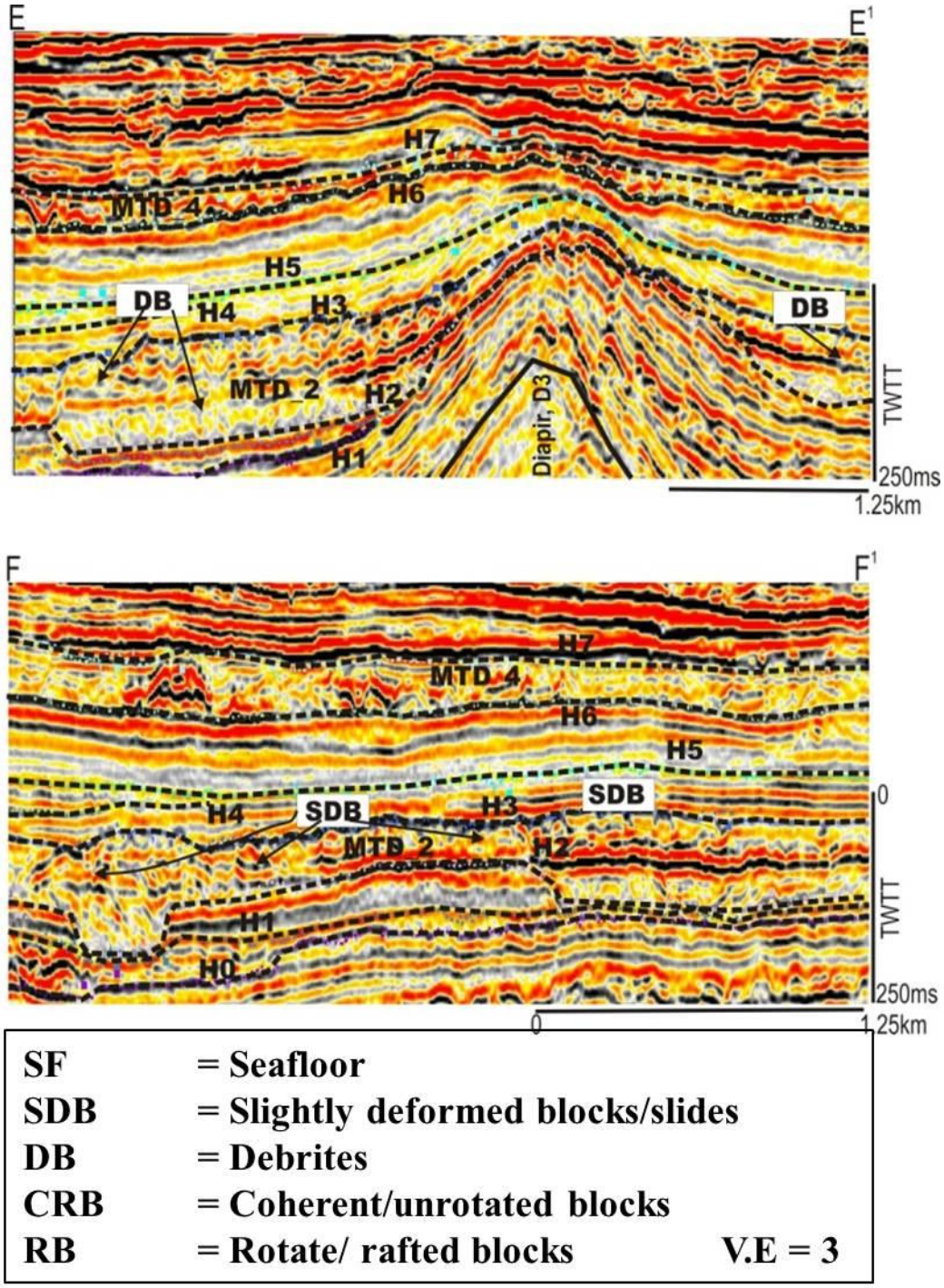

AIII. 9: MTD facies interpreted within drag zone 2_2.

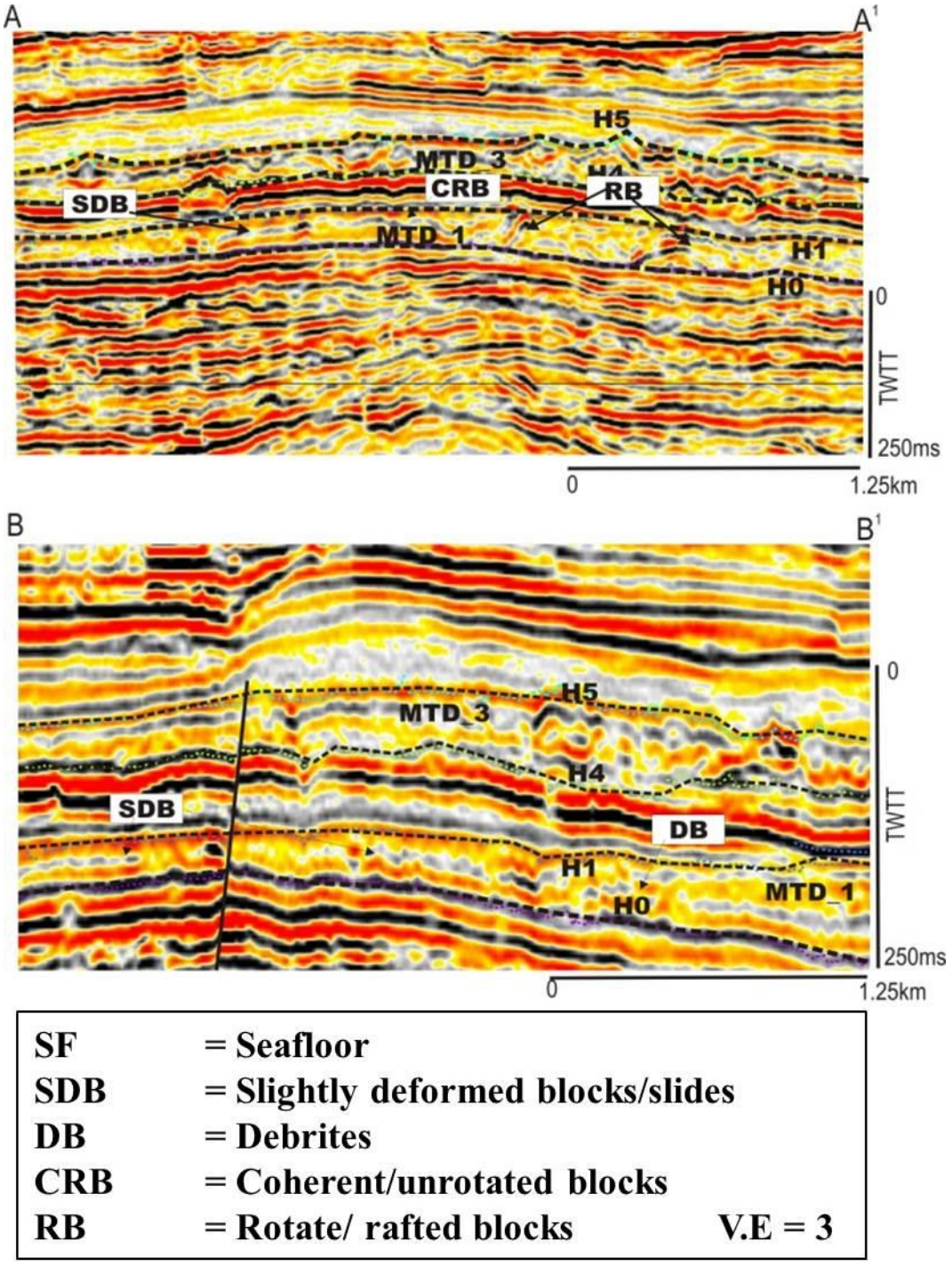

AIII. 5: MTD facies interpreted within drag zone 1_1.

Appendix IV: Review of kinematic indicators of MTDS

Extensional domain or depletion Zone

- The headwall scarp defines the upslope margins of mass-transport deposits, where the basal shear surface ramps up to cut stratigraphically higher, younger strata and intersect the surface (Bull et al., 2009; Frey Martinez et al., 2005).
- Headwall scarps are characterised by an arcuate geometry in plan-view.
- They are often fragmented and sinuous which help to distinguish them from tectonic normal faults (Lastras et al., 2006;Lastras et al., 2004; Imbo et al., 2003; Boe et al., 2000).
- Headwall scarps forms in the same way as extensional faults. The headwall propagates along-strike perpendicular to the direction of the minimum compressive stress σ3; (Anderson, 1936), which will generally be oriented parallel to the slope due to the effect of gravity acting on the sediment mass.

Translational domain

- Sigmoidal scarps run parallel to the direction of mass flow
- Grooves and striation are oriented parallel to the direction of mass flows (Bull et al., 2006 Gee et al., 2005).

Lateral margins

- Lateral margins are the dip-parallel side boundaries of a mass-transport deposit; they form parallel to the gross flow direction, and offer a primary constraint on the gross general transport direction (Bull et al., 2009).
- Lateral margins are associated with strike-slip movement, although transpressional or transtensional deformations may occur if the MTC scar

widens or narrows (Frey Martinez et al., 2005; Martinsen and Bakken, 1990; Martinsen, 1994).

Basal shear surface

- The basal shear surface is often continuous and concordant with bedding, but may be affected by faults, bedding plane or material variations (Varnes, 1978).
- A ramp is defined as a segment of the basal shear surface that cuts discordantly across bedding, whereas the 'flat' sections are bedding-parallel segments of the basal shear surface.
- The ramps, therefore, connect 'flat' segments of the basal shear surface at differing stratigraphic levels (Trincardi and Argnani, 1990).
- Slots are kinds of ramps that run parallel to the flow direction (Bull et al., 2009; O'Leary, 1986).

Toe domain/Accumulation Zone

- *Pressure ridges* are defined here as positive, parallel to sub-parallel, linear to arcuate ridges orientated perpendicular to flow direction (Boe et al., 2000; Masson et al., 1993; Moscardelli et al., 2006; Posamentier and Kolla, 2003).
- Pressure ridges are commonly observed in both submarine and subaerial mass-transport deposits, and are usually confined to the toe domain.
- They can, however, occur elsewhere due to localised topographical variations in the basal shear surface, or obstacles to flow (Masson et al., 1993).
- Pressure ridges are best viewed on top-MTD surface maps.
- Pressure ridges have been associated with debris flow deposits (Posamentier and Kolla, 2003), and occur where Mass-transport deposits are free to spread-out in

an unconfined manner to form convex-downslope, lobe like morphologies ‘frontally emergent’, after (Frey-Martínez et al., 2006; Lucente and Pini, 2003; Prior and Coleman, 1984).

Examples of Kinematic indicators for MTDs

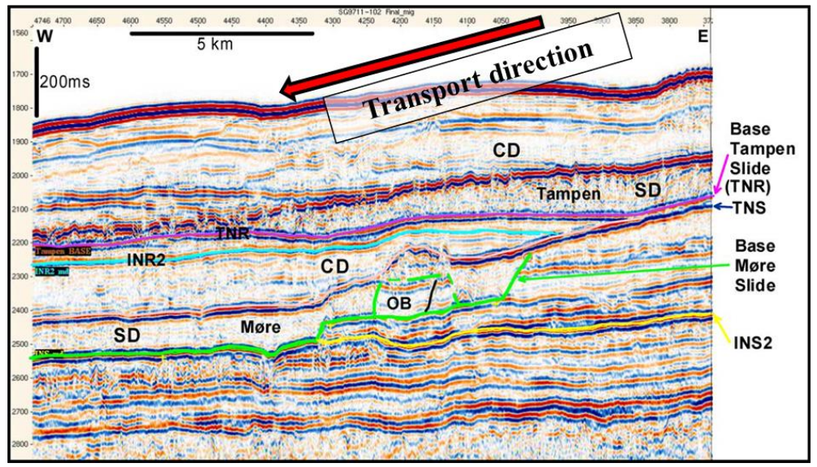

Headwall region of several submarine landslides including the Storegga slide from the Norwegian margin (Solheim et al., 2005).

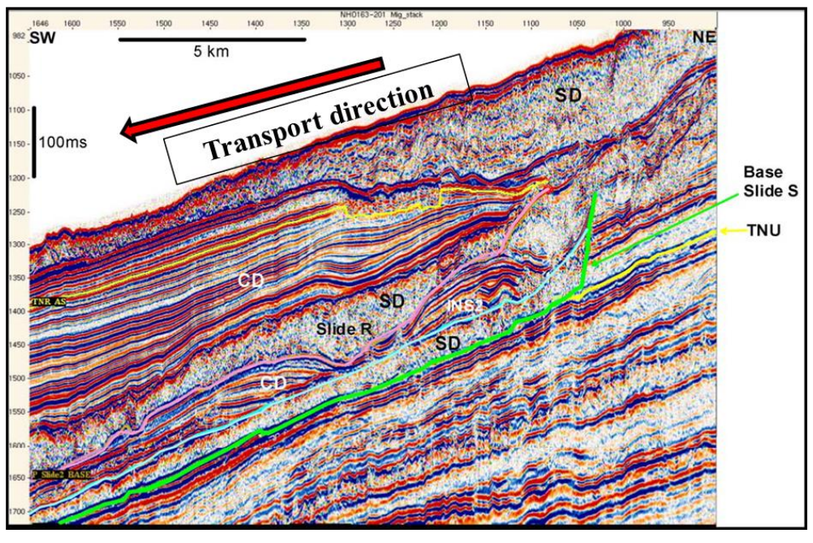

Headwall region of several submarine landslides including the Storegga slide from the Norwegian margin (Solheim et al., 2005).

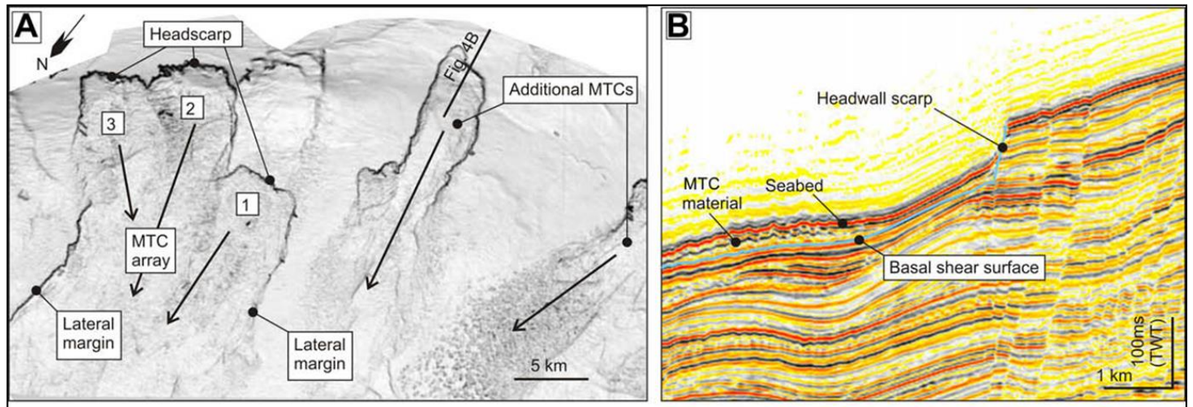

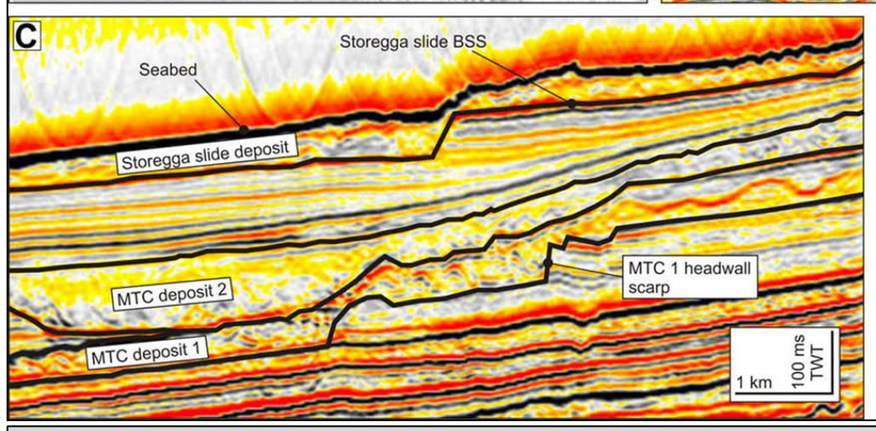

Headwall scarps from the headwall domain of several MTCs from the Levant Basin area. The headwall scarps are characterised by arcuate geometry (B) Seismic section through headwall scarp of a Levant Basin MTC (location shown in A). (C) Seismic section from the headwall domain of the Storegga Slide showing Storegga Slide deposits and older MTC deposits (labelled 1 and 2, respectively) lower in the succession. Note the infilling of the earlier headscarp (labelled 'MTC 1 headscarp') by the subsequent MTC deposit 2 (From Bull et al., 2009)

N.B: MTC – Mass transport complex, CD- Contouritic deposits and SD- Slide

HEADWALL REGION

Examples of Kinematic indicators for MTDs

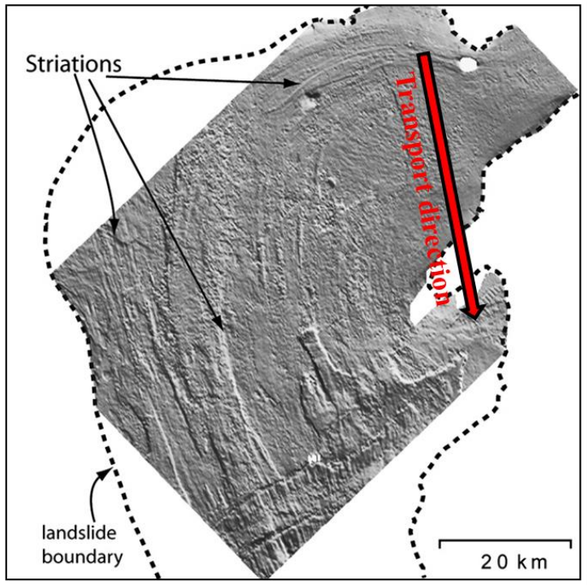

Striations from the Brunei Slide (Gee et al., 2005)

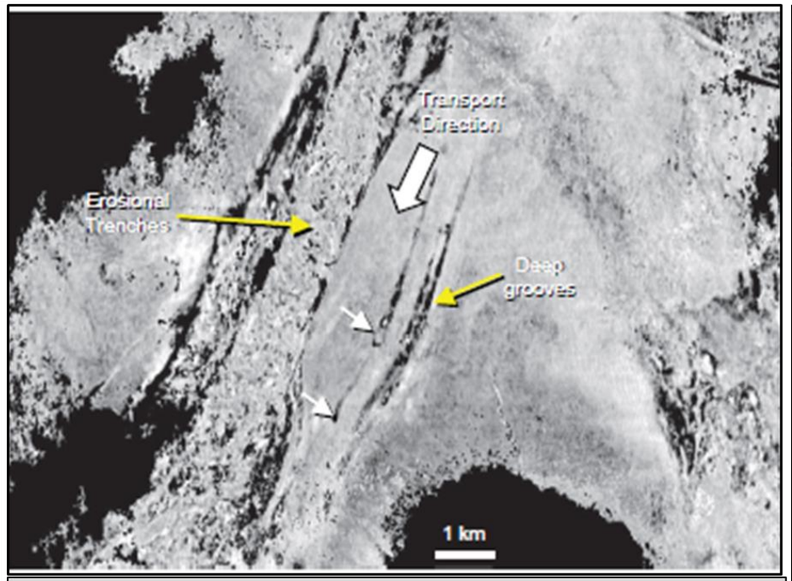

Seismic amplitude stratal slice illustrating outrunner blocks and associated grooves; white arrows indicate outrunner blocks; yellow arrows indicate erosional grooves and trenches (Posamentier and Martinsen, 2003).

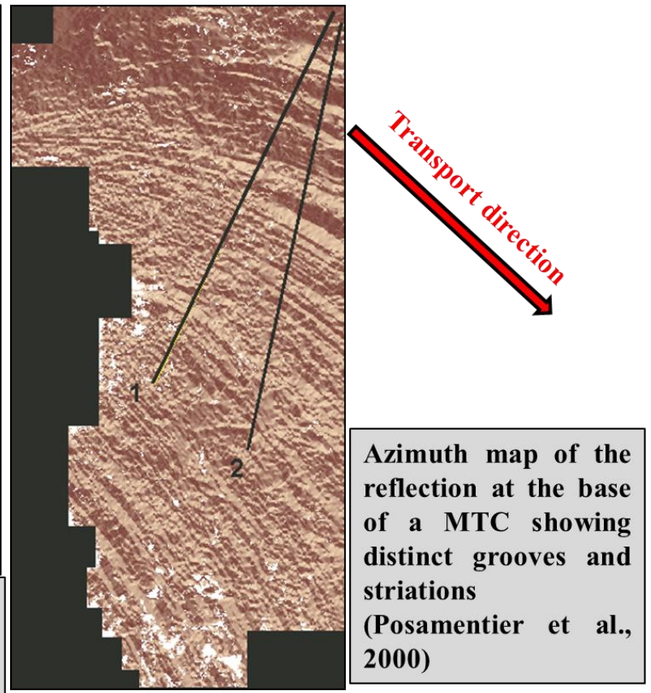

Azimuth map of the reflection at the base of a MTC showing distinct grooves and striations (Posamentier et al., 2000)

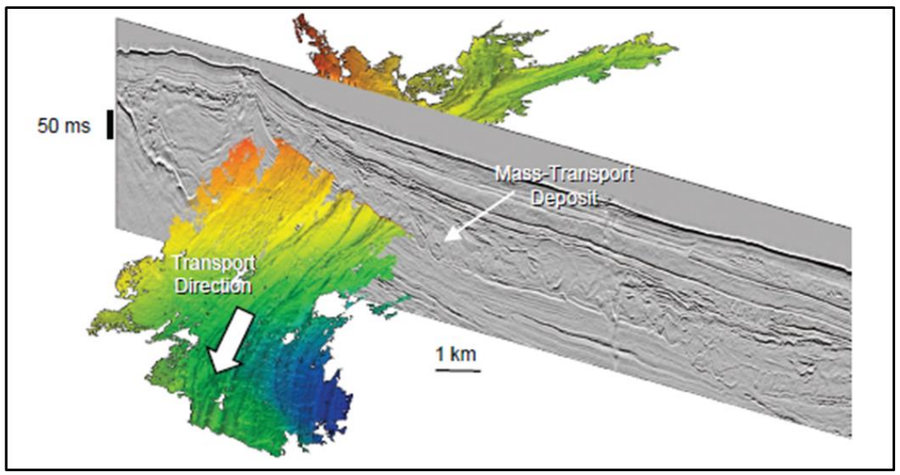

Time (isochron) map illustrating basal grooves beneath mass-transport deposits within channels (Posamentier and Martinsen, 2003)

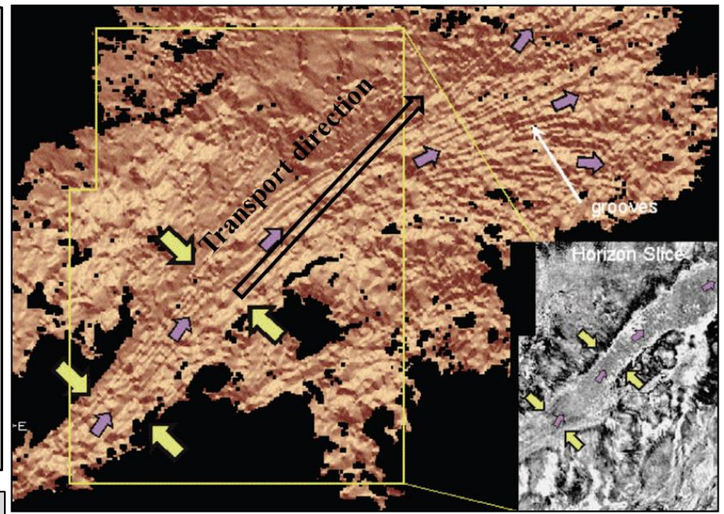

Dip azimuth horizon attribute illustrating pseudo-relief illustrating basal grooves beneath a mass transport channel. Small inset represents a seismic amplitude stratal slice illustrating channelized morphology. Yellow arrows indicate margins of mass-transport channel; (Posamentier and Martinsen, 2003).

BASAL SHEAR SURFACE

Examples of Kinematic indicators for MTDs

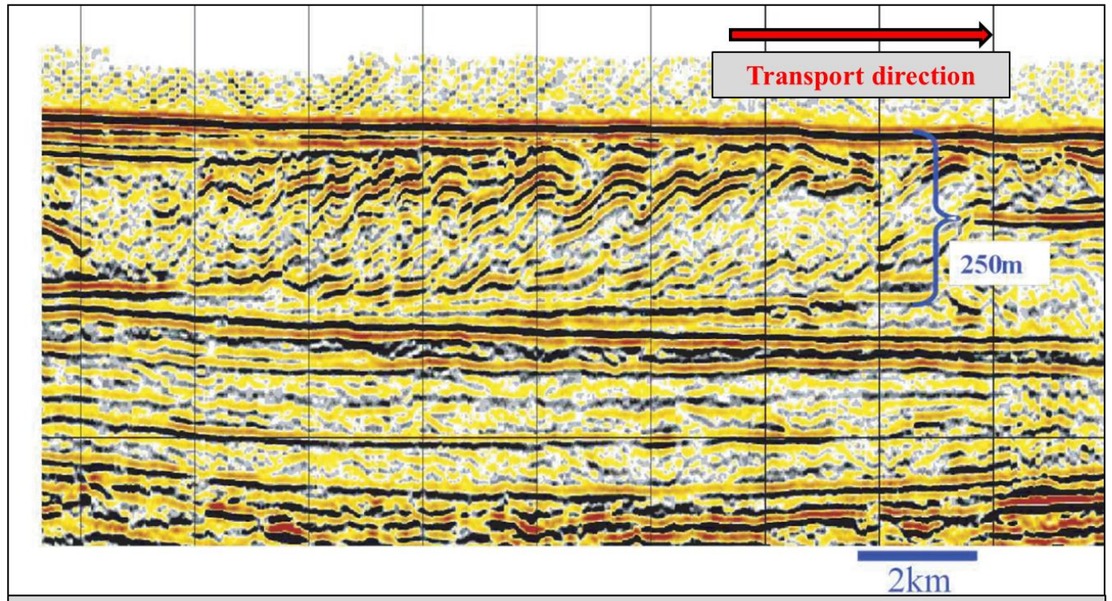

Pleistocene MTD, offshore Trinidad (Brami et al., 2000)

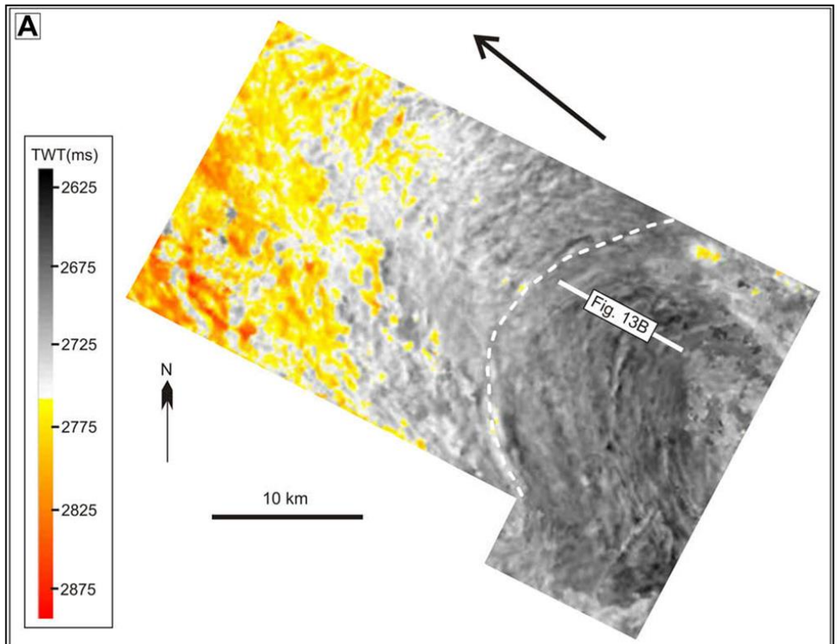

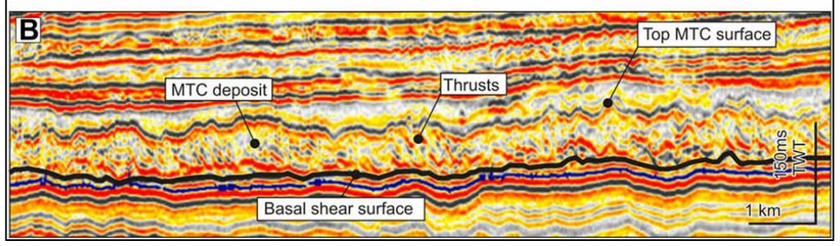

Example of pressure ridges. (A) Time structure map of the top surface of a buried MTC from within the PL251 3D survey area. Note steeply dipping parallel reflections separated by offsets within the MTC body. These are interpreted as small-scale thrusts which form the ridges seen in planform. Arrow indicates transport direction. (B) Seismic section through pressure ridges (location shown in A). Arrow indicates general transport direction (NW) (From Bull et al., 2009).

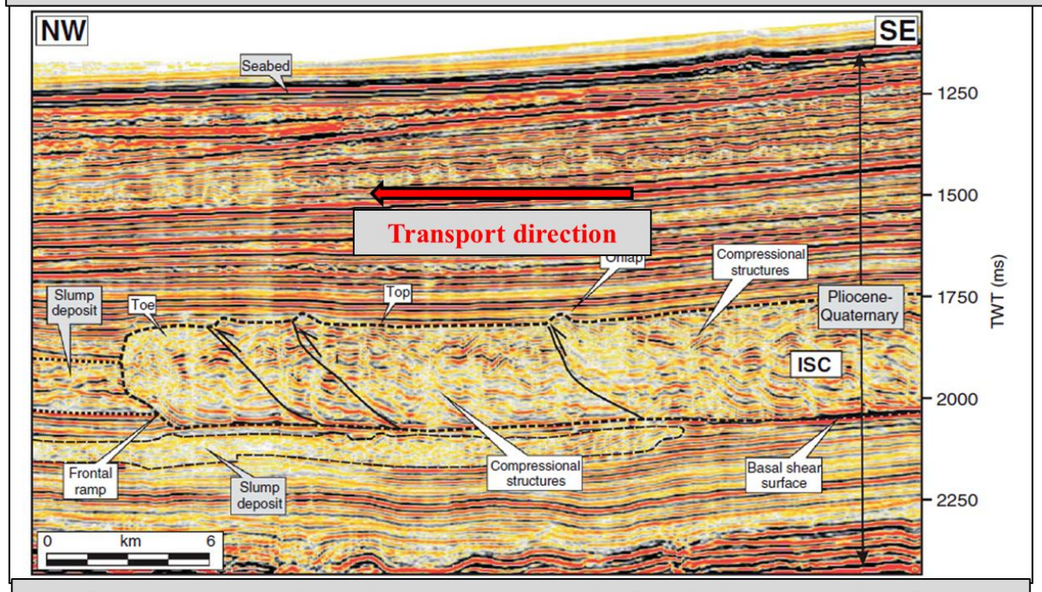

3D seismic profile through the toe region of the Israel Slump Complex (ISC), Frey-martinez et al., 2006.

TOE REGION

Appendix V: Chapter 7, Atlas of MTD outcrops and reservoir rocks

ATLAS OF MTD OUTCROPS AND RESERVOIRS IN MTDs

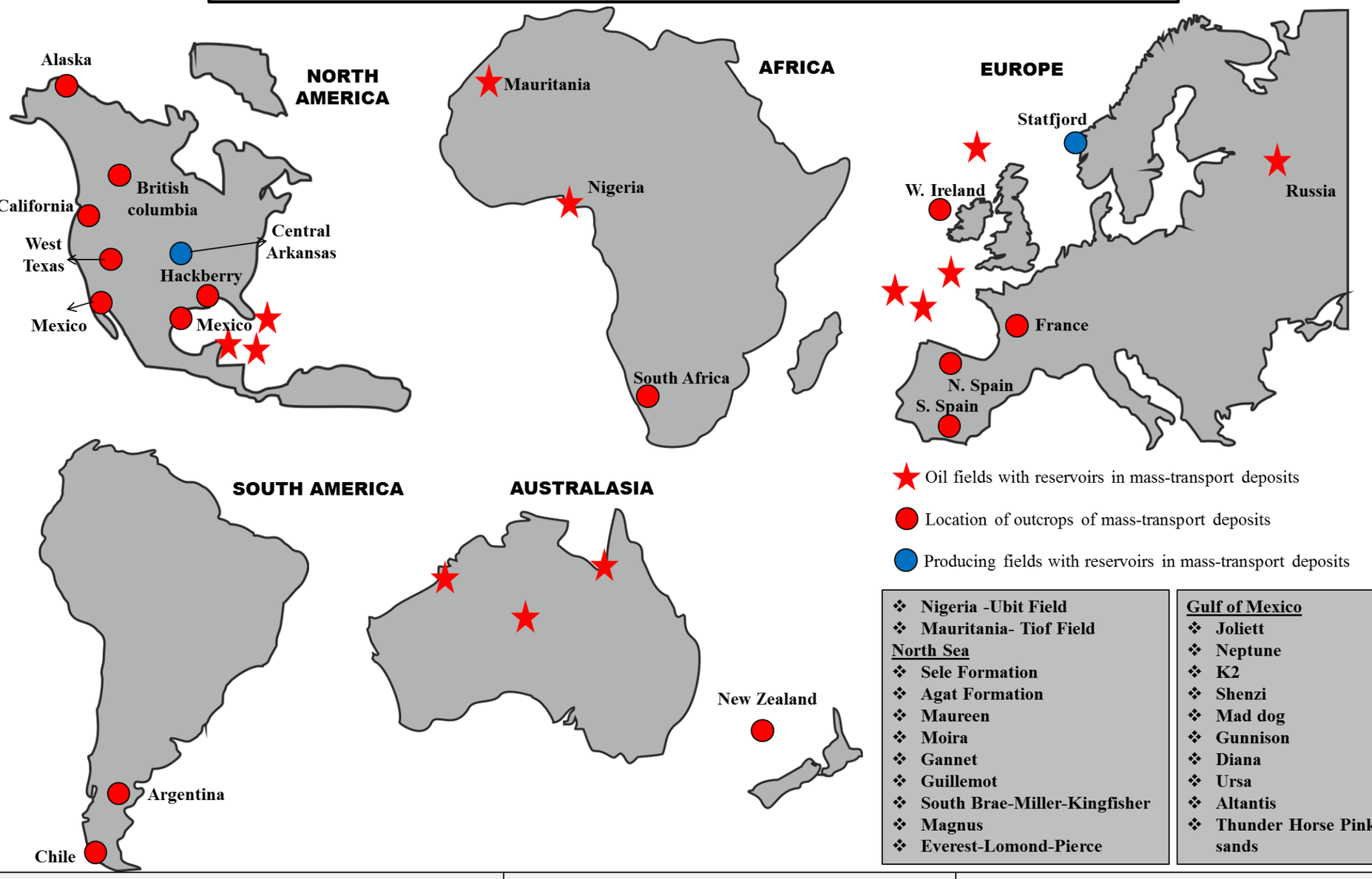

- Nigeria -Ubit Field
- Mauritania- Tiof Field

North Sea

- Sele Formation
- Agat Formation
- Maureen
- Moira
- Gannet
- Guillemot
- South Brae-Miller-Kingfisher
- Magnus
- Everest-Lomond-Pierce

Gulf of Mexico

- Joliett
- Neptune
- K2
- Shenzi
- Mad dog
- Gunnison
- Diana
- Ursa
- Altantis
- Thunder Horse Pink sands

REFERENCES

1. Alaska – Houseknecht and Schenk, 2006
2. Northwestern British Columbia, Canada – Gammon et al,.2006
3. Central California – Clifton, 2006
4. Delaware Mountains, West Texas- King 1948
5. Ouachita Mountains, central Arkansas- Slatt et al., 2000
6. Baja California, Mexico – Dykstra and Kneller (2006)
7. Eastern Mexico – Cossey, 2006
8. Southern Chile – Romans et al., 2006
9. Quebrada de la Lajas, Argentina- Dystra et el., 2006
10. Western Ireland (County Clare)- Strachan, 2002
11. Peira Cava, Southern France- Amy et al., 2006
12. Ainsa Basin, Northern Spain -Pickering and Corregidor, 2005
13. Tabernas – Kleverlaan, 1987
14. Karoo, south Africa- Flint et al, 2006
15. New Zealand, western North Island- King et al., 2006.

Appendix VI to VII: Statistical data for Chapters 4 and 6 (on attached CD)

Appendix VIII: Fault terminology as used in this thesis

Hanging wall: The rock mass above a fault, i.e. the downthrown side of a normal fault (Peacock et al., 2000).

Footwall: The rock mass that is below a lode or fault i.e. the upthrown side of a normal fault (Peacock et al., 2000).

Displacement: The relative movement between two originally adjacent points on the surface of a fault. The displacement can be curved, so need not be a direct line between two originally adjacent points (Peacock et al., 2000).

Throw: The vertical component of the *dip-separation* of a normal or reverse fault, measured in a vertical cross-section perpendicular to the strike of a fault (Peacock et al., 2000). The throw is equivalent to the vertical component of the *displacement* only for a pure *dip-slip* fault (Peacock et al., 2000).

Fault zones: Represent the zone of disturbed rocks between faulted blocks. A fault zone can include fault segments with a wide range of orientations, and these can be both *synthetic* and *antithetic* to the overall displacement of the zone (Peacock et al., 2000).

*Stratigraphic separation***:** The apparent displacement of a planar marker (e.g. bed) across a fault, measured in any indicated direction (Peacock et al., 2000).

Fault linkage: The process by which, two originally separate faults become connected (Pollard and Aydin, 1984).

Growth fault: Defines faults that are active during sedimentation and apparently cut the earth surface. A growth fault is characterised by (a) an increase in displacement down the dip of the fault; and by (b) thicker sediments in the *hanging wall* near the fault than in the *footwall* or in the *hanging wall* away from the fault (Peacock et al., 2000).

Normal drag: Folding adjacent to a fault such that a marker is convex towards the slip direction, usually caused by resistance to slip (Biddle and Christie-Blick, 1985).

Fault reactivation: used for overturning or reversal of strata (Peacock, 2002), which involves renewed displacement along a previously passive or inactive fault. *Inversion* is now commonly used for the *reactivation* of a dip-slip fault such that there is a reversal of the sense of throw (Buchanan and Buchanan, 1995; Sibson, 1985). *Reverse-reactivation* of a normal positive inversion involves the reverse-reactivation of a normal fault or a contraction of a region that previously witnessed extension. Alternatively, *negative inversion* is the normal reactivation of a reverse fault or the extension of a region that previously underwent contraction (Needham, 1989).

Faults may be reactivated either by upward propagation (Richard and Krantz, 1991) or through dip linkage (Mansfield and Cartwright, 1996; Baudon and Cartwright, 2008). The fault propagation by dip linkage has wider implications for reactivation in fault systems where strong mechanical layer anisotropy favours localization of new faults in different mechanical ‘tiers'. In contrast, reactivation by upward propagation implies that faults were generated at depth and subsequently grow upward from pre-existing structures.

Both modes of reactivation are recognised by typical stepped profiles with a major break in throw gradients. Subtle differences over the throw distribution provide insights into the recognition of the mode referred to above (Baudon and Cartwright, 2008). Upward propagation is characterized by profiles exhibiting a regular decrease in throw values and gradients up to the upper tip point, whereas reactivation by dip linkage can be identified by throw maxima in the upper part of the fault plane separated from the pre-existing parts by throw minima. Further growth of the two hard-linked segments after reactivation might attenuate the throw variations and obscure the differentiation of these two types of reactivation. The probability of reactivation is directly related to the orientation of the fault planes relative to the principal stresses and their ability to accommodate the imposed strains (Richard and Krantz, 1991; White et al., 1986), as well as differences in friction coefficients and cohesion in the fault planes and gouges (Sibson, 1985).

Index